ornl

NUREG/CR-4219
Vol. 4, No. 2
ORNL/TM-9593/V4&N2

OAK RIDGE
NATIONAL
LABORATORY

MARTIN MARIETTA

Heavy-Section Steel Technology Program Semiannual Progress Report for April–September 1987

W. R. Corwin

Prepared for the U.S. Nuclear Regulatory Commission
Office of Nuclear Regulatory Research
Under Interagency Agreements DOE 0551-0551-A1 and 0552-0552-A1

OPERATED BY
MARTIN MARIETTA ENERGY SYSTEMS, INC.
FOR THE UNITED STATES
DEPARTMENT OF ENERGY

Printed in the United States of America. Available from
National Technical Information Service
U.S. Department of Commerce
5285 Port Royal Road, Springfield, Virginia 22161
NTIS price codes—Printed Copy: A15 Microfiche A01

NUREG/CR-4219
Vol. 4, No. 2
ORNL/TM-9593/V4&N2
Dist. Category RF

Engineering Technology Division

HEAVY-SECTION STEEL TECHNOLOGY PROGRAM SEMIANNUAL PROGRESS REPORT FOR APRIL—SEPTEMBER 1987

W. R. Corwin

Manuscript Completed — March 31, 1988
Date Published — April 1988

Prepared for the
U.S. Nuclear Regulatory Commission
Office of Nuclear Regulatory Research
under Interagency Agreements DOE 0551-0551-A1 and 0552-0552-A1

NRC FIN No. B0119

Prepared by the
OAK RIDGE NATIONAL LABORATORY
Oak Ridge, Tennessee 37831
operated by
MARTIN MARIETTA ENERGY SYSTEMS, INC.
for the
U.S. DEPARTMENT OF ENERGY
under Contract No. DE-AC05-840R21400

CONTENTS

LIST OF FIGURES

LIST OF TABLES

PREFACE

The Heavy-Section Steel Technology (HSST) Program, which is sponsored by the Nuclear Regulatory Commission, is an engineering research activity devoted to extending and developing the technology for assessing the margin of safety against fracture of the thick-walled steel pressure vessels used in light-water-cooled nuclear power reactors. The program is being carried out in close cooperation with the nuclear power industry. This report covers HSST work performed in April–September 1987. The work performed by Oak Ridge National Laboratory (ORNL) and by subcontractors is managed by the Engineering Technology Division (ETD). Major tasks at ORNL are carried out by the ETD and the Metals and Ceramics Division. Prior progress reports on this program are ORNL-4176, ORNL-4315, ORNL-4377, ORNL-4463, ORNL-4512, ORNL-4590, ORNL-4653, ORNL-4681, ORNL-4764, ORNL-4816, ORNL-4855, ORNL-4918, ORNL-4971, ORNL/TM-4655 (Vol. II), ORNL/TM-4729 (Vol. II), ORNL/TM-4805 (Vol. II), ORNL/TM-4914 (Vol. II), ORNL/TM-5021 (Vol. II), ORNL/TM-5170, ORNL/NUREG/TM-3, ORNL/NUREG/TM-28, ORNL/NUREG/TM-49, ORNL/NUREG/TM-64, ORNL/NUREG/TM-94, ORNL/NUREG/TM-120, ORNL/NUREG/TM-147, ORNL/NUREG/TM-166, ORNL/NUREG/TM-194, ORNL/NUREG/TM-209, ORNL/NUREG/TM-239, NUREG/CR-0476 (ORNL/NUREG/TM-275), NUREG/CR-0656 (ORNL/NUREG/TM-298), NUREG/CR-0818 (ORNL/NUREG/TM-324), NUREG/CR-0980 (ORNL/NUREG/TM-347), NUREG/CR-1197 (ORNL/NUREG/TM-370), NUREG/CR-1305 (ORNL/NUREG/TM-380), NUREG/CR-1477 (ORNL/NUREG/TM-393), NUREG/CR-1627 (ORNL/NUREG/TM-401), NUREG/CR-1806 (ORNL/NUREG/TM-419), NUREG/CR-1941 (ORNL/NUREG/TM-437), NUREG/CR-2141, Vol. 1 (ORNL/TM-7822), NUREG/CR-2141, Vol. 2 (ORNL/TM-7955), NUREG/CR-2141, Vol. 3 (ORNL/TM-8145), NUREG/CR-2141, Vol. 4 (ORNL/TM-8252), NUREG/CR-2751, Vol. 1 (ORNL/TM-8369/V1), NUREG/CR-2751, Vol. 2 (ORNL/TM-8369/V2), NUREG/CR-2751, Vol. 3 (ORNL/TM-8369/V3), NUREG/CR-2751, Vol. 4 (ORNL/TM-8369/V4), NUREG/CR-3334, Vol. 1 (ORNL/TM-8787/V1), NUREG/CR-3334, Vol. 2 (ORNL/TM-8787/V2), NUREG/CR-3334, Vol. 3 (ORNL/TM-8787/V3), NUREG/CR-3744, Vol. 1 (ORNL/TM-9154/V1), NUREG/CR-3744, Vol. 2 (ORNL/TM-9154/V2), NUREG/CR-4219, Vol. 1 (ORNL/TM-9593/V1), NUREG/CR-4219, Vol. 2 (ORNL/TM-9593/V2), NUREG/CR-4219, Vol. 3, No. 1 (ORNL/TM-9593/V3&N1), NUREG/CR-4219, Vol. 3, No. 2 (ORNL/TM-9593/V3&N2), and NUREG/CR-4219, Vol. 4, No. 2 (ORNL/TM-9593/V4&N1).

SUMMARY

1. PROGRAM MANAGEMENT

The Heavy-Section Steel Technology (HSST) Program is arranged into 12 tasks: (1) program management, (2) fracture methodology and analysis, (3) material characterization and properties, (4) environmentally assisted crack-growth studies, (5) crack-arrest technology, (6) irradiation effects studies, (7) stainless steel cladding evaluations, (8) intermediate vessel tests and analyses, (9) thermal-shock technology, (10) pressurized-thermal-shock (PTS) technology, (11) Pressure-Vessel-Research Users' Facility (PVRUF), and (12) shipping cask material evaluations. Progress reports are issued on a semiannual basis, and the report chapters correspond to the tasks.

The work is performed by the Oak Ridge National Laboratory (ORNL) and through a number of research and development (R&D) subcontracts. During the report period, 47 program briefings, reviews, or presentations were made; 8 technical documents were published.

2. FRACTURE MECHANICS AND ANALYSIS

Experimental and analytical studies were carried out to provide an improved basis for establishing transferable fracture criteria governing inelastic crack propagation-arrest behavior in pressure vessel steels. These studies included developments and applications of viscoplastic-dynamic finite-element techniques, small-scale fracture experiments, and viscoplastic material characterization testing. Intensive metallographic and fractographic studies of various heats of steels were conducted to investigate the transition from purely ductile fracture at high temperature to brittle cleavage at lower temperature.

3. MATERIAL CHARACTERIZATION AND PROPERTIES

Posttest properties-characterization studies were completed for the low-upper-shelf material used in the second pressurized thermal-shock experiment (PTSE-2). Tests included drop-weight, tensile, Charpy V-notch (CVN) impact, fracture toughness, and crack-arrest toughness. Comparison of results shows the posttest vessel insert to be stronger than the pretest characterization material, and the four types of toughness tests showed transition temperatures from 15 to 30 K higher for the posttest material. Analyses of all the data resulted in a conclusion that the differences were largely a result of strain hardening during the vessel experiment and that the material properties of the vessel insert prior to PTSE-2 are reasonably well represented by the pretest characterization block. Fractographic evaluations of the PTSE-2 fracture surface were also completed and confirmed the existence of an intermediate arrest at a depth of about 70 mm.

Material characterization and fracture surface evaluations were performed for the clad-plate materials. Tensile, drop-weight, CVN impact, and microhardness tests were completed. The Charpy results from specimens with a TL orientation, as required by the *ASME Code*, resulted in an RT_{NDT} of 72°C, as opposed to the previously determined value of 36°C using LT-oriented specimens.

4. ENVIRONMENTALLY ASSISTED CRACK-GROWTH TECHNOLOGY

Fatigue crack-growth rate and static-load cracking studies at Westinghouse have been completed. The goal of the task has been to generate data and to propose, as appropriate, revisions to the *ASME Code* reference crack-growth curves with environmental considerations. The report summarizing the program from its inception was received from Westinghouse and is being edited.

5. CRACK-ARREST TECHNOLOGY

Twelve wide-plate crack-arrest tests have been completed to date (three during this reporting period). When combined with other large specimen test results, the wide-plate crack-arrest toughness values form a consistent trend, showing that arrest can and does occur at temperatures up to and above that which corresponds to the onset of Charpy upper-shelf behavior. Also, the measured K_{Ia} values extend above the limit in Sect. XI of the *ASME Code*.

6. IRRADIATION EFFECTS STUDIES

In the Fifth Irradiation Series, tests of irradiated 2TCS and 4TCS were completed by Materials Engineering Associates (MEA). Testing of irradiated 1TCS and unirradiated 4TCS were completed by ORNL. The results show that the irradiated 4TCS gave K_{Jc} values in the scatter band of data from 1TCS and 2TCS specimens tested at the same temperatures; in fact, at the highest test temperature, the 4TCS results were quite high relative to those from the smaller specimens. Preliminary analyses indicate that the shift of fracture toughness K_{Jc} for 73W, the higher copper weld, is somewhat greater than that determined from Charpy impact testing.

In the Seventh Irradiation Series, irradiated Charpy impact specimens were tested and showed upper-shelf energy decreases of 15 and 20% for fluences of 2 and 5×10^{19} neutrons/cm^2, respectively. The 41-J transition temperatures were 13 and 28°C, respectively. Fracture toughness and tensile testing will be performed during the next reporting period.

7. CLADDING EVALUATIONS

A three-pronged effort on cladding evaluations has included (1) study of the crack-arrest behavior of clad plates by the testing of one unclad and five clad specimens (second series of tests), (2) a development of analysis techniques to permit the evaluation of the clad-plate tests, and (3) a study of flaw density of nuclear vessels by continued nondestructive evaluations of segments of the shells from cancelled boiling-water reactor (BWR) and pressurized-water reactor (PWR) power plants. A comparison of the achieved arrest loads of the clad specimens to that of the unclad specimen, which was loaded to yield stress and then failed, shows a remarkable flaw-arresting capability for this series of clad specimens. Two notable complications were discovered in these tests: (1) the apparent overriding influence of the heat-affected zone (HAZ) on the flaw-arrest capability of the cladding (i.e., cladding/HAZ combined layer) and (2) the propensity for tunneling of the flaw at arrest. The first discovery indicates that this test series represents conditions of only limited radiation damage of the HAZ region. The deeply tunneled flaw profiles present a difficult analytical problem. The results to date using finite-element analyses of pseudo flaws have been informative but have not quantitatively defined stress intensities at arrest. Nondestructive and destructive examinations of the plate segments from the salvaged nuclear pressure vessels, although not significant statistically, have revealed defect/size distributions departing from those used in the *UKAEE 1982 Marshall Report* and the Octavia function developed by the U.S. Nuclear Regulatory Commission (NRC) for probabilistic studies of failure. The implication of the examinations is that these previous estimates may be nonconservative to some degree for small flaws.

8. INTERMEDIATE VESSEL TESTS AND ANALYSIS

A topical report was issued on the test of the HSST intermediate test vessel V-8A containing low-upper-shelf steel. This test was the twelfth fracture test of a 150-mm-thick steel vessel in the HSST Program. This series of tests is a set of experiments on a scale large enough to simulate realistically important aspects of fracture behavior of reactor pressure vessels. Such experiments are the means by which theoretical models of fracture behavior can be evaluated for possible application to fracture analysis of vessels in nuclear plants.

This experiment demonstrated that the V-8A vessel, pressurized in a ductile state with a large flaw in a region of low tearing resistance, withstood a pressure twice the nominal *ASME Code* design pressure. The study also indicated that accurate prediction of instability pressures of a ductile vessel requires (1) methods of analysis that account for plasticity and (2) good representations of the properties of the material with respect to tearing resistance and stress-strain behavior.

9. THERMAL-SHOCK TECHNOLOGY

There was no activity in the thermal-shock technology task for this period.

10. PRESSURIZED-THERMAL-SHOCK TECHNOLOGY

During this reporting period, the results of the second pressurized-thermal-shock experiment PTSE-2 were evaluated, posttest properties of the vessel insert containing the flaw were determined, and a topical report on the experiment was written. The PTSE-2 experiment was concerned, primarily, with the behavior of a crack in material with low tearing resistance, and, secondarily, with warm prestressing. The PTSE-2 experiment employed a steel that had low toughness in the ductile fracture regime, so that fracture behavior representative of irradiated low-upper-shelf steel could be observed under conditions relevant to a flawed nuclear reactor pressure vessel (RPV) undergoing an overcooling transient. The insert of material containing the flaw in the vessel was characterized before the PTSE-2 experiment by testing specimens cut from a piece of the plate from which the insert was made. After the experiment, material from the insert was tested to evaluate its tensile and toughness properties.

This experiment produced, for the first time with stress and toughness states representative of RPVs, (1) the arrest of a brittle fracture with an immediate tearing instability and (2) brittle fracture following warm prestressing. Principal conclusions are that (1) low-upper-shelf material can exhibit very high arrest toughness, (2) ductile tearing promotes more severe fractures in low-upper-shelf material, (3) warm prestressing inhibits brittle fracture to some degree even when crack-driving forces are increasing with time, (4) benefits of warm prestressing are diminished by ductile tearing, (5) a simple theoretical analysis of warm prestressing represented fracture conditions reasonably well, and (6) calculations of ductile tearing based on resistance curve test data did not consistently predict the observed tearing. Warm prestressing elevated the fracture initiation toughness significantly above the level of the pristine K_{Ic}, even with the complications of precleavage tearing.

11. ESTABLISHMENT OF A PRESSURE VESSEL RESEARCH USERS' FACILITY

The ORNL undertook an initiative in concert with the NRC and Department of Energy (DOE) to establish a Pressure Vessel Research Users' Facility (PVRUF). The facility is to be centered around a complete PWR pressure vessel and is to provide unique R&D opportunities for a number of organizations. Internal ORNL funds were used to procure the PVRUF vessel from Combustion Engineering, who had fabricated it for use in a four-loop 1100-MW(e) PWR plant. The vessel, the head, and supportive stands were delivered to Oak Ridge in late September.

The overall research plan and conceptual design of the facility to house the vessel will begin as appropriate funding is arranged. Initial R&D activities, however, will proceed with the vessel in its temporary location at the K-25 Plant in Oak Ridge. One early HSST-funded task will characterize the density, size, location, and orientation of flaws in this vessel for use in probabilistic integrity assessment methods. It is anticipated that domestic and foreign organizations will supplement their pressure vessel integrity research programs by conducting PVRUF studies in several technical areas through cooperative or independent programming. In addition to the NRC and DOE, the domestic interests are anticipated to include the Electric Power Research Institute, light-water reactor (LWR) component vendors, and utilities.

12. SHIPPING CASK MATERIAL EVALUATIONS

In June 1987, a fact-finding team traveled to the Federal Republic of Germany to attend a seminar on nodular cast iron (NCI) held at the Bundesanstalt für Materialprüfung (BAM) and to visit other sites doing related work. An overall impression was that, for static loading, NCI is probably a more ductile material than has previously been believed but the material's resistance to crack propagation needs considerable further study. The only existing measurements of crack arrest for NCI were made during this reporting period. The first meeting of the HSST Expert Panel on Shipping Casks was held at ORNL September 24--25, 1987, to consider the proposed use of NCI as a primary structural material for nuclear spent-fuel shipping casks. Within the information available, it was determined that there were no overriding reasons for NCI to be disqualified as a candidate structural material for spent-fuel shipping casks at this time, but that several factors pertaining to its use need substantially more study before a fully supported regulatory decision can be made.

HEAVY-SECTION STEEL TECHNOLOGY PROGRAM SEMIANNUAL PROGRESS REPORT FOR APRIL–SEPTEMBER 1987*

W. R. Corwin

ABSTRACT

The Heavy-Section Steel Technology (HSST) Program is conducted for the Nuclear Regulatory Commission (NRC). The studies relate to all areas of the technology of materials fabricated into thick-section primary-coolant containment systems of light-water-cooled nuclear power reactors. The focus is on the behavior and structural integrity of steel pressure vessels containing cracklike flaws. The program is organized into 12 tasks: (1) program management, (2) fracture methodology and analysis, (3) material characterization and properties, (4) environmentally assisted crack-growth studies, (5) crack-arrest technology, (6) irradiation effects studies, (7) cladding evaluations, (8) intermediate vessel tests and analysis, (9) thermal-shock technology, (10) pressurized-thermal-shock (PTS) technology, (11) Pressure Vessel Research Users' Facility (PVRUF), and (12) shipping cask material evaluations. During this period, extensions were made to fracture-analysis codes, including the addition of more constitutive models and inelastic fracture criteria in the dynamic viscoplastic fracture version of the ADINA-ORMGEN-ORVIRT analysis codes at Oak Ridge National Laboratory (ORNL). Elastodynamic analyses and development work on viscoplastic fracture-analysis techniques were performed by ORNL and the Southwest Research Institute (SwRI) in support of the wide-plate crack-arrest tests that are being performed by the National Bureau of Standards (NBS) for the HSST Program. Three additional wide-plate crack-arrest tests were performed by NBS, bringing to 12 the total of such tests. Crack-arrest and other fracture characterization data were obtained for wide-plate and pressurized-thermal-shock (PTS) test materials. The draft of the final report on the crack-growth-rate task with vessel steels was prepared. Testing of irradiated 1TCT, 2TCT, and 4TCT specimens was completed in the Fifth HSST Irradiation Series for the study of K_{Ic} shifts for welds with different copper contents. Nondestructive examinations were begun on a segment of a clad pressurized-water reactor (PWR) vessel, and the results of similar examinations on a segment of a boiling-water reactor vessel to determine flaw density

---

*This report is written in terms of metric units. Conversions from SI to English units for all SI quantities are listed on a foldout page at the end of this report.

were published. The report covering a test of ITV-8A (which contained a low-upper-shelf weldment) was published. Six of the second series of the clad-plate fracture tests of reactor vessel steels were performed. The report on the second PTS test (PTSE-2) was drafted. The delivery of the PWR pressure vessel to be used in the ORNL PVRUF was completed. The use of NCI as a primary material in spent-fuel shipping casks was evaluated by the HSST expert panel.

---

1. PROGRAM MANAGEMENT

W. R. Corwin

The Heavy-Section Steel Technology (HSST) Program, a major safety program sponsored by the Nuclear Regulatory Commission (NRC) at Oak Ridge National Laboratory (ORNL), is concerned with the structural integrity of the primary systems [particularly, the reactor pressure vessels (RPVs)] of light-water-cooled nuclear power reactors. The structural integrity of these vessels is ensured by (1) designing and fabricating RPVs according to standards set by the code for nuclear pressure vessels, (2) detecting flaws of significant size that occur during fabrication and in service, and (3) developing methods of producing quantitative estimates of conditions under which fracture could occur. The program is concerned mainly with developing pertinent fracture technology, including knowledge of (1) the material used in these thick-walled vessels, (2) the flaw growth rate, and (3) the combination of flaw size and load that would cause fracture and, thus, limit the life and/or operating conditions of this type of reactor plant.

The program is coordinated with other government agencies and with the manufacturing and utility sectors of the nuclear power industry in the United States and abroad. The overall objective is a quantification of safety assessments for regulatory agencies, professional code-writing bodies, and the nuclear power industry. Several activities are conducted under subcontract by research facilities in the United States and through an informal cooperative effort on an international basis. Six research and development subcontracts are currently in force.

The program tasks are arranged according to the work breakdown structure shown in Fig. 1.1. Accordingly, the chapters of this progress report correspond to these 12 tasks. During this report period, the 5-year program plan[1] applicable to FY 1986–1990 was published.

During this period, 18 program briefings, reviews, or presentations were made by the HSST staff during program reviews and visits with NRC staff or others. Five technical documents, including one technical progress report[2] and four topical reports,[3-6] were published, as well as two technical papers.[7,8] In addition 29 technical presentations were made: twenty[9-28] at the Third Annual Workshop on Dynamic Fracture and Crack-Arrest Technology, organized on behalf of NRC by the HSST program, held at the National Bureau of Standards (NBS) in Gaithersburg on May 13–15, 1987; one[29] at the Fifth National Congress on Pressure Vessels and Piping

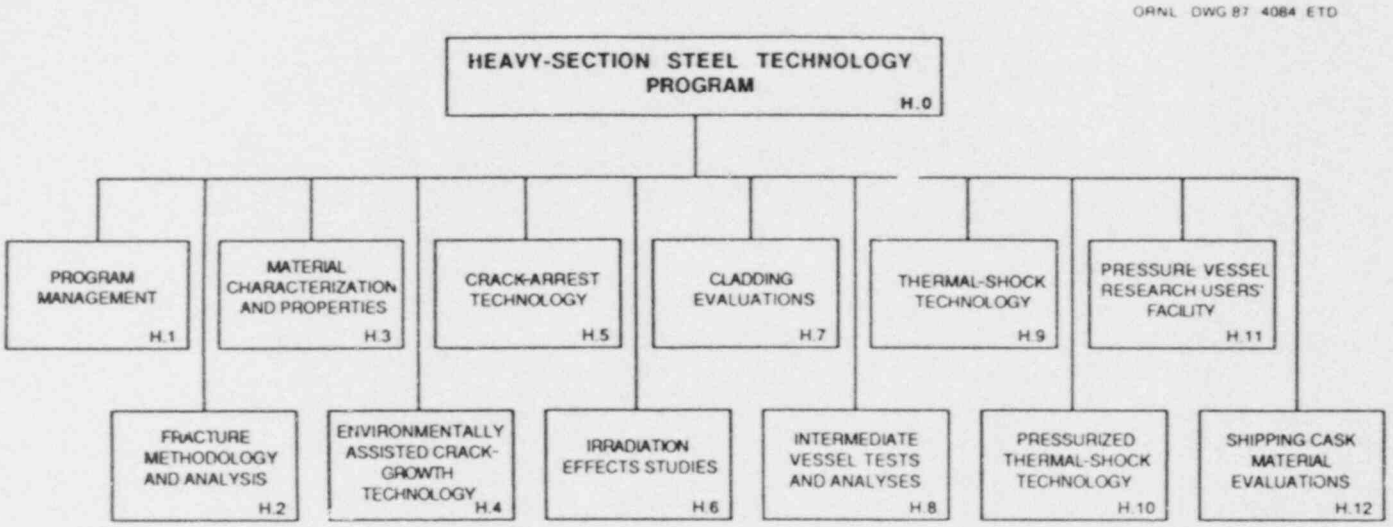

Fig. 1.1. Level-2 work breakdown structure for HSST Program.

Technology held in San Diego, California, on June 28—July 2, 1987; one[30] at the Plant Lifetime Improvement Materials Workshop held in Albuquerque, New Mexico, on Sept. 15—16, 1987; two[31,32] at the NRC Workshop on Modified J-Integral held at the U.S. Naval Ship Research and Development Command in Annapolis, Maryland, on August 5, 1987; two[33,34] at the MPC Workshop on Scatter of Fracture Toughness Data in the Transition Temperature Regime held at the National Bureau of Standards in Boulder, Colorado, on July 16, 1987; two[35,36] at the ASTM-IAEA Specialists Meeting on Irradiation Embrittlement and Aging of Reactor Pressure Vessel Steels held in Philadelphia, Pennsylvania, on May 27—29, 1987; and one[37] at the 9th International Conference on Structural Mechanics in Reactor Technology held in Lausanne, Switzerland, on August 17—21, 1987.

References

1. *Heavy-Section Steel Technology Program — Five Year Plan FY 1986—1990*, NUREG/CR-4990 (ORNL/TM-10526), Martin Marietta Energy Systems, Inc., Oak Ridge Natl. Lab., July 1987.

2. C. E. Pugh, *Heavy-Section Steel Technology Program Semiann. Prog. Rep. October 1986—March 1987*, NUREG/CR-4219, Vol. 4, No. 1 (ORNL/TM-9593/V4&N1), Martin Marietta Energy Systems, Inc., Oak Ridge Natl. Lab., August 1987.

3. K. V. Cook and R. W. McClung, *Flaw Density Examinations of a Clad Boiling Water Reactor Pressure Vessel Segment*, NUREG/CR-4860 (ORNL/TM-10364), Martin Marietta Energy Systems, Inc., Oak Ridge Natl. Lab., April 1987.

4. R. H. Bryan et al., *Test of 6-in.-Thick Pressure Vessels. Series 3: Intermediate Test Vessel V-8A — Tearing Behavior of Low Upper Shelf Material*, NUREG/CR-4760 (ORNL-6187), Martin Marietta Energy Systems, Inc., Oak Ridge Natl. Lab., May 1987.

5. J. J. McGowan, R. K. Nanstad, and K. R. Thoms, *Characterization of Irradiated Current-Practice Welds and A533 Grade B Class 1 Plate for Nuclear Pressure Vessel Service*, NUREG/CR-4880 (ORNL/TM-10387), Martin Marietta Energy Systems, Inc., Oak Ridge Natl. Lab., September 1987.

6. D. J. Naus et al., *Crack-Arrest Behavior in SEN Wide-Plates of Quenched and Tempered A533B Steel Tested Under Nonisothermal Conditions*, NUREG/CR-4930 (ORNL-6388), Martin Marietta Energy Systems, Inc., Oak Ridge Natl. Lab., September 1987.

7. C. E. Pugh et al., "Crack Run-Arrest Behavior in Wide SEN Plates of an LWR Pressure Vessel Material," the *9th International Conference on Structural Mechanics in Reactor Technology*, Lausanne, Switzerland, August 17—21, 1987, Vol. G, pp. 21—26, A. A. Balkema Publishers, Rotterdam.

8. C. E. Pugh et al., "Wide-Plate Crack-Arrest Tests Utilizing a Prototypical Pressure Vessel Steel," *International Journal of Pressure Vessels and Piping*, Paper PVP 130, September 1987.

9. B. R. Bass, "Development of ADINA/VPF at ORNL," *Third Annual HSST Workshop on Dynamic Fracture and Crack-Arrest Technology*, May 13–15, 1987, National Bureau of Standards, Gaithersburg, Md.

10. B. R. Bass, "Elastodynamic Analyses of HSST Wide-Plate Tests," *Third Annual HSST Workshop on Dynamic Fracture and Crack-Arrest Technology*, May 13–15, 1987, National Bureau of Standards, Gaithersburg, Md.

11. R. H. Bryan, "Pressurized-Thermal-Shock Tests PTSE-1 and PTSE-2," *Third Annual HSST Workshop on Dynamic Fracture and Crack-Arrest Technology*, May 13–15, 1987, National Bureau of Standards, Gaithersburg, Md.

12. R. J. Dexter, "Development of VISCRK Code at SwRI and Analysis of Duplex- and Wide-Plate Specimens," *Third Annual HSST Workshop on Dynamic-Fracture and Crack-Arrest Technology*, National Bureau of Standards, Gaithersburg, Md., May 13–15, 1987.

13. R. J. Fields, "Overview of HSST Wide-Plate Test Procedures," *Third Annual HSST Workshop on Dynamic-Fracture and Crack-Arrest Technology*, National Bureau of Standards, Gaithersburg, Md., May 13–15, 1987.

14. W. L. Fourney and R. Chona, "ASTM Standard Test Method for Crack-Arrest Fracture Toughness, K_{Ia}," *Third Annual HSST Workshop on Dynamic-Fracture and Crack-Arrest Technology*, National Bureau of Standards, Gaithersburg, Md., May 13–15, 1987.

15. L. B. Fruend, "Dislocation Model of Viscoplastic Crack Growth," *Third Annual HSST Workshop on Dynamic-Fracture and Crack-Arrest Technology*, National Bureau of Standards, Gaithersburg, Md., May 13–15, 1987.

16. A. Gilat, "Contributions to Viscoplastic Characterization," *Third Annual HSST Workshop on Dynamic-Fracture and Crack-Arrest Technology*, National Bureau of Standards, Gaithersburg, Md., May 13–15, 1987.

17. J. H. Giovanola, "Contributions to Viscoplastic Characterization," *Third Annual HSST Workshop on Dynamic-Fracture and Crack-Arrest Technology*, National Bureau of Standards, Gaithersburg, Md., May 13–15, 1987.

18. G. T. Hahn, "Analysis of Crack-Arrest Under Elastic-Plastic Conditions," *Third Annual HSST Workshop on Dynamic-Fracture and Crack-Arrest Technology*, National Bureau of Standards, Gaithersburg, Md., May 13–15, 1987.

19. S. J. Hudak, "Dynamic Fracture of A533B Steel," *Third Annual HSST Workshop on Dynamic-Fracture and Crack-Arrest Technology*, National Bureau of Standards, Gaithersburg, Md., May 13–15, 1987.

20. J. W. Hutchinson, "Background Review of Viscoplastic Crack Growth," *Third Annual HSST Workshop on Dynamic-Fracture and Crack-Arrest Technology*, National Bureau of Standards, Gaithersburg, Md., May 13–15, 1987.

21. R. K. Nanstad, "Properties of HSST WP-1 and -2 Materials," *Third Annual HSST Workshop on Dynamic-Fracture and Crack-Arrest Technology*, National Bureau of Standards, Gaithersburg, Md., May 13–15, 1987.

22. D. J. Naus, "Summary of HSST Wide-Plate Tests," *Third Annual HSST Workshop on Dynamic-Fracture and Crack-Arrest Technology*, National Bureau of Standards, Gaithersburg, Md., May 13–15, 1987.

23. P. E. O'Donoghue, "Viscoplastic-Dynamic Crack-Tip Characterization," *Third Annual HSST Workshop on Dynamic Fracture and Crack-Arrest Technology*, May 13–15, 1987, National Bureau of Standards, Gaithersburg, Md.

24. E. Z. Polch and P. E. O'Donoghue, "Plane Stress Considerations in Viscoplasticity," *Third Annual HSST Workshop on Dynamic Fracture and Crack-Arrest Technology*, May 13–15, 1987, National Bureau of Standards, Gaithersburg, Md.

25. C. H. Popelar, "Tunneling Effects on Crack-Arrest Toughness Calculations," *Third Annual HSST Workshop on Dynamic Fracture and Crack-Arrest Technology*, May 13–15, 1987, National Bureau of Standards, Gaithersburg, Md.

26. C. E. Pugh, "Objective of HSST Wide-Plate Testing Program," *Third Annual HSST Workshop on Dynamic Fracture and Crack-Arrest Technology*, May 13–15, 1987, National Bureau of Standards, Gaithersburg, Md.

27. A. R. Rosenfield, "Battelle K_{Ia} Data Base," *Third Annual HSST Workshop on Dynamic Fracture and Crack-Arrest Technology*, May 13–15, 1987, National Bureau of Standards, Gaithersburg, Md.

28. C. W. Schwartz, "Algorithms for Viscoplastic Finite Element Analysis," *Third Annual HSST Workshop on Dynamic Fracture and Crack Arrest Technology*, May 13–15, 1987, National Bureau of Standards, Gaithersburg, Md.

29. B. R. Bass, C. E. Pugh, and J. Keeney-Walker, "Viscoplastic Dynamic Fracture Analyses of Crack Run-Arrest Events in Nonisothermal Specimens," *Fifth National Congress on Pressure Vessels and Piping Technology*, San Diego, Calif., June 28–July 2, 1987.

30. W. R. Corwin, "Effects of 50°C Surveillance and Test Reactor Irradiations on Ferritic Pressure Vessel Steel," *Plant Lifetime Improvement Materials Workshop*, Albuquerque, N.M., September 15—16, 1987.

31. J. G. Merkle, "Comparison of Specimen and Vessel Tearing Modulus Behavior for the Low Upper-Shelf V-8A Weldment," *NRC Workshop on Modified J-Integral*, U.S. Naval Ship Research and Development Command, August 5, 1987, Annapolis, Md.

32. R. K. Nanstad, "Comparison of J-R Curves for Low and High-R Curve Materials," *NRC Workshop on Modified J-Integral*, U.S. Naval Ship Research and Development Command, August 5, 1987, Annapolis, Md.

33. G. R. Irwin, "Sequential Role of Local Events in the Initiation of Rapid Cleavage," MPC Workshop on Scatter of Fracture Toughness Data in the Transition Regime, National Bureau of Standards, Boulder, Colo., July 16, 1987.

34. J. G. Merkle, "Engineering Approaches to the Application of Fracture Toughness Data in the Nuclear Industry," MPC Workshop on Scatter of Fracture Toughness Data in the Transition Regime, National Bureau of Standards, Boulder, Colo., July 16, 1987.

35. C. W. Marschall, "Status of Research to Assess Radiation Effects on Crack-Arrest Toughness of RPV Steels," ASTM-IAEA Specialists Meeting on Irradiation Embrittlement and Aging of Reactor Pressure Vessel Steels, May 27—29, 1987, Philadelphia, Pa.

36. R. K. Nanstad, "Effects of 50°C Irradiation Embrittlement of Reactor Pressure Vessel Steel," ASTM-IAEA Specialists Meeting on Irradiation Embrittlement and Aging of Reactor Pressure Vessel Steels, May 27—29, 1987, Philadelphia, Pa.

37. C. E. Pugh et al., "Crack Run-Arrest Behavior in Wide SEN Plates of an LWR Pressure Vessel Material," *9th International Conference on Structural Mechanics in Reactor Technology*, Lausanne, Switzerland, August 17—21, 1987.

2. FRACTURE METHODOLOGY AND ANALYSIS

Oak Ridge National Laboratory (ORNL) performed additional static and dynamic fracture-mechanics analyses to evaluate the usefulness for crack-arrest experiments of a relatively small panel specimen intermediate in size between conventional crack-arrest specimens and the wide-plate specimens. The ORNL viscoplastic-dynamic fracture analysis program ADINA/VPF was extended by the addition of the Robinson viscoplastic constitutive model and an improved crack-propagation algorithm. Benchmark viscoplastic-dynamic fracture-mechanics analyses of a wide-plate test were performed with the ADINA/VPF program to compare results with those obtained from applications of the VISCRK program to the same problem at the Southwest Research Institute (SwRI).

SwRI made improvements to the viscoplastic-dynamic fracture-mechanics program VISCRK by identifying and resolving a problem arising in the treatment of out-of-plane strain in plane stress conditions. Other improvements to increase the efficiency and generality of VISCRK were made and verified through the benchmark wide-plate analyses performed in concert with ORNL and the ADINA/VPF program. A detailed study of the temperature field at the tip of a rapidly propagating crack in a viscoplastic material was also developed for eventual incorporation into VISCRK. A series of crack-arrest experiments were conducted with duplex compact specimens to demonstrate the veracity of crack-length vs time measurements and other key experimental observations.

The University of Maryland (UM) began a study of triaxial constraint effects and the transition from plane stress to plane strain yielding conditions in the crack-tip region through a series of fine-mesh, static, nonlinear, three-dimensional analyses of a cracked plate. Cleavage-fibrous transition studies continued with an investigation of the influence of nonuniformities of microstructure produced by carbide banding on cleavage initiation and loss-of-cleavage behavior. Work continued on the development of two dynamic crack-initiation experiments involving a notched short bar with integral dog-bone ends and a notched round-bar configuration.

SRI International performed 15 split Hopkinson torsion bar experiments on A 533 grade B steel at engineering shear-strain rates varying from 400 to 3000 s^{-1} to provide additional data for characterizing viscoplastic constitutive models at higher strain rates. A final report documenting these experiments was prepared by SRI and transmitted to ORNL.

2.1 Analysis of a Stub-Panel Crack-Arrest Specimen

J. Keeney-Walker B. R. Bass

2.1.1 Introduction

The role of nonlinear rate-dependent effects in the interpretation of crack run-arrest events in ductile materials is being investigated by the Heavy-Section Steel Technology (HSST) Program through analytical and

experimental studies. Research efforts at ORNL and at several subcontracting groups are developing viscoplastic-dynamic analysis techniques and validating their utility through the analysis of carefully performed crack-arrest experiments. Portions of the crack-arrest data used in these studies are being provided by the HSST Program through tests of several types of large specimens.[1-6] In particular, tests of wide plates[4-6] are under way to allow a significant number of data points to be generated at affordable cost. These tests are extending the crack-arrest data base for ductile steels to temperatures that are higher than those generally imposed in conventional small specimen tests. It is within the range of this higher temperature data that crack arrest is most likely to occur in a pressurized-thermal-shock (PTS) scenario.

Studies[7-9] have been conducted by the HSST Program at ORNL to evaluate the usefulness for crack-arrest experiments of a relatively small panel specimen intermediate in size between conventional crack-arrest specimens and the wide-plate specimens. For the design of the specimen geometry, the following requirements were adopted:

1. measurement of crack-arrest toughness values >200 MPa$\cdot\sqrt{m}$,
2. measurements of toughness values in a rising field of stress-intensity factor, and
3. a limit capacity of 2.5 MN for the available testing machines.

In Ref. 8 a panel specimen with a stub similar to that depicted in Fig. 2.1 (but having different dimensions) was proposed to meet the above requirements. A gradient in fracture toughness is achieved by cooling the stub region and heating the panel edge to produce a nonuniform steady-state temperature distribution across the plate. A tensile load is applied to the panel to produce a rising driving force. The stub is mechanically loaded to provide K_I levels that are high enough for initiation of the chilled crack in cleavage. Arrest of the fast-running crack then occurs in the ductile high-temperature region of the panel. Static and dynamic analyses[8,9] were carried out for the stub-panel configuration of Ref. 8 to assess its utility for producing K_{Ia} data in the temperature regime of upper-shelf material behavior. These analyses indicated that crack-arrest toughness values >200 MPa$\cdot\sqrt{m}$ could be measured in a rising K_I field by using available testing machines and appropriate thermal boundary conditions.

During this reporting period, plans were formulated at ORNL for fabricating, instrumenting, and testing the 45.1 × 99.1 × 3.39 cm stub-panel specimen shown in Fig. 2.1. Some dimensions of the specimen in Fig. 2.1 have been modified from those of Ref. 8 to accommodate mechanical and thermal loading equipment at ORNL. The plate is side-grooved to a depth of 12.5% of the thickness, resulting in a net thickness of 2.54 cm at the crack plane. The first specimen will be fabricated from the same plate (13-A) of A 533 grade B class 1 steel as that used in the WP-1 series of wide-plate tests. Material properties for these plates have been described previously in Refs. 9–10. To record pertinent data during the test, the specimen will be instrumented with thermocouples, strain gages, and displacement gages, using a placement configuration and instrumentation chain similar to that employed for the wide-plate specimens (described in Sect. 5 of this report). An improved ladder-type crack

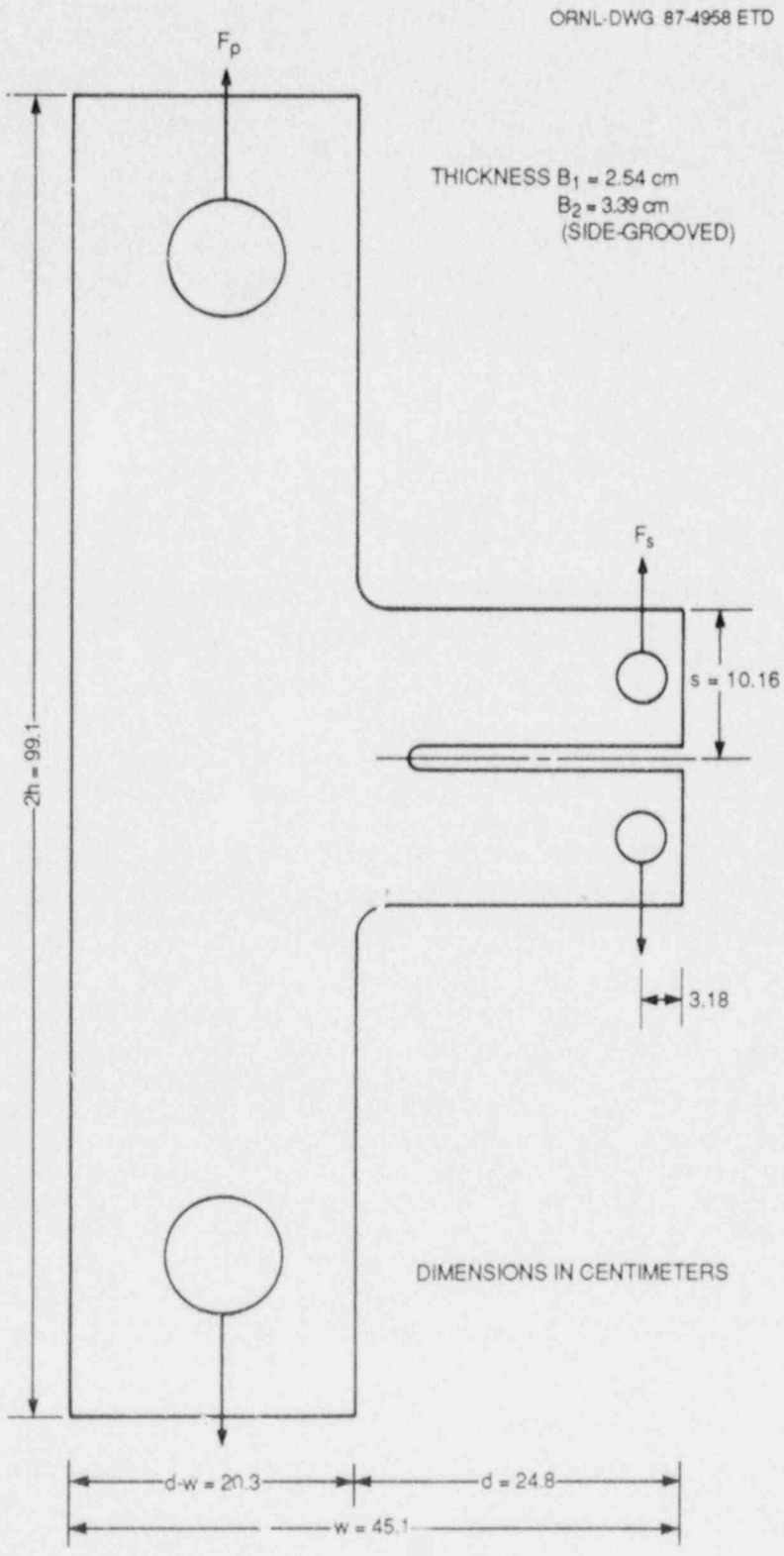

Fig. 2.1. Geometry and loading system of stub-panel crack-arrest specimen.

gage[11] developed at SwRI will be attached to the specimen to provide crack velocity data that can be compared with analogous data derived from the crack-line strain-gage output. Steps taken during this report period to transfer the ladder-gage technology to ORNL include training sessions conducted at SwRI for ORNL personnel in techniques for applying the gages and for interpreting output signals from the gages.

As part of the pretest planning, the stub-panel specimen of Fig. 2.1 was subjected to further static and dynamic fracture analyses. These studies were carried out using the finite-element programs ADINAT[12] for temperature analysis and ADINA/VPF[13-15] for static and dynamic fracture analyses. Material properties for the analyses are those for A 533 grade B class 1 steel described in Refs. 8 and 9. Results from these analyses are summarized in Sect. 2.1.2.

2.1.2 Analyses to assess the stub-panel specimen capabilities

The geometry of the specimen proposed in Fig. 2.1 is based on design calculations described in this report and in Refs. 7-9. Several static and dynamic analyses for different loading conditions were performed to assess the specimen capabilities for providing dynamic fracture-toughness data above 200 MPa$\cdot\sqrt{m}$ in the upper-shelf regime and to determine effects of mechanical loading and thermal gradient on the run-arrest event. The thermal boundary conditions used in the analyses are shown in Fig. 2.2. The surface region denoted by T_1 in Fig. 2.2 is cooled down to temperature T_{min}, which is close to RT_{NDT} so that the crack can be initiated in cleavage. The back surface of the panel (region T_2) is heated to a temperature T_{max}. The surface region T_3 is assumed to be at ambient temperature; all other surfaces are insulated. The resulting (nondimensional) steady-state temperature distribution in the crack plane ($y = 0$) is depicted in Fig. 2.3. Because the initiation and arrest fracture toughness relations are strongly temperature dependent, the length of the crack jump can be adjusted by an appropriate choice of the temperatures T_{min} and T_{max}.

Finite-element analyses of the stub-panel specimen were performed using the two-dimensional (2-D) plane-stress model illustrated in Fig. 2.4. Loading pin forces are approximated in the model by point loads F_s and F_p applied to nodes located at the top of the stub and panel pin holes, respectively; the pin holes are not included in the model. Assuming crack initiation for a given combination of F_s^{in} and F_p^{in}, there is some uncertainty concerning the boundary conditions at the load points during crack propagation. Both fixed-load and fixed-displacement boundary conditions were used to determine upper and lower limits for the dynamic response of the specimen. The fixed-displacement condition was emphasized in the study under the assumption that during the short time of the event, the testing machine cannot react to the change in specimen compliance resulting from the increase in crack length.

For crack initiation, the applied stress-intensity factor $K_I^F(a_i)$ must exceed the temperature-dependent plane strain initiation toughness $K_{Ic}(T_{min})$ at the crack tip located at $x = a_i$. Crack-tip temperatures of $T_{min} = -55$ and -23°C were selected for these analyses; for the A 533

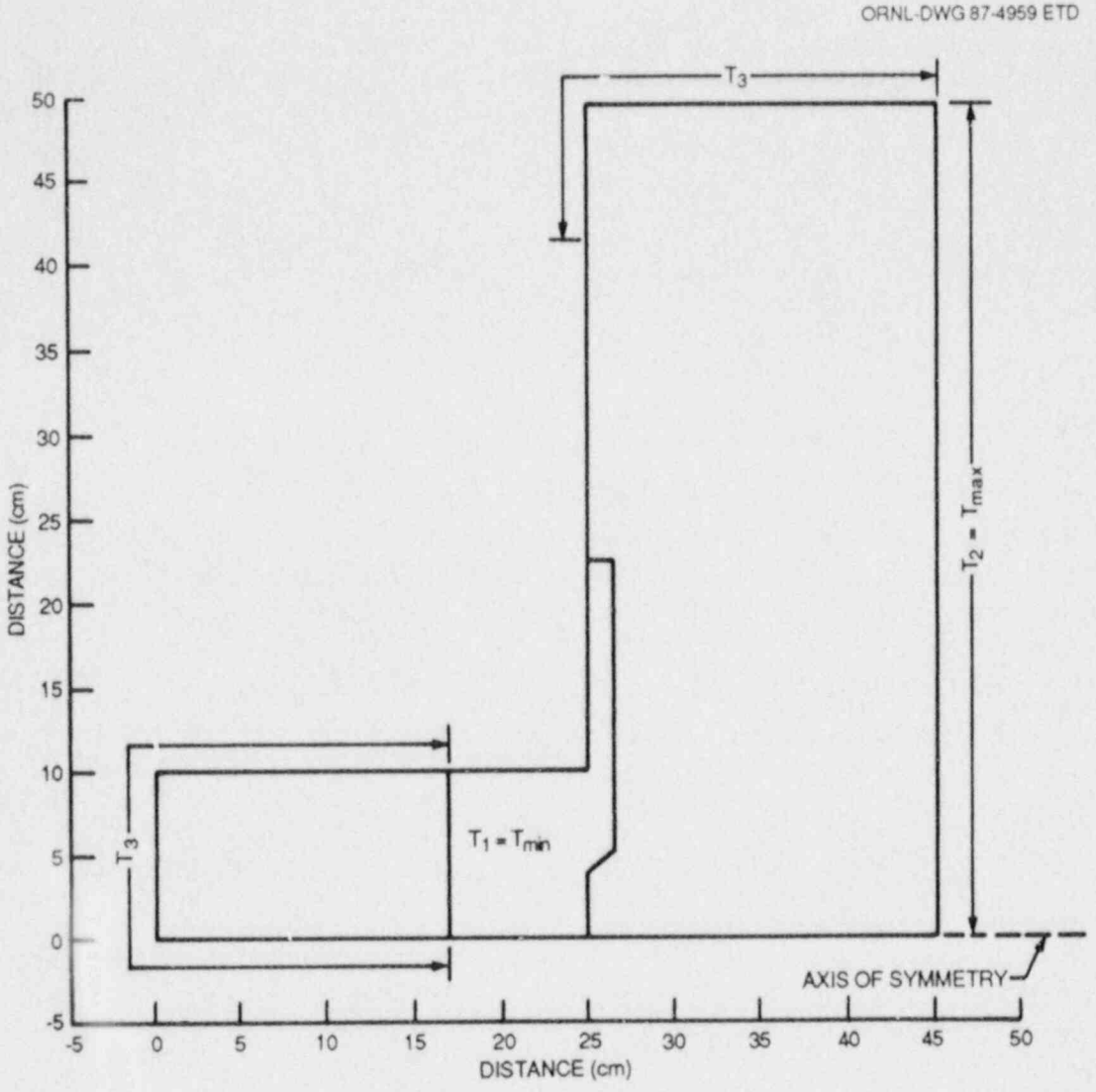

Fig. 2.2. Thermal boundary conditions of stub-panel crack-arrest specimen.

grade B plate material, $RT_{NDT} = -23°C$. From the initiation fracture-toughness relation of Refs. 8 and 9, these temperatures correspond to K_{Ic} values of 67.8 and 103.2 MPa$\cdot\sqrt{m}$, respectively. According to Figs. 2.5 and 2.6, $K_I^F(a_i)$ is almost exclusively determined by the magnitude of the stub force F_s. The temperature T_{max} of the heated edge is determined by specifying the location, X_{US} (measured from the cold edge), in the crack plane where the temperature is T_{US}, which defines the onset of Charpy upper-shelf material. Charpy data[8,9] for this material suggests that $T_{US} = 55°C$; the range of values specified in these analyses for crack-tip temperature T_{min} and for X_{US} (from 0.3493 to 0.3620 m) required a variation in T_{max} from 119.5 to 173°C. The tensile load F_p applied to the

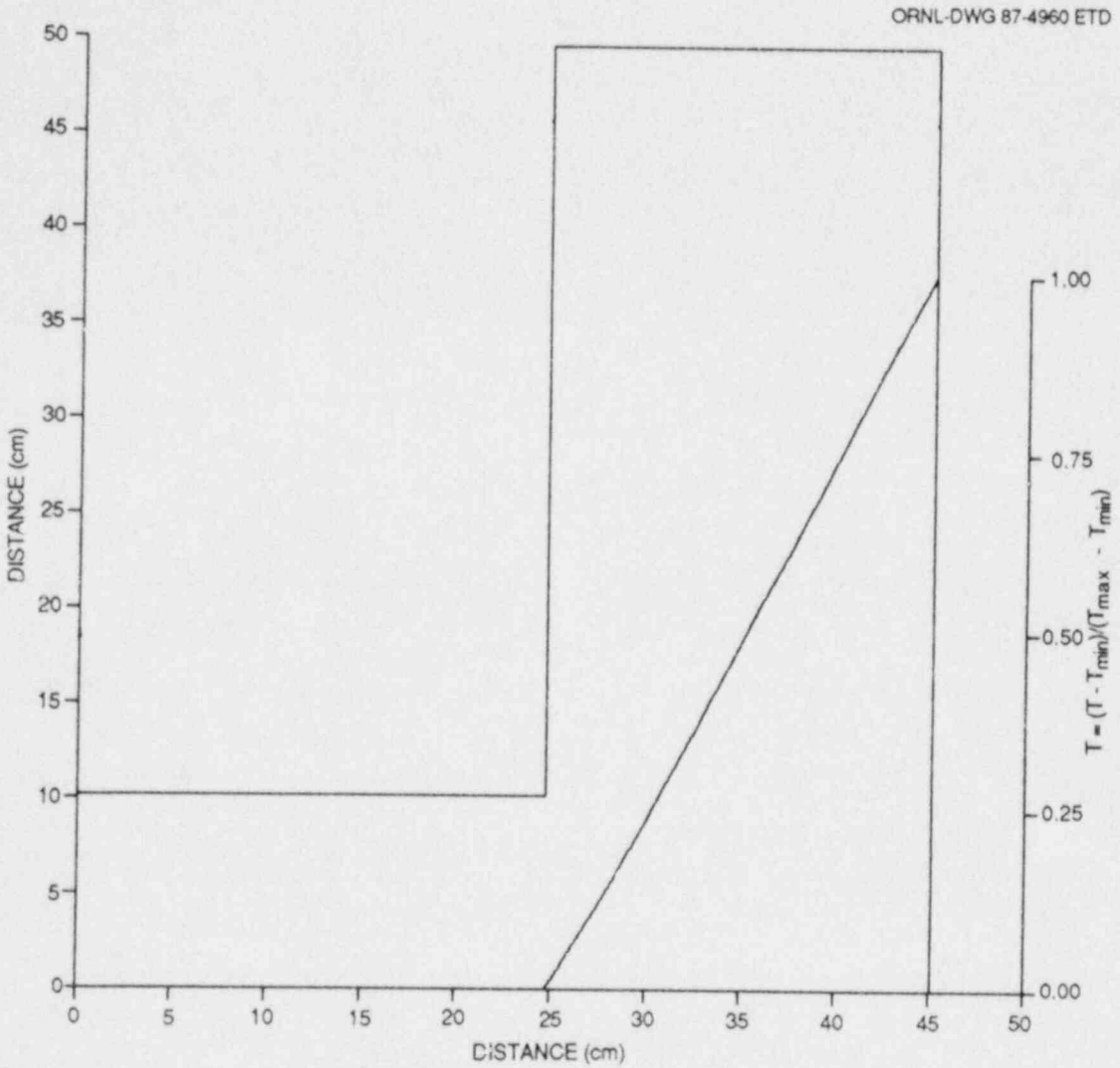

Fig. 2.3. Nondimensional steady-state temperature distribution $\bar{T}(x, y = 0)$ in crack plane $y = 0$ of stub-panel specimen.

panel must be high enough to produce crack-arrest toughness data in the range of interest but low enough to avoid general yielding in the crack plane. Based on yield properties described in Refs. 8 and 9, a panel load of $F_p = 1.85$ MN was used in all but one of these analyses.

Calculations are reported here for 11 different loading conditions listed in Table 2.1. Results from the application-mode elastodynamic analyses included in Table 2.1 are the crack-jump length Δa, the arrested crack depth a_f, the arrested crack-depth ratio a_f/W, the temperature T_{arr} at the point of crack arrest, and the crack-arrest toughness calculated from ADINA/VPF and from a static crack-arrest toughness relation taken from Refs. 8 and 9. The ratio K_I/K_{Ic} specified for each load case in Table 2.1 is based on a probable elevation in apparent toughness from

Table 2.1. Analytical results for stub-panel crack-arrest specimen

No.[a]	Loads (MN)		T_{min} (°C)	T_{max} (°C)	X_{US} at 55.0°C (M)	$K_I^F(a_1)$[b] (MPa·√m)	K_{Ic}[c] (MPa·√m)	K_I/K_{Ic}	Δa (m)	a_f (m)	a_f/W	T_{arr} (°C)	K_{Ia} (MPa·√m)	
	F_S	F_P											ADINA[d]	K_{Ia}[e] function
A^{DC}	0.10	1.80	−55	173	0.3493	103.2	67.8	1.5	0.1302	0.3524	0.7817	58.8	213.5	226.9
B^{DC}	0.10	1.85	−55	173	0.3493	103.7	67.8	1.5	0.1302	0.3524	0.7817	58.8	214.2	226.9
D_1^{DC}	0.124	1.85	−23	119.5	0.3620	123.8	103.2	1.2	0.1461	0.3683	0.8169	59.6	224.0	231.2
D_2^{FC}	0.124	1.85	−23	119.5	0.3620	123.8	103.2	1.2	0.1778	0.4000	0.8873	82.7	417.7	401.5
E_1^{DC}	0.149	1.85	−23	119.5	0.3620	144.6	103.2	1.4	0.1493	0.3715	0.8239	61.9	235.9	243.6
E_2^{FC}	0.149	1.85	−23	119.5	0.3620	144.6	103.2	1.4	0.1778	0.4000	0.8873	82.7	422.0	401.5
F_1^{DC}	0.0833	1.85	−55	146	0.3620	89.7	67.8	1.3	0.1429	0.3651	0.8099	58.3	214.4	224.7
F_2^{FC}	0.0833	1.85	−55	146	0.3620	89.7	67.8	1.3	0.1778	0.4000	0.8873	94.1	507.0	538.4
G^{DC}	0.10	1.85	−55	146	0.3620	103.7	67.8	1.5	0.1461	0.3683	0.8169	61.6	227.4	241.9
H^{DC}[f]	0.0833	1.85	−55	146	0.3620	89.7	67.8	1.3	0.1429	0.3651	0.8099	58.3	213.9	224.7
I^{DC}[g]	0.091	1.85	−55	146	0.3620	83.3	67.8	1.2	0.1397	0.3619	0.8028	55.1	200.3	209.2

[a] DC = displacement-controlled boundary condition; FC = force-controlled boundary condition.

[b] Stress-intensity factor from ADINA/VPF static analysis, where $a_1 = 0.222$ m.

[c] Fracture toughness computed at crack-tip temperature: $K_{Ic} = 51.276 + 51.897\, e^{0.036(T-RT_{NDT})}$; $RT_{NDT} = -23°C$.

[d] Dynamic stress-intensity factor computed by ADINA/VPF using time step $\Delta t = 1$ μs.

[e] Toughness computed at arrest-point temperature: $K_{Ia} = 49.957 + 16.878\, e^{0.28738(T-RT_{NDT})}$.

[f] One fixed displacement at panel load point.

[g] Load pin moved on stub from 0.03175 to 0.0762 m (measured from stub edge to center of pin).

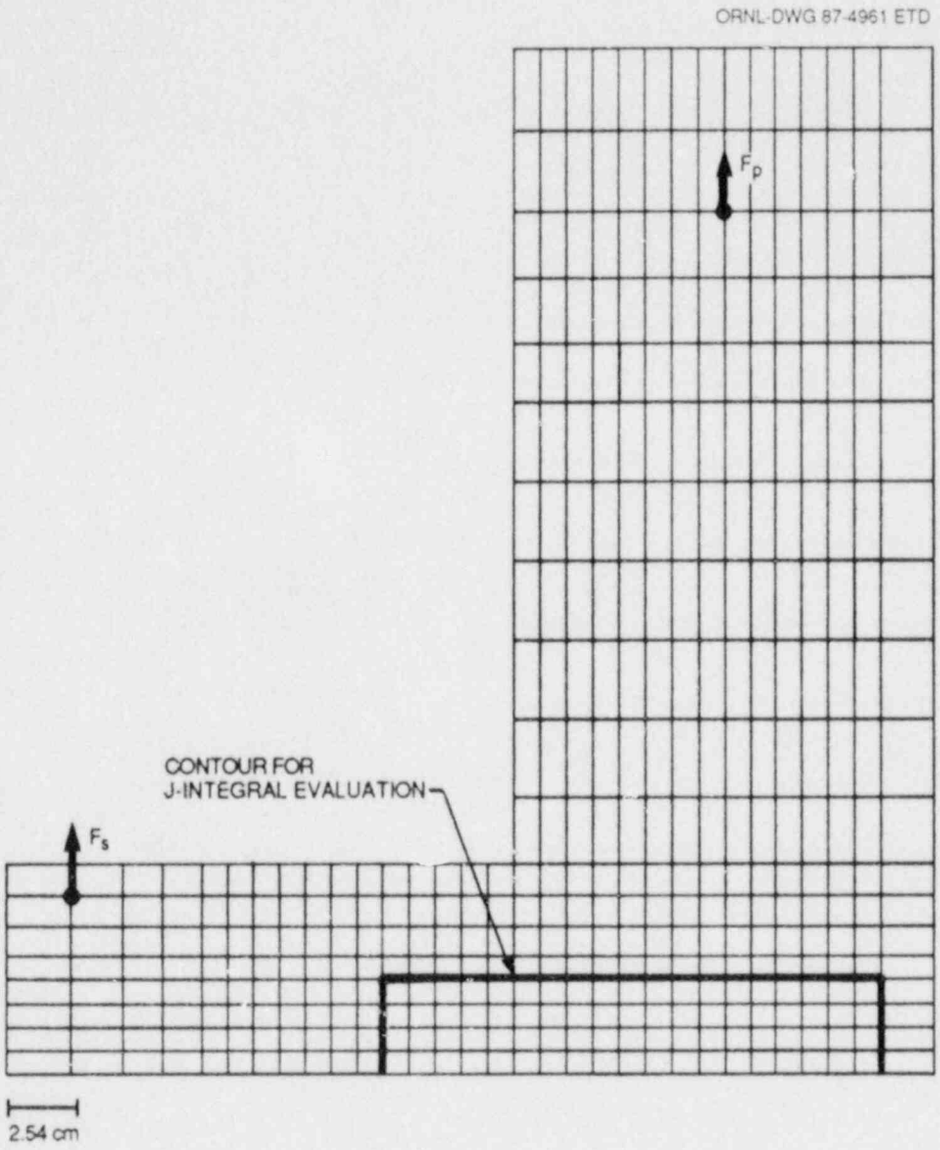

Fig. 2.4. Mesh for static and dynamic finite-element analyses of the stub-panel specimen.

prevailing plane-stress conditions; elevations ranging from 20 to 50% above K_{Ic} were examined in these studies. For analyses D and E in Table 2.1, Fig. 2.7(*a*–*d*) shows the dynamically calculated stress-intensity factor K_I^{DYN}, the static crack-arrest toughness K_{Ia}, and the crack velocity $\dot{a}$ vs crack-depth ratio a/W. Figure 2.7 indicates that in both cases, crack arrest takes place in a rising K_I field. A comparison of cases D and E for displacement control indicates that increasing the stub force sufficiently to elevate the K_I/K_{Ic} ratio from 1.2 to 1.4 only slightly increases the length of the crack jump. There was no difference

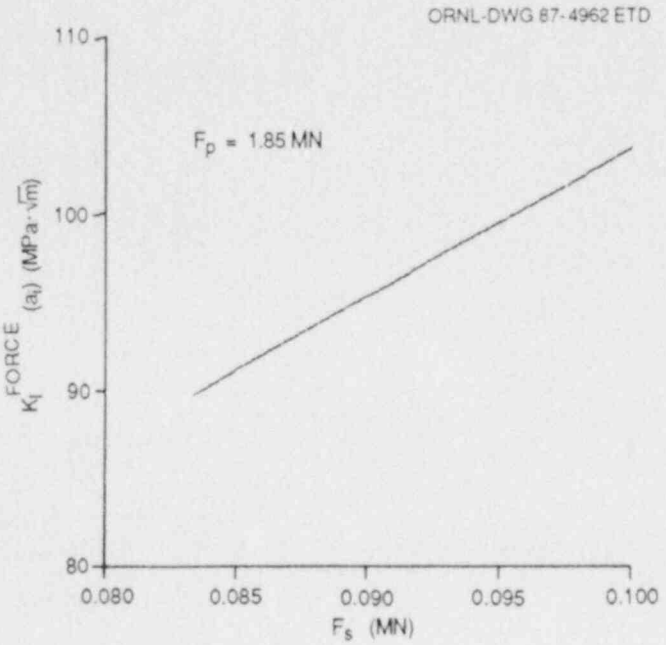

Fig. 2.5. Dependence of $K_I^F(a_i)$ of initial crack on stub forces.

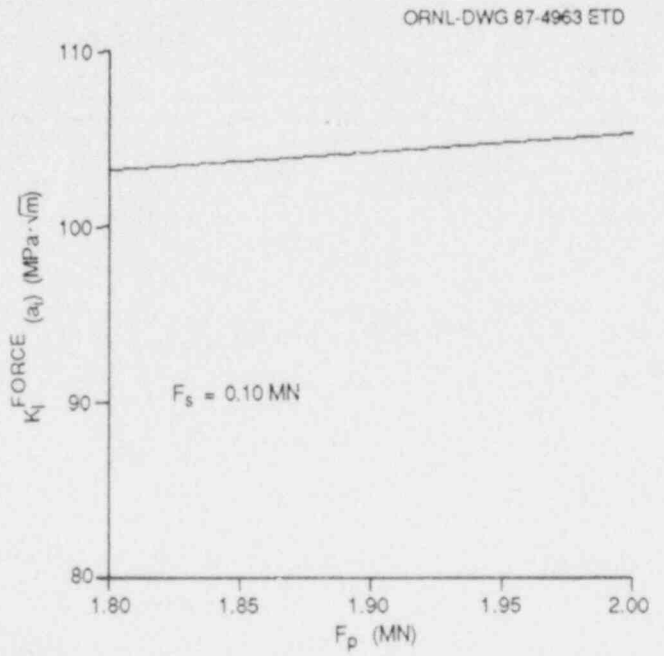

Fig. 2.6. Dependence of $K_I^F(a_i)$ of initial crack on panel forces.

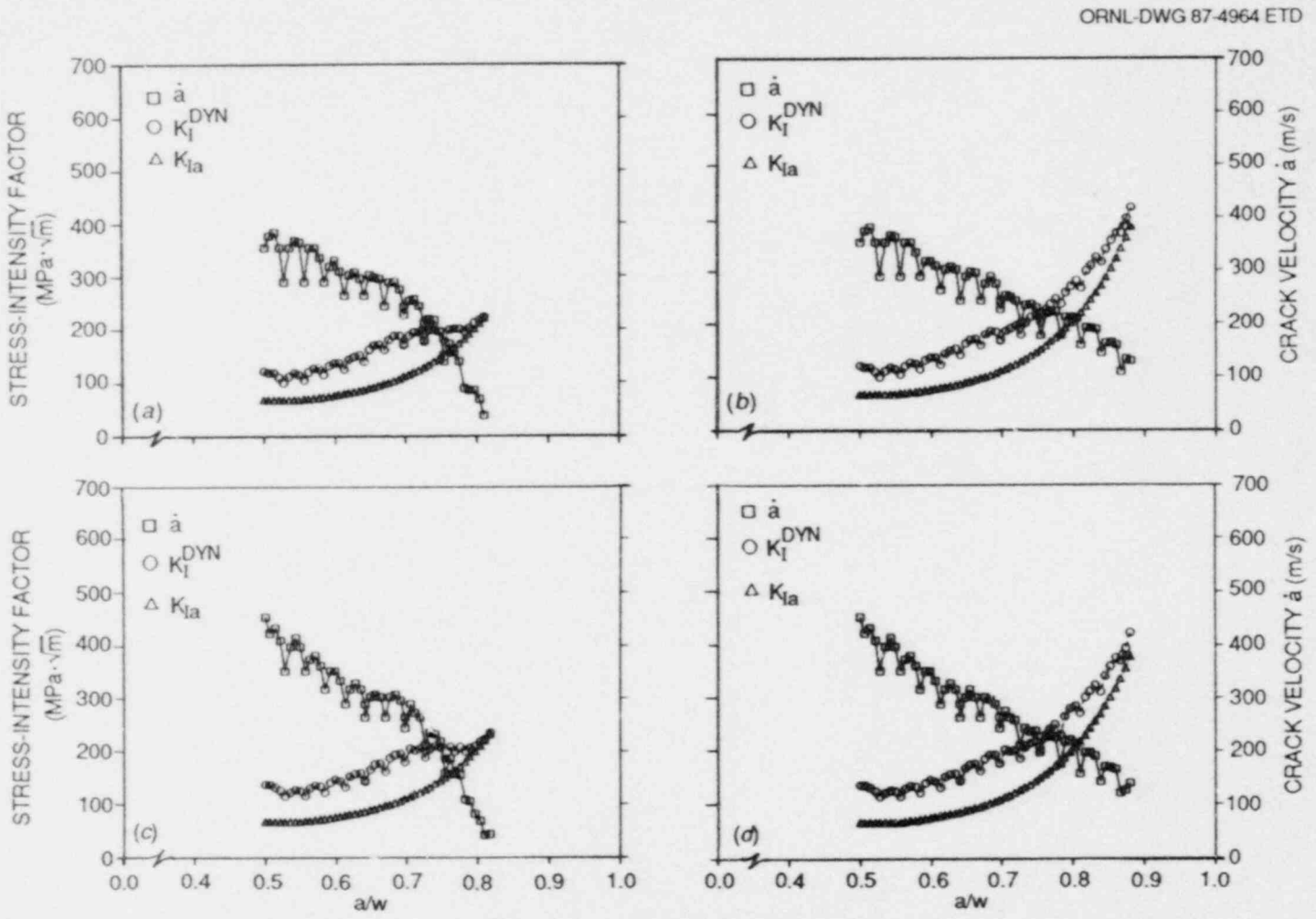

Fig. 2.7. Results from application-mode elastodynamic analyses of stub-panel specimen for load cases D and E in Table 2.1. (*a*) Load case D (displacement control), (*b*) load case D (force control), (*c*) load case E (displacement control), (*d*) load case E (force control).

in final crack length for cases D and E when force-controlled conditions were used. But when different boundary conditions for the same case (D and E) were compared, the final crack length is ~8% longer using force control than displacement control. The calculated K_{Ia} values for cases D and E ranged from 224 to 422 MPa$\cdot\sqrt{m}$.

When cases D and I for displacement-controlled conditions were compared, elevation of the crack-tip temperature with K_I/K_{Ic} at initiation held fixed results in a slightly larger crack jump and a higher K_{Ia} value at arrest. Also, a somewhat longer crack jump is obtained by shifting the onset of the upper shelf (X_{US}) further toward the back surface of the specimen (analyses B and G), resulting in a slightly higher K_{Ia} value. Analyses A and B, together with G, indicate that crack-jump length is much more sensitive to temperature gradient than to changes in the panel load F_p.

The analyses presented in this section demonstrate that if crack arrest in the tensile instability region is acceptable, then the stub-panel specimen of Fig. 2.1 is compatible with measurements in the ORNL testing machine of toughness values >200 MPa$\cdot\sqrt{m}$ under fixed-displacement conditions and >400 MPa$\cdot\sqrt{m}$ under fixed-load conditions.

2.2 Computational Methods Development for Dynamic-Fracture Analysis

B. R. Bass* J. Keeney-Walker*
C. W. Schwartz†

In support of HSST crack-arrest studies, the viscoplastic constitutive models and the proposed inelastic fracture criteria described in Refs. 14 and 15 have been implemented for evaluation in finite-element computer programs. At ORNL and UM a strategy was adopted to modify the well-known ADINA[13] general-purpose, finite-element structural analysis program for inelastic dynamic fracture-mechanics applications. The modified program (designated ADINA/VPF)[14,15] is designed for 2-D elasto-dynamic and viscoplastic-dynamic fracture-mechanics analysis of thermo-mechanically loaded structures. The ADINA/VPF code was constructed through modifications of existing ADINA subroutines (primarily the 2-D element module) and through the addition of 37 new subroutines. In addition to the fracture capabilities, ADINA/VPF has available from the standard ADINA program many options that are useful for applications in crack-arrest studies. The ADINA code uses a displacement-based finite-element formulation and includes the implicit Newmark and Wilson-Theta methods and the explicit central difference method for time integration of the equations of motion. Additional capabilities of ADINA that are

*Computing and Telecommunications Division, Martin Marietta Energy Systems, Inc., Oak Ridge National Laboratory, Oak Ridge, Tennessee.

†Department of Civil Engineering, University of Maryland, College Park.

relevant to fracture applications include one-dimensional (1-D), 2-D, and three-dimensional (3-D) element libraries; a substructure option; an equilibrium iteration option; an out-of-core equation solver; and a range of other options for geometric and materially nonlinear analysis.

During this report period, the ADINA/VPF program was extended by the additions of the Robinson[16,17] viscoplastic constitutive model and an improved crack propagation algorithm. In addition, benchmark viscoplastic-dynamic fracture-mechanics analyses were performed using the ADINA/VPF and the SwRI VISCRK[18] programs to compare the computational techniques implemented in the two programs. These developments of ADINA/VPF and applications of the program are summarized in Sects. 2.2.1 through 2.2.3.

2.2.1 Robinson constitutive model

The Robinson[16,17] viscoplastic constitutive model implemented in ADINA/VPF makes use of the formulation for isotropic and kinematic hardening described by Robinson and Bartolotta[19] and summarized in Table 2.2. This formulation has been used in finite-element applications previously by Hornberger et al.[20] at Kernforschungzentrum Karlsruhe (KfK); substantial portions of the Robinson computational algorithm implemented in ADINA/VPF were obtained from KfK during a recent site visit[21] there by ORNL personnel. The equations in Table 2.2 are valid for small deformations and initially isotropic materials. The model employs an equilibrium (back) stress internal variable α_{ij} and a drag stress internal variable κ to represent kinematic and isotropic hardening, respectively. A characteristic feature of Robinson's model is the subdivision of the state space defined by the stress σ_{ij} and the internal variables α_{ij} and κ into regions with boundaries defined by stress-function inequalities. Both the flow law and the evolutionary law for the kinematic internal variable exhibit discontinuous changes at the transition between the different regions of the state space. The form of the evolutionary law for isotropic hardening (K in Table 2.2) was specified by Robinson and Bartolotta[19] to qualitatively account for thermomechanical hereditary behavior in cyclic hardening with emphasis on that induced through metallurgical changes (e.g., through dynamic strain aging).

Applications to a problem from Ref. 19 of uniaxial isothermal cycling over a fixed strain range and strain rate were performed to validate the implementation of the Robinson model in ADINA/VPF. Figure 2.8 shows predicted isothermal stress-strain loops for cycling over a strain range of $\Delta\varepsilon = \pm 0.25\%$ and a strain rate of $\dot{\varepsilon} = 0.4\%/m$ at temperatures of 600, 700, and 800 K, using material properties for 2 1/4 Cr-1 Mo steel from Refs. 17 and 19. The results for T = 600 K [Fig. 2.8(a)] and for T = 800 K [Fig. 2.8(c)] are in good agreement with Ref. 19; the solution for T = 700 K was verified through comparison with KfK results for the same problem. Material constants for the Robinson model that are applicable to strain rates and temperature regimes characteristic of dynamic-fracture events in reactor pressure vessel (RPV) steels are currently under development by the HSST Program.

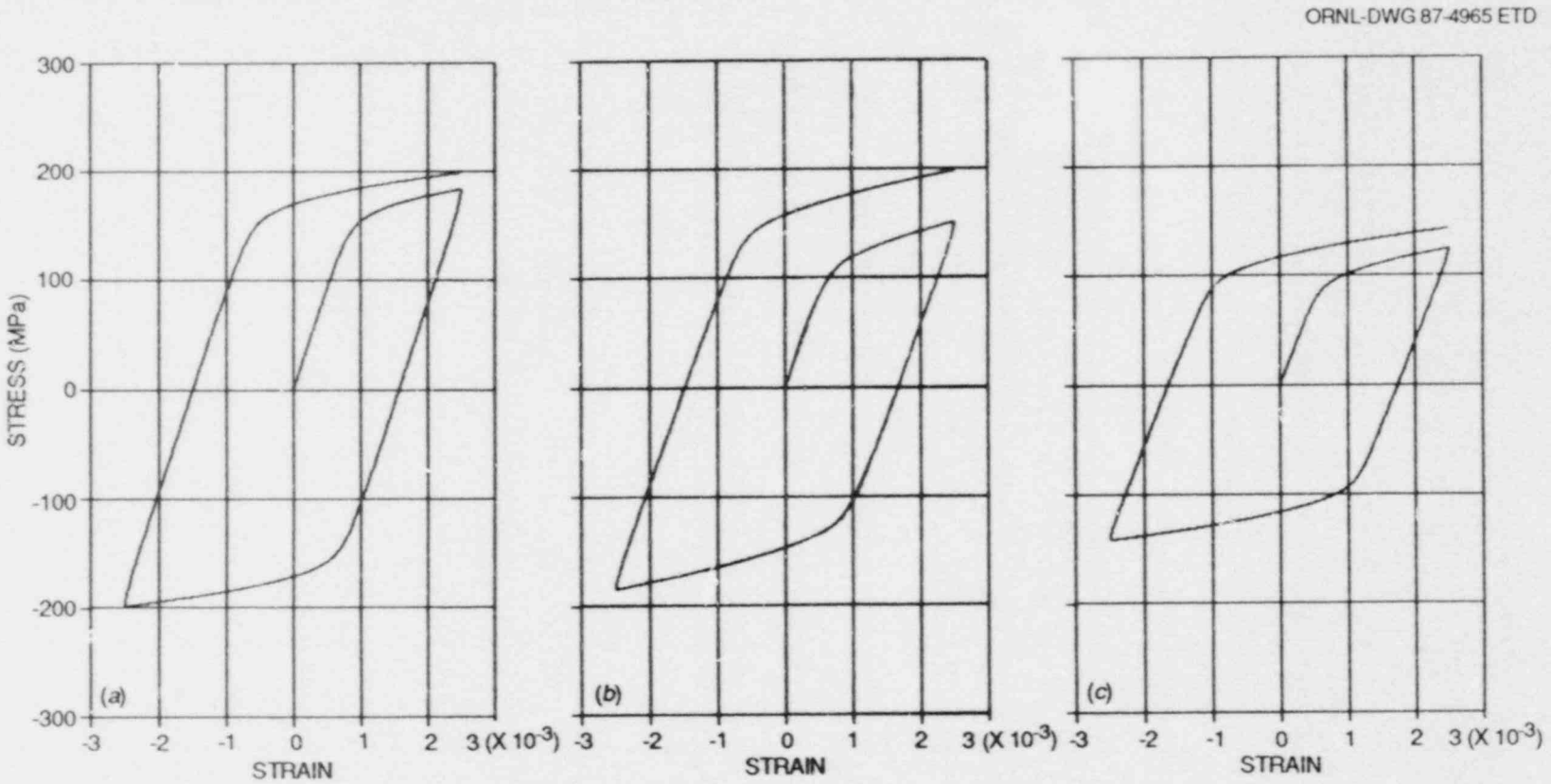

Fig. 2.8. Isothermal hysteresis loops predicted by Robinson model for strain rate 0.004/m at three different temperatures. (*a*) T = 600 K, (*b*) T = 700 K, (*c*) T = 800 K.

Table 2.2. Summary of relations for the Robinson model for nonisothermal conditions

1. Flow law:

$$\dot{\varepsilon}_{ij} = \dot{\varepsilon}^{e}_{ij} + \dot{\varepsilon}^{p}_{ij}$$

$$2\mu\,\dot{\varepsilon}^{p}_{ij} = \begin{cases} F^{n}\,\dfrac{\Sigma_{ij}}{\sqrt{J_2}} & \text{if } F > 0 \text{ and } S_{ij}\Sigma_{ij} > 0 \\ 0 & \text{if } F \leq 0 \text{ or} \\ & \quad F > 0 \text{ and } S_{ij}\Sigma_{ij} \leq 0 \end{cases},$$

where

$$S_{ij} = \sigma_{ij} - \frac{1}{3}\,\delta_{ij}\sigma_{kk} ,$$

$$a_{ij} = \alpha_{ij} - \frac{1}{3}\,\delta_{ij}\alpha_{kk} ,$$

$$\Sigma_{ij} = S_{ij} - a_{ij} ,$$

$$J_2 = \frac{1}{2}\,S_{ij}S_{ij} ,$$

$$F = \frac{J_2}{\kappa^2} - 1 .$$

2. Evolution equation of kinematic hardening internal variable:

$$\dot{a}_{ij} = \begin{cases} \dfrac{H}{G^{\beta}}\,\dot{\varepsilon}^{p}_{ij} - \dfrac{R\,G^{m-\beta}}{\sqrt{I_2}}\,a_{ij} & \text{if } G > G_o \text{ and } S_{ij}a_{ij} > 0 \\ \dfrac{H}{G_o^{\beta}}\,\dot{\varepsilon}^{p}_{ij} - \dfrac{R\,G_o^{m-\beta}}{\sqrt{I_2}}\,a_{ij} & \text{if } G \leq G_o \text{ or } S_{ij}a_{ij} \leq 0 \end{cases},$$

where

$$G = \frac{I_2}{\kappa_o^2} ,$$

$$I_2 = \frac{1}{2}\,a_{ij}a_{ij} .$$

Table 2.2 (continued)

3. Evolution equation for isotropic hardening internal variable:

$$\dot{K} = \Gamma(W_p,T)\ \dot{W}_p + \theta(W_p,T)\ \dot{T}\ ,$$

where

$$K = 3\ \kappa^2\ ,$$

$$\Gamma(W_p,T) = \frac{K_s(T) - K_i(T)}{W_o(T)}\ e^{-W/W_o(T)}\ ,$$

$$\theta(W_p,T) = \frac{Q(W_p)}{T^2}\ e^{-Q(W_p)(1/T_o - 1/T)}\ ,$$

$$W_p = \sigma_{ij}\dot{\epsilon}^p_{ij}$$

(functional forms of K_s, K_i, W_o, and Q are described in Ref. 19).

4. Material constants:

μ, n, β, m, H, R, κ_o^2, G_o, and elastic constants

2.2.2 Modifications to the crack propagation algorithm

In the crack-growth modeling technique employed in ADINA/VPF, the element immediately ahead of the crack tip is divided into N subelement divisions. During propagation the tip is moved through these subelements along the crack plane in discrete jumps. The position of the crack tip relative to these subelement divisions is determined from restraining forces placed on the crack-plane nodes of the element adjacent to the crack tip; these forces are released incrementally as the tip propagates through the element. Modifications were made to ADINA/VPF to vary the restraining forces with the crack-tip location according to the relation

$$\frac{F_i}{F_{oi}} = [1 - a(t)/\Delta X]^R\ , \qquad (2.1)$$

where F_i is the force at node "i," F_{oi} is the force at node "i" just before node release, and a is the length of the crack in the element of length ΔX. Before this modification, the exponent in Eq. (2.1) was restricted to the value R = 1.0. Studies are described in Sect. 2.2.3 that examine the effects varying R in viscoplastic-dynamic analyses of crack-run/-arrest events.

Additional modifications that relate to the method of calculating the restraining forces F_{oi} placed on crack-plate nodes were made to ADINA/VPF. Previously, nodes were restrained normal to the crack plane by 1-D truss elements that were assigned an appropriate stiffness. At the time of release for a crack-plane node, the associated truss element was deactivated. In the current version of ADINA/VPF, the truss element algorithm has been replaced with one in which the restraining forces are calculated from virtual work principles. This modification has significantly improved the efficiency of the program by reducing the memory requirements for loading the program and by reducing the number of input/output (I/O) operations required for a dynamic-fracture analysis.

2.2.3 Benchmark wide-plate analysis

Benchmark analyses of wide-plate test WP-1.2 (Ref. 22) were performed using the ADINA/VPF and VISCRK computer programs to compare and evaluate the computational techniques implemented in the two codes. Figure 2.9 shows the single-edge-notched (SEN) plate specimen (1 × 1 × 0.1 m) that was cooled on the notched edge and heated on the other edge to give a linear temperature gradient (T_{min} = 97°C, T_{max} = 207°C) along the plane of crack propagation. Upon initiating propagation of the crack in cleavage, arrest was intended to occur in the higher-temperature ductile region of the specimen. The specimen had an initial crack depth-to-plate width ratio (a/w) of 0.2. Each surface was side-grooved to a depth equal to 12.5% of the plate thickness. The specimen was welded to pull-plates that have a pin-to-pin length of 9.6 m to minimize stress wave effects. Drop-weight and Charpy test data indicate that RT_{NDT} = −23°C for this material. Material properties of the wide-plate material are described in Refs. 10 and 23. Previously reported elastodynamic and viscoplastic-dynamic analyses of the WP-1.2 tests include those described in Refs. 24 and 15, respectively.

The 2-D plane-stress finite-element model (Fig. 2.10) used in the benchmark analyses was generated by R. J. Dexter of SwRI. The model consists of 2040 nodes and 637 eight-noded isoparametric elements. Figure 2.11 depicts the viscoplastic element group (consisting of 399 elements) adjacent to the crack plane and the fixed contours used in one of the analyses to evaluate the fracture parameters. The elements along the crack path have dimensions of 37.5 by 45 mm. The mesh configuration of the benchmark model was selected by SwRI to conform with criteria derived from wave propagation studies conducted by SwRI and by UM.[25]

Generation-mode viscoplastic-dynamic analyses of the benchmark model were performed with ADINA/VPF at ORNL and with VISCRK at SwRI, using the estimate of crack position vs time from Fig. 2.12 and the Bodner-Partom model from Refs. 26 and 27. Figure 2.12 shows the two measured crack arrests at a_{fm_1} = 0.55 m and at a_{fm_2} = 0.65 m, which occurred at times

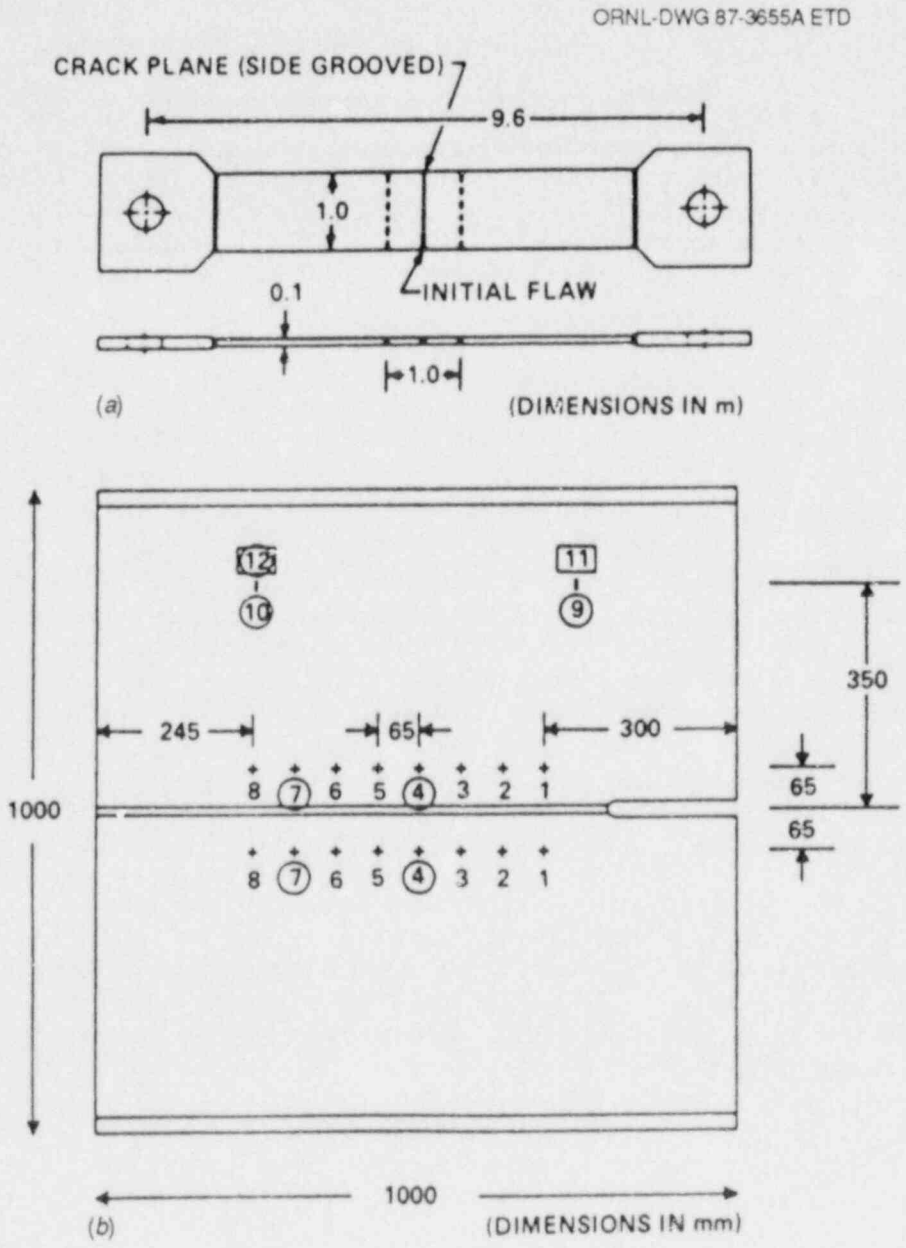

Fig. 2.9. Wide-plate assembly and crack-arrest specimen. (*a*) Pull-plate assembly, (*b*) specimen with strain-gage locations.

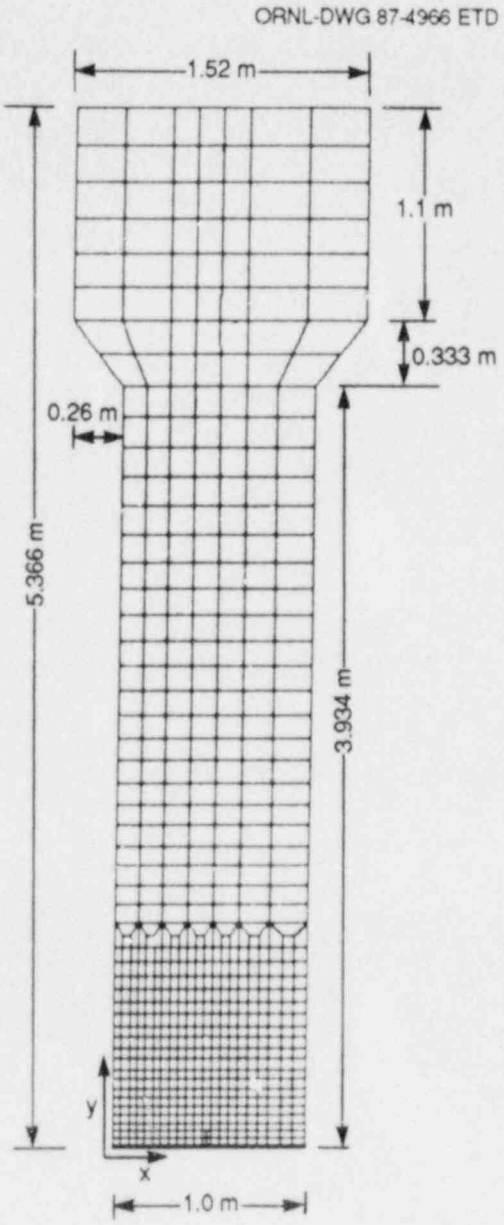

Fig. 2.10. Finite-element model of wide-plate assembly used in benchmark viscoplastic analyses.

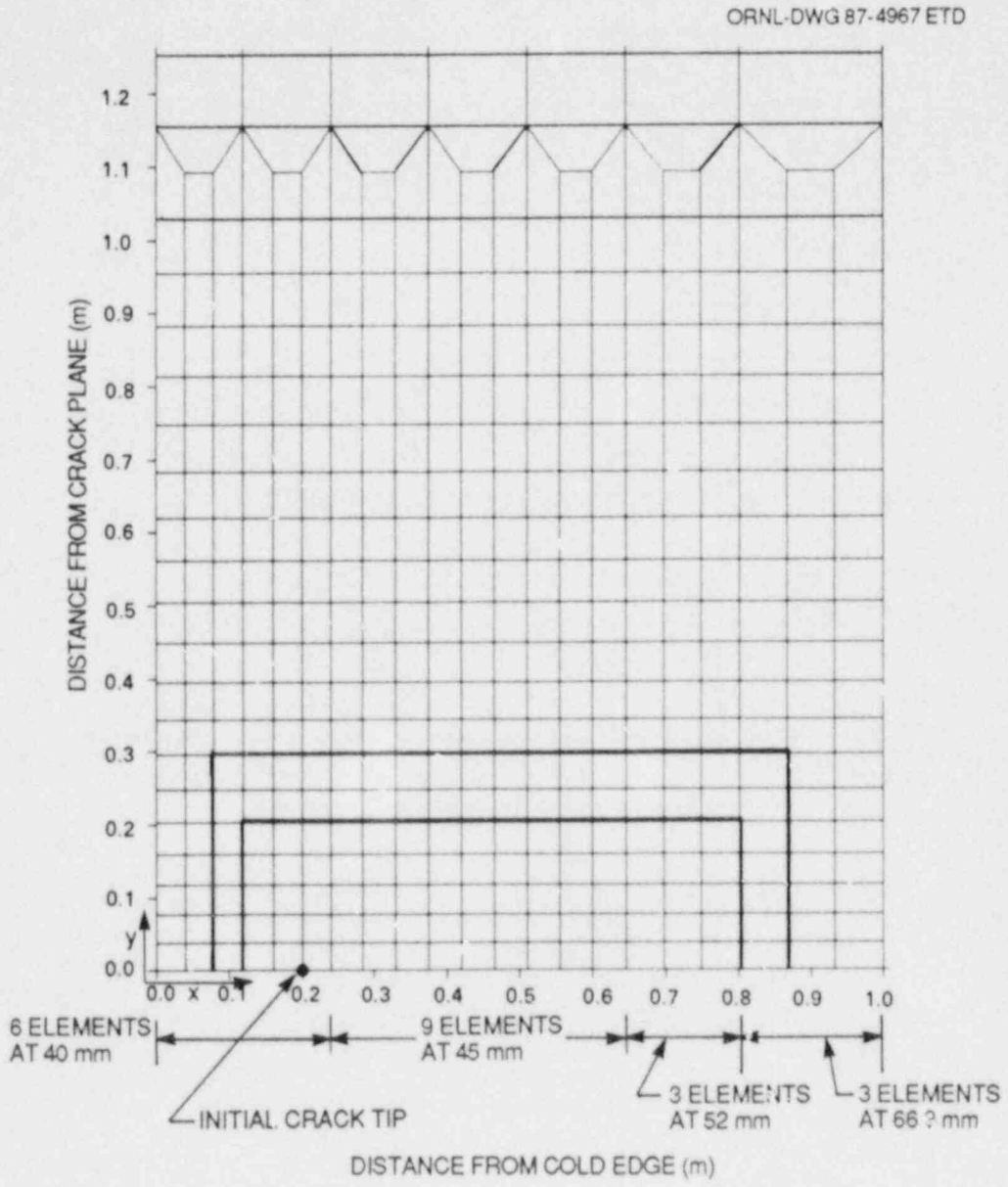

Fig. 2.11. Crack-plane viscoplastic element group of finite-element model used in benchmark analyses.

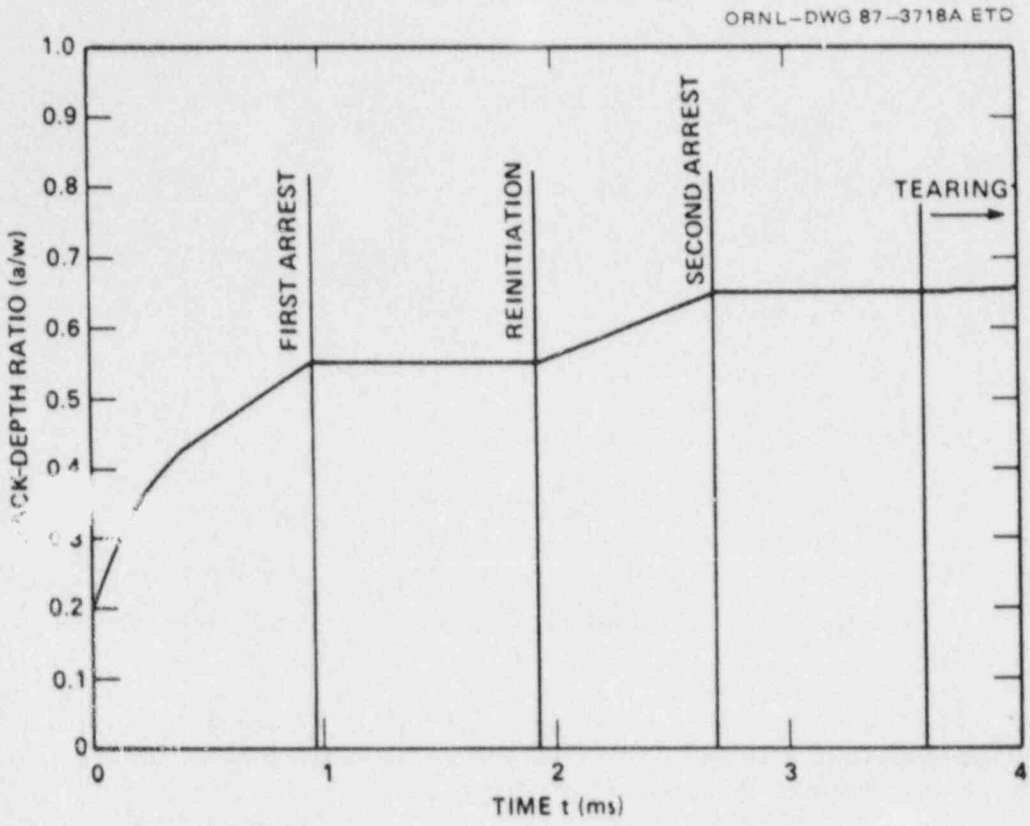

Fig. 2.12. Crack-depth history derived from strain-gage data for wide-plate test WP-1.2.

t_{m_1} = 0.96 ms and at t_{m_2} = 2.7 ms, respectively, after crack initiation. The in-plane thermal bending of the plate as a result of the imposed linear temperature gradient was ignored in the analyses. For these analyses, the applied load was fixed at the value that prevailed at initiation (F_{in} = 18.9 MN). A 3 × 3 Gauss point rule was selected for both the stiffness matrix and the consistent mass matrix; the time step was set at Δt = 1 μs. The ADINA/VPF analysis used the Wilson-Theta (Theta = 1.4) scheme for time integration of the equations of motion; VISCRK employed the fourth-order accurate Runge-Kutta scheme. Time integration of the Bodner-Partom equations was performed in ADINA/VPF by using the Euler forward one-step explicit method and in VISCRK by using a mixed implicit scheme.[18] For the ADINA/VPF analysis, the exponent in the node release function [Eq. (2.1)] was set at R = 1.5. Results from these two analyses are compared in Fig. 2.13 for the first 3 ms of the event, where the time-history of the T^*-integral[28] is expressed in terms of pseudo-K_I values [K_I (T^*) = $\sqrt{ET^*}$, E = 206.9 GPa]. Values computed by ADINA/VPF for the rate of work function γ (Refs. 14 and 29) are also included in Fig. 2.13. The ADINA/VPF and VISCRK codes were found to be in good agreement for the benchmark problem despite the significant differences in finite-element formulation, time-stepping routines, and the algorithms for integration of the viscoplastic equations. The run

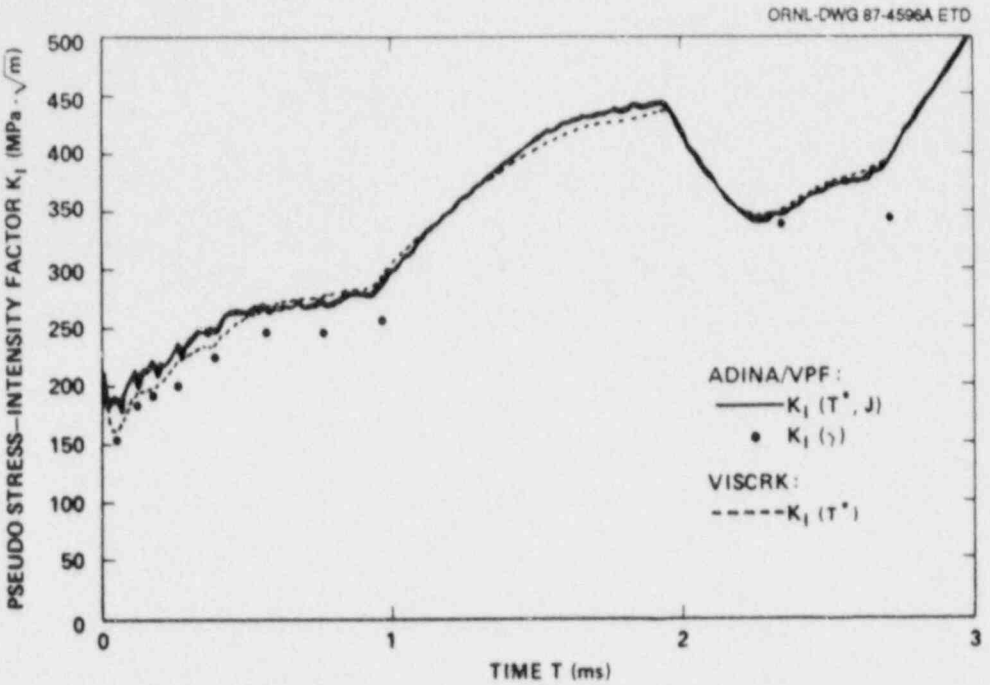

Fig. 2.13. Comparison between pseudo-stress-intensity-factor histories computed by ADINA/VPF and VISCRK in benchmark generation-mode viscoplastic-dynamic analyses of test WP-1.2.

times for the two codes were approximately the same, requiring about 16 h of central processer unit (CPU) time on the Oak Ridge CRAY X-MP computer.

Additional viscoplastic-dynamic analyses of test WP-1.2 were performed with ADINA/VPF to compare solutions for different values of the exponent R in the node-release function (Eq. 2.1). The analyses were carried out using the benchmark model as described above, except that a 2 × 2 Gauss point rule was used for the stiffness matrix calculation. Results for values of the exponent R = 0.5, 1.0, and 1.5 expressed in terms of the pseudo-stress-intensity factor $K_I(T^*)$ are compared in Fig. 2.14 up to time t = 1 ms. The sharp "cusps" in the solution for R = 0.5 coincide with the crack tip located instantaneously at an inter-element boundary and are an artifact of the node-release function; they are least evident in the solution for R = 1.5. Results from these analyses expressed in terms of $K_I(\gamma)$ are shown in Fig. 2.15.

Figure 2.16 compares results from generation-mode viscoplastic analyses of wide-plate test WP-1.2 obtained from models having different mesh refinements along the crack plane. The results are expressed in terms of pseudo-K_I values computed from the rate-of-work function γ and plotted vs crack length for the first run/arrest event. The characteristic mesh size is defined as the ratio of the crack path element width to the plate width. The ORNL results shown in Fig. 2.16 for mesh sizes 1/22 and 1/40 were obtained from the ADINA/VPF benchmark analysis described in this section and from the Perzyna model analysis of Refs. 14 and 15, respectively. Also shown in Fig. 2.16 are results obtained by

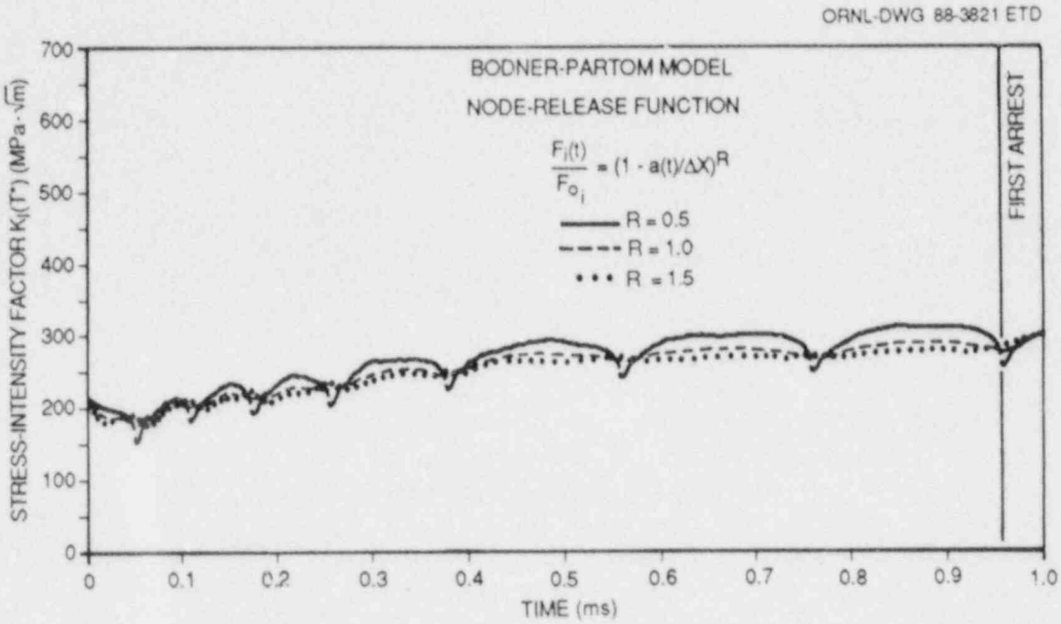

Fig. 2.14. Comparison of results [$K_I(T^*)$ vs time] from generation-mode viscoplastic-dynamic analysis of test WP-1.2 for three node-release functions.

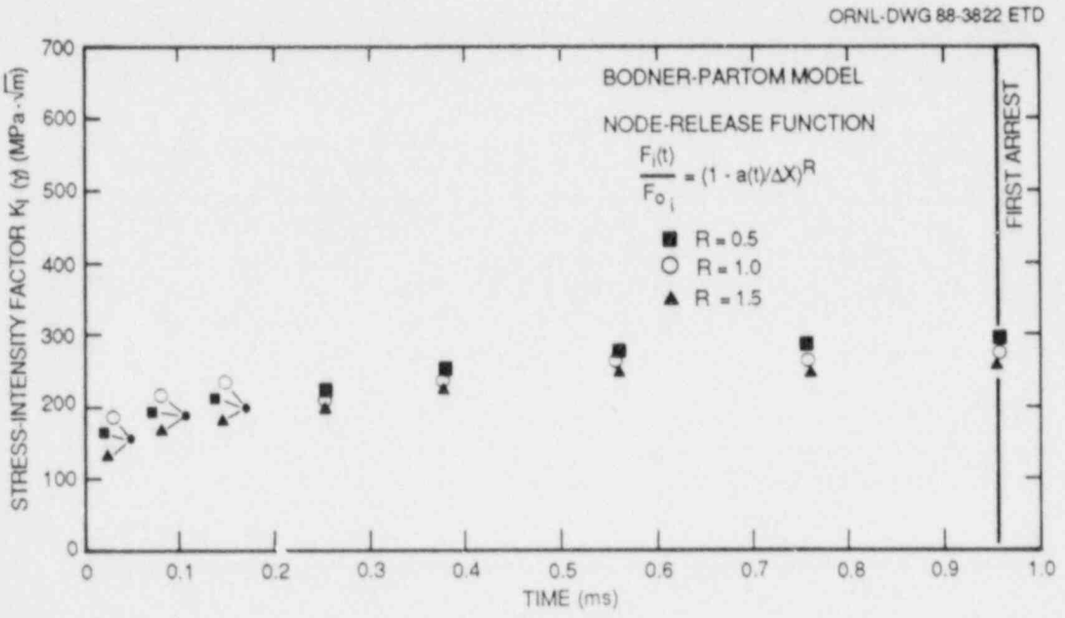

Fig. 2.15. Comparison of results [$K_I(\gamma)$ vs time] from generation-mode viscoplastic-dynamic analysis of test WP-1.2 for three node-release functions.

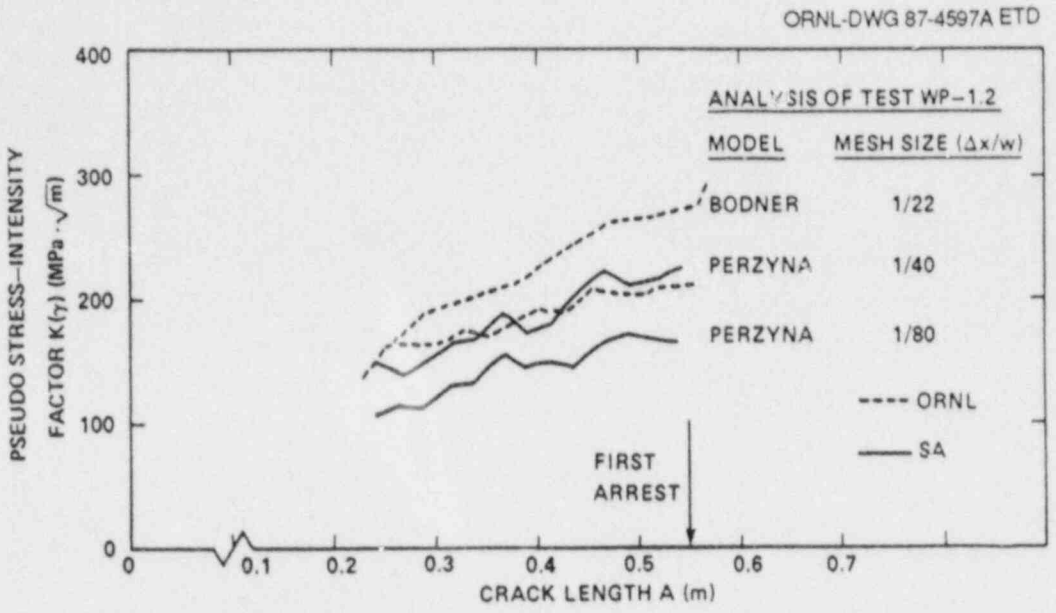

Fig. 2.16. Comparison of results [$K_I(\gamma)$ vs crack depth] from generation-mode viscoplastic-dynamic analyses of test WP-1.2 for three different crack-path mesh refinements.

Brickstad[30] at the Swedish Plant Inspectorate (SA) using mesh sizes 1/40 and 1/80 and the Perzyna viscoplastic model described in Refs. 14 and 15. The results in Fig. 2.16 reported by Brickstad[30] were obtained using finite-element models constructed from four-noded linear elements and an SA-developed computer program employing the explicit central difference time integration scheme. These combined results indicate that the viscoplastic-dynamic solutions of the wide-plate tests expressed in terms of the inelastic fracture parameters (T* and γ) have not yet converged for the mesh refinements employed thus far in these studies (for ratios of element width-to-plate width as low as 1/80). It has not yet been established what degree of mesh refinement is necessary to get convergence of the fracture parameters or whether the parameters will converge to nonzero values (see Moran and Shih[31] for further discussion of this topic).

The finite-element calculations carried out for the wide-plate tests thus far have assumed plane-stress conditions over the entire plate. Recent discussions among participants in these studies (e.g., comments by Freund[32] and by Hutchinson[33]) indicate that a plane-stress elastic field is expected to prevail in the specimen during rapid crack propagation at distances greater than one plate thickness (approximately) from the crack. However, in the vicinity of the crack tip, there must be a transition from this plane-stress field to a zone dominated by 3-D effects. Within this region, the most significant of the 3-D effects may be transverse constraint. Insight into the importance of the plane-stress vs plane-strain issue is found in results reported by Freund and Hutchinson[32] for the extension of the asymptotic analysis of Ref. 34 to plane stress. In that study, the plastic dissipation under plane stress was found to be

about two times that under plane strain, all other factors being equal. Thus, the development of valid inelastic fracture criteria from applications of 2-D finite-element formulations will require that techniques be implemented to model this transition from far-field plane-stress to near-tip plane-strain conditions.

Future development plans include mesh refinement studies to determine whether the proposed fracture parameters (e.g., T*) converge to nonzero values in viscoplastic-dynamic analyses or whether they are controlled by the element length used along the path of crack propagation. As refinement in the vicinity of the crack tip is increased, the stress and strain fields ahead of the propagating crack will be better defined. This should lead to improved understanding of the significance of the proposed fracture criteria. Studies will also be initiated to investigate the significance of 3-D constraint in crack-tip deformation with respect to the evaluation of these fracture parameters. The error inherent in assuming plane-stress deformation at the crack tip will be assessed. Alternative techniques that account for 3-D constraint will be evaluated with emphasis on modifications that can be incorporated into 2-D finite-element programs.

Parallel research efforts will involve the measurement of dynamic stress-strain data at higher strain rates ($\geq 10^3$ s^{-1}) that are representative of peak values generated by running cracks in RPV steels. Material constants for various viscoplastic constitutive models will be improved to take into account this additional high-strain-rate data and the effects of dynamic strain aging. The necessary improvements in computational techniques to make use of these updated constitutive models will be developed and implemented in ADINA/VPF and VISCRK. Small specimen tests of RPV steels are currently under way at ORNL (Sect. 2.1) and SwRI[11] to supplement the dynamic-fracture data being generated by the series of wide-plate tests at National Bureau of Standards (NBS). Extensive generation- and application-mode analyses of these tests will be performed with ADINA/VPF and VISCRK to assess the utility of the inelastic material models and trial fracture parameters in constructing a transferable fracture-mechanics model capable of predicting crack-propagation/crack-arrest behavior.

2.3 Investigation of Triaxial Constraint and Yielding in the Crack-Tip Region*

C. W. Schwartz†

Triaxial constraint effects and the transition from plane-stress to plane-strain yielding conditions in the crack-tip region are being investigated through a series of fine-mesh, static, nonlinear, 3-D analyses

---

*Work sponsored by the HSST Program under Subcontract No. 7778 between Martin Marietta Energy Systems, Inc., and the University of Maryland.

†Department of Civil Engineering, University of Maryland, College Park.

of a single crack in an infinite plate. For the preliminary series of analyses, the target ratio of element size to specimen thickness is 1/20 (or smaller). Initial analyses are focusing on mesh convergence behavior to determine whether this target element size is adequate for modeling the nonlinear stress and strain fields in the crack-tip region.

A key feature of the proposed computations is the use of a combined boundary-element–finite element formulation for the analyses. Finite elements, which are advantageous for modeling nonlinear material behavior, are used in the nonlinear near-crack-tip regions; boundary elements, which are advantageous for modeling linear infinite-boundary domains, are employed to represent the far-field conditions. This combined formulation permits very fine mesh discretization in the crack-tip region of interest without the overhead of large numbers of elements and degrees of freedom in the far field. An evaluation of the performance of the combined method relative to pure finite-element or boundary-element formulations for linear problems can be found in Ref. 35. Details of the combined boundary-element–finite-element formulation are outlined in Sects. 2.3.1 and 2.3.2.

2.3.1 Numerical formulation of coupled boundary-element–finite-element analysis

The finite-element algorithm is based on the standard virtual displacement formulation.[36] The well-known matrix form of finite-element equations is given by

$$[K]\{U\} = \{F\} , \tag{2.2}$$

where [K] is the global stiffness matrix, $\{U\}$ is the nodal displacements vector, and $\{F\}$ is the nodal force vector. Four-node, quadrilateral, isoparametric elements with linear interpolation are used throughout this study.

The boundary-element formulation employed in this study is based on the weighted residual procedure described by Brebbia et al.[37-39] This formulation is often referred to as the direct boundary element formulation in the literature. The matrix form of the boundary element formulation for elastostatics problems in the absence of body forces is given by

$$[H]\{U\} = [G]\{P\} , \tag{2.3}$$

where [H] and [G] are the boundary-element influence coefficient matrices, $\{U\}$ is the nodal displacements vector, and $\{P\}$ is the nodal tractions vector. For a general mixed-boundary value problem, some elements of $\{U\}$ and $\{P\}$ are prescribed boundary conditions. Equation (2.3) can then be rearranged such that all unknown boundary quantities appear on the left side of the equation and all prescribed boundary conditions

appear on the right, yielding

$$[A]\ \{X\} = \{Y\} \ . \tag{2.4}$$

In Eq. (2.4), $\{X\}$ is the vector of unknown boundary traction and displacement quantities, [A] is the matrix of influence coefficients corresponding to the entries in $\{X\}$, and $\{Y\}$ is the product of the vector of prescribed boundary quantities premultiplied by the matrix of corresponding influence coefficients. Two-noded boundary elements with linear interpolation functions for boundary displacements and tractions are used throughout this study.

In the hybrid finite-element—boundary-element formulation, the boundary-element region is treated as a "super" finite element that can be incorporated into the standard finite-element global stiffness matrix. Consider a problem discretized in part by finite elements and in part by boundary elements (Fig. 2.17). In Eq. (2.3) the boundary-element domain is rearranged to give

$$[G]^{-1}\ [H]\ \{U\} = \{P\} \ . \tag{2.5}$$

The nodal traction vector $\{P\}$ can be converted to an equivalent nodal force vector $\{F\}$ through use of the transformation matrix [M] according to the relation

$$\{F\} = [M]\ \{P\} \ . \tag{2.6}$$

If Eq. (2.5) is multiplied by the matrix [M] to obtain

$$[M]\ [G]^{-1}\ [H]\ \{U\} = [M]\ \{P\} = \{F\} \ , \tag{2.7}$$

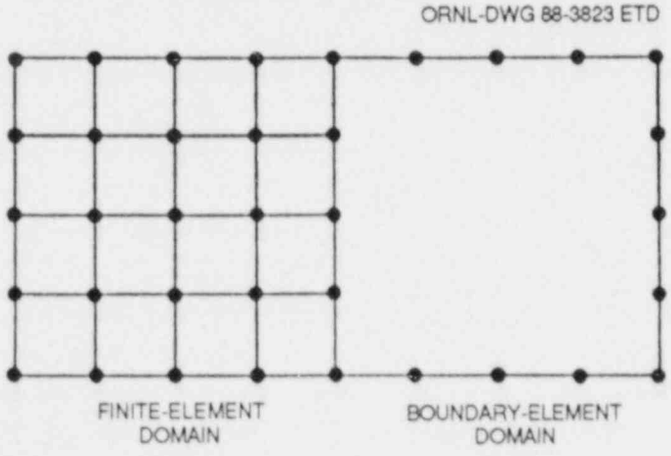

Fig. 2.17. Hybrid boundary-element—finite-element discretization.

and the matrix $[K_B]$ is defined according to

$$[K_B] = [M]\,[G]^{-1}\,[H]\ , \tag{2.8}$$

then Eq. (2.7) can then be expressed as

$$[K_B]\,\{U\} = \{F\}\ . \tag{2.9}$$

Equation (2.9) is in a form similar to the standard finite-element formulation given by Eq. (2.2). However, $[K_B]$ is not symmetric and, thus, cannot be solved using the symmetric equation solvers found in standard finite-element codes. Symmetry can be imposed on Eq. (2.9) through the procedure suggested by Brebbia, Telles, and Worbel.[38] In this procedure, a symmetric equivalent stiffness matrix $[K_{BS}]$ is defined for the boundary-element regions according to the relations

$$[K_{BS}] = ([K_B] + [K_B]^T)/2\ , \tag{2.10}$$

or

$$[K_{BS}] = ([M][G]^{-1}\,[H] + ([M][G]^{-1}\,[H])^T)/2\ . \tag{2.11}$$

This equivalent stiffness matrix can be assembled into the finite-element stiffness matrix by using standard procedures. If similar interpolation functions are used for both the boundary elements and finite elements along the interface, then displacement compatibility is ensured.

2.3.2 Implementation of coupled-boundary-element–finite-element algorithm

Implementation of the coupled-boundary-element–finite-element algorithm for the crack-tip analysis problem is straightforward. The 1984 version of ADINA[13] permits direct input of an element stiffness matrix. Thus, all that is required is a preprocessor program to generate the stiffness matrix given by Eq. (2.11) for the outer-boundary-element region of the problem in a format suitable for direct input to ADINA. The basic version of this preprocessor has been developed and is currently being enhanced to include the necessary symmetry and far-field stress boundary conditions. These enhancements are also based upon standard boundary-element formulations.[40]

2.3.3 Acknowledgments

Computational resources for this work were provided in part by the San Diego Supercomputer Center, which is administered and operated by GA Technologies, Inc., with major funding from the National Science Foundation.

2.4 Elastodynamic and Viscoplastic-Dynamic Fracture Mechanics*

M. F. Kanninen[†]
S. J. Hudak, Jr.[†]
R. J. Dexter[†]
H. Couque[†]
E. Z. Polch[†]
P. E. O'Donoghue[†]
J. D. Achenback[‡]
C. H. Popelar**

2.4.1 Introduction and summary

This research is carried out under subcontract and is designed to assist the HSST Program in developing procedures needed for the prediction of crack arrest at the high-upper-shelf toughness conditions involved in postulated PTS events. The objective is to provide analytical methods for use in pressure vessel integrity assessments that include the effects of reflected stress waves and large-scale inelastic and time-dependent material deformation that could arise in PTS conditions. This objective is being accomplished by combining dynamic fracture-mechanics finite-element analyses, viscoplastic material characterization testing, small-scale fracture experimentation, near-tip mathematical analyses, and elastic-plastic tearing instability computations. The specific aim is to quantify an inelastic-dynamic crack-propagation/-arrest criterion for PTS conditions through analyses of fracture experiments on compact duplex (A 533 B/4340 steel) laboratory specimens. The fracture criterion drawn from these analyses will next be applied to the NBS wide-plate tests in the proof-of-principle mode. Satisfactory agreement will then validate a crack-arrest assessment procedure for the entire range of PTS conditions.

The analytical work in this reporting period has centered on SwRI's viscoplastic-dynamic fracture-mechanics finite-element code VISCRK. A problem arising in the treatment of out-of-plane strain in plane-stress conditions was identified and resolved. Other improvements to increase the efficiency and generality of VISCRK were made and verified through a benchmark study performed in concert with ORNL. However, it was found that some limitations on the refinement of the near-tip region still exist that must be circumvented before meaningful analyses of actual experiments can be made. A detailed study of the temperature field at the tip of a rapidly propagating crack in a viscoelastic material was also

---

*Work sponsored by the HSST Program under Subcontract No. 12X-97306C between Martin Marietta Energy Systems, Inc., and the Southwest Research Institute.

[†]Engineering and Materials Sciences Division, Southwest Research Institute, San Antonio, Texas.

[‡]Department of Civil Engineering, Northwestern University, Evanston, Illinois.

**Engineering Mechanics Department, The Ohio State University, Columbus.

developed for eventual incorporation into VISCRK. Finally, a series of duplex 4340/A 533 grade B steel compact specimen crack-propagation/-arrest experiments was conducted. These results demonstrate the veracity of the crack length vs time measurements and other key experimental observations. They also provide helpful insights that will be useful for the design and interpretation of subsequent experiments.

2.4.2 Dynamic-viscoplastic fracture-mechanics finite-element analyses

The dynamic-viscoplastic fracture analysis program VISCRK has been benchmarked through applications to the SwRI small-specimen experiments and to the NBS wide-plate tests. Early benchmarking of the viscoplastic constitutive model implementation in VISCRK at first revealed accuracy problems in plane-stress conditions. These problems resulted from an improper assumption in the treatment of out-of-plane strain. The correction of this problem necessitated rewriting the algorithms governing the constitutive behavior. The approach used is the same mixed implicit/explicit approach originally used.

Following this correction, extensive assessments of the constitutive model implementation were successfully completed. Comparisons of the results obtained from VISCRK were made to closed-form solutions for simple uniaxial cases and to an independent numerical integration scheme in an SwRI "single-element" computer program for complex stress states and loading histories. Preliminary applications of VISCRK revealed a large computational cost for viscoplastic computations relative to elastic computations. This finding motivated several efficiency improvements that have cut the "penalty" for viscoplastic computations by ~60%.

The T* integral[28] as a fracture criterion (Sect. 2.4.3) was added to VISCRK, complementing the existing J′ integral. Because the J′ integral can be obtained as a special case from the T* integral, once this was verified, the existing J′ formulation was discarded. The terms of the T* integral that are contained in the standard J integral were benchmarked by comparison with analytical static solutions for double-edge-notched geometry. The elastodynamic terms (J′) were benchmarked by comparison with analytical elastodynamic solutions for a semi-infinite SEN geometry.

A preliminary analysis of the 4340/A 533 grade B steel duplex specimen E was completed. The mesh was composed of elements having linear dimensions of ~12 mm (Fig. 2.18). The results of this analysis in terms of K (not corrected for side-grooves) derived from T* from two different domains are shown in Fig. 2.19. The results from the two domains superpose, indicating good path independence of the T* integral.

As shown in Fig. 2.20, the experimental crack-gage data exhibited slow crack propagation (or arrests and reinitiations) for up to 400 μs. During this period, the driving force was oscillating by some ±25% (Fig. 2.19), making identification of the K_A value very difficult. If it is assumed that the crack arrest occurred shortly after 120 μs, a K_A value of ~100 MPa·$\sqrt{m}$ would be obtained. This falls on the "ORNL equation" fit to existing crack-arrest data for A 533 grade B steel. However, it would appear that there was some subsequent crack extension up to 400 μs. The crack penetrated less than one thickness into the A 533 grade B steel,

ORNL-DWG 88-3824 ETD

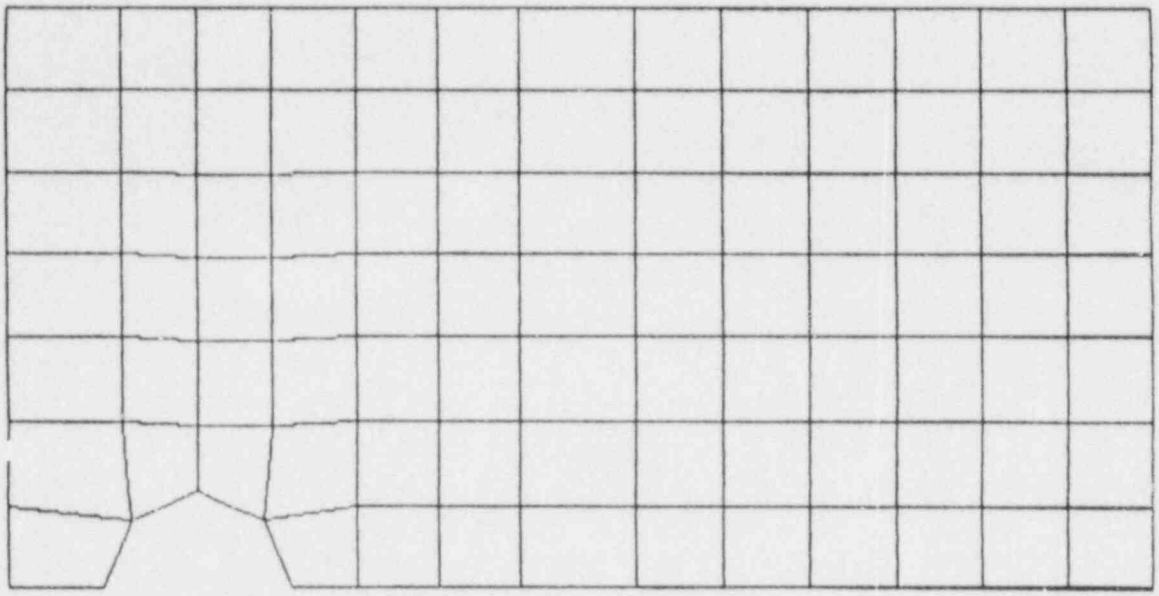

Fig. 2.18. Finite-element mesh for analysis of 4340/A 533 grade B steel duplex specimen E.

part of which was electron-beam (EB) weld and heat-affected zone (HAZ), and had a very irregular crack front with patches of unbroken ligament existing behind the point of maximum penetration. Thus, it is not clear that coplanar dynamic crack propagation actually took place in the A 533 grade B steel or that the experiment measured the full capacity of A 533 grade B steel to arrest a running crack. Analyses of additional SwRI small-specimen tests have been initiated and will be reported subsequently.

Because the plastic zones attending the running crack tip were on the order of one element, the mesh shown in Fig. 2.18 is not considered fine enough. The time step required for stability of the integration with this nodal spacing is 0.1 μs. This preliminary analysis required 4000 steps and was relatively expensive. Reduction of element size will require a proportionate reduction in time step, so meshes that are considered fine enough to represent the crack-tip region [e.g., as shown in Fig. 2.21 (2-mm-square elements)] will require time steps on the order of 10^{-8} s. Such computations are prohibitively expensive.

The problem of time-step size is further exacerbated by the fact that the mesh shown in Fig. 2.21 allows the crack-tip region to exhibit strain rates $>10^5$ s^{-1}. When integrating the constitutive equations in VISCRK, the strain increment must be limited to $<10^{-3}$. Therefore, the time step must be on the order of 10^{-9} s. This secondary problem can be eliminated by integrating the constitutive equations in subincrements decoupled from the finite-element integrations. This solution is currently being pursued. Finally, the primary problem of stability can be addressed by using implicit finite-element integration schemes with some

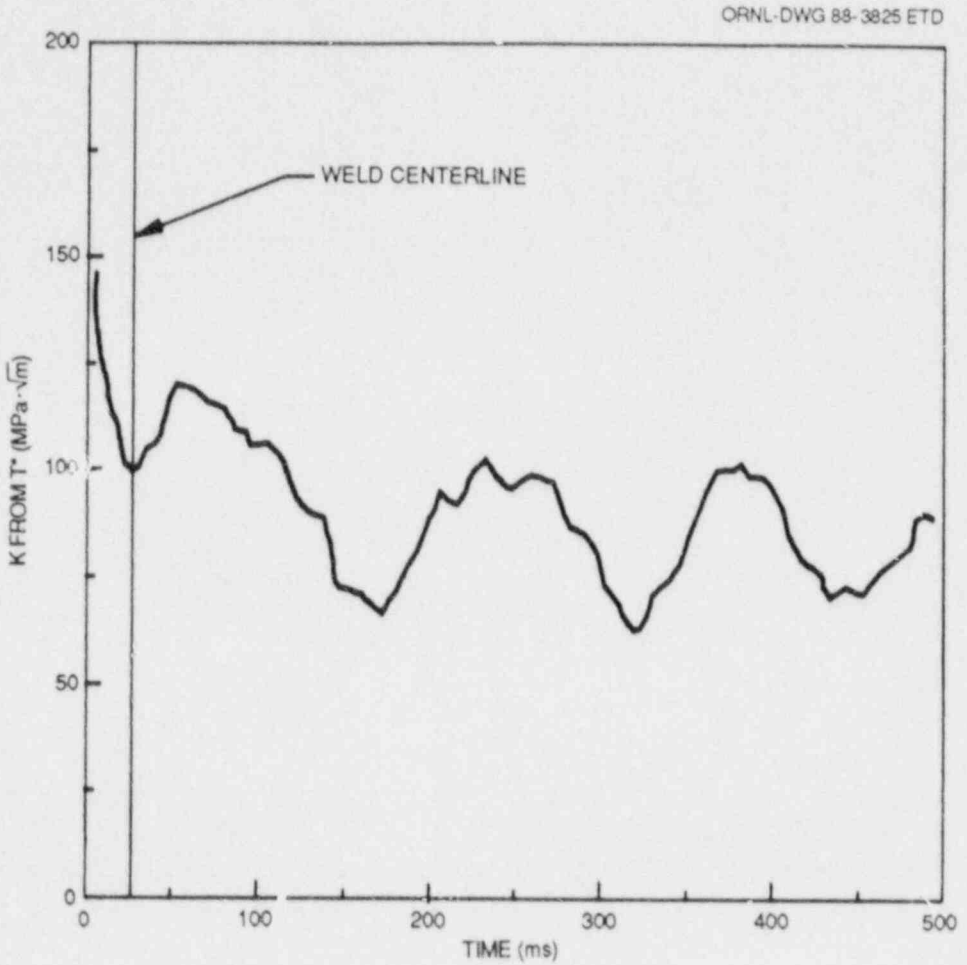

Fig. 2.19. Stress-intensity factors obtained from T* on two different domains in analysis of duplex specimen E.

sacrifice in accuracy and some cost in refactoring the matrix. Implementation of implicit integration is also currently being pursued.

Benchmark analyses of the HSST wide-plate test WP-1.2 were performed with VISCRK at SwRI and with ADINA/VPF at ORNL as described in Sect. 2.2.3 of this report. The agreement of the two different results is within 10%, which is excellent in view of the significantly different methods employed in the two computer programs. Thus, it has been established that the results of these computations are reproducible and correct.

The ADINA/VPF code uses an Euler one-step explicit method to integrate the Bodner equations. This method can lead to significant errors (which are not calculated) unless very small strain increments are used. However, ADINA lumps all out-of-balance forces from a time step into the next time step, which allows the method to maintain stability in the presence of these errors. The VISCRK code uses a mixed implicit scheme to integrate the constitutive equations. This scheme is inherently very accurate. However, some iteration is required at each step. This can be

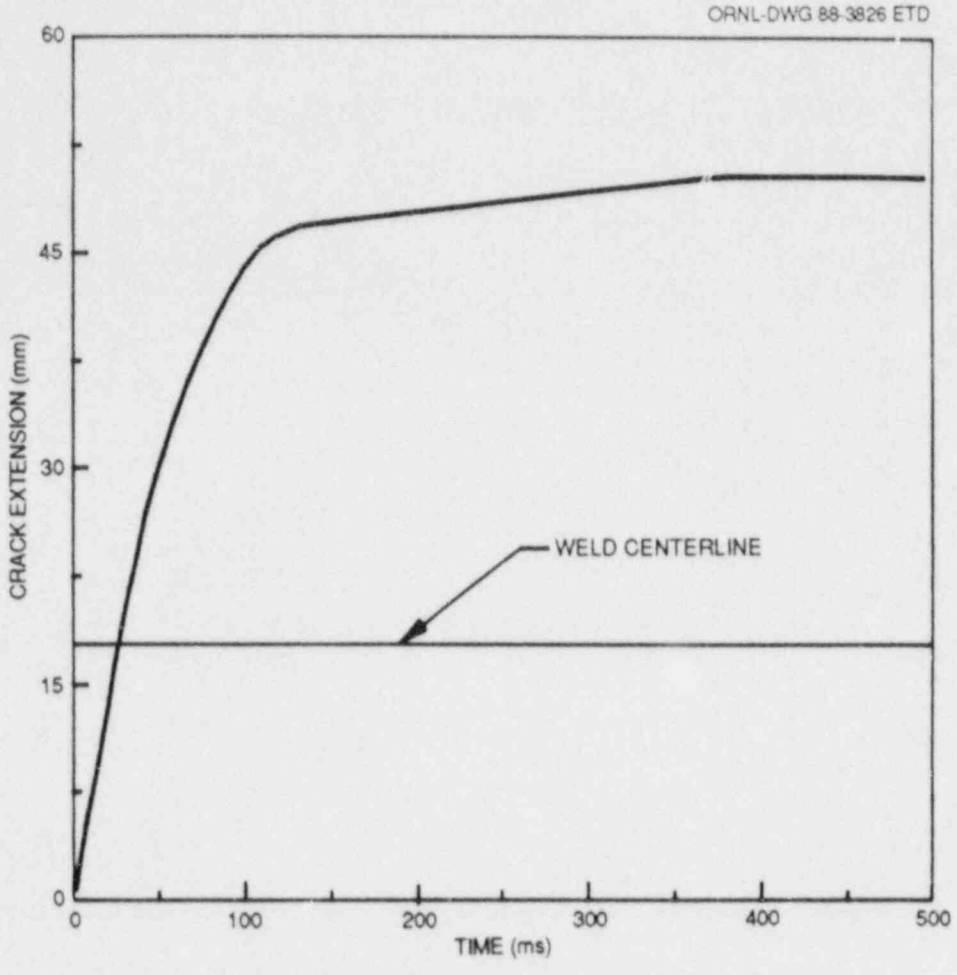

Fig. 2.20. Crack-extension history for duplex specimen E.

time consuming, and the method breaks down if it cannot converge. Thus, small strain increments are absolutely required. This scheme is in contrast to the ADINA/VPF method, which allows error to occur and compensates with out-of-balance load control. The agreement of the benchmark results indicates that the latter method does not introduce an intolerable error in the analysis, at least for these coarse meshes.

In addition to the T* integral (which embodies the J′ and other integrals as special cases), the capability of monitoring the crack tip and remote opening displacement and crack-opening angle has been added to VISCRK. The rate of work dissipated by the artificial nodal forces as each element is released is also monitored. The capability of monitoring and displaying the stress and strain fields around the crack has also been added. The objective of monitoring these quantities is to identify a crack-tip parameter with a value during crack propagation and arrest that is consistent from small specimen to wide-plate test to pressure vessel (i.e., a transferable crack-tip parameter).

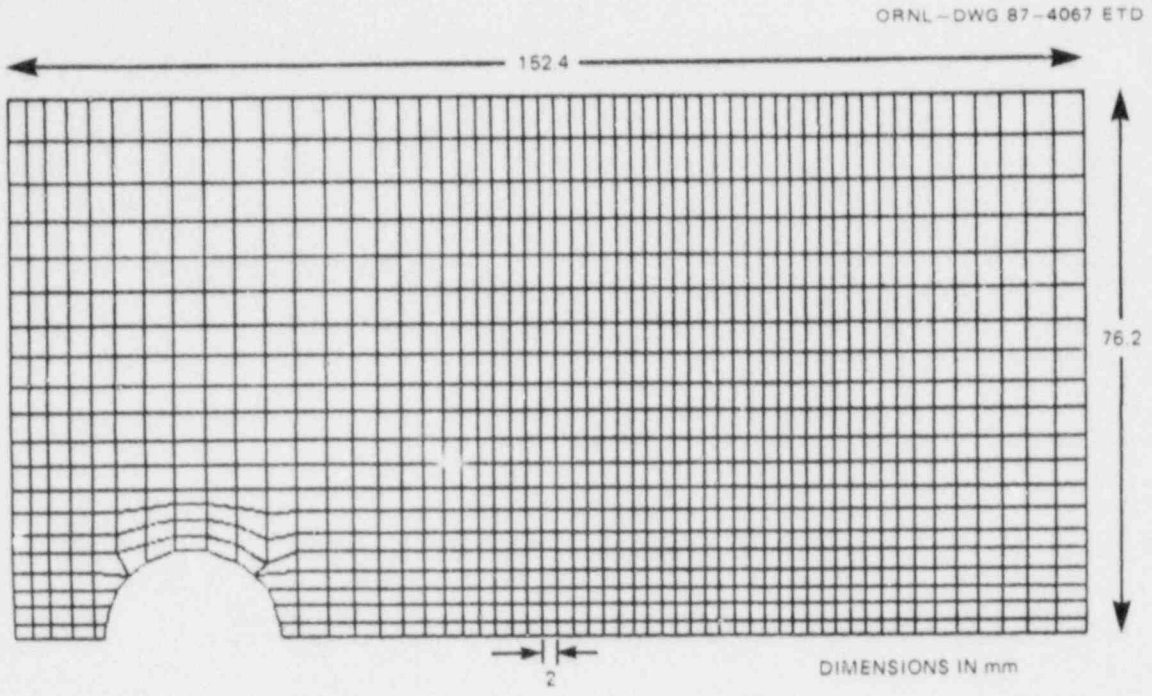

Fig. 2.21. Fine-mesh finite-element model of duplex specimen E.

Improvements in node-release algorithms were considered. It was shown in benchmark analyses that the solution is accurate at points of complete node release; between these points, errors of up to 5% may be introduced by the nodal release algorithm. It is believed that the algorithm can be improved, but this work is now thought to be a lower priority than establishing mesh convergence.

Standardized mesh generation was installed in VISCRK. A typical block of elements can now be generated with only a few lines of input. Transitions from three columns to one column of elements can be automatically generated, as well as holes in the mesh. Meshes can be re-oriented following generation to minimize computer memory requirements. Also, the ductile tearing model was established in VISCRK. This tearing model allows crack propagation in the dynamic or quasi-static mode.

To achieve the mesh refinement around the crack path necessary in these analyses, it is advantageous to grade the meshes such that larger elements are used in parts of the specimen remote from the crack path. The automatic transition described above was largely created for this purpose. Work at UM showed that large changes in the size of adjacent elements would introduce spurious wave reflections.[25] SwRI extended this investigation and established the limitations and maximum element size capable of accurately transmitting a waveform of a given period.

An estimate of the smallest period of interest was based on significant features in the experimentally recorded strain histories. Wave

propagation studies with VISCRK also showed that

1. the 3:1 column transition does not cause any significant dispersion in the solution,
2. there is no limitation on the ratio of smallest to largest element in a mesh provided other limitations (on adjacent element size ratio and absolute element size) are met,
3. the thickness change in the wide-plate specimens does cause real and significant wave reflection, and
4. the mesh used in the benchmark analysis of WP-1.2 is capable of transmitting waves of the smallest period of interest.

2.4.3 Crack-tip characterization for viscoplastic material response

A suitable fracture criterion must be robust if it is to predict the various fracture events. In the HSST wide-plate tests, the initial cleavage crack growth is followed by crack arrest as the result of a temperature increase. This is followed by a reinitiation of cleavage crack growth and, finally, by ductile tearing. The most appropriate fracture criterion must be capable of predicting all of these events. The T* integral selected for this work is believed to be appropriate for these purposes. To justify its inclusion in VISCRK, this section outlines the fundamental basis for this parameter and the techniques that can be used to evaluate it in an efficient manner.

In the following, a superposed dot will be used to denote derivatives with respect to time; spatial derivatives are indicated with a comma and subscript. Because a 2-D analysis is being conducted, the indices i,j range from 1 to 2. For convenience the crack is taken to lie along the x axis (Fig. 2.22).

The ΔT^* integral, which has the meaning of energy flow to the crack tip, can be established from a mechanical energy balance.[28,31] It is given by

$$\Delta T^* = \lim_{\Gamma \to 0} \int_{\Gamma} [(\Delta W + \Delta K) n_1 - (\sigma_{ij} + \Delta\sigma_{ij})\, n_j \Delta u_{i,1} - \Delta\sigma_{ij} n_j u_{i,1}]\, d\Gamma \,, \qquad (2.12)$$

where the quantities n_i are the components of the vector normal to the contour Γ (Fig. 2.22). Here, ΔW and ΔK are the incremental stress work density and kinetic energy density, respectively. The important point about Eq. (2.12) is that its value is independent of the inner contour Γ only in the limit as this contour shrinks onto the crack tip. If this were not the case, then the physical significance of ΔT^* would be lost.

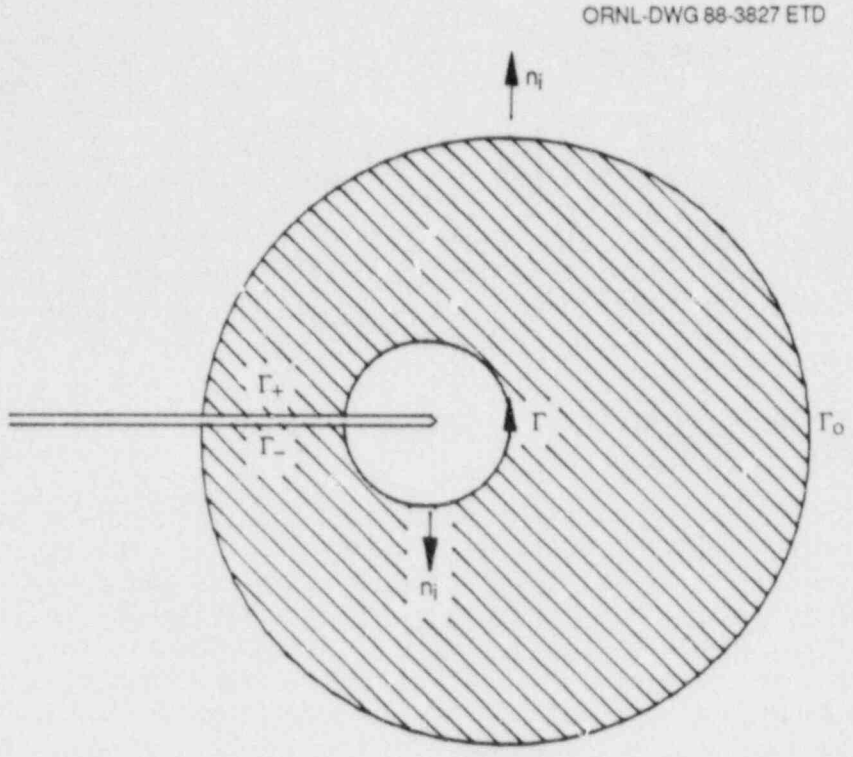

Fig. 2.22. Integral path definition in crack vicinity.

Application of the divergence theorem transforms the above integral to far-field contour and volume terms given by

$$\Delta T^* = \int_{\Gamma_0} [(\Delta W + \Delta K)\, n_1 - (\sigma_{ij} + \Delta\sigma_{ij})\, n_j \Delta u_{i,1} - \Delta\sigma_{ij} n_j u_{i,1}]\, d\Gamma$$

$$+ \int_{A_0} [\Delta\sigma_{ij}(\varepsilon_{ij,1} + 1/2\ \Delta\varepsilon_{ij,1}) - \Delta\varepsilon_{ij}(\sigma_{ij,1} + 1/2\ \Delta\sigma_{ij,1})$$

$$+ \rho\,(\ddot{u}_i + \Delta\ddot{u}_i)\,\Delta u_{i,1} - \rho\,(\dot{u}_i + \Delta\dot{u}_i)\,\Delta\dot{u}_{i,1}$$

$$+ \rho\Delta\ddot{u}_i u_{i,1} - \rho\Delta\dot{u}_i \dot{u}_{i,1}]\, dA\ . \quad (2.13)$$

This form of the integral is independent of the selection of the outer contour Γ_0. Because of the presence of the domain terms, this is a path-area integral.

When the computation of Eq. (2.13) is being performed, one particular difficulty becomes evident: the second line of this equation contains derivatives of the stresses and the strains. Because these quantities are calculated from the displacement-based finite-element method,

they will be inaccurate. One remedy is to use a least-squares fitting for the nodal stresses/strains based on the corresponding Gauss point values. These stresses and strains are then averaged at the nodal points. These nodal values, in conjunction with the shape functions, are then used to calculate the derivatives. This technique has been found to improve greatly the accuracy of the solution.

To this point, no restrictions have been imposed on material response because the integral has been established from a very general form of the mechanical energy balance. Because of this, several specializations may be deduced from the integral expression of Eq. (2.13) when the appropriate restrictions are introduced. This includes the standard J integral in elastostatics and the J′ integral for elastodynamic response. However, for crack propagation in a viscoplastic medium, ΔT^* must be used directly as given in Eq. (2.13).

The ΔT^* integral of Eq. (2.13) consists of both a volume term and a contour term. This is not always the most convenient from the computational standpoint, and there may be some inaccuracies associated with the calculation of the contour term. However, with the use of weighting functions, it is possible to convert the contour integral into a domain integral.[31] Specifically, a domain form can be established by the introduction of weighting functions to the original path-independent expression given by Eq. (2.12). The weighting function, q_1, is defined over the domain indicated in Fig. 2.22. This function is equal to unity on inner contour Γ and is equal to zero on the outer contour Γ_0. In the interior region, q_1 is an arbitrary smooth function of the coordinates that ranges between zero and one. Assuming traction-free crack surfaces Γ_+ and Γ_-, Eq. (2.12) may be rewritten as

$$\Delta T^* = \int_S [(\Delta W + \Delta K)\, m_1 - (\sigma_{ij} + \Delta\sigma_{ij})\, m_j \Delta u_{i,1} - \Delta\sigma_{ij} m_j u_{i,1}]\, q_1 d\Gamma \,, \quad (2.14)$$

where m_i has been used to denote the normal components $m_i = n_i$ on Γ_0 and $m_i = -n_i$ on Γ and S is used to denote the entire closed contour (i.e., $S = \Gamma + \Gamma_0 + \Gamma_+ + \Gamma_-$).

If the divergence theorem is applied in a similar fashion to Eq. (2.14), the resulting expression for ΔT^* is given by

$$\begin{aligned}\Delta T^* = \int_{A_0} \{ & [\Delta\sigma_{ij}\, (\varepsilon_{ij,1} + 1/2\, \Delta\varepsilon_{ij,1}) - \Delta\varepsilon_{ij}\, (\sigma_{ij,1} + 1/2\, \Delta\sigma_{ij,1}) \\ & + \rho\, (\ddot{u}_i + \Delta\ddot{u}_i)\, \Delta u_{i,1} - \rho\, (\dot{u}_i + \Delta\dot{u}_i)\, \Delta\dot{u}_{i,1} \\ & + \rho\Delta\ddot{u}_i u_{i,1} - \rho\Delta\dot{u}_i \dot{u}_{i,1}]\, q_1 - [(\Delta W + \Delta K)\, \delta_{ij} \\ & - (\sigma_{ij} + \Delta\sigma_{ij})\, \Delta u_{i,1} - \Delta\sigma_{ij} u_{i,1}]\, q_{1,j} \}\, dA \,. \quad (2.15)\end{aligned}$$

The distinctive feature of this equation is that it consists entirely of a domain integral, and it does not involve a contour term as in Eq. (2.13). The penalty for this is the presence of the weighting function, but this is relatively easy to calculate.

A number of options are available in the selection of the weighting functions. One choice is to allow q_1 to vary linearly between the inner and outer contours. This will be used to establish functional quantities at the nodal points. Within each element, the shape functions are then used to calculate values of the weighting functions. Another possible approach is to use an analytical expression for the weighting functions. This may be a simpler technique from the computational standpoint.

The path-area form of the T* integral has been incorporated into the VISCRK code. Several analyses were performed to check the accuracy of the formulation. Perhaps the most appropriate of these was the benchmark analysis of WP-1.2. As discussed in Sect. 2.2.3, very good agreement was achieved between the two methods of analyses. For convenience, the results have been expressed in terms of a stress-intensity-like quantity, and its relationship to T* is

$$K_I = \sqrt{ET^*} \ . \tag{2.16}$$

This can be taken as a definition of K_I for inelastic conditions where its usual linear elastic fracture-mechanics interpretation is invalid.

2.4.4 Thermoviscoplastic analysis of crack-tip fields

Two versions of the Bodner-Partom constitutive model have been considered. For these two versions the inelastic strain rates are represented by

$$\dot{\underset{\sim}{\varepsilon}}^i = D_o \frac{\underset{\sim}{\tau}'}{\sqrt{J_2}} \exp[-(Z^2/3J_2)^n/2] \ , \tag{2.17}$$

and

$$\dot{\underset{\sim}{\varepsilon}}^i = D_o \frac{\underset{\sim}{\tau}'}{Z/\sqrt{3}} \exp[-(Z^2/3J_2)^n/2] \ , \tag{2.18}$$

respectively. Most of the results have been obtained for the version of the Bodner-Partom constitutive model for which the inelastic strain rate is represented by Eq. (2.17). Because this version has a bounded inelastic strain rate near a crack tip, the maximum value of this strain rate is proportional to the parameter D_o of Eq. (2.17). The near-tip fields strongly depend on the value that is selected for D_o. This is particularly true for the temperature at a rapidly propagating crack tip. The maximum temperature that is achieved as a result of the dissipation of

mechanical energy near the crack tip shows a rather steep increase as larger values are selected for D_o.

The Bodner-Partom model predicts a square-root singular field for the stress components as the crack tip is approached. The corresponding stress-intensity factor is a function of time, and for uniform external loads, this factor decreases with time because of conversion of elastic deformation into viscoplastic deformation. The specific results show that the square-root singular term presents a poor approximation to the crack-tip field even at very small distances from the crack tip. The approximation becomes worse as time increases. The use of additional terms in the asymptotic expression is needed for agreement between the asymptotic representation and the numerically computed stress component at a crack-line point just ahead of the crack tip. Accordingly, a new method has been developed for the analysis of such additional terms.

The fields near a *propagating* crack tip predicted using the Bodner-Partom model have also been discussed in some detail. These are transient rather than the usually computed steady-state fields. Square-root singular fields were found to prevail again. This is true for both versions of the Bodner-Partom model, represented by Eqs. (2.17) and (2.18), respectively. For a point ahead of a propagating crack tip, some interesting competing effects affect the dependence of the stress-intensity factor on time. There exists a certain range of crack-tip velocities for which a higher velocity gives rise to a faster decrease of the stress-intensity factor.

This phenomenon can happen if during crack growth the crack-tip velocity is slow enough for sufficient stress relaxation to take place near the crack tip. However, if the crack-tip velocity is higher, effects as a result of crack growth will become more important than stress relaxation effects. For higher crack-tip velocities, the time-dependent stress-intensity factor decreases less, and it approaches the far-field linear elastic stress-intensity factor K_I^E. This is to be expected because at very high crack-tip velocities the solid behaves essentially like a linear elastic material.

If the strain rate is represented by Eq. (2.18), the near-tip fields decay more rapidly with time. The presence of an unbounded plastic strain rate has a significant effect on the time dependence of the stress-intensity factor.

2.4.5 Dynamic crack propagation experimentation

The experimental research is aimed at obtaining dynamic crack propagation data in A 533 grade B steel by using small-scale specimens. A series of duplex A 533 grade B/4340 specimens supplied by ORNL were instrumented and tested at room temperature. Crack growth was monitored on both surfaces of the specimen by using crack gages. Crack-opening displacements were measured using an eddy-current transducer. Dynamic strain measurements were also obtained and used to examine the relationship between stress wave propagation and crack growth response. Crack length vs time measurements for three specimen are compared in Fig. 2.23.

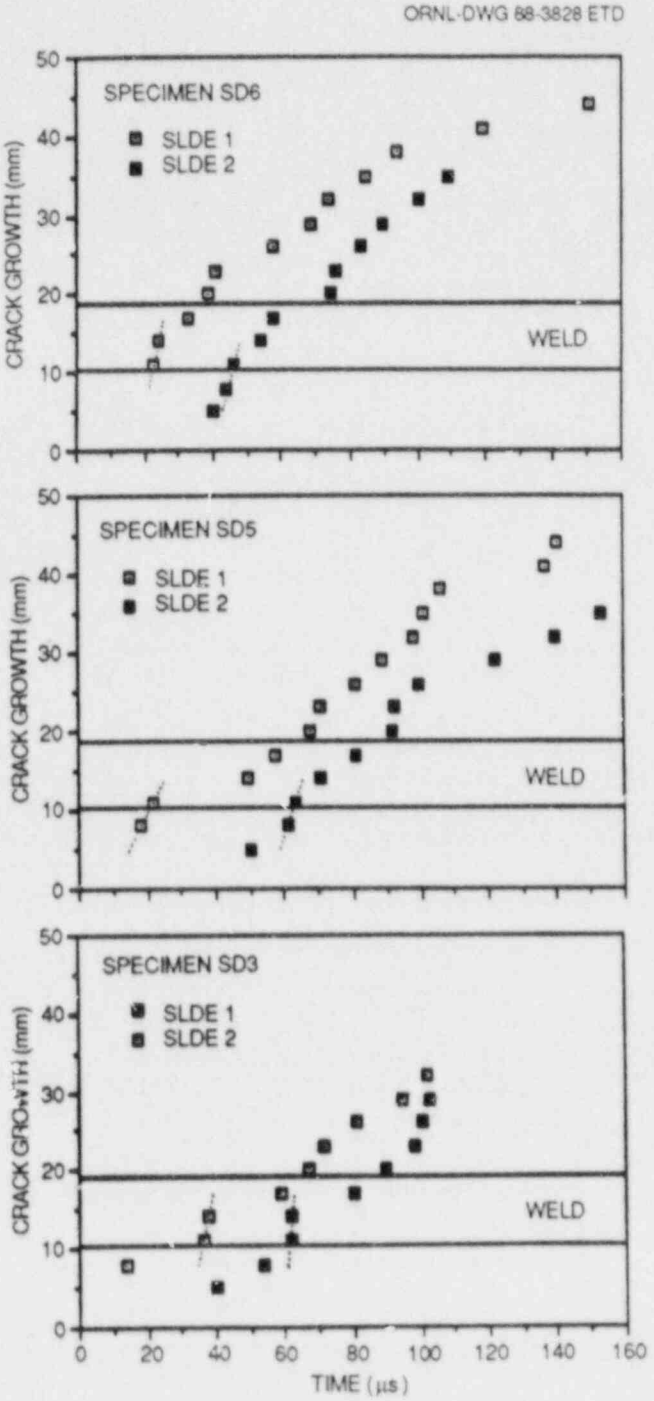

Fig. 2.23. Crack length vs time measurements in duplex 4340/A 533 grade B steel specimens.

For each test shown in Fig. 2.23, the comparison of the crack-gage responses indicates that the crack length on each side of the specimen differed by about 20 μs. Such behavior was found to be consistent with observations on the fracture surface (i.e., that the crack initiates at one corner of the starter notch). Nevertheless, the average velocities were quite similar, ranging from 200 to 400 m/s.

Strain measurements were performed on the planar surface of the specimens with strain gages located symmetrically at 13 mm from the machine notch (Fig. 2.24). As indicated, the magnitude and period of oscillation of the strain records from both gages were in excellent agreement. This confirms the reproducibility of these measurements. The strain oscillations were found to be in agreement with the arrival of reflected longitudinal stress waves emitted during crack initiation (Fig. 2.25). Correspondence in time was also found between increased crack velocity and the arrival of reflected tensile longitudinal waves.

The arrival of the first reflection and the corresponding increase in velocity occur when the crack is at the EB weld of the duplex specimen. Such behavior has been found for all of the specimens tested thus far (Fig. 2.23). This process may, in fact, assist the crack in penetrating the weld and entering the tougher A 533 grade B steel. In the development of larger duplex specimens, the weld will need to be located at a specific distance from the starter notch to take advantage of the arrival of these boundary-reflected tensile waves.

Emission of Rayleigh waves during crack initiation was investigated using two perpendicular strain gages located on the starter notch surface of the specimen 15 mm from the machine notch. Evidence of Rayleigh waves was found in the strain record corresponding to the axial gage oriented perpendicular to the crack front (Fig. 2.26). However, no significant effect of the reflected Rayleigh waves on crack velocity was found.

Dynamic strain-gage measurements are also being used to investigate the correspondence between the crack-gage response and the actual crack position. Two strain gages were located above crack gages 7 and 8 at a distance of 6.5 mm from the side groove (Fig. 2.27). The time differences between the successive strain peaks and between the failure times of the crack gages were found to be similar. The peak of strain is occurring at an earlier time than the failure of the crack gage. This delay corresponds to a peak of strain ahead of the crack tip with an angle of 73° (Fig. 2.28). This angle is similar to the peak-strain angle of 70° for the elastostatic plane-stress field. Based on this static calculation, the failure of the crack gage apparently occurs 2 μs before the crack actually reaches the crack-gage location.

These experiments will be analyzed using SwRI's elastodynamic/viscoplastic finite-element code. From such analyses, strain measurements will be obtained and compared with the experimental strain measurements. These results will be reported in the next period.

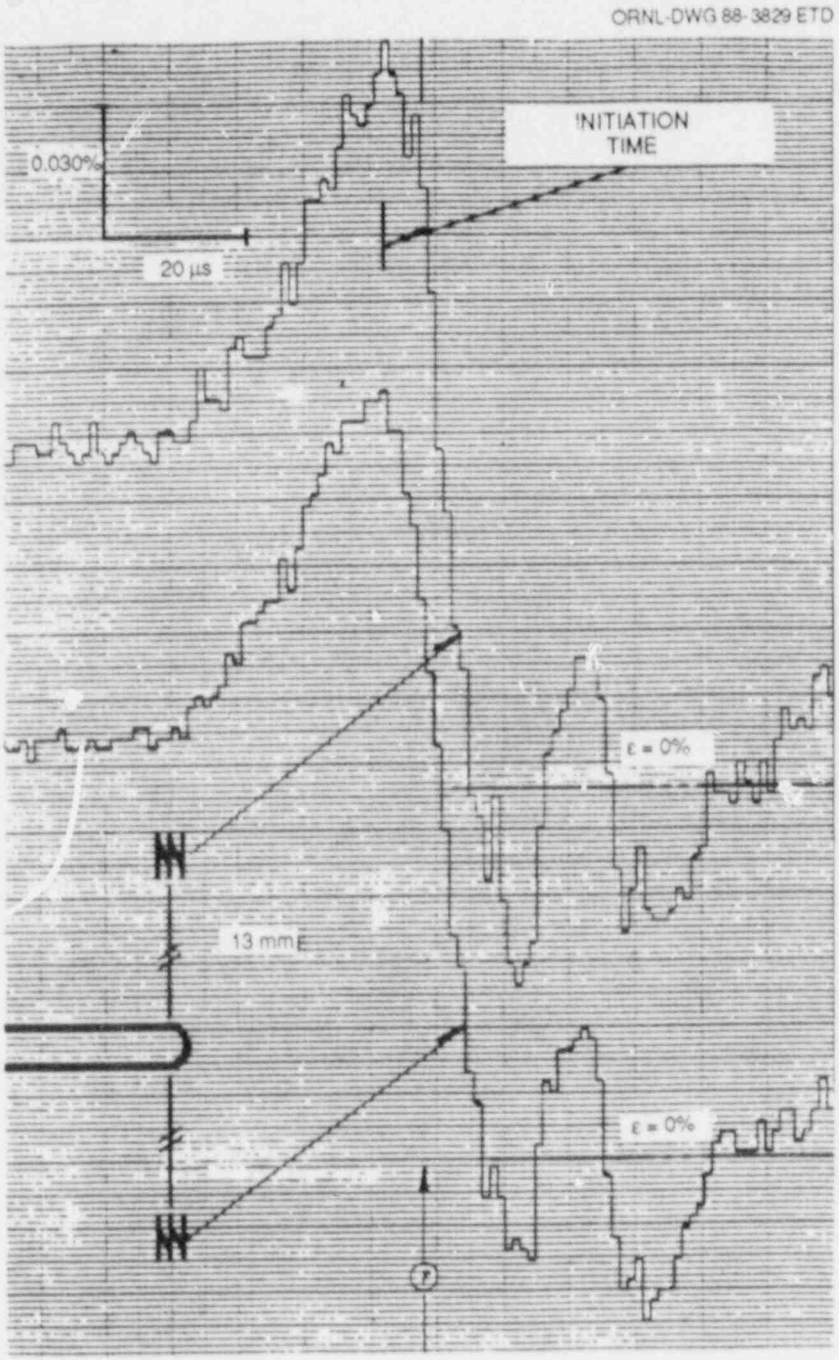

Fig. 2.24. Comparison of dynamic strains from symmetric locations about machined notch.

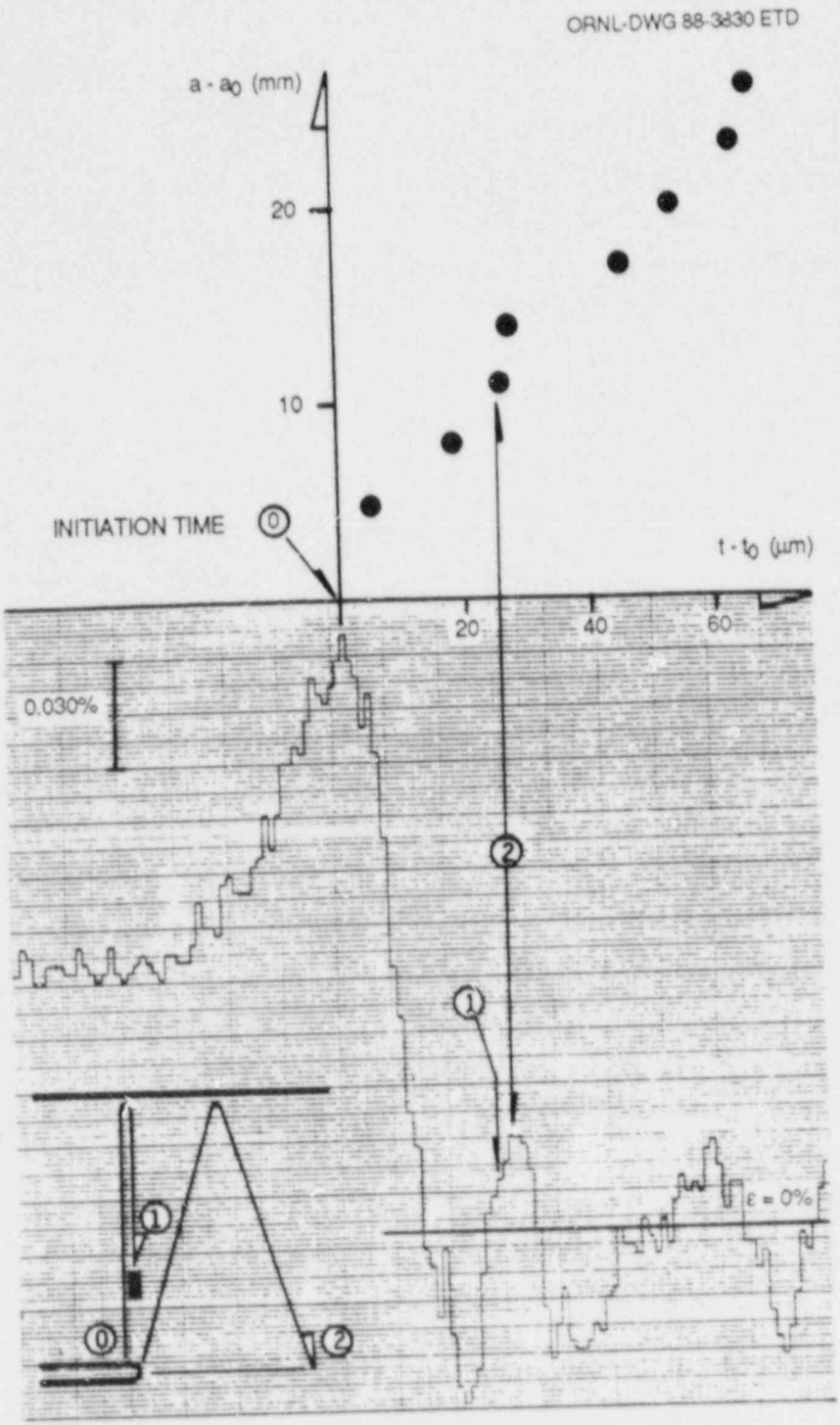

Fig. 2.25. Dynamic strain record of axial strain gage located 13 mm from machined notch. Arrival times of reflected longitudinal wave at strain-gage and crack-tip locations are indicated.

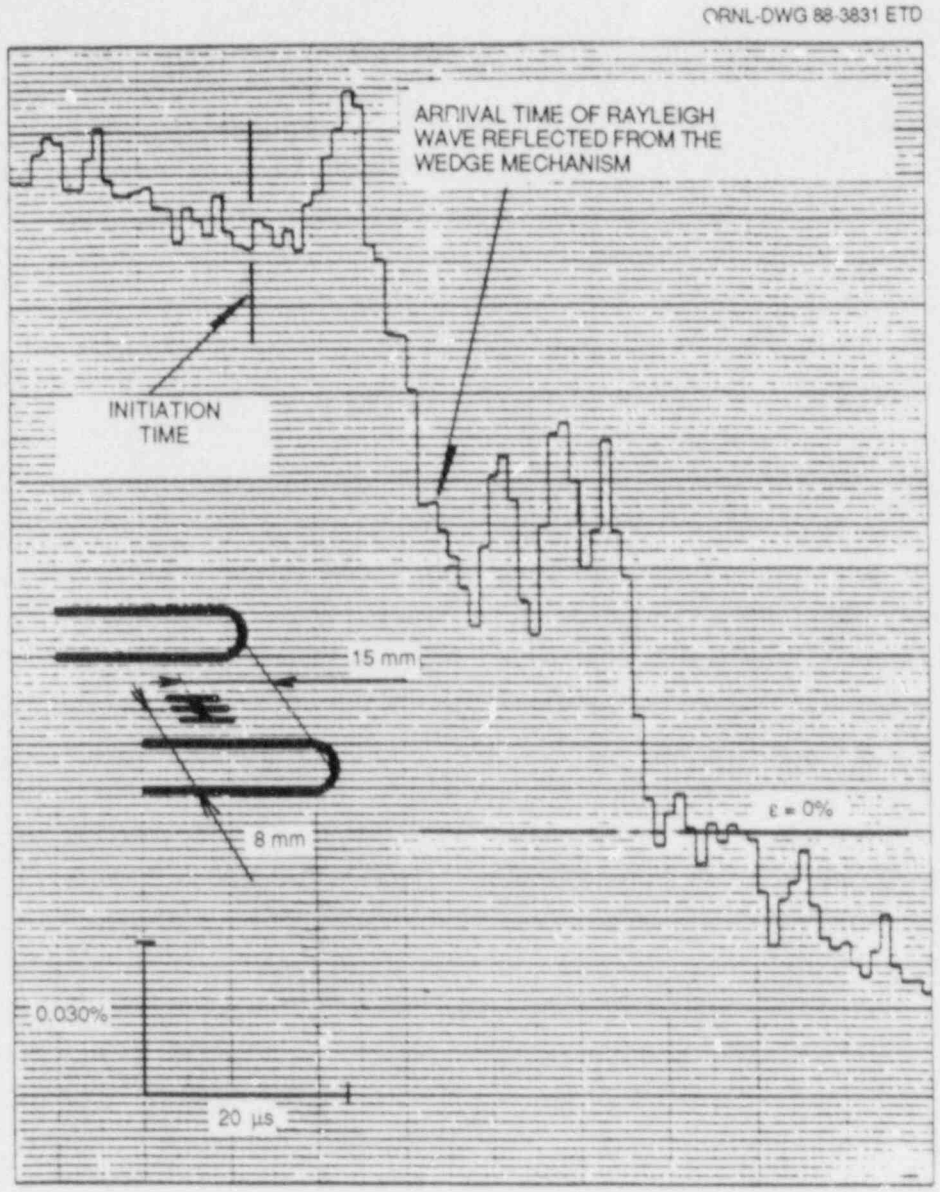

Fig. 2.26. Dynamic strain record of axial strain gage located on crack face.

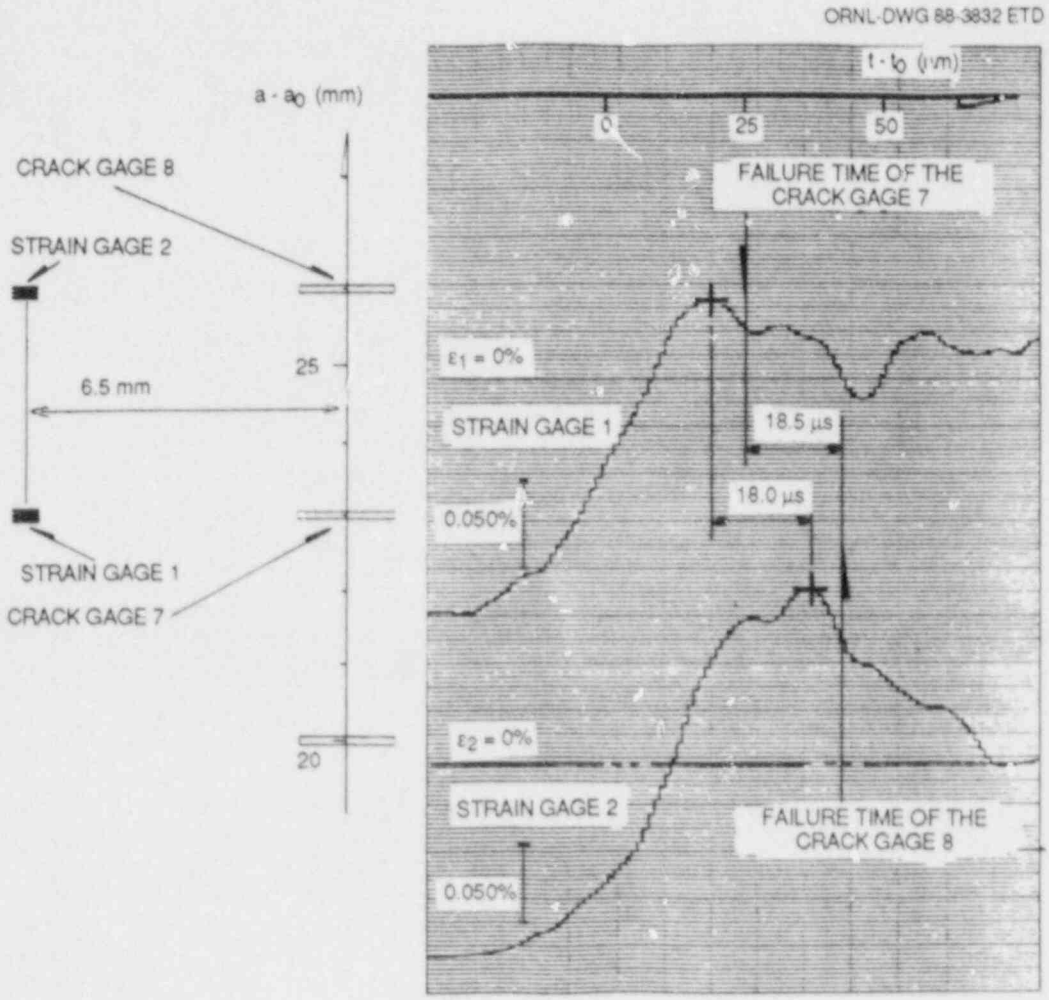

Fig. 2.27. Dynamic strain records of two axial strain gages located at levels of crack gages 7 and 8.

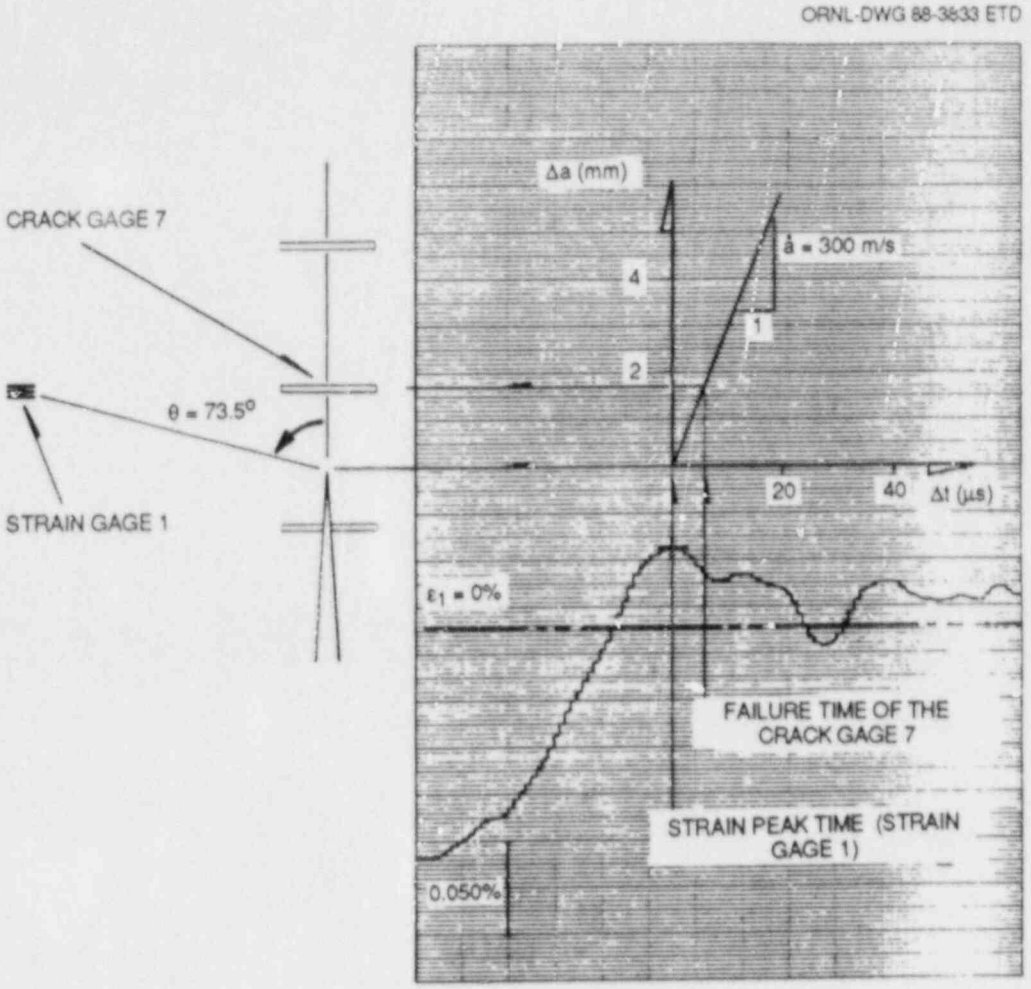

Fig. 2.28. Dynamic strain record of axial strain gage located at level of crack gage 7.

2.5 Fracture-Mechanics Studies at the University of Maryland*

W. L. Fourney† C. W. Schwartz‡
G. R. Irwin† D. B. Barker†
J. W. Dally† X. J. Zhang†

The work conducted by UM in this report period included studies of cleavage-fibrous transition behavior in reactor vessel steels and of dynamic crack initiation in notched bars. Progress achieved in each topic will be briefly reviewed in the following sections.

2.5.1 Cleavage-fibrous transition behaviors

In nuclear pressure vessel steels, cleavage initiation and loss of cleavage behaviors are closely linked to nonuniformities of microstructure and to variations of local deformation across a broad range of dimensional size. Carbide banding represents a relatively large-scale nonuniformity feature. The influence of this feature upon scatter of fracture-toughness values was explored by comparing Charpy V-notch (CVN) test values for a sample of heavy-section A 508 material with those for the same material after the banding inhomogeneity had been reduced by a homogenizing treatment. The original heavy-section A 508 plates had been quenched from 900°C into water and tempered at 613°C for 4 h before they were delivered to the University of Maryland (UM). A 2-cm-thick slice of the material was homogenized at 1100°C for 48 h and followed by the same quenching and tempering treatment performed for the original material. Figure 2.29 shows a typical region of carbide density banding before the homogenizing treatment. Figure 2.29(*b*) indicates the substantial degree of carbide density uniformity achieved by homogenizing. Figure 2.30 shows the comparison of CVN toughness values as a function of testing temperature. The expected result was a reduction of scatter of the CVN results. Although the scale of the experiment permitted only a limited number of CVN measurements, the CVN results for the homogenized material conform closely to a smooth trend curve with very little scatter. Because of the small size of the homogenized specimen block (2 cm thick), the subsequent heat treatment resulted in a yield strength of 978 MPa (145 ksi), which is substantially higher than the yield strength of the original A 508 material, 620 MPa (90 ksi). The failure of the homogenized specimens to achieve high toughness values at loss-of-cleavage temperature can be reasonably ascribed to the elevation of yield strength.

---

*Work sponsored by the HSST Program under Subcontract No. 7778 between Martin Marietta Energy Systems, Inc., and the University of Maryland.

†Department of Mechanical Engineering, University of Maryland, College Park.

‡Department of Civil Engineering, University of Maryland, College Park.

ORNL PHOTO 0122-88

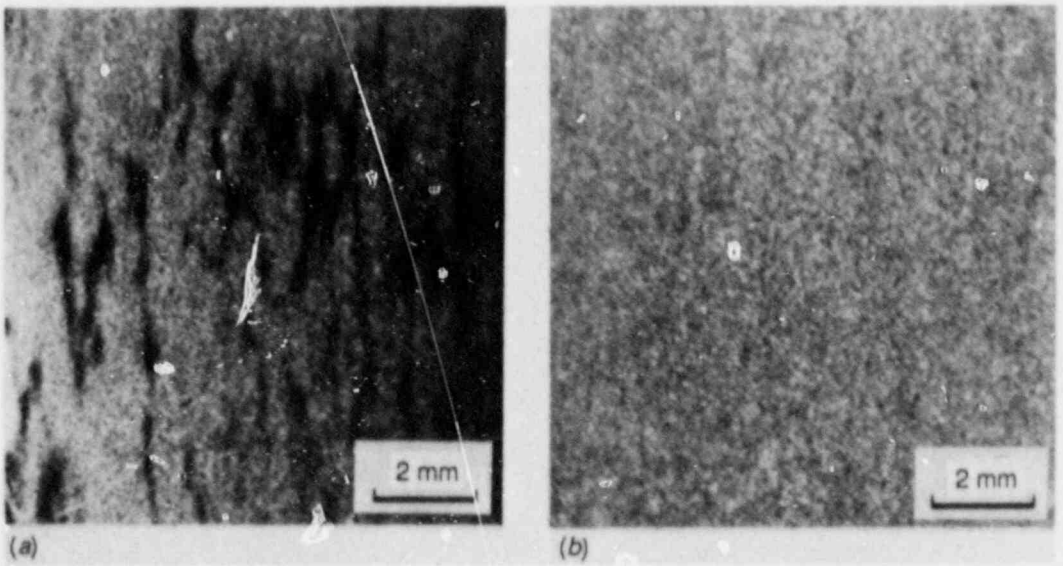

Fig. 2.29. Comparison of carbide banding structures in original A 508 material and in homogenized A 508 material. (*a*) Original material (large-section thickness) was quenched from 900°C and tempered at 613°C for 4 h, (*b*) homogenized material (2-cm-thick plate) was homogenized at 1100°C for 48 h, followed by water quench from 900°C and same tempering treatment used for original material.

ORNL-DWG 88-3834 ETD

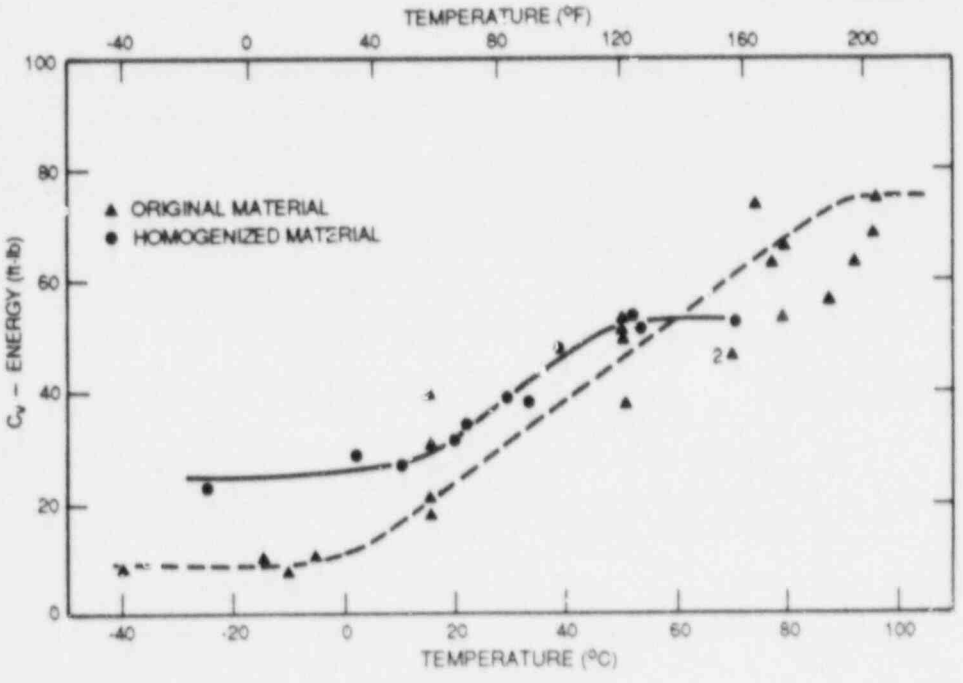

Fig. 2.30. CVN energy loss results for A 508 steel before and after reduction of carbide banding by homogenizing treatment that elevated yield strength.

An influence of homogenizing upon the sulphide inclusions was neither expected nor observed. Figure 2.31 shows a comparison of typical sulphide inclusion regions in the original A 508 material and in a homogenized specimen. The influence of homogenizing and of the subsequent heat treatment upon the microstructures and the carbides was substantial. The microstructures of dark banding regions and light banding regions in the original material contain tempered martensite and tempered bainite, a fact presented in a previous report.[41] Figure 2.32 shows that the homogenized material has a rather uniform tempered martensite appearance.

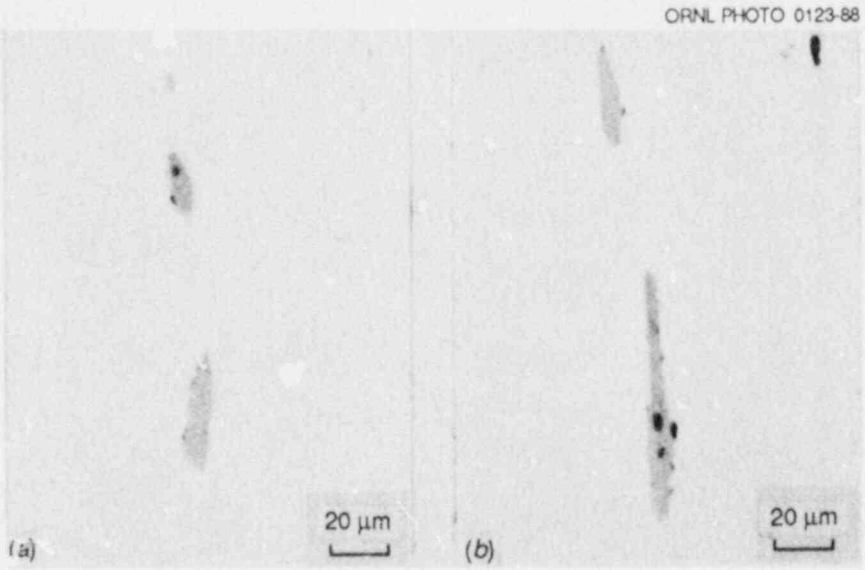

Fig. 2.31. Comparison of typical sulphide inclusions. (*a*) Original A 508 material, (*b*) homogenized specimen.

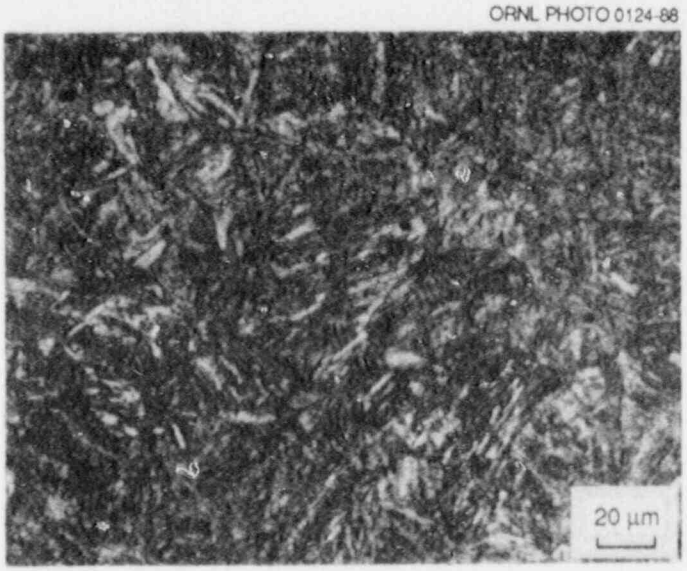

Fig. 2.32. Optical micrograph of tempered martensite structure in homogenized A 508 sample.

Figure 2.33 shows TEM micrographs of two different carbide morphologies obtained in this manner. In the original A 508 [Fig. 2.33(*a*)], thin-foil TEM micrographs show that the carbides tend to form into small plates with crystallographic alignment. This is particularly evident in the ferrite grains of relatively large size. In some regions, particularly in small ferrite grains, the carbides form into small, rounded particles.

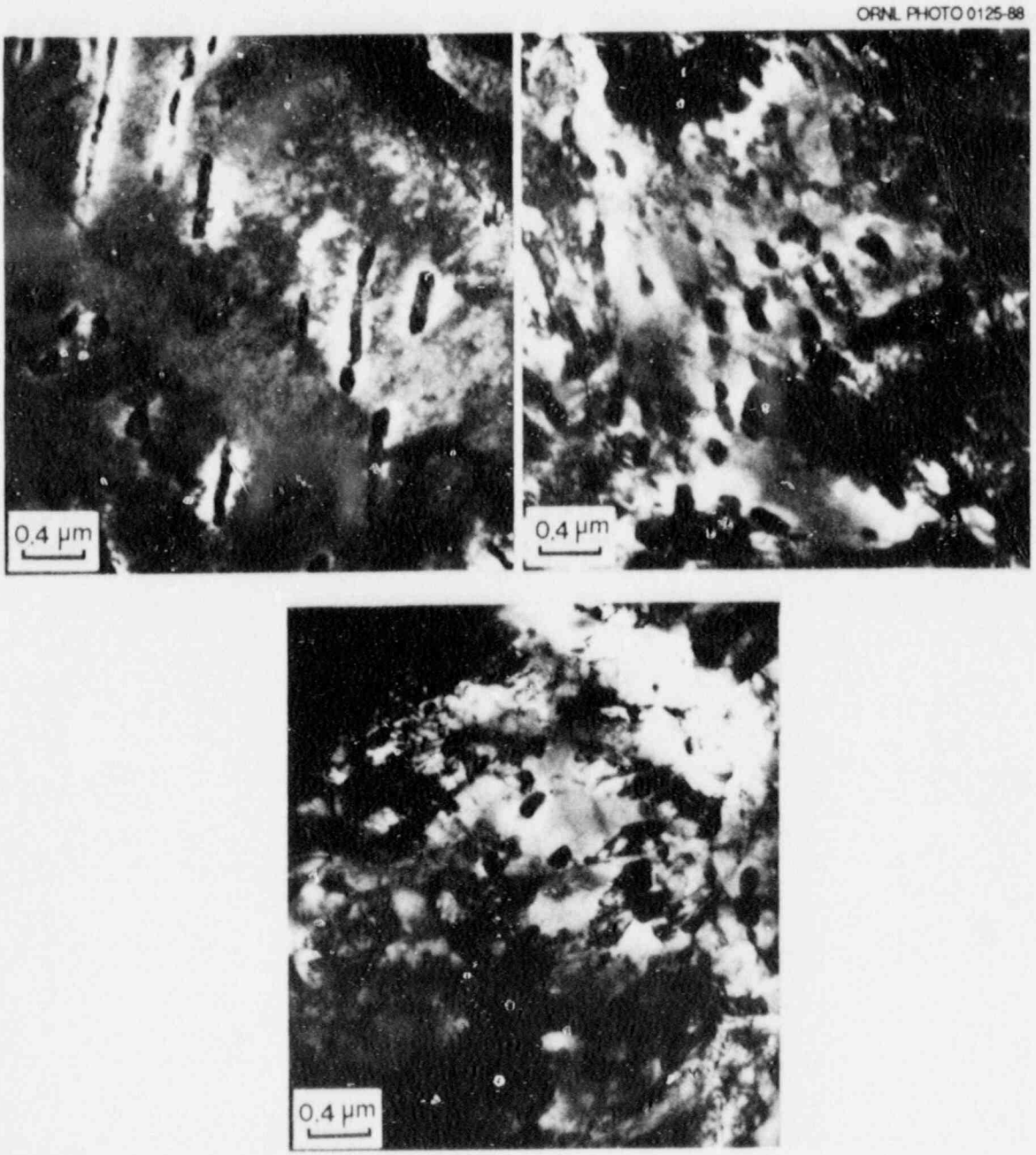

Fig. 2.33. Thin-foil TEM micrographs of carbide morphologies in A 508 material. (*a*) Original material, (*b*) homogenized sample.

Thus, the microstructure varies between tempered bainite and tempered martensite, producing substantial differences of local region brittleness. In the homogenized material [Fig. 2.33(*b*)] the carbides are almost entirely small, rounded particles of the type expected in tempered martensite. These microstructural changes affected the fracture mechanism of the material. An atypical cleavage fracture appearance, called "quasi-cleavage fracture," dominates the fracture mechanism within the cleavage region on the fractured surface of homogenized material (Fig. 2.34). Further fractographic study on the homogenized material is in progress.

For the weld metals that have been studied, the most significant nonuniformities are thought to be local variations of inclusion density and of ferrite grain size. From observations of cleavage initiation adjacent fractured silicate particles, it was noted that the particle size was consistently in the range of 2 to 3 μm. Why larger particles, which are numerous, did not fracture and initiate cleavage is not clear. X-ray emissions from silicate particles of various sizes were examined with regard to particle composition. It was found that there is a moderate trend for the indication of calcium content to increase with particle size (Fig. 2.35). This can be noted as a possible aid toward clarification.

Among the conditions that may interfere with spreading of cleavage after initiation, the ability of cleavage to achieve passage through grain boundaries is a significant aspect. Some information of interest in regard to this was obtained by topographic studies of the change of crystalline orientation where cleavage was observed to achieve passage through a grain boundary.

ORNL PHOTO 0126-88

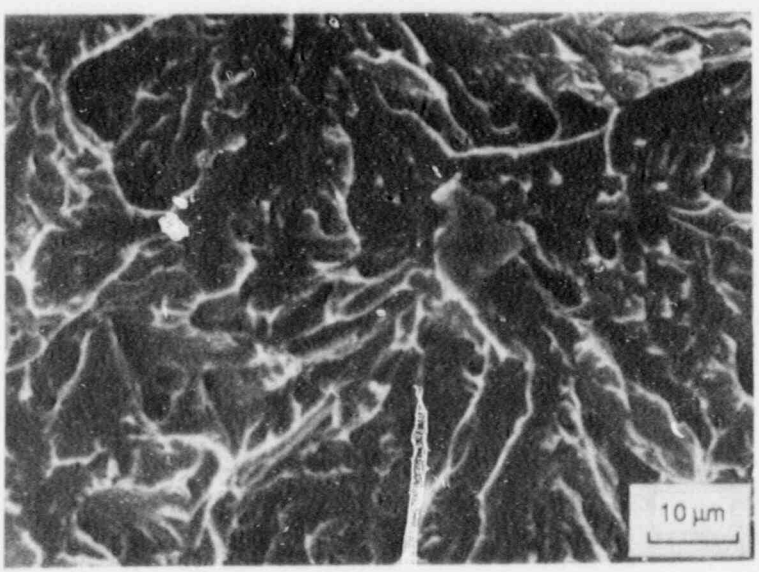

Fig. 2.34. SEM micrograph of quasi-cleavage fracture in homogenized A 508 sample.

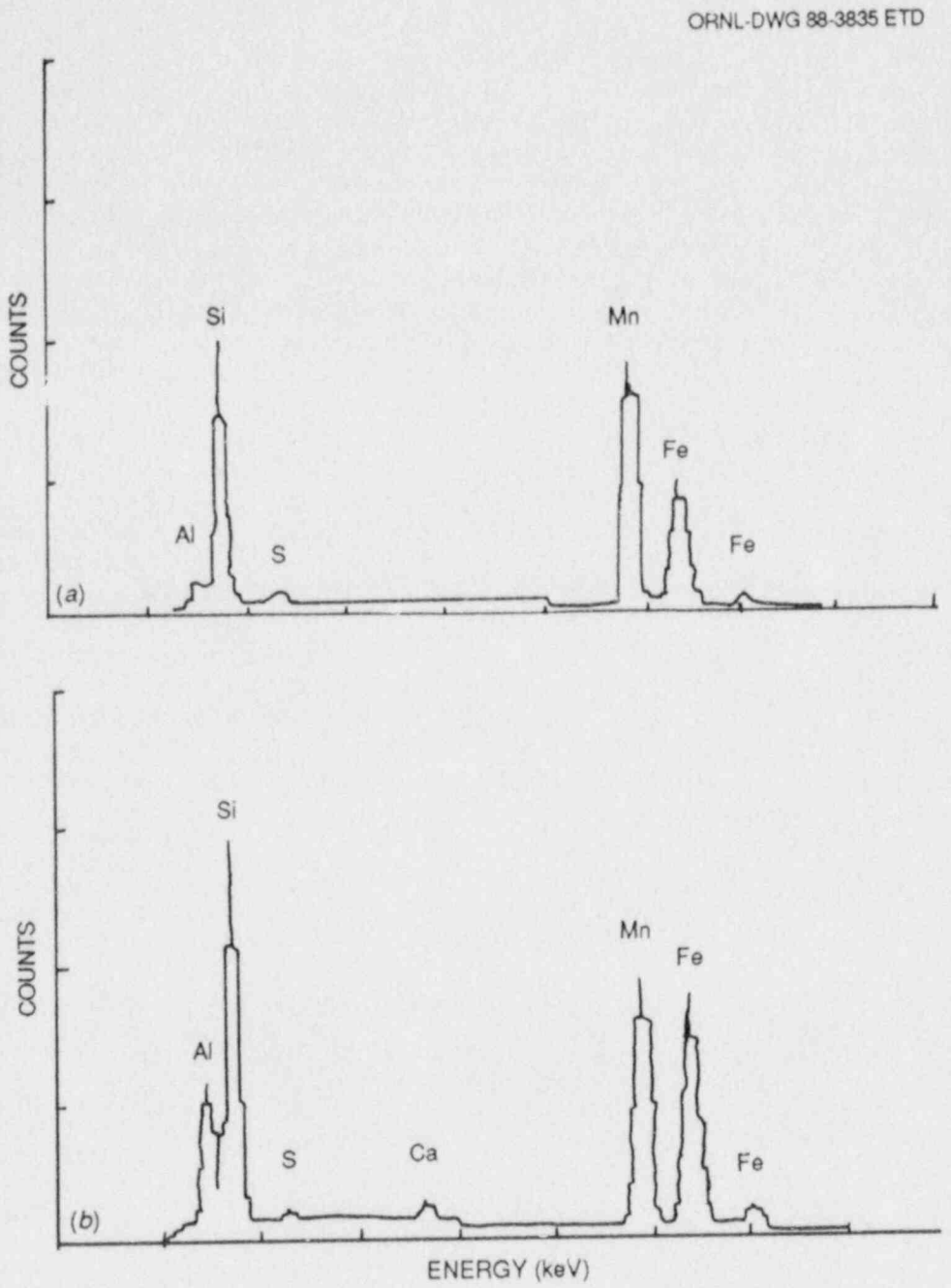

Fig. 2.35. X-ray spectral analysis results for (*a*) small, and (*b*) large silicate inclusions.

Several isolated cleavage regions, observed at shelf temperature with weld metal, were reexamined using stereo scanning electron microscopy (SEM) to determine the change of angle of the normal to the cleavage surface of the adjacent ferrite grains traversed by the cleavage. The results were further analyzed to determine the components of "tilt" (in the direction of cleavage extension) and of "twist" (rotation about the

direction of cleavage extension). This experiment was then repeated using similar-sized areas of grain boundary passage on a fracture of the same weld metal at liquid air temperature. For the high temperature, the angles of twist were consistently small. The angles of tilt were larger but generally <20°. For the low-temperature fracture, both angles were significantly of larger average size. These results will be available soon in a technical paper for an October 1987 American Society for Metals meeting.

With regard to a comprehensive report on the topic of this investigation, the major descriptive aspects have not changed appreciably from the account given in Ref. 42. The current difficulty in completing the comprehensive report is the desire to include illustrative analytical modeling of cleavage behaviors in the transition range. A satisfactory method for modeling in a significantly property-dependent manner is still not clear.

2.5.2 Dynamic crack initiation

Work on dynamic crack initiation has followed two different lines of investigation: notched short-bar experiments and notched round-bar experiments. Progress made to date in both of these areas will be described.

2.5.2.1 Notched short-bar experiments. Earlier work was completed to establish the feasibility of the notched short bar as a new specimen for dynamic initiation studies. This feasibility study demonstrated that either photoelasticity or strain gages could be employed to measure K_I at initiation. The loading of the short bar with its integral dog-bone ends was accomplished with four explosive charges that were detonated simultaneously. Tensile stress waves produced at both ends of the bar propagated to the central region of the bar where they combined to produce a rapidly increasing K field that initiates a stationary crack. The crack initiates before the arrival of the shear wave.

The current effort with the short-bar specimen involves specimens fabricated from 12.7-mm-thick (0.5-in.) 4340 steel hardened to Rc = 51. Fatigue-sharpened cracks 17.5 mm (0.6875 in.) long were used as initiators. Two strain gages were deployed near the crack tip to sense K_I, and two additional gages were mounted in the bar section to monitor the incident stress waves. Loading was accomplished with boosted detonators coupled to data sheet. Each of the four charges weighed 3.95 g, giving a total charge of 15.8 g.

The first test indicated that symmetric loading was achieved as the ears separated with near-perfect symmetry and the central crack extended straight across the midsection of the bar. Indeed, the extensive damage at the ears indicate that the charge weight was higher than necessary. A photograph showing the specimen shape before and after failure is presented in Fig. 2.36.

The fracture surfaces are illustrated in Fig. 2.37 and indicate cleavage-type propagation with evidence of only very small shear lips. The crack propagated about 13 mm and arrested. The fracture surface shows signs of several arrests with reinitiation.

Strain-gage traces were obtained from all four gages, indicating that the electronic noise associated with the detonation decayed before

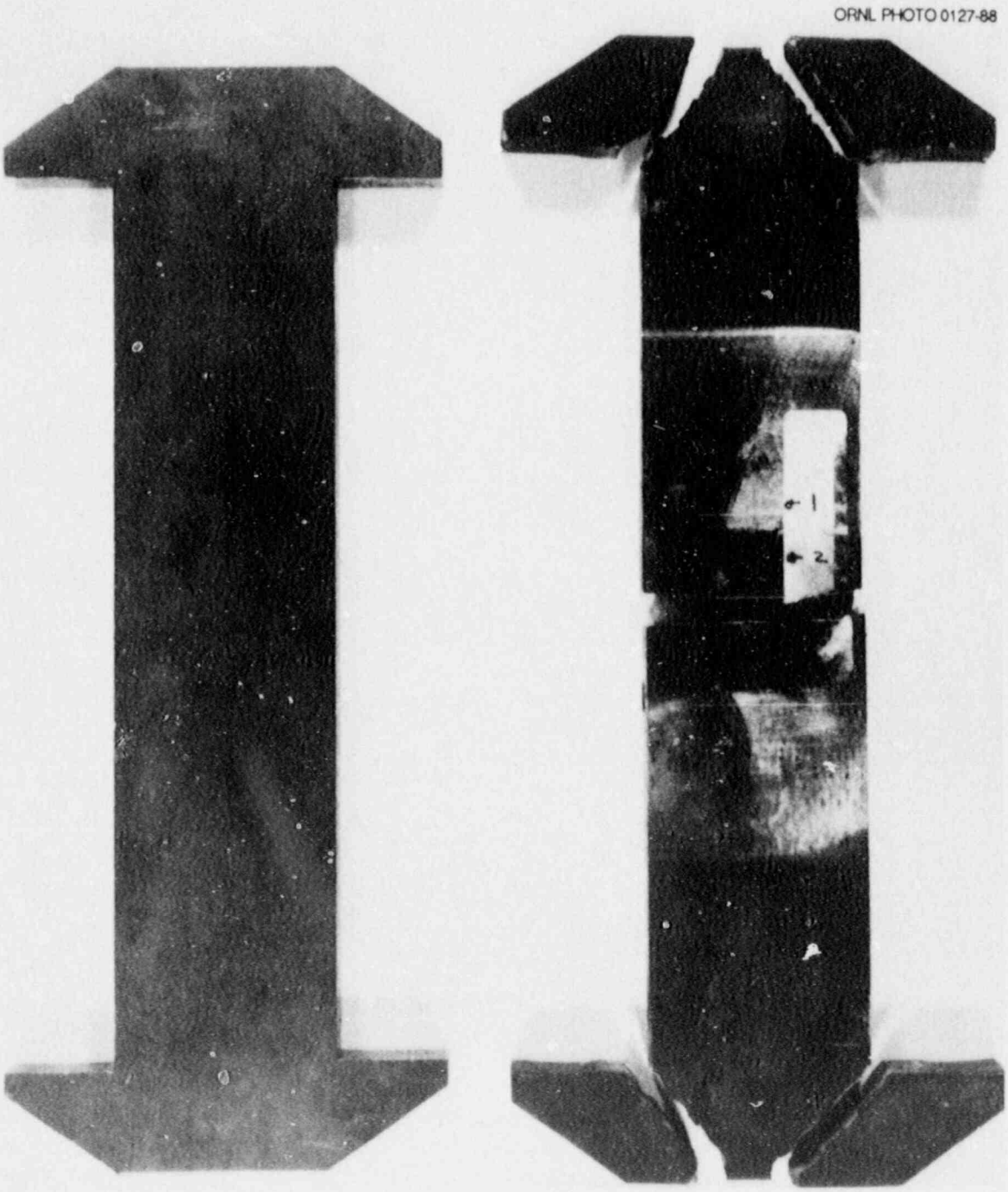

Fig. 2.36. Short-bar specimen before and after explosively induced fracture.

ORNL PHOTO 0128-88

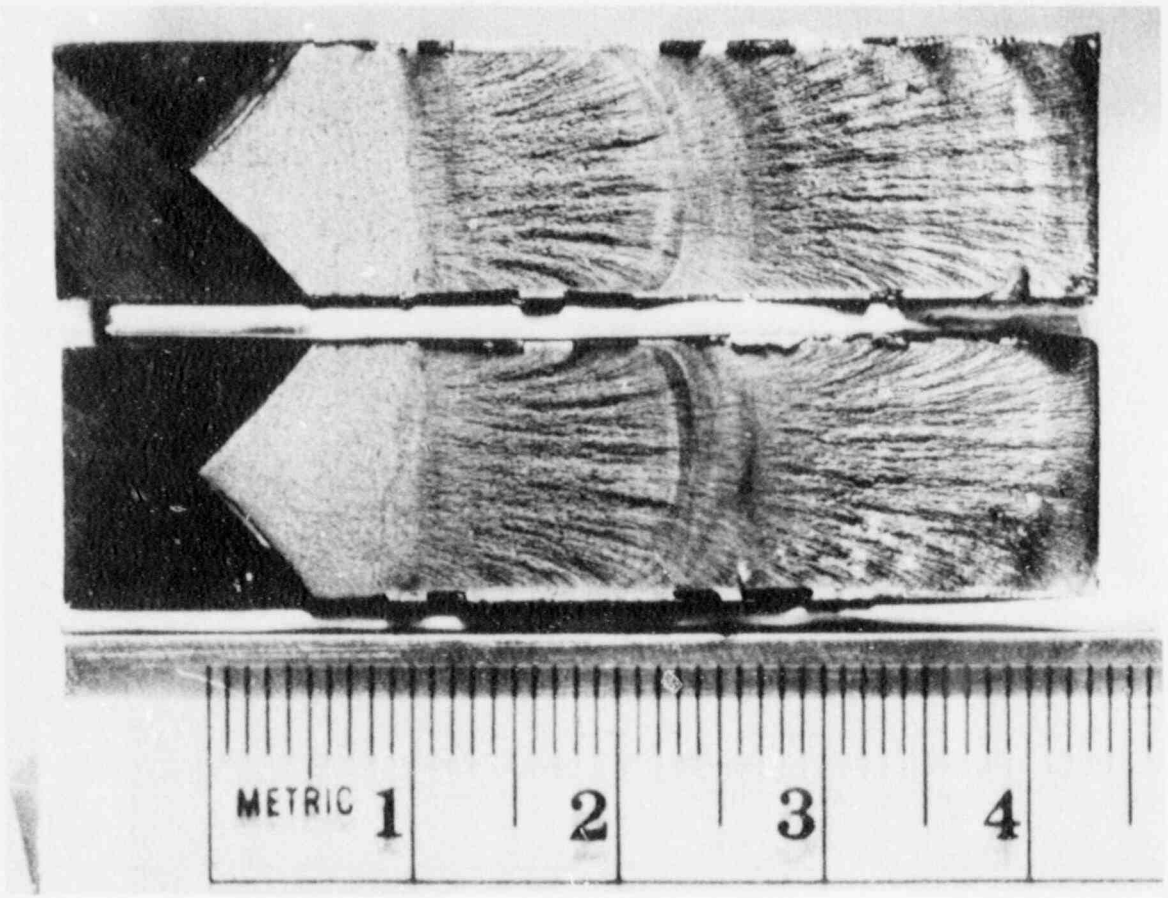

Fig. 2.37. Fracture surface for 4340 short-bar specimen.

the arrival of the stress wave. Unfortunately, the sensitivity of the strain amplifiers used was not adjusted to the proper setting, and the strain-gage records were off scale. For this reason, dynamic initiation toughness and the rate of loading dK/dt achieved in the experiment cannot be reported at this time.

Future work will involve more experiments of this type. Four additional specimens with 203-mm-long (8-in.) central bar regions have been machined. Experiments will be conducted with these specimens, initially holding the hardness at Rc = 51 and reducing the explosive charge. In later tests specimens with lower hardness will be investigated; also, the length of the bar will be increased. This added length will provide more time for the detonation signal to decay and give more room to protect the lead wires from the blast waves produced by the explosives. It is also planned to test welded specimens where the center section of the bar is welded into more or less permanent ends. This will conserve test material and will reduce machining costs by permitting straight bar segments to be employed.

2.5.2.2 Notched round-bar specimens. The purpose of employing notched round-bar experiments for dynamic fracture initiation is an

attempt to simulate the effects of constraint of a very thick specimen with a relatively small round bar. The cylindrical shape of the bar should increase the effective thickness of the specimen by a factor of ~3.

The first requirement in this study was to develop a loading system that would apply impact loading to round-bar specimens ~38.1 mm (1.5 in.) in diameter. Accordingly, a drop-weight system was designed and constructed (Fig. 2.38). This loading system is capable of delivering 1051 J (775 ft-lb) of energy when the weight of 58.8 kg (129.4 lb) drops through a distance of 1.83 m (6 ft). The weight strikes a hardened steel tube that transmits the impact force to the anvil at the bottom of the delivery rod. The test specimen is fastened to the delivery tube and the anvil with a 25.4-mm-diam UNC thread. The bottom of the impacting weight, the transmission tube, and the anvil are all fabricated from 4340 hardened steel to reduce the impact time.

The specimen configuration used in testing is shown in Fig. 2.39. The outside diameter of the round bar is 38.1 mm (1.5 in.), and the diameter of the machined notch is 19.1 mm (0.75 in.). The notch was machined with an overly sharp Charpy notch-cutting tool with a notch tip radius of 0.127 mm (0.005 in.). The specimen was shouldered to facilitate alignment of the specimen during the assembly operation and ensure axial impact conditions.

The initial experiments were made with strain-gaged specimens: three gages were placed at 120° intervals around the specimen below the notch, and three additional gages were positioned about the circumference above the notch. Results from these strain-gage studies indicate that a full height drop of 1778 mm produces a strain of 0.001 in 60 μs, which is equivalent to a strain rate of 16.7 s^{-1}. The symmetry of the loading was excellent, showing that the alignment features incorporated into the design of the load frame and the specimen are effective. Also, the strain-time trace taken above and below the notch were essentially identical, indicating that stress-wave effects in the specimen were minimized.

A total of nine specimens have been machined from A 508 steel. One of these specimens has been used in characterizing the dynamic response of the impact loading system. The others will be tested to determine the fracture initiation toughness of A 508 steel as a function of temperature over the transition range for this material.

2.6 Viscoplastic Stress-Strain Characterization of A 533 Grade B Class 1 Steel*

J. H. Giovanola† R. W. Klopp†

The HSST Program is currently involved in a research effort to develop rate- and temperature-sensitive constitutive equations for A 533 grade B class 1 pressure vessel steel. These constitutive equations will

*Work sponsored by the HSST Program under Subcontract No. 32X-5A193V between Martin Marietta Energy Systems, Inc., and SRI International.

†SRI International, Menlo Park, California.

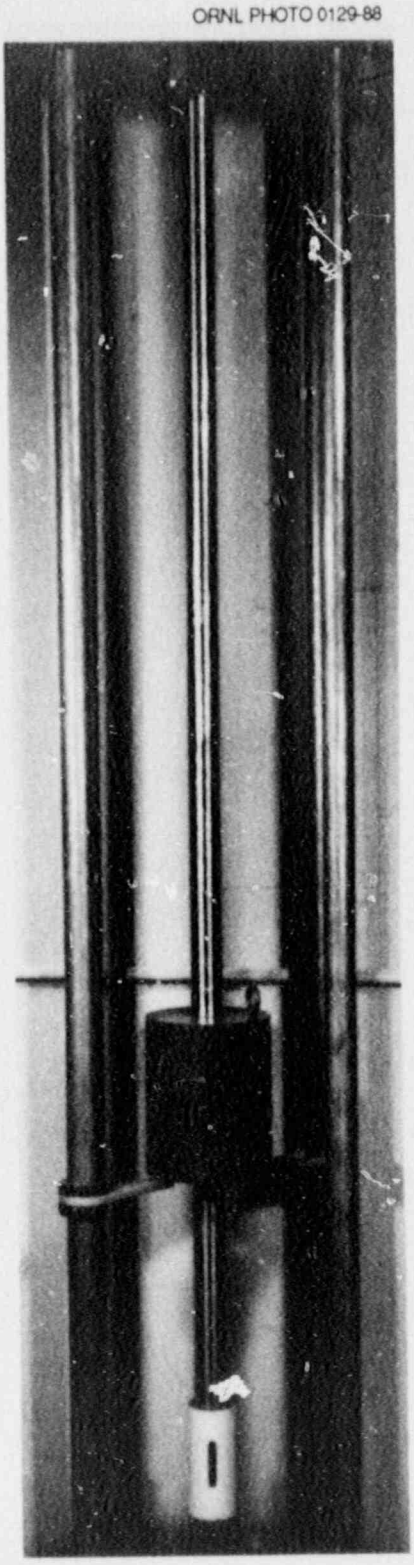

Fig. 2.38. Photograph of impact loading fixture used with notched round bars.

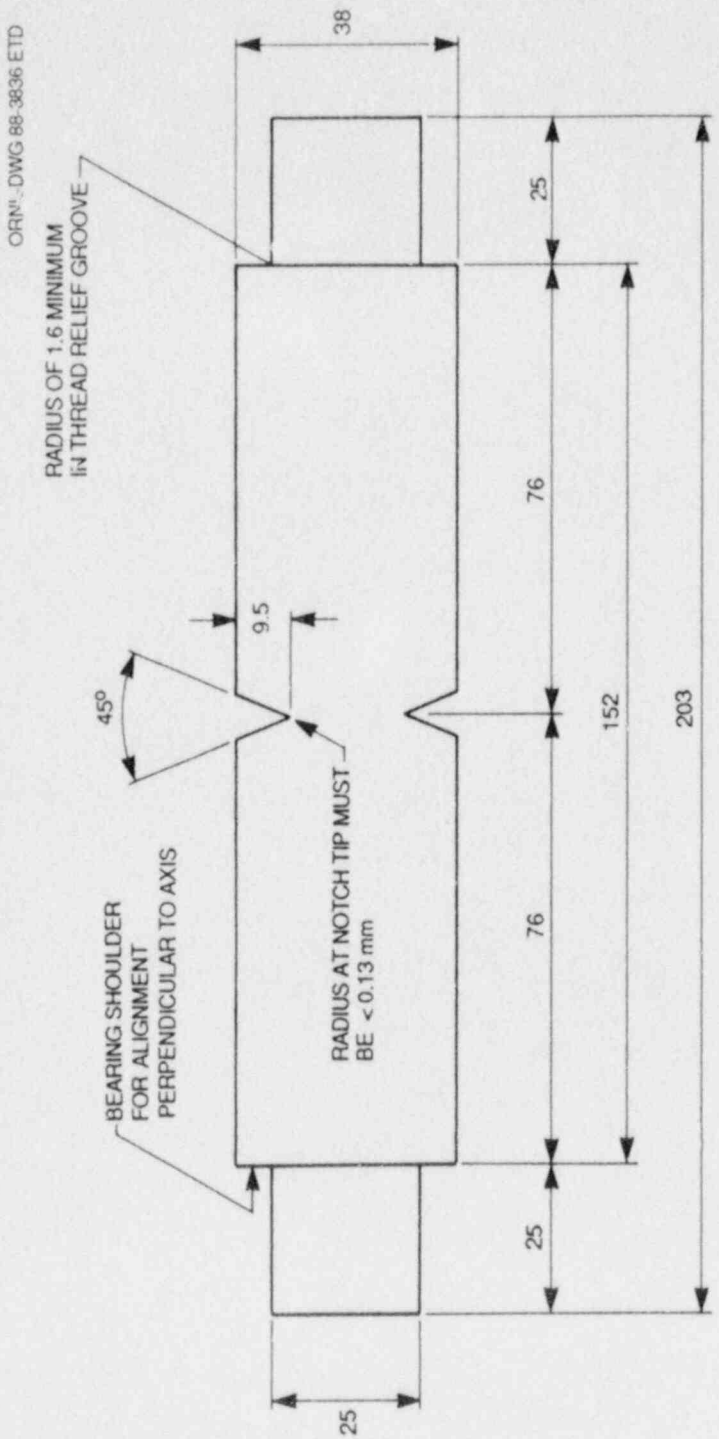

Fig. 2.39. Geometry of notched round-bar specimen.

be used in conjunction with numerical simulations and dynamic fracture analyses to assess the effect of viscoplastic material behavior on cleavage crack propagation and arrest in reactor pressure vessel steels. To help evaluate candidate viscoplastic constitutive models for A 533 grade B class 1 steel and to augment the available data base, SRI International performed 15 split Hopkinson torsion bar experiments at engineering shear strain rates ranging from 400 to 3000 s^{-1} and at temperatures of −60, 20, and 150°C. A final report[43] documenting these experiments has been prepared by SRI International and transmitted to ORNL. A summary of a portion of the results is given in the following sections of this report.

2.6.1 Experimental setup and test procedure

The high-strain-rate torsional tests, performed by SRI International, used a split Hopkinson torsion bar consisting of an input and output bar with a specimen placed between the bars (Fig. 2.40). The specimen is deformed during the test by the sudden release of a static torque applied at the end of the bar by means of a hydraulic wrench; the torque is stored in a section of the input bar between a fixed clamp at the far end of the input bar and a movable release clamp. The location of the release clamp can be varied to adjust the total strain input to the specimen. Strain rate can be varied by adjusting the specimen diameter and gage length or, more effectively, by adjusting the magnitude of the

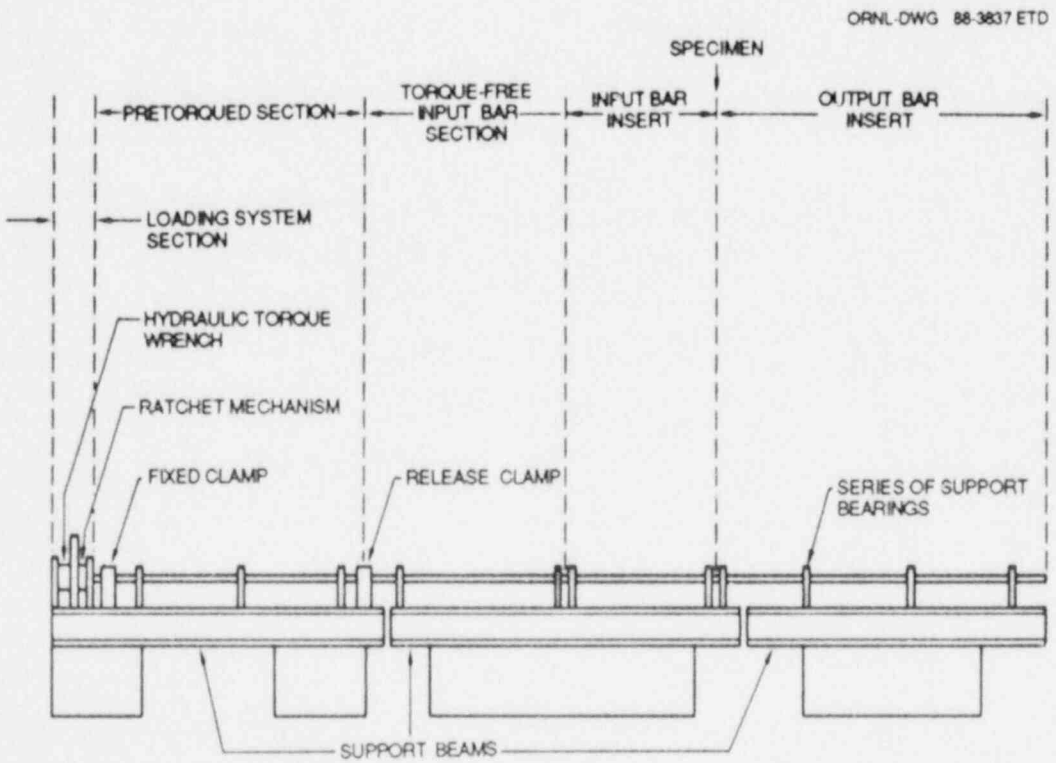

Fig. 2.40. Split Hopkinson torsion bar used by SRI in high-strain-rate experiments on A 533 grade B class 1 steel.

stored input torque. Strain gages are mounted on the input and output bars to record the incident and the reflected and transmitted stress waves. A stress-strain curve is obtained from the analysis of these strain-gage records by using 1-D elastic wave theory.

The material used in these high strain-rate tests was an A 533 grade B class 1 steel supplied by ORNL. The test material was taken from HSST plate 13A, which was the same source plate for the WP-1 series[4] of wide-plate specimens and for strain-rate specimens previously tested by SwRI.[27] A total of 15 specimens were prepared by SRI International for testing.

Fifteen experiments were performed at −60, 20, and 150°C and at nominal engineering shear strain rates of 400, 1500, and 3000 s^{-1}. The experiments at 400 and 3000 s^{-1} strain rates were duplicated; however, only single experiments were performed at a strain rate of 1500 s^{-1}. These latter experiments were not originally planned but were included to provide intermediate data points and to utilize spare specimens. With this choice of strain rates, data that could be compared with the previously available high-rate data for A 533 grade B steel were obtained.[27]

2.6.2 Summary of results

A portion of the results of the SRI Hopkinson torsion bar experiments are summarized in Figs. 2.41–2.46 and in Table 2.3. Figures 2.41 and 2.42 are composite figures showing the effect of strain rate on the

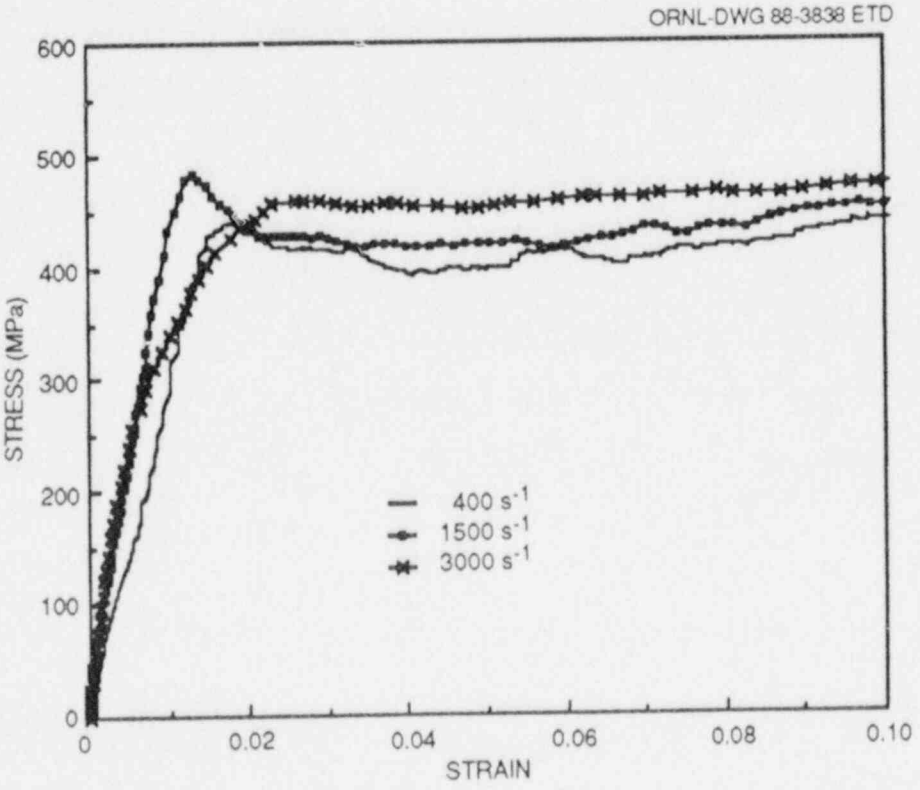

Fig. 2.41. Influence of strain rate on shear stress-shear strain curve for A 533 grade B class 1 steel at −60°C.

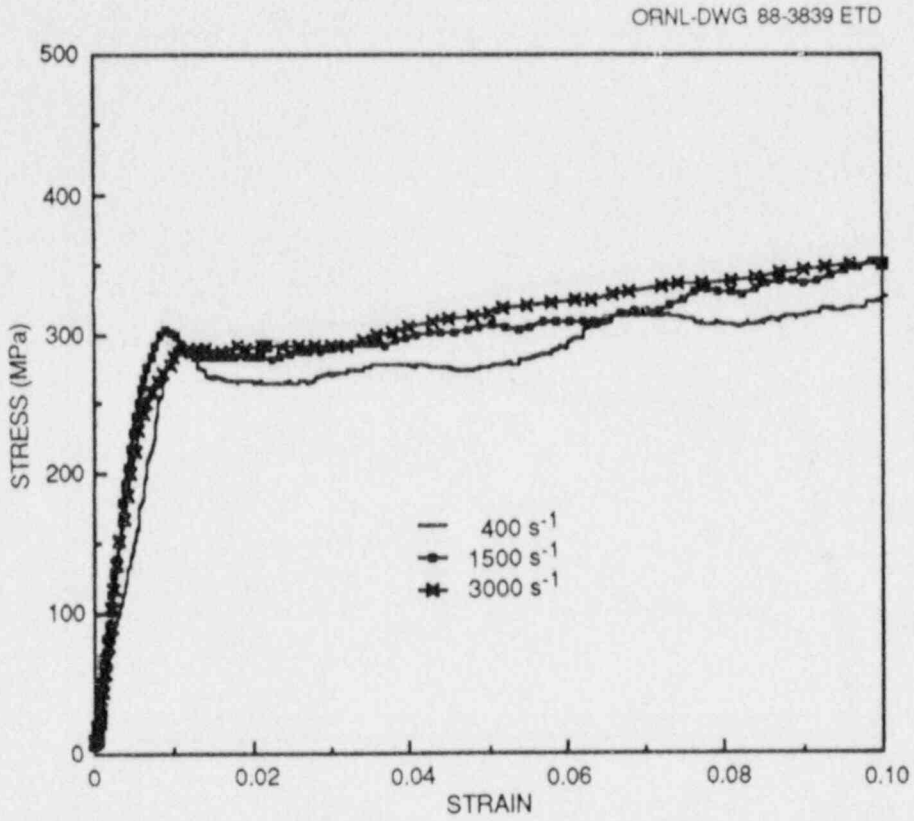

Fig. 2.42. Influence of strain rate on shear stress-shear strain curve for A 533 grade B class 1 steel at 150°C.

Table 2.3. Summary of flow stress data for A 533 grade B class 1 steel used in SRI high-strain rate tests

Strain rate (s^{-1})	Flow stress (MPa)		Failure strain
	At 0.05 strain	At 0.4 strain	
	Test temperature −60°C		
400	398	498	No failure
1500	422	517	1.22
3000	455	540	0.98/0.80
	Test temperature 20°C		
Static	235[a]	323[b]	
400	331	458	No failure
1500	349	461	1.28
3000	366	477	1.48/1.19
	Test temperature 150°C		
400	277	390	No failure
1500	305	416	No failure
3000	315	422	2.20/2.10

[a]Converted from tensile yield strength.

[b]Converted from ultimate tensile strength.

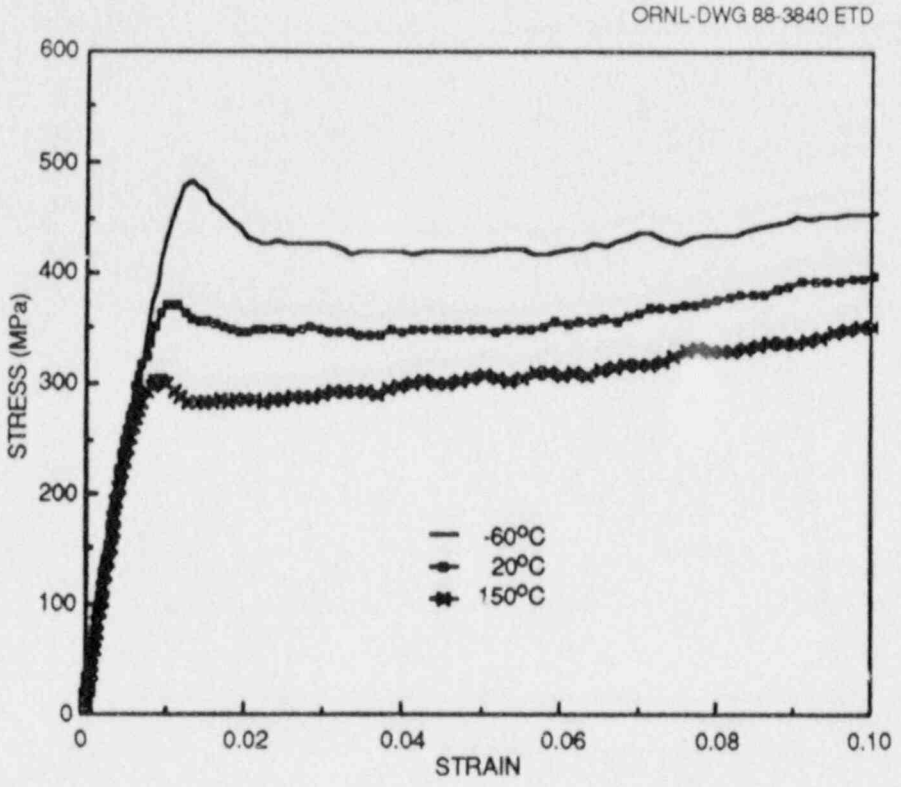

Fig. 2.43. Influence of temperature on shear stress-shear strain curve for A 533 grade B class 1 steel at 1500-s^{-1} strain rate.

flow curve at −60 and 150°C, respectively. Figures 2.43 and 2.44 are similar figures showing the effect of temperature on the flow curve at strain rates 1500 and 3000 s^{-1}, respectively. Table 2.3 compares the value of the flow stress at two fixed strain values, 0.05 and 0.4, for the three strain rates and the three temperatures investigated. The failure strains are also listed in Table 2.3. Finally, for comparison Table 2.3 also lists the room-temperature static yield strength and ultimate strength provided by ORNL and converted to equivalent shear stress values.

The data in Figs. 2.41 and 2.42 and in Table 2.3 show that at all strain rates, the temperature has a significant effect on the flow curve of A 533 grade B class 1 steel. Moreover, at all temperatures, the strain rate has a less-pronounced, yet clearly measurable effect on the flow curve in the relatively narrow strain-rate range investigated here. Another significant observation is that at all temperatures and strain rates, an identifiable yield-point phenomenon occurs with upper and lower yield points. In the 400-s^{-1} strain-rate experiments, the specimens were unloaded by the relief edge of the incident wave at ~50% strain and did not fail. For the two other strain rates, failure strains were all well above 50% (Table 2.3).

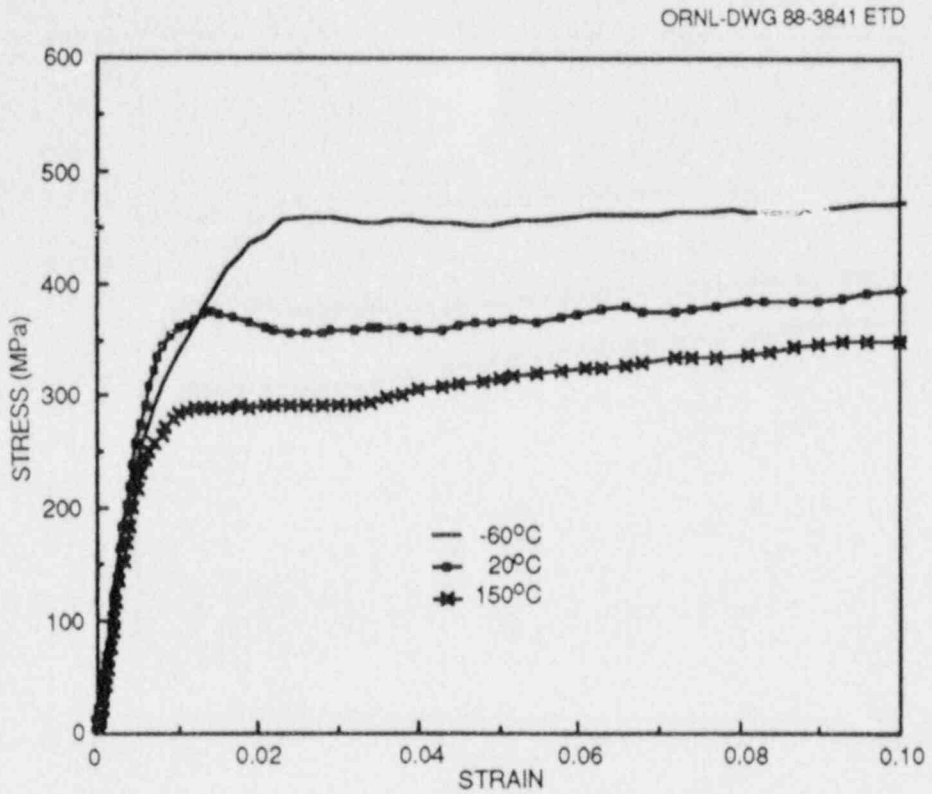

Fig. 2.44. Influence of temperature on shear stress-shear strain curve A 533 grade B class 1 steel at 3000-s^{-1} strain rate.

The torsion data generated at −60 and 150°C are compared in Figs. 2.45 and 2.46, respectively, with the tensile data[27] obtained previously by SwRI. A von Mises type conversion has been used in transforming the tensile data to equivalent torsion data; that is, the tensile stresses have been divided by $\sqrt{3}$ and the tensile strains have been multiplied by $\sqrt{3}$. The agreement between the two sets of results is good, given the difference in the geometry of the experiments. Noticeable differences between the torsion data and the tensile data are the lack of a yield-point phenomenon and the lower failure strains in the tensile experiments. The latter may be attributed to the geometrical differences, in particular the formation of a neck in the tensile experiments, which raises the tensile hydrostatic component of stress and, thus, favors the onset of fracture. However, no explanation is offered for the different yield-point behavior.

Higher strain-rate data can be obtained in the future by using a different specimen geometry for the Hopkinson torsion bar experiments, by performing rod impact experiments, or by performing pressure-shear impact experiments.[44] The rod impact experiment can also be used to evaluate various viscoplastic constitutive models at strain rates approaching those expected near a rapidly propagating cleavage crack (e.g., Ref. 45).

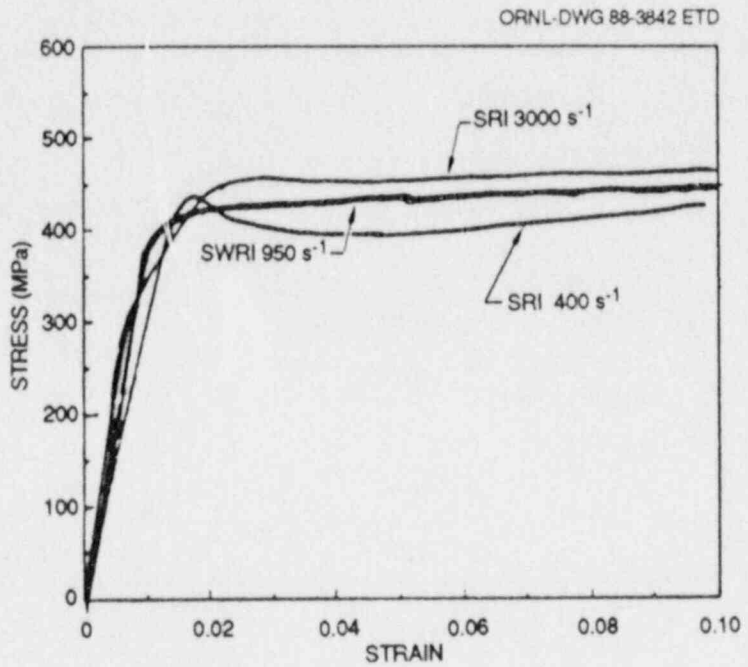

Fig. 2.45. Comparison of high-rate data generated by SwRI (tensile data converted to equivalent shear data) with data generated by SRI (temperature = −60°C).

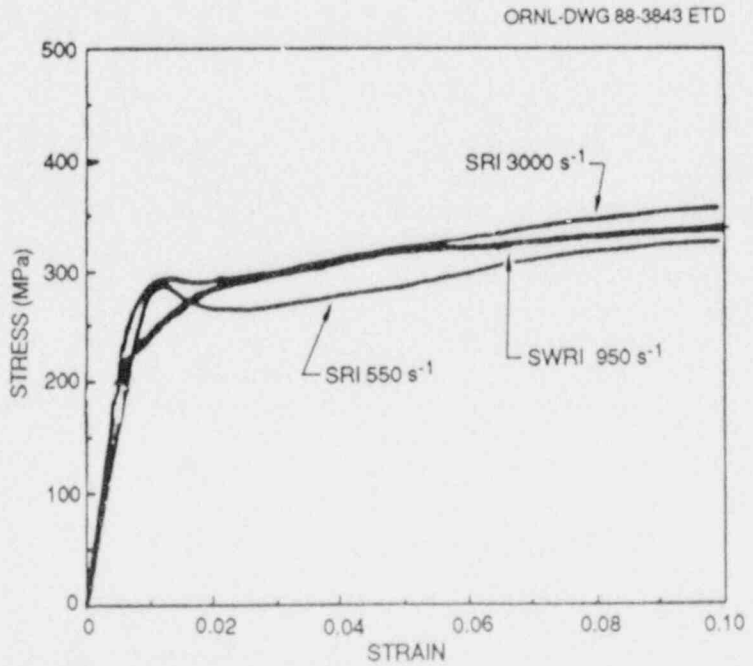

Fig. 2.46. Comparison of high-rate data generated by SwRI (tensile data converted to equivalent shear data) with data generated by SRI (temperature = 150°C).

References

1. R. D. Cheverton et al., "Fracture Mechanics Data Deduced from Thermal-Shock and Related Experiments with LWR Pressure Vessel Material," *J. Pressure Vessel Tech.* 105, 102–10 (May 1983).

2. R. H. Bryan et al., "The Heavy-Section Steel Technology Pressurized-Thermal Shock Experiment, PTSE-1," *Eng. Fract. Mech.* 23(1), 81–97, (1986).

3. R. H. Bryan et al., *Pressurized-Thermal-Shock Test of 6-in.-Thick Pressure Vessels. PTSE-2: Investigation of Low Tearing Resistance and Warm Prestressing*, NUREG/CR-4888 (ORNL-6377), Martin Marietta Energy Systems, Inc., Oak Ridge Natl. Lab., to be published.

4. D. J. Naus et al., *Crack Arrest Behavior in SEN Wide Plates of Quenched and Tempered A533B Steel Tested under Nonisothermal Conditions*, NUREG/CR-4930 (ORNL-6388), Martin Marietta Energy Systems, Inc., Oak Ridge Natl. Lab., September 1987.

5. B. R. Bass et al., "Fracture Analyses of Heavy-Section Steel Technology Wide-Plate Crack-Arrest Experiments," *Proc. 19th Natl. Symp. on Fracture Mechanics, San Antonio, TX, June 30–July 2, 1986.*

6. C. E. Pugh et al., "Crack Run-Arrest Behavior in Wide SEN Plates of a LWR Pressure Vessel Material," Vol. G, pp. 21–26 in *Transactions of the 9th International Conference on Structural Mechanics in Reactor Technology, Lausanne, Switzerland, Aug. 17–21, 1987.*

7. H. K. Stamm, "Analysis of a Panel Crack-Arrest Specimen," pp. 9–17 in *Heavy-Section Steel Technology Program Semiann. Prog. Rep. April–September 1984*, NUREG/CR-3744, Vol. 2 (ORNL/TM-9154/V2), Martin Marietta Energy Systems, Inc., Oak Ridge Natl. Lab.

8. B. R. Bass, H. K. Stamm, and C. E. Pugh, "Fracture Analysis of a Small Panel Crack-Arrest Specimen," pp. 11–18 in *Heavy-Section Steel Technology Program Semiann. Prog. Rep. October 1984–March 1985*, NUREG/CR-4219, Vol. 1 (ORNL/TM-9593/V1), Martin Marietta Energy Systems, Inc., Oak Ridge Natl. Lab., June 1985.

9. H. K. Stamm, B. R. Bass, and C. E. Pugh, "Dynamic Analysis of a Crack-Arrest Specimen," *Nucl. Eng. Des.* 96, 255–68 (1986).

10. B. R. Bass, C. E. Pugh, and H. K. Stamm, "Dynamic Analyses of a Crack Run-Arrest Experiment in a Nonisothermal Plate," *Pressure Vessel Components Design and Analysis* 4, ASME PVP Vol. 98-2, 175–84 (1985).

11. S. J. Hudak et al., *Techniques for Measuring Displacements and Crack Growth During Dynamic Fracture*, submitted for publication from Southwest Research Institute, San Antonio, Tex.

12. K. J. Bathe, *ADINAT — A Finite Element Program for Dynamic Incremental Nonlinear Analysis of Temperatures*, Report AE 84-2, Massachusetts Institute of Technology, Cambridge, December 1984.

13. K. J. Bathe, *ADINA — A Finite Element Program for Automatic Dynamic Incremental Nonlinear Analysis*, Report AE 84-1, Massachusetts Institute of Technology, Cambridge, December 1984.

14. B. R. Bass et al., "Computational Methods Development for Dynamic-Fracture Analysis," pp. 7–16 in *Heavy-Section Steel Technology Program Semiann. Prog. Rep. October 1986–March 1987*, NUREG/CR-4219, Vol. 4, No. 1 (ORNL/TM-9593/V4&N1), Martin Marietta Energy Systems, Inc., Oak Ridge Natl. Lab., August 1987.

15. B. R. Bass et al., "Late-Event Viscoplasticity in Wide-Plate Crack Arrest Tests," to be published in the *Int. J. Vessels Piping*.

16. C. E. Pugh and D. N. Robinson, "Some Trends in Constitutive Equation Model Development or High-Temperature Behavior of Fast-Reactor Structural Alloys," *J. Nucl. Eng. Des.* 48, 269–76 (1978).

17. D. N. Robinson and R. W. Swindeman, *Unified Creep-Plasticity Constitutive Equations for Structural Alloys at Elevated Temperature*, ORNL/TM-8444, Martin Marietta Energy Systems, Inc., Oak Ridge Natl. Lab., October 1982.

18. R. J. Dexter et al., "Dynamic-Viscoplastic Analysis and Small-Specimen Experimental Methods for the Study of Fracture in A533B Steel," in *Proceedings of the Fourth International Conference on Numerical Methods in Fracture Mechanics, March 23–27, 1987, San Antonio, TX*.

19. D. N. Robinson and P. A. Bartolotta, *Viscoplastic Constitutive Relationships with Dependence on Thermomechanical History*, NASA CR 174836, March 1985.

20. K. Hornberger et al., "Numerical Integration and Implementation of Viscoplastic Models into Finite Element Codes," pp. 477–90 in *Proceedings of Third International Conference on Computational Plasticity, Barcelona, Spain, April 6–10, 1987*, Pineridge Press, Swansea, U.K., 1987.

21. B. R. Bass, *Report of Foreign Travel, March 27 through April 17, 1987*, ORNL/FTR-2526, Martin Marietta Energy Systems, Inc., Oak Ridge Natl. Lab., May 1987.

22. R. deWit et al., "Wide-Plate Crack-Arrest Testing," pp. 62–82 in *Heavy-Section Steel Technology Program Semiann. Prog. Rep. October 1984–March 1985*, NUREG/CR-4219, Vol. 1 (ORNL/TM-9593/V1), Martin Marietta Energy Systems, Inc., Oak Ridge Natl. Lab., June 1985.

23. J. J. McGowan et al., "Properties of Wide-Plate Crack-Arrest Test Material," pp. 82–86 in *Heavy-Section Steel Technology Program Semiann. Prog. Rep. October 1984–March 1985*, NUREG/CR-4219, Vol. 1 (ORNL/TM-9593/V1), Martin Marietta Energy Systems, Inc., Oak Ridge Natl. Lab., June 1985.

24. C. E. Pugh, "Crack Arrest Technology," pp. 71–164 in *Heavy-Section Steel Technology Program Semiann. Prog. Rep. April–September 1985*, NUREG/CR-4219, Vol. 2 (ORNL/TM-9593/V2), Martin Marietta Energy Systems, Inc., Oak Ridge Natl. Lab., January 1986.

25. C. W. Schwartz, "Mesh Refinement for Viscoplastic-Dynamic Fracture Analysis," pp. 16–24 in *Heavy-Section Steel Technology Program Semiann. Prog. Rep. October 1986–March 1987*, NUREG/CR-4219, Vol. 4, No. 1 (ORNL/TM-9593/V4&N1), Martin Marietta Energy Systems, Inc., Oak Ridge Natl. Lab., August 1987.

26. S. R. Bodner and Y. Partom, "Constitutive Equations for Elastic Viscoplastic Strain Hardening Materials," *J. Appl. Mech.* 42, 385 (1975).

27. M. F. Kanninen et al., "Viscoplastic Characterization of A 533 Grade B Steel," pp. 35–41 in *Heavy-Section Steel Technology Program Semiann. Prog. Rep. April–September 1986*, NUREG/CR-4219, Vol. 3, No. 2 (ORNL/TM-9593/V3&N2), Martin Marietta Energy Systems, Inc., Oak Ridge Natl. Lab., December 1986.

28. S. N. Atluri, T. Nishioka, and M. Nakagaki, "Incremental Path Independent Integrals in Inelastic and Dynamic Fracture Mechanics," *Eng. Fract. Mech.* 20(2), 209–44 (1984).

29. B. Brickstad, "A Viscoplastic Analysis of Rapid Crack Propagation Experiments in Steel," *J. Mech. Phys. Solids* 31, 307–27 (1983).

30. B. Brickstad, *Wide-Plate Analysis of WP-1.2 and WP-1.5*, presented at the Third Annual Workshop on Crack Arrest Technology, National Bureau of Standards, Gaithersburg, Md., May 1987.

31. B. Moran and C. F. Shih, *Crack Tip and Associated Domain Integrals from Momentum and Energy Balance*, Office of Naval Research Report ONR0365/2, Brown University, Providence, R.I., May 1986.

32. L. B. Freund, *Notes on the 3rd HSST Workshop on Dynamic Fracture and Crack Arrest*, letter report to C. E. Pugh, Heavy-Section Steel Technology Program, Oak Ridge Natl. Lab., May 26, 1987.

33. J. W. Hutchinson, letter report on the 3rd HSST Workshop on Dynamic Fracture and Crack Arrest, to C. E. Pugh, Oak Ridge Natl. Lab., July 1, 1987.

34. L. B. Freund and J. W. Hutchinson, "High Strain-Rate Crack Growth in Rate-Dependent Plastic Solids," *J. Mech. Phys. Solids* 33(2), 169–91 (1985).

35. C. W. Schwartz and C. W. Lee, "Comparative Efficiency of Finite, Boundary, and Coupled Methods in Elastostatics," submitted to *J. Eng. Mech.*, ASCE.

36. K. J. Bathe and E. L. Wilson, *Numerical Methods in Finite Element Analysis*, Prentice-Hall, Inc., New York, 1976.

37. C. A. Brebbia, *The Boundary Element Method for Engineers*, Pentech Press, London, 1978.

38. C. A. Brebbia, J. C. F. Telles, and L. C. Worbel, *Boundary Element Techniques — Theory and Application in Engineering*, Springer-Verlag, 1984.

39. C. A. Brebbia and S. Walker, *Boundary Element Techniques in Engineering*, Newnes-Butterworths, London, 1980.

40. S. L. Crouch and A. M. Starfield, *Boundary Element Methods in Solid Mechanics*, George Allen and Unwin, Boston, 1983.

41. W. L. Fourney, G. R. Irwin, and R. Chona, "Investigation of Damping and of the Cleavage-Fibrous Transition in Reactor-Grade Steel," pp. 21–58 in *HSST Program Quart. Prog. Rep. October–December 1982*, NUREG/CR-2751, Vol. 4 (ORNL/TM-8369/V4), Union Carbide Corp. Nuclear Div., Oak Ridge Natl. Lab.

42. G. R. Irwin et al., title unknown, pp 251–78 in *Proceedings of the 14th Water Reactor Safety Information (WRSI) Meeting*, NUREG/CP-0082, Vol. 2, February 1987.

43. J. H. Giovanola and R. W. Klopp, *Viscoplastic Stress-Strain Characterization of A5333 Class 1 Steel*, Final Report HSST Subcontract No. 32X-5A193V, SRI International, Menlo Park, Calif., September 1987.

44. R. J. Clifton and R. W. Klopp, "Pressure Shear Impact Testing," pp. 230–38 in *Metals Handbook Ninth Edition, Vol. 8, Mechanical Testing*, American Society for Metals, Metals Park, Ohio, 1985.

45. D. Bois and A. Grave, "Simulation Numerique d'Eassais d'Impact et Comparaison de Lois de Comportement," pp. C5-101 to C5-108 in *Dymat 85, International Conference on Mechanical and Physical Behaviour of Materials under Dynamic Loading*, les Editions de Physique, Les Ulis, France, 1985.

3. MATERIAL CHARACTERIZATION AND PROPERTIES

R. K. Nanstad

Primarily for internal management and budgetary control, the Heavy-Section Steel Technology (HSST) Program created a separate task (Task H.3) for the work on material characterization and properties determinations. However, for the reader's convenience some contributions to this report are placed within other chapters according to the larger tasks that correspond to the particular material studies. For example, in addition to the work reported here, refer to Sect. 7.1 for crack-arrest studies in clad plates and Sect. 7.2 for nondestructive examination studies in support of cladding evaluations.

3.1 Low-Upper-Shelf Material Characterization

R. K. Nanstad R. L. Swain
S. K. Iskander E. T. Manneschmidt
J. P. Strizak

Pretest characterization of material for the second pressurized-thermal-shock experiment (PTSE-2) and the second wide-plate crack-arrest series (WP-2) has been conducted primarily with characterization block PTC1, 2 1/4 Cr-1 Mo steel. Virtually all test results from that material were reported in the previous two progress reports.[1,2] Subsequent testing and analysis have concentrated on material removed from the PTSE-2 test cylinder for comparison of posttest and pretest data. The results and detailed discussions are included in the final report[3] for PTSE-2 and are summarized here.

3.1.1 Metallography and hardness testing

As reported previously,[1] the PTSE-2 vessel insert had an average pretest surface hardness of about Rockwell B (HRB) 94 compared with HRB 86 for PTC1. Using the standard American Society for Testing and Materials (ASTM) correlation of hardness with tensile strength gives 675 MPa for the vessel and 558 MPa for PTC1. This difference is substantial in terms of strength and implies higher yield strength, as well as a higher transition temperature. Mechanical testing with specimens removed from the vessel insert following the PTSE-2 test shows somewhat higher tensile strength for the insert, but, as explained later, vessel test conditions obscure the conclusions.

Figures 3.1 and 3.2 show representative micrographs of PTC1 and the PTSE-2 insert, respectively, at the quarter-thickness (1/4t) depth. As shown, the two materials have similar amounts of pearlite. That observation is not consistent with posttest hardness testing, which showed the insert to be harder than PTC1. At the 1/4t depth the insert has a hardness of HRB 90, and that of PTC1 is HRB 86, corresponding to tensile strengths (by correlation) of 620 and 558 MPa, respectively. As shown in

M&C PHOTO Y209275

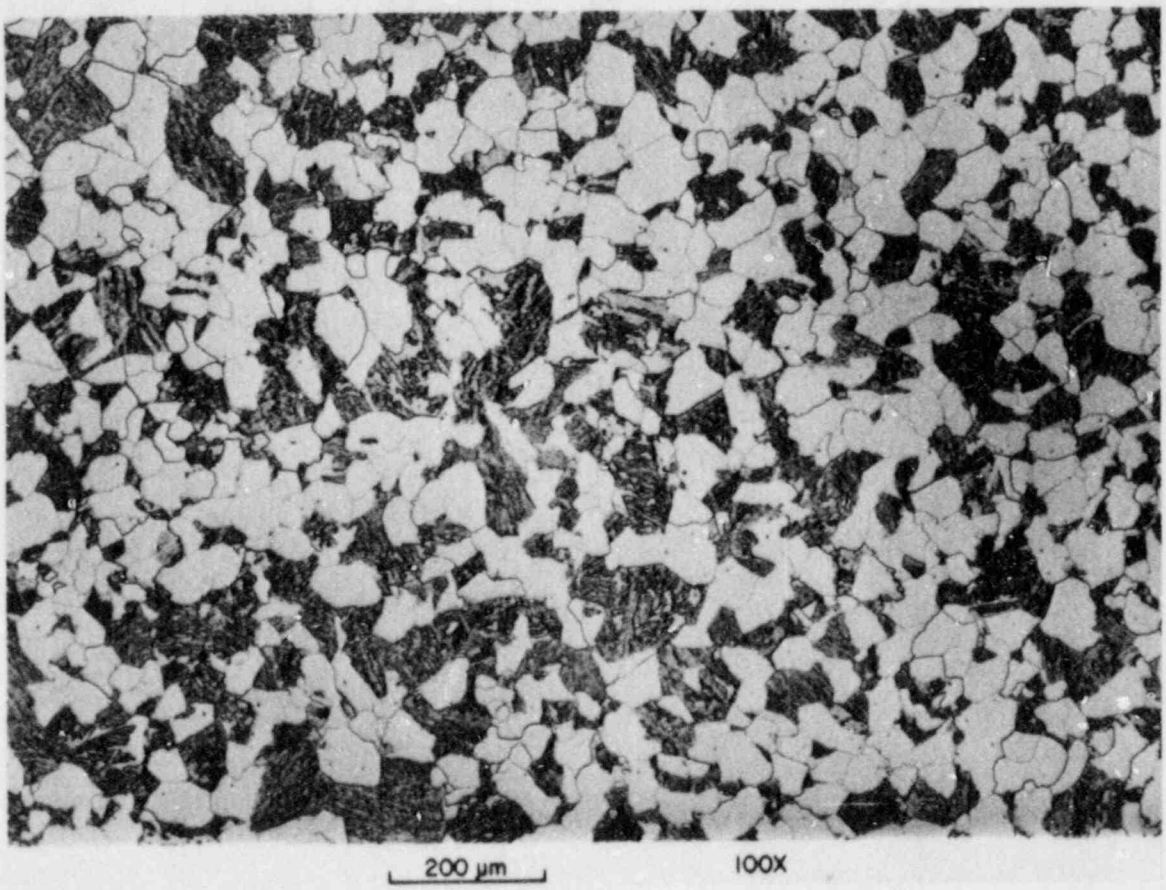

Fig. 3.1. Microstructure of characterization block PTC1, 2 1/4 Cr-1 Mo steel, near the 1/4t depth, longitudinal orientation.

M&C PHOTO Y209118

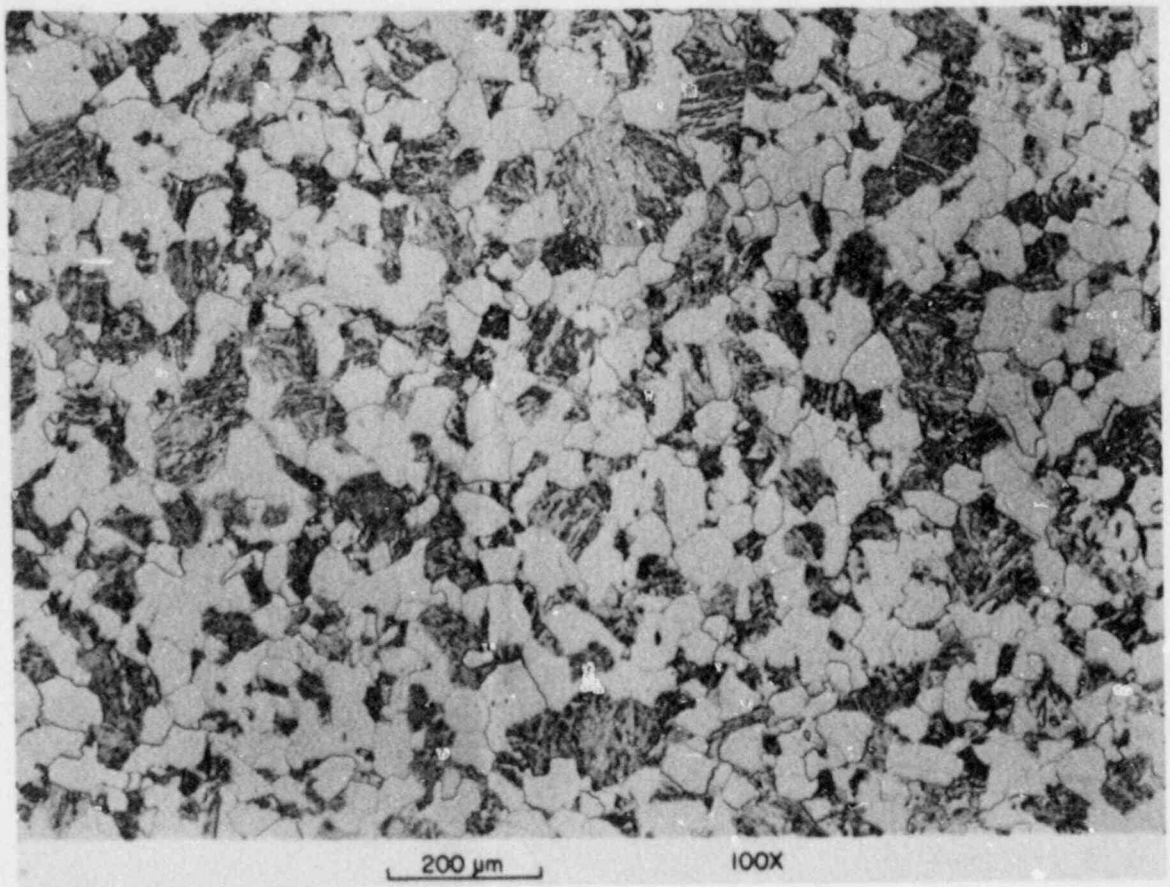

Fig. 3.2. Microstructure of PTSE-2 posttest insert, 2 1/4 Cr-1 Mo steel, near the 1/4t depth, longitudinal orientation.

Sect. 3.1.4, the measured tensile strengths are in quite good agreement with the correlative predictions from hardness. The hardness variations through the thickness of PTC1 are summarized in Table 3.1 and do not show significant variation in hardness as a function of plate depth. A hardness traverse of the vessel insert is discussed in a later section on fractography.

Table 3.1. Hardness variation through thickness of characterization block PTC1, 2 1/4 Cr-1 Mo steel

Depth location (mm)	Portable tester[a]		Laboratory Rockwell tester[b] (HRB)
	Raw No.	Converted to HRB	
Near surface	444	87	84
12.7	440	86	85.5
25.4	437	85	85
38.1	445	87	87.5
50.8	447	88	87.5
63.5	450	88	89
76.2	451	88	87.5
88.9	437	85	85.5
101.6	438	86	85
114.3	431	84	86
127.0	343	85	85.5
139.7	428	83	84
Near surface	431	84	85

[a]Equotip portable hardness tester measured average value (five readings) of HRB 94 on calibration block calibrated to HRB 96.6 ± 1.0.

[b]Laboratory Rockwell hardness tester measured average (five readings) of HRB 96.5 on calibration block calibrated to HRB 96.6 ± 1.0.

3.1.2 Physical properties

Physical properties of PTC1 were determined for consideration in determining the contribution of the insert to thermal stresses during the PTSE-2 experiment and for demonstration of the properties, including bulk density, electrical resistivity, and thermal expansion.

Bulk density measurements (diameter, length, and weight) were determined at 27°C for 12 specimens with an average result of 7.847 g/cm^3 ± 0.1%. The density of pure iron is 7.873 g/cm^3 at 20°C.

Electrical resistivity was also determined at 27°C for the 12 specimens with an average value of 28.744 μΩ-cm ± 0.5%.

Thermal expansions were determined using a modification[4] of a technique described by Kollie et al.[5] The modification uses a fused quartz push rod dilatometer considered to provide expansion measurements accurate within 2% of expected values. Within the range 0 to 350°C, the thermal expansion data can be described by the equation

$$\alpha \cdot 10^6 = 10.20 + 12.496 \cdot 10^{-3} \cdot T \pm 0.93\% ,$$

where α [=] $°C^{-1}$ and T [=] °C.

The results compare favorably with other measurements on similar materials and are ~10% lower than those for pure iron.

3.1.3 Drop-weight testing

Drop-weight testing was conducted with standard P-3 specimens per ASTM Method E208-84a. A single welding pass was used for application of the brittle weld bead. Pretest specimens were removed from PTC1 at the 1/4t depth in the plate. Posttest specimens were removed from portions of the vessel insert at the 1/4t and 3/4t depths. Table 3.2 shows the

Table 3.2 Results of drop-weight testing on 2 1/4 Cr-1 Mo material

Specimen	Test temperature (°C)	Test results	
		Break	No break
PTC1 characterization block (TS)[a]			
PI261	66		✓
PI262	54		✓
PI263	38	✓	
PI264	49	✓	
PI265	54		✓
PI266	49	✓	
Flaw insert material segments (LS)[a]			
PE94	65		✓
PE95	45	✓	
PE96	55	✓	
PE97	60	✓	
PE98	65	✓	
PE99	70	✓	
PE100	75	✓	
PE101	85		✓
PE102	80		✓
PE103	80		✓
PE104	60	✓	
PE105	70		✓

[a]The drop-weight test is insensitive to specimen orientation per ASTM E208.

drop-weight results for each specimen. Using the procedures of E208, the nil-ductility transition (NDT) temperatures are 49°C for PTC1 and 75°C for the vessel insert, a substantial difference. The specific test results reveal a fairly high degree of scatter, however, and further examination of the drop-weight specimens will be conducted to provide an explanation for such differences. A comparison between drop-weight NDT temperatures and Charpy V-notch (CVN) results is presented in a later section. Note that the previous characterization material (PTC2B), unacceptable because of a high CVN upper shelf and low CVN transition temperature, revealed a drop-weight NDT of 32°C.

3.1.4 Tensile testing

3.1.4.1 Pretest tensile tests. Results of tensile tests performed with several different specimen sizes made from characterization block material PTC1 are shown in Table 3.3. All results except those for the 12.7-mm-thick specimens were reported previously.[1,2]

Noteworthy is the difference (shown for the 6.35-mm-diam specimens) between the yield strengths obtained from strip charts and those obtained from an x-y plotter. A strip chart records the load vs crosshead speed (which is easily converted to strain); an x-y plotter records load vs an extensometer strain. Experience has shown that for most materials, the 0.2% yield strength derived from strip charts correlates very well with that derived from the x-y plotter. The use of strip charts does not require the attachment of an extensometer (which in case of testing in a hot cell is difficult); thus, it is more efficient to use strip charts to determine the 0.2% yield strength.

In the case of the 2 1/4 Cr-1 Mo material used for PTSE-2, a verification of this correlation revealed differences between strip chart and x-y plot values of the 0.2% yield strength. The difference also occurred for the one 12.7-mm-diam specimen for which the two methods of calculating the 0.2% yield strength was used.

The most likely cause of this difference is the apparent lack of a proportional limit for this material. Schematic engineering stress-strain diagrams for this material obtained from a strip chart and an x-y plotter recording are shown in Fig. 3.3(*a*) and (*b*), respectively. The method used to determine the 0.2% yield requires some judgment in choosing the linear portion on the autographic record of the test beyond possible initial perturbations caused by "play" in the screw threads, crosshead, etc. Such perturbations do not show up on x-y plots that use extensometers. As can be seen from Fig. 3.3, the slope of the stress-strain curve obtained from a strip chart is less than that obtained from an x-y plotter, and, thus, higher yields are derived from strip charts. Thus, the use of strip charts to obtain 0.2% yield stresses can lead to errors. It follows that a necessary condition for the strip-chart method to give a reliable 0.2% yield stress is a sufficiently high proportional limit stress. Obviously, a material whose stress-strain curve has a relatively shallow slope beyond a well-defined yield point is not as sensitive to errors in determining the 0.2% yield as is the case with this 2 1/4 Cr-1 Mo.

Table 3.3. Pretest tensile results for PTC1, 2 1/4 Cr-1 Mo steel

Specimen[a]	Temperature (°C)	Strength (MPa)			Fracture stress (MPa)	Elongation[d] (%)	Reduction of area (%)
		Yield		Ultimate			
		[b]	[c]				
4.52-mm-diam (0.18-in.) specimens							
PI97	−100		512	715	573	35	50
PI93	−100		503	719	572	41	51
PI94	− 50		348	664	470	28	51
PI127	0		321	603	466	26	53
PI118	0		346	599	468	25	56
PI123	100		320	537	441	21	48
PI98	200		269	493	411	20	50
PI114	300		327	533	478	15	38
6.35-mm-diam (0.25-in.) specimens							
PI283	24	266	348	574	467	26	51
PI291	24	314	314	586	501	25	44
PI285	100	265	359	530	446	22	47
PI286	100	266	337	523	432	24	50
PI292	100	259	340	530	449	26	47
PI287	200	241	315	511	447	20	46
PI288	200	248	315	509	434	19	46
PI293	200	234	330	513	442	20	45
PI289	300	290	344	520	454	16	41
PI290	300	244	325	513	454	17	43
PI294	300	248	335	515	461	16	41
12.7-mm-diam (0.5-in.) specimens							
PI369	24	275	336	578		26	47
PI370	25	295		603		27	50
PI371	100	256		536		23	46
PI372	100	276		554		24	46
PI374	200	263		534		23	47
PI373	300	254		524		21	42

[a]All specimens machined from 1/4t depth in plate with transverse orientation.

[b]Yield strength obtained from x-y plot of load vs strain extensometer (25.4-mm gage length).

[c]Yield strength obtained from strip-chart recording of load vs crosshead speed.

[d]Computed from strip-chart readings of elongation of specimen, corrected to a gage length of 4 diameters when necessary. The elongations for the 12.7-mm-diam specimens were computed from gage marks on the specimens.

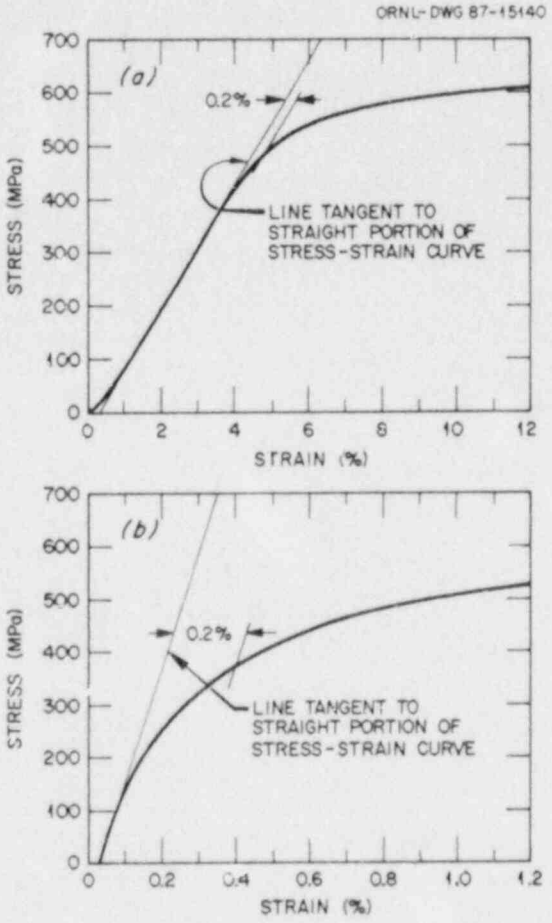

Fig. 3.3. Schematic stress-strain curves for 2 1/4 Cr-1 Mo material from (*a*) strip charts and (*b*) x-y plotter.

3.1.4.2 Posttest tensile testing and evaluation of flaw insert. Results of tensile testing performed at different temperatures on flaw insert material are given in Table 3.4. The specimens were T-oriented and were from different depth locations. Material from the 1/4t and the 3/4t depths was assumed to be the same. Figure 3.4 compares the tensile strengths of 1/4t material from the PTC1 characterization block to that from the flaw insert. The 0.2% yield strength of the flaw insert material is ~60 to 70% higher than the 0.2% yields obtained for characterization block material. All of the tensile specimens had some weld metal that extended to one end of the uniform section of the specimen. It was not possible to manufacture 6.35-mm-diam tensile specimens from flaw insert material alone because of the limitations imposed by the material availability. Except for specimen PE09, which is not shown in the table, most of the necked area and the fracture location in the specimens during tensile testing occurred in the base metal, determined by etching of the specimens after testing. Assuming the necked area to be the "weakest link" of the specimen, then the effect of weld metal on the ultimate tensile strength (UTS) of the flaw insert material is small.

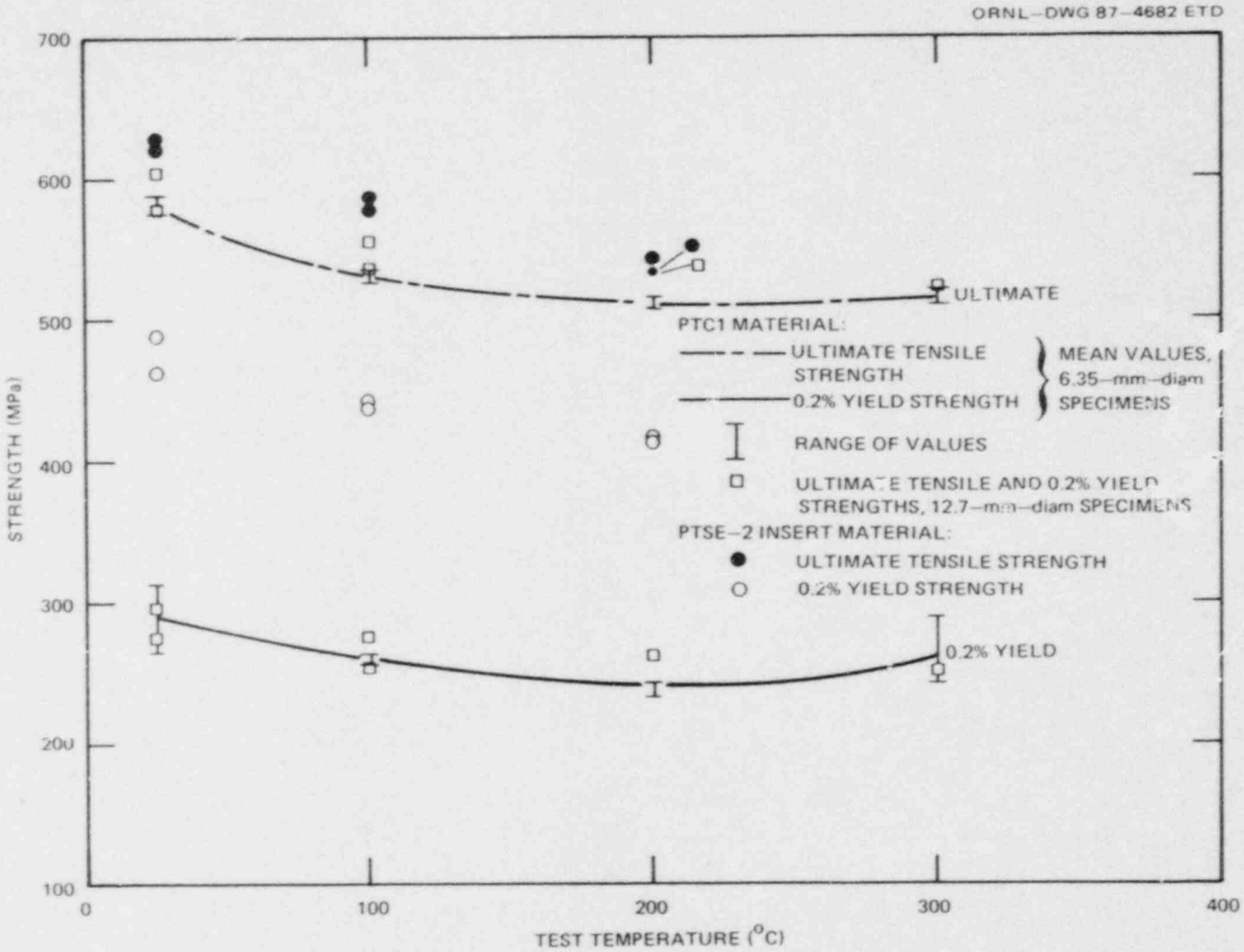

Fig. 3.4. Comparison of tensile strengths of PTC1 characterization block with flaw insert material, all from the 1/4t depth and T orientation. Values for the 0.2% yield are from the x-y plotter.

Table 3.4. Posttest tensile results from PTSE-2 flaw insert 2 1/4 Cr-1 Mo material, T-orientation, 6.35-mm-diam specimens

Specimen	Location (t)	Test temperature (°C)	Strength (MPa)		Elongation[a] (%)	Reduction of area (%)
			0.2% yield[a]	Ultimate		
PE01	0	25	461	620	18	52
PE04	0	25	478	623	18	52
PE02	1/4	25	462	620	21	52
PE05	1/4	25	488	627	19	50
PE03	1/2	25	460	627	20	51
PE06	1/2	25	452	620	22	49
PE10	0	100	443	578	16	49
PE08	1/4	100	442	585	17	49
PE11	1/4	100	440	579	16	46
PE09	1/2	100	422	580	19	48
PE12	1/2	100	423	577	20	47
PE13	0	200	436	545	13	45
PE16	0	200	449	550	14	47
PE14	1/4	200	415	534	17	46
PE17	1/4	200	414	541	17	48
PE15	1/2	200	403	548	19	46
PE18	1/2	200	403	549	20	42

[a]Determined from extensometer, x-y chart.

The UTS of the flaw insert material is about 10% higher than the characterization block; thus, the 60 to 70% increase in yield strength cannot be due solely to differences in heat treatment. In the following discussion much of this difference is assumed to be due to strain hardening that does not affect the UTS of the material. Among the possible causes for this strain hardening could be the residual stresses resulting from welding the insert into the vessel, various degrees of straining during the tests on the vessel, or both. The UTS will be used as a "normalizing" parameter in estimating the amount of strain hardening subjected on the flaw insert material.

As a step in estimating the amount of strain that could lead to such an elevation of yield stress, L-oriented specimens 6.35 mm in diameter were manufactured from both the characterization block PTC1 and the flaw insert. L-orientation specimens were used to avoid the material limitations mentioned above that are associated with T-oriented specimens.

The tensile test results for the L-oriented specimens are shown in Table 3.5. Comparison of the UTS for the 1/4t location material tested

Table 3.5. Results of tensile tests performed on L-orientation, 6.35-mm-diam 2 1/4 Cr-1 Mo material

Specimen	Location (t)	Test temperature (°C)	Strength (MPa)		Elongation[b] (%)	Reduction of area (%)
			0.2% yield[a]	Ultimate		
PTC1 characterization block material						
PC1	1/4	100	288	541	24	51
PC2	1/4	100	280	542	26	51
Flaw insert material						
PE109	1/2	26	365	617	29	48
PE115	1/2	26	377	621	23	47
PE111	1/4	100	389	538	22	49
PE117	1/4	100	374	567	22	52

[a]Extensometer, x-y chart.

[b]Measured from gage marks on specimens.

at 100°C shows that the averages for both of these materials agree within 2%. The 0.2% yield strength (average of two specimens) for the flaw insert is 35% higher compared with the 60 to 70% yield strength observed for the T-orientation specimens. If the cause of the strain hardening was either welding residual stresses or pressure stress during the test, then this would preferentially strain-harden the T-orientation.

The L-orientation PTC1 tensile specimens were subjected during the tensile tests to three cycles of loading and unloading. The purpose was to verify that after reloading, the stress-strain curve would follow the same curve had there been no unloading. Such a behavior was indeed observed. Thus, it is possible to estimate from stress-strain curves for PTC1 the amount of strain necessary to result in the increases of yield strength observed for the vessel insert. The strain required for such an elevation was estimated as follows. Using an average of 475 and 624 MPa for the 0.2% yield and UTS, respectively, their ratio is ~0.76 for the flaw insert material tested at room temperature (6.35-mm specimens, Table 3.4). The corresponding averages for the PTC1 material are 290 and 580 MPa, respectively. Using the UTS of specimen PI283 of 574 MPa and the 0.76 ratio would correspond to a 0.2% yield of 436 MPa if the material has hardened in the same manner as the flaw insert. This increase of 64% over the actual 0.2% yield stress corresponds to a strain of ~2%. Thus, the amount of strain hardening is ~1.8%.

As mentioned above, L-orientation tensile specimens from PTC1 were subjected to three cycles of loading and unloading. In each cycle,

unloading was initiated when the total strain was ~1, 2, and 3% respectively, as shown in Fig. 3.5(*a*). The 0.2% yield of PTC1 material is 288 MPa. If the 0.2% yield had been measured after 1.8% total strain, the yield would have been 455 MPa, an increase of 58%. Figure 3.5(*b*) is a comparison of the stress-strain curves of T-orientation materials, the lower one from PTC1 material and the upper from flaw insert material. This illustrates the sensitivity of the 0.2% yield of this 2 1/4 Cr-1 Mo material to strain levels >0.2%. It also graphically describes the differences in tensile behavior of the two materials. As discussed previously, some uncertainties exist concerning the exact representation of the vessel insert by the pretest characterization material. Although the cyclic tests described above do not mitigate all of those uncertainties, they have shown that the differences in tensile properties between the posttest insert and the pretest material likely are due largely to strain hardening that occurred during the PTSE-2 experiments.

3.1.4.3 Determination of Young's modulus. Two L-orientation 1/4t specimens 6.35 mm in diameter from each of the flaw insert and characterization block material PTC1 have been instrumented with electric resistance strain gages to measure Young's modulus E and Poisson's ratio ν. Two axial and two circumferential gages on each specimen were connected in series and placed diametrically opposite to each other to average any bending strains caused by misalignment. The measurements were performed at two temperatures, 25 and 150°C. At each temperature, the specimens were first subjected to three loading and unloading cycles between 0 and 55 MPa. The 0.2% yield for this material is ~280 MPa, but because of the apparent lack of a proportional limit, the maximum stress was restricted to 20% of the yield.

Measurements of the strain from the electric resistance strain gages were performed at loads corresponding to 7 and 57 MPa, and E was calculated as the secant modulus between the two stresses. The E and ν values reported in Table 3.6 for each temperature are the average of four measurements: two each during loading and unloading. Also given are the standard deviations calculated from each set of four measurements. The accuracy of the E and ν values reported is estimated to be ~5 and 10%, respectively, because the strains were ~250 με for the axial direction and 70 με for the circumferential direction.

Young's modulus was also estimated from autographic records made using an averaging linear variable differential transformer (LVDT) placed over a 50-mm gage length. The value of E ranged from 213 GPa at room temperature to 205 GPa at 300°C. However, the variation of E with temperature is of the same order of magnitude as the estimated accuracy of the measurements and, therefore, should be ignored.

Ultrasonic wave velocity measurements were also performed at room temperature on a 6.35-mm-thick coupon of PTC1 to give a dynamic Young's modulus of 213 ± 1 GPa and a dynamic Poisson's ratio of 0.286 ± 0.003.

Within the limits of the accuracy of these measurements, Young's modulus can be taken to be ~205 GPa and Poisson's ratio to be 0.26 with no temperature dependence detected in the range 25 to 150°C.

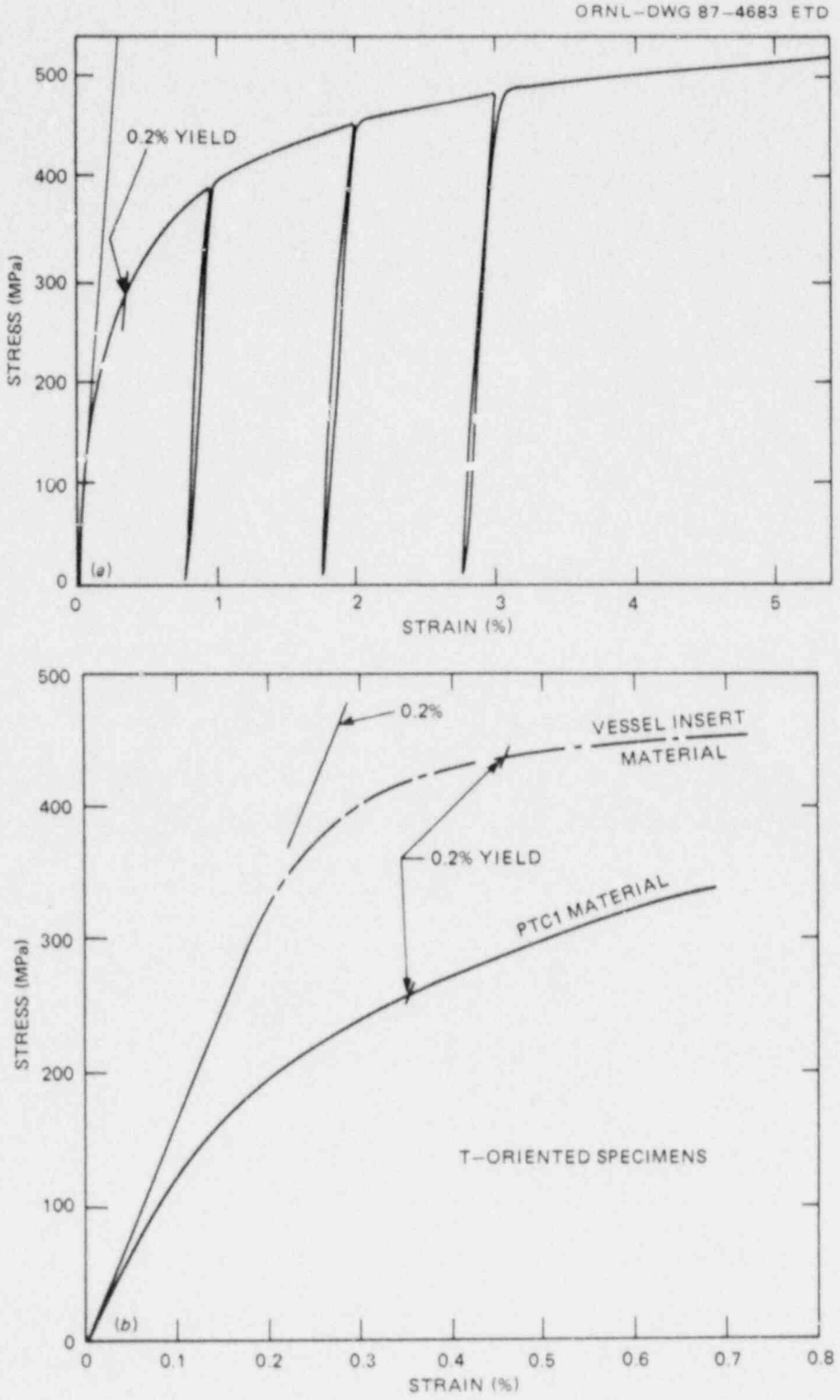

Fig. 3.5. (*a*) The 0.2% yield of 2 1/4 Cr-1 Mo material used in PTC1 increased 50% when strain hardened 1.8%, (*b*) comparison of the stress-strain curves of 2 1/4 Cr-1 Mo material from PTC1 and flaw insert.

Table 3.6. Pretest and posttest determination of Young's modulus E and Poisson's ratio ν

Specimen	Temperature (°C)	Young's modulus E (GPa)	Poisson's ratio ν
	PTC1, T orientation[a]		
PI369	24	211	
PI370	25	211	
PI371	100	216	
PI372	100	211	
PI374	200	216	
PI373	300	206	
	PTC1, L orientation[b]		
PC5	25	212	0.259
	150	205	0.267
PC6	25	206	0.258
	150	203	0.256
	Vessel insert, L orientation[b]		
PE107	25	206	0.257
	150	210	0.260
PE113	25	204	0.260
	150	194	0.263

[a]From extensometer data and 12.7-mm-diam specimens.

[b]From strain-gaged 6.35-mm-diam specimens.

3.1.5 CVN testing

Pretest CVN impact testing was performed with PTC1 material of varying depths in the plate and in both the TS (crack propagation in thickness direction) and TL (crack propagation in rolling direction) orientations. Those results were reported previously.[1]

Table 3.7 summarizes the curve fit parameters and, based on the curve fits, the energy corresponding to the drop-weight NDT and the 41-J (30-ft-lb) transition temperature for each data set. The NDT corresponds to an average CVN energy of 19.5 J (14.3 ft-lb) for the TS orientation and 15.5 J (11.4 ft-lb) for the TL orientation. Note that specimens from 1/2t depth showed the highest 41-J temperature in both orientations.

Posttest CVN specimens in the TS orientation were removed from the vessel insert at the surface, 1/4t, and 1/2t depths. The CVN data and curve fits are shown in Figs. 3.6–3.8. The curve fit parameters are

Table 3.7. Curve fit parameters of Charpy energy for PTC1, 2 1/4 Cr-1 Mo steel

Depth (t)	$E = (A/2)\{1 + \tanh[B(T - C)]\}^a$			E at NDT, 49°C (J)	Temperature at 41 J (°C)
	A (J)	B ($°C^{-1}$)	C (°C)		
			TS orientation		
0	59.85	0.03046	76.8	*b*	89.6
1/4	68.15	0.01755	75.03	19.5	86.8
1/2	61.34	0.01913	85.98	*b*	104.3
3/4	68.90	0.02214	73.16	*b*	81.8
1	72.81	0.01959	74.26	*b*	80.7
			TL orientation		
0	59.89	0.02062	80.6	*b*	99.4
1/4	59.43	0.01998	74.4	15.5	94.4
1/2	50.42	0.01675	75.8	*b*	119.7
3/4	63.63	0.02255	73.32	*b*	86.5
1	63.33	0.02112	77.74	*b*	92.1

[a] E = CVN energy at temperature T,
A = upper-shelf energy,
B = related to slope of curve in transition region,
C = temperature corresponding to energy equal to one-half of upper-shelf energy.

[b] Not calculated, drop-weight NDT was determined with specimens from 1/4t.

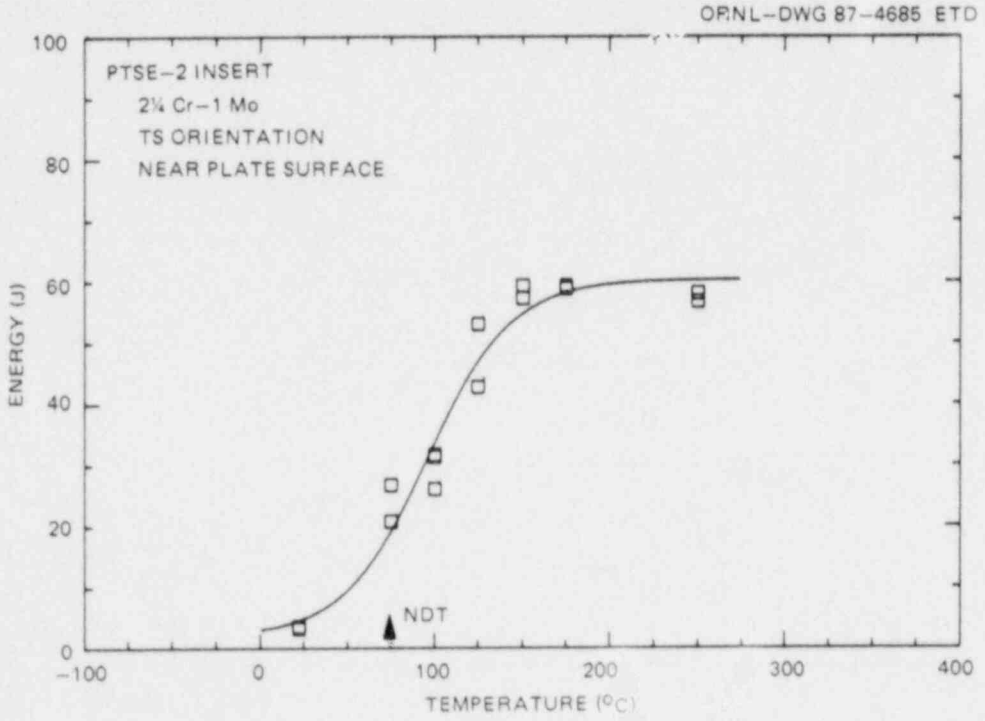

Fig. 3.6. CVN impact energy vs temperature for PTSE-2 posttest vessel insert, 2 1/4 Cr-1 Mo steel, with TS orientation near plate surface.

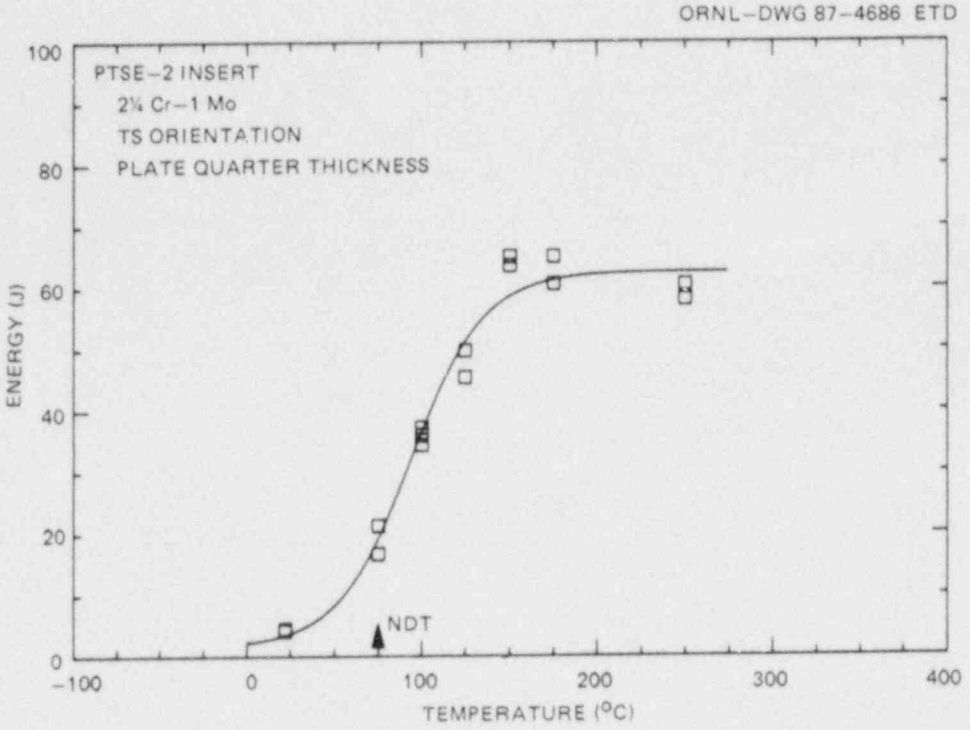

Fig. 3.7. CVN impact energy vs temperature for PTSE-2 posttest vessel insert, 2 1/4 Cr-1 Mo steel, with TS orientation at the 1/4t depth in the insert.

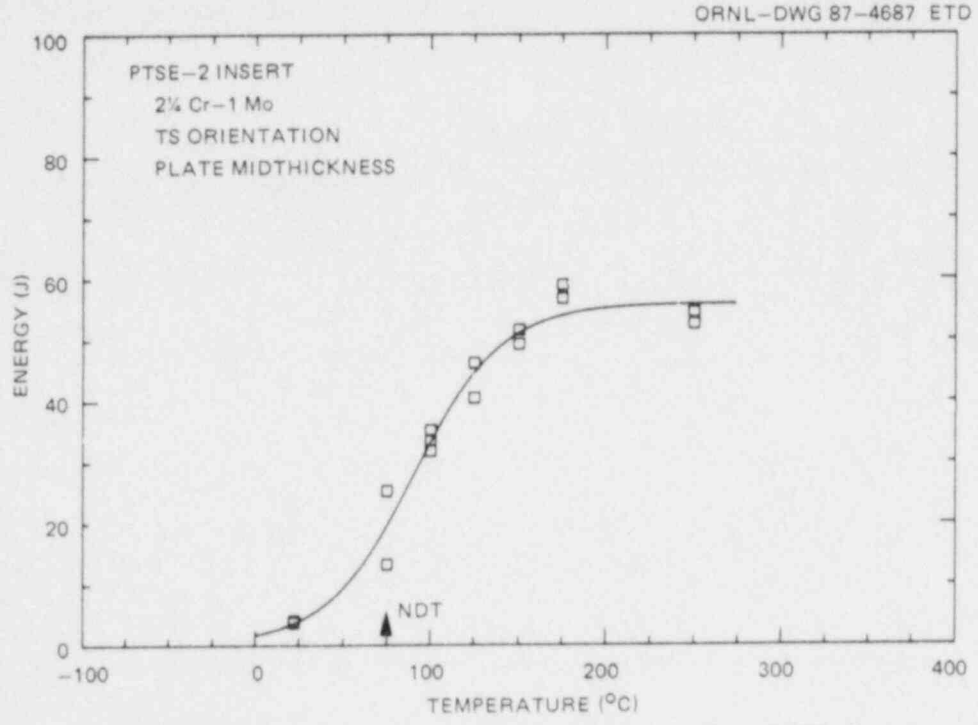

Fig. 3.8. CVN impact energy vs temperature for PTSE-2 posttest vessel insert, 2 1/4 Cr-1 Mo steel, with TS orientation at the mid-thickness depth in the insert.

given in Table 3.8. Figure 3.9 is a comparison of the pretest and posttest CVN results for specimens removed from the 1/4t depth in the plate. Comparison of the midenergy transition temperatures (parameter C) and the 41-J temperatures from Tables 3.7 and 3.8 reveals that the PTSE-2 vessel insert transition is ~20°C higher than that for the pretest characterization block PTC1 in the TS orientation at the 1/4t depth. The tables also show that the CVN upper-shelf energies of the insert are, on the average, slightly lower than those for PTC1 in the TS orientation.

Table 3.8. Curve-fit parameters of Charpy energy for PTSE-2 posttest vessel insert, 2 1/4 Cr-1 Mo steel, TS orientation

Depth (t)	$E = (A/2)\{1 + \tanh[B(T - C)]\}^{a}$			E at NDT, 75°C (J)	Temperature at 41 J (°C)
	A (J)	B ($°C^{-1}$)	C (°C)		
0	60.57	0.01966	94.16	*b*	113.0
1/4	63.16	0.02293	93.92	18.6	107.3
1/2	66.03	0.01988	90.69	*b*	116.0

[a] E = CVN energy at temperature T,
A = upper-shelf energy,
B = related to slope of curve in transition region,
C = temperature corresponding to energy equal to one-half of upper-shelf energy.

[b] Not calculated, drop-weight NDT was determined with specimens from 1/4t.

These results follow the implications mentioned earlier relative to the higher surface hardness of the insert and, especially, the posttest drop-weight NDT and tensile results. The differences in the 1/4t Charpy transition temperatures are ~20°C, compared with a difference in the NDT temperatures of 26°C, a reasonably similar result. Inspection of Tables 3.7 and 3.8 shows that the curve-fit-determined CVN energy at the NDT temperature is about the same for the insert (18.6 J) as for PTC1 (19.5 J). As discussed earlier, the drop-weight tests for the vessel insert showed relatively high scatter. In spite of that, however, the CVN and drop-weight NDT results reflect similar differences between the pretest characterization of PTC1 and the posttest characterization of the PTSE-2 vessel insert.

Regarding determinations of a reference NDT temperature, RT_{NDT}, according to the *ASME Boiler and Pressure Vessel Code*, Sect. III (Ref. 6), none of the CVN data sets would result in an RT_{NDT} equal to the NDT because all sets have CVN energies at NDT + 33°C (60°F) <68 J (50 ft-lb). From the curve fit, the pretest material at the 1/4t achieves 68 J at

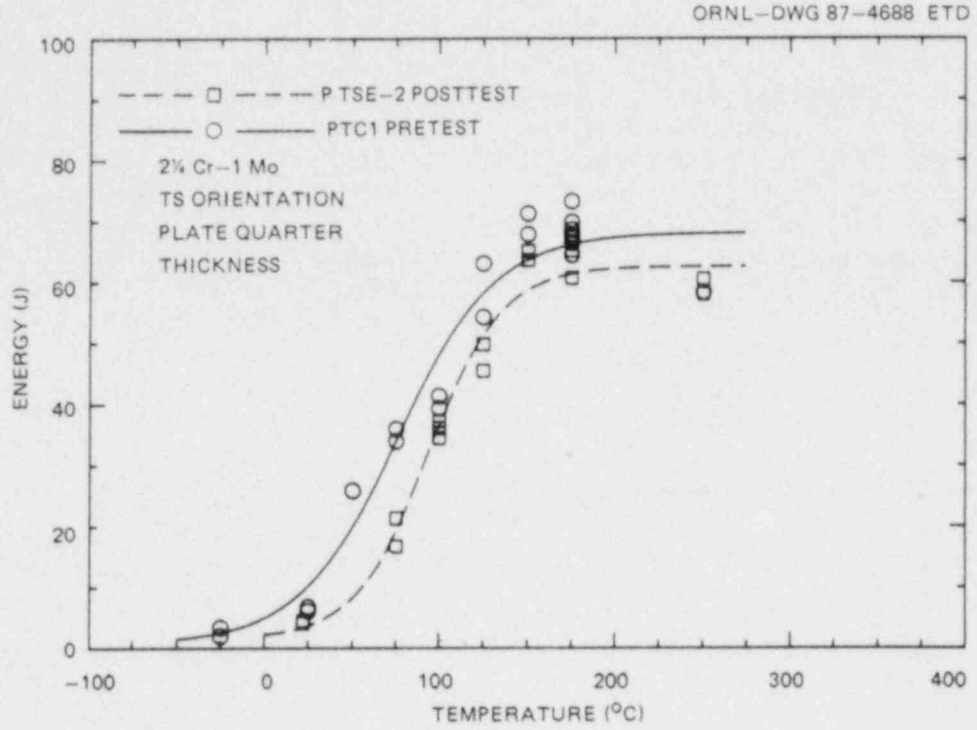

Fig. 3.9. Comparison of CVN results for pretest characterization block PTC1 and PTSE-2 posttest vessel insert, 2 1/4 Cr-1 Mo steel, with TS orientation at the 1/4t depth.

~132°C (T_{68}), which, by defining RT^*_{NDT} as T_{68} − 33°C, gives an RT^*_{NDT} of 99°C. The vessel insert did not achieve 68 J even on the upper shelf, and an RT_{NDT} cannot be defined.

3.1.6 Fracture-toughness testing

Pretest fracture-toughness testing was conducted from −75 to 250°C with 25.4-mm-thick compact specimens machined from near the surface of PTC1. Specimens were fatigue precracked and have been tested with both TS and TL orientations. The results are reported in Refs. 1 and 2.

Posttest fracture-toughness testing was completed from 50 to 250°C with fatigue-precracked 25.4-mm-thick compact specimens machined from near the 1/4t depth in the PTSE-2 vessel insert. All specimens were tested in the TS orientation. All specimens except those tested at 50°C were side-grooved to 10% of the specimen thickness on each side. Values of K_{Jc}, $K_{\beta c}$, J_{Ic}, and T were determined as described previously[1,2] for the pretest characterization tests.

Table 3.9 shows the results of posttest fracture toughness tests with specimens that experienced cleavage. Only the specimens tested at 50°C were smooth sided. Five specimens with TS orientation were tested at each of three temperatures, 50, 75, and 100°C. Figure 3.10 shows the data graphically and a comparison with the pretest data from PTC1. The

Table 3.9. Transition region fracture-toughness results for PTSE-2 vessel insert, 2 1/4 Cr-1 Mo steel, TS orientation

Specimen	Test temperature (°C)	Side-groove (%)	K_{Jc} (MPa·√m)	$K_{\beta c}$ (MPa·√m)	Stable crack extension (mm)
PE64	50	0	122.3	75.4	0.226
PE66	50	0	124.2	75.9	0.249
PE68	50	0	122.6	75.5	0.274
PE70	50	0	125.3	76.2	0.371
PE72	50	0	100.4	68.8	0.071
PE74	75	20	139.0	74.0	0.947
PE76	75	20	104.4	65.5	0.300
PE78	75	20	105.7	65.8	0.297
PE80	75	20	128.7	71.7	0.752
PE82	75	20	124.4	70.7	0.627
PE85	100	20	139.2	73.0	1.209
PE67	100	20	179.9	80.9	3.726
PE69	100	20	220.2	87.3	7.000
PE71	100	20	187.0	82.1	4.050
PE73	100	20	185.6	81.8	3.655

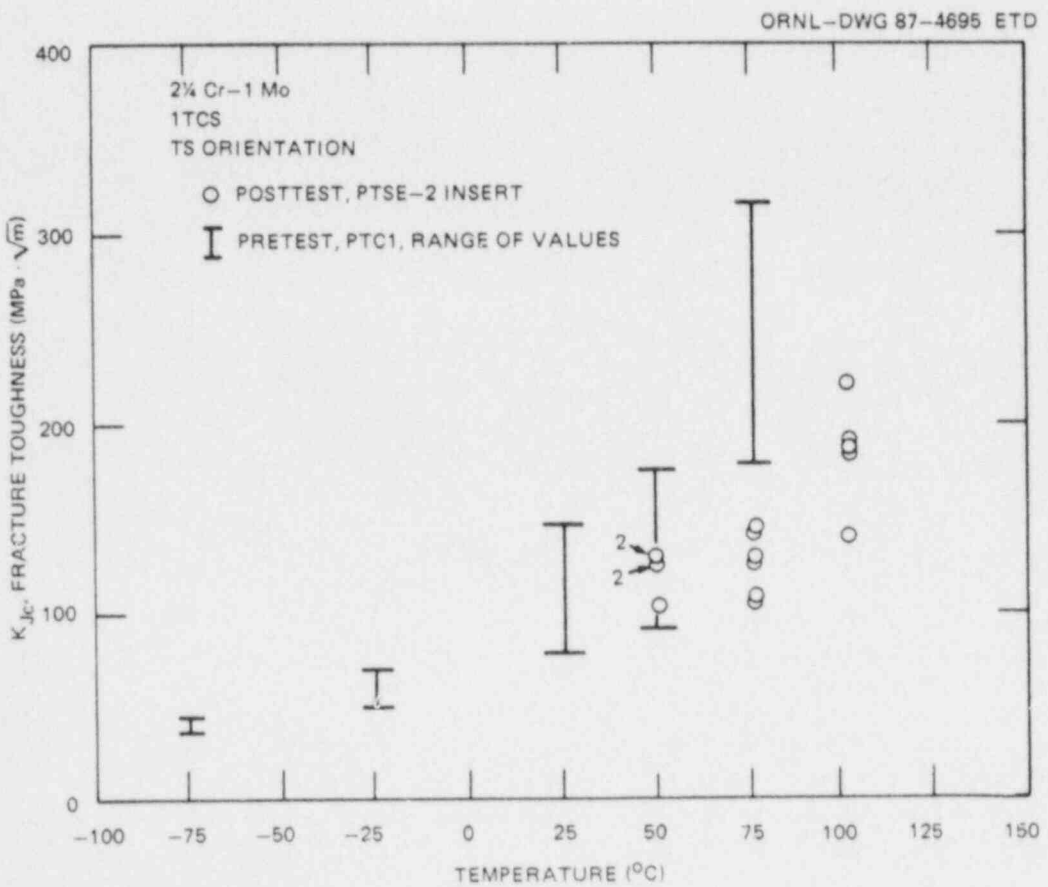

Fig. 3.10. Fracture toughness K_{Jc} vs temperature for PTSE-2 posttest vessel insert with TS orientation compared with similar specimens from pretest characterization block PTC1. All posttest specimens cleaved.

results indicate an upward temperature shift in fracture toughness for the posttest material compared with pretest material from characterization block PTC1. This observation is substantiated by the fact that no pretest specimens tested at 100°C experienced cleavage; all five posttest specimens, however, cleaved at 100°C. Additionally, comparison of the data reveals that the stable crack extensions at a given K_{Jc} level are less for the posttest material than for the pretest material. That is an indication of an increase in yield strength that is reflected in the discussion in Sect. 3.1.4 on tensile testing. At an arbitrarily chosen K_{Jc} of 150 MPa$\cdot\sqrt{m}$, the posttest material achieves that level of toughness at a temperature 30°C higher than the pretest material. That upward shift is slightly greater than shown by the Charpy impact results and the drop-weight NDT results.

Table 3.10 shows the results of testing side-grooved specimens from the vessel insert at 175 and 250°C to obtain full J-R curves without cleavage intervention. The posttest material exhibited slightly lower J_{Ic} values but significantly lower tearing modulus values than did the pretest material, ~30 and 75, respectively. Typical J-R results using modified J are shown in Fig. 3.11. The effect of plastic deformation during the vessel experiment increased the flow strength significantly and because the flow strength occurs in the denominator of the equation for tearing modulus, will cause a 40 to 50% decrease in the tearing modulus even if the J-R curves are the same. In this case, however, the J-R curve slopes for the posttest material are much less than those for the pretest material. Thus, both the flow strength increase and a real degradation in the material tearing resistance have resulted in the lower tearing modulus results for the posttest material.

3.1.7 Crack-arrest toughness testing

Crack-arrest toughness data obtained from the PTC1 characterization block for TS and TL specimens were reported previously.[1,2]

The ASME Sect. XI K_{Ia} curve included has been adjusted with respect to the drop-weight NDT rather than RT_{NDT} because the Charpy upper-shelf energy of this material is <68 J, and, thus, it is not possible to define an RT_{NDT}. The NDT for this material is 49°C.

Material from the flaw insert has been used to fabricate TS-orientation "nugget" type specimens.[7] The results, together with the TS data for PTC1 material, are given in Table 3.11 and plotted in Fig. 3.12. The crack-arrest toughness of the vessel insert is less than that of the PTC1 material. Using a toughness level of 150 MPa$\cdot\sqrt{m}$ for comparison, the arrest toughness of the flaw insert is shifted ~15 K toward a higher temperature than that of PTC1 material. This shift to a higher temperature is consistent with shifts noticed for other toughness measures discussed in Sect. 3.1.8.

3.1.8 Summary

In Sect. 3.1.1 it was pointed out that pre-experiment hardness testing performed on the vessel insert outer surface and PTC1 characterization material indicated a substantially higher strength (by correlation

Table 3.10. Ductile shelf fracture-toughness results for PTSE-2 vessel insert, 2 1/4 Cr-1 Mo steel, TS orientation

Specimen[a]	Test temperature (°C)	J_{Ic}[b] (kJ/m^2)	$K_{J_{Ic}}$ ($MPa\cdot\sqrt{m}$)	Final crack extension (mm)	Tearing modulus[c]	Power-law curve fit parameters[d]			
						A	B	C	D
PE75	175	46.3	95.5	8.49	28	70.7	0.075	0.373	2.76
PE77	175	52.7	102	8.87	28	67.9	0.195	0.379	4.75
PE79	175	45.3	94.6	9.09	31	71.3	0.110	0.407	1.26
PE81	250	49.8	98.0	9.42	19	43.9	0.195	0.371	18.58
PE83	250	35.9	83.3	8.70	20	56.1	0	0.296	1.70

[a] 25.4-mm-thick compact specimens.

[b] J_{Ic} determined by power-law curve intersection with 0.15-mm offset line; J is deformation theory J per ASTM E813.

[c] Calculated using linear fit to data between offset lines.

[d] $J = A(\Delta a + B)^C + D$, where Δa = crack extension.

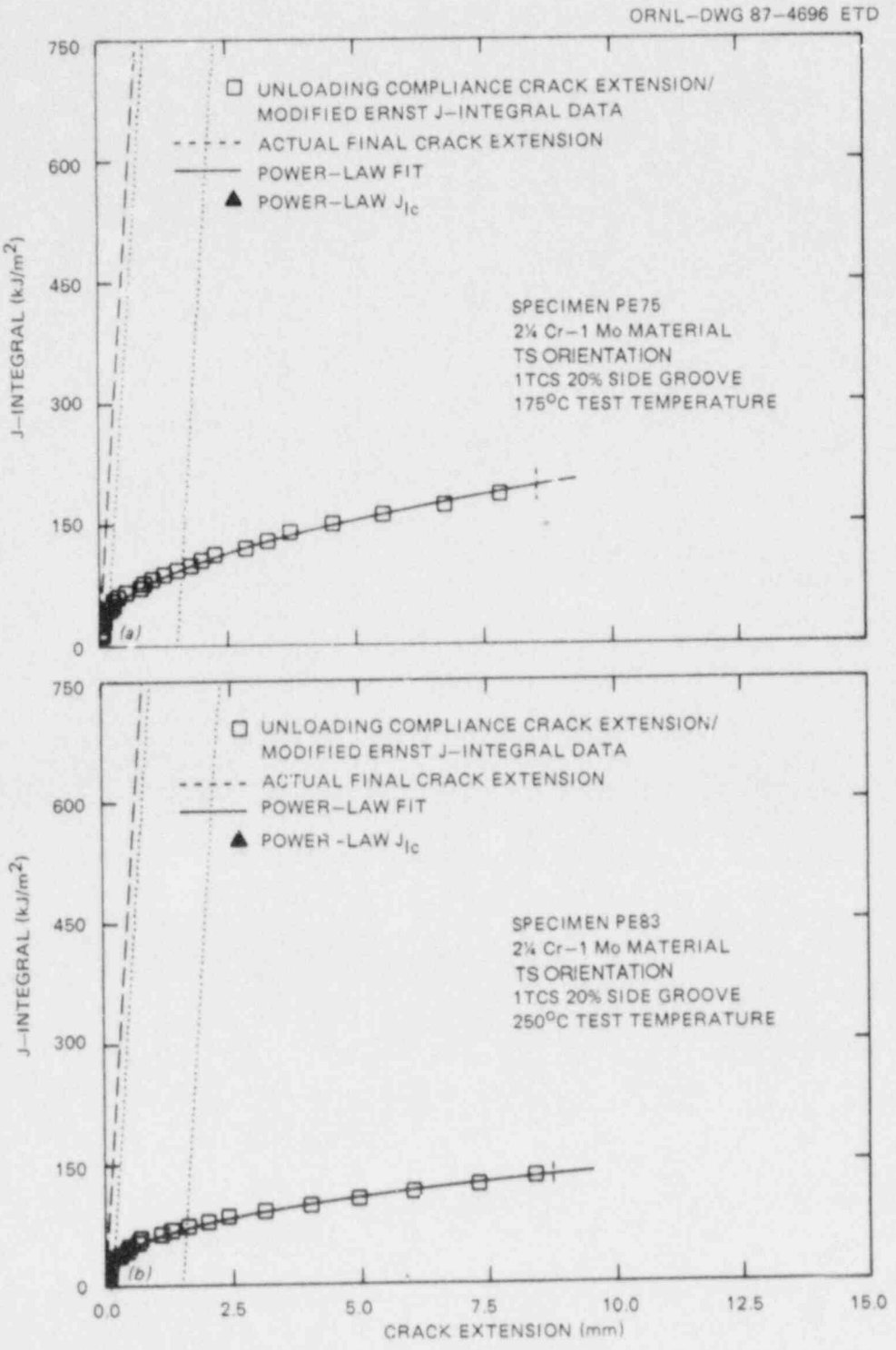

Fig. 3.11. J-integral resistance curves at (*a*) 175°C and (*b*) 250°C for PTSE-2 posttest vessel insert, 2 1/4 Cr-1 Mo steel, TS orientation.

Table 3.11. Crack-arrest K_a data for flaw insert material, TS orientation

Specimen	Test temperature (°C)	K_a (MPa·√m)
Weld embrittled, 33 × 152 × 152 mm (1.3 × 6 × 6 in.)		
PE86	50	58
PE87	50	58
PE88	50	62
PE84	80	64
PE85	80	76
Duplex, 33 × 152 × 152 mm (1.3 × 6 × 6 in.)		
PE89	110	139
PE90	110	179
PE91	110	119
PE92	110	136
PE93	110	148

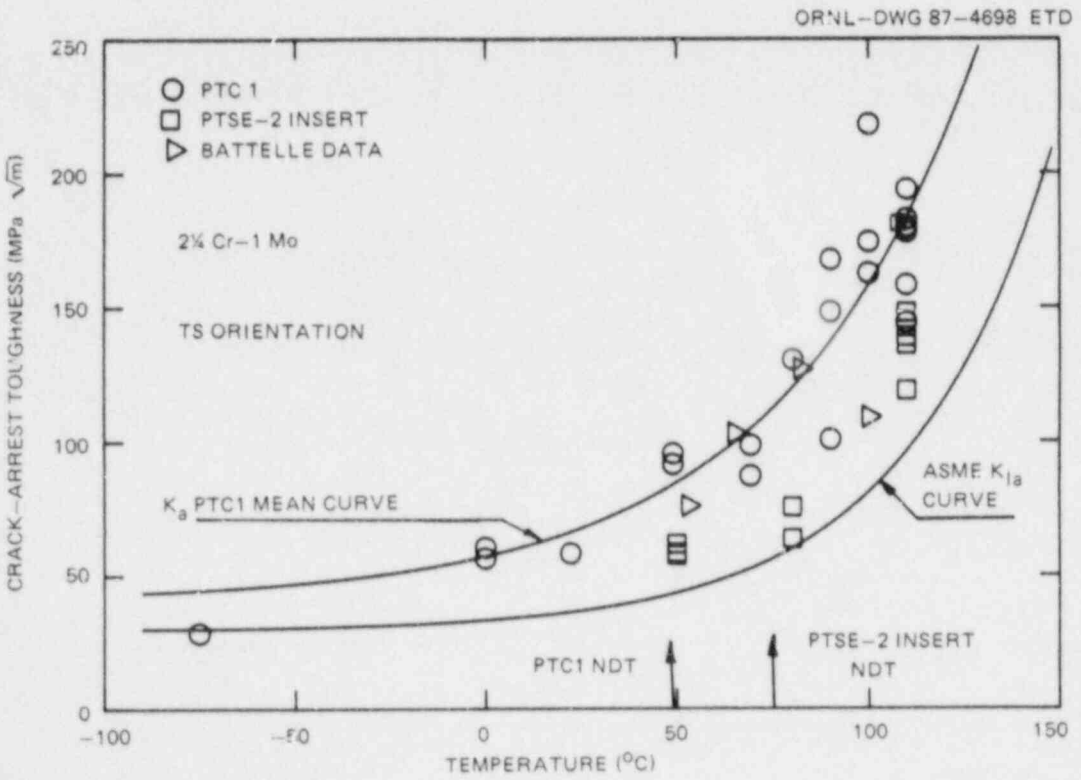

Fig. 3.12. Crack-arrest test results of the flaw insert material compared with characterization block PTC1, both in TS orientation (low-upper-shelf 2 1/4 Cr-1 Mo steel).

with hardness) for the vessel insert. It was realized following the PTSE-2 tests that the strains that developed in the vessel wall during testing were large enough to cause significant strain hardening, thus an increase in yield strength and, possibly, increases in toughness transition temperatures. As discussed in Sect. 3.1.4.2, the posttest yield strength of the vessel insert is ~70% higher than that of PTC1; the ultimate strength is ~8% higher.

Relative to toughness, the behavior is quite consistent. All of the posttest vessel insert material tests showed higher transition temperatures than did those for PTC1. The increases were 26 K for the drop-weight NDT temperature, 20 K for the CVN 41-J temperature, 30 K for the K_{Jc} 150-MPa$\cdot\sqrt{m}$ temperature, and 15 K for the K_a 150-MPa$\cdot\sqrt{m}$ temperature. Thus, the various measures of toughness transition temperature are from 15 to 30 K higher for the posttest vessel insert.

The cyclic tests described in Sect. 3.1.4.2 demonstrated that the differences in tensile properties likely are due largely to strain hardening that occurred during the vessel experiments, and, therefore, it is likely that the effects of strain hardening were also manifested by the increases in toughness transition temperatures. A definitive experiment would be desirable but is outside the scope of this report.

It is believed that the material properties of the vessel insert prior to the PTSE-2 experiments is reasonably well represented by the PTC1 pretest characterization block for the following reasons: (1) the vessel insert and PTC1 were heat treated simultaneously, (2) the changes in the tensile results are reasonably consistent with strain-hardening predictions of yield strength increases, and (3) four different measures of toughness transition temperatures changed similarly from the pretest characterization block to the posttest vessel insert.

3.2 Fractographic and Metallographic Evaluation

R. K. Nanstad R. S. Crouse

PTSE-2 was designed to produce a cleavage crack propagation and arrest followed by unstable ductile tearing in a material of low ductile-shelf toughness. Preliminary visual measurements in comparison with the instrumentation outputs during the test concluded that two initiation and arrest events occurred, one during each of two transients performed with the PTSE-2 test vessel. The second transient concluded with a tearing instability that breached the inner surface of the vessel. Figure 3.13 shows a photograph of the fracture surface reassembled with the sections cut from the vessel. Figure 3.14 shows a photograph of one section near the center portion of the fracture surface.

Fractographic examination in the scanning electron microscope (SEM) confirmed that initial ductile tearing and crack propagation in a cleavage mode occurred in the first transient with arrest at a depth of ~40 mm. The second transient showed ductile tearing preceded cleavage crack propagation with final cleavage arrest at a depth of ~80 mm. However, it seems evident that an intermediate arrest occurred at a depth of ~70 mm with subsequent reinitiation by ductile tearing before the final cleavage

M&C PHOTO YP3644A

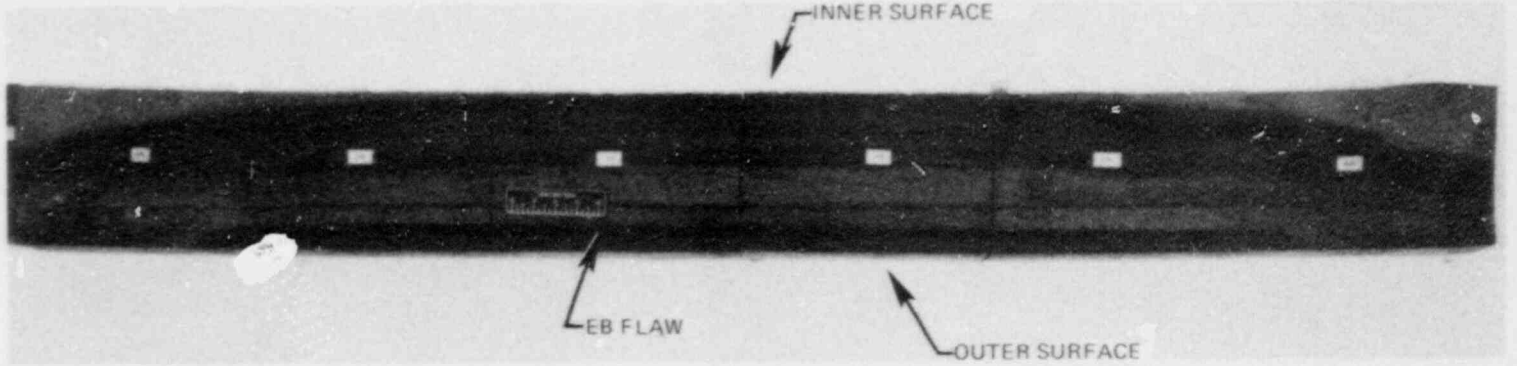

Fig. 3.13. Photograph of fracture surface from PTSE-2. The fracture surface was reassembled from Sects. 1A–6A, which were cut from the test section.

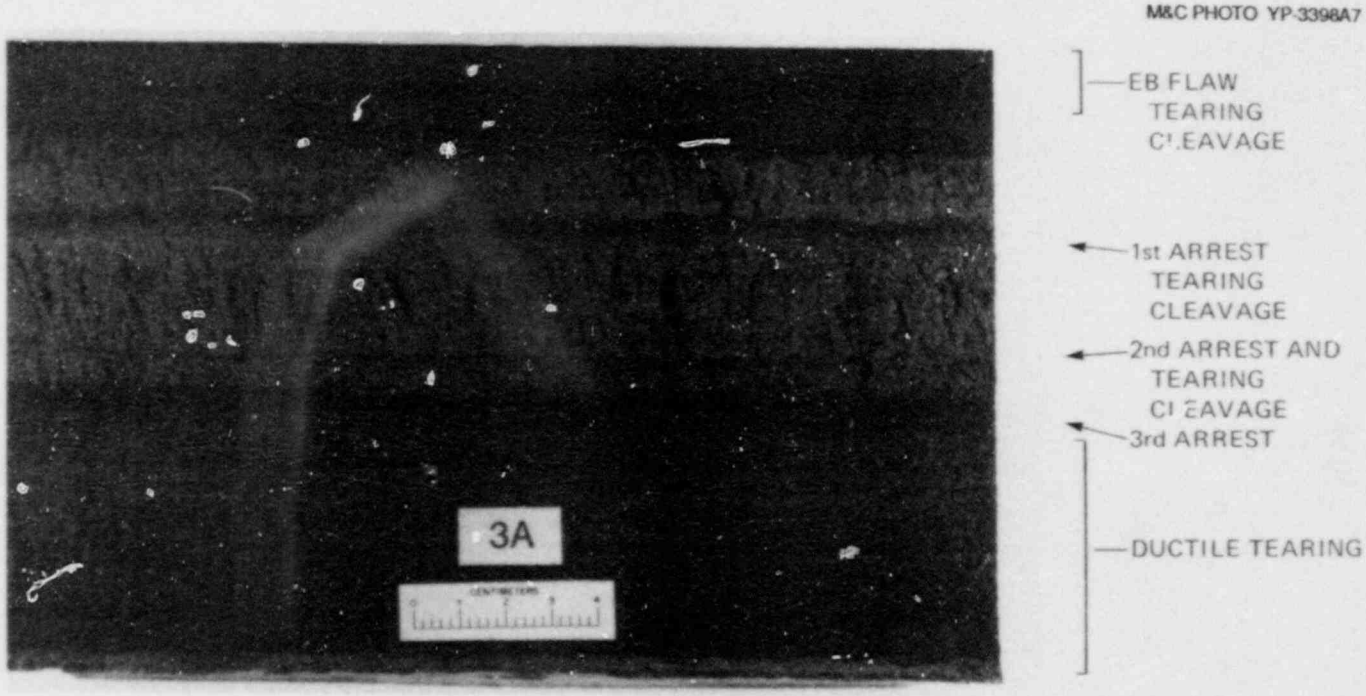

Fig. 3.14. Photograph of Sect. 3A from the fracture surface of PTSE-2. The initial electron-beam flaw is evident at the top of the photograph, and the various crack events, as well as propagation modes, are denoted on the right.

propagation. Beyond a depth of 80 mm, the fracture occurred by ductile tearing.

Preparatory to performing the scanning electron fractography, a portion of the fracture surface was removed from segment 4A and cut to approximate size for the SEM. Punch marks (PMs) were placed onto the fracture surface at or near various features of interest for reference. Figure 3.15 is a macrograph of the punch-marked pieces and identifies the boundaries (y marks) given in Table 3.12, as well as the PMs (painted white) and distances between them. Figure 3.16 shows the surface just beyond PM1 near the end of the electron-beam weld. The ductile tearing is evident in the fractographs. Figure 3.17 is a series of three fractographs in the region between PM2 and PM3, which show the end of the ductile tearing in the first transient and the start of the transgranular cleavage propagation (boundary y_2).

Table 3.12. Description of boundary designations on fracture surface of PTSE-2

Boundary designation	Description
y_1	Cracked EB weld; smooth, dark gray
y_2	Precleavage ductile tear in PTSE-2, dark gray, rough
y_3	Cleavage fracture in PTSE-2A, light gray
y_4	Postcleavage ductile tear in PTSE-2A, brown or gray band
y_5	Precleavage ductile tear in PTSE-2B, medium gray
y_6	Cleavage fracture in PTSE-2B, light gray
y'_6	Narrow band of ductile tearing, medium gray
y_7	Cleavage fracture in PTSE-2B, light gray
y_8	Postcleavage ductile tear in PTSE-2B
y_9	Light-gray shear lip in ruptured portion; unbroken ligament, very light gray, near both ends of flaw

Figure 3.18 shows an area beyond PM3 and confirms that the dominant cleavage mode of crack propagation occurred with only a small amount of tearing in the form of tear ridges between cleavage facets. Figure 3.19 was taken in the region just before PM4 and shows that the fracture mode was still predominantly cleavage at that point, just before arrest. Between PM4 and PM5 is a dark band thought to be ductile tearing associated with reloading during the first transient immediately following crack arrest. Figure 3.20 was taken in that region and shows the predominant ductile tearing behavior.

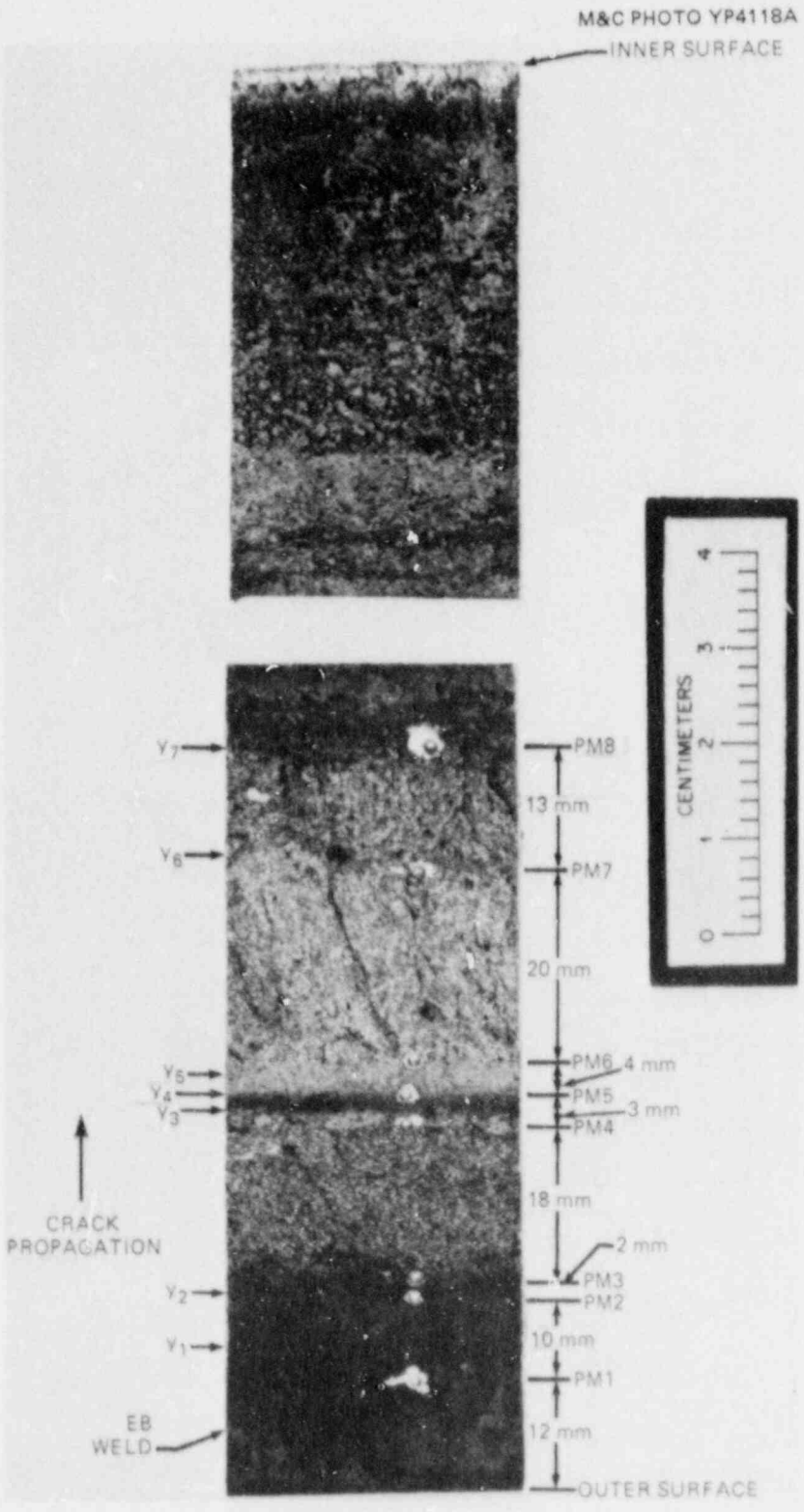

Fig. 3.15. Photograph of PTSE-2 fracture surface showing PMs used as reference points for scanning electron fractography. The "y" numbers refer to boundary designations defined in Table 3.12.

ORNL PHOTO 7739-87

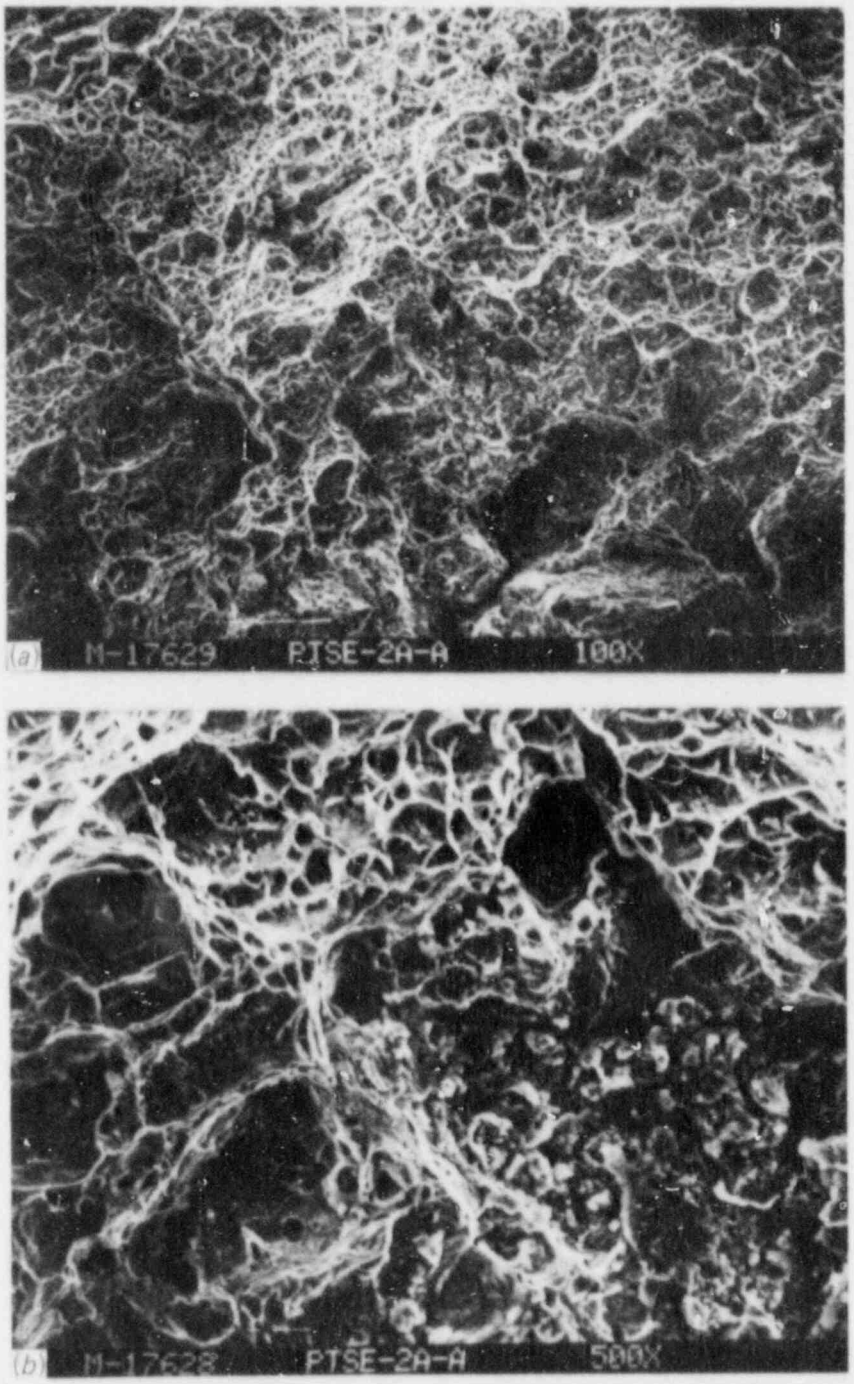

Fig. 3.16. Scanning electron fractographs of PTSE-2 showing the ductile tearing region between PM1 and PM2 preceding cleavage initiation during the first transient. (*a*) 100×, (*b*) 500× in center of part (*a*).

ORNL PHOTO 7740-87

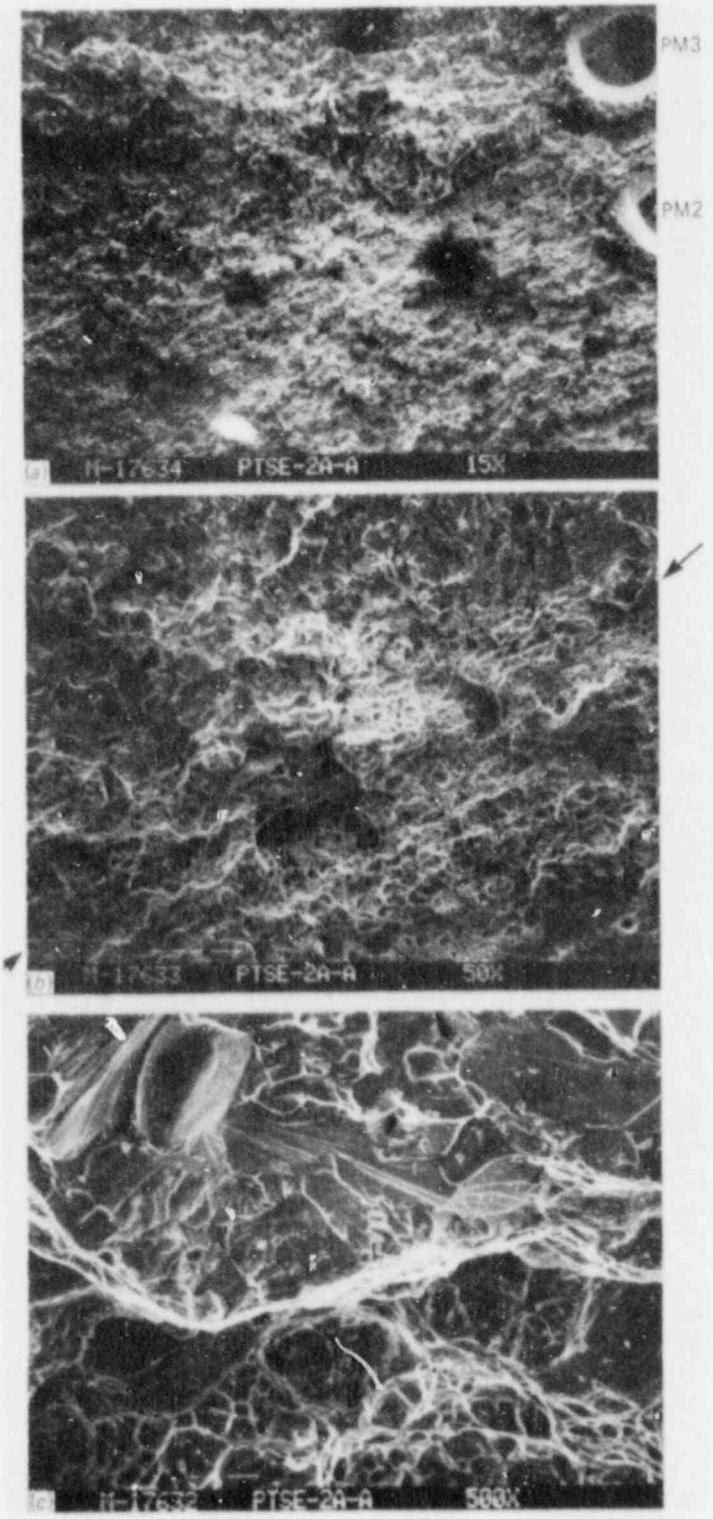

Fig. 3.17. Scanning electron fractographs of PTSE-2 at the boundary between ductile tearing and cleavage regions. (*a*) 15× showing PM2 and PM3, (*b*) 50× in center of part (*a*), (*c*) 500× in center of part (*b*).

ORNL PHOTO 7741-87

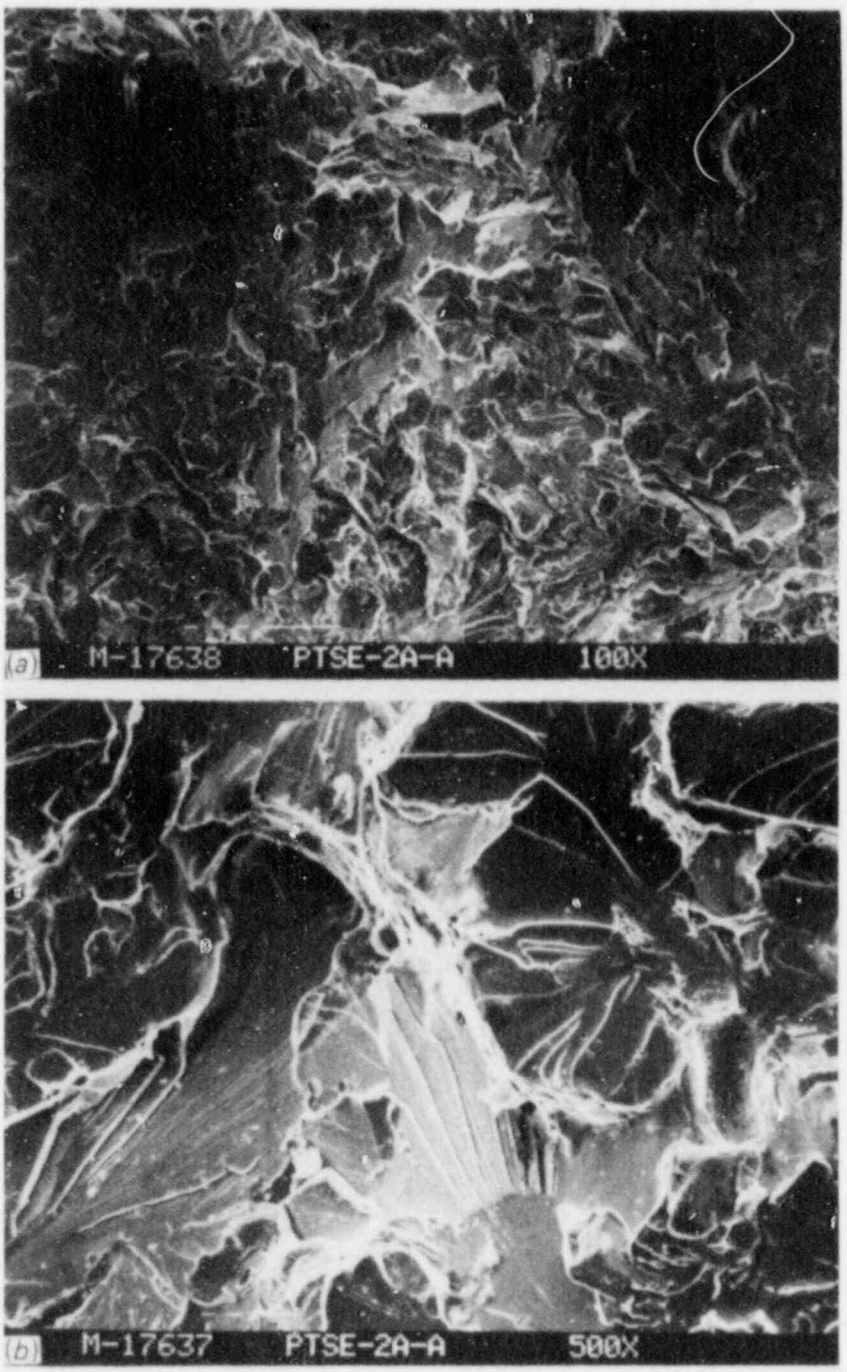

Fig. 3.18. Scanning electron fractographs of PTSE-2 showing transgranular cleavage as mode of fracture during the crack run event in the first transient. (*a*) 100× just beyond PM3, (*b*) 500× in center of part (*a*).

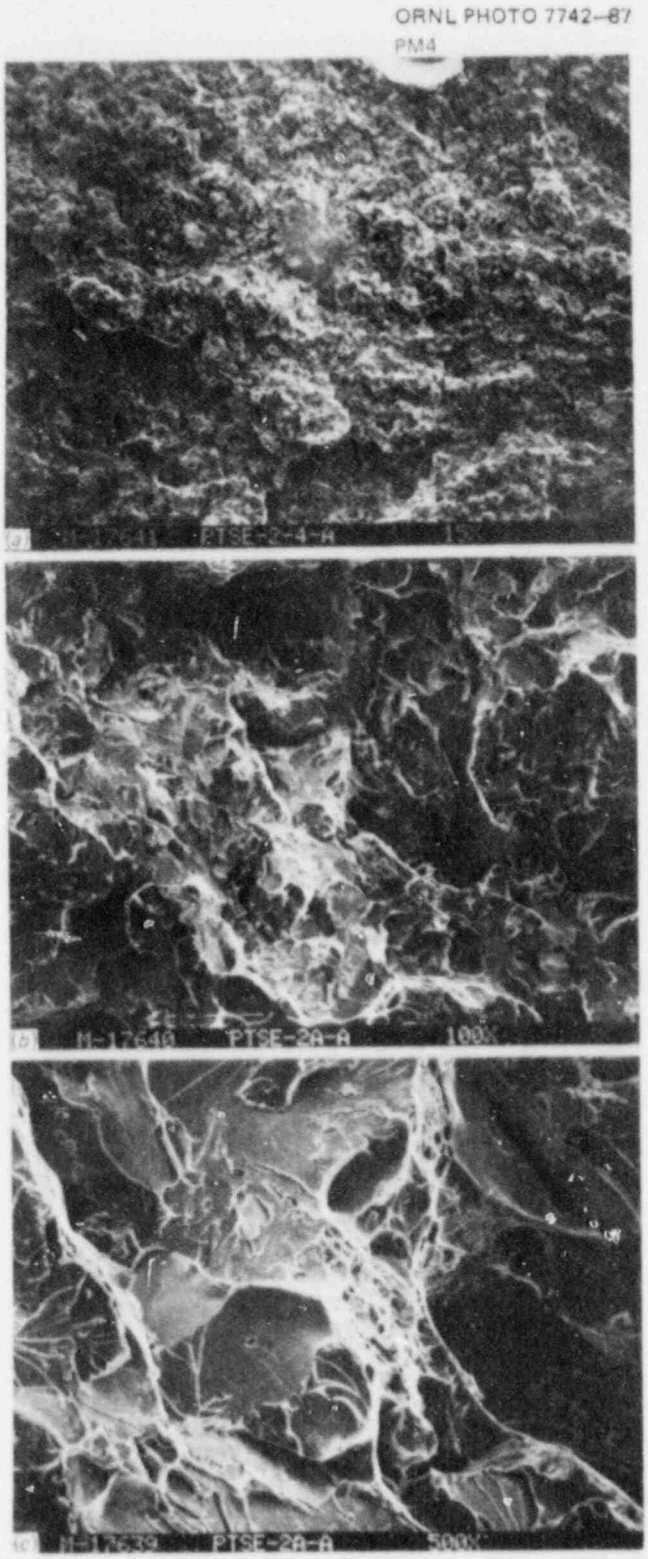

Fig. 3.19. Scanning electron fractographs of PTSE-2 in region just preceding PM4 showing that cleavage was primary mode of fracture with some ductile tearing occurring as tear ridges between cleavage planes. (*a*) 15×, (*b*) 100×, (*c*) 500×, in center of part (*a*).

ORNL PHOTO 7743-87

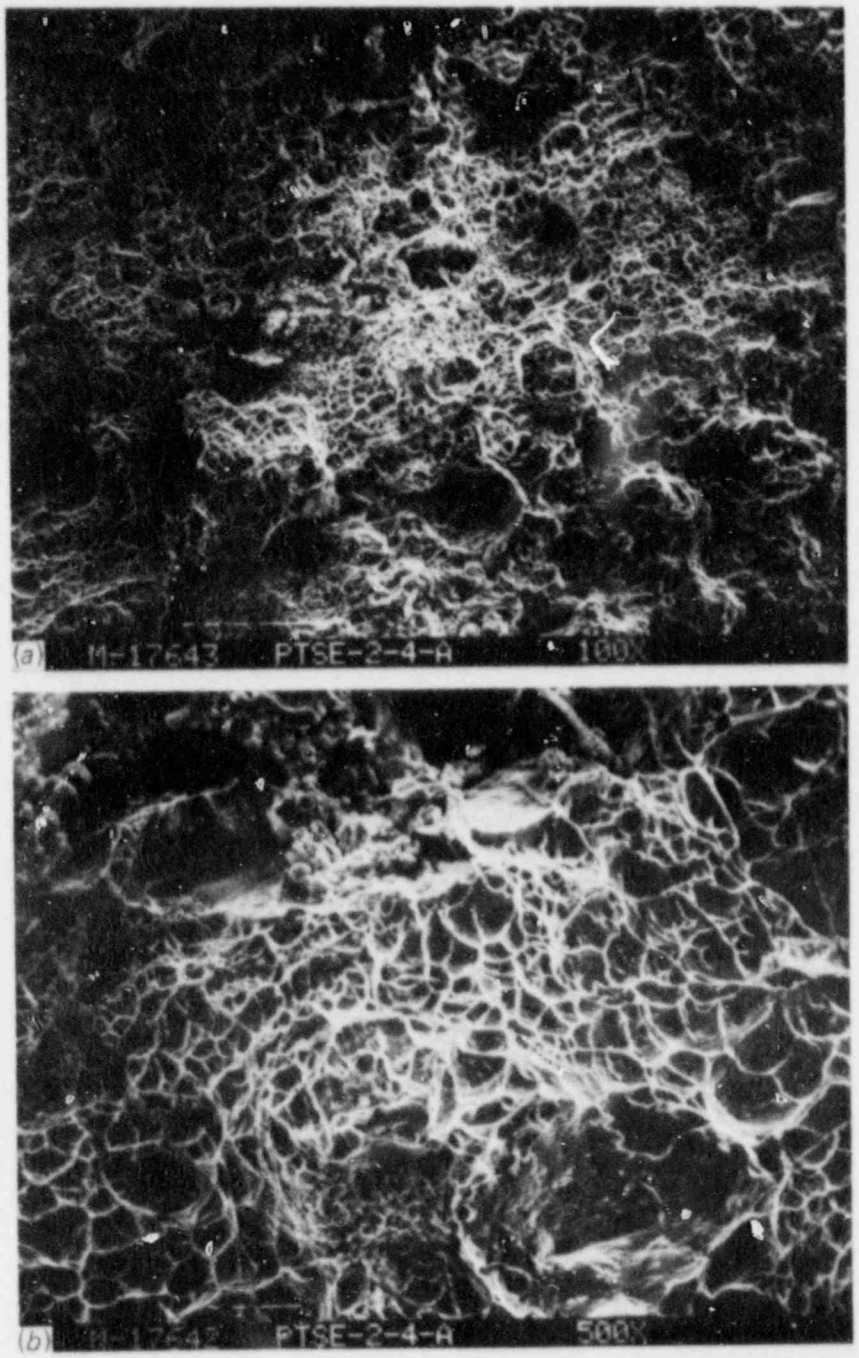

Fig. 3.20. Scanning electron fractographs of PTSE-2 in region of ductile tearing that followed cleavage arrest during the first transient. Region is between PM4 and PM5. (*a*) 100×, (*b*) 500× in center of part (*a*).

The light band between y_4 and y_5 is ductile tearing that is thought to have occurred during the second transient before mode conversion to cleavage. Figure 3.21 shows the region near PM6 at the boundary y_5 with the change from tearing to cleavage quite evident in Fig. 3.21(*b*). The region from y_5 to y_6 was examined also and was shown to be predominantly cleavage similar to that of the first transient but with slightly more predominant tear ridges.

The boundary y_6 visually appeared to be a possible momentary crack arrest followed by a small region of ductile tearing before cleavage initiation and propagation. The y_6 boundary is evident on the entire fracture surface (see Fig. 3.14). Figure 3.22 is a series of fractographs taken in the vicinity of PM7, located near that boundary, and showing the narrow band of ductile tearing between the two regions of cleavage. The SEM fractography likewise confirmed the cleavage mode of propagation from y_6 to y_7 and the fact that ductile tearing was the fracture mode beyond y_7 to the inner surface.

The vessel insert was also examined with optical metallography. Figures 3.23 and 3.24 show the general microstructures near the outer surface and at the 1/4t depth, respectively. The microstructures are quite similar, consisting of ferrite and ~40% pearlite. The higher magnification in Fig. 3.24(*b*) shows the pearlite interspersed with carbides.

Figure 3.25 is a plot of the measured diamond pyramid hardness (DPH) numbers as a function of distance from the vessel outer surface through the thickness. The figure has been annotated with approximate locations of the various boundary features discussed earlier. As mentioned earlier, the various boundary indications are not parallel across the surfaces, and distances between features in one location may be a few millimeters different than in another location.

There are wide variations in DPH, shown in Fig. 3.25, ranging from ~160 to 240 DPH (neglecting the two peaks at ~260 DPH). That range corresponds to HRB 82 to HRB 98. A nominal average then would be ~200 DPH (HRB 91). As discussed in Sect. 3.1, a hardness of HRB 90 was measured at the 1/4t depth of the vessel insert with a larger indenter (Rockwell B). There are also two peak hardnesses at midthickness at ~260 DPH (HRB 101).

The microstructures in the regions of some of the microhardness indentations were examined, and two are shown in Fig. 3.26. Figure 3.26(*a*) was taken ~4 mm from the outer surface; Fig. 3.26(*b*) was taken at about midthickness. Apparently, the percentage of pearlite was greater in the midthickness and the indenter was located in a fairly large patch of pearlite (harder than ferrite). It has been concluded that most of the variations in DPH are associated with the amount of pearlite sampled by the indenter. However, it is apparent that the average hardnesses at midthickness and near the inner surface are higher than near the outer surface.

Without additional detailed work, it is not possible to make any conclusions regarding possible correspondence between the crack events and microstructural features. No significant features that allow for such conclusive evidence have been observed in this study.

ORNL PHOTO 7744-87

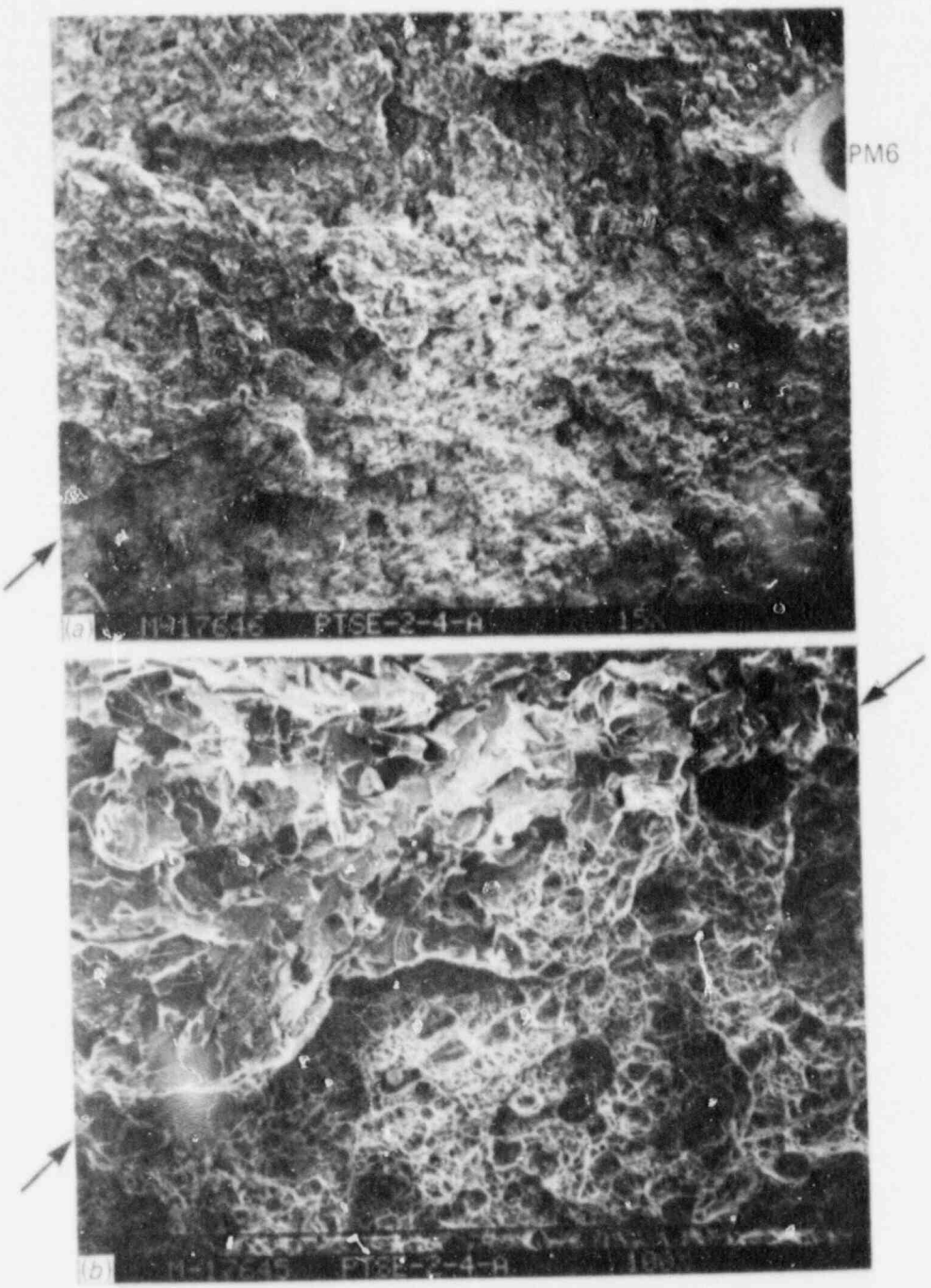

Fig. 3.21. Scanning electron fractographs of PTSE-2 at boundary between ductile tearing and cleavage regions of the second transient. (*a*) 15× showing PM6, (*b*) 100× in center of part (*a*).

ORNL PHOTO 7745-87

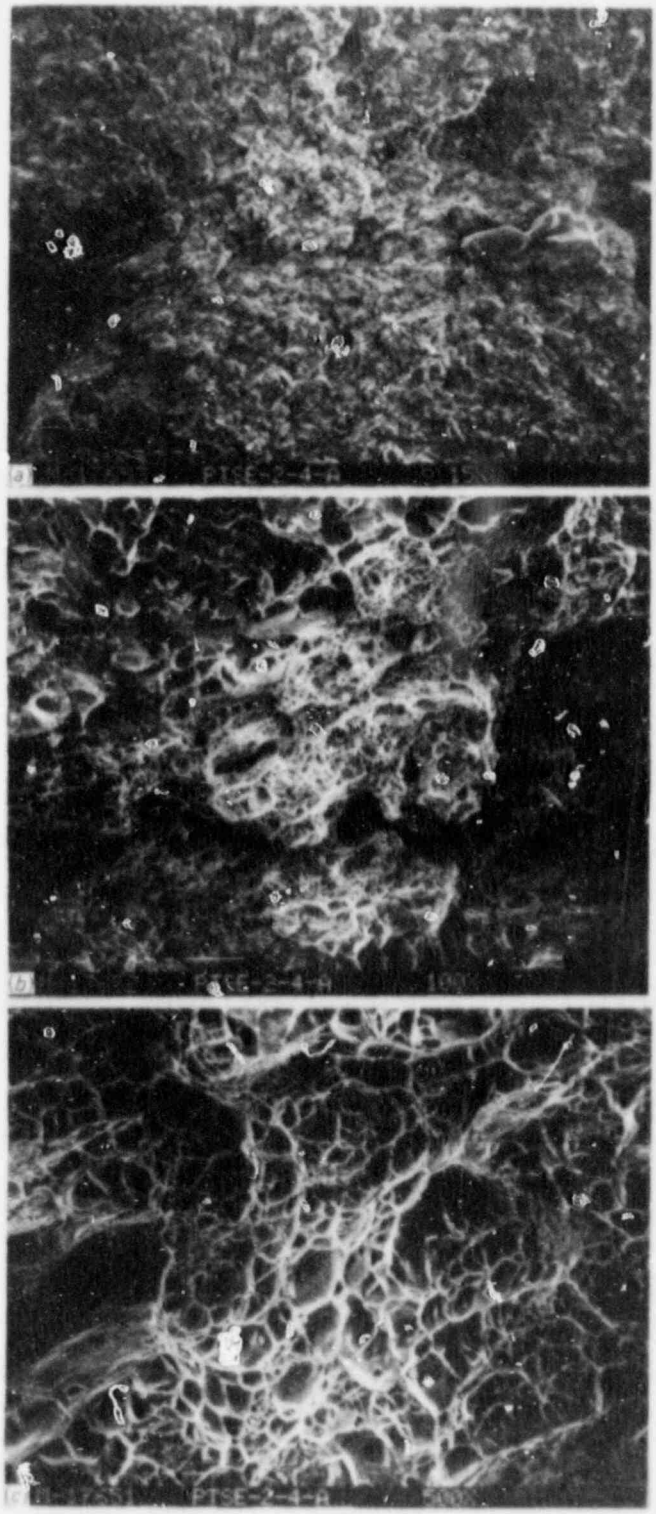

Fig. 3.22. Scanning electron fractographs of PTSE-2 in region of momentary crack arrest during second transient. (*a*) 15× showing PM7, (*b*) 100× showing band of ductile tearing with cleavage before and after tearing band, (*c*) 500× from center of part (*b*) clearly showing tearing mode.

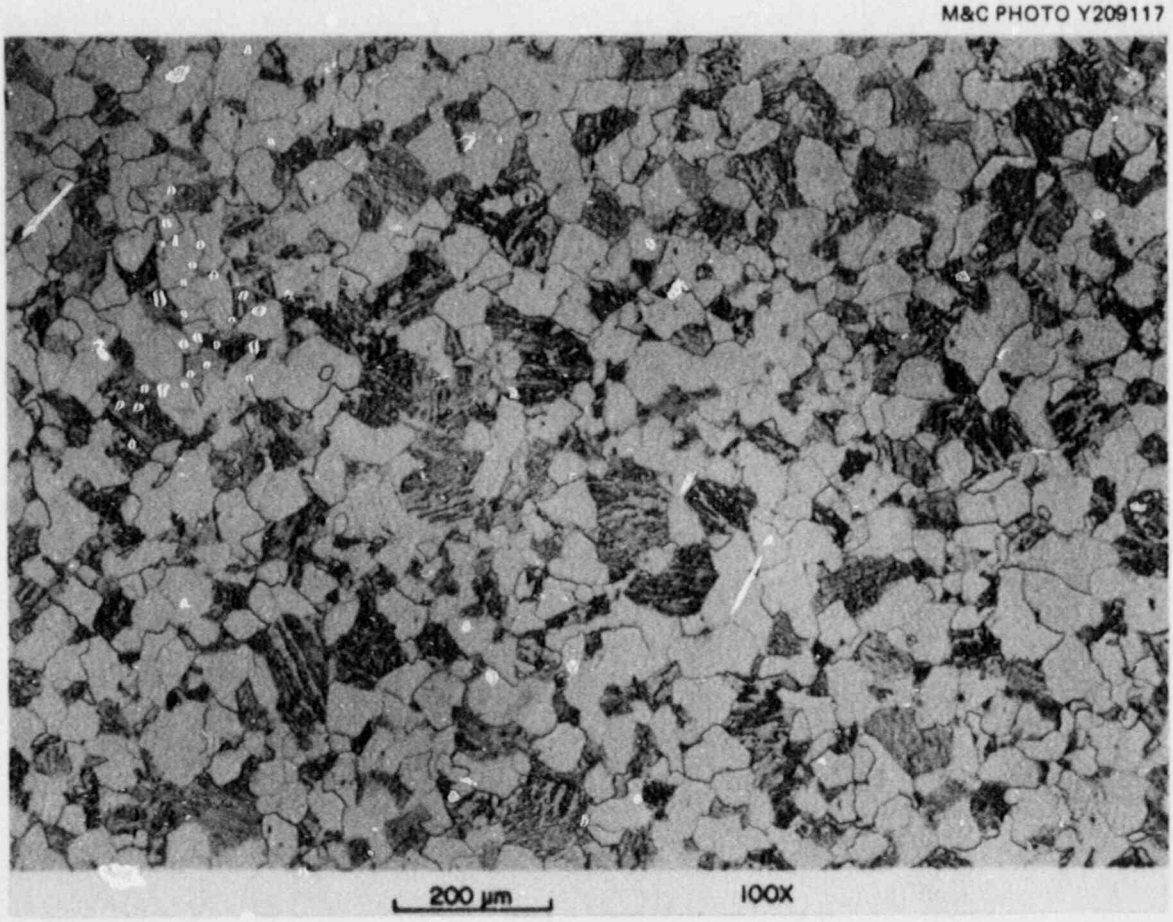

Fig. 3.23. Microstructure of PTSE-2 insert near the outer surface of the vessel taken in the transverse direction. The microstructure consists of ferrite with ~40% pearlite.

ORNL PHOTO 7746-87

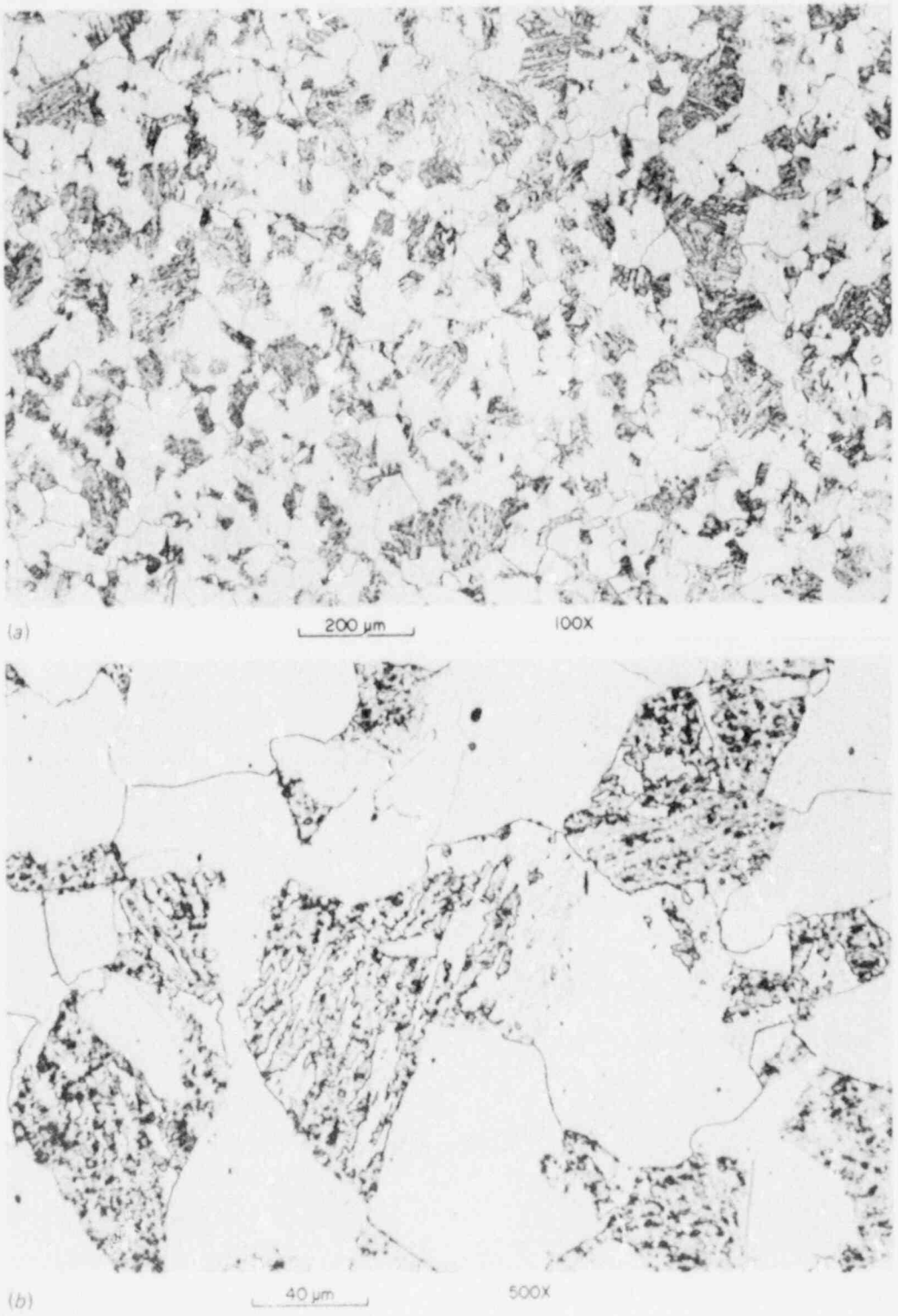

Fig. 3.24. Microstructure of PTSE-2 insert near the 1/4t depth taken in the transverse direction. (*a*) 100× showing a microstructure similar to that of Fig. 3.23, (*b*) 500× showing details of the pearlite patches interspersed with carbides.

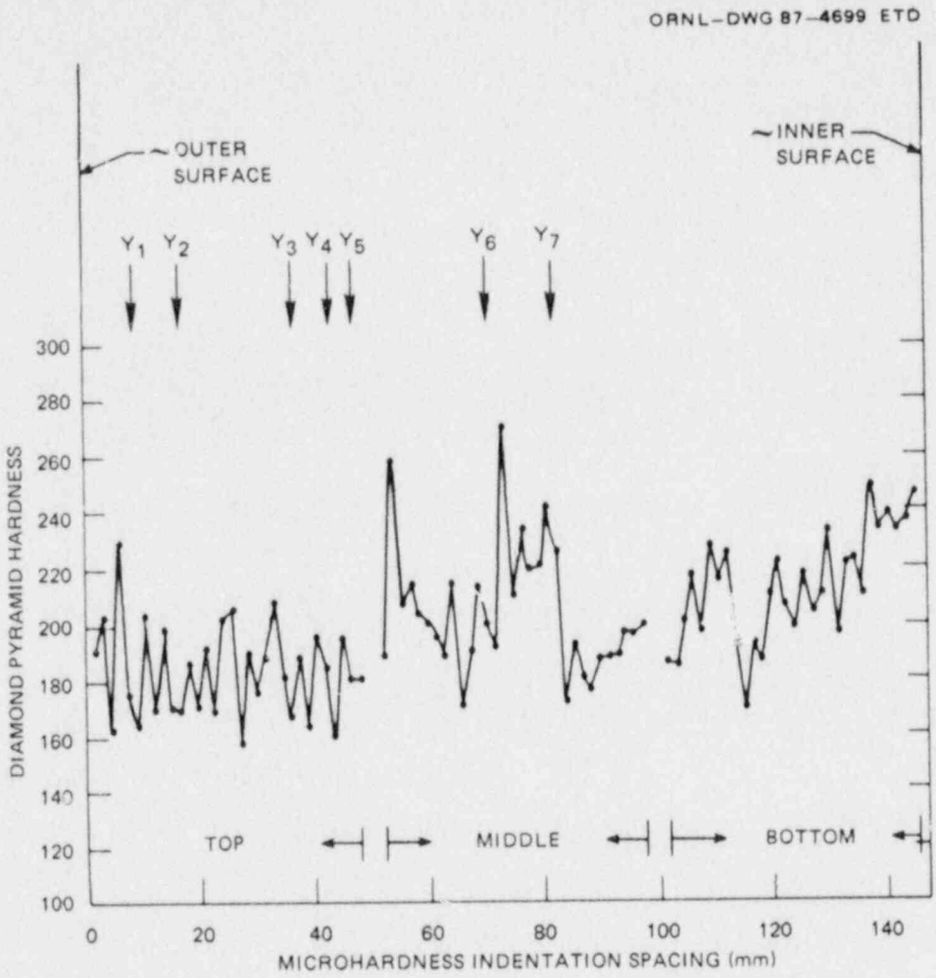

Fig. 3.25. Plot of microhardness (DPH) vs indentation spacing across the thickness of the PTSE-2 vessel insert following testing. The "y" numbers refer to boundary designations defined in Table 3.12.

ORNL PHOTO 7748-87

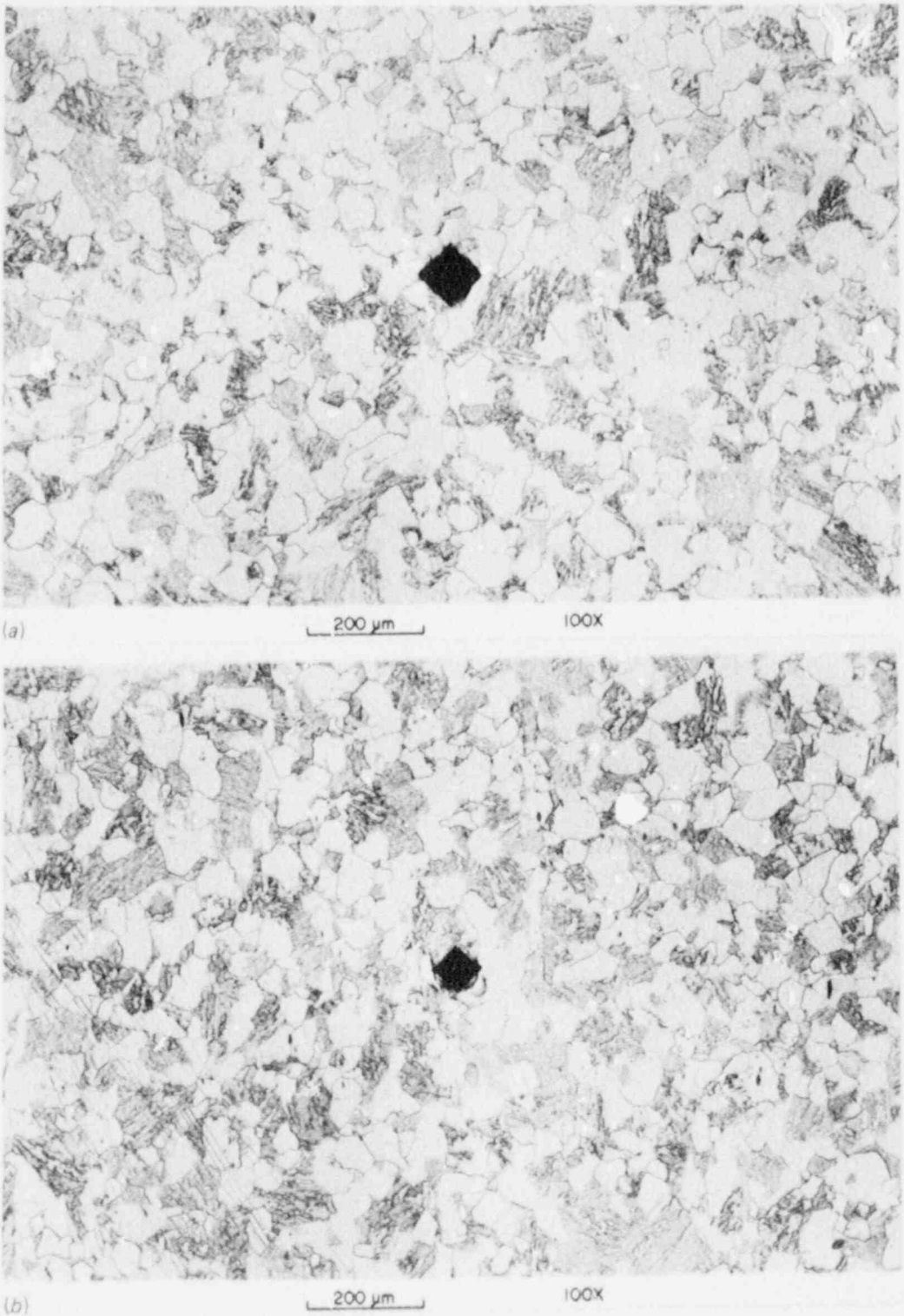

Fig. 3.26. Micrographs of PTSE-2 insert taken near microhardness indentations from (*a*) 162.3 DPH ~4 mm from the outer surface, (*b*) 267.9 DPH near midthickness. The amount of pearlite appears to be somewhat greater at the midthickness.

3.3 Posttest Material Characterization of Clad Plate Materials

S. K. Iskander D. J. Alexander
R. H. Baldwin E. T. Manneschmidt

Pretest material characterization has been reported in Ref. 8. Some posttest material characterization has been performed and is reported in this chapter. Tensile tests were performed to determine Young's modulus; Poisson's ratio; and stress-strain curves for base metal, heat-affected zone (HAZ), and cladding. The stress-strain curves will be used in finite-element analyses. Some room temperature tensile testing has been performed on the HAZ from one of the broken halves of the first plate tested because of differences between the characterization block and the clad plates. The RT_{NDT} of the base metal and the variation of hardness across the thickness of the plate have been determined, and some metallographic examinations have been performed. The hardness and metallurgical structures determined for the first plate are typical of all the other plates.

3.3.1 Tensile tests performed

To obtain stress-strain curves for use in the finite-element analysis of the experiments, tensile tests at room temperature have been performed on the base metal, HAZ, and 308 stainless steel weld metal. In conjunction with such tests, Young's modulus was also determined. In both cases, L-orientation specimens were employed, where L refers to the rolling direction of the base metal and is also parallel to the welding direction.

The size of the specimens used for both the stress-strain curves and Young's modulus (E) was limited by the available material. For clad metal, 4.55-mm-diam specimens were machined from the same three-layer clad block that was used in pretest material characterization but has received extra postweld heat treatment (PWHT).[8] Specimens from the HAZ of one of the broken halves of the clad plate CP-15 were machined such that the 6.35-mm-gage diameter of the specimen was just below the cladding. The clad plates have been clad with a single layer of stainless steel and given a slightly milder PWHT (593°C for 10 h) than typical for a clad reactor pressure vessel (621°C for 40 h). The HAZ from the single-layer clad plates has not received the additional tempering from the subsequent weld layers as has the three-layer clad material. HAZ from single-layer clad material is, therefore, expected to give a higher yield and ultimate strength than HAZ material from the three-layer characterization block. The base metal specimens used were 12.7 mm in diameter.

The results of the tensile tests are given in Table 3.13. Also included are the averages of the tests performed on material from the characterization block.[8] Note that the average yield and ultimate strengths of the present HAZ tests are ~20 and 15% higher, respectively, than averages of the characterization block, but, as expected, the base metal and cladding agree very closely with the previously determined

Table 3.13. Clad plate tensile properties at room temperature for L-orientation specimens[a]

Specimen	Test temperature (°C)	Strength (MPa)		Total elongation (%)	Reduction of area (%)
		0.2% yield	Ultimate		
		1/4t base metal			
3UAE5	26	575	708	20	58
3UAE6	24	575	710	19	58
Average[b]	22	589	727	16	59
		Heat-affected zone			
CP-3	26	674	793	19	66
CP-6	26	720	820	20	63
Average[b]	22	572	700	16	62
		Clad (weld metal)[c]			
A26A	24	301	574	46	53
A26B	26	297	577	48	57
Average[b]	22	308	561	52	50

[a]L orientation refers to rolling direction of base metal and welding direction of clad metal.

[b]Average values from characterization block material.

Source: W. R. Corwin, "Seventh HSST Irradiation Series: Stainless Steel Cladding," pp. 70–87 in *Heavy-Section Steel Technology Program Semiann. Prog. Rep. October 1985–March 1986*, NUREG/CR-4219, Vol. 3, No. 1 (ORNL/TM-9593/V3&N1), Martin Marietta Energy Systems, Inc., Oak Ridge Natl. Lab.

[c]Material also from characterization block but with extra postweld heat treatment.

values. Apparently, the extra PWHT has not affected the tensile properties of the cladding to any significant extent.

3.3.2 Determination of Young's modulus

Two L-orientation 1/4t specimens from each of the base metal, HAZ, and cladding and of the same dimensions as those used in the tensile tests described above were instrumented with electric resistance strain gages to measure Young's modulus E and Poisson's ratio ν. Two axial and two circumferential gages on each specimen were connected in series and placed diametrically opposite to each other to average out any bending

strains as a result of misalignment. The measurements were performed at room temperature, ~25°C. At each temperature, the specimens were first subjected to three loading and unloading cycles between zero and ~25% of the estimated 0.2% yield strength.

Table 3.14 shows the E and ν values for the clad plate materials. Strain measurements were performed at loads corresponding to the stress range shown for each material in Table 3.14, and E was calculated as the secant modulus between the two stresses. The values reported here for each temperature are the average of four measurements: two each during loading and unloading. Also given are the standard deviations (S) calculated from each set of four measurements. The accuracies of the E and ν values reported are estimated to be ~5 and 10%, respectively, because the strains were ~500 με for the axial direction and 140 με for the circumferential direction.

Young's modulus for base metal was also estimated from autographic records made using an averaging LVDT placed over a 50-mm gage length on specimens 3UAE5 and 3UAE6 (Table 3.14). The E-values obtained using the LVDTs are in close agreement with those obtained using electric-

Table 3.14. Young's modulus and Poisson's ratio for clad plates at room temperature for L-orientation specimens[a]

Specimen	Specimen diameter (mm)	Stress range (MPa)	Young's modulus (GPa)		Poisson's ratio	
			E	S[b]	ν	S[b]
1/4t base metal						
3UAE2	12.8	17–138	205	0.7	0.26	0.01
3UAE3	12.8	17–138	210	0.6	0.26	0.002
3UA35	12.8	17–138	206			
3UAE6	12.8	17–138	204			
Heat-affected zone[c]						
CP-1	5.08	11–109	205	2	0.27	0.01
CP-2	5.08	11–109	205	1	0.26	0.01
Cladding						
WC04E	4.55	13–68	151.7	0.4	0.47	0.06
WC15E	4.55	13–68	143.8	1.4	0.43	0.01

[a] L orientation refers to rolling direction of base metal and welding direction of clad metal.

[b] S = standard deviation of four values obtained.

[c] From clad plate CP-15, single-layer cladding.

resistance strain gages. Other E-modulus determinations on low-upper-shelf 2 1/4 Cr-1 Mo material using an averaging, 50-mm gage length LVDT also gave close agreement with E-moduli determined with electric-resistance strain gages. Thus, E-modulus determination with a 50-mm LVDT appears to be a more viable method than the use of electric-resistance strain gages.

Initially, the low values for the cladding were thought to be incorrect because of specimen misalignment. However, steps to improve the load train alignment with the specimen centerline by remachining the ends of the specimen and using dead loads still gave essentially the same results. A literature search for the elastic constants of 308 stainless steel weld cladding was unsuccessful, but Ref. 9 gives the plane-orthotropic elastic constants of type 308 stainless steel electroslag weld. For the same metallographic direction as in this case, Young's modulus and Poisson's ratio are 142 GPa and 0.53, respectively. The values reported for cladding are assumed reasonable.

Figures 3.27–3.29 are the stress-strain curves generated for base metal, HAZ, and cladding, respectively. These curves are composed of an initial slope that reflects average values of E reported above, merged with a stress-strain curve deduced from an x-y plotter record of load vs displacement. These curves have also been digitized for use in finite-element analysis.

The linear portion of the load-displacement curves for both cladding and HAZ were inaccurate, a reflection of the insufficient accuracy of the

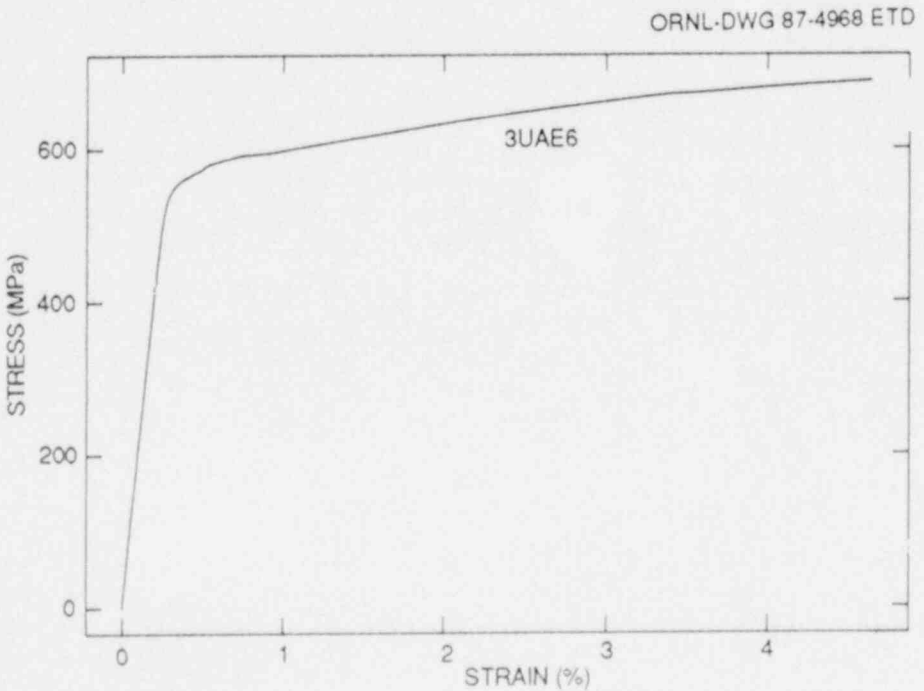

Fig. 3.27. Stress-strain curve for normalized and PWHT A 533 grade B base metal of clad plates.

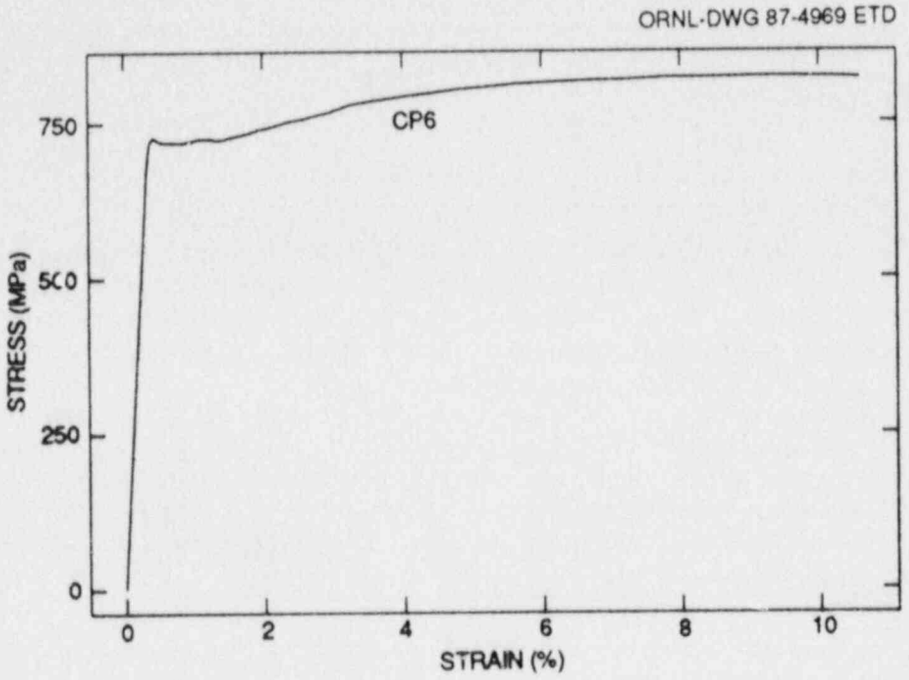

Fig. 3.28. Stress-strain curve for HAZ of single-layer clad plates.

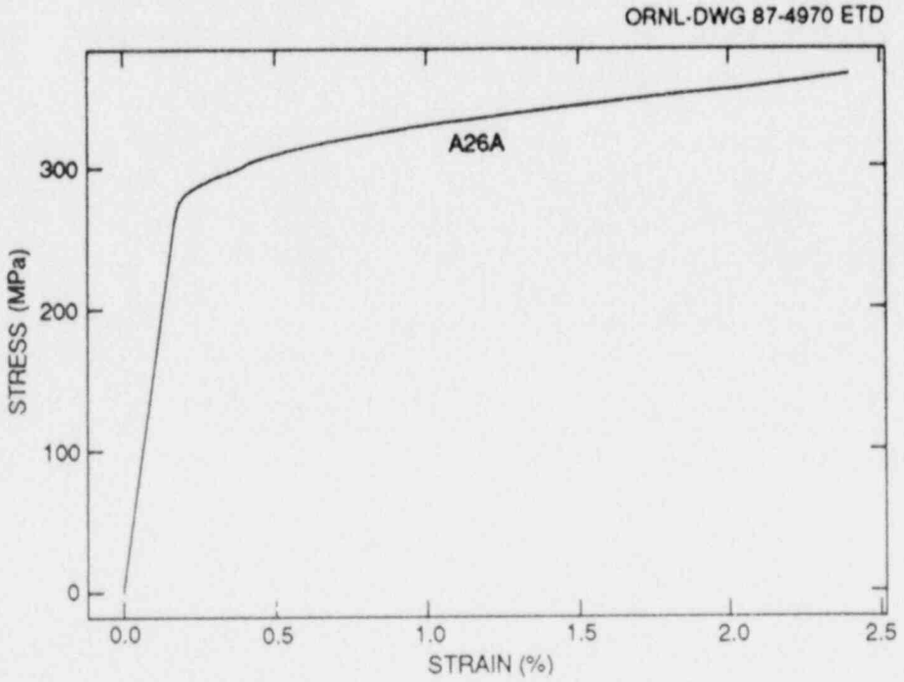

Fig. 3.29. Stress-strain curve for 308 stainless steel cladding.

small gage lengths of the specimens and the mechanical extensometers. As previously mentioned, tests on base metal with a 50-mm LVDT extensometer gave an initial slope that was in good agreement with E-values determined using electric-resistance strain gages as mentioned previously, and no adjustment was necessary.

3.3.3 Determination of RT_{NDT} for base metal

In accordance with NB-2330 of the *ASME Boiler and Pressure Vessel Code*, Sect. III, RT_{NDT} is the higher of the drop-weight NDT temperature and (T—33)°C, where T is defined as the higher temperature at which (for TL-orientation Charpy specimens) 67.8 J (50 ft-lb) and a lateral expansion of 0.89 mm (35 mils) are attained.

A drop-weight NDT of 36°C for the base metal of the plate has been previously determined.[6] A full Charpy energy curve has been developed for the TL orientation, and the results are given in Table 3.15. Figures 3.30—3.32 show plots vs temperature of the Charpy energy, lateral expansion, and percent shear fracture appearance, respectively. The temperature T as defined above has been determined to be 105°C, so the RT_{NDT} of the material is 72°C.

Table 3.15. Charpy impact test results for A 533 grade B, 1/4t depth material in TL orientation

Specimen[a]	Test temperature (°C)	Energy (J)	Lateral expansion (mm)	Fracture appearance (% shear)
CP-02	0	5	0.051	6
CP-03	0	5	0.025	3
CP-09	21	29	0.432	21
CP-10	21	24	0.356	12
CP-11	50	49	0.762	39
CP-12	50	36	0.533	30
CP-22	66	40	0.660	40
CP-23	66	37	0.635	40
CP-24	66	36	0.660	35
CP-08	80	36	0.787	52
CP-13	80	48	0.813	44
CP-14	80	53	0.914	57
CP-15	100	77	1.321	99
CP-16	100	67	1.092	73
CP-17	100	67	1.118	70
CP-18	105	72	1.092	90
CP-19	105	77	1.194	95
CP-20	105	81	1.295	100
CP-21	120	74	1.245	98
CP-01	120	69	1.245	100
CP-04	200	66	1.168	100
CP-07	200	81	1.359	100
CP-05	300	81	1.524	100
CP-06	300	83	1.397	100

[a]Heat treatment: normalized at 1032°C for 2 h, air cooled; postweld heat treated at 593°C for 10 h.

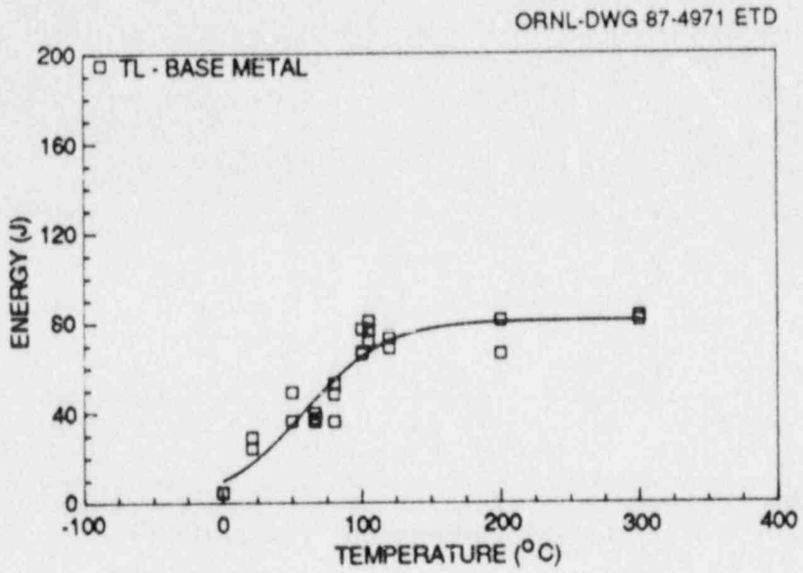

Fig. 3.30. Charpy impact energy for A 533 grade B, 1/4t depth material in the TL orientation.

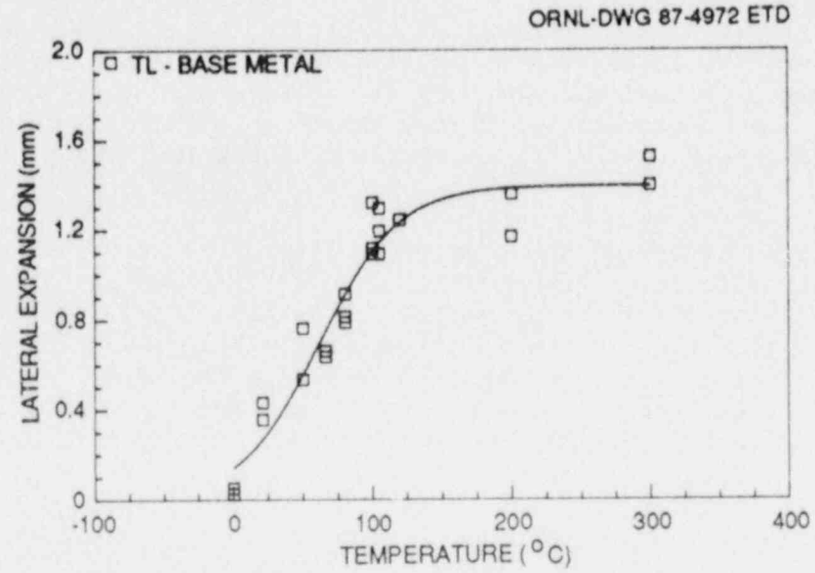

Fig. 3.31. Lateral expansion for A 533 grade B, 1/4t depth material in the TL orientation.

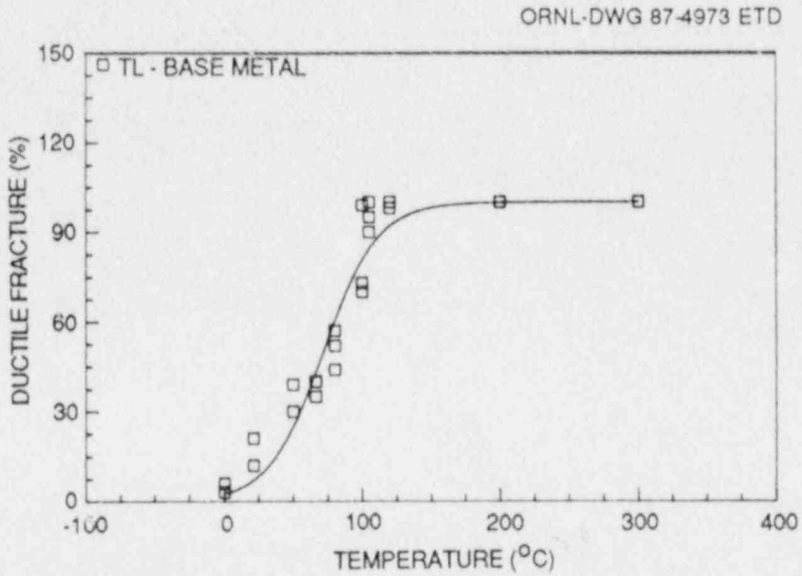

Fig. 3.32. Percent shear fracture appearance for A 533 grade B, 1/4t depth material in the TL orientation, respectively.

3.3.4 Metallography and hardness

Samples of the base metal from plate CP-15 were polished and etched to allow the microstructure to be examined. Sections were made corresponding to the L, S, and T planes of the plate (Fig. 3.33). Unetched samples allowed the inclusions to be examined, and etching revealed the microstructure. The HAZ was examined on sections from plate CP-15 taken parallel and also perpendicular to the fracture surface (L) in the direction of crack growth (T). A piece of the cladding from plate CP-15 was also sectioned along the L, S, and T planes and examined in the etched and unetched conditions.

The microstructure of the base metal (Fig. 3.34) consists of coarse ferrite grains with large grains of fine upper bainite. As the cladding is approached, the HAZ is encountered. Initially, the HAZ consists of the coarse ferrite grains with a decoration of fine bainite around the edges, which is the result of these grains being heated only slightly into the austenite region. Closer to the cladding, the material is heated further during the cladding application, so more of the ferrite is transformed to austenite, which then forms a fine bainite on recooling. Eventually, the entire structure is heated into the austenite region and then transforms into fine grains of ferrite and bainite as it cools. Close to the fusion line, the material is heated to higher temperatures and forms coarse austenite grains that transform to an acicular bainitic structure on cooling. All of these microstructures are then tempered somewhat during the application of subsequent passes of cladding with the amount of tempering dependent on the location of the material. The material near the edge of the HAZ that is adjacent to the next strip of cladding will be reheated and tempered significantly; the material at the

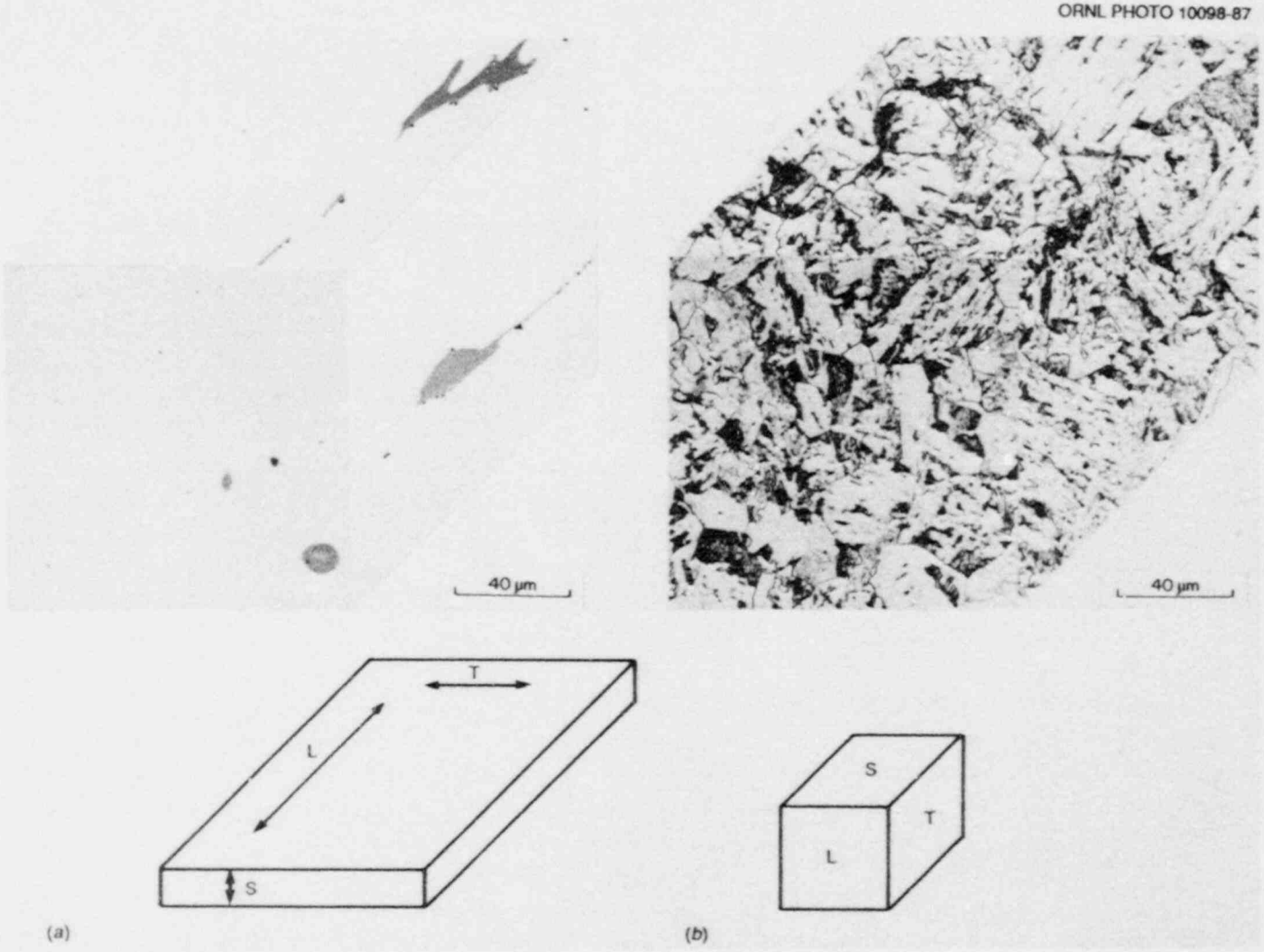

Fig. 3.33. Microstructure of the normalized A 533 grade B base plate, showing the orientation of the L, S, and T planes with respect to the plate. (*a*) Unetched plate directions, (*b*) etched plate designations.

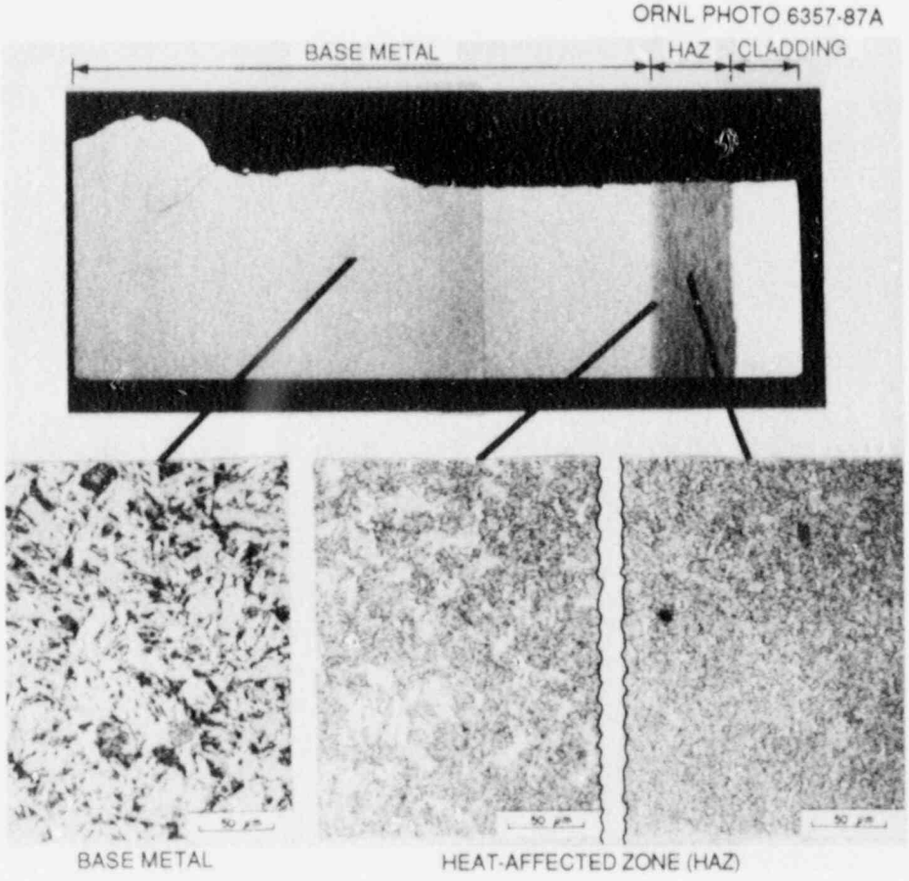

Fig. 3.34. Microstructure of the normalized A 533 grade B base plate and the HAZ.

other edge of that strip of the HAZ, however, will be unaffected. Thus, there will be a gradient in the microstructure and the mechanical properties both through the thickness of the HAZ and also across each strip of the HAZ resulting from the strips of cladding.

The cladding consists of three types of stainless steel wires, deposited simultaneously. This weld metal will also be diluted with some amount of the base metal. The three types of stainless steel wire used were 304, 308, and 309. The welding parameters and wire compositions were chosen to reflect current commercial practice. The cladding microstructure is shown in Fig. 3.35. Immediately adjacent to the HAZ, the cladding is fully austenitic. The bulk of the cladding consists of thin layers of ferrite dispersed among the austenite. The amount of ferrite varies from the bottom of the cladding toward the top with ~6% near the bottom of the cladding, increasing to ~10% at the top of the clad layer.

A microhardness traverse was made across the thickness of the plate on a section taken perpendicular to the final fracture surface (plane T). The result of this traverse is shown in Fig. 3.36. Some scatter exists

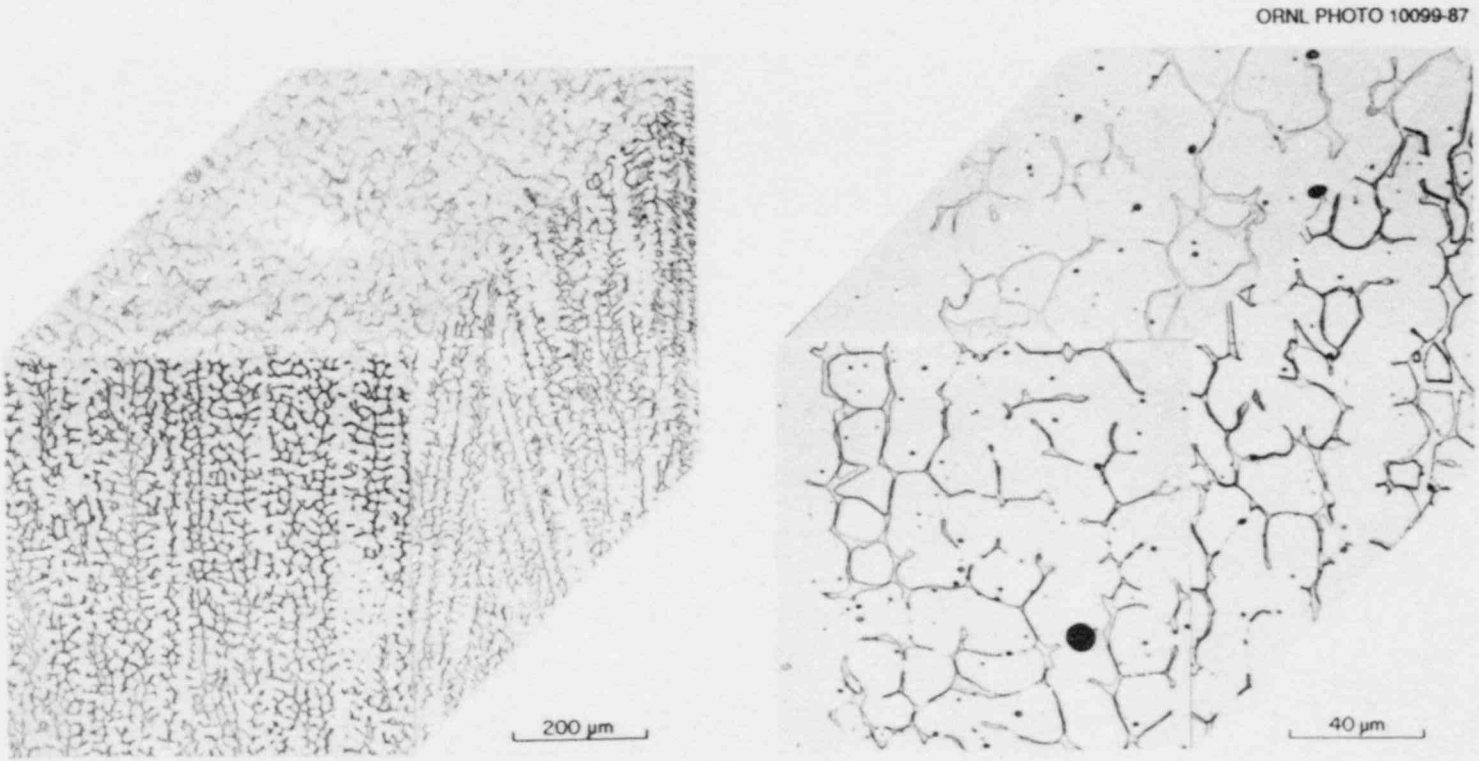

Fig. 3.35. Microstructure of the three-wire, series-arc, stainless steel cladding.

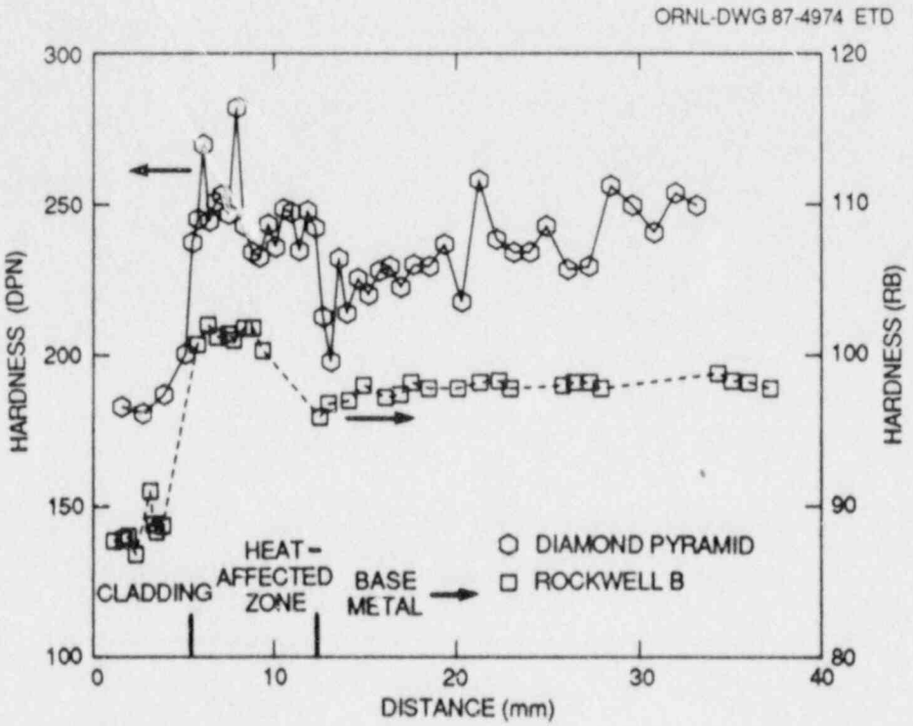

Fig. 3.36. Hardness traverse through cladding, HAZ, and base metal of clad plate CP-15.

in the data, the result of the small indenter sampling different regions in the inhomogeneous microstructure. In spite of this, several features can be noted from the traverse. The cladding has the lowest hardness, and there is a definite gradient in the microhardness of the cladding with the hardness increasing as the HAZ is approached. In the HAZ itself, the hardness tends to decrease as the base metal is approached although there are two somewhat harder points. The base metal has a lower hardness, and there seems to be a gradient in the plate also with the hardness tending to increase as the back of the plate is approached.

To confirm these results, a second traverse was made using the much larger indenter of the Rockwell B hardness tester. To achieve a fine spacing of the hardness measurements yet prevent interference between adjacent measurements, the readings were staggered across the specimen surface. These data are plotted in Fig. 3.36 for comparison with the microhardness data. The same trends are shown by the second set of hardness data, confirming the microhardness results.

References

1. R. K. Nanstad et al., "Pressurized Thermal Shock and Wide-Plate Crack Arrest Characterization," pp. 55–57 in *Heavy-Section Steel Technology Program Semiann. Prog. Rep. April–September 1986*, NUREG/CR-4219, Vol. 3, No. 2 (ORNL/TM-9593/V3&N2), Martin Marietta Energy Systems, Inc., Oak Ridge Natl. Lab.

2. R. K. Nanstad et al., "Low-Upper-Shelf Material Characterization," pp. 42–55 in *Heavy-Section Steel Technology Program Semiann. Prog. Rep. October 1986–March 1987*, NUREG/CR-4219, Vol. 4, No. 1 (ORNL/TM-9593/V4&N1), Martin Marietta Energy Systems, Inc., Oak Ridge Natl. Lab.

3. R. H. Bryan et al., *Pressurized-Thermal-Shock Test of Six-in.-Thick Pressure Vessels. PTSE-2: Investigation of Low Tearing Resistance and Warm Prestressing*, NUREG/CR-4888 (ORNL-6377), to be published.

4. R. L. Graves, F. J. Weaver, and D. L. McElroy, internal memorandum to J. P. Strizak, Oak Ridge National Laboratory, September 15, 1986.

5. T. G. Kollie et al., "A Computer Operated Fused Quartz Differential Dilatometer," pp. 12–146 in *Thermal Expansion – 1973, AIP Conference Proceedings No. 17*, American Institute of Physics, New York, 1974.

6. *ASME Boiler and Pressure Vessel Code. An American National Standard*, ANSI/ASME BPV-III-1-NB, American Society of Mechanical Engineers, New York, 1986.

7. W. R. Corwin et al., "Nugget Specimen," p. 58 in *Heavy-Section Steel Technology Program Semiann. Prog. Rep. October 1986–March 1987*, NUREG/CR-4219, Vol. 4, No. 1 (ORNL/TM-9593/V4&N1), Martin Marietta Energy Systems, Inc., Oak Ridge Natl. Lab.

8. W. R. Corwin, "Seventh HSST Irradiation Series: Stainless Steel Cladding," pp. 70–87 in *Heavy-Section Steel Technology Program Semiann. Prog. Rep. October 1985–March 1986*, NUREG/CR-4219, Vol. 3, No. 1 (ORNL/TM-9593/V3&N1), Martin Marietta Energy Systems, Inc., Oak Ridge Natl. Lab.

9. B. R. Dewey et al., "Measurements of Anisotropic Elastic Constants of Type 308 Stainless-Steel Electroslag Welds," *Exp. Mech.* 17(11), 420–26 (November 1977).

4. ENVIRONMENTALLY ASSISTED CRACK-GROWTH TECHNOLOGY*

C. E. Pugh

This task has been carried out through subcontract with Westinghouse Electric Corporation, Generation Technology Systems Division (W. H. Bamford, principal investigator) and was concluded at the end of FY 1986. Follow-on work will be performed by other ongoing Nuclear Regulatory Commission (NRC) programs [e.g., at Materials Engineers Associates (MEA)] to the degree necessary. The first priority was to complete the characterization of two major known influences on the enhancement of crack-growth rates in water environments: the influences of the material chemistry through sulfur content and the influence of the water environment. Both of these tasks have been concluded.

Another important task was to develop a relationship between cyclic-fatigue and static-load crack growth. This work is interrelated with the mechanisms of environmental enhancement of crack growth and should considerably improve understanding in this area. This work will continue at MEA.

The ultimate goal of the task has been to propose, as appropriate, revisions to the *American Society of Mechanical Engineers (ASME) Code* reference crack-growth curves based on environmental considerations. A report[1] summarizing the results of this program from its inception (early 1970s) was drafted and transmitted to Oak Ridge National Laboratory in August. Photomasters for the report and graphics preparations are under way for the report to be issued during the next period.

Reference

1. W. H. Bamford, *A Summary of Environmentally Assisted Crack-Growth Studies Performed at Westinghouse Electric Corporation: Under Funding from the Heavy-Section Steel Technology Program*, NUREG/CR-5020 (ORNL/Sub/82-21598/1), Martin Marietta Energy Systems, Inc., Oak Ridge Natl. Lab.

---

*Work sponsored by Heavy-Section Steel Technology Program under Subcontract 11X-21598C between Martin Marietta Energy Systems, Inc., and Westinghouse Electric Corporation, Generation Technology Systems Division, W. H. Bamford, principal investigator.

5. CRACK-ARREST TECHNOLOGY

D. J. Naus

5.1 Background

Current light-water reactor (LWR) pressure vessel safety assessment methods are based in large measure on Sects. III and XI of the *American Society of Mechanical Engineers (ASME) Boiler and Pressure Vessel Code (B&PVC)*. In pressurized-thermal-shock (PTS) scenarios, inner surface flaws have the greatest propensity to propagate because they are in the region of highest thermal stress, lowest temperature, and greatest irradiation damage. If such a flaw begins to propagate radially through the vessel wall, it will extend into a region of higher fracture toughness because of higher temperatures and less irradiation damage. Although the thermal stresses may decrease with propagation depth, the stress-intensity factor caused by the elevated pressure loading will be increasing. Assessment of the integrity of a reactor vessel under such a postulated crack run-arrest scenario requires prediction of the arrest location, potential reinitiation, stable and unstable ductile crack growth, and structural instability of the remaining vessel wall ligament.

The primary objective of the crack-arrest studies under the Heavy-Section Steel Technology (HSST) Program is to generate data for understanding the crack-arrest behavior of prototypical pressure vessel steels at temperatures near and above the onset of the Charpy upper-shelf region. Program goals include (1) extending the existing K_{Ia} data bases beyond those associated with the upper limit in the *ASME B&PVC*; (2) clearly establishing that crack arrest occurs before fracture-mode conversion; (3) observing the relationship between arrest data and machine/specimen compliance behavior; and (4) validating the predictability of crack arrest, stable tearing, and/or unstable tearing sequences for ductile materials. Additionally, the tests and analyses provide bases for obtaining and interpreting dynamic fracture data (with relatively long crack runs) and bases for validation of viscoplastic fracture models and analysis methods. During the current report period, the program objectives and goals were investigated for a low-upper-shelf base material (specially heat-treated, 2 1/4 Cr-1 Mo steel) and prototypical pressure vessel materials, A 533 grade B class 1 steels. Future studies will also investigate a low-upper-shelf weld material.

The wide-plate tests are being conducted at the National Bureau of Standards (NBS), Gaithersburg, Maryland, under an interagency agreement. The tests are designed to provide fracture-toughness measurements at temperatures approaching or above the onset of the Charpy upper-shelf regime in a rising toughness region and with an increasing driving force. In addition to providing crack-arrest data, the wide-plate tests provide information on dynamic fracture (run and arrest) processes that are being used by researchers at Oak Ridge National Laboratory (ORNL), Southwest Research Institute (SwRI), and the University of Maryland (UM) to develop and evaluate improved fracture-analysis methods (see Chap. 2).

Crack-arrest-related work is also being sponsored by the HSST Program at UM to coordinate an American Society for Testing and Materials (ASTM) round-robin on crack-arrest test procedures and at Battelle-Columbus Laboratories (BCL) to maintain and document available crack-arrest toughness K_{Ia} data. These activities are reported in Sects. 5.5 and 5.6, respectively.

5.2 Wide-Plate Crack-Arrest Testing*

R. deWit† S. R. Low†
R. J. Fields†

5.2.1 Introduction

The HSST wide-plate crack-arrest tests are being performed with the 27-MN-capacity testing machine at NBS. The first series of six tests (WP-1.1 through WP-1.6) has been completed, using specimens fabricated from HSST plate 13A of A 533 grade B class 1 steel. The first three tests using a low-upper-shelf base material (WP-2.4, WP-2.1, and WP-2.5) were completed during the two previous report periods. During this report period, three additional tests were conducted: one using the low-upper-shelf material (WP-2.3) and two using A 533 grade B class 1 materials (WP-1.7 and WP-CE-1). Each test used a single-edge notched (SEN) plate specimen that was subjected to a thermal gradient along the plane of crack propagation. The linear thermal gradient, which provides a rising toughness field, was achieved by cooling the notched edge of the plate and heating the other edge. During each test, strain and temperature were obtained as functions of time and position. Also, load, crack-opening-displacement (COD), acoustic emission (AE), and accelerometer data were obtained during each test as functions of time. Figure 5.1 presents a schematic of a wide-plate crack-arrest specimen, and Fig. 5.2 shows a specimen positioned in the NBS testing machine. More details on the specimen assembly can be obtained from Ref. 1.

The ninth (WP-2.5) HSST wide-plate crack-arrest test was performed on January 8, 1987. During this report period, posttest analyses for WP-2.5, as well as testing of three additional wide-plate crack-arrest specimens (WP-2.3, WP-1.7, and WP-CE-1), were conducted. Tests WP-2.3 (low-upper-shelf material), WP-1.7 (A 533 B class 1 material), and WP-CE-1 (A 533 B class 1 material) were conducted on May 28, 1987; July 23, 1987; and September 14, 1987. The 1 × 1 × 0.15 m specimens (0.1 m for specimen

---

*Work sponsored by the HSST Program under Interagency Agreement No. DE-AC05-840R21432 between the U.S. Department of Energy and the National Bureau of Standards.

†Fracture and Deformation Division, National Bureau of Standards, Gaithersburg, Maryland.

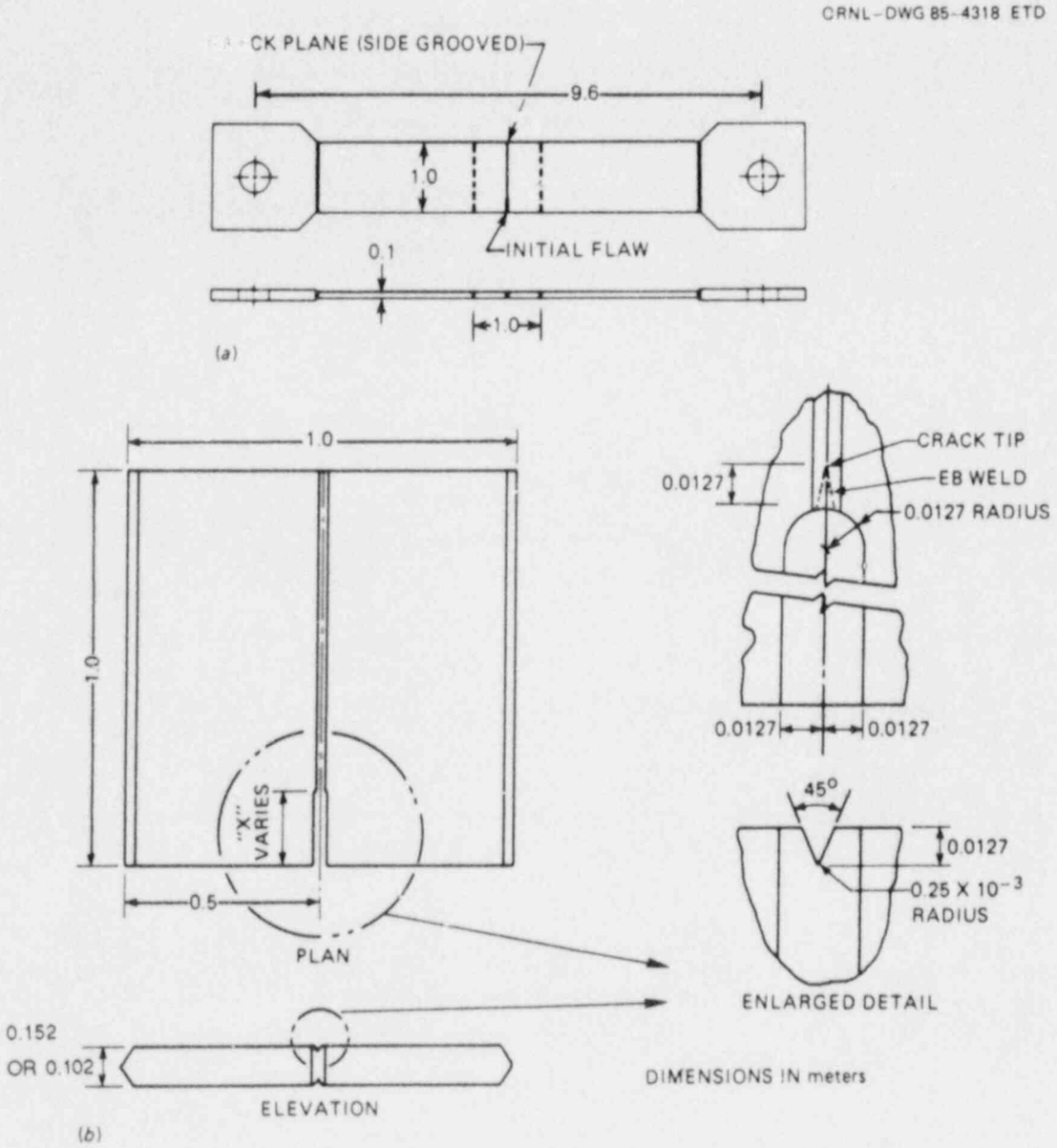

Fig. 5.1. Schematic of HSST wide-plate crack-arrest specimen.

WP-CE-1) were provided by ORNL. The specimens had been precracked by hydrogen charging an electron-beam (EB) weld located at the base of a premachined notch in the plate (Fig. 5.1). The crack front of specimens WP-1.7 and WP-CE-1 had also been cut into the chevron configuration shown schematically in Fig. 5.3. Table 5.1 presents specific dimensions for each of the plate specimens.

ORNL PHOTO 6718-85

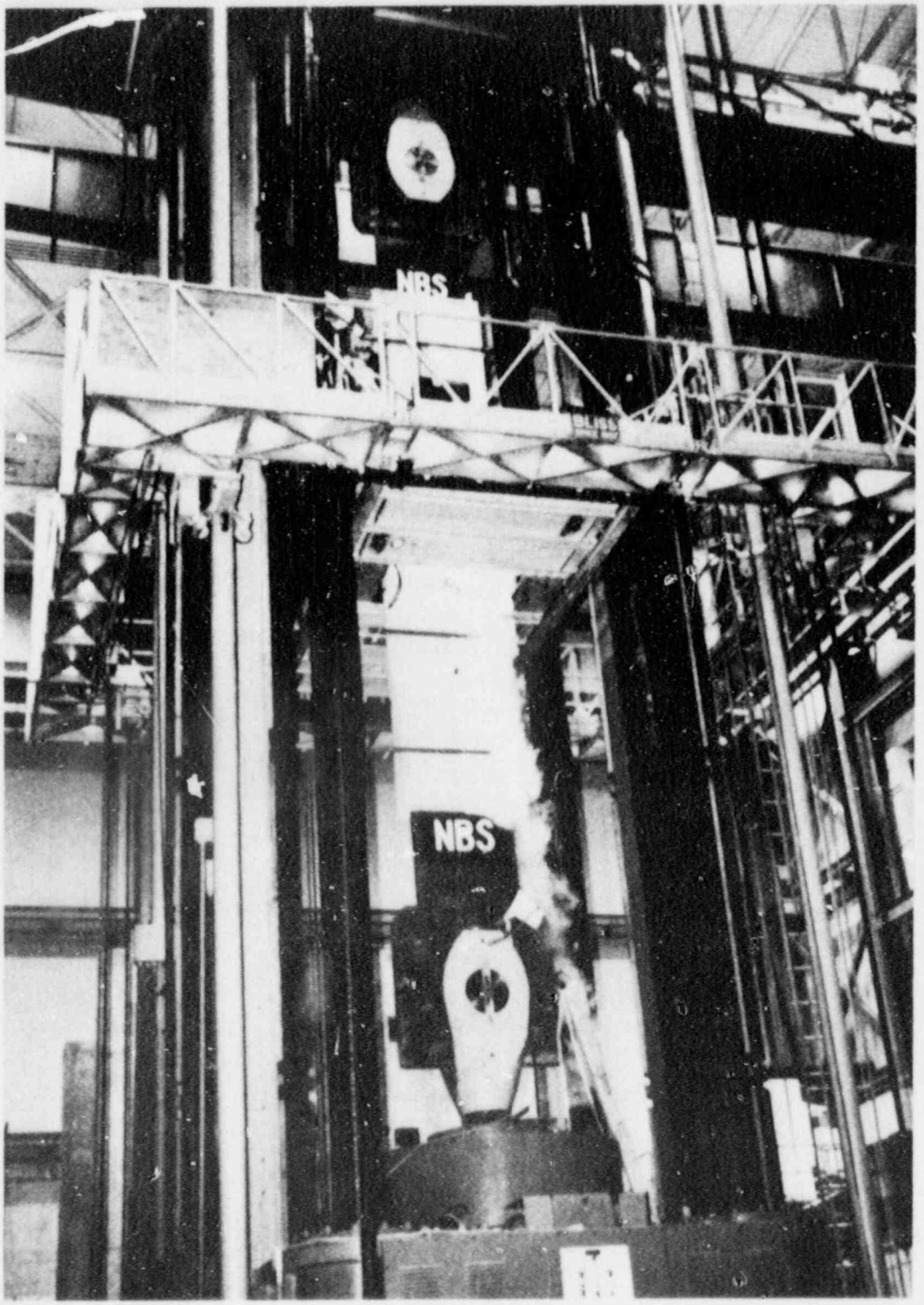

Fig. 5.2. Wide-plate crack-arrest test in progress using the 27-MN capacity tensile machine at NBS Gaithersburg fracture laboratory.

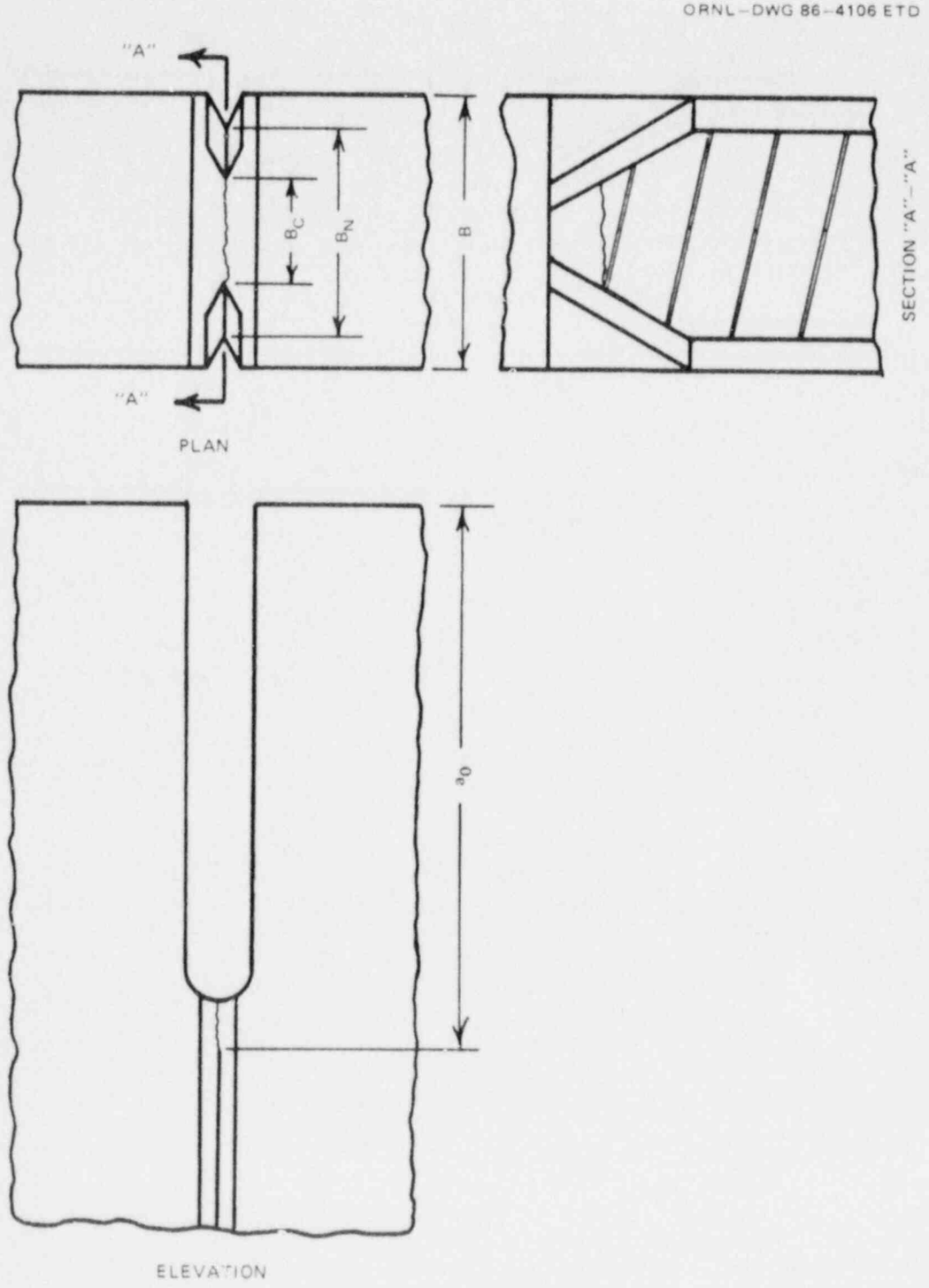

Fig. 5.3. Schematic of chevron configuration of crack front.

Table 5.1. Detailed dimensions of wide-plate crack-arrest specimens

Specimen feature	Symbol[a]	Dimension (mm)			
		WP-2.5	WP-2.3	WP-1.7	WP-CE-1
Initial crack length	a_o	199	200	202	[c]
Thickness	B	101.6	152.4	152.4	101.7
Notch thickness	B_N	76.2	113.8	114.3	76.3
Chevron thickness (thickness a_o)	B_C	40.7	NA[b]	61.0	[c]
Width	W	999	1000	1000	1000
Pop-in crack length	a'_o	264	NA[b]	NA[b]	NA[b]

[a]See Fig. 5.3.

[b]Not applicable.

[c]Initial crack length and chevron thickness dimensions for specimen WP-CE-1 were not available because the test was performed late in the reporting period.

5.2.2 Instrumentation and testing procedure

NBS welded the plate specimen to pull plates; the overall specimen dimensions for WP-2.5, -2.3, -1.7, and -CE-1 are presented in Fig. 5.4. (The length of pull plates changed from test to test as a result of the cutting procedure used to remove a specimen before welding of the next specimen.) The specimens were then instrumented with 40 thermocouples positioned as shown in Fig. 5.5. Biaxial and uniaxial strain gages were placed on the specimen and pull plates as shown in Fig. 5.6. Additional instrumentation included two COD gages installed on the front (F-COD) and back (B-COD) plate faces at a/w = 0.150 (the gages measured the displacement between points 30 mm above and 30 mm below the crack plane), an AE transducer located on the lower pull tab, and two accelerometers mounted at the top and bottom pull plates near the pull tabs. A measurement of tensile load applied to the specimen was obtained from the testing machine load cell.

After being instrumented, the specimen was placed into the testing machine and insulated. A temperature gradient was then imposed across the plate by liquid nitrogen cooling of the notched edge while the other edge was heated. Liquid nitrogen flow and power to the heaters were continuously adjusted to obtain the desired thermal gradient. Final calibrations of the strain gages, CODs, and load were completed just before

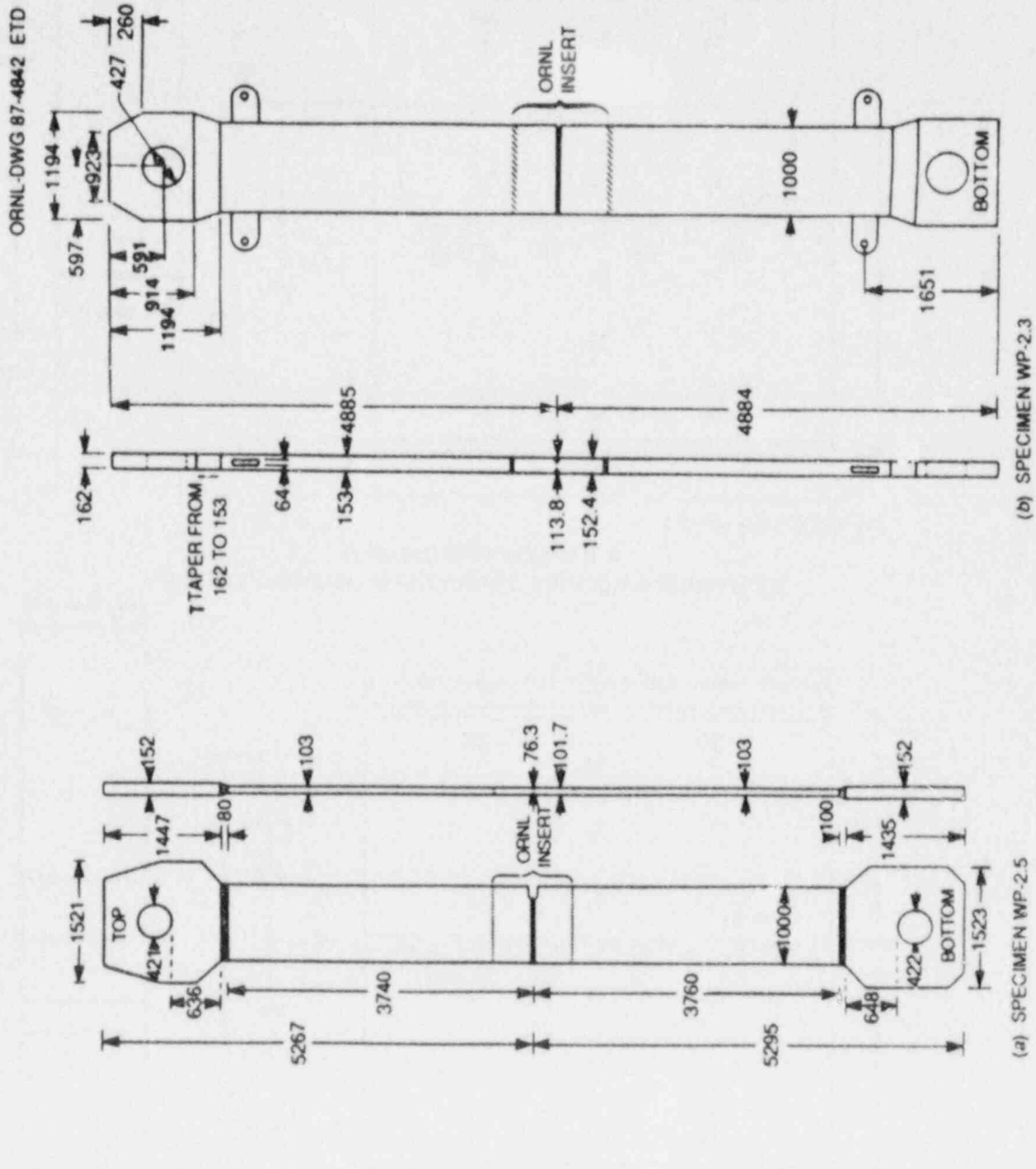
ORNL-DWG 87-4842 ETD
427
260
1194
923
597
591
914
1194
ORNL
INSERT
1000
BOTTOM
1651
4885
4884
162
TAPER FROM
162 TO 153
64
153
113.8
152.4
(b) SPECIMEN WP-2.3
152
103
76.3
101.7
103
152
1447
80
ORNL
INSERT
100
1435
1521
TOP
421
1000
1523
422
BOTTOM
636
3740
3760
648
5267
5295
(a) SPECIMEN WP-2.5

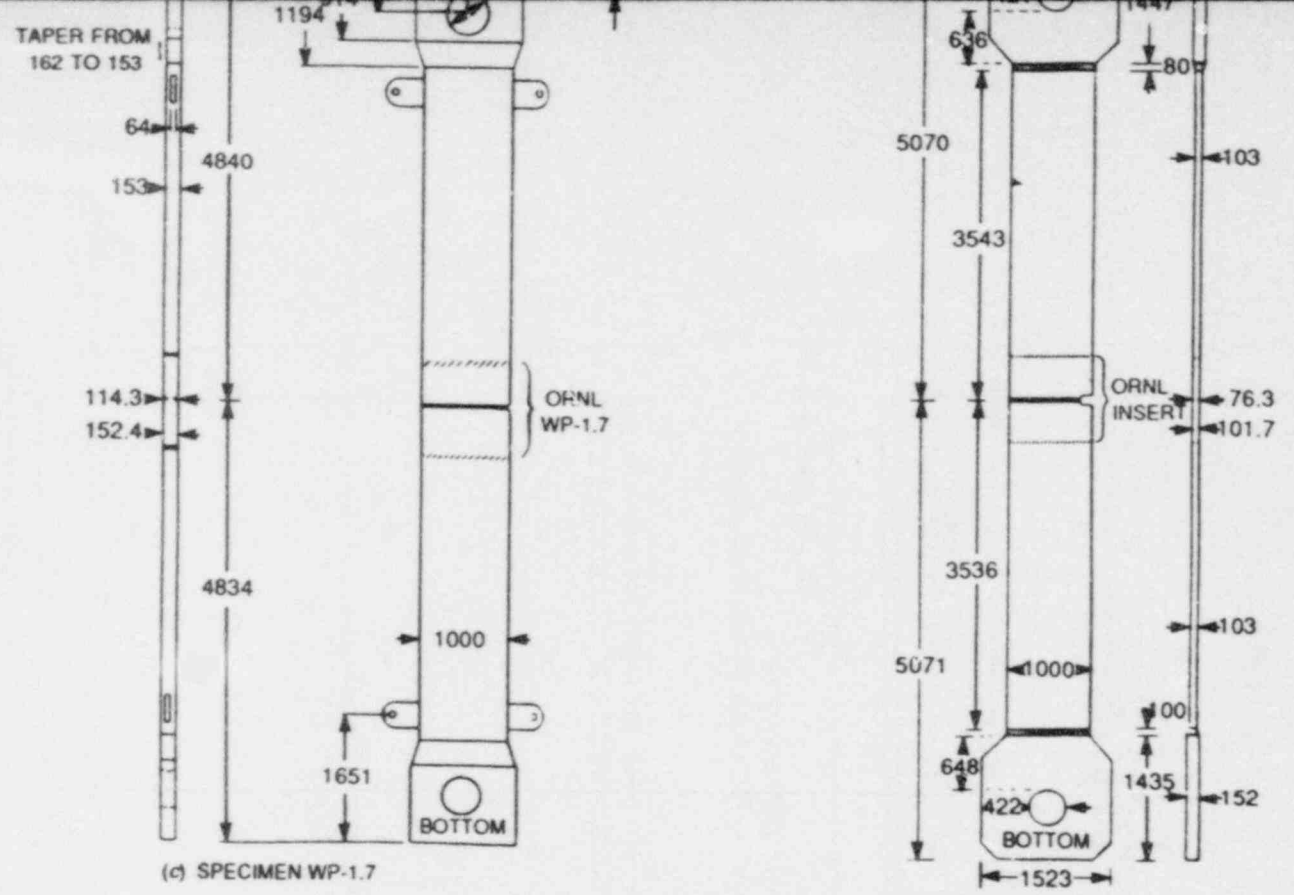

Fig. 5.4. Overall dimensions for HSST wide-plate crack-arrest specimens and pull-plates for (*a*) specimen WP-2.5, (*b*) specimen WP-2.3, (*c*) specimen WP-1.7, and (*d*) specimen WP-CE-1.

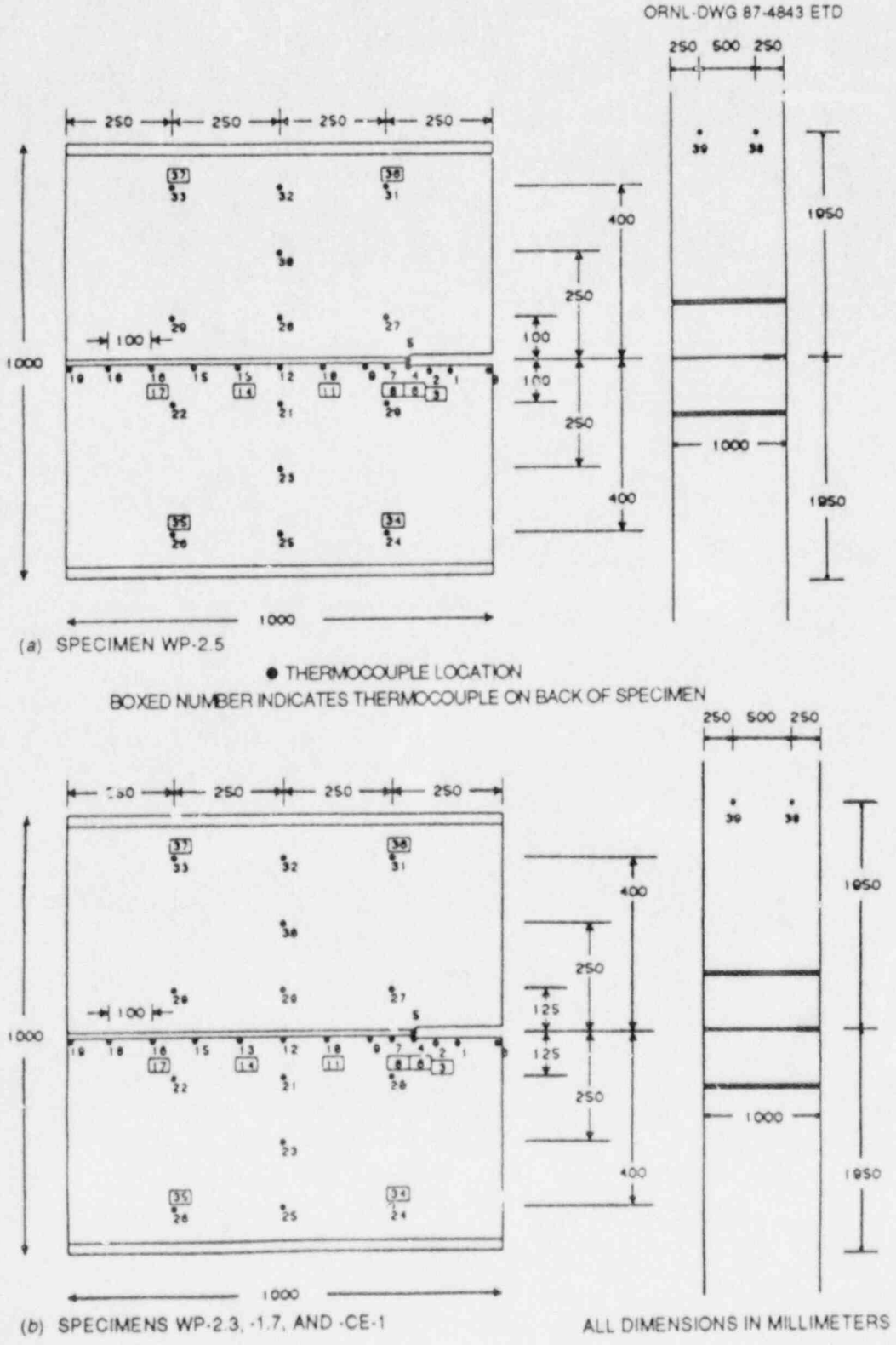

Fig. 5.5. Thermocouple locations for wide-plate crack-arrest specimens. (*a*) Specimen WP-2.5, (*b*) specimens WP-2.3, -1.7, and -CE-1.

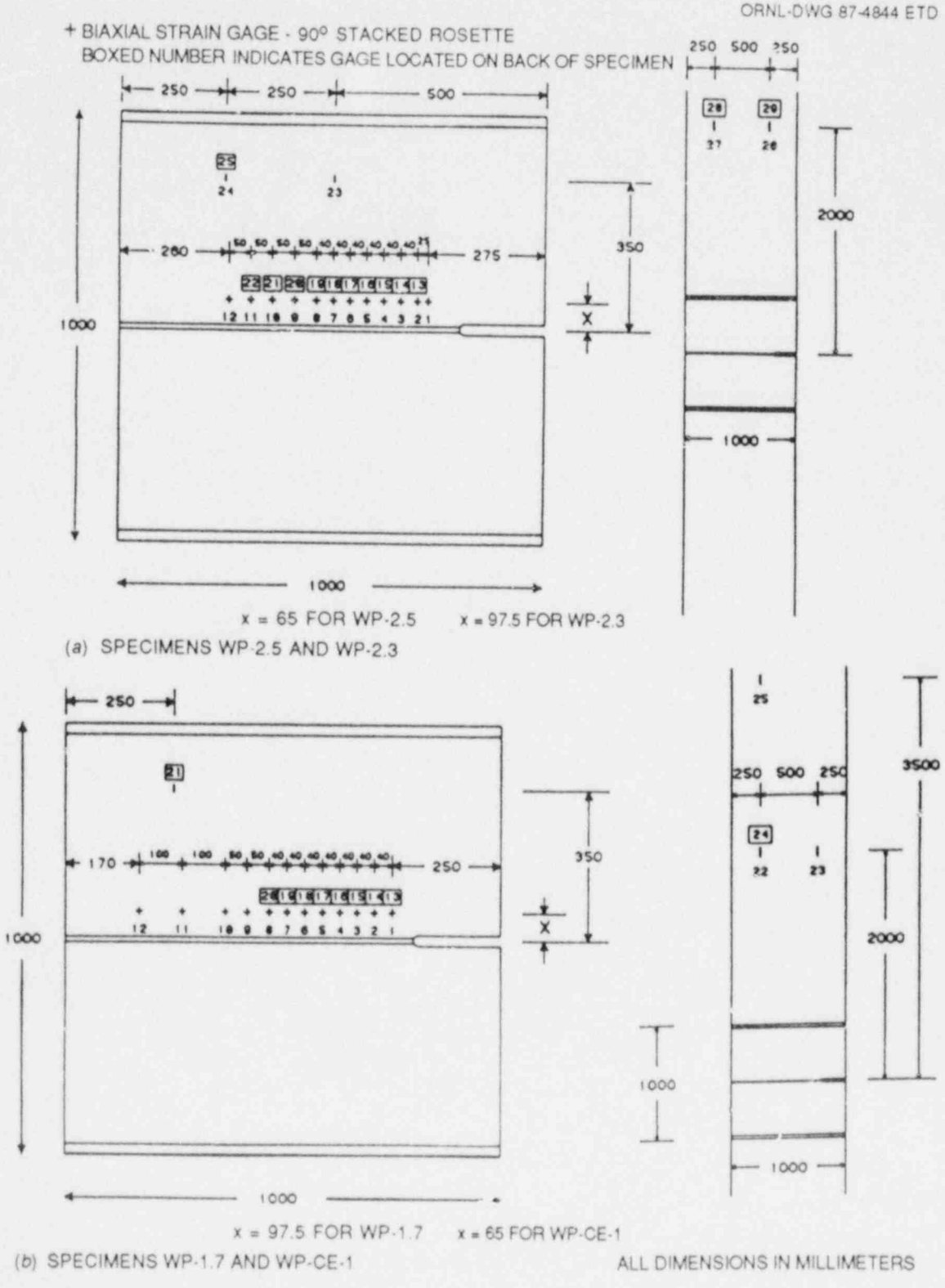

Fig. 5.6. Strain-gage locations for HSST wide-plate crack-arrest test specimens. (*a*) Specimens WP-2.5 and -2.3, (*b*) specimens WP-1.7 and -CE-1. x = 65 for WP-2.5, x = 97.5 for WP-2.3, x = 97.5 for WP-1.7, and x = 65 for WP-CE-1.

specimen loading. The specimen was then loaded until crack propagation occurred.

5.2.3 Test description summary*

5.2.3.1 Test WP-2.5. The WP-2.5 test was performed at NBS on January 8, 1987.[2] This was the third test using the low-upper-shelf base material. After the thermal gradient shown in Fig. 5.7(*a*) was obtained, specimen loading was initiated at an average rate of 25 kN/s. At 7.53 MN or 86% of peak load, a pop-in was heard that was later supported by the strain-gage outputs, accelerometer readings, and examination of the fracture surface. Specimen loading was continued; at a load of 8.9 MN, the fracture event began and lasted about 90 ms (cleavage fracture plus ductile tearing). The strain-gage output and the fracture surface indicated that six cleavage crack run-arrest events occurred before the onset of ductile tearing. A small, 8.5-mm, plate ligament remained intact after the fracture event.

5.2.3.2 Test WP-2.3. The tenth wide-plate crack-arrest test, WP-2.3, was performed on May 28, 1987.[3] This fourth test used the low-upper-shelf base material and was the first to use a nonchevroned crack front. Test WP-2.3 also was the second test in the WP-2 series that used a 152-mm-thick plate. After a satisfactory thermal gradient was obtained [Fig. 5.7(*b*)], the specimen was loaded at an average rate of 14 kN/s. At a load of 15.3 MN, the fracture event began and lasted about 900 ms (crack run-arrest events plus ductile tearing). Examination of the strain-gage records and fracture surface indicated that three cleavage crack run-arrest events were detectable at the front face and four at the back face of the plate.

5.2.3.3 Test WP-1.7. The WP-1.7 test was performed at NBS on July 23, 1987.[4] This seventh test in the WP-1 series was the first to use a 152-mm-thick plate. After a satisfactory thermal gradient was obtained [Fig. 5.7(*c*)], the specimen was loaded at an average rate of 17 kN/s. At the testing machine's 26.7-MN tensile load capacity, the crack run-arrest event(s) had not occurred, so the load was held constant for 176 s. During this constant load period, the crack run-arrest event(s) did not occur, so the specimen was rapidly unloaded in an effort to sharpen the crack tip before application of a second load cycle. Two changes were made in the testing procedure before application of the second load cycle. The crack-tip temperature was lowered ~5°C to −23.7°C, and the specimen loading rate was increased by a factor of ~5. Approximately 4700 s after the beginning of the first load cycle, specimen loading was reinitiated at a rate of 90 kN/s. At a load of 26.2 MN, the crack run-arrest events initiated and lasted ~27.5 ms (crack run-arrest events plus ductile tearing). Examination of the strain-gage records and fracture surface indicated that two cleavage crack run-arrest events occurred.

---

*Although the WP-2.5 test was described in the previous semiannual progress report, a summary of the material is repeated as background for the posttest analyses that are described later in this chapter.

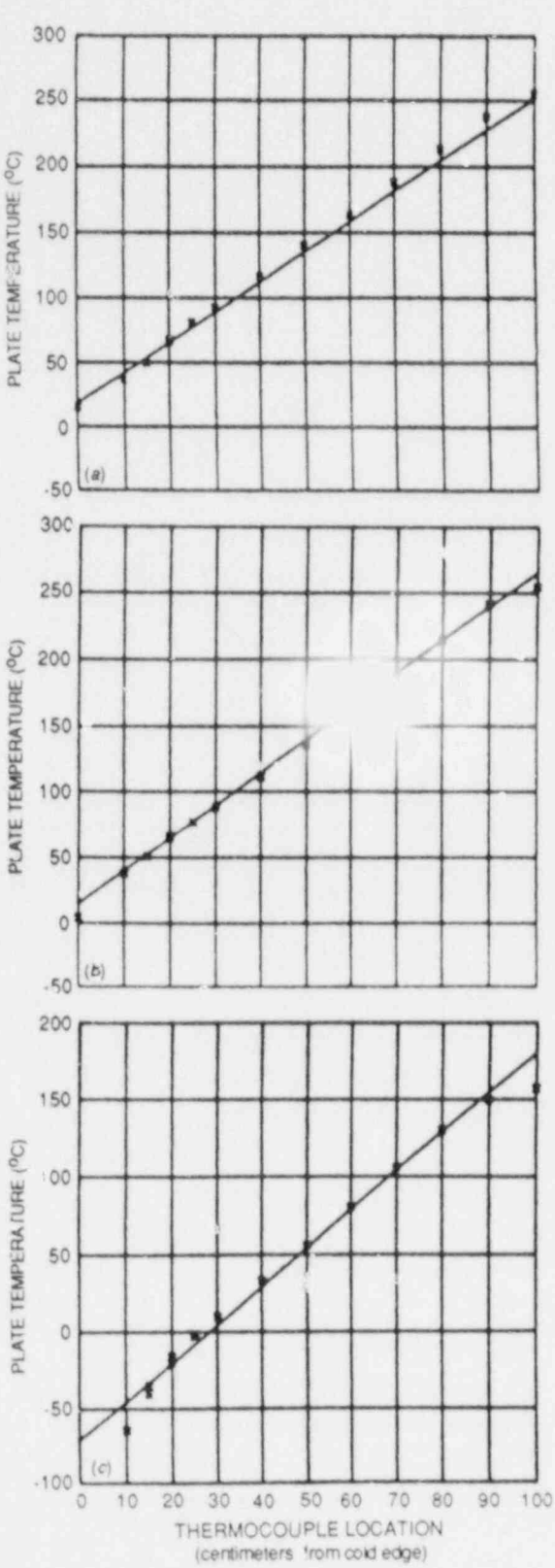

CENTIMETERS	TEMPERATURE (°C) REAL	IDEAL
0	15	18
10	36	41
15	50	53
15	49	53
20	66	64
20	67	64
20	66	64
25	81	76
25	80	76
30	92	88
40	116	111
40	116	111
50	140	134
60	163	158
60	163	158
70	188	181
80	213	205
80	214	205
90	238	228
100	255	251

CENTIMETERS	TEMPERATURE (°C) REAL	IDEAL
0	4	15
10	37	39
15	51	52
15	51	52
20	65	64
20	67	64
20	66	64
25	77	77
25	77	77
30	88	89
40	111	114
40	112	114
50	136	140
60	160	164
60	160	164
70	188	189
80	214	214
80	214	214
90	242	239
100	255	265

CENTIMETERS	TEMPERATURE (°C) REAL	IDEAL
0	-119	-70
10	-65	-46
15	-40	-33
15	-35	-33
20	-20	-21
20	-16	-21
20	-17	-21
25	-2	-8
25	-1	-8
30	10	4
40	33	29
40	33	29
50	56	55
60	80	79
60	80	79
70	106	104
80	130	129
80	130	129
90	150	154
100	157	180

Fig. 5.7. Actual and target temperature distributions across specimen width at approximate time of fracture for (*a*) specimen WP-2.5, (*b*) specimen WP-2.3, and (*c*) specimen WP-1.7 (first loading cycle). (Temperature distribution for specimen WP-CE-1 not available.)

5.2.3.4 Test WP-CE-1.* The twelfth wide-plate crack-arrest test was conducted at NBS on September 14, 1987. After a thermal gradient approximately equal to that desired (T_{min} = −83.3°C, T_{CT} = −30°C, T_{mid} = 50°C, and T_{max} = 183.3°C) was obtained, specimen loading was initiated. At a maximum load of ~10.2 MN, the crack run-arrest event initiated with a stable arrest occurring at a/w ≈ 0.37 at the front face and a/w ≈ 0.43 at the back face. After the load was held constant for ~1 min, loading was reinitiated. As the load was increased, ductile tearing occurred.

5.2.4 Test result summary

5.2.4.1 Test WP-2.5. The test results for WP-2.5 were presented in the previous semiannual progress report and will not be repeated in this section. Some results associated with analyses of test WP-2.5 are available, however, in Sect. 5.4.1.1.

5.2.4.2 Test WP-2.3. The entire fracture surface of WP-2.3 is shown in Fig. 5.8. A close-up of cleavage and loss-of-cleavage regions is presented in Fig. 5.9. As noted in the figures, three cleavage crack run-arrest events occurred at the front side of the plate and four at the back side. Examination of the fracture surface indicates that initiation of crack growth in cleavage was in the plane of the side grooves, but as it extended, it deviated from this plane at several places. The maximum deviation was 6 mm below the plane of the side grooves on the lower half of the surface. Once fibrous fracture took over (a/w = 0.457, T = 125°C), the crack returned to the plane of the side grooves. As observed in previous tests in the WP-2 series, the fibrous fracture zone at a/w > 0.457 was extremely fine or flat as compared with the fibrous fracture zones observed in the WP-1 material (A 533 grade B class 1 material). Figure 5.10 presents reduction-in-thickness contours surrounding the crack plane. As in previous tests, little reduction-in-thickness was detected before the first arrest position.

Strain-gage records, shown in Figs. 5.11–5.13 for companion crack-line gages located adjacent to the crack plane, indicate that four major cleavage crack run-arrest events occurred during the test. Available near- and far-field strain-gage results are presented in Fig. 5.14. Evaluations of the strain-gage records and fracture surface were used to deduce the crack length (position of the crack front) during the fracture process, and the results are summarized in Table 5.2. The strain-gage positions have been modified from those shown in Fig. 5.6(*a*) to account for the fact that the peak strain occurs at an angle of 72° in front of the crack tip. A plot of the strain-gage-derived crack-front position vs time from the front- and back-face strain gage results for the first 50 ms of the test is presented in Fig. 5.15(*a*). Results indicate that the crack-front advance at comparable elapsed times during the cleavage crack run-arrest events was more rapid near the back face of the plate than near the front face. An expanded plot of the strain-gage-derived crack-front position vs time from the front- and back-face strain-gage

*Results presented for WP-CE-1 are tentative because the data had not been reduced at the time this report was prepared.

ORNL PHOTO 9835-87

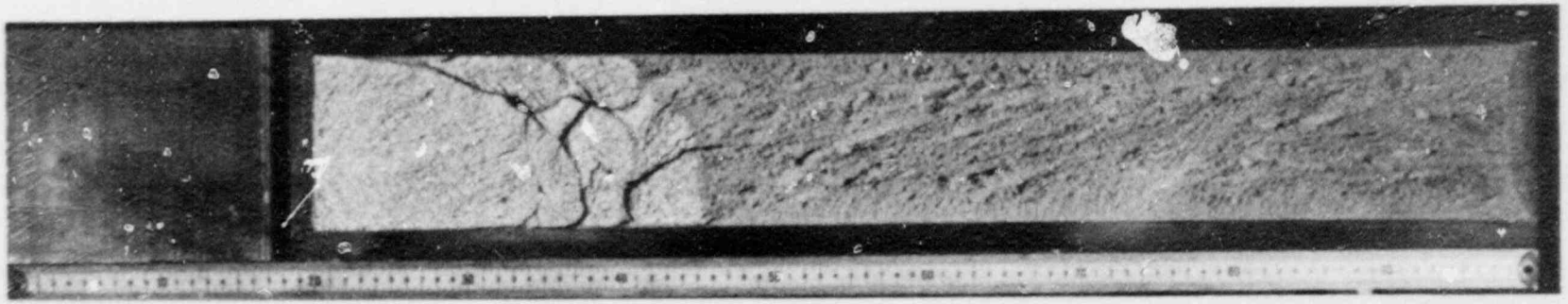

Fig. 5.8. Overall fracture surface of test specimen WP-2.3.
(F and B denote front- and back-plate faces, respectively.)

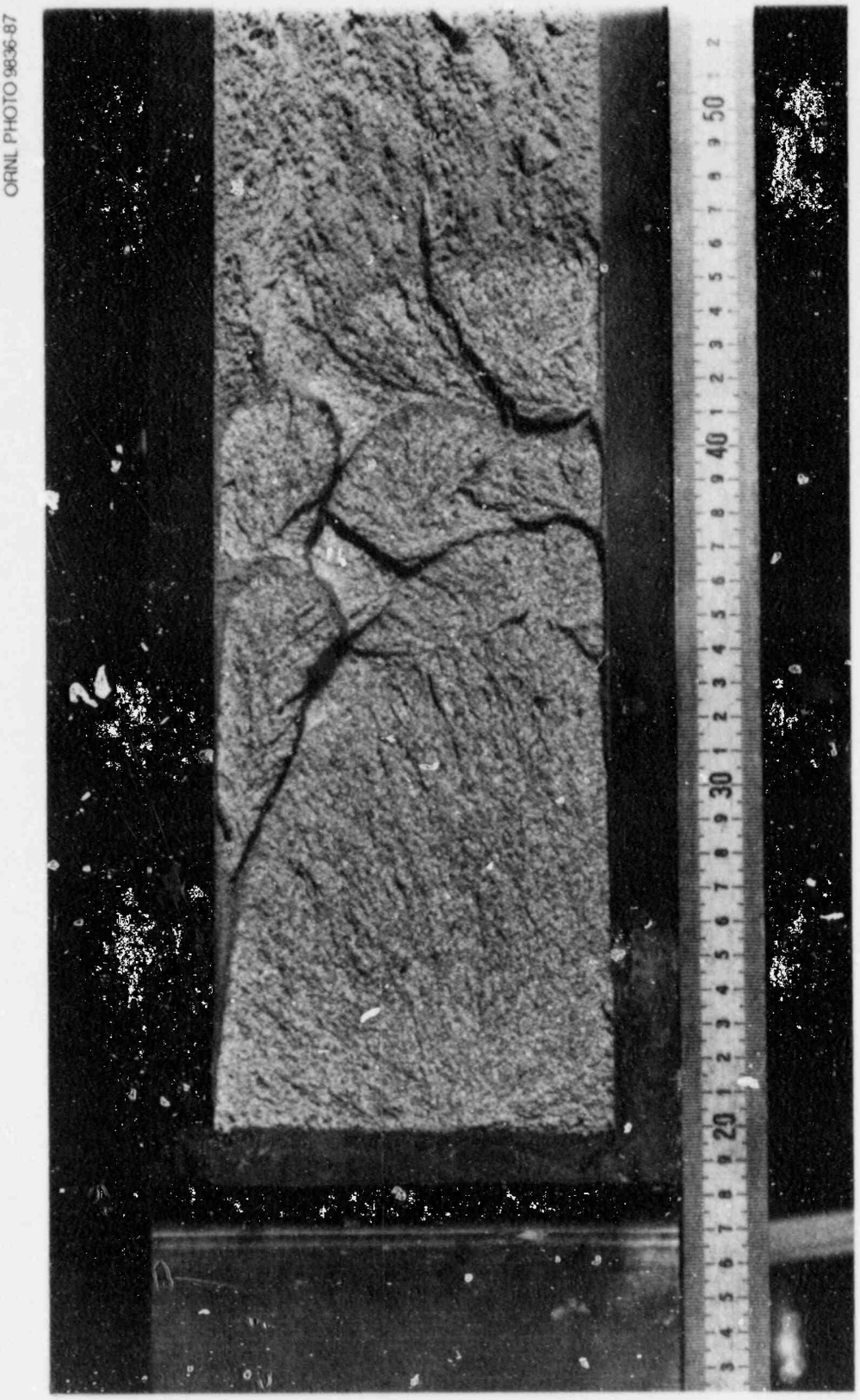

Fig. 5.9. Close-up of cleavage and loss-of-cleavage regions of specimen WP-2.3.

Table 5.2. Crack position and velocity vs time

Indicator[a]	Crack length (mm)	Time (ms)	Velocity (m/s)[b]
Front-face measurements: WP-2.3			
a_o	200	0	
			729
SG1	243	0.059	
			1667
SG2	268	0.074	
			47
Arrest A	275	0.222	
Reinitiation	275	12.489	
			388
SG3	308	12.574	
			211
Arrest C	345	12.749	
Reinitiation	345	37.344	
			150
SG4	348	37.364	
			2000
SG5	388	37.384	
			86
Arrest E	400	37.524	
Reinitiation	400	43.324	
			0.3
SG6	428	136	
			0.06
SG7	468	812	
			0.9
SG8	508	856	
			2.6
SG9	558	875	
			6.7
SG10	608	882.5	
			(8.3)
SG11[c]	658	(888.5)	
			(14.3)
SG12[c]	708	(892)	
			(11.4)
Ligament	(993)	917.0	
			0.3
End of plate	1000	942.5	

Table 5.2 (continued)

Indicator[a]	Crack length (mm)	Time (ms)	Velocity (m/s)[b]
Back-face measurements: WP-2.3			
a_o	200	0	
			1700
SG13	268	0.040	
			541
SG14	308	0.114	
			327
Arrest A	340	0.212	
Reinitiation	340	3.160	
			98
SG15	348	3.242	
			338
Arrest B	375	3.322	
Reinitiation	375	13.004	
SG16	338	Not working	314
Arrest D	397	13.074	
Reinitiation	397	38.464	
SG17	428	Too noisy	500
Arrest F	457	38.584	
Reinitiation	457	44.304	
			0.02
SG18	468	688	
			0.26
SG19	508	842	
			2.17
SG20	558	865	
			2.94
SG21	608	882	
			6
SG22	650	889	
			12
Ligament	993	917	
			0.27
End of plate	1000	942.5	

[a]Gage positions in the table are all reduced by 32 mm from the actual gage position to account for the fact that the peak strain occurs at an angle of 72° in front of the crack tip.

[b]Velocity is an average calculated velocity for crack propagation.

[c]Gage broke before peak formed.

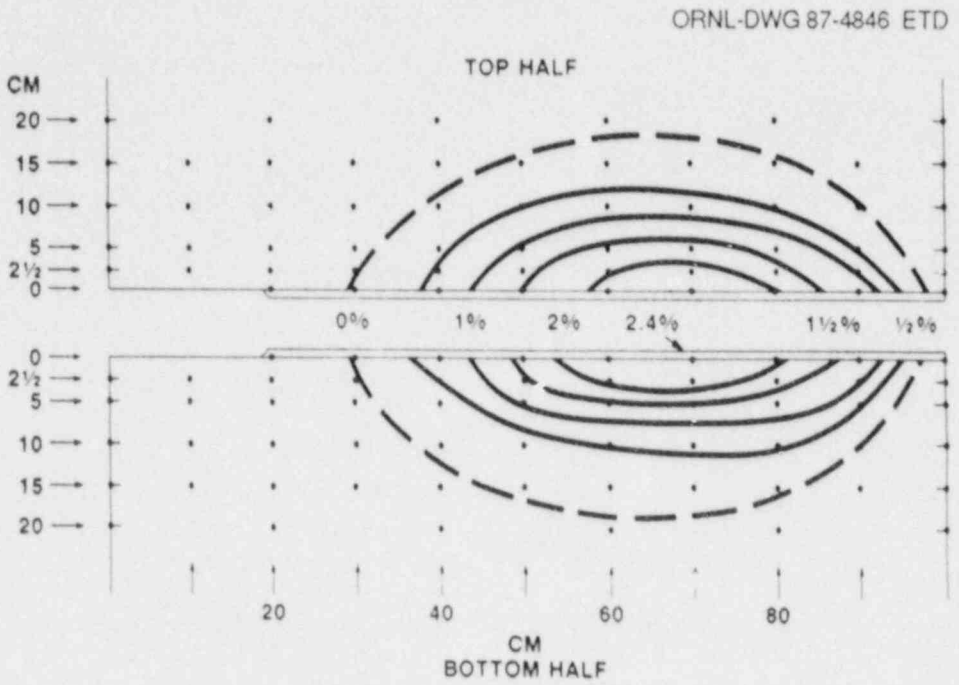

Fig. 5.10. Posttest reduction-in-thickness contours: Test WP-2.3.

results over the ≈950-ms duration of the test is presented in Fig. 5.15(*b*). The results presented in this plot indicate that the crack-front advance across the plate width did not become fairly uniform until the crack advance had reached an a/w ~ 0.6 while ductile tearing was occurring.

Longitudinal accelerations recorded by "damped" accelerometers mounted on the specimen's centerline at 3.585 m above (top) and 3.589 m below (bottom) the crack plane are presented in Fig. 5.16. Results obtained from the displacement gage mounted at the same location as the bottom accelerometer are presented in Fig. 5.17. The F- and B-COD results obtained from gages located at a/w = 0.150 are presented in Fig. 5.18. AE results obtained from a transducer mounted on the lower pull tab are presented in Fig. 5.19 for four levels of resolution.

5.2.4.3 Test WP-1.7. The results for test WP-1.7 were being analyzed at the time this report was prepared. Final results and conclusions from test WP-1.7 will be presented in the next semiannual progress report.

5.2.4.4 Test WP-CE-1. Data from test WP-CE-1 were being reduced at the time this report was prepared. Results and conclusions from test WP-CE-1 will be presented in the next semiannual progress report.

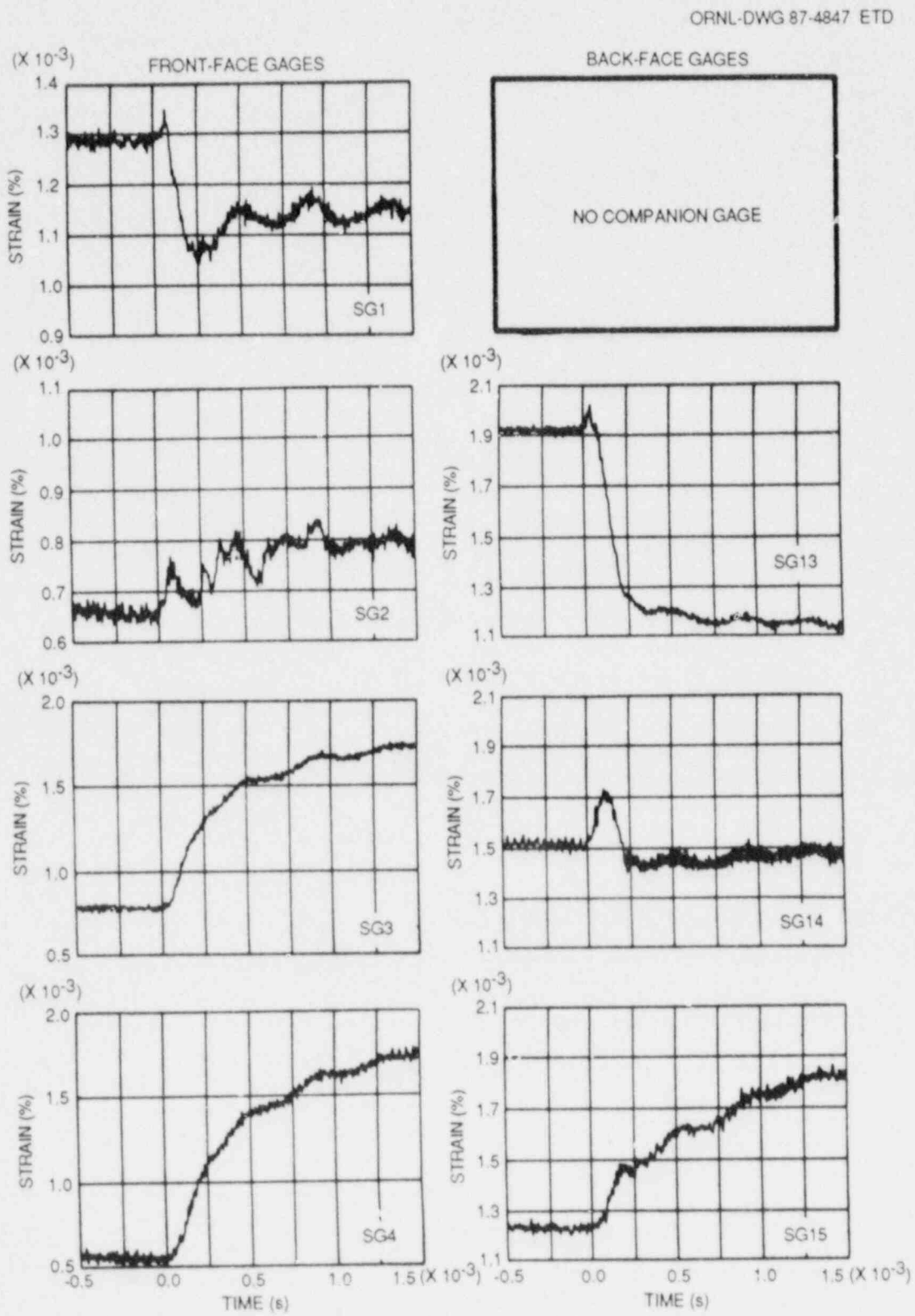

Fig. 5.11. Strain histories for companion crack-line gages: Test WP-2.3.

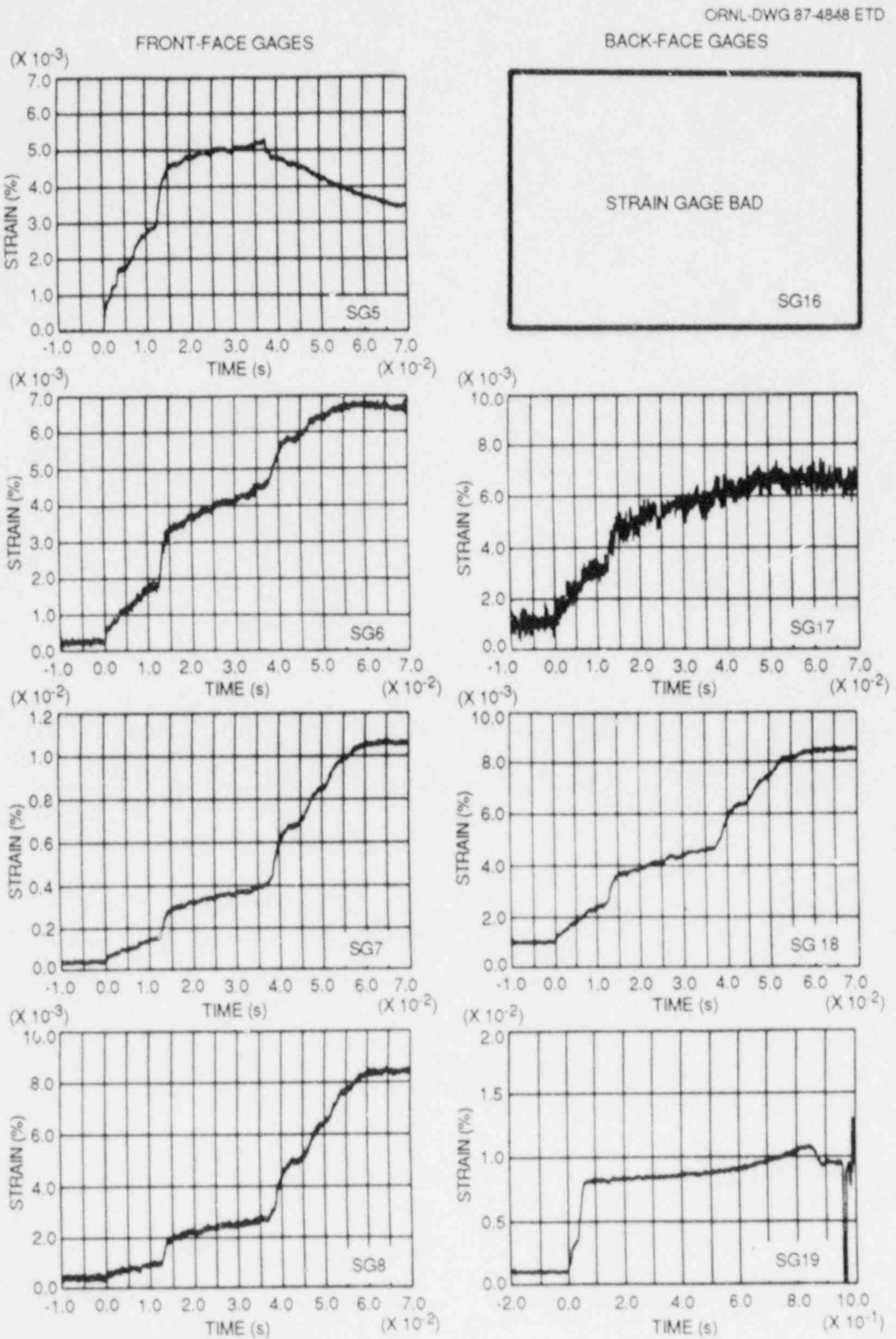

Fig. 5.12. Strain histories for companion crack-line gages: Test WP-2.3.

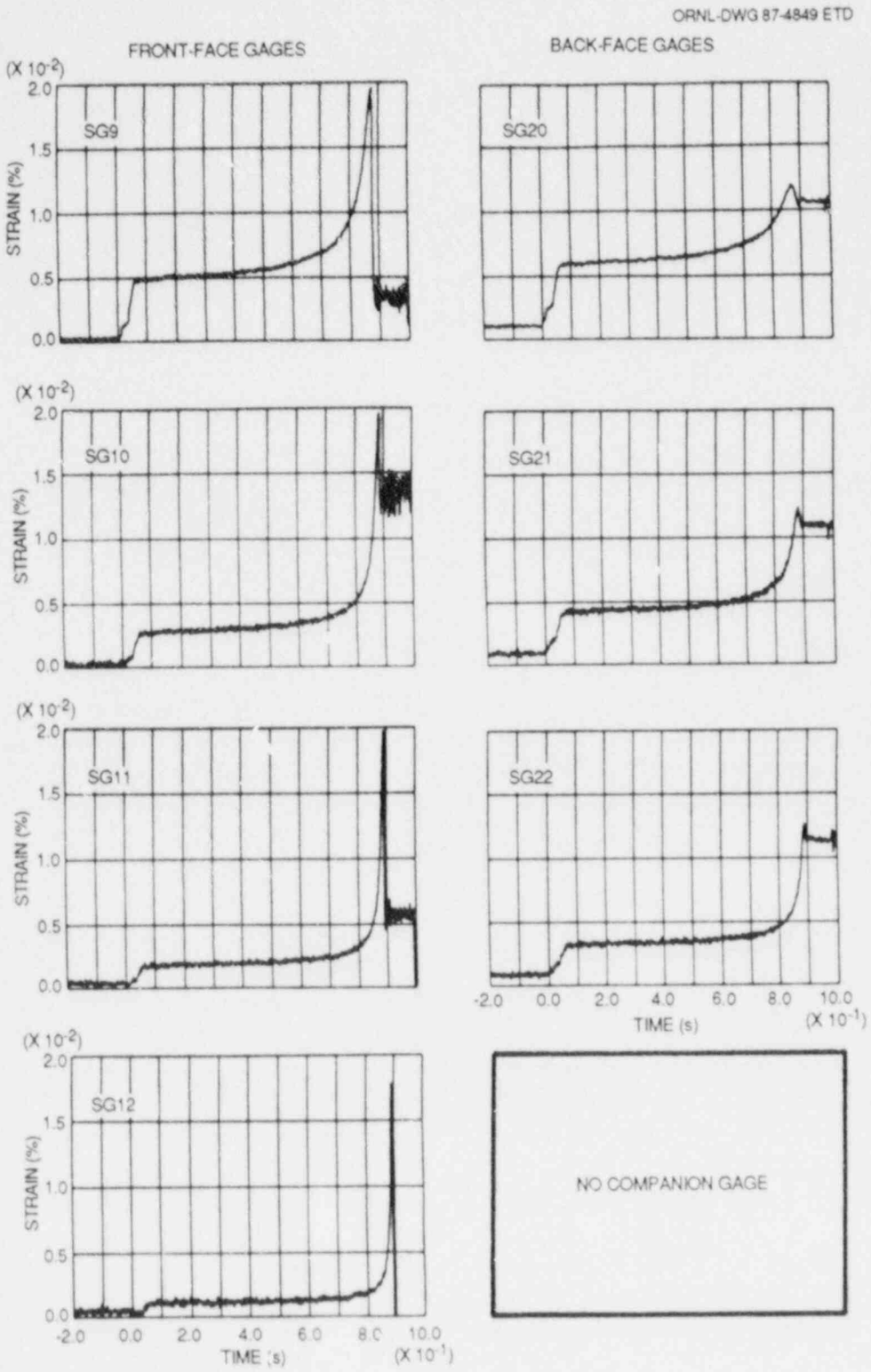

Fig. 5.13. Strain histories for companion crack-line gages: Test WP-2.3.

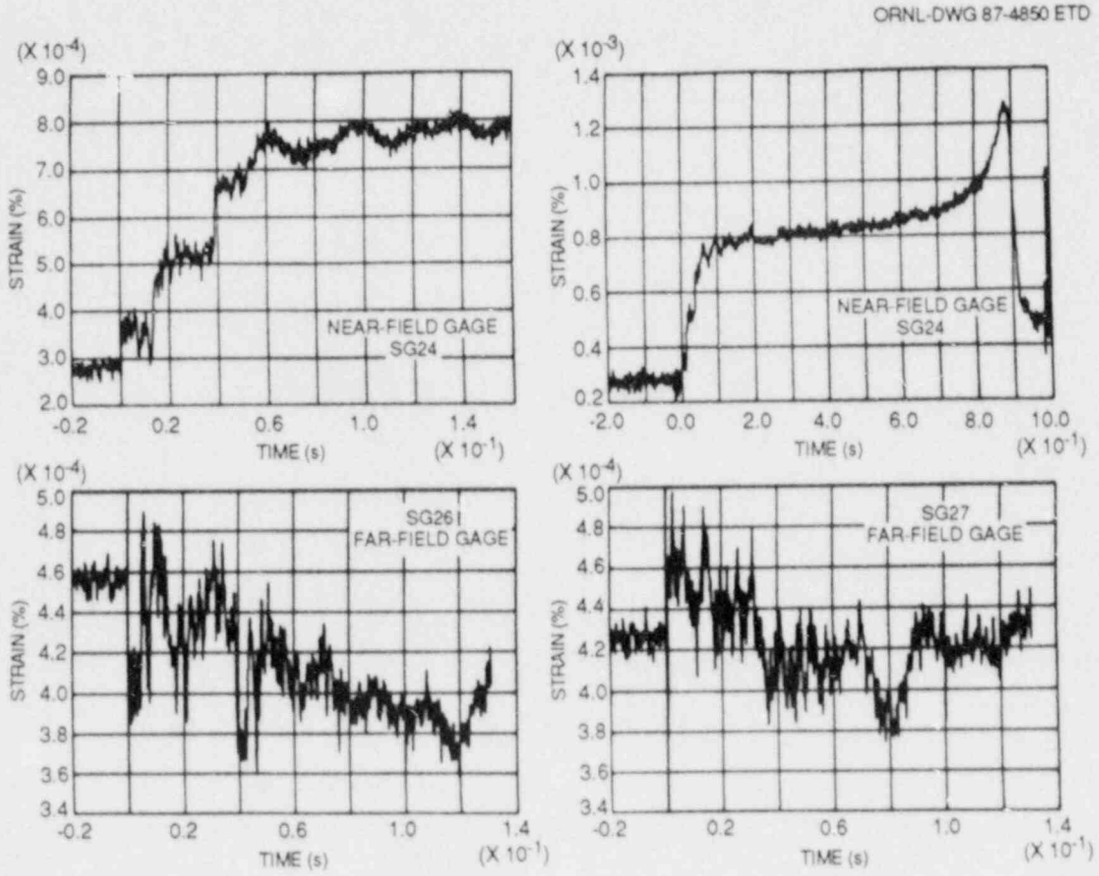

Fig. 5.14. Crack run-arrest events as detected by near- and far-field strain gages: Test WP-2.3. Note: since strain gage Nos. 26 and 27 were recorded on a transient oscilloscope, their records end at 130 ms.

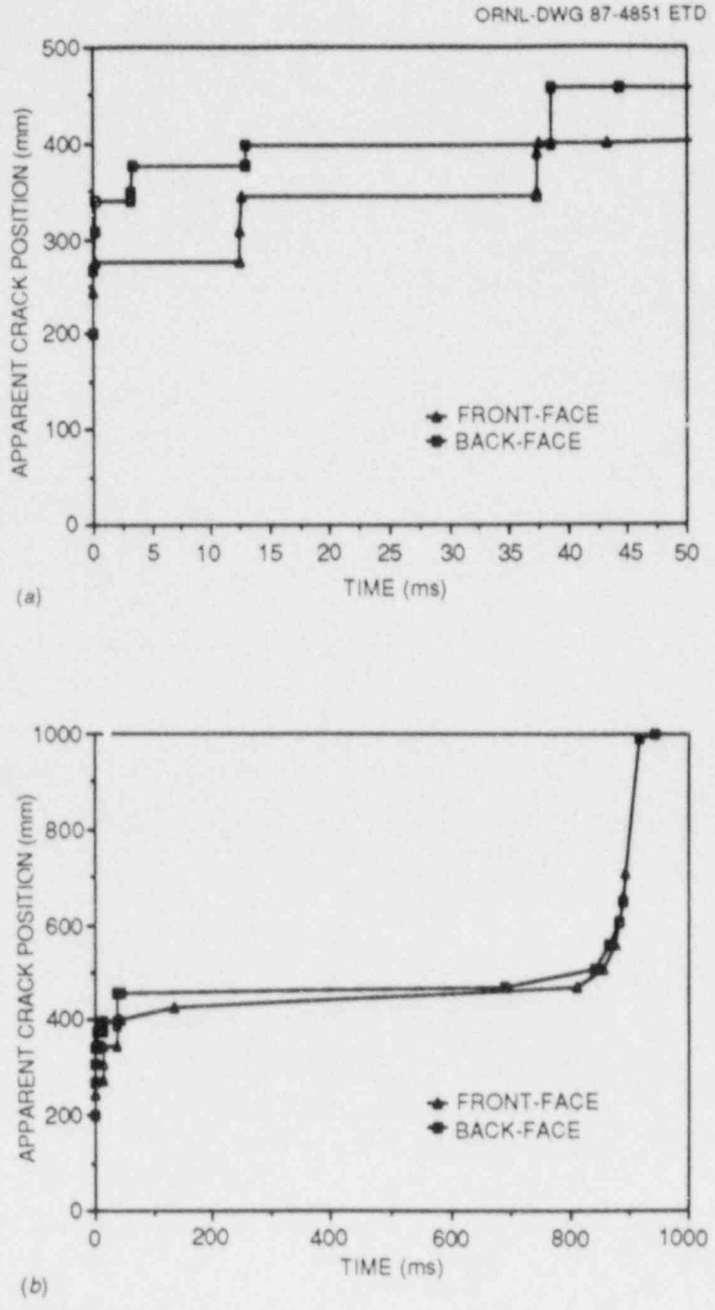

Fig. 5.15. Apparent crack-front position vs time: Test WP-2.3. (*a*) Results for first 50 ms of the test, and (*b*) results for the entire ~950 ms of the test.

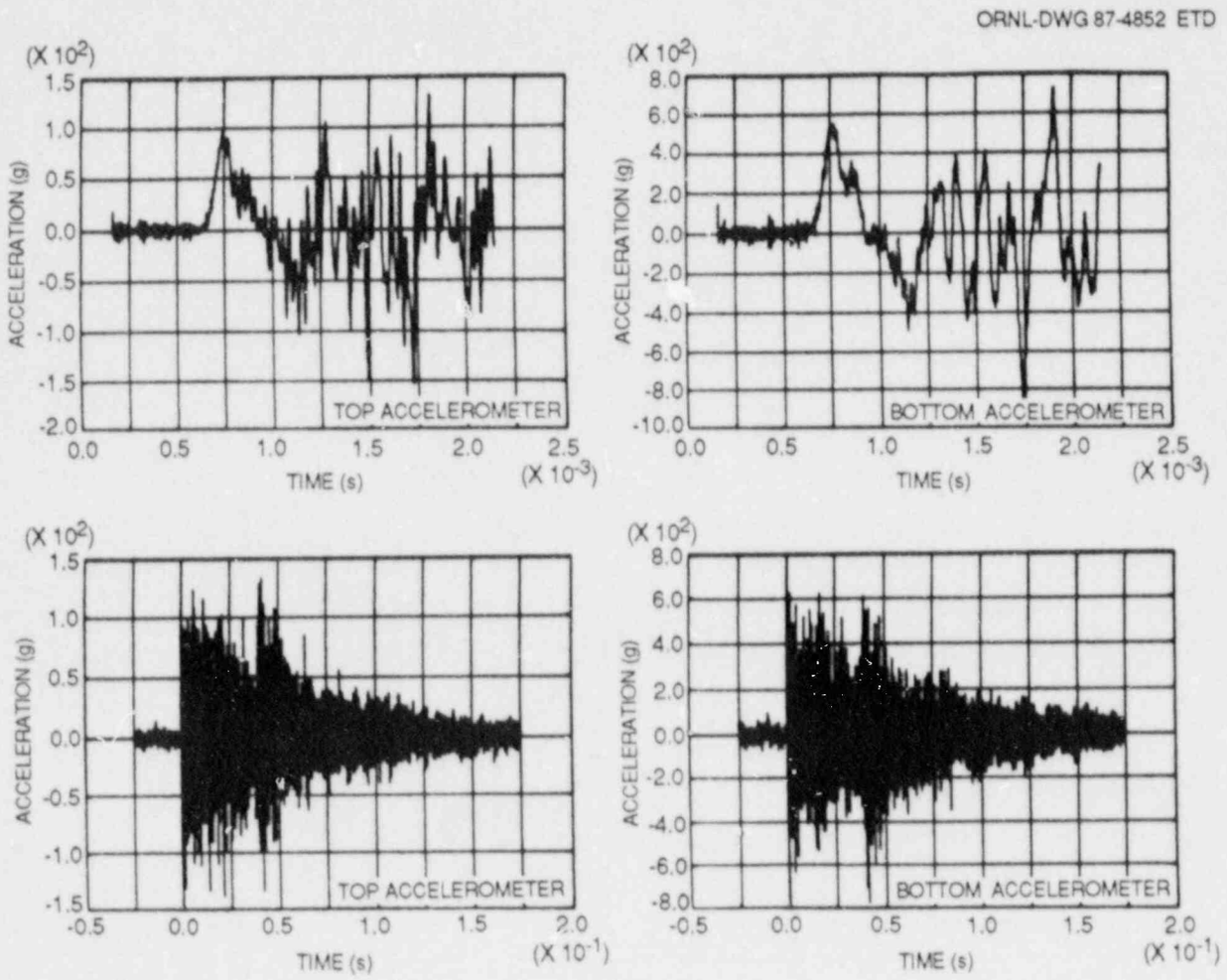

Fig. 5.16. Longitudinal acceleration results at two levels of time resolution measured by top and bottom "damped" accelerometers mounted 3.585 m above and 3.589 m below the crack plane, respectively: Test WP-2.3.

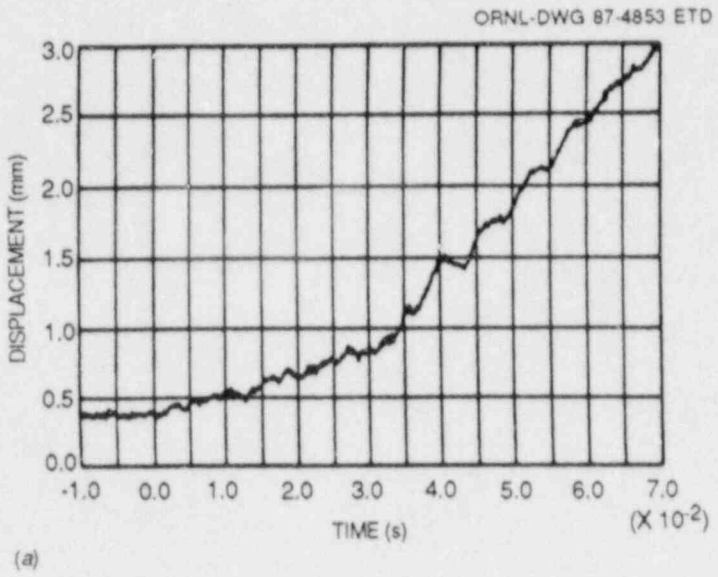

(a)

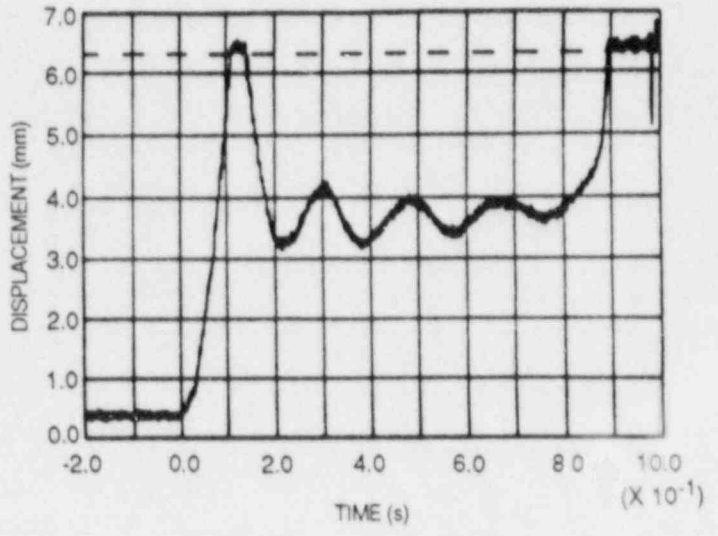

(b)

Fig. 5.17. Bottom displacement gage results: Test WP-2.3. (*a*) During initial crack run-arrest events, and (*b*) during the entire test.

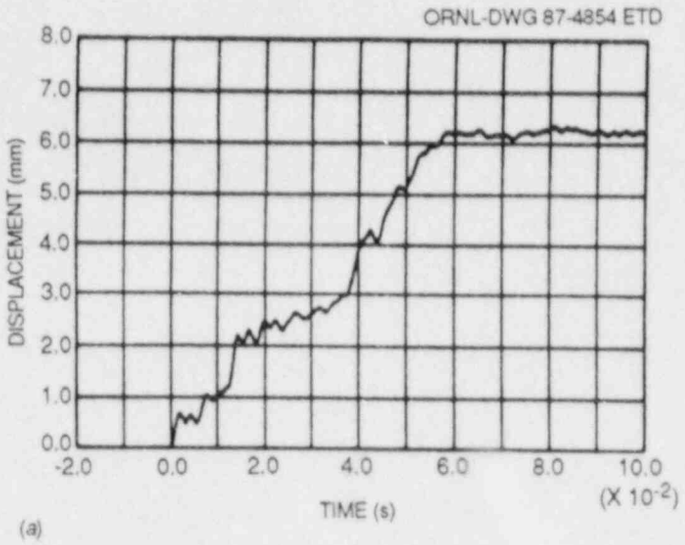

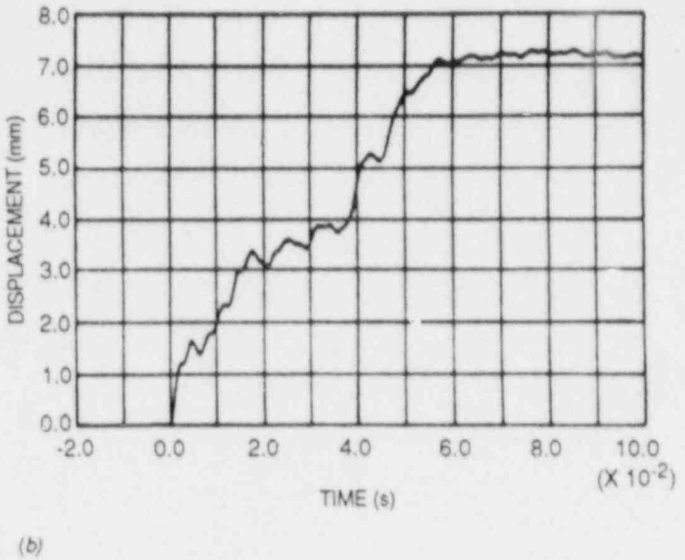

Fig. 5.18. COD gage results during the initial crack run-arrest events: Test WP-2.3. (*a*) F-COD, and (*b*) B-COD.

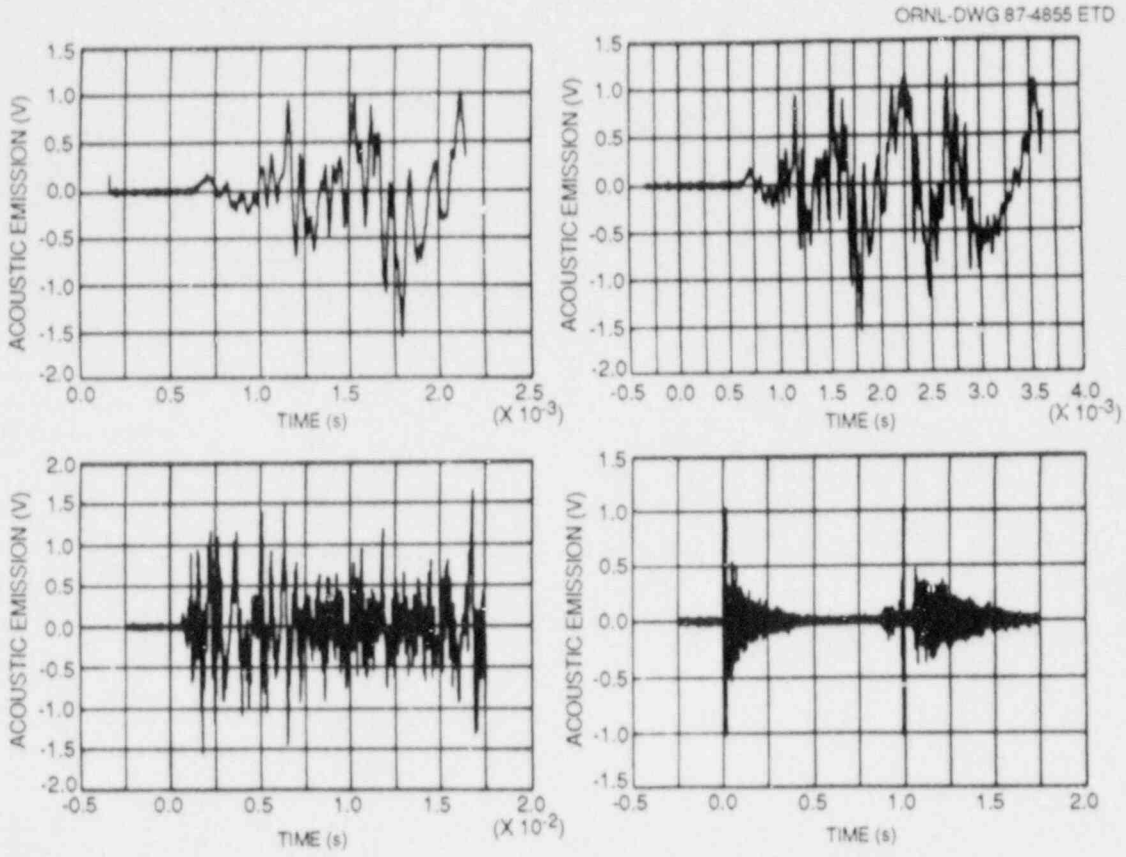

Fig. 5.19. AE results for various time resolutions: Test WP-2.3.

5.3 Properties of Wide-Plate Crack-Arrest Test Materials

5.3.1 Prototypical pressure vessel materials

5.3.1.1 WP-1 series. The initial series of wide-plate crack-arrest specimens is taken from the central portion of the 18.73-cm-thick HSST plate 13A of A 533 grade B class 1 steel that is in a quenched and tempered condition. Properties of this plate include Young's modulus (E) = 206.9 GPa, Poisson's ratio (ν) = 0.3, coefficient of thermal expansion (α) = 11 × 10^{-6}/°C, and density (ρ) = 7850 kg/m^3. Temperature-dependent fracture-toughness relations for initiation and arrest, based on small-specimen data, are given by

$$K_{Ic} = 51.276 + 51.897\, e^{0.036(T-RT_{NDT})}, \tag{5.1}$$

$$K_{Ia} = 49.957 + 16.878\, e^{0.028738(T-RT_{NDT})}, \tag{5.2}$$

with units of K and T being megapascals times root meters and degrees Celsius, respectively. Drop-weight and Charpy V-notch test data indicate that $RT_{NDT} = -23°C$, and the Charpy upper-shelf energy is 160 J with its onset occurring at 55°C.

Analytical studies have used a dynamic fracture-toughness relation in the following form:

$$K_{ID} = K_{Ia} + A(T)\,\dot{a}^2 \ , \tag{5.3}$$

where K_{Ia} is given by Eq. (5.2) and

$$A(T) = [329.7 + 16.25\,(T - RT_{NDT})] \times 10^{-6} \ , \tag{5.4}$$

or

$$A(T) = [121.71 + 1.296\,(T - RT_{NDT})] \times 10^{-6} \ , \tag{5.5}$$

if $(T - RT_{NDT})$ is greater or less than −13.9°C, respectively. Units for K_{ID}, A, $\dot{a}$, and T are megapascals times root meters, megapascals times square seconds times meters to the −3/2, meters per second, and degrees Celsius, respectively. The form of the K_{ID} expression in Eq. (5.3) and relations for A(T) [Eqs. (5.4) and (5.5)] are derived from Ref. 5 by estimating that $RT_{NDT} = -6.1°C$ for the material used in that study.

5.3.1.2 WP-CE series. The WP-CE specimens were fabricated from a second heat of A 533 grade B class 1 material that was provided to ORNL by Combustion Engineering, Inc. (CE), in the form of a plate 244 × 1016 × 1016 mm. The material was characterized by CE, and the detailed results are presented in Ref. 6. Pertinent material properties include an ultimate tensile strength ranging from ≈580 MPa at room temperature to ≈560 MPa at 66°C to ≈520 MPa at 120°C, a nil-ductility transition temperature from approximately equal to −34 to approximately equal to −23°C, a Charpy upper-shelf energy of ≈180 to ≈203 J, and the minimum temperature for fully ductile behavior occurring at ≈43 to ≈49°C. Temperature-dependent fracture-toughness relations for the WP-CE material used for pretest planning were the same as Eqs. (5.1) and (5.2) with the RT_{NDT} changed to the appropriate value for the WP-CE material.

5.3.2 Low-upper-shelf material (WP-2 series)

The WP-2 series of wide-plate crack-arrest specimens is taken from the left-hand portion of a 158.75-mm-thick plate of 2-1/4 Cr-1 Mo steel. The material was supplied by Babcock and Wilcox after being heat treated in an effort to obtain a Charpy upper-shelf energy of 68 J (50 ft-lb) or less. Characterization of this material has not been completed, so detailed property data are not available.

Based on a limited number of tests, the tentative drop-weight nil-ductility temperature for the material is >60°C, and the onset of Charpy

upper shelf is at ~150°C. The ultimate strength of the material for use in tensile instability calculations is based on the average stress in the remaining ligament (σ_u) equal to 500 MPa, which represents the lowest value determined for the temperature range of interest. For tearing instability calculations, the material tearing resistance is assumed to be given in the form of a power-law J-resistance curve

$$J_R = c(\Delta a)^m , \tag{5.6}$$

where c = 0.1114, m = 0.3832, and the units of J_R and Δa are megajoules per square meter and millimeters, respectively. Based on results of a limited number of small-specimen tests, temperature-dependent fracture-toughness relations for initiation and arrest that are being used for planning the WP-2 series tests are given by

$$K_{Ic} = 39.53 + 93.47\, e^{0.036(T-RT_{NDT})} , \tag{5.7}$$

$$K_{Ia} = 22.31 + 62.69\, e^{0.0177(T-RT_{NDT})} , \tag{5.8}$$

with units of K and T being megapascals times root meters and degrees Celsius, respectively.

5.4 Wide-Plate Analyses at ORNL

B. R. Bass J. Keeney-Walker

5.4.1 Posttest analyses of series WP-2 tests

5.4.1.1 Test WP-2.5

Posttest three-dimensional (3-D) static analyses. The 3-D static finite-element analyses were performed on the WP-2.5 plate assembly to ascertain the static stress-intensity factor at the time of the pop-in with a/w = 0.199. These analyses were performed with the ORMGEN/ORVIRT[7,8] fracture analysis system in conjunction with the ADINA-84 (Ref. 9) finite-element code. The 3-D finite-element model incorporated a segment of the plate assembly 4.9035 m in length measured from the crack plane to the top of the load pin hole. The crack-tip region of the model included the chevron cutout, the side grooving, and the edge notch, the dimensions of which are taken from Table 5.1. From symmetry conditions neglecting out-of-plane eccentricity, one-quarter of the partial pull-plate assembly was modeled using 3751 nodes and 720 20-noded isoparametric elements.

The thermal deformations computed from a posttest two-dimensional (2-D) analysis were superposed on the 3-D finite-element model to account for the in-plane thermal bending effect in the 3-D analyses. The boundary conditions of the 2-D thermoelastic analysis assumed that the heated

and cooled edges of the plate were fixed at T_{max} = 263.3°C and T_{min} = 16.7°C, respectively, along a 2.4-m length (centered relative to the crack plane) and that the pull-tab edges were prescribed to be T = 20.0°C. The remaining surfaces of the assembly were assumed to be insulated. The in-plane thermal bending produced a load-line (through the top of the load-pin hole) eccentricity of 1.97 cm relative to the geometric center of the plate.

In the 3-D analysis, thermal stress effects were neglected, and a uniform line-load statically equivalent to the WP-2.5 test load of 7.53 MN at pop-in was applied at the location corresponding to the top of the load-pin hole. The result of this analysis produced a static stress-intensity factor of K_I = 119.5 MPa•$\sqrt{m}$ at the center plane of the plate. Comparison of this computed K_I value with the static initiation value of K_{Ic} = 155.5 MPa•$\sqrt{m}$, evaluated from the relationship presented in Eq. (5.7) using the material RT_{NDT} = 60°C and the crack-tip temperature of 66°C, yields a ratio of K_I/K_{Ic} = 0.768.

Posttest 2-D static and dynamic analyses

Static and stability analysis. Posttest 2-D analyses were carried out using computer codes based on both quasistatic and elastodynamic techniques. For the quasistatic analyses, the ORNL computer code WPSTAT[10] was used to perform both crack-arrest and crack-stability analyses. As described in Ref. 10, the WPSTAT code evaluates static stress-intensity factors as a function of crack length a and temperature differential $\Delta T = T_{max} - T_{min}$ across the plate. These factors are computed for fixed-force conditions K_I^F (a, ΔT) and for fixed load-pin displacement conditions K_I^{DSP} (a, ΔT) by superposing contributions from te ion and bending finite-element and handbook solutions. In addition, WPSTAT categorizes arrested crack lengths in terms of three types of instability limits that are enumerated below.

The posttest WPSTAT calculations of static factors K_I^F (a, ΔT) and K_I^{DSP} (a, ΔT) utilized the actual temperature profile provided in Fig. 5.7(a). For this specified temperature profile, the dependence of the arrested crack length and crack stability upon the applied initiation load F_{in} was investigated with WPSTAT, and the results are presented in Fig. 5.20. Figure 5.20 includes the statically calculated final crack length a_{fc} and the instability-limit crack lengths for reinitiation a_{rein} (F_{in}) for tensile instability a_{I1} (F_{in}) and for tearing instability a_{I2}(F_{in}). The tensile instability calculation is based on the average stress in the remaining ligament equal to an ultimate stress of σ_u = 500 MPa, which represents the lowest value for the temperature range of interest. For the tearing instability calculation, the material tearing resistance is assumed given in the form of the power-law J-resistance curve, presented in Eq. (5.6). In Fig. 5.20 the statically computed arrest length corresponding to the measured initiation load F_{in} = 8.9 MN is given by a_{fc} = 0.370 m. The computed arrest point is below the tearing instability curve (a_{I2}), implying a stable condition. The measured initial arrest point after the pop-in event a_{fm_1} = 0.350 m [Arrest B,

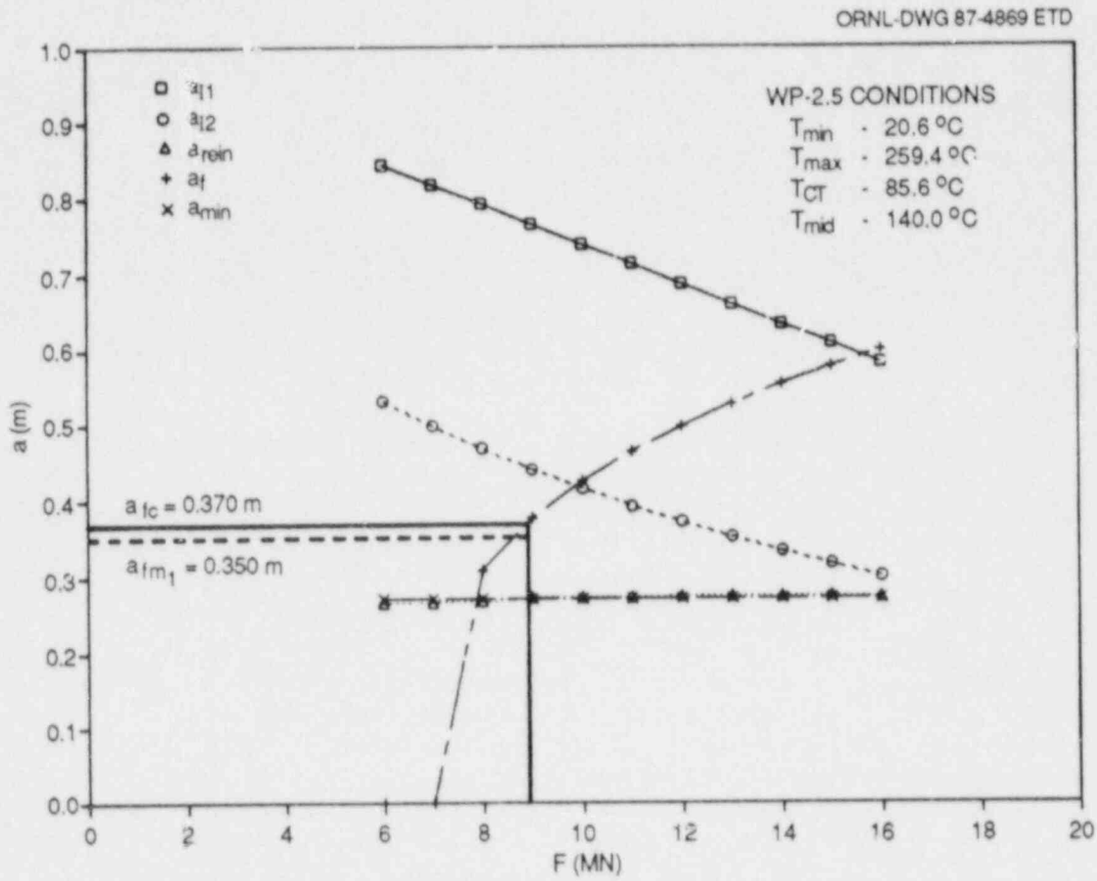

Fig. 5.20. Statically calculated crack lengths: Test WP-2.5.

back-face gages (Table 5.4, Ref. 2)] is also below the tearing instability curve. Figure 5.20 indicates that tearing instability is not expected until the crack length exceeds ≈0.45 m, which occurs between measured arrest positions C and D in Table 5.4 (back-face measurements) of Ref. 2.

In Fig. 5.21 the K_{Ia} function presented in Eq. (5.8) is evaluated on the arrest crack length curve $a_f(\ )$, on the incipient tearing instability curve $a_{I2}(F)$, and on the cleavage reinitiation curve $a_{rein}(F)$; the K_{Ic} function presented in Eq. (5.7) is also evaluated on the curve $a_{rein}(F)$. Evaluation of the $K_{Ia}(a_f)$ curve at the initiation load F_{in} = 8.9 MN yields an arrest toughness of K_{Ia} = 171.2 MPa·$\sqrt{m}$ at the predicted arrest point a_{fc} = 0.370 m where the crack-tip temperature would be T = 108.9°C.

The complete static fracture-mechanics and stability analyses are depicted in Fig. 5.22 for the initiation load of F_{in} = 8.9 MN. Included in the figure are curves for initiation toughness K_{Ic}, arrest toughness K_{Ia}, displacement-controlled stress-intensity factor K_I^{DSP}, and force-controlled stress-intensity factor K_I^F. The regions of tearing and tensile instability and the computed cleavage arrest point (a_{fc}) are also identified in Fig. 5.22.

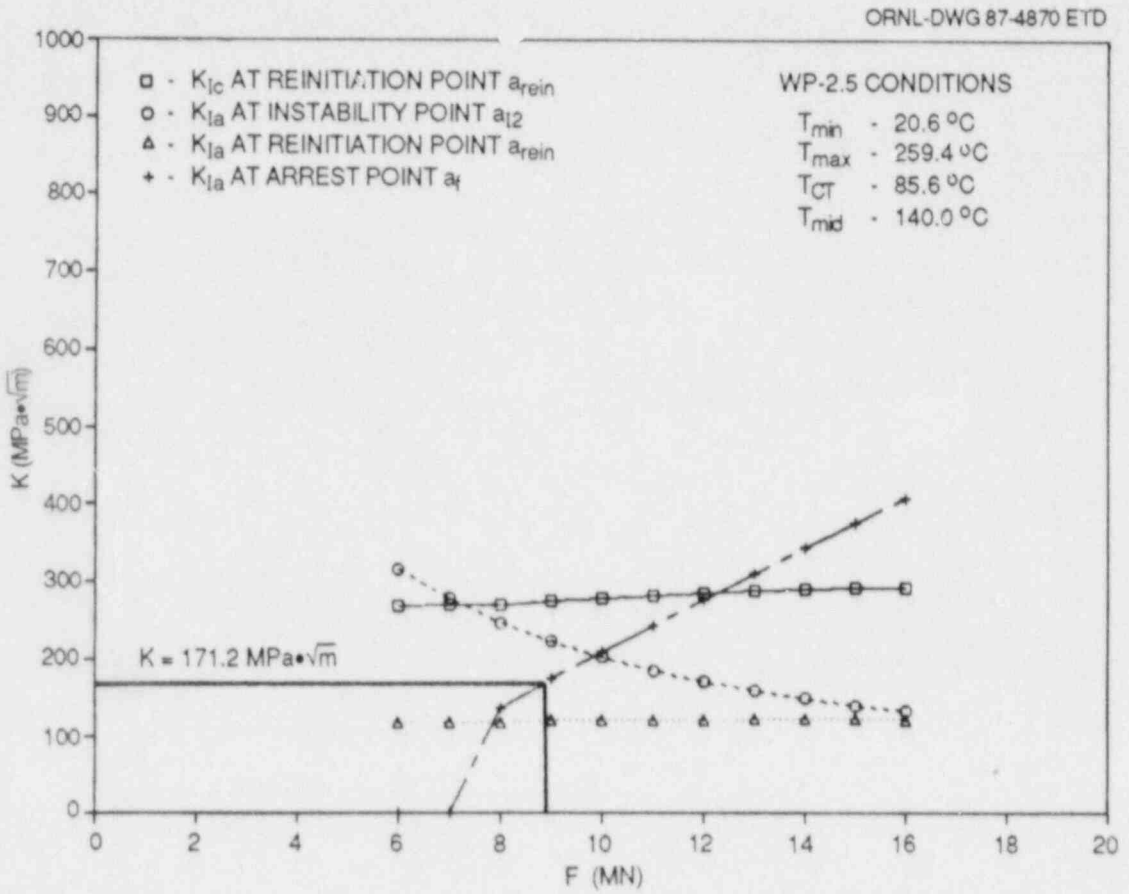

Fig. 5.21. Determination of arrest toughness at initiation load of 8.9 MN: Test WP-2.5.

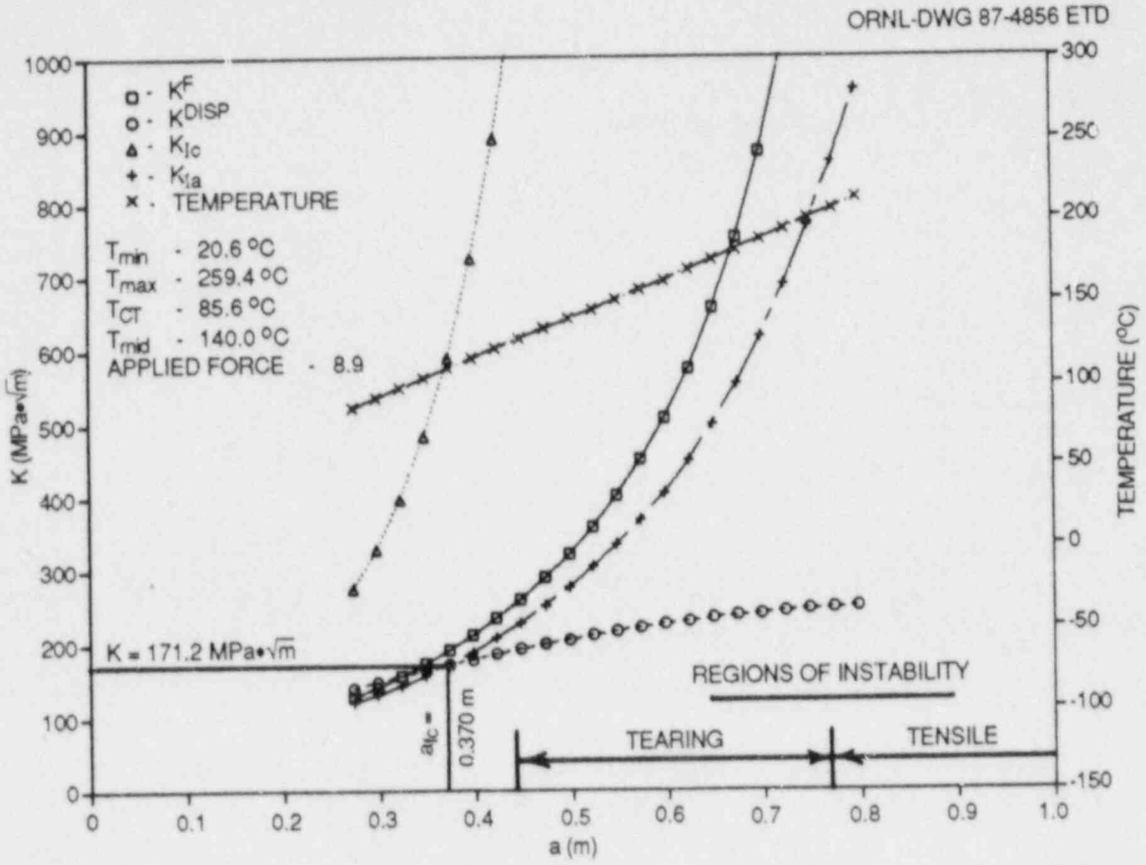

Fig. 5.22. Complete static and stability analyses for the initiation load of 8.9 MN: Test WP-2.5.

Application-mode dynamic analysis

Displacement control. Elastodynamic analyses of wide-plate test WP-2.5 were carried out with the ADINA/VPF[11] dynamic crack analysis code. The 2-D plane-stress finite-element model of the wide-plate configuration used in the analyses consisted of 935 nodes and 277 eight-noded isoparametric elements. A total of 31 spring elements were used in the crack plane to model propagation of the crack tip. Side grooves were taken into account by adjusting the resulting stress-intensity factor calculated in each time step of the analysis. The in-plane bending of the plate assembly caused by the thermal gradient across the plate was also incorporated into the analyses.

A posttest application-mode analysis of WP-2.5 was performed using the temperature gradient of Fig. 5.7(a) and the material properties given in Sect. 5.3. The measured fracture load of F_{in} = 8.90 MN was applied at the location of the top of the load-pin hole to determine the load-point displacement U_{LL} = 0.22790 × 10^{-2} m. For the dynamic analysis, the load point was fixed at the displacement value of the initiation load, and the time step was set at Δt = 5 μs. The calculated crack-depth history from this analysis is depicted in Fig. 5.23 and indicates a predicted arrest

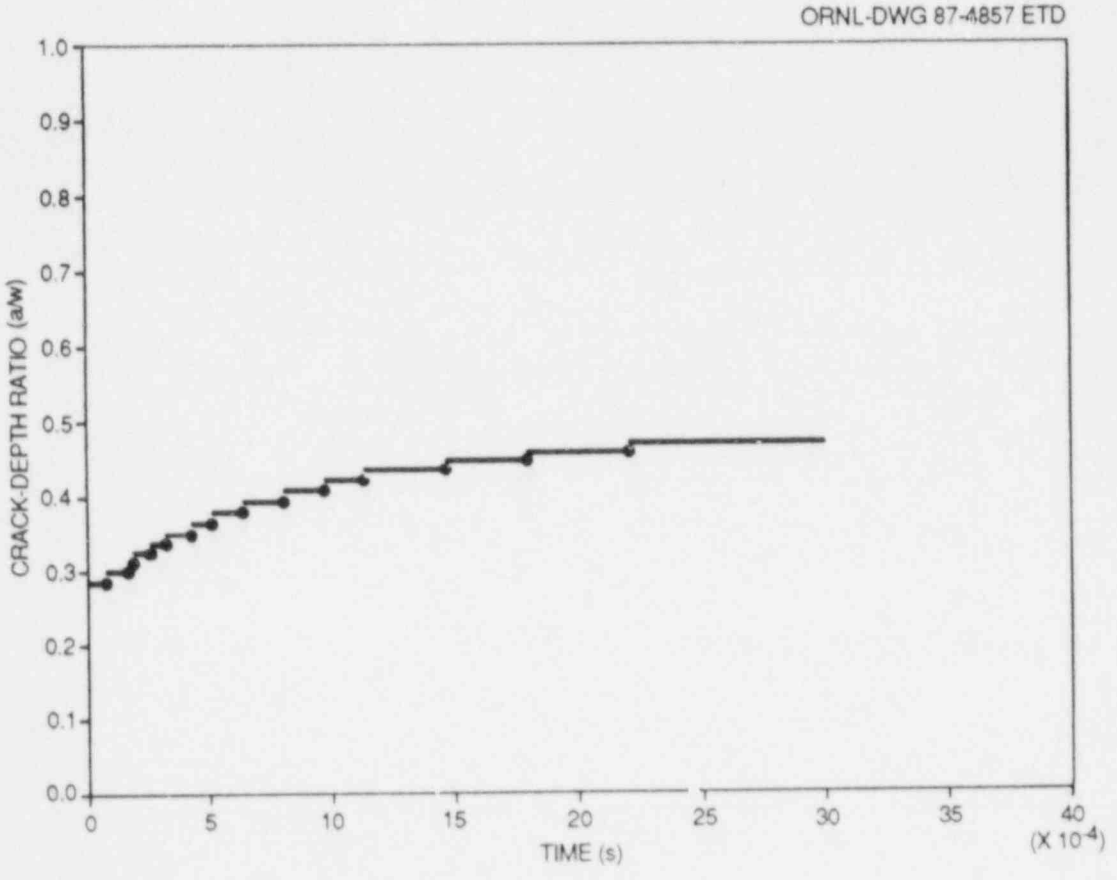

Fig. 5.23. Calculated crack-depth history from an application-mode dynamic analysis (displacement control boundary condition): Test WP-2.5.

at a_f = 0.467 m. Figure 5.24 presents the dynamic stress-intensity factor K_I^{DYN}, the static toughness K_{Ia}, and the crack velocity $\dot{a}$ as a function of instantaneous crack length. The crack propagates into a rising K_I field, followed by arrest at a point where the crack-tip temperature would have been T = 132.1°C. The arrest toughness at the arrest-point temperature is determined to be K_{Ia} = 246.8 MPa•$\sqrt{m}$ [Eq. (5.8)]. The computed arrest length exceeds the measured initial arrest length at a_{fm_1} = 0.350 m (back face) with crack-tip temperature T = 104.0°C and corresponding arrest toughness 158.8 MPa•$\sqrt{m}$. The computed arrest length is between measured arrest points C and D in Table 5.4 of Ref. 2 (back-face measurements) where $a_{f_{mC}}$ = 0.435 m, T = 124.4°C, K_{Ia} = 218.8 MPa•$\sqrt{m}$, and $a_{f_{mD}}$ = 0.478 m, T = 134.7°C, K_{Ia} = 257.4 MPa•$\sqrt{m}$, respectively. The application-mode analysis was terminated at time t = 3 ms, which precludes any prediction from the analysis of the reinitiation that occurred in the test at time t = 7.90 ms.

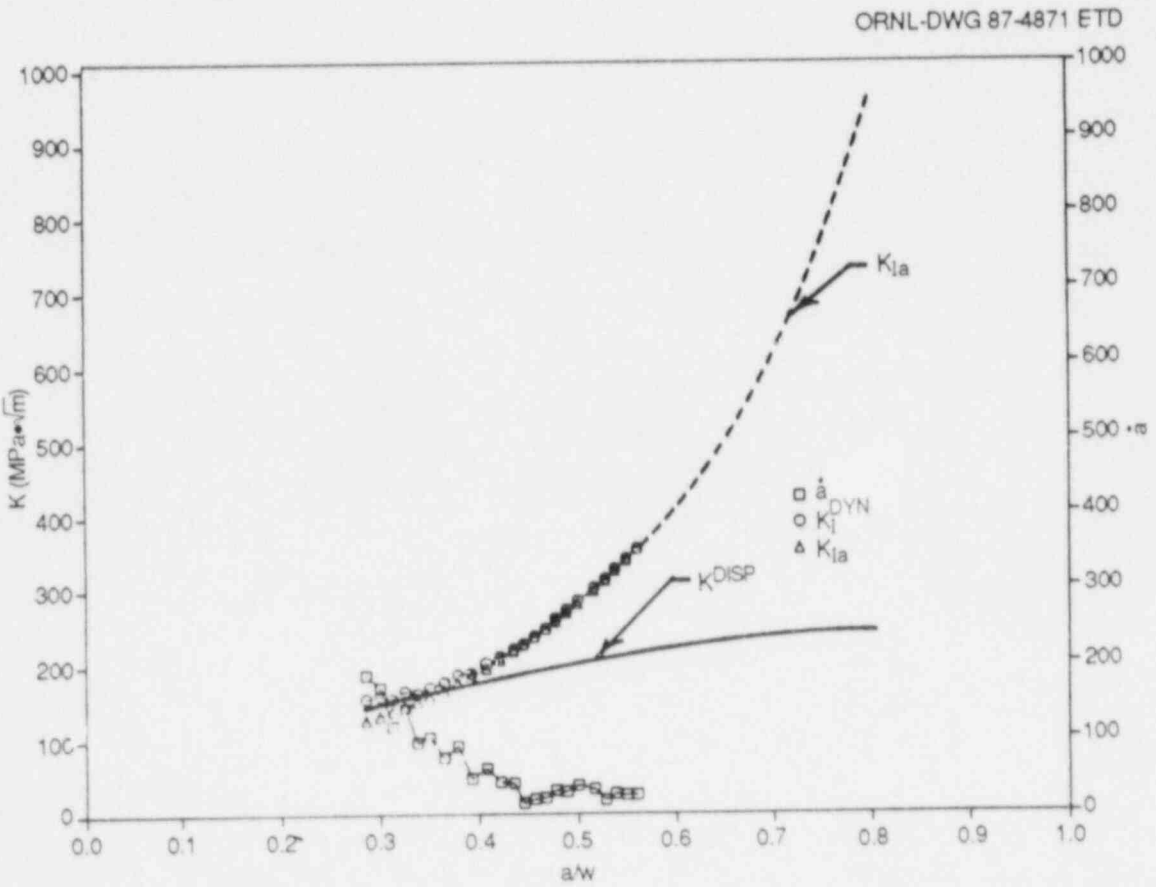

Fig. 5.24. Dynamic factor, static toughness, quasi-static displacement-controlled factor, and crack velocity vs instantaneous crack length (displacement control boundary condition): Test WP-2.5.

Force control. A posttest application-mode analysis of WP-2.5 was also performed with a fixed-load boundary condition. Utilizing the same finite-element model and material properties as for the displacement-control analysis, the load point was fixed at the value of the measured fracture load, 8.9 MN, as a prescribed concentrated load. The time step was set at $\Delta t = 5$ μs. The calculated crack-depth history from this analysis is depicted in Fig. 5.25 and indicates three predicted arrests at $a_{f_{P1}} = 0.456$ m, $a_{f_{P2}} = 0.527$, and $a_{f_{P3}} = 0.575$ m. Figure 5.26 presents the dynamic stress-intensity factor K_I^{DYN}, the static toughness K_{Ia}, and the crack velocity $\dot{a}$ as a function of instantaneous crack length. The crack propagates into a rising K_I field, followed by arrest at a point where the crack-tip temperatures would have been $T_{P1} = 129.4°C$, $T_{P2} = 146.2°C$, and $T_{P3} = 157.2°C$, respectively, for the three predicted arrest points given above. The arrest toughnesses at the arrest-point temperatures, evaluated from the relationship in Eq. (5.8), are determined to be $K_{Iap_1} = 237.1$ MPa·$\sqrt{m}$, $K_{Iap_2} = 311.0$ MPa·$\sqrt{m}$, and $K_{Iap_3} = 372.3$ MPa·$\sqrt{m}$. The first computed arrest length ($a_{f_{P1}}$) exceeds the initial measured arrest length at $a_{f_{m1}} = 0.350$ m but is closer to the measured value

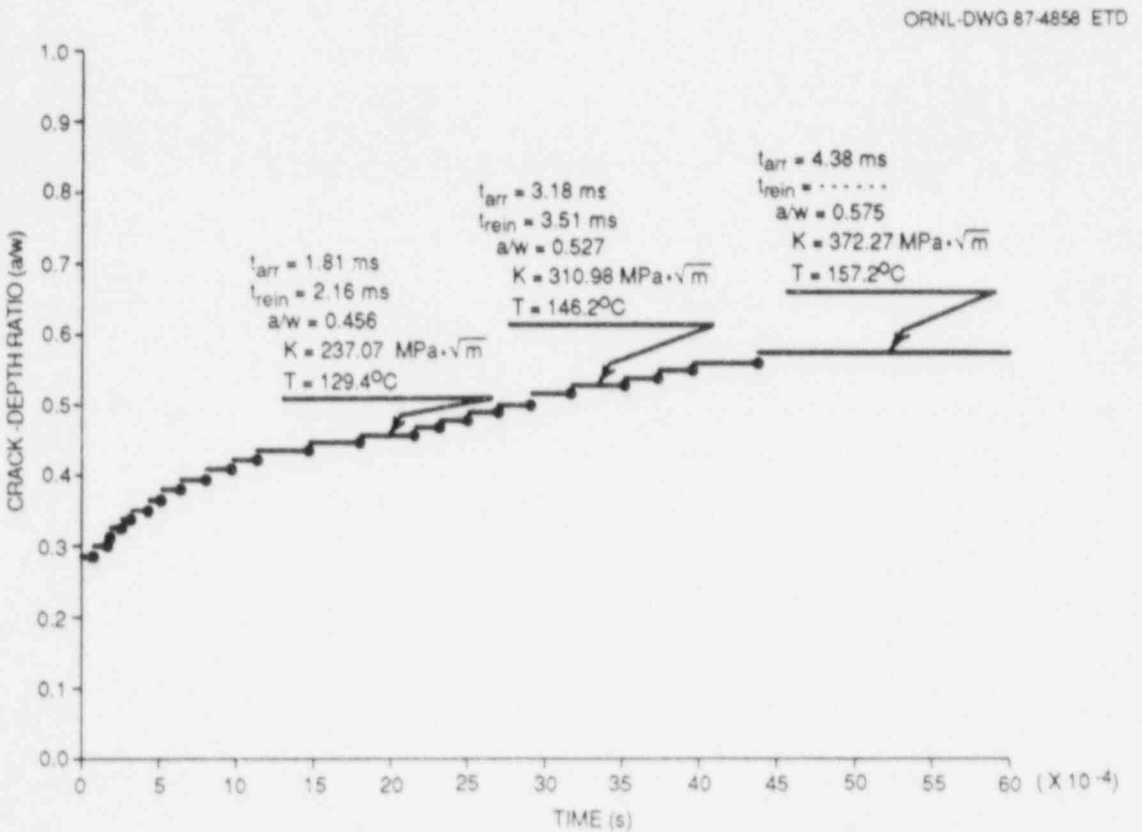

Fig. 5.25. Calculated crack-depth history from an application-mode dynamic analysis (force control boundary condition): Test WP-2.5.

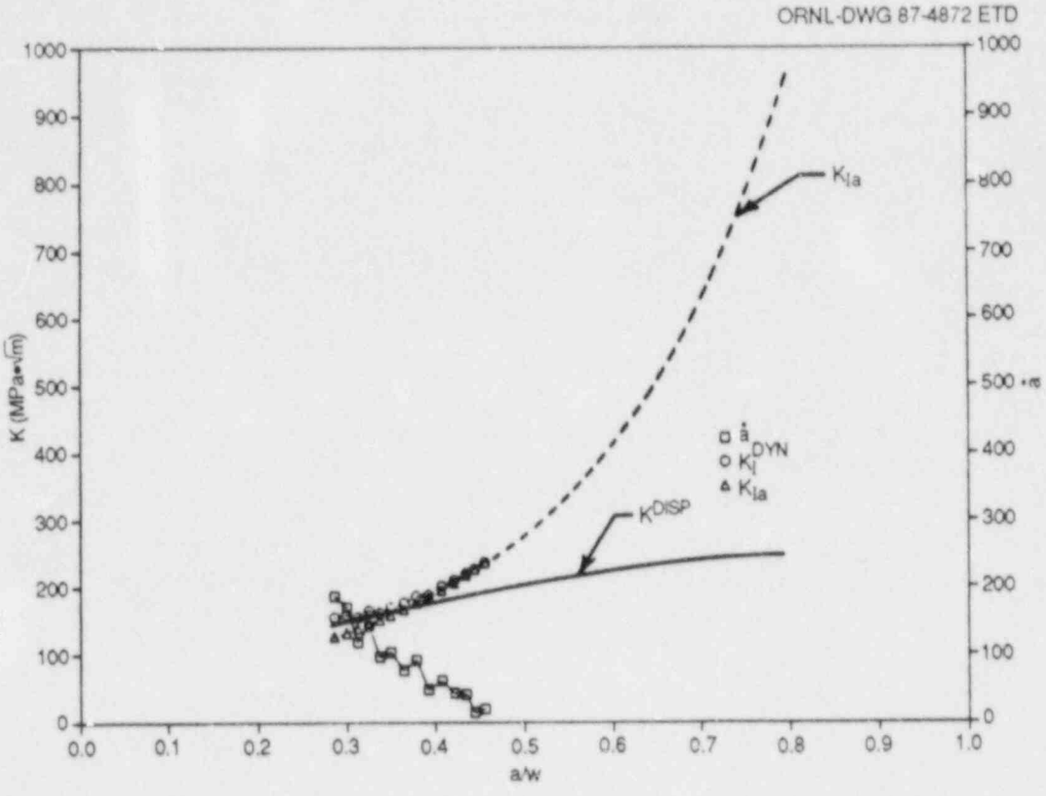

Fig. 5.26. Dynamic factor, static toughness, quasi-static displacement-controlled factor, and crack velocity vs instantaneous crack length (force control boundary condition): Test WP-2.5.

than the arrest length computed using the fixed-displacement boundary condition. The first computed arrest length is between measured arrest points C and D in Table 5.4 of Ref. 2 (back-face measurements). The second computed arrest length (a_{tp2}) is close to measured arrest point E in Table 5.4 of Ref. 2 where a_{fm_E} = 0.516 m, T = 143.7°C, and K_{Ia} = 297.8 MPa•$\sqrt{m}$. The third computed arrest length ($a_{f_{p3}}$) exceeds measured arrest point F in Table 5.4 of Ref. 2 where a_{fm_F} = 0.560 m, T = 153.8°C, and K_{Ia} = 351.8 MPa•$\sqrt{m}$. The application-mode analysis was terminated at time t = 6 ms, which precludes any prediction from the analysis of the reinitiation that occurred in the test at time t = 7.90 ms.

Generation-mode dynamic analyses

From the output of the crack-line strain gages and from an inspection of the fracture surface, estimates of the crack position as a function of time were constructed and given in Table 5.4 of Ref. 2 for the front- and the back-side strain gages. Figure 5.28 of Ref. 2 (back-face gages) presents the crack-time curve derived from Table 5.4 (Ref. 2) that

was used as input to ADINA/VPF for a posttest generation-mode elasto-dynamic analysis of test WP-2.5. The curve in the figure incorporates the five measured crack arrests as determined from the back-surface strain measurements (see Table 5.4 of Ref 2). For the dynamic analysis, the load point was fixed at the value of the initiation load, 8.9 MN, as a prescribed concentrated load, and the time step was set at Δt = 10 μs. From these calculations, the stress-intensity factor as a function of time is given in Fig. 5.27. The generation-mode analysis results for the five arrest events after the pop-in are given in Table 5.3.

The computed strain histories from selected points close to the back-side crack-line strain gages 13–22 [see Fig. 5.6(*a*) for strain-gage locations], along with measured data from the gages, are depicted in Figs. 5.28–5.30 for the generation-mode analysis (fixed load). The sharply defined strain peaks are associated with the fast-running crack passing under a gage point, with the peak being transformed into a more blunted curve as the crack tip slows down. The comparisons of strain histories in these figures indicate generally good agreement between measured and computed times for the occurrence of the peak strain values. The transition of the strain pulse from a sharp peak for gage 14 to a

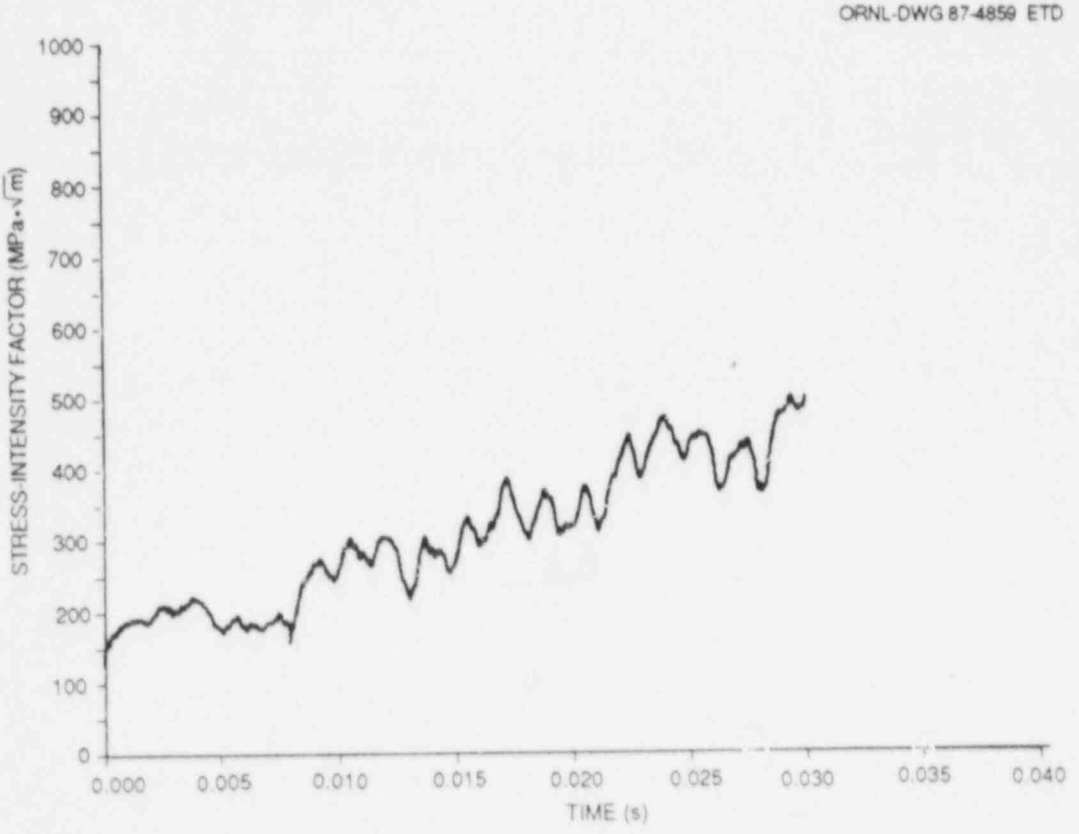

Fig. 5.27. Calculated stress-intensity factor vs time from the generation-mode dynamic analysis (force control boundary condition): Test WP-2.5.

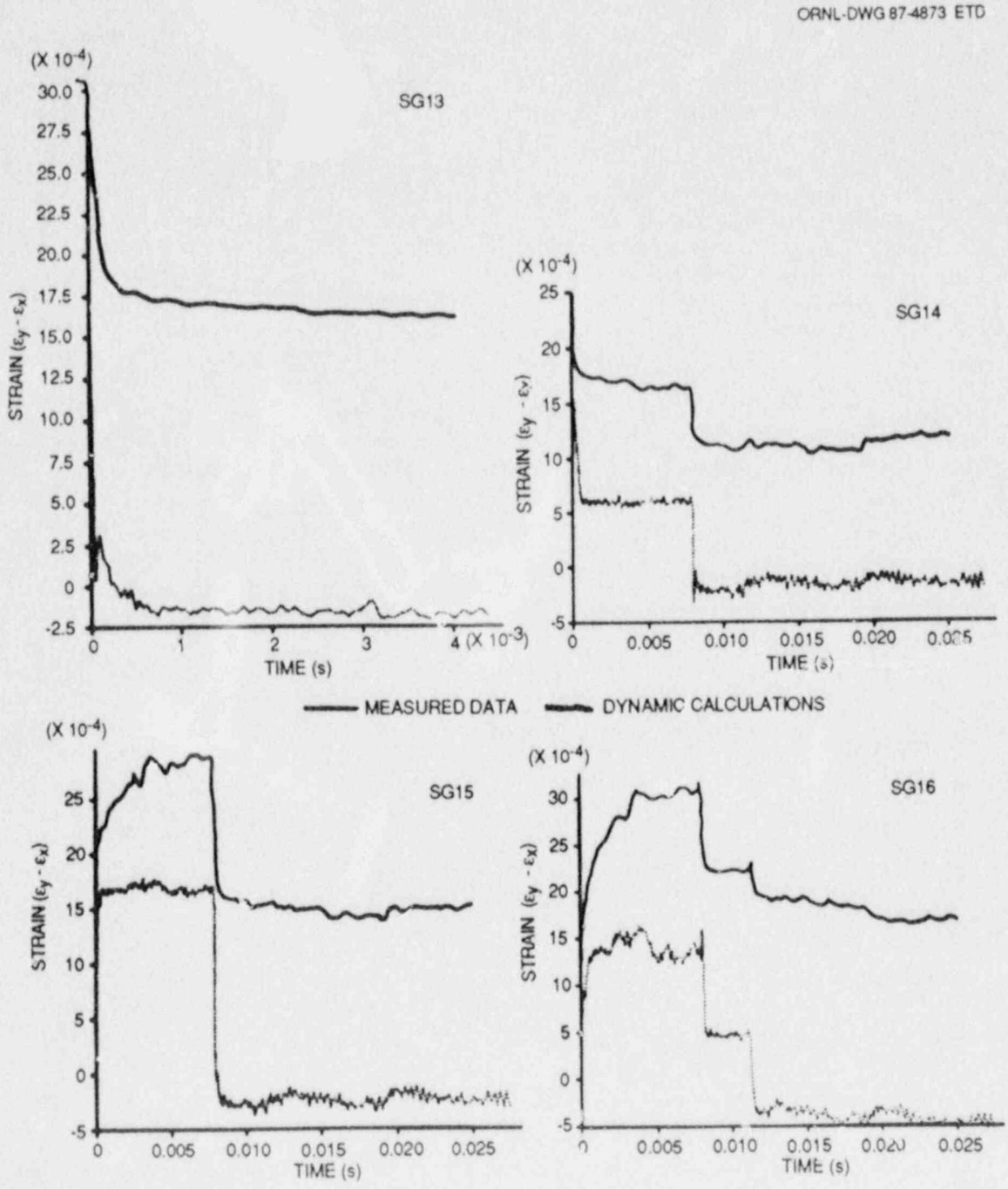

Fig. 5.28. Actual and computed strain histories for back-face crack-line gages 13–16: Test WP-2.5.

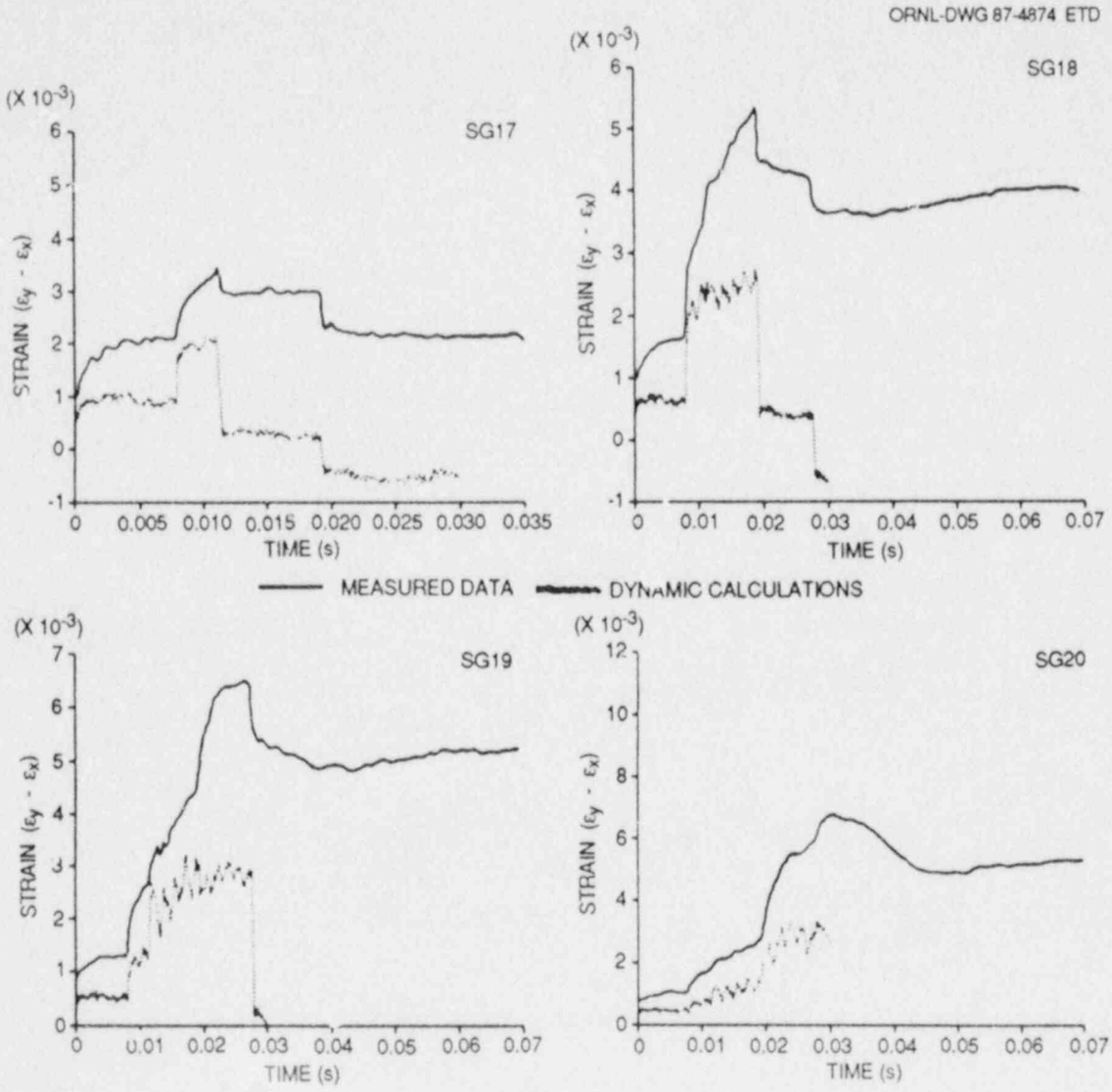

Fig. 5.29. Actual and computed strain histories for back-face crack-line gages 17–20: Test WP-2.5.

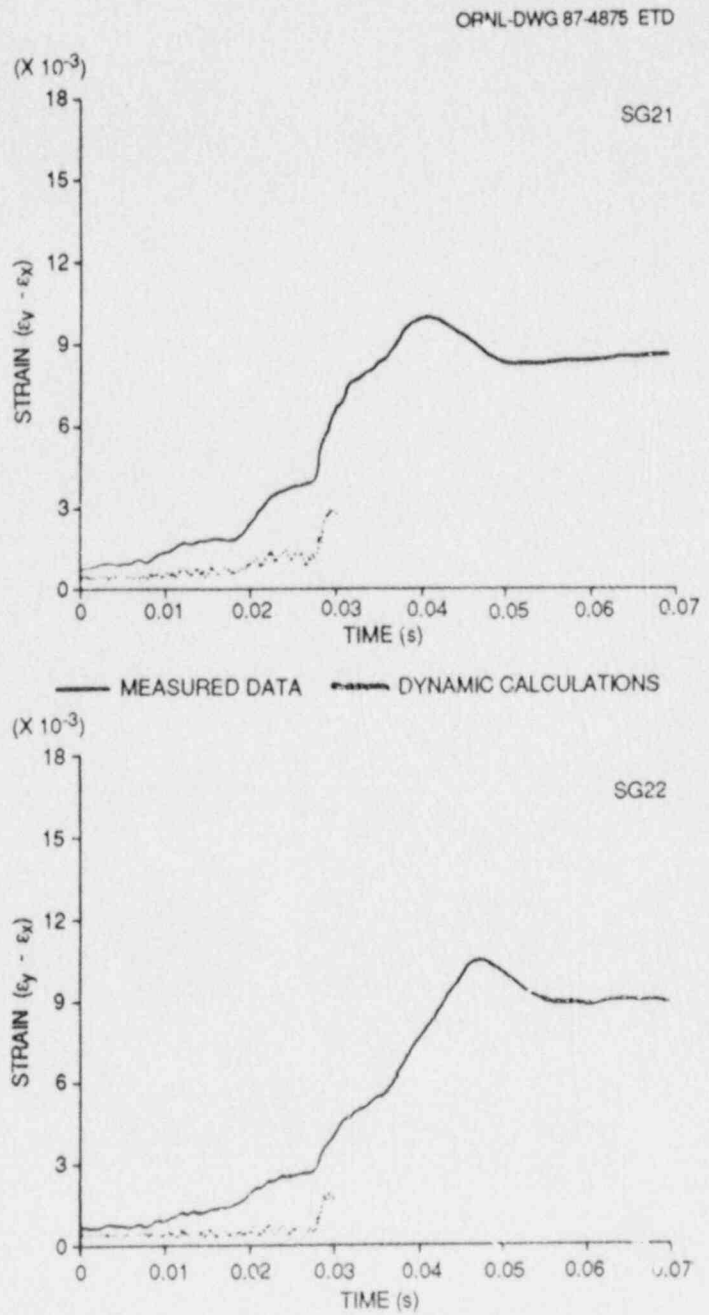

Fig. 5.30. Actual and computed strain histories for back-face crack-line gages 21–22: Test WP-2.5.

Table 5.3. Summary of computed results for test WP-2.5 (back-face gages)

Event[a]	Time (ms)	A (m)	K[b] (MPa·√m)
Initiation[c]	0.0	0.272	154.22[d]
Arrest B	0.54	0.350	171.09
Reinitiation	7.90	0.350	183.77
Arrest C	8.16	0.435	190.36
Reinitiation	11.16	0.435	276.55
Arrest D	11.49	0.478	268.18
Reinitiation	19.11	0.478	356.65
Arrest E	19.43	0.516	305.74
Reinitiation	27.63	0.516	428.90
Arrest F	27.95	0.560	365.98
Reinitiation	29.01	0.560	475.08

[a]Plate back-face determinations.

[b]Generation-mode, fixed-load dynamic analysis.

[c]After pop-in.

[d]From ADINA static analysis.

blunted curve for gage 15 in Fig. 5.28 reflects the arrest event (Arrest B) between the back-side crack-line strain gages 14 and 15. This same occurrence can be viewed for the remainder of the arrest events in the figures for the back-side crack-line gages.

In Fig. 5.31 the COD calculated at x = 0.15 m from the cold edge of the plate using a generation-mode analysis is compared with measured data from the COD gages installed on the F- and B-COD surfaces of the plate. The COD values calculated are reasonably consistent with the measured values up to an elapsed time of ≈25 ms into the fracture event.

5.4.1.2 WP-2.3

Posttest 3-D static analyses. The 3-D finite-element model used for test WP-2.3 incorporated a segment of the plate assembly 4.6245 m in length measured from the crack plane to the top of the load-pin hole. The crack-tip region of the model included the side grooving and the edge notch, the dimensions of which were taken from Table 5.1. From symmetry

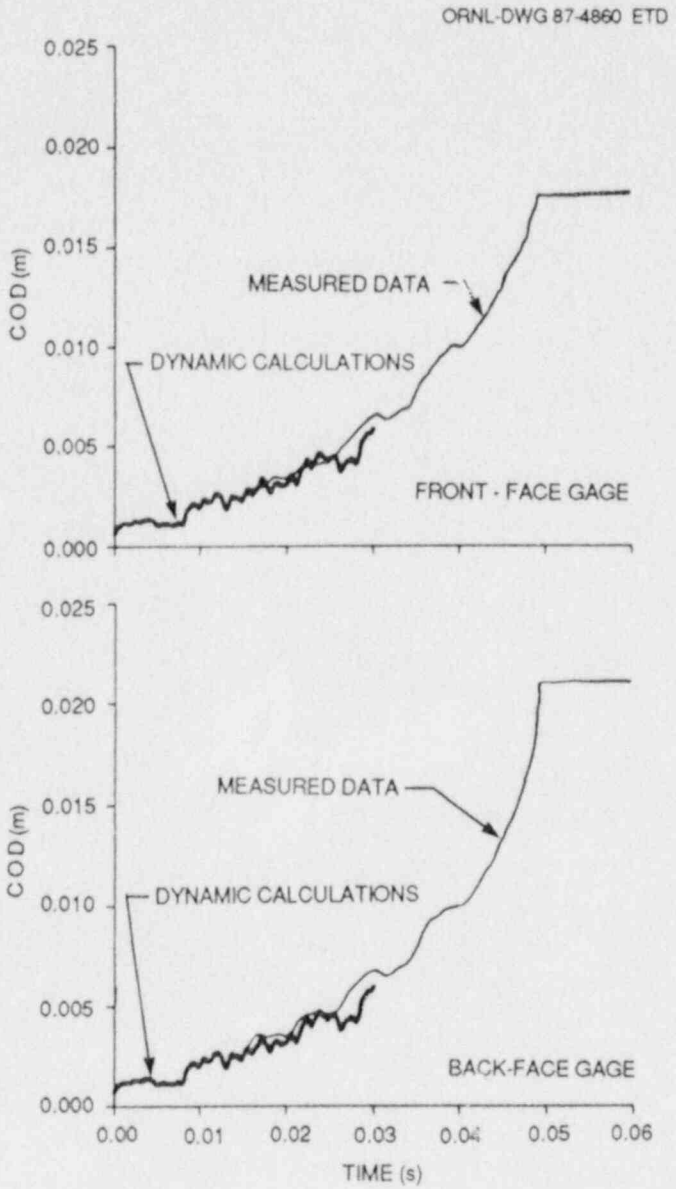

Fig. 5.31. Actual and computed CODs at a/w = 0.15 for front-face and back-face gage locations: Test WP-2.5.

conditions neglecting out-of-plane eccentricity, one-quarter of the partial pull-plate assembly was modeled using 3751 nodes and 720 20-noded isoparametric elements. Test WP-2.3 did not have the crack front cut into a chevron configuration.

Thermal deformations to be superposed on the 3-D finite-element model to account for the in-plane bending effect were computed from a 2-D analysis which assumed that the heated and cooled edges of the plate were fixed at T_{max} = 252.7°C and T_{min} = 19.3°C, respectively. The in-plane thermal bending produced a load-line (through the top of the load-pin hole) eccentricity of 1.74 cm relative to the geometric center of the plate.

In the 3-D analysis, thermal stress effects were neglected, and a uniform line-load statically equivalent to the WP-2.3 test initiation load of 15.3 MN was applied at the location corresponding to the top of the load-pin hole. The result of this analysis produced a static stress-intensity factor of K_I = 136.1 MPa•$\sqrt{m}$ at the center plane of the plate. Comparison of this computed K_I value with the static initiation value of K_{Ic} = 155.5 MPa•$\sqrt{m}$, evaluated from the relationship presented in Eq. (5.7) using the crack-tip temperature of 66°C, yields a ratio of K_I/K_{Ic} = 0.875. A comparison of initiation stress-intensity factors obtained from the WP-1 series tests and the previous WP-2 series tests (WP-2.4, WP-2.1, and WP-2.5) is presented in Table 5.4.

Table 5.4. Initiation stress-intensity factor comparisons

Test designation	Crack-tip temperature (°C)	Calculated static[a] K_I (MPa•$\sqrt{m}$)	Property correlation K_{Ic} (MPa•$\sqrt{m}$)	K_I/K_{Ic}
WP-1.2	−33	251.5	87.5[b]	2.87
WP-1.3	[illegible]	173.5	70.1[b]	2.48
WP-1.4	−62	213.0	63.9[b]	3.33
WP-1.5	−30	179.8	91.6[b]	1.96
WP-1.6	−19	233.8	111.2[b]	2.10
WP-2.4A	45	123.0	93.9[c]	1.31
WP-2.4B[d]	60.8	143.3	135.7[c]	1.06
WP-2.1	55	126.4	117.6[c]	1.07
WP-2.5	66	119.5	155.5[c]	0.77
WP-2.3	66	136.1	155.5[c]	0.88

[a]Computed from 3-D static analysis using ORMGEN/ADINA/ORVIRT.

[b]Calculated from $K_{Ic} = 51.276 + 51.897\, e^{0.036\,(T-RT_{NDT})}$ using crack-tip temperature of initial flaw.

[c]Calculated from $K_{Ic} = 39.53 + 93.47\, e^{0.036(T-DW_{NDT})}$ using crack-tip temperature of initial flaw.

[d]After crack pop-in.

Posttest 2-D static and dynamic analyses

Static and stability analysis. Posttest 2-D analyses of WP-2.3 were carried out in the same manner as for test WP-2.5. Using a temperature profile as defined by specifying the crack-tip temperature of T_{CT} = 65°C and midplate temperature T_{MP} = 140°C, implying T_{min} = 15°C and T_{max} = 265°C, the dependence of arrested crack length and crack stability upon the applied initiation load F_{in} = 15.3 MN was investigated with WPSTAT; the results are presented in Fig. 5.32. Evaluation of the K_{Ia} function of Eq. (5.8) on the arrest crack length curve $a_f(F)$, on the incipient tearing instability curve $a_{I2}(F)$, and on the reinitiation curve $a_{rein}(F)$ is presented in Fig. 5.33; the K_{Ic} function of Eq. (5.7) is also evaluated on the curve $a_{rein}(F)$. Evaluation of the $K_{Ia}(a_f)$ curve at the initiation load F_{in} yields an arrest toughness K_{Ia} = 224 MPa•$\sqrt{m}$ at the predicted arrest point a_{fc} = 0.460 m, where the crack-tip temperature would be T = 126.1°C. The complete static fracture mechanics and stability analyses are depicted in Fig. 5.34.

Application-mode dynamic analyses (fixed-load boundary condition). The 2-D plane-stress finite-element model of the wide-plate configuration

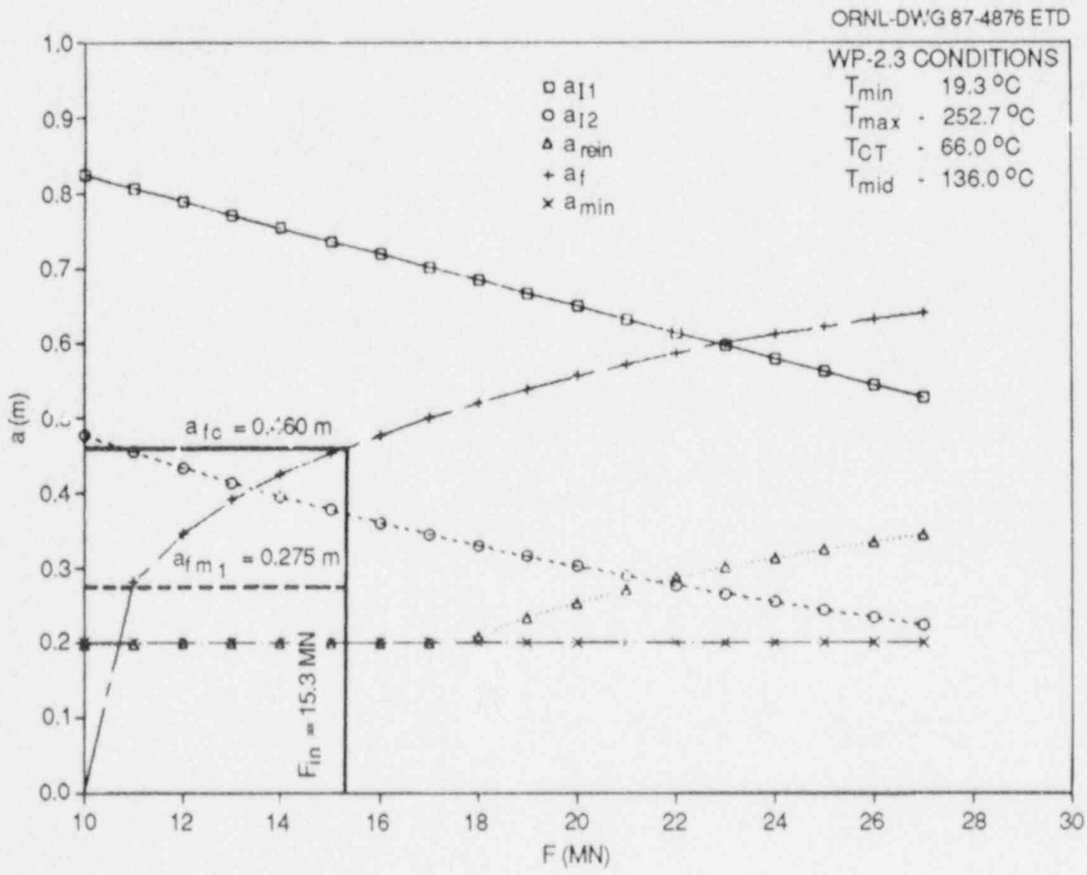

Fig. 5.32. Statically calculated crack lengths: Test WP-2.3.

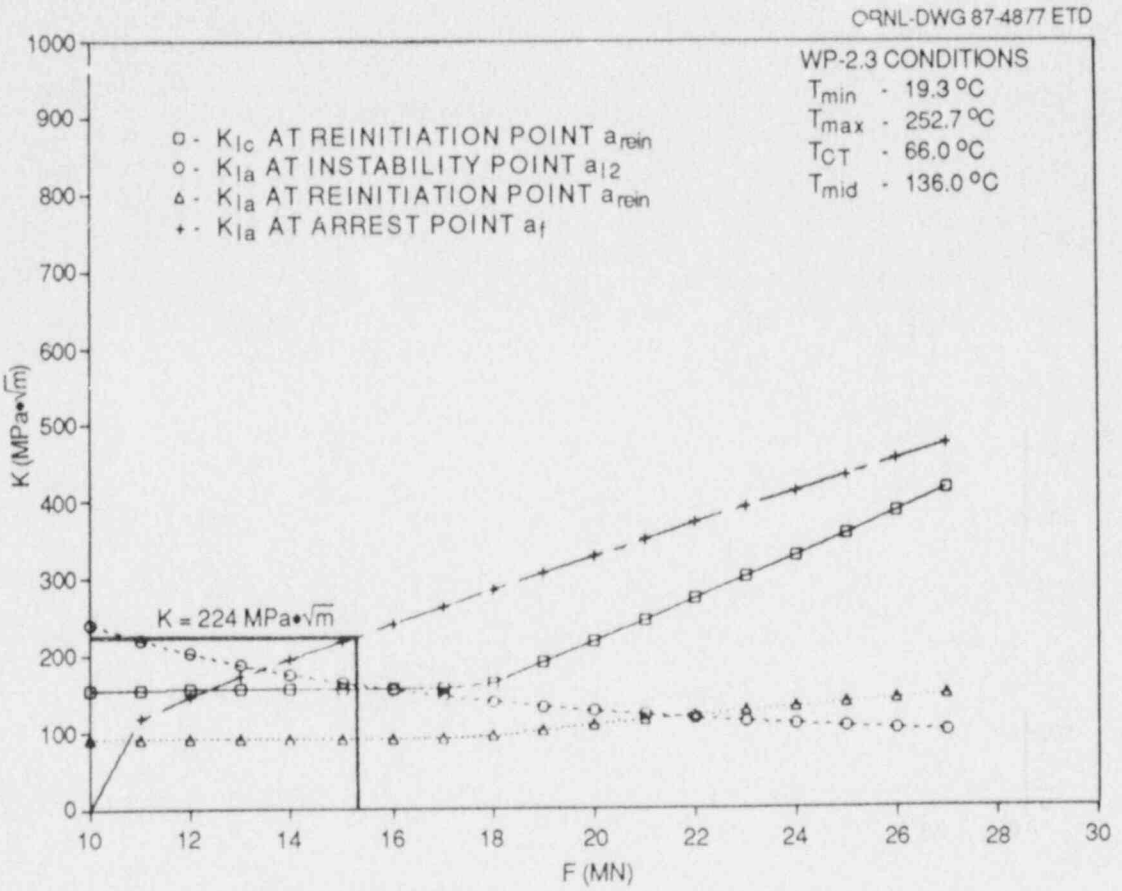

Fig. 5.33. Determination of arrest toughness at initiation load of 15.3 MN: Test WP-2.3.

used in the analyses consisted of 939 nodes and 277 eight-noded isoparametric elements. A total of 35 spring elements were used in the crack plane to model propagation of the crack tip. For the dynamic analysis, the load point was fixed at the value of the measured fracture load, 15.3 MN, as a prescribed concentrated load. The time step was set at Δt = 5 μs. Figure 5.35 presents the calculated crack depth history from this analysis and indicates a predicted arrest a_{fp} = 0.667 m. The dynamic stress-intensity factor K_I^{DYN}, the static toughness K_{Ia}, and the crack velocity a as a function of instantaneous crack depth are presented in Fig. 5.36. The crack propagates into a rising K_I field, followed by a predicted arrest at a point where the crack-tip temperature would have been T = 178.7°C. The arrest toughness at the arrest-point temperature is determined to be K_{Ia} = 534 MPa•√m. The computed arrest length exceeds the last measured arrest point, a_{fm_3} = 0.400 (Arrest E, front face in Table 5.2) where T = 111.5°C and K_{Ia} = 178.2 MPa•√m. The application-mode analysis was terminated at time t = 6 ms, which precludes any prediction from the analysis of the reinitiation that occurred at time t ~ 12.5 ms.

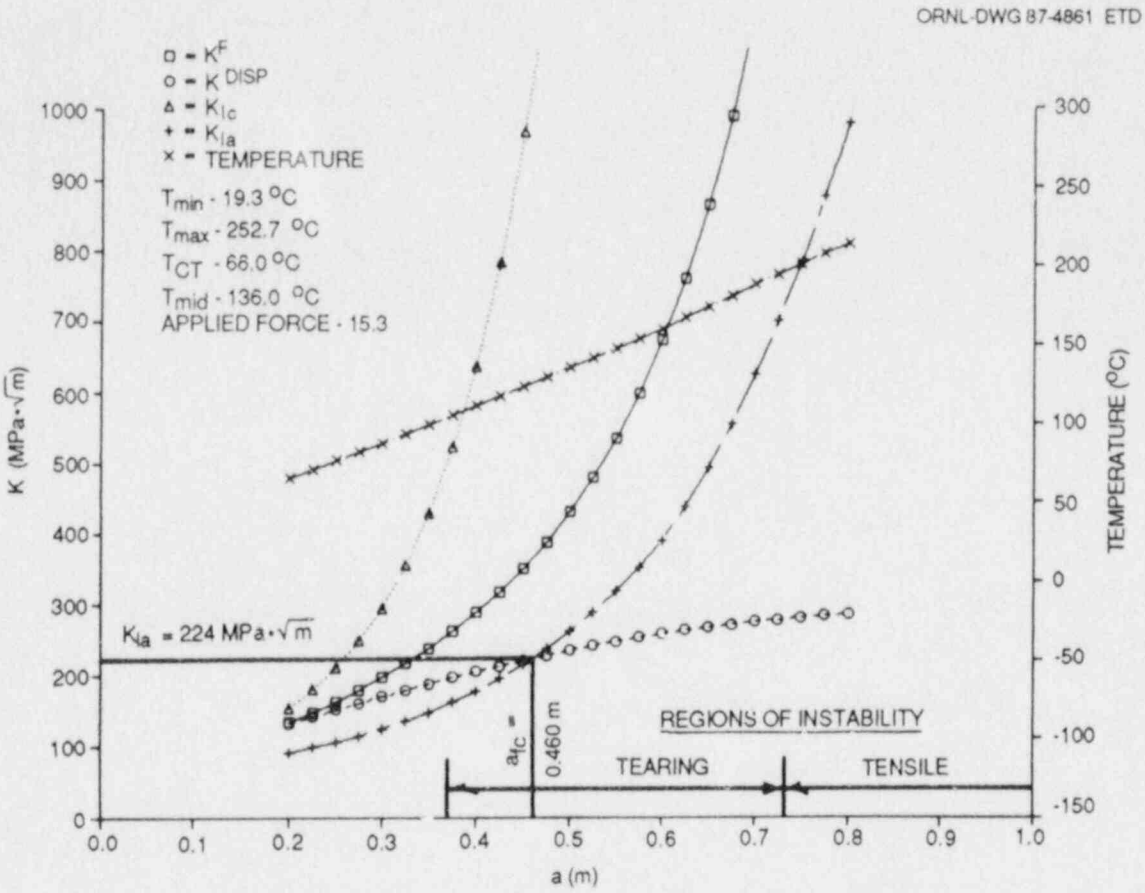

Fig. 5.34. Complete static and stability analyses for initiation load of 15.3 MN: Test WP-2.3.

Generation-mode dynamic analysis (fixed-load boundary condition). Figure 5.15 depicts the apparent crack position vs time curve that was used as input for the posttest generation-mode elastodynamic analysis of test WP-2.3. For these analyses, the load point was fixed at the value of the initiation load, 15.3 MN, as a prescribed concentrated load, and the time step was set at Δt = 10 μs. From these calculations, the stress-intensity factor as a function of time is given in Fig. 5.37. Table 5.5 presents the generation-mode analysis results for the seven arrest events (three front plus four back face).

The computed strain histories from selected points close to the crack-line strain gage Nos. 1–22* [see Fig. 5.6(*a*) for strain-gage locations] are shown in Figs. 5.38–5.44 for measured data from the gages. The F- and B-COD results calculated at x = 0.15 m from the cold edge of

*Results are not presented for gage Nos. 16 and 17 because of inoperability (No. 16) or a noisy signal (No. 17).

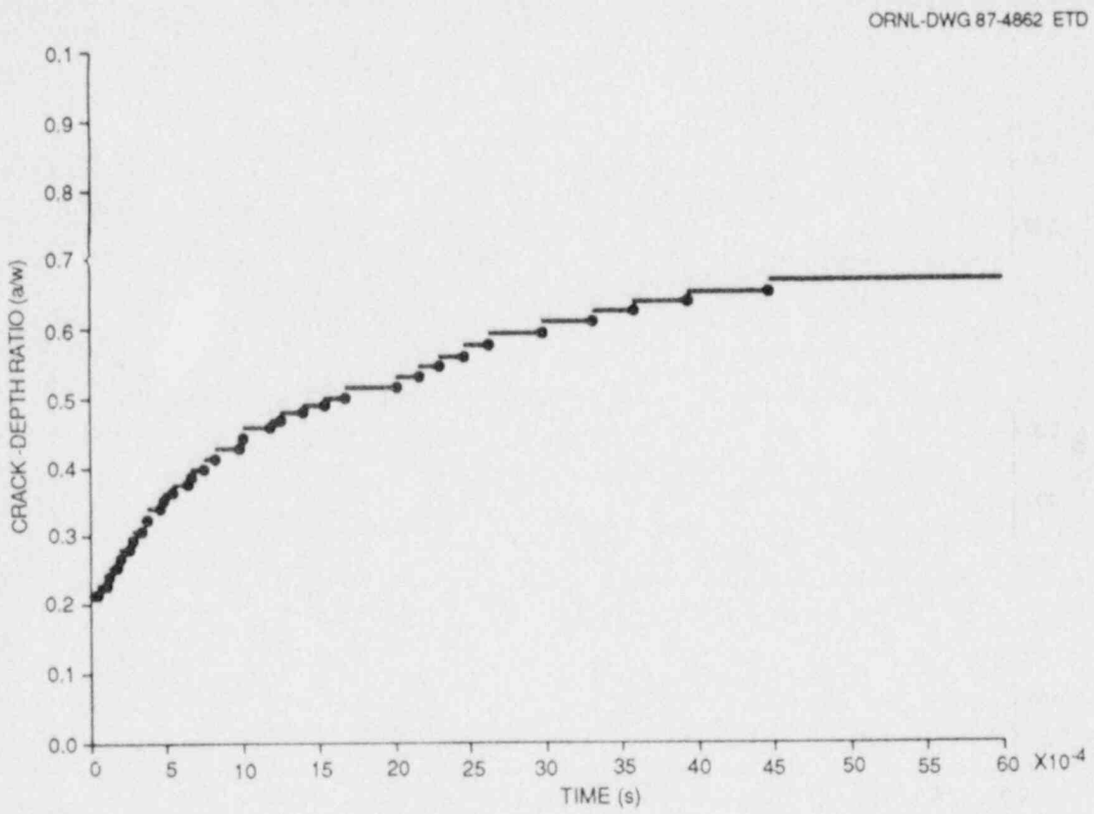

Fig. 5.35. Calculated crack-depth history from an application-mode dynamic analysis (fixed-load boundary condition): Test WP-2.3.

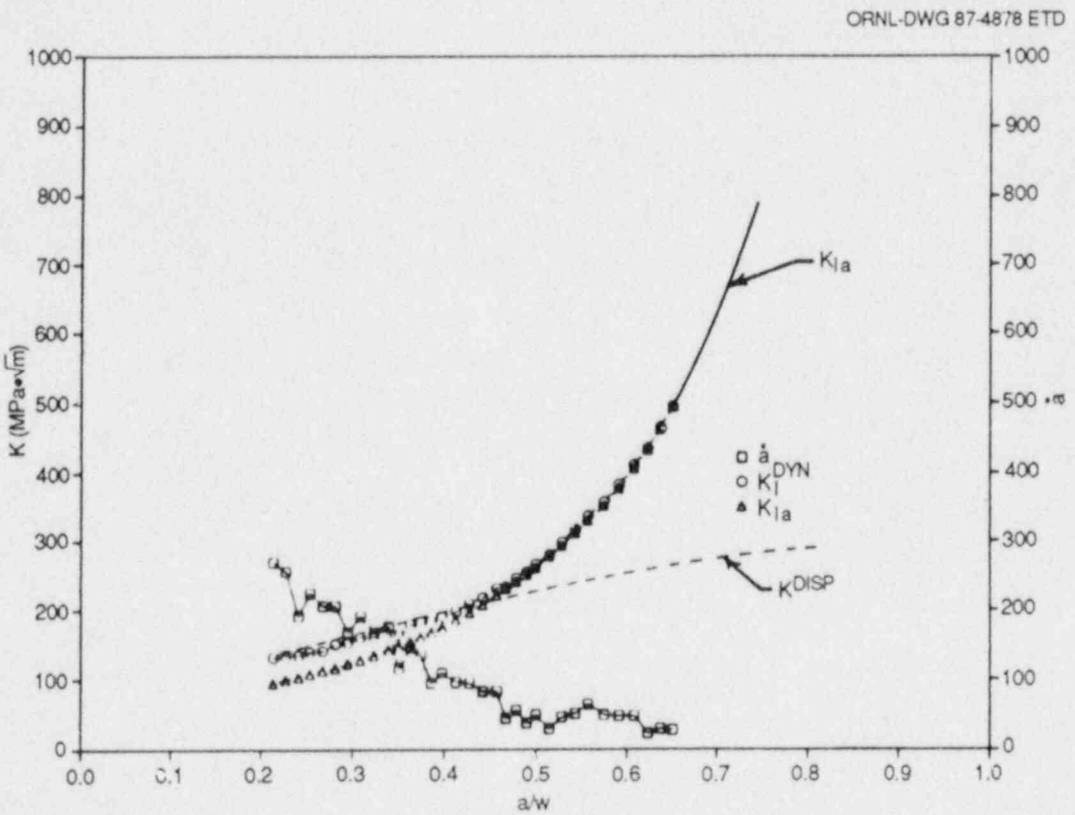

Fig. 5.36. Dynamic factor, static toughness, quasi-static displacement-controlled factor, and crack velocity vs instantaneous crack length (fixed-load boundary condition): Test WP-2.3.

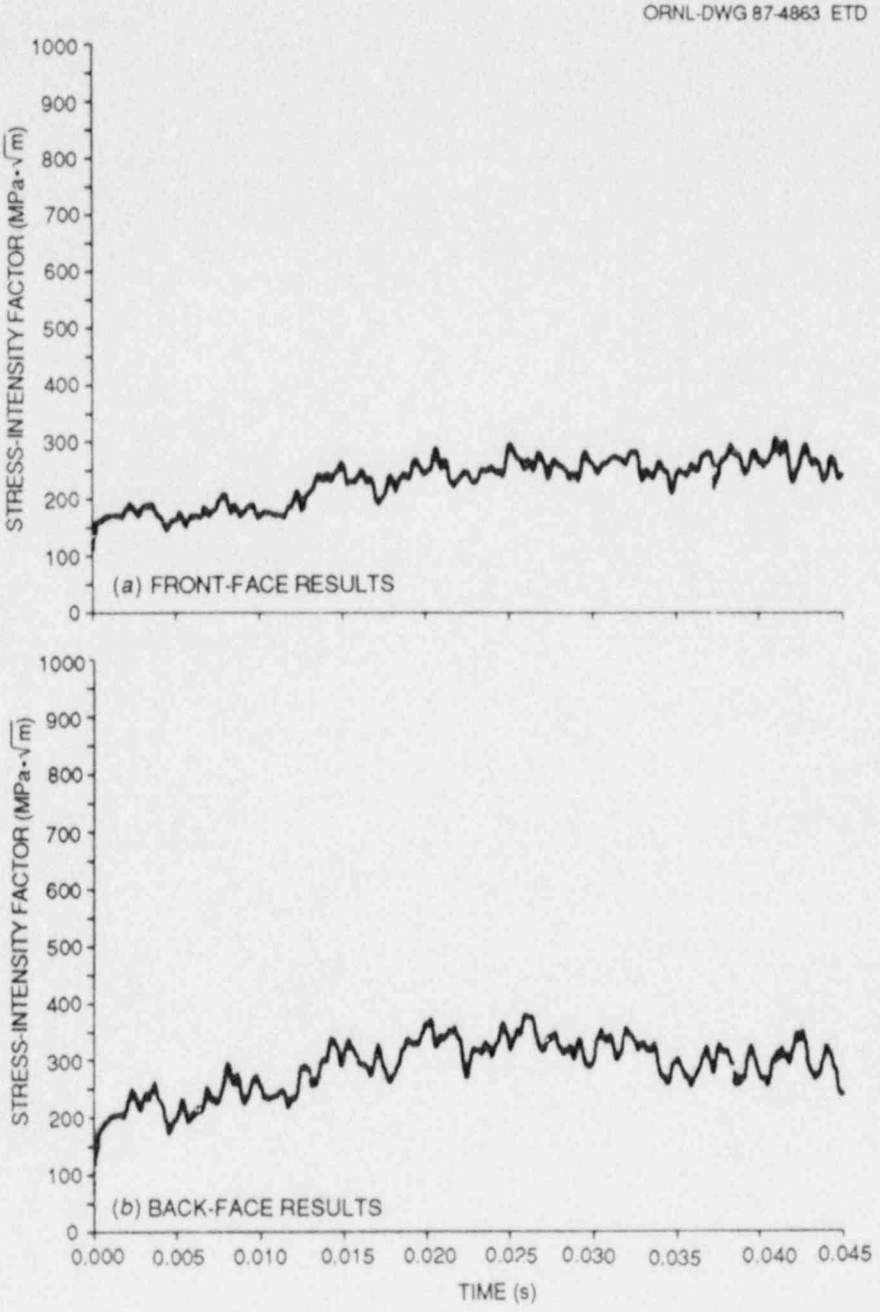

Fig. 5.37. Calculated stress-intensity factor vs time from the generation-mode dynamic analysis (fixed-load boundary condition): Test WP-2.3.

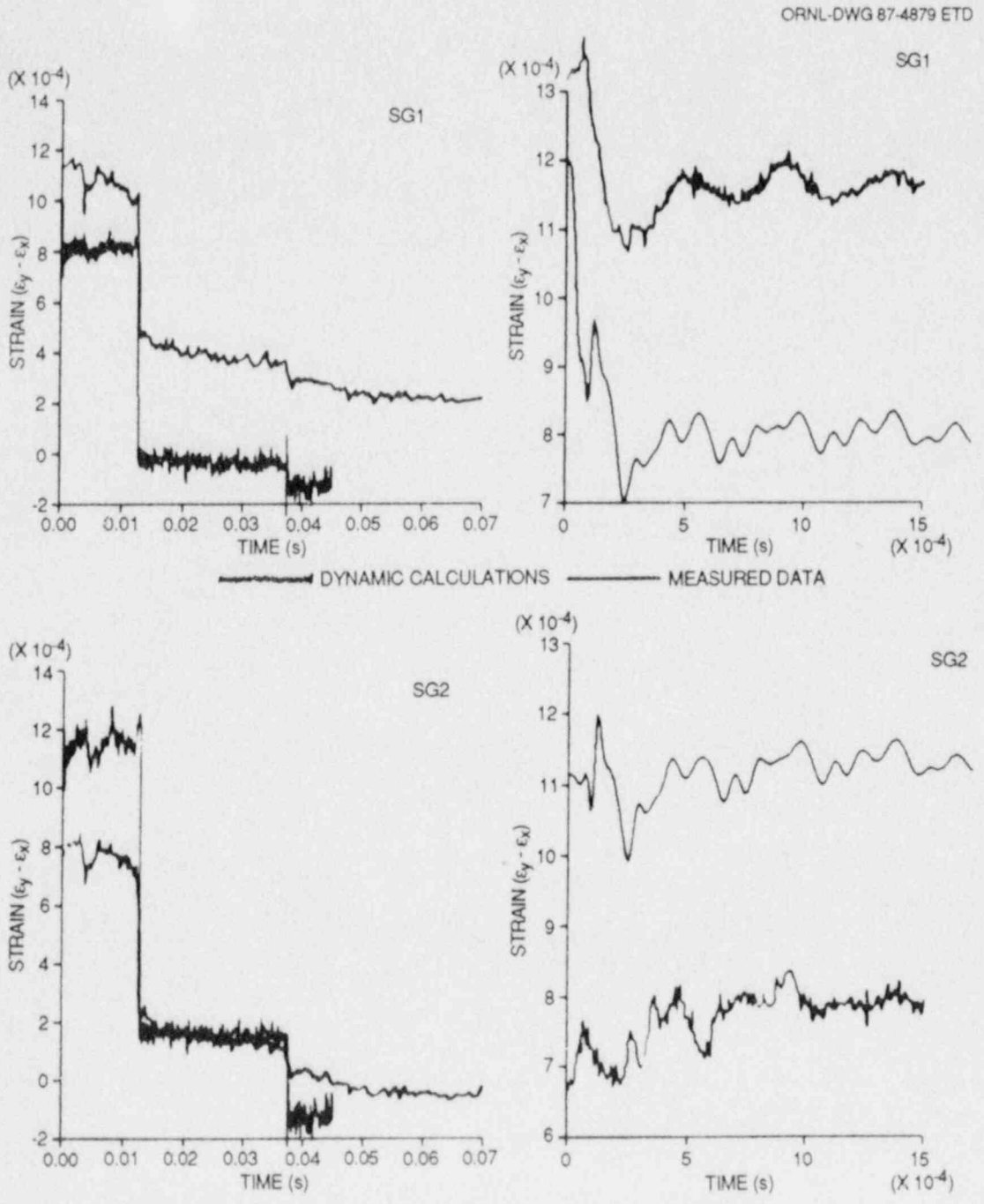

Fig. 5.38. Actual and computed strain histories for front-face crack-line gages 1 and 2 at two time resolutions: Test WP-2.3.

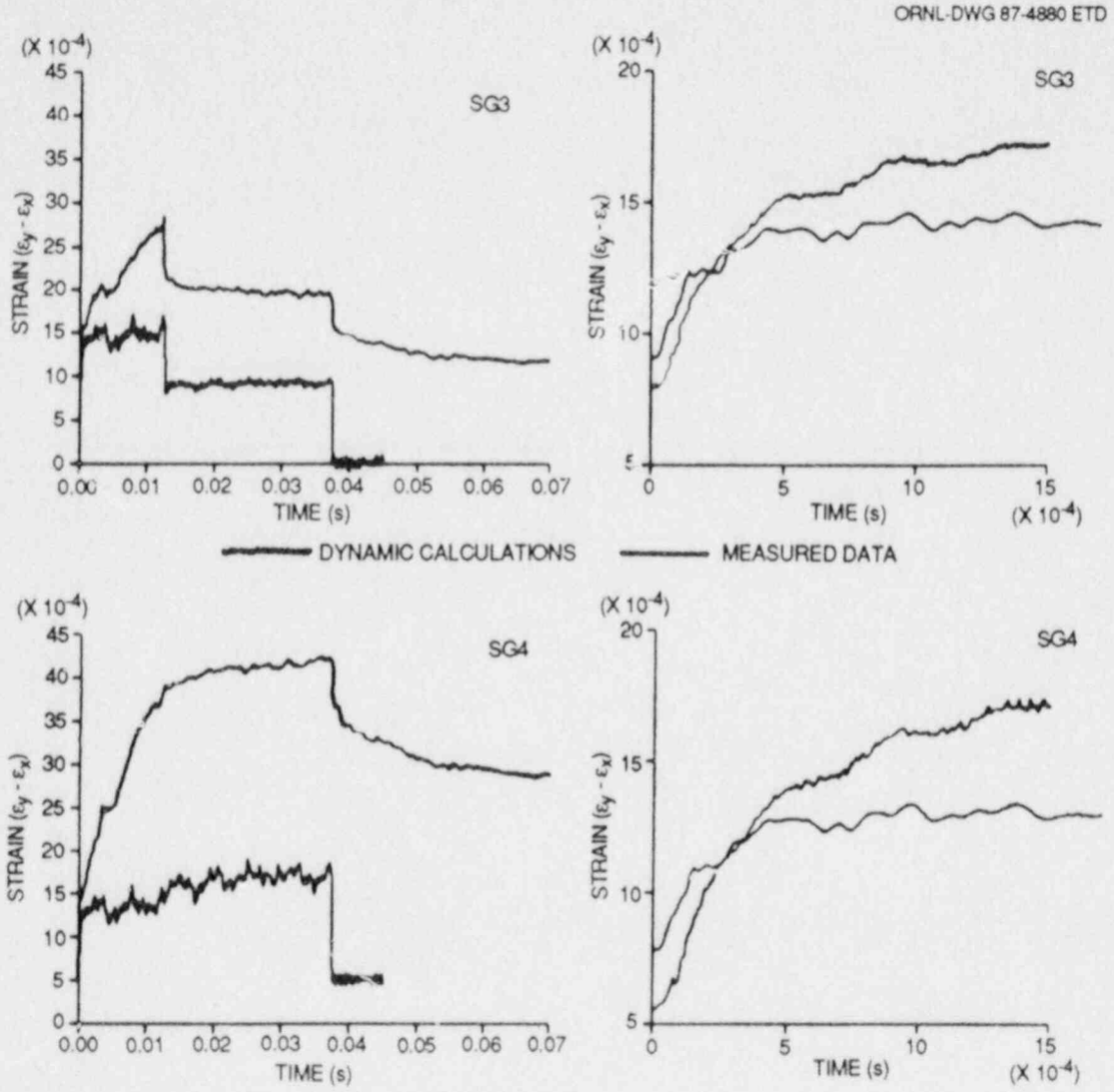

Fig. 5.39. Actual and computed strain histories for front-face crack-line gages 3 and 4 at two time resolutions: Test WP-2.3.

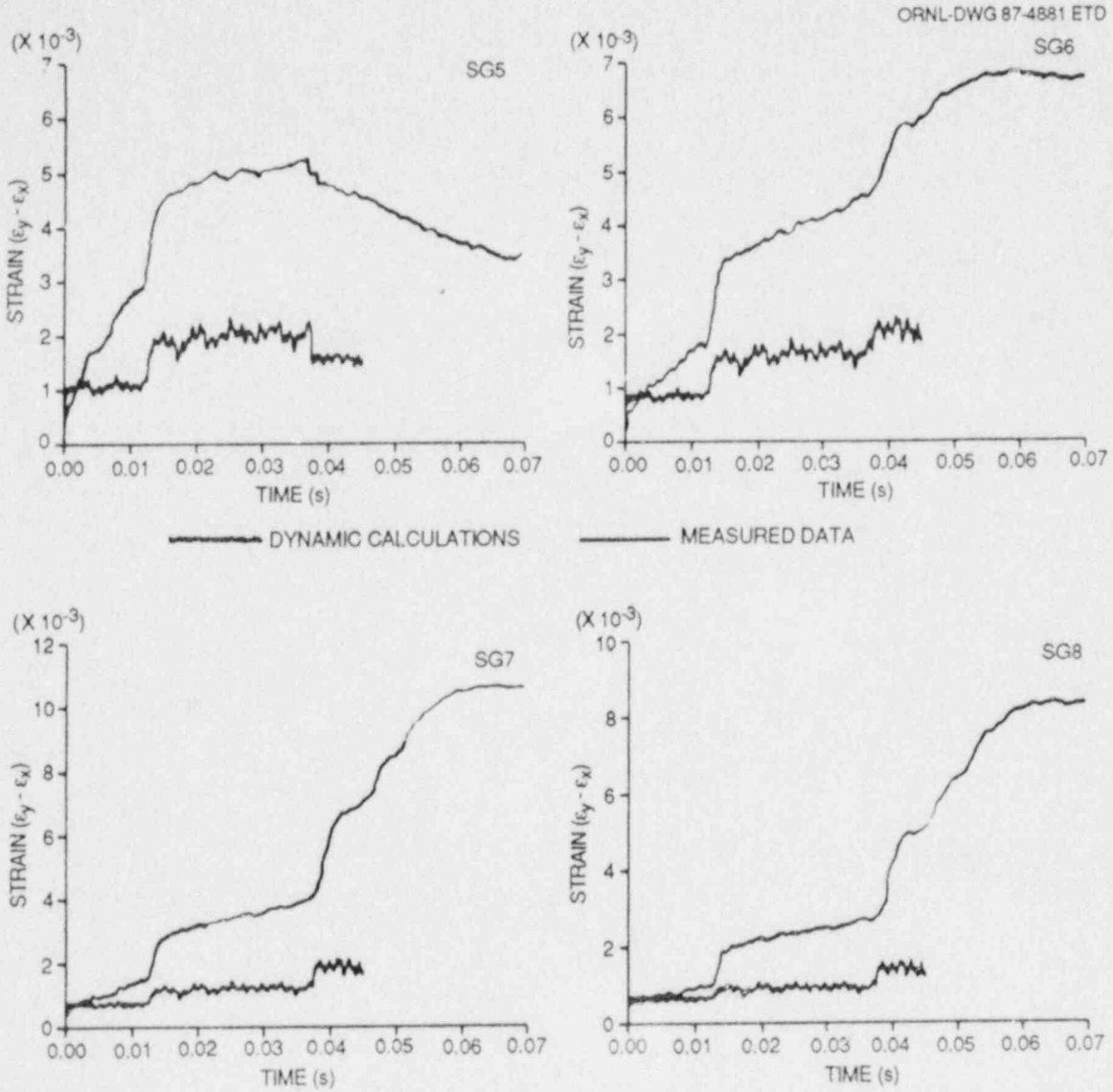

Fig. 5.40. Actual and computed strain histories for front-face crack-line gages 5–8: Test WP-2.3.

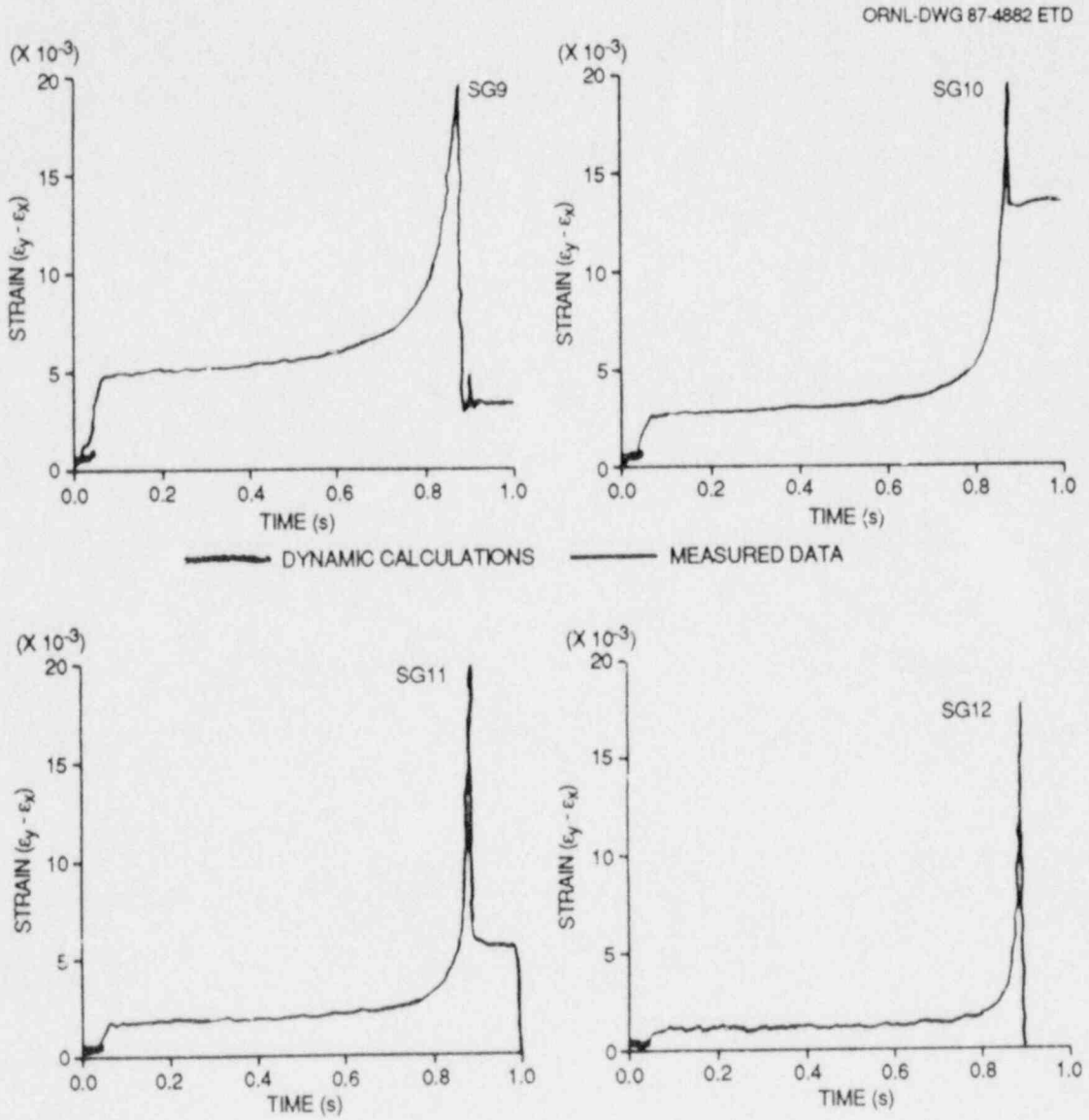

Fig. 5.41. Actual and computed strain histories for front-face crack-line gages 9–12: Test WP-2.3.

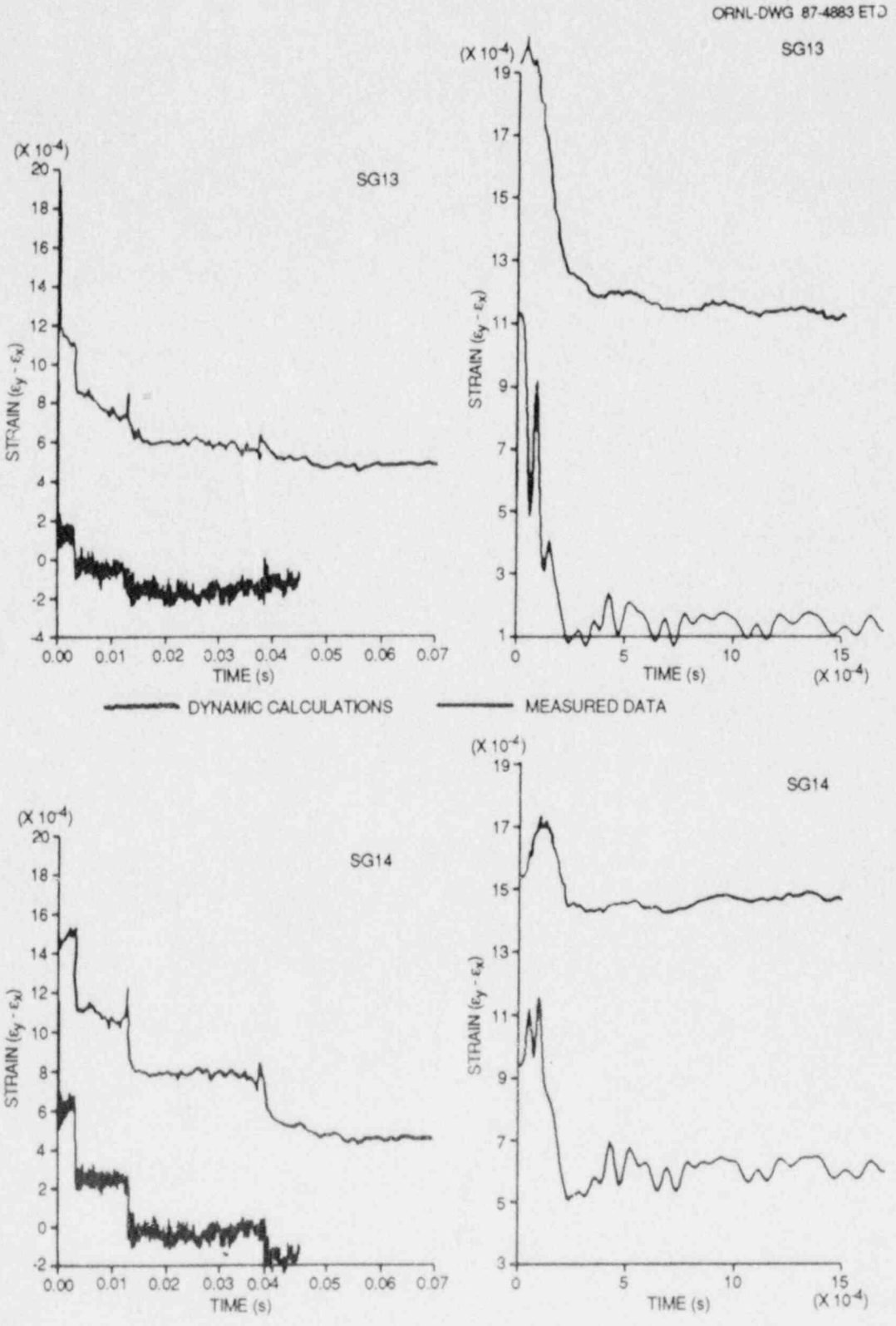

Fig. 5.42. Actual and computed strain histories for back-face crack-line gages 13 and 14 at two time resolutions: Test WP-2.3.

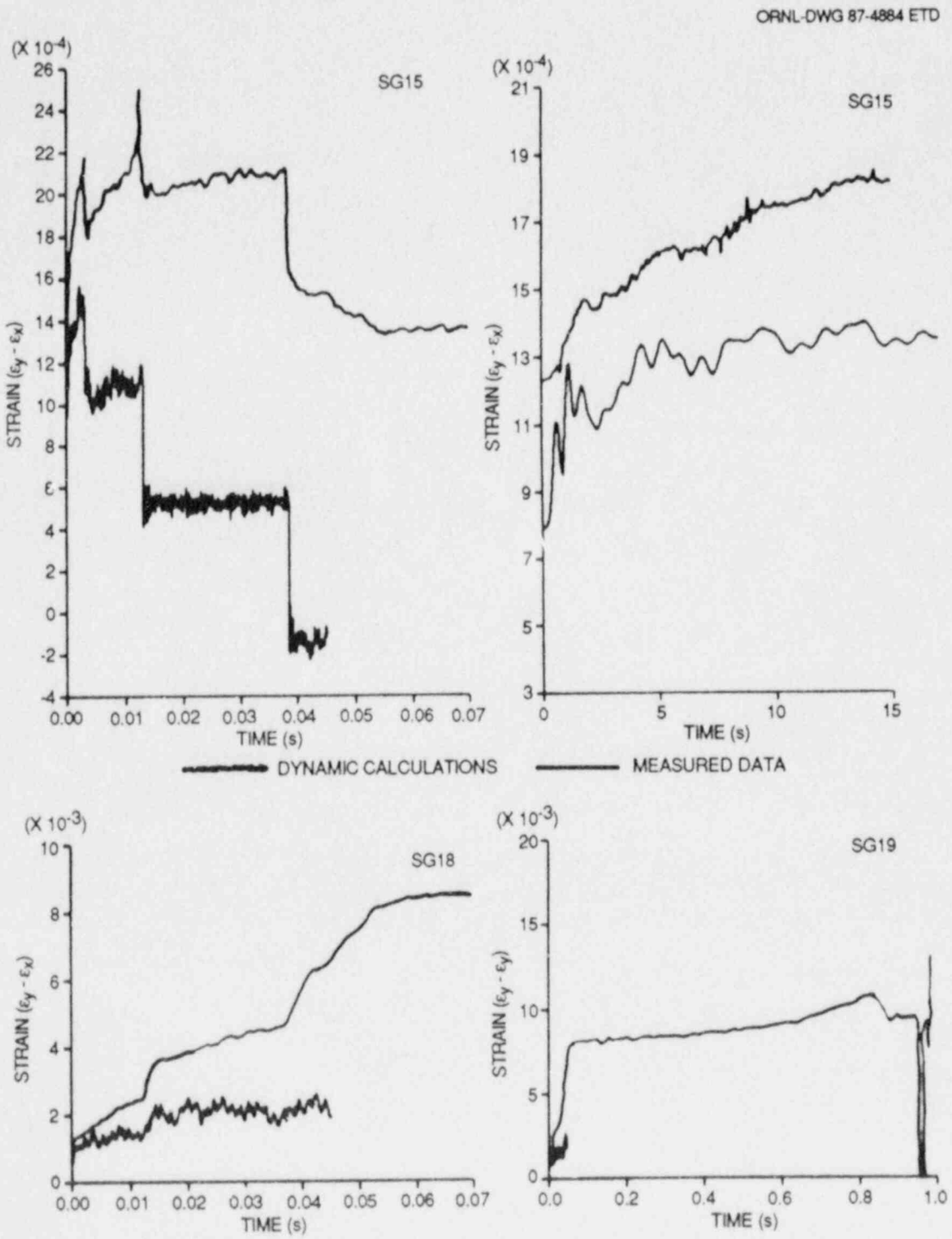

Fig. 5.43. Actual and computed strain histories for back-face crack-line gage 15 at two time resolutions and gages 18 and 19: Test WP-2.2.

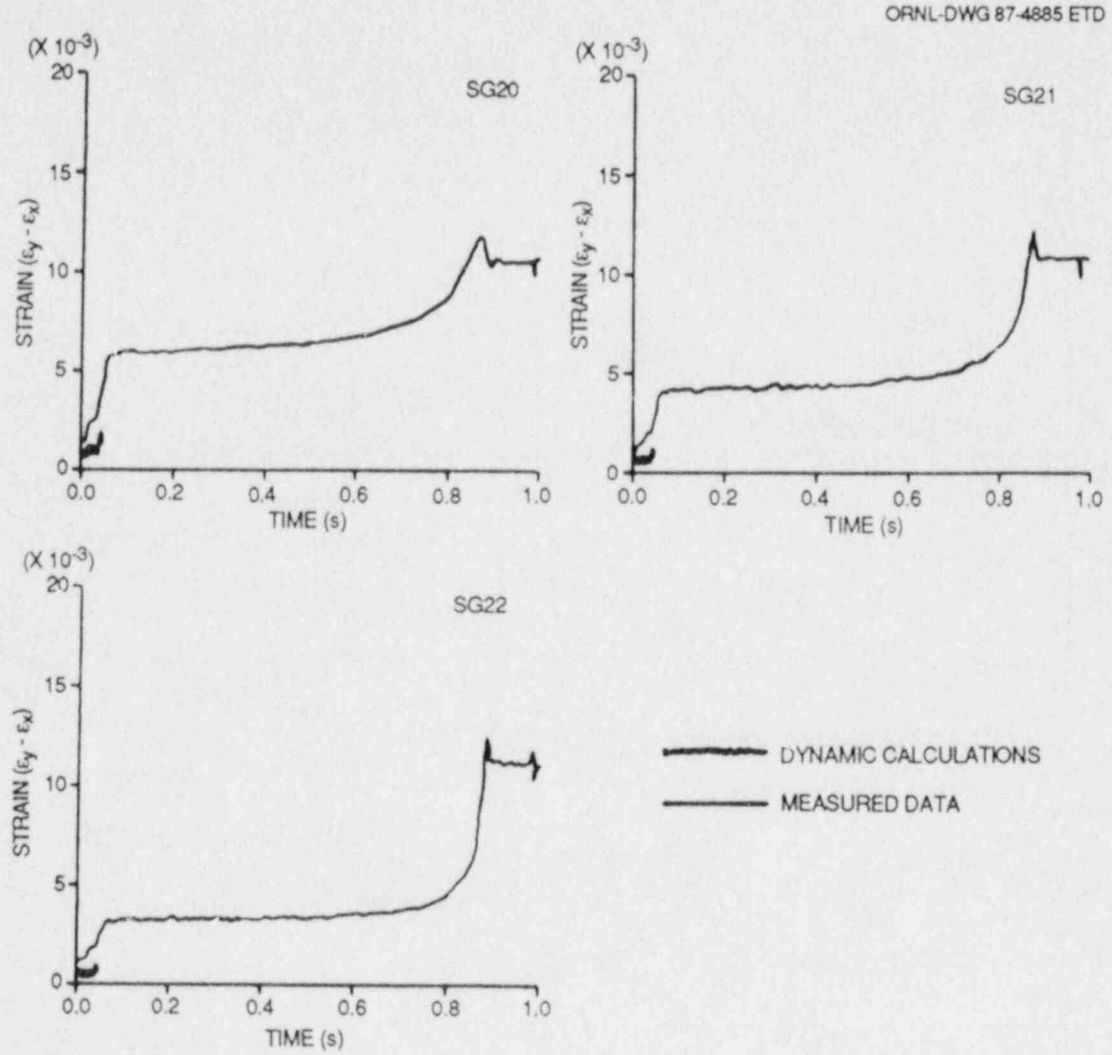

Fig. 5.44. Actual and computed strain histories for back-face crack-line gages 20–22: Test WP-2.3.

Table 5.5. Summary of computed results for test WP-2.3

Event	Time (ms)	A (m)	K[a] (MPa•√m)
Initiation	0	0.200	132.0[b]
Front-face gages			
Arrest A	0.222	0.275	140.9
Reinitiation	12.489	0.275	201.5
Arrest C	12.749	0.345	183.7
Reinitiation	37.344	0.345	259.3
Arrest E	37.524	0.400	230.8
Reinitiation	43.324	0.400	268.4
Back-face gages			
Arrest A	0.212	0.340	144.3
Reinitiation	3.160	0.340	241.0
Arrest B	3.322	0.375	232.2
Reinitiation	13.004	0.375	277.1
Arrest D	13.074	0.397	255.0
Reinitiation	38.464	0.397	294.3
Arrest F	38.584	0.457	257.9
Reinitiation	44.304	0.457	303.3

[a]Generation-mode, fixed-load dynamic analysis.

[b]From ADINA static analysis.

the plate are compared with measured data from the COD gages in Fig. 5.45. The COD values calculated are reasonably consistent with the measured values up to an elapsed time of ~10 ms into the fracture event. At elapsed times >10 ms, the calculated and measured COD values diverge, but the overall trend between them is consistent.

5.4.1.3 Test WP-1.7. The test results for test WP-1.7 were still being analyzed at the time this report was prepared. Thus, test WP-1.7 results will be presented in the next semiannual progress report.

5.4.1.4 Test WP-CE-1. Because data from test WP-CE-1 still were being reduced at the time this report was being prepared, the analysis results will not be available until the next report period.

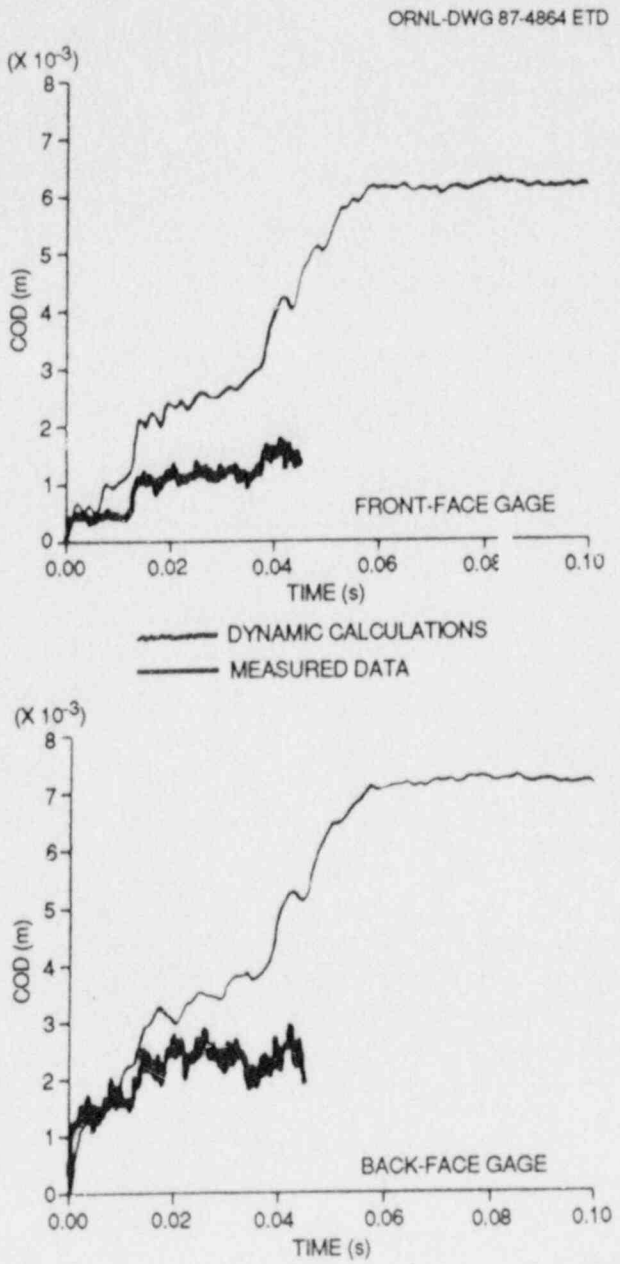

Fig. 5.45. Actual and computed CODs at a/w = 0.15 for front- and back-face gage locations: Test WP-2.3.

5.4.2 Crack-arrest toughness determinations for wide-plate tests

Tables 5.6 and 5.7 present a summary of the general conditions for tests WP-2.5 and WP-2.3, respectively. (Results for previous tests in the WP-1 and WP-2 test series were presented in the previous semiannual progress report.[2]) Posttest analyses have been carried out for each of these tests using both static and dynamic fracture analysis codes, as well as by application of handbook techniques. Some of these values[12] are presented in Table 5.8 for specimen WP-2.5 and Table 5.9 for specimen WP-2.3. As noted in the previous semiannual progress report,[2] values computed from the alternate static formula[13,14]

$$K_I = \sigma \left\{ \pi a \sec\left(\frac{\pi a}{2w}\right) \right\}^{1/2} \tag{5.9}$$

represent approximate lower bounds to the results and are presented only for completeness of test results. The most meaningful K_{Ia} values for the WP-2 series tests will reflect the considerable load adjustment that takes place during one of these tests as a result of specimen/pull-plate compliance. The dynamic generation-mode (fixed-load point) analysis results represent one type of such calculation. Figure 5.46 presents

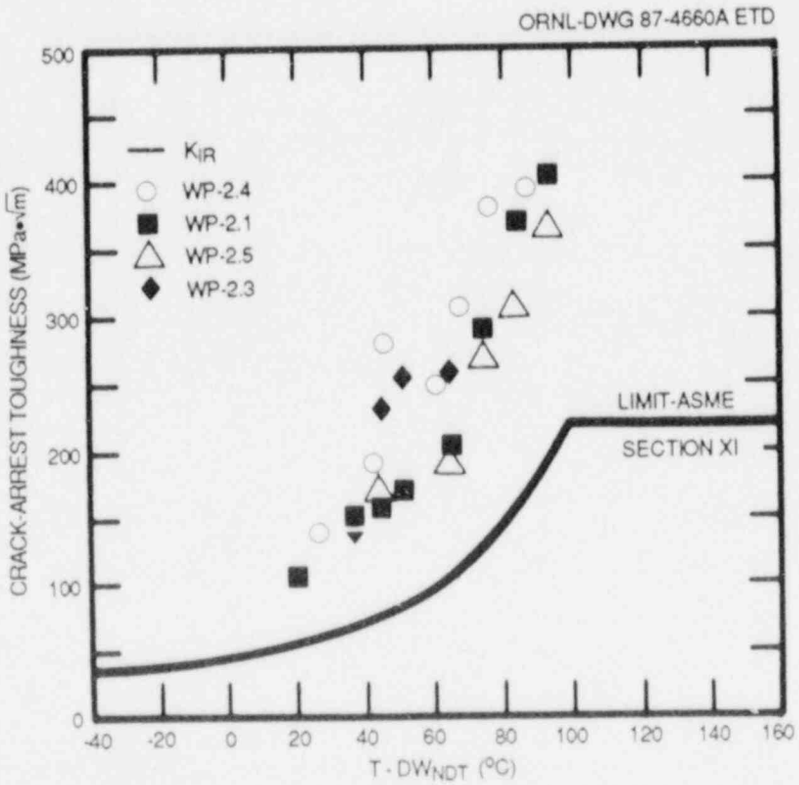

Fig. 5.46. Fixed-load, generation-mode dynamic finite-element determinations of crack-arrest toughness values for test specimens WP-2.4, -2.1, -2.5, and WP-2.3 (back-face results).

Table 5.6. Summary of HSST wide-plate crack-arrest test conditions for 2 1/4 Cr-1 Mo steel: WP-2 Series, specimen WP-2.5

Test No.	Crack location (cm)	Crack temperature (°C)	Initiation load (MN)	Arrest location[a] (cm)	Arrest temperature (°C)	Arrest $T - DW_{NDT}$ (°C)
WP-2.5A[b]	19.9	66.0	7.53	27.2	85.6	25.6
WP-2.5B	27.2[c]	85.6	8.90	35.0	104.0	44.0
WP-2.5C	35.0	104.0	8.90	43.5	124.4	64.4
WP-2.5D	43.5	124.4	8.90	47.8	134.7	74.7
WP-2.5E	47.8	134.7	8.90	51.6	143.7	83.7
WP-2.5F	51.6	143.7	8.90	56.0	153.8	93.8

[a]Arrest location is average of plate quarter-thickness crack length and crack length at the side groove of the back face of the plate.

[b]Crack front cut to chevron configuration.

[c]After pop-in.

Table 5.7. Summary of HSST wide-plate crack-arrest test conditions for 2 1/4 Cr-1 Mo steel: WP-2 Series, specimen WP-2.3

Test No.	Crack location (cm)	Crack temperature (°C)	Initiation load (MN)	Arrest location (cm)	Arrest temperature (°C)	Arrest $T - DW_{NDT}$ (°C)
			Front-face results			
WP-2.3A	0.200	66.0	15.3	0.275	82.5	22.5
WP-2.3C	0.275	82.5	15.3	0.345	98.6	38.6
WP-2.3E	0.345	98.6	15.3	0.400	111.5	51.5
			Back-face results			
WP-2.3A	0.200	66.0	15.3	0.340	97.4	37.4
WP-2.3B	0.340	97.4	15.3	0.375	105.6	45.6
WP-2.3D	0.375	105.6	15.3	0.397	110.8	50.8
WP-2.3F	0.397	110.8	15.3	0.457	125.5	65.5

Table 5.8. Computed crack-arrest toughness values for HSST wide-plate test WP-2.5 of 2 1/4 Cr-1 Mo steel: WP-2 Series

Test No.	Crack-arrest toughness values ($MPa\cdot\sqrt{m}$)			
	Static SEN formulas		Alternate static formula[c]	Dynamic FE
	Displacement control[a]	Load control[b]		Generation mode[d]
WP-2.5A[e]	108	123	83	
WP-2.5B	165	196	114	171
WP-2.5C	184	273	134	190
WP-2.5D	193	326	144	268
WP-2.5E	200	382	155	306
WP-2.5F	209	464	167	366

[a] From Ref. 12 (pp. 2.10–2.11) while assuming $a = a_f$ and no further bending occurs because of crack propagation.

[b] From Ref. 12 (pp. 2.10–2.11) while assuming $a = a_f$ and full bending according to SEN formula when the final crack depth is used.

[c] $K_I = \sigma \left\{ \pi a \sec \left(\frac{\pi a}{2w} \right) \right\}^{1/2}$, with σ = far-field tensile stress, $a = a_f$ = final crack length, and w = full-plate width.

[d] Fixed-load condition.

[e] Pop-in event.

Table 5.9. Computed crack-arrest toughness values for HSST wide-plate test WP-2.3 of 2 1/4 Cr-1 Mo steel: WP-2 Series

Test No.	Crack-arrest toughness values ($MPa\cdot\sqrt{m}$)			
	Static SEN formulas		Alternate static formula[c]	Dynamic FE
	Displacement control[a]	Load control[b]		Generation mode[d]
Front-face results				
WP-2.3A	147	169	113	141
WP-2.3C	165	221	130	184
WP-2.3E	178	274	144	231
Back-face results				
WP-2.3A	164	217	129	144
WP-2.3B	172	249	138	232
WP-2.3D	177	271	144	255
WP-2.3F	190	344	160	258

[a] From Ref. 12 (pp. 2.10–2.11) while assuming $a = a_f$ and no further bending occurs because of crack propagation.

[b] From Ref. 12 (pp. 2.10–2.11) while assuming $a = a_f$ and full bending according to SEN formula when the final crack depth is used.

[c] $K_I = \sigma \left\{ \pi a \sec \left(\frac{\pi a}{2w} \right) \right\}^{1/2}$, with σ = far-field tensile stress, $a = a_f$ = final crack length, and w = full-plate width.

[d] Fixed-load condition.

fixed-load, generation-mode, dynamic finite-element determinations of K_{Ia} for the WP-2 series tests conducted to date.

5.4.3 Comparison of wide-plate crack-arrest toughness data with other large-scale test results

Results presented in Fig. 5.46 show that the WP-2 series K_{Ia} test results exhibit an increase in arrest-toughness values with increasing temperature. The trend for K_{Ia} values to extend consistently above the limit provided in ASME Sect. XI is further substantiated in Fig. 5.47, which presents data from several large-scale tests plus the WP-2 series test results.[15-19]

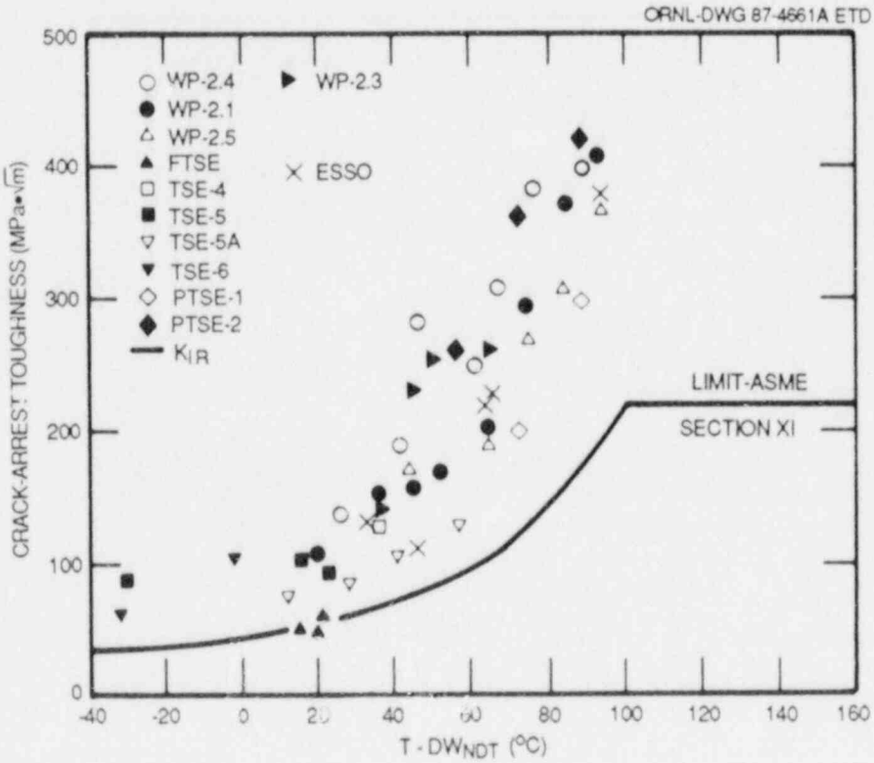

Fig. 5.47. Relationship of fixed-load, generation-mode dynamic finite-element determinations of crack-arrest toughness values for WP-2 series tests to selected large-specimen test results. (Note: PTSE-2 data points are preliminary and subject to change as posttest analyses become more complete.)

5.5 ASTM Round-Robin on K_{Ia} Testing (UM)*

D. B. Barker† W. L. Fourney†
R. Chona† G. R. Irwin†

ORNL review of the report entitled *A Report on the Round Robin Program Conducted to Evaluate the Proposed ASTM Standard Test Method for Determining the Plain Strain Crack Arrest Fracture Toughness K_{Ic} of Ferritic Materials* has been completed. It is anticipated that the report will be published during the next reporting period.

The proposed ASTM Standard, which resulted in large part from the round robin, has successfully passed subcommittee and main committee balloting. It will appear in the October issue of *Standardization News* to be balloted by the Society. It is anticipated that the Standard, known as E1221, will be in effect by the end of October 1987.

5.6 Battelle-Columbus HSST Support Program‡

A. R. Rosenfield** P. N. Mincer**
H. J. Cialone**

5.6.1 Crack-arrest test procedures for nodular cast iron

A small block (41 × 43 × 432 mm) of Type GGG-40 (German designation with no current U.S. equivalent standard) nodular cast iron from a cask designated CASTOR V/21 No. 500 11-002 was supplied to Battelle by Fracture Corporation investigators, who have also characterized the material.[20] Approximately half of the block was used for the initial development of crack-arrest test procedures. The other half will be used to fabricate a second series of specimens using procedures discussed below, which will be further modified on the basis of experience.

The Battelle block is designated I-7 and was cut from the bottom of the cask.†† Reference 20 contains data for nearby blocks I-5 and -6. The

---

*Work sponsored by the HSST Program under Subcontract No. 7778 between Martin Marietta Energy Systems, Inc., and the University of Maryland.

†Department of Mechanical Engineering, University of Maryland, College Park.

‡Work sponsored by the HSST Program under Subcontract No. 85X-17624C between Martin Marietta Energy Systems, Inc., and Battelle-Columbus Laboratories.

**Battelle-Columbus Laboratories, 505 King Avenue, Columbus, Ohio.

††According to Ref. 20, this location corresponds to the top of the casting. Discussion with Siempelkamp foundry personnel and the metallographic evidence of Fig. 11c in Ref. 20 indicate that Block I-7 came from the bottom of the casting.

chemical composition is fairly insensitive to location within the cask, and averages for the nearby blocks, in weight percent, are C = 3.13, Si = 2.08, Mn = 0.15, P = 0.029, S = 0.001, Mg = 0.054, Cr = 0.01, Ni = 0.56, Cu = 0.02, and Mo = 0.01. Figure 5.48 is an optical micrograph taken at Battelle from Block I-7 that was used to fabricate the crack-arrest specimens. According to Ref. 20, the average microstructural dimensions of the neighboring blocks are ferrite grain size = 65 μm, graphite = 9.9 vol %, and nodule size = 40 μm. The appearance of the microstructure in Fig. 5.48 suggests that these values are also appropriate for the crack-arrest specimens.

The nodular-iron data reported in Ref. 20 has very low Charpy-impact energies, with an upper-shelf energy of 16.5 J (12.2 ft-lb) being attained at about 18°C. An estimated fracture appearance transition temperature (FATT) of −28°C is based on the temperature at which the impact energy is half of its upper-shelf value. Based on these data, it was decided that a temperature range from −40°C to +25°C would be an acceptable range for crack-arrest experiments to characterize ductile/brittle transition behavior.

Because the nodular iron has a very low yield strength (248 MPa = 36 ksi), duplex specimens[21] are required to initiate fast-moving cracks with minimal notch-tip plasticity. This specimen consists of a block of SAE 4340 steel EB welded to the material being investigated. While this procedure is fairly routine for testing of reactor-pressure-vessel (RPV) steels, a concern arose that a brittle layer of white iron might form in either the fusion zone or in the nodular-iron heat-affected zone. Transverse fracture in the weld region of the first specimen tested, before

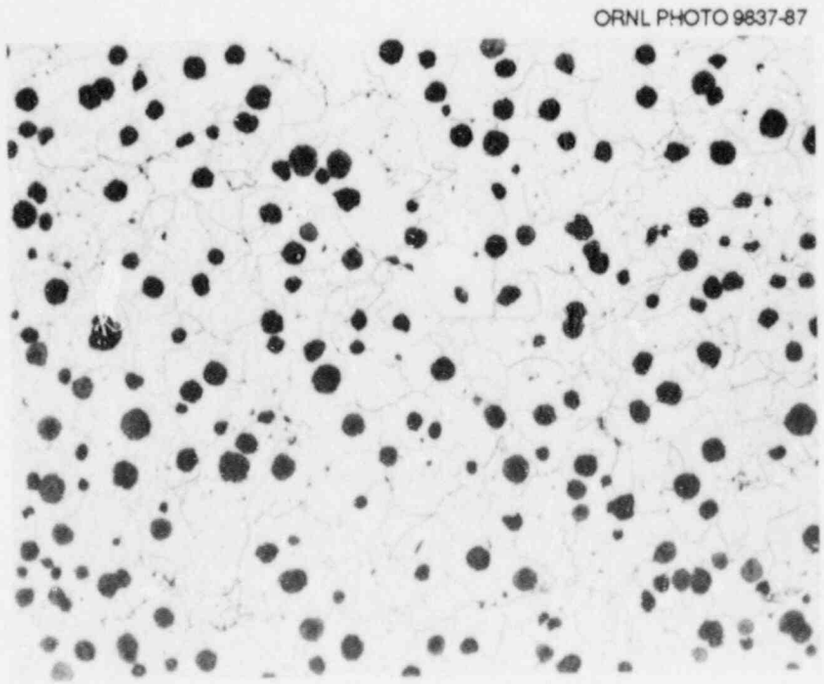

Fig. 5.48. Photomicrograph of nodular-iron slab I-7, 100×.

crack initiation at the starter notch, apparently confirmed this concern, although subsequent evaluations showed that the transverse fracture was not related to the formation of white iron, and thus should not be an intractable problem.

Micrographic examination of a specimen that broke prematurely in the weld region, shown in Fig. 5.49, revealed that the fracture occurred in the weld zone, a material that contained large martensite needles. This microstructure is believed to form as the result of intermingling between the SAE 4340 steel and the nodular iron and should be rendered less brittle by proper heat treatment. In fact, the weld cracking problem was considerably alleviated by a postweld heat treatment at 400°C for 1 h, conditions limited by the need to retain sufficient hardness in the SAE 4340 steel. All but one of the specimens that were postweld heat treated underwent rapid crack initiation at the starter notch, with limited transverse weld fracture.

Table 5.10 summarizes the results of this test development effort. Seven crack-arrest values were obtained, with a typical fracture surface being shown in Fig. 5.50. In addition to the specimens yielding crack-arrest toughnesses, several specimens were tested at too high a temperature (>0°C), and the crack did not penetrate the test section. Others, tested at low temperatures (<−25°C), broke completely in two. Thus, the transition region was only partially characterized.

Table 5.10 also indicates that it was necessary to increase the depth of the side grooves to 60% to inhibit crack deflection at the weld line. This depth was chosen because it had been used successfully in early crack-arrest experiments at Battelle.[22] Additional evidence supporting the use of deep side grooves has been obtained for several plain

ORNL PHOTO 9838-87

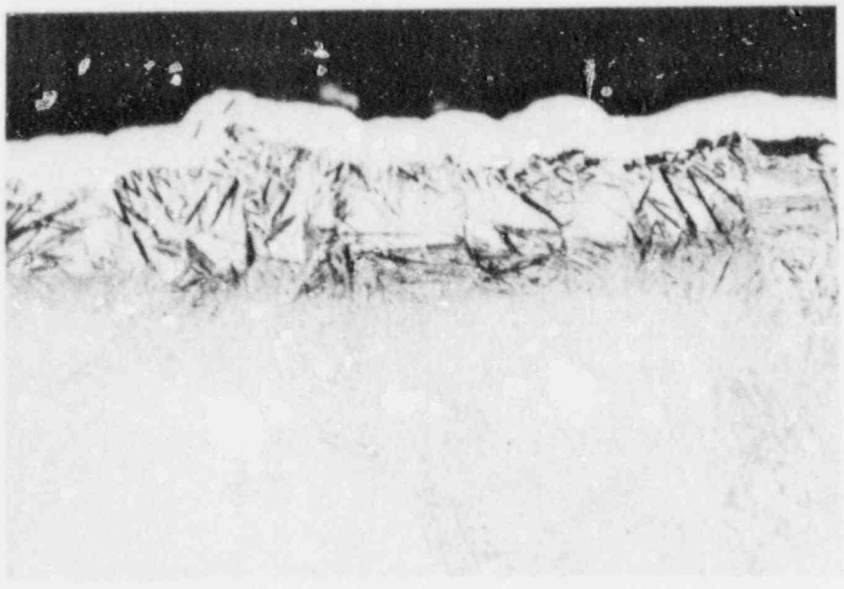

Fig. 5.49. Photomicrograph of fusion zone of weld that split prematurely; SAE 4340 half of the fracture, 500×.

Table 5.10. Results of crack-arrest trials on nodular iron

Specimen No.	Test temperature (°C)	K_a (MPa•$\sqrt{m}$)
I-7-1	24	[c]
-2[a,b]	25	[d]
-3[b]	−39	[c]
-4[a,b]	−36	[e]
-5[b]	−29	[d]
-6[a,b]	−28	[e]
-7[a,b]	0	[c]
-8[a,b]	−13	121
-9[a,b]	11	[f]
-10[a,b]	−29	63
-11[a,b]	0	96
-12[a,b]	26	[f]
-13[a,b]	0	101
-14[a,b]	−29	60
-15[a,b]	−22	67
-16[a,b]	−12	99

[a] Postweld heat treated.

[b] 60% side grooved.

[c] Split along weld, no crack initiation.

[d] Slight crack penetration into test section.

[e] Complete fracture.

[f] Arrested at weld line.

carbon steels by Mejias and Vedia,[23] who have shown that K_{Ia} is independent of side-groove depth between 25 and 75% depth. Their result confirms Battelle work on SAE 4340 steel[24] and lends confidence to the use of deep side grooves for the nodular-iron experiments.

The range of K_a values in Table 5.10 is considered tentative because they indicate violations of the size requirements of the proposed ASTM Test Procedure and are likely to be higher than linear-elastic plane-strain values. It is estimated that K_a values on the order of 60 MPa•$\sqrt{m}$ would be valid according to the proposed standard. Problems in meeting specimen size requirements have been reported for determining static fracture toughness of nodular iron, as described in the trip reports by Cialone. The highest values determined here are also much higher than the dynamic initiation data of Ref. 22.

ORNL PHOTO 9839-87

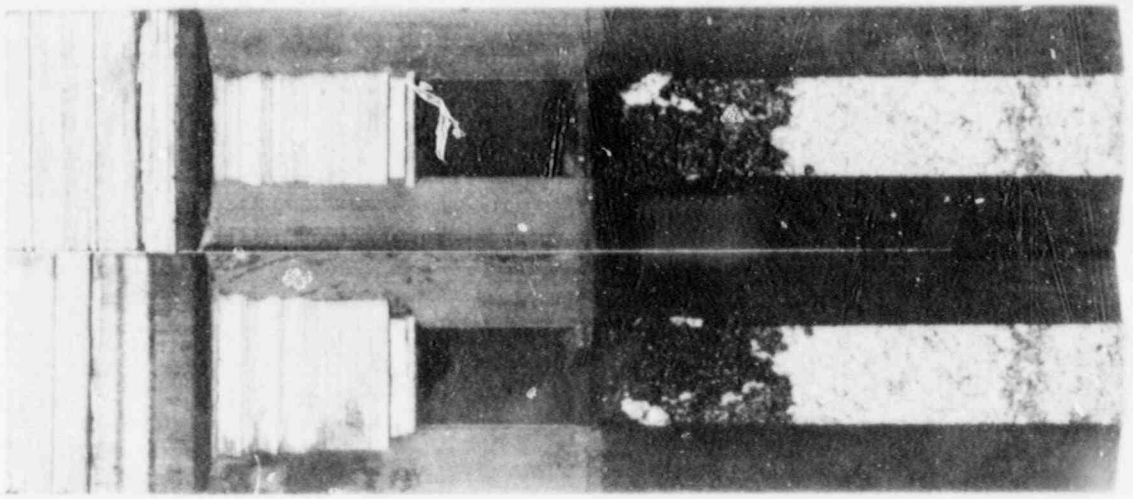

Fig. 5.50. Specimen I-7-8 that experienced a successful run-arrest event, 2×.

In addition to not meeting the size requirements, the reported values do not account for the differing elastic moduli of duplex specimens made from alloys whose elastic moduli differ by 20%, as is the case for this series of experiments. However, this latter effect is believed to be small.

Figure 5.51 is a plot of the results. To provide a context, these results have been compared to characteristic values for RPV steels. Because of the small Charpy upper-shelf energies of the nodular iron, the only possible estimate of the ductile/brittle transition temperature is the FATT (estimated as the temperature at which the impact energy is half of the upper-shelf value). While the graph suggests that the crack-arrest data are roughly comparable to typical RPV data, the uncertainties previously discussed, plus the need for a significantly larger data base, preclude drawing any conclusions at the present time.

5.6.2 Crack-arrest data bank

During the current reporting period, 147 new crack-arrest data were added, bringing the total to 1017, not including summary tables of the ASTM Coooperative Test Program and [illegible] Robin. As was the case for the February 1987 Addendum, the new data were all foreign (German and Italian). One of the German steels was close to A 508 but was heat treated to produce a Charpy upper-shelf energy of only 45 J (33 ft-lb). The K_{Ia} values for this steel were unusually weakly dependent on temperature, with the result that the high-temperature data fell below the ASME K_{IR} curve. The reasons for this behavior are not clear from the publication. The Italian data are consistent with typical behavior of RPV steels and lend support to use of their electric-resistance method of hardening the starter notch tip.

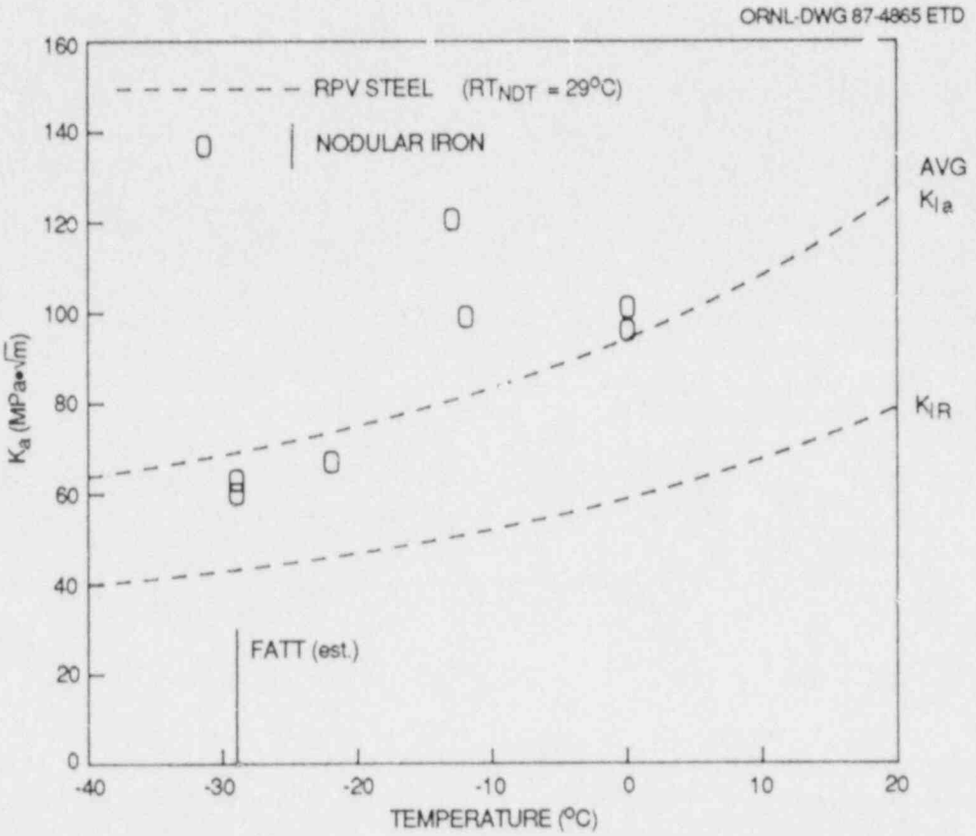

Fig. 5.51. Preliminary nodular-iron crack-arrest data.

5.7 Dynamic Fracture Propagation Relations Inferred from WP-1 Test Series*

C. W. Schwartz†

Accurate prediction of fracture propagation and arrest for many problems requires specification of the relationship among instantaneous crack-tip velocity ($\dot{a}$), dynamic stress-intensity factor (K_{ID}), and temperature (T) for the fracturing material. This relationship, which is often unknown or poorly defined for many materials, is a primary input for predictive "application-mode" dynamic fracture finite-element codes. The recently completed WP-1 series of large-scale wide-plate crack-arrest tests has generated sufficient data to estimate the $\dot{a}$ vs K_I vs T relation for A 533 grade B class 1 nuclear pressure vessel steel.

---

*Work sponsored by the HSST Program under Subcontract No. 7778 between Martin Marietta Energy Systems, Inc., and the University of Maryland.

†Department of Civil Engineering, University of Maryland, College Park.

5.7.1 Methodology for determining dynamic fracture relation

The methodology followed in estimating the $\dot{a}$ vs K_I vs T relation from the test results is summarized as follows:

1. Smooth crack-tip position vs time curves are fit (through nonlinear regression techniques) to the discrete crack history data points measured in the tests.

2. "Generation-mode" dynamic finite-element analyses[25] are performed to determine the K_I vs time history and the dynamic arrest toughness (K_{Ia}) for each test. An elastodynamic formulation was employed for all analyses, because only the first millisecond of response was considered and previous analyses[26] have shown that viscoplastic yielding is negligible during this interval. Thermal bowing of the specimen caused by the applied thermal gradient is considered in the analyses.

3. The K_{Ia} values computed in the WP-1 generation-mode analyses, together with other large-scale crack-arrest data, are used to develop a revised relation between arrest toughness and temperature.

4. A simple form is assumed for the $\dot{a}$ vs K_I vs T relation for the material:

$$\dot{a} = c_0 + c_1 \times (K_I/K_{Ia}) \quad K_I/K_{Ia} > 1 \ , \tag{5.10}$$

in which the coefficients c_0 and c_1 are temperature dependent. [Note that the K_{Ia} relation determined in step 3 is used to normalize Eq. (5.10)]. A two-stage regression analysis is performed to determine these coefficients:

(a) Crack-tip velocity vs K_I data points are extracted from the generation-mode analysis results at various selected temperatures. Data at constant temperature values are fit with linear relations of the form of Eq. (5.9); a different set of c_0 and c_1 coefficients are determined for each temperature.

(b) The sets of coefficients determined in step 4a are regressed against temperature.

Note that the $\dot{a}$ vs K_I relation could be derived from a single test if there were no temperature dependence of the fracture properties. Data from several tests are required to include the effects of temperature.

5. Application-mode dynamic finite-element analyses[25] are performed as an initial check of the validity of the derived $\dot{a}$ vs K_I vs T relation. This predicted response is compared with the experimental data.

The results presented in this paper are a refined and modified version of preliminary findings presented earlier by Schwartz.[27]

5.7.2 Results of application to WP-1 data

Only data from tests WP-1.2, -1.3, -1.5, and -1.6 were considered in this study. Test WP-1.1 suffered an instrumentation malfunction, and test WP-1.4 is difficult to interpret because of a pillow jack inserted in the notch to promote fracture initiation.

Figures 5.52 and 5.53 illustrate the crack position vs time data obtained from the crack-line strain gages for tests WP-1.2 and -1.6. Data for the other tests are similar. Also shown in the figures are the computed regression curves for the crack position histories. Cubic polynomials were found to provide an excellent fit to the data; R^2 values exceeded 0.98 in all cases.

Determination of the initiation time from the instrumentation records involves considerable subjective interpretation. For tests WP-1.5 and -1.6, an initiation time correction procedure was developed from the regression analyses. A polynomial curve is first fit to the raw strain-gage data points without constraining the curve to pass through the initial crack-tip location at time zero. The curve is extrapolated to the initial crack-tip location, and the corresponding time (usually negative) is computed. This computed time is taken as the corrected initiation time, and all strain-gage data points are adjusted accordingly. A new corrected polynomial curve is then fit to the adjusted crack position vs time data. The computed time corrections were 32 and 70 μs for tests WP-1.5 and -1.6, respectively. The initiation time correction procedure was not applied to tests WP-1.2 and -1.3 because of the limited number of experimental data points.

The polynomial relations for crack position history are used as input to the generation-mode dynamic-fracture analyses. The generation-mode analysis results at arrest, including the computed dynamic arrest toughness K_{Ia}, are summarized in Table 5.11.

Figure 5.54 shows the relationship between K_{Ia} and temperature, normalized as $T - RT_{NDT}$, computed for the WP-1 tests. Also plotted on the figure are data from other large-scale crack-arrest tests.[28] A revised nonlinear regression relationship between K_{Ia} and temperature is given by

$$K_{Ia} = 69.56 + 5.111*e^{[0.04658(T-RT_{NDT})]} \qquad (5.11)$$

in which K_{Ia} is in units of MN-m$^{3/2}$ and $(T - RT_{NDT})$ is in units of degrees Celsius. The revised K_{Ia} relation exhibits a steeper rise in the high-temperature region as compared with the original ORNL relation.[29]

Contours of $(\dot{a}, K_I)$ data points at constant temperature computed from the generation-mode analyses are illustrated in Fig. 5.55. Each test provides one data point on each temperature contour. The data at each temperature contour are fit with linear equations; each temperature contour is defined by a different set of coefficients. The variation of these coefficients with temperature is shown in Fig. 5.56. Quadratic polynomial equations providing excellent fits to the data in Fig. 5.55 have the form

$$c_0 = 193 + 14.1*(T - RT_{NDT}) - 0.183*(T - RT_{NDT})^2 , \qquad (5.12)$$

$$c_1 = 168 - 5.62*(T - RT_{NDT}) + 0.0484*(T - RT_{NDT})^2 , \qquad (5.13)$$

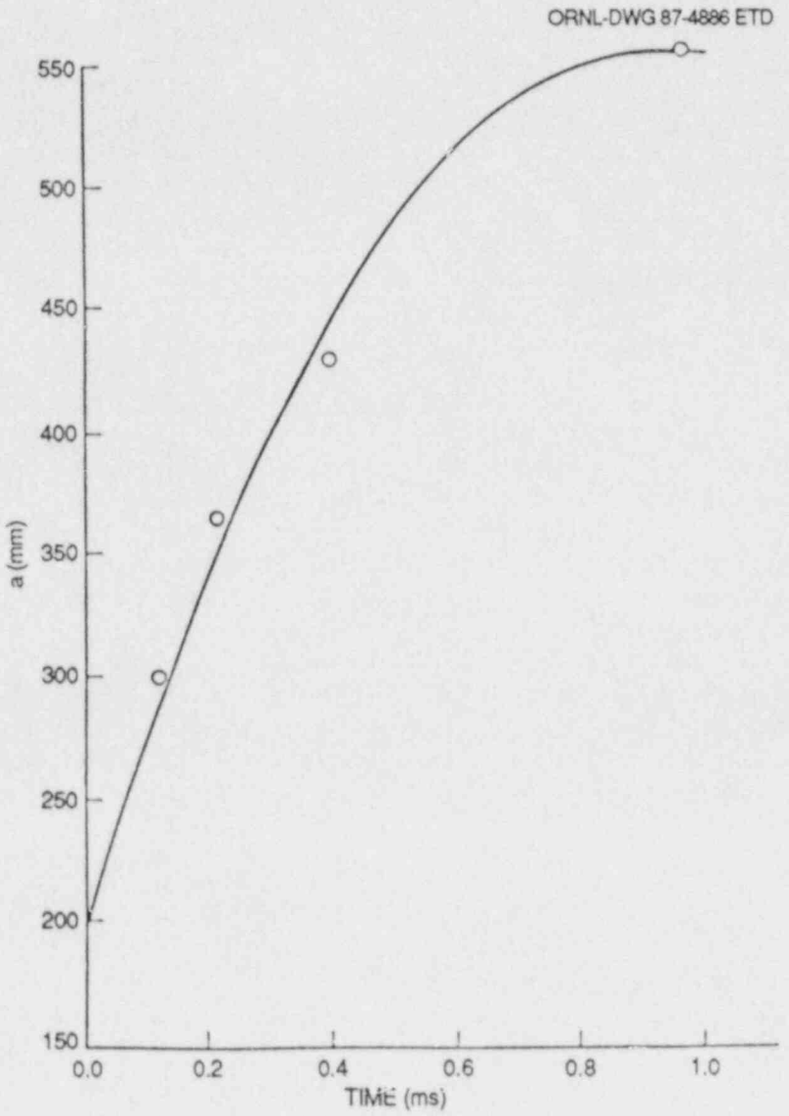

Fig. 5.52. Cubic polynomial fit of measured crack-tip position history for test WP-1.2.

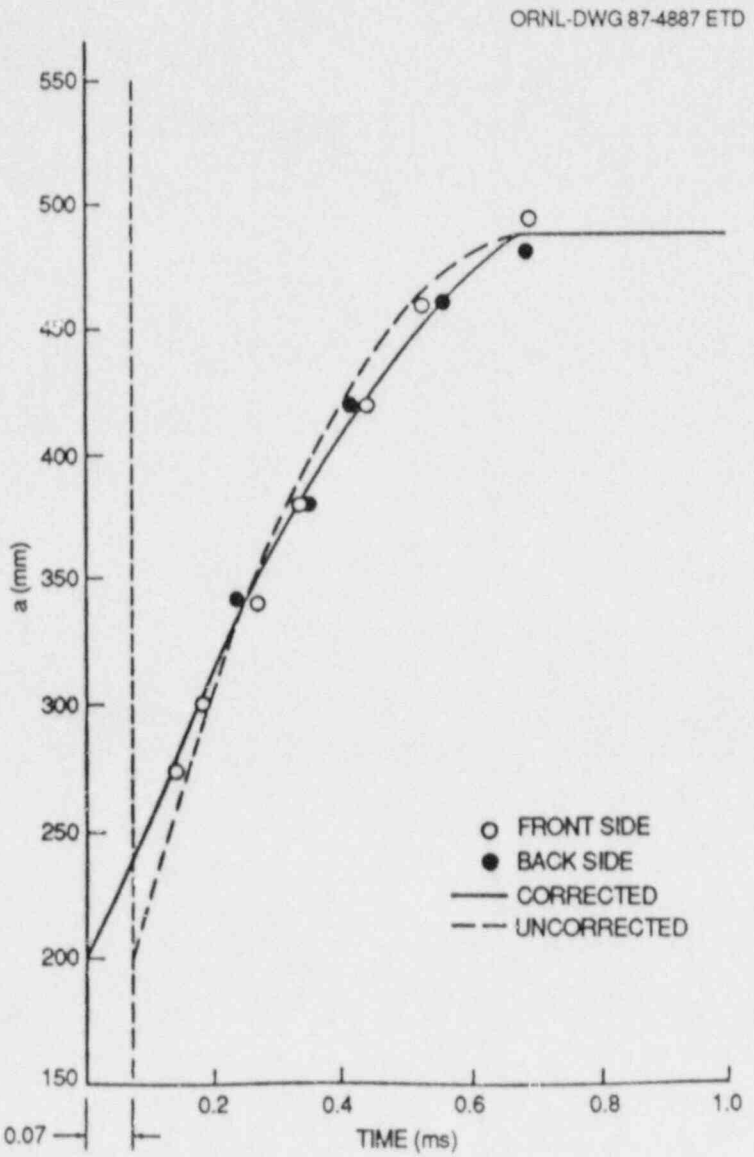

Fig. 5.53. Cubic polynomial fit of measured crack-tip position history for test WP-1.6.

Table 5.11. Summary of elastodynamic analysis results at arrest for four tests in the WP-1 series

	WP-1.2		WP-1.3		WP-1.5		WP-1.6	
	GEN[a]	APP[b]	GEN	APP	GEN	APP	GEN	APP
Arrest time, ms	0.907	0.700–0.783	0.680	0.559–0.596	0.762	0.610–0.656	0.701	0.633–0.652
Crack length at arrest, m	0.555	0.565–0.580	0.493	0.473–0.482	0.518	0.493–0.504	0.487	0.500–0.506
K_{Ia}, MN-m$^{3/2}$	457	381–441	252	214–231	233	209–226	305	278–291
$T - RT_{NDT}$, °C	85.6	88.8–93.6	79.5	72.3–75.5	77.7	71.1–74.0	76.9	80.0–81.4

[a]Generation-mode analysis.

[b]Application-mode analysis.

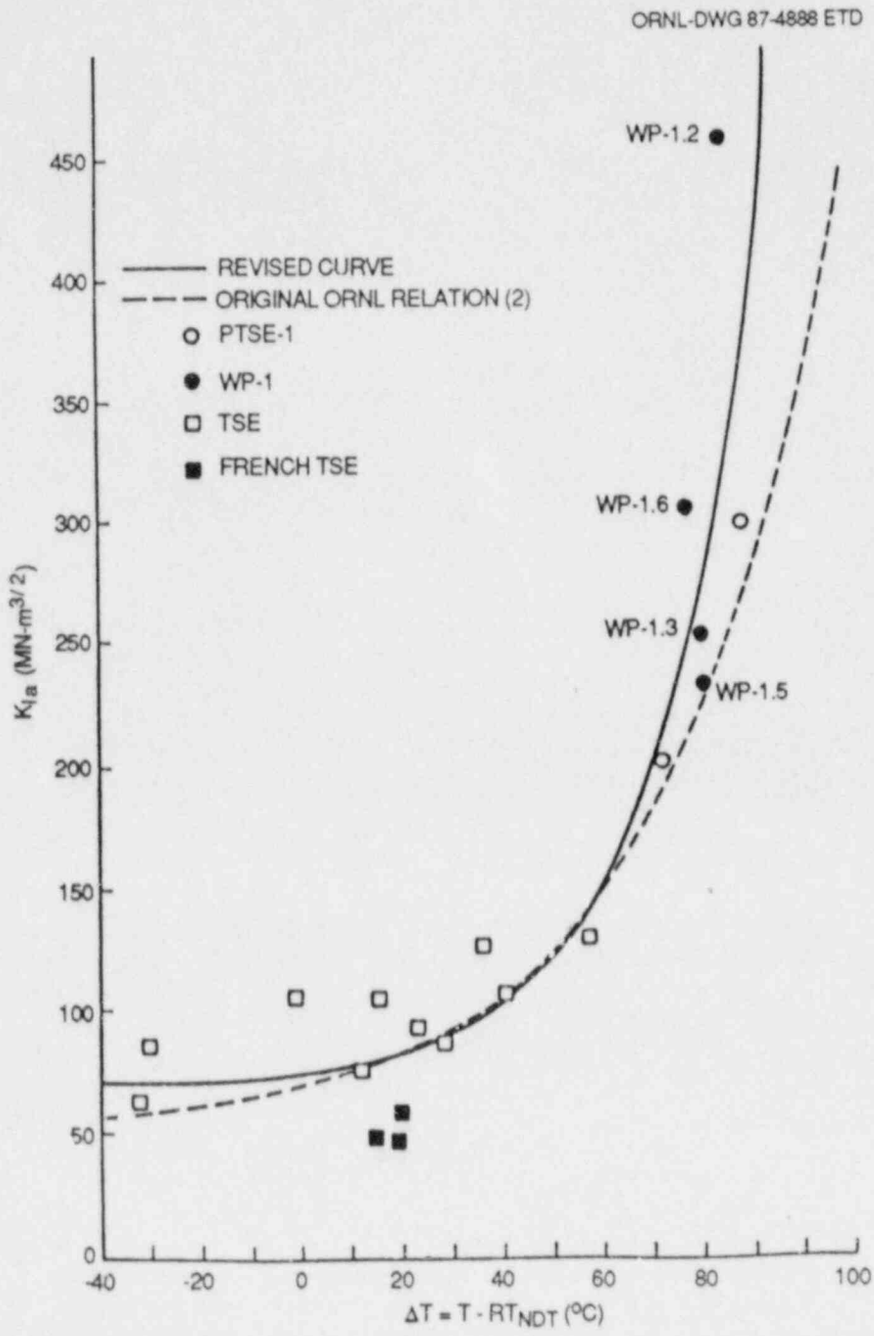

Fig. 5.54. Arrest toughness vs temperature for A 533 grade B class 1 steel.

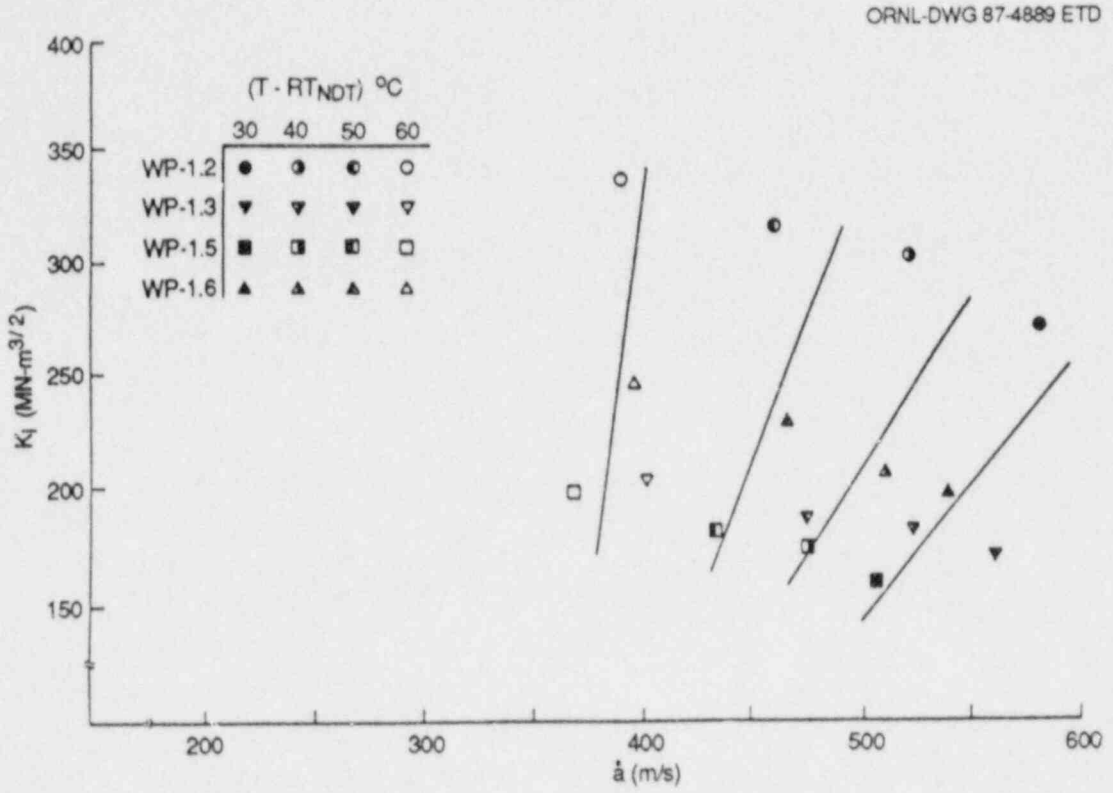

Fig. 5.55. Dynamic stress-intensity and crack-tip velocity relationships for various temperature contours.

in which c_0 and c_1 are in units of meters per second and $(T - RT_{NDT})$ is in units of degrees Celsius.

The final $\dot{a}$ vs K_I vs T relationship inferred for A 533 grade B class 1 steel from the four WP-1 tests is shown in Fig. 5.57. The relationship is based upon the general form given in Eq. (5.10), with terms as defined in Eqs. (5.11)--(5.13). The relationship is bilinear with a vertical stem at $K_I/K_{Ia} = 1$. Both the slope and the velocity cutoff for the upper portion of the relationship are temperature dependent. In an application-mode dynamic finite-element analysis, the computed instantaneous K_I and T values [and the associated K_{Ia} values from Eq. (5.11)] would be used with this relationship to determine the instantaneous crack-tip velocity for the next increment of crack advance.

Application-mode analyses, using the relationship in Fig. 5.57, were performed for tests WP-1.2, -1.3, -1.5, and -1.6. Table 5.11 compares the results from the application-mode analyses against those from the generation-mode computations. (Note that the experimentally measured arrest positions and times are by definition identical to the generation-mode analysis values.) The precise instant of arrest was somewhat difficult to identify using current application-mode analysis algorithms. In the analyses, the crack typically arrests and immediately (e.g., within 1

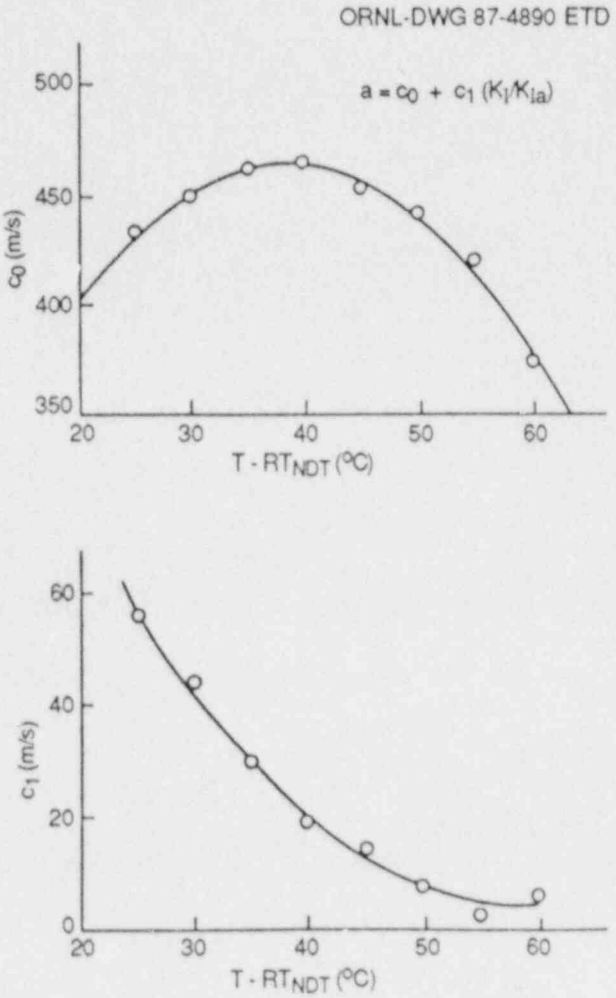

Fig. 5.56. Temperature dependence of crack speed regression coefficients for dynamic fracture-toughness relation.

or 2 μs) reinitiates several times before reaching a "final" arrest. Consequently, values for two arrest conditions are included in Table 5.11: the computed values at the initial instantaneous arrest and the computed values at the first arrest lasting 20 μs or longer. The first arrest lasting 20 μs or longer in the analyses is believed to be a good estimate for the actual experimental arrest condition. Additional crack growth computed in the application-mode analyses after the first 20 μs arrest typically occurs in isolated jumps spread out over long periods of time; the total additional crack growth due to these jumps is very small (<5% of the crack length).

As detailed in Table 5.11, the application-mode analyses consistently underestimate the time of arrest by up to 15% as compared with the experimental/generation-mode values. The application-mode predictions for final crack length are closer to the experimental/generation-mode

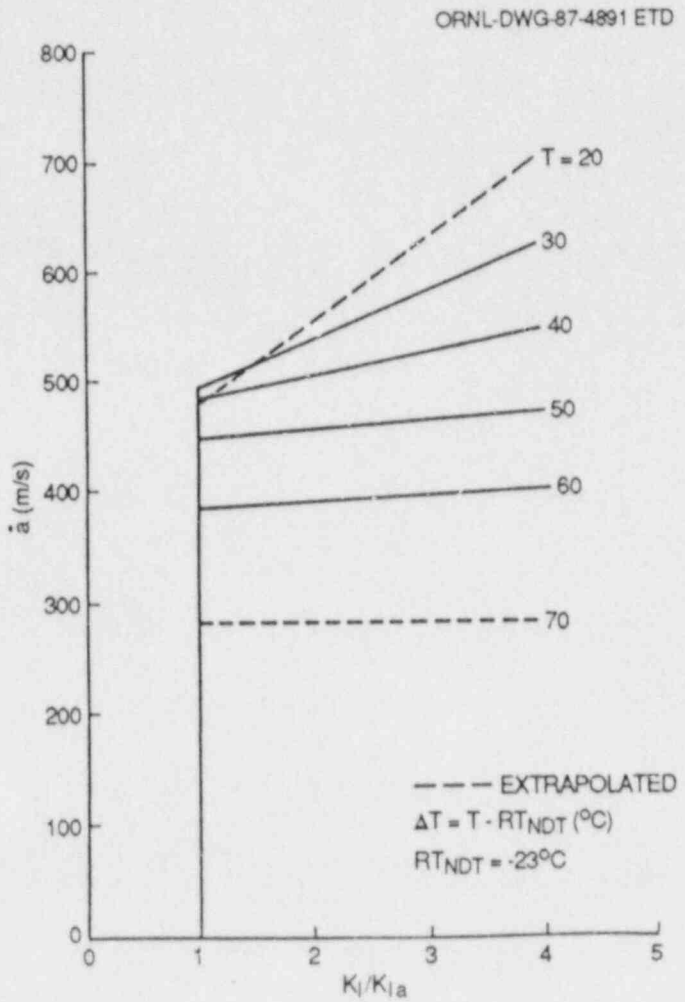

Fig. 5.57. Crack-tip velocity vs dynamic stress intensity vs temperature relation inferred for A 533 grade B class 1 steel.

values, with a mix of underestimation and overestimation and a maximum error of 5%. The computed dynamic stress intensity at arrest is underestimated by ~5% in the application-mode analyses as compared with the generation-mode results. These errors are judged acceptable. Previous application-mode analyses using hypothesized a vs K_I vs T relations predicted arrest times up to several times later and final crack lengths up to 30% longer than observed experimentally.[26,29]

5.7.3 Conclusions

A methodology for inferring crack-tip speed vs dynamic stress intensity vs temperature relations from instrumented dynamic fracture tests has been developed and applied to data from four wide-plate experiments on A 533 grade B steel. Application-mode dynamic finite-element analyses

using the inferred relationship produce results that are acceptably close to experimental and generation-mode analytical results.

The preliminary validation of the proposed speed vs stress intensity vs temperature relationship must be expanded through comparisons with other specimen geometries. Further validation studies are planned using results from smaller scale instrumented tests currently under way at ORNL. Updates to the proposed relationship reflecting recent experimental results from the two 0.15-m-thick WP-1 tests are also in progress; changes are expected to be relatively small.

5.7.4 Acknowledgments

Computational resources for this study were provided in part by the San Diego Supercomputer Center, which is administered and operated by GA Technologies Inc. with major funding from the National Science Foundation.

References

1. C. E. Pugh, "Crack Arrest Technology," pp. 83--137 in *Heavy-Section Steel Technology Program Semiann. Prog. Rep. April–September 1984*, NUREG/CR-3744, Vol. 2 (ORNL/TM-9154/V2), Martin Marietta Energy Systems, Inc., Oak Ridge Natl. Lab., April 1985.

2. C. E. Pugh, *Heavy-Section Steel Technology Program Semiann. Prog. Rep. October 1986–March 1987*, NUREG/CR-4219, Vol. 4, No. 1 (ORNL/TM-9593/V4&N1), Martin Marietta Energy Systems, Inc., Oak Ridge Natl. Lab., August 1987.

3. D. J. Naus et al., *Summary of the Tenth Heavy-Section Steel Technology (HSST) Wide-Plate Crack-Arrest Test (WP-2.3)*, Attachment to letter, HSST Wide-Plate Crack Arrest Test WP-2.3, from W. R. Corwin, Oak Ridge National Laboratory, to M. Mayfield, Nuclear Regulatory Commission, dated August 11, 1987.

4. R. deWit and R. J. Fields, *Preliminary Results from the Eleventh Wide Plate Test: WP-1.7*, letter report from R. Fields, National Bureau of Standards, to D. J. Naus, Oak Ridge National Laboratory, dated August 20, 1987.

5. M. F. Kanninen et al., *Preliminary Analysis of Japanese Wide-Plate Dynamic Crack Propagation Arrest Experiments*, Subcontract report from Battelle Columbus Laboratories to Oak Ridge National Laboratory, December 1983.

6. D. J. Ayres et al., "Appendix G, Material Characterization," in *Tests and Analyses of Crack Arrest in Reactor Vessel Materials*, EPRI NP5121-SP, prepared by Combustion Engineering, Inc., Windson, Conn., for Electric Power Research Institute, Palo Alto, Calif., April 1987.

7. B. R. Bass and J. W. Bryson, *Applications of Energy Release Rate Technique to Part-Through Cracks in Plates and Cylinders, Volume 1, ORMGEN-3D: A Finite Element Mesh Generator for 3-Dimensional Crack Geometries*, NUREG/CR-2997, Vol. 1 (ORNL/TM-8527/V1), Union Carbide Corp. Nuclear Div., Oak Ridge Natl. Lab., December 1982.

8. B. R. Bass and J. W. Bryson, *Applications of Energy Release Rate Technique to Part-Through Cracks in Plates and Cylinders, Volume 2, ORVIRT: A Finite Element Program for Energy Release Rate Calculations for 2-D and 3-D Crack Models*, NUREG/CR-2997, Vol. 2 (ORNL/TM-8527/V2), Union Carbide Corp. Nuclear Div., Oak Ridge Natl. Lab, February 1983.

9. K. J. Bathe, *ADINA — A Finite Element Program for Automatic Dynamic Incremental Nonlinear Analyses*, Report A-1, Massachusetts Institute of Technology, Cambridge, Mass., 1984.

10. B. R. Bass, C. E. Pugh, and H. K. Stamm, "Dynamic Analyses of a Crack Run-Arrest Experiment in a Nonisothermal Plate," *Pressure Vessel Components Design and Analysis*, ASME Publication PVP, 98-2, 175–84, 1985.

11. B. R. Bass and J. Keeney-Walker, "Computer Program Development for Dynamic Fracture Analysis," pp. 5–12 in *Heavy-Section Steel Technology Program Semiann. Prog. Rep. April–September 1985*, NUREG/CR-4219, Vol. 2 (ORNL/TM-9593/V2), Martin Marietta Energy Systems, Inc., Oak Ridge Natl. Lab., January 1986.

12. R. Tada, P. C. Paris, and G. R. Irwin, *The Stress Analysis of Cracks Handbook*, Del Research Corp., Hellertown, Pa., 1973.

13. C. F. Fedderson, *Current Status of Plain Strain Crack Toughness Testing of High-Strength Metallic Materials*, Crack Arrest Methodology and Applications, ASTM STP-410, American Society for Testing and Materials, Philadelphia, Pa., 1967.

14. G. R. Irwin, University of Marvland, private communication to C. E. Pugh, Oak Ridge National Laboratory, "Notes on Testing Arrangements for Crack-Arrest Tests Using an SEN Specimen and a Temperature Gradient," October 1983.

15. R. D. Cheverton et al., "Fracture Mechanics Data Deduced from Thermal-Shock and Related Experiments with LWR Pressure Vessel Material," *J. Pressure Vessel Technol.* 105, 102–10 (May 1983).

16. R. H. Bryan et al., *Pressurized-Thermal-Shock Test of 6-in.-Thick Pressure Vessels. PTSE-1: Investigation of Warm Prestressing and Upper-Shelf Arrest*, NUREG/CR-4106 (ORNL-6135), Martin Marietta Energy Systems, Inc., Oak Ridge Natl. Lab., April 1985.

17. Japan Welding Council, *Structural Integrity of Very Thick Steel Plate for Nuclear Reactor Pressure Vessels*, JWES-AE-7806, Tokyo, 1977 (in Japanese).

18. A. Pellissier-Tanon, P. Sollogoub, and B. Houssin, "Crack Initiation and Arrest in an SA 508 Class-3 Cylinder Under Liquid Nitrogen Thermal-Shock Experiment," *Transactions of the 7th International Conference on Structural Mechanics in Reactor Technology, Chicago*, Vols. G and H, 132–42 (August 1983).

19. R. H. Bryan et al., *Quick-Look Report on the Second HSST Pressurized-Thermal-Shock Test, PTSE-2*, ORNL/PTSE-2, Martin Marietta Energy Systems, Inc., Oak Ridge Natl. Lab., Feb. 19, 1987.

20. P. McConnell and W. Sheckherd, *Fracture Toughness Characterization of a Ductile Iron Spent Nuclear Fuel Cask*, Fracture Control Corp. Report on EPRI Research Project 2717-2, June 1986.

21. A. R. Rosenfield, P. N. Mincer, and C. N. Marschall, "High Temperature Crack-Arrest Toughness Measurements Using Compact Specimens," to appear in *Proc. 18th National Fracture Mechanics Symposium*, published as an ASTM STP.

22. R. G. Hoagland et al., *A Crack Arrest Measuring Procedure for K_{Im}, K_{ID}, and K_{Ia} Properties*, ASTM STP 627, pp. 177–202 (1977)

23. H. D. Mejias and L. A. de Vedia, "Influence of Side Grooving in Crack Arrest Toughness of C-Mn Steels," *Eng. Fract. Mech.* 26, 625–36 (1987).

24. G. T. Hahn et al., *Critical Experiments, Measurements and Analyses to Establish a Crack Arrest Methodology for Nuclear Pressure Vessel Steels*, Battelle Report to Nuclear Regulatory Commission No. BMI-1937, 1975.

25. C. W. Schwartz et al., *SAMCR: A Two-Dimensional Dynamic Finite Element Code for the Stress Analysis of Moving Cracks*, NUREG/CR-3891 (ORNL/Sub/79-7778/3) Martin Marietta Energy Systems, Inc., Oak Ridge Natl. Lab., November 1984.

26. B. R. Bass and J. Keeney-Walker, "Wide-Plate Analyses at ORNL," *Heavy-Section Steel Technology Program Semiann. Prog. Rep. April–September 1986*, NUREG/CR-4219, Vol. 3, No. 2 (ORNL/TM-9593/V3&N2), Martin Marietta Energy Systems, Inc., Oak Ridge Natl. Lab., December 1986.

27. C. W. Schwartz, "Algorithms for Viscoplastic Finite Element Analysis," presented at the Third Annual HSST Workshop on Dynamic Fracture and Crack Arrest Technology, U.S. National Bureau of Standards, Gaithersburg, Md., May 1987.

28. R. H. Bryan et al., *Pressurized-Thermal-Shock Test of 6-in.-Thick Pressure Vessels. PTSE-1: Investigation of Warm Prestressing and Upper-Shelf Arrest*, NUREG/CR-4106 (ORNL-6135), Martin Marietta Energy Systems, Inc., Oak Ridge Natl. Lab., April 1985.

29. C. E. Pugh, "Crack Arrest Technology," *Heavy-Section Steel Technology Program Semiann. Prog. Rep. October 1984—March 1985*, NUREG/CR-4219, Vol. 1 (ORNL/TM-9593/V1), Martin Marietta Energy Systems, Inc., Oak Ridge Natl. Lab., June 1985.

6. IRRADIATION EFFECTS STUDIES

R. K. Nanstad

The Heavy-Section Steel Technology (HSST) Irradiation Effects Task (Task H.6) consists of a number of projects concerned with the effects of neutron irradiation on the fracture toughness and mechanical properties of reactor pressure vessel materials. The task currently involves seven designated series of experiments, the first four completed. The active series described here include (1) the Fifth and Sixth Series, which will characterize the shifts and shapes of the irradiated K_{Ic} and K_{Ia} curves, respectively, and (2) the Seventh Series, concerned with the irradiation resistance of stainless steel cladding.

6.1 Fifth HSST Irradiation Series

R. K. Nanstad F. M. Haggag
R. L. Swain T. N. Jones

Fracture-toughness investigations have continued with testing of unirradiated 4TCS and scoping tests of 1TCS and 2TCS. All tests were conducted with a computer-interactive test system using the single-specimen compliance technique. Nc unloadings are performed before the P_Q load defined in American Society for Testing and Materials (ASTM) test method E399. Tests that do not satisfy the ASTM criteria for a valid K_{Ic} are analyzed by computing the J-integral at the onset of cleavage J_c. An elastic-plastic fracture-toughness value K_{Jc} is calculated from the relationship

$$K_{Jc}^2 = EJ_c \quad , \tag{1}$$

where E ≡ Young's modulus, MPa.

Table 6.1 gives the results of tests conducted with irradiated 4TCS by Materials Engineering Associates (MEA). Those tests were conducted in the hot cells at the Naval Research Laboratory. Test temperatures were selected to provide K_{Ic} and K_{Jc} results from a sufficiently broad temperature range to allow for construction of a fracture-toughness curve to high values relative to the existing K_{Ic} curve in the ASME Code, as well as to provide large-specimen results for comparison with those from small specimens. As shown in the table, valid K_{Ic} values (by ASTM E399) were obtained for both welds at 50°C. All data at higher temperatures were not valid K_{Ic} values; note, however, that one specimen of 73W at 65°C is invalid only because maximum load exceeded the P_Q load by >10%. Additionally, the 73W test at 75°C was only very slightly outside the plastic-zone size limit, and maximum load was equal to the P_Q load. Thus, interpretation of the data in terms of E399 provides quite restrictive results and amplifies the need for using elastic-plastic fracture mechanics in

Table 6.1. Fracture-toughness results for irradiated 4TCS of Fifth HSST Irradiation Series[a]

Specimen	Test temperature (°C)	J at cleavage[b] (kJ/m^2)	K_{Jc} (MPa·$\sqrt{m}$)	$K_{\beta c}$ (MPa·$\sqrt{m}$)	K_Q (MPa·$\sqrt{m}$)	K_J values at pop-ins (MPa·$\sqrt{m}$)
		Weld 72W, 0.23% Cu, 0.60% Ni				
72W-19	50	45.6		93.1	93.2[c]	75.8, 90.2
-26	50	54.9	105.9	100.9	111.4[e]	
-20	75	144.7	171.4	142.7	176.3	
-25	75	93.7	137.9	123.5	144.4	
-13	85	129.8	162.2	137.5	169.8	
-16	85	161.8		147.2	156.6	145
-11	95	371.7	274.0	182.9	198.0	
-14	95	258.8	228.6	167.3	153.0	135
		Weld 73W, 0.31% Cu, 0.60% Ni				
73W-22	50	64.9	115.2	109.0	105.1[c]	76.0
-18	50	70.4		112.7	103.1[c]	96.0
-21	65	84.1	130.8	120.4	140.0	
-19	65	78.8	126.7	117.4	102.0[d]	93.9
-16	75	69.4	118.7	111.4	127.2[e]	
-12	85	102.1	143.8	128.7	151.3	
-15	95	294.2	243.7	176.7	208.7	
-11	95	363.8	271.0	186.3	207.9	

[a]Tests performed by MEA.

[b]Value calculated using load-line deflection data.

[c]Valid K_{Ic} values according to ASTM E399.

[d]Not a valid K_{Ic} because $P_{max}/P_Q > 1.10$.

[e]Very slightly above the maximum allowable K_Q (126.2 MPa·$\sqrt{m}$) to satisfy ASTM E399 as a valid K_{Ic}.

the interpretation of material behavior. Table 6.1 also points out the values of K_J calculated where pop-ins occurred during certain tests. In those cases where a K_{Jc} value is not shown, a large pop-in occurred that increased area under the load-displacement curve sufficient to elevate significantly the calculated value of the J-integral. In those cases, interpretation of the results has not yet been performed. All recorded pop-ins occurred at loads lower than the P_Q loads subsequently determined. The interpretation of significance of pop-ins has not yet been determined but will be in the final analyses of program results.

Additional testing of irradiated 1TCS and unirradiated 4TCS has been completed at Oak Ridge National Laboratory (ORNL); irradiated 2TCS were tested by MEA. For 72W, nine 1TCS were tested at 85°C, and five 1TCS were tested at 95°C. For 73W, ten 1TCS were tested at 85°C, and five 1TCS were tested at 105°C. Two of the specimens at 105°C showed some pop-in events, but none failed in cleavage. For each weld, four irradiated 2TCS were tested at 95°C and four at 105°C.

Four irradiated 2TCS of each weld remain to be tested by ORNL. Final crack-length measurements have not yet been completed for the 1TCS and 2TCS tests, and results will be reported in the next progress report.

The unirradiated 4TCS results are presented in Table 6.2. The results for 73W are all relatively high and have relatively small scatter. The results for 72W, however, show a much wider scatter band. Preliminary estimates of crack extension for the unirradiated 4TCS indicated extensions up to ~0.5 mm with the average value ~0.25 mm, and all indications are that only blunting took place with no in-plane stable tearing. More detailed analyses will be performed and reported in the next progress report.

Table 6.2. Fracture-toughness results for unirradiated 4TCS of Fifth HSST Irradiation Series

Specimen	Test temperature (°C)	J at cleavage[a] (kJ/m^2)	K_{Jc} (MPa·$\sqrt{m}$)	K_{Bc} (MPa·$\sqrt{m}$)	K_Q (MPa·$\sqrt{m}$)
		Weld 72W, 0.23% Cu, 0.60% Ni			
72W-30	20	112.5	152.3	124.0	138.8
-31	20	173.8	193.1	141.5	130.7
-32	20	271.7	252.2	161.1	144.0
-33	20	101.6	144.7	120.2	144.6
		Weld 73W, 0.31% Cu, 0.60% Ni			
73W-30	5	203.9	208.8	147.0	147.7
-31	5	282.3	254.6	161.2	146.5
-32	5	240.7	225.3	152.6	143.3
-33	5	271.7	238.9	156.9	146.9

[a]Value calculated using load-line deflection data.

6.2 Sixth HSST Irradiation Series: Crack Arrest

S. K. Iskander T. D. Owings, Jr.
R. K. Nanstad

The fixture (described in Ref. 1) to be used for remote testing of irradiated crack-arrest specimens has undergone minor reworking and preliminary evaluations, including heating and cooling experiments to examine the rate of thermal conditioning, as well as uniformity throughout the test specimen. Specimens of various sizes are being evaluated. Initial results have shown excellent thermal distribution within the specimens and the ability to condition the specimens at a reasonable

rate. A new contact thermocouple based on the same technology used in the past for Charpy impact testing was fabricated and is being evaluated during this series of performance tests.

The additional submerged-arc weldments of 72W and 73W have been fabricated by Combustion Engineering, Inc. (CE), and shipped to ORNL. Some of the welds will be used for specimen fabrication; the remainder will be stored for archival purposes.

6.3 Seventh HSST Irradiation Series

F. M. Haggag R. K. Nanstad
T. N. Jones E. T. Manneschmidt

6.3.1 Phase 1

The first phase of the Seventh Irradiation Series evaluated stainless steel cladding applied in three layers by the single-wire oscillating submerged-arc method. In this phase, completed and reported earlier, Charpy impact and tensile specimens were irradiated to 2×10^{19} neutrons/cm^2 (>1 MeV) at 288°C. Details of the test results are given in Ref. 1.

6.3.2 Phase 2

In the second phase, currently in progress, a commercially produced, three-wire series-arc weldment was evaluated under identical irradiation and testing conditions as in the first phase. The three-wire series-arc procedure, developed by CE, Chattanooga, Tennessee, produced a highly controlled weld chemistry and microstructure and highly controlled fracture properties in all three layers of the weld. The three layers of cladding were required to allow the fabrication of tensile, Charpy impact, and 0.5TCS from the cladding. Irradiations of the specimens [Charpy V-notch (CVN), tensile, and 12.7-mm compact specimens] to 2 and 5×10^{19} neutrons/cm^2 (>1 MeV) have been completed. The results of the unirradiated (control) tensile and Charpy impact specimens are discussed below. Preparations have been made to complete testing of the irradiated tensile and Charpy impact specimens by the middle of October 1987.

6.3.3 Results and discussion

Charpy impact specimens were machined in the LT, LS, TL, and TS orientations, corresponding to crack extension across and through the thickness of the plate and across and through the length of the plate, respectively. These four specimen orientations were chosen to simulate the possibilities of crack extension in the axial and circumferential orientations both across and through the cladding of a pressure vessel. The results of the CVN tests are shown in Figs. 6.1–6.3. The transition temperature and the upper- and lower-shelf energies did not vary significantly for the four orientations (Table 6.3). Hence, CVN irradiated

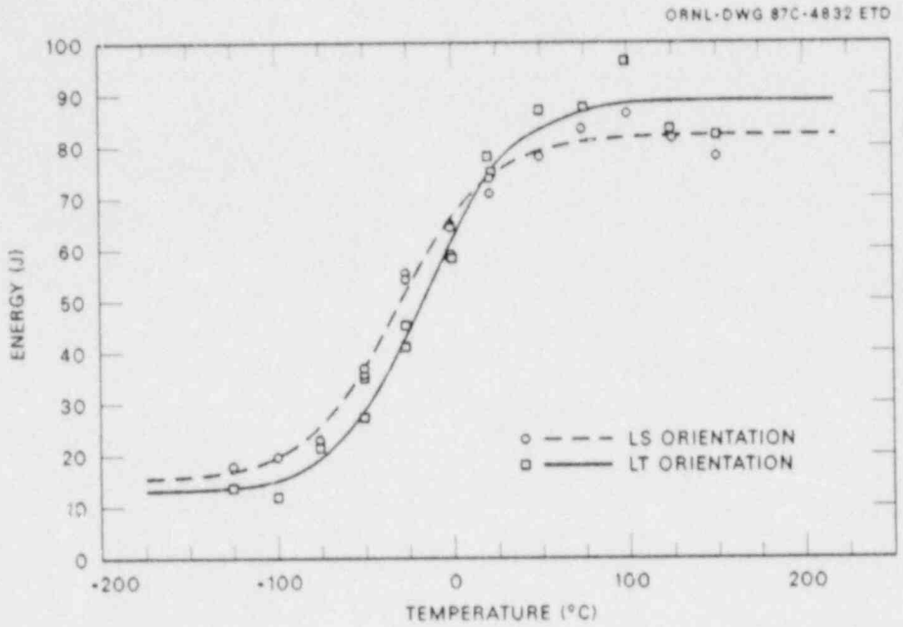

Fig. 6.1. Charpy impact energy of unirradiated three-wire cladding in the LS and LT orientations.

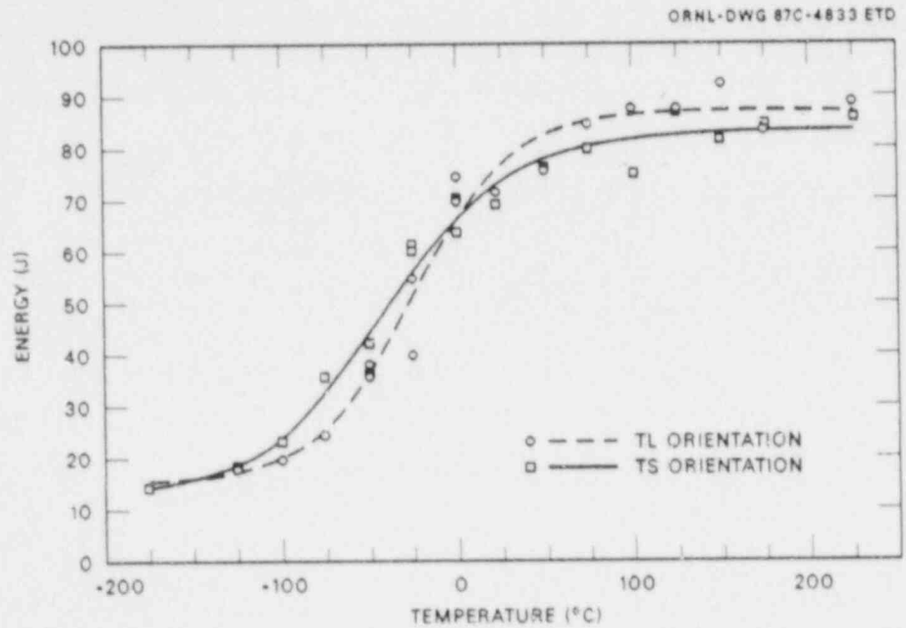

Fig. 6.2. Charpy impact energy of unirradiated three-wire cladding in the TL and TS orientations.

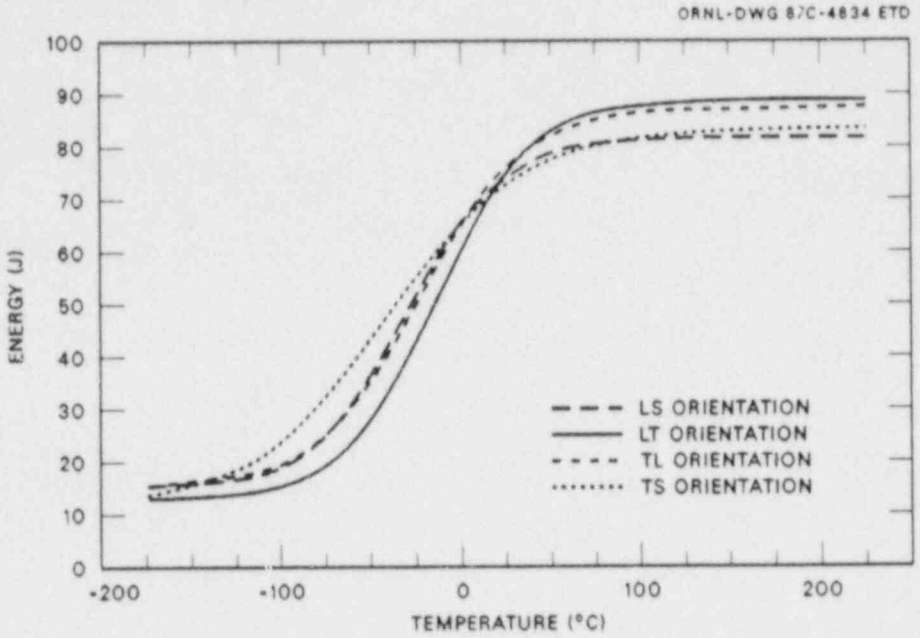

Fig. 6.3. Charpy impact energy of three-wire series-arc stainless steel cladding in four different orientations.

Table 6.3. Charpy impact test results for stainless steel three-wire series-arc cladding

Orientation[a]	Neutron fluence [neutrons/cm^2 (>1 MeV)]	Transition temperature criterion (°C)		Energy (J)	
		41 J	68 J	Upper shelf	Lower shelf
LS	0	−42	6	80	15
	2×10^{19}	−28	56	70	9
	5×10^{19}	−15		68	12
LT	0	−31	10	89	13
TL	0	−41	3	86	16
TS	0	−58	7	81	14

[a]With respect to the base metal where L is the rolling, as well as the welding, direction.

specimens were machined only from the cladding with their notches in the LS orientation because that orientation exhibited a typical transition temperature, as well as a slightly lower upper-shelf energy. Note that the L-orientation is the longitudinal (rolling direction of base plate), as well as the welding, direction for all three-wire cladding specimens.

The CVN test results, obtained here for cladding material that has received a postweld heat treatment (PWHT) typical of that for pressure vessel three-wire cladding, are compared in Figs. 6.4 and 6.5 with results of cladding from the characterization material for the clad plate tests that received only a partial PWHT (see Sect. 3.3). The typical PWHT resulted in a slightly higher upper-shelf energy, as well as a slightly lower transition temperature compared with the partial PWHT data for both the LS and LT orientations.

One-half of the tensile specimens were fabricated with their axes in the L-orientation; the other half were fabricated in the T-direction. The results of these tensile tests are shown in Figs. 6.6–6.9. As shown, the effect of test specimen orientation on the test results was very small. Thus, specimens for irradiation tests were machined only in the longitudinal orientation. The cladding exhibits an extremely rapid rise in tensile strength below ~0°C. The ductility properties show increases from high temperatures to about −50°C and then decreases at lower temperatures.

6.3.3.1 Effect of irradiation on the Charpy impact energy. Irradiation of the three-wire stainless steel cladding specimens at 288°C to fluence levels of 2 and 5 × 10^{19} neutrons/cm^2 (>1 MeV) has resulted in decreases of the CVN upper-shelf energy by 12 and 16% and increases of the transition temperatures by 15 and 30°C, respectively (see Fig. 6.10).

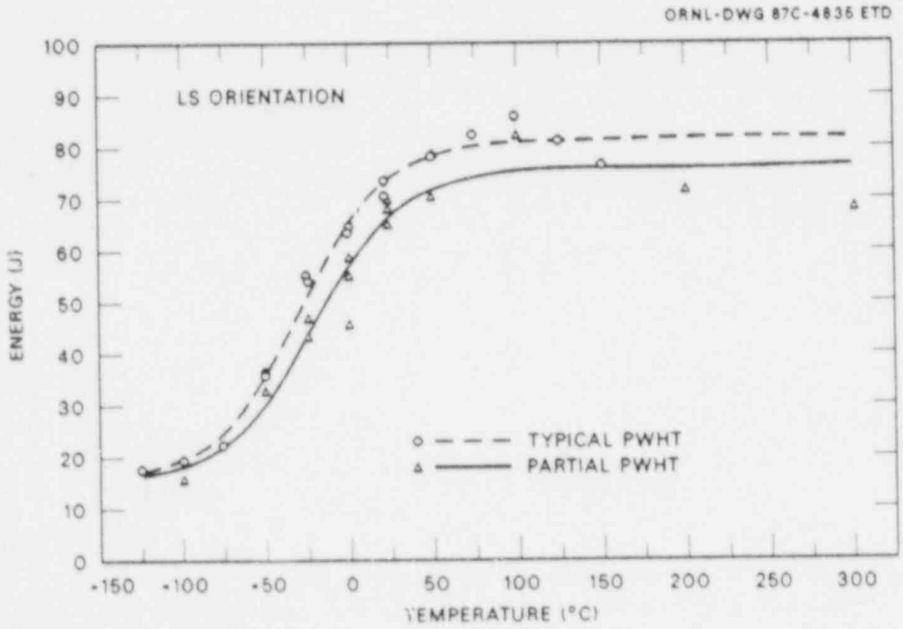

Fig. 6.4. Effect of PWHT on the Charpy impact energy of three-wire series-arc stainless steel cladding in the LS orientation.

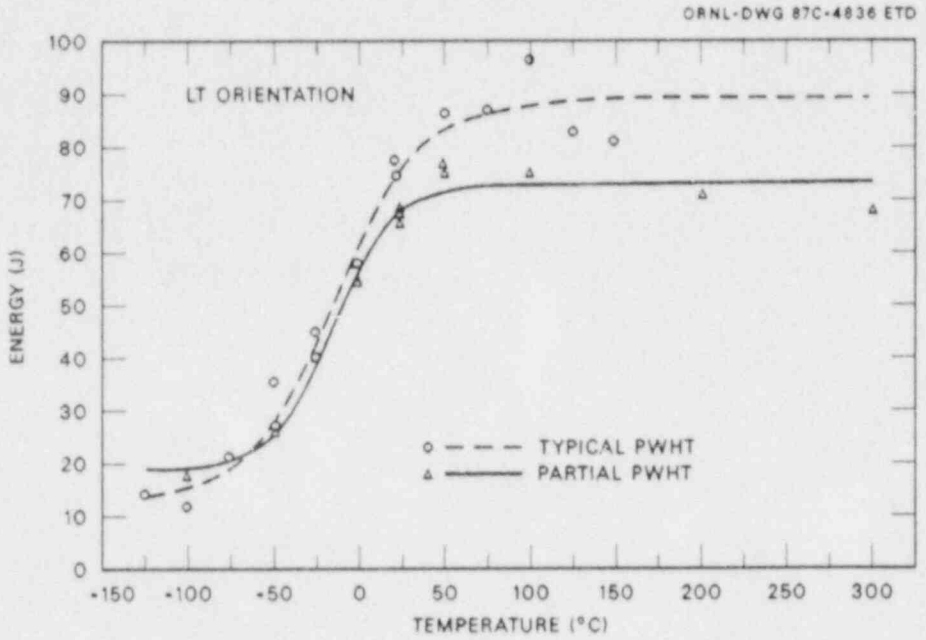

Fig. 6.5. Effect of PWHT on the Charpy impact energy of three-wire series-arc stainless steel cladding in the LT orientation.

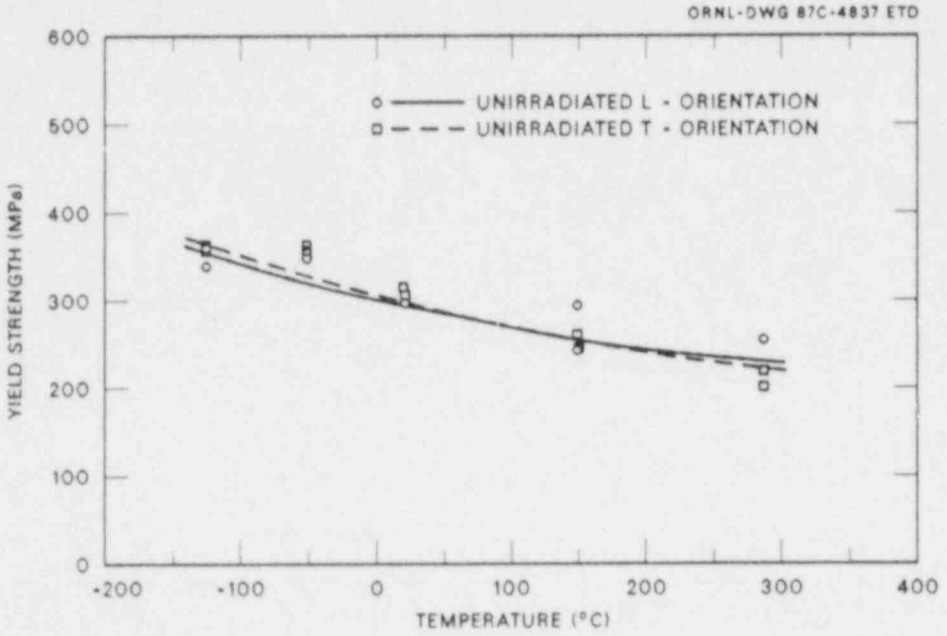

Fig. 6.6. Effect of test temperature on yield strength of unirradiated three-wire series-arc stainless steel cladding.

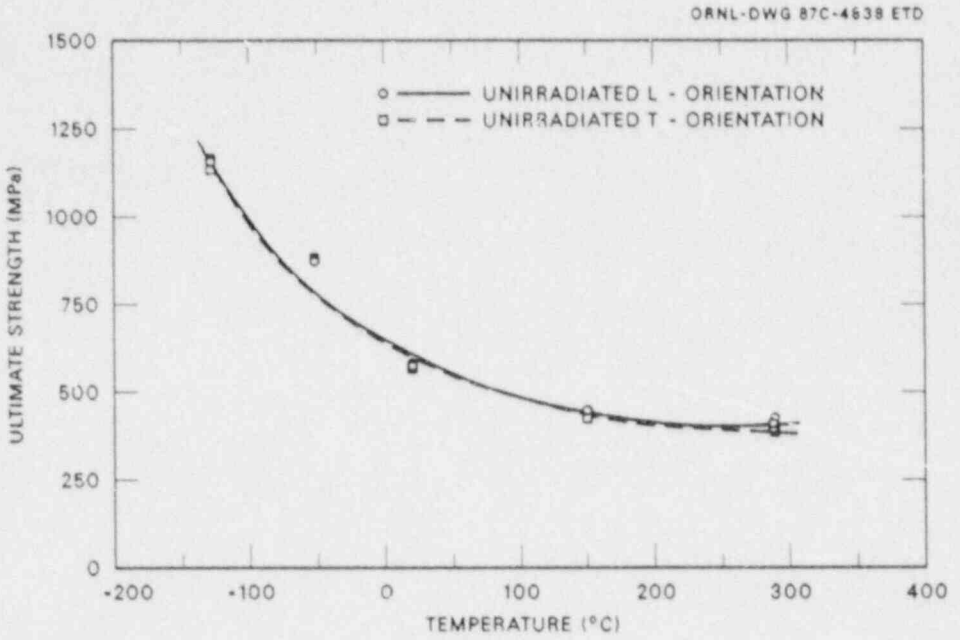

Fig. 6.7. Effect of test temperature on ultimate strength of unirradiated three-wire series-arc stainless steel cladding.

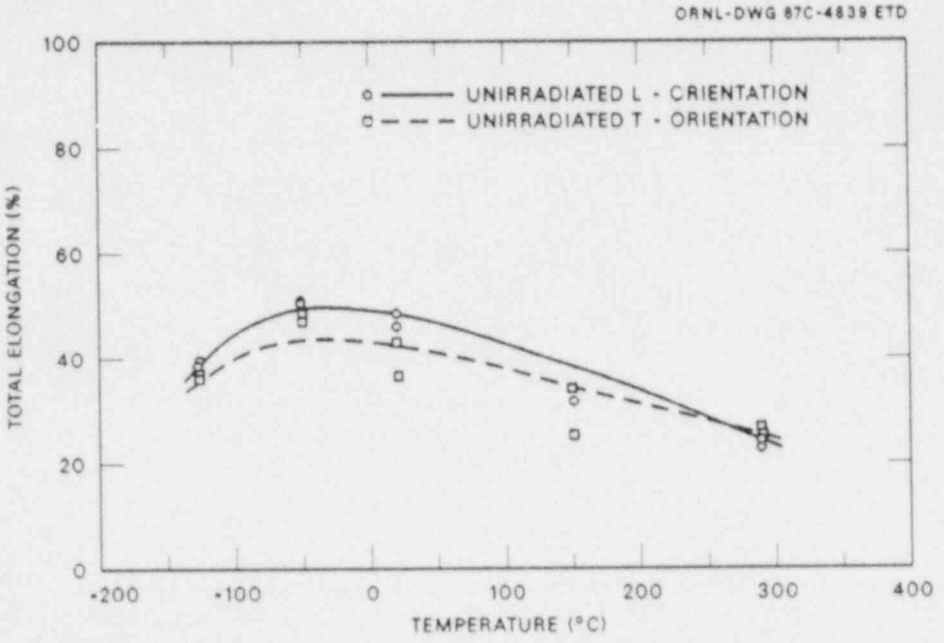

Fig. 6.8. Effect of test temperature on total elongation of unirradiated three-wire series-arc stainless steel cladding.

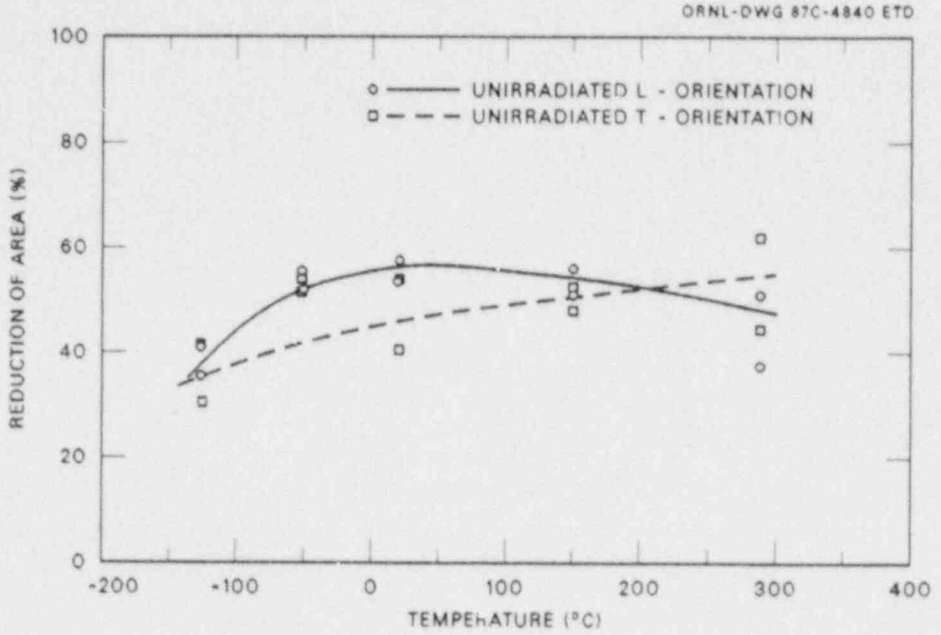

Fig. 6.9. Effect of test temperature on reduction of area of unirradiated three-wire series-arc stainless steel cladding.

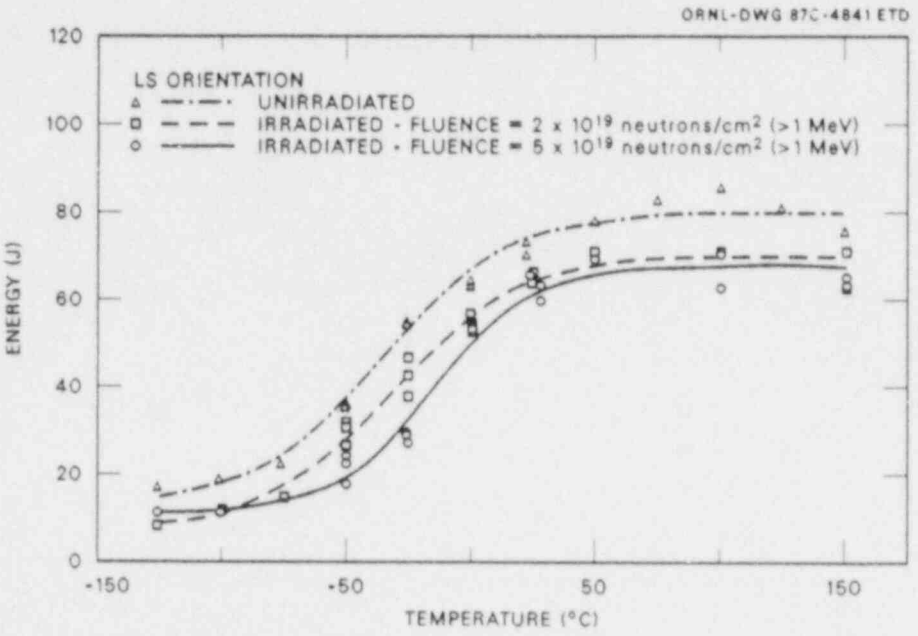

Fig. 6.10. Effect of irradiation on Charpy impact energy of three-wire series-arc stainless steel cladding.

These results are in agreement with those for the single-wire cladding produced with good welding practice. Table 6.3 also provides the curve-fit results for the unirradiated and irradiated CVN test results.

6.3.3.2 Effect of irradiation on the tensile properties. Irradiated tensile specimens in the longitudinal orientation are scheduled for testing in late October 1987. The testing temperatures will be room temperature, 288, and −125°C. Six specimens available for each fluence level will be tested in duplicates.

6.3.3.3 Effect of irradiation on the fracture toughness. Unirradiated and irradiated 12.7-mm compact specimens are scheduled for testing in November and December 1987.

Reference

1. W. R. Corwin et al., "Sixth HSST Irradiation Series: Crack Arrest," pp. 185–92 in *Heavy-Section Steel Technology Program Semiann. Prog. Rep. April–September 1986*, NUREG/CR-4219, Vol. 3, No. 2 (ORNL/TM-9593/V3&N2), Martin Marietta Energy Systems., Inc., Oak Ridge Natl. Lab.

7. CLADDING EVALUATIONS

7.1 Crack-Arrest Behavior in Clad Plates

S. K. Iskander
S. E. Bolt
D. J. Alexander
K. V. Cook
G. C. Robinson
B. C. Oland

7.1.1 Introduction

The objective of the clad plate experiments is to determine the effect, if any, of stainless steel cladding on the propagation of small surface cracks subjected to stress states similar to those produced by thermal shock conditions. During this reporting period, five clad and one unclad plate have been tested.

The test specimen was described in a previous report.[1] The pretest material characterization was reported in Ref. 2.

Posttest material characterizations have recently been performed. Young's modulus and stress-strain curves were determined for the base metal, heat-affected zone (HAZ), and cladding. The stress-strain curves will be used in finite-element analyses. Some room temperature tensile testing has been performed on the HAZ from one of the broken halves of the first plate tested because of differences between the characterization block and the clad plates. The RT_{NDT} of the base metal and the variation of hardness across the thickness of the plate were determined, and some metallographic examinations were performed. The hardness and metallurgical structures observed for the first plate are typical of all the other plates. All such material characterizations are reported in Sect. 3.3.

Fractography and scanning electron microscopy (SEM) of the fracture surface of the first plate have been completed and are reported here.

7.1.2 General description of the test

In the six tests performed, the general test procedure was essentially the same. The instrumented plate was mounted in a 1-MN Instron testing machine. For tests at other than room temperature, the plate was cooled to the specified temperature. The variation in temperature at chosen locations was kept within 3°C. The plate was then loaded in four-point bending to induce a pure bending moment in the span, including the electron-beam (EB) weld. The loads were chosen to induce a specified strain level on the surface of the base metal. The EB weld was then hydrogen-charged, while the load was kept constant by using stroke control, until a flaw initiated. This portion of the experiment on an initially unflawed plate is essentially an "arrest" experiment — the purpose of which is to study the effect of cladding on a running flaw.

In cases in which the flaw arrested, the plate is removed from the testing machine and heat-tinted to define the arrested flaw shape. Some nondestructive examination was performed on the first and second plates

tested to determine the extent of flaw propagation. After partial reinstrumentation, the plate is put back into the testing machine and cooled to a specified temperature. The load is increased at a uniform rate until the plate either ruptures or further pop-in occurs. In case of the latter event, the process is repeated. The purpose of reloading the arrested flaw shapes is to obtain data on the residual load-bearing capacity of flawed clad plates. This portion of the experiment is designated an "initiation" one, in contrast with the "arrest" portion previously described.

Figure 7.1 shows typical instrumentation for the arrest portion of the experiment. The gages designated ZE are weldable, stainless-steel-sheathed strain gages that are used as crack-opening-displacement (COD) gages. Only the end portions of the gage are welded and a sufficient length is left unbonded so that the expected COD, when averaged over the unbonded length, is within the maximum strain capacity of the gage. They have been used successfully many times before in this manner by the HSST Program. On the top surface only, in addition to the COD gages, there are four foil strain gages on each of the base metal and clad portions of the plate and two thermocouples. Heat-tinting destroyed the foil strain gages, and the plate was partially reinstrumented for the initiation test as shown in Fig. 7.2. On the first plate tested, an attempt was made to reuse the weldable strain gages, but with mixed success; subsequently, a clip gage was used to measure the COD. Extra thermocouples were added for tests at other than room temperature to ensure uniform temperature through the plate thickness.

A data acquisition system was used to record the readings from the instrumentation on magnetic tape at suitable time and load intervals. In addition to the strain/COD and the temperature at various locations in the plate, the load and the displacement of the testing machine ram were also recorded.

Using an assumed flaw shape that corresponded approximately to the EB weld zone, the loading rate was chosen to be within the range prescribed by ASTM E399 (0.55 to 2.75 MPa$\cdot\sqrt{m}$/s).

For the six plates tested, the target surface strains and corresponding loads are given in Table 7.1. For applicable cases, the load that the specimen can support after pop-in, the "arrest" load, is also given. The surface strain (in the uniform bending moment span of the plate) is the independent parameter used in the selection of the target load. All arrest experiments were performed at either −25 or 25°C, and Fig. 7.3 shows the point on the load vs surface strain curve at which the six plates have been tested. The loads (and strains) were maintained constant under stroke control during the period of hydrogen charging and are a measure of the crack-driving force during the instant the flaw initiated in the EB weld.

For the first plate tested, CP-15, the surface strain was chosen to be approximately the yield strain of the base metal. The plate did not rupture. The target surface strain was increased for each of plates CP-17 and -19. In all three cases, the flaw initiated and arrested after propagating, beneath the cladding, a distance that increased with increasing target strain. An unclad plate, CP-21, ruptured when loaded to approximately the base metal yield strain on the surface. The pop-in, arrest loads, and corresponding crack lengths for the four plates tested at room temperature are shown schematically in Fig. 7.4.

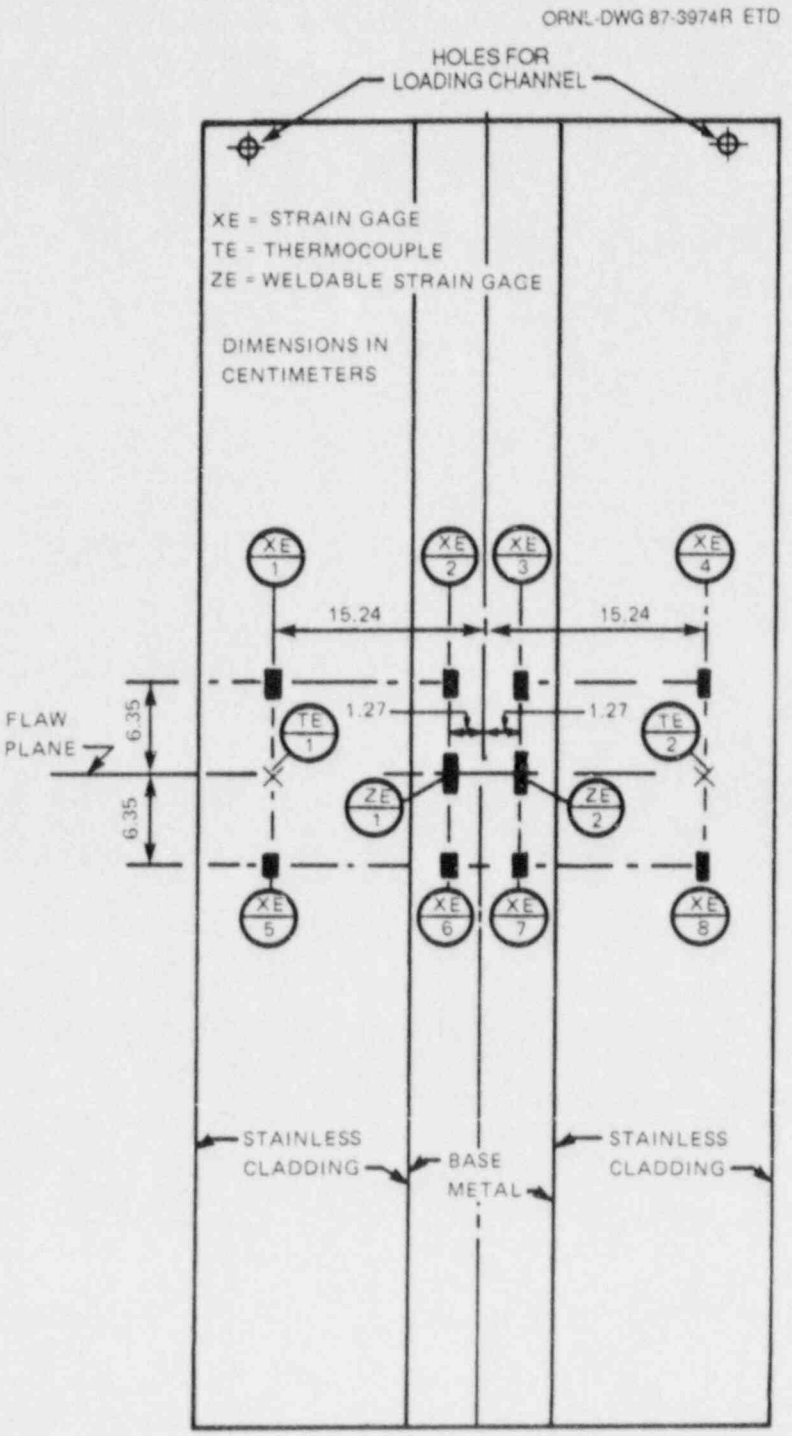

Fig. 7.1. Typical instrumentation for arrest portion of experiment.

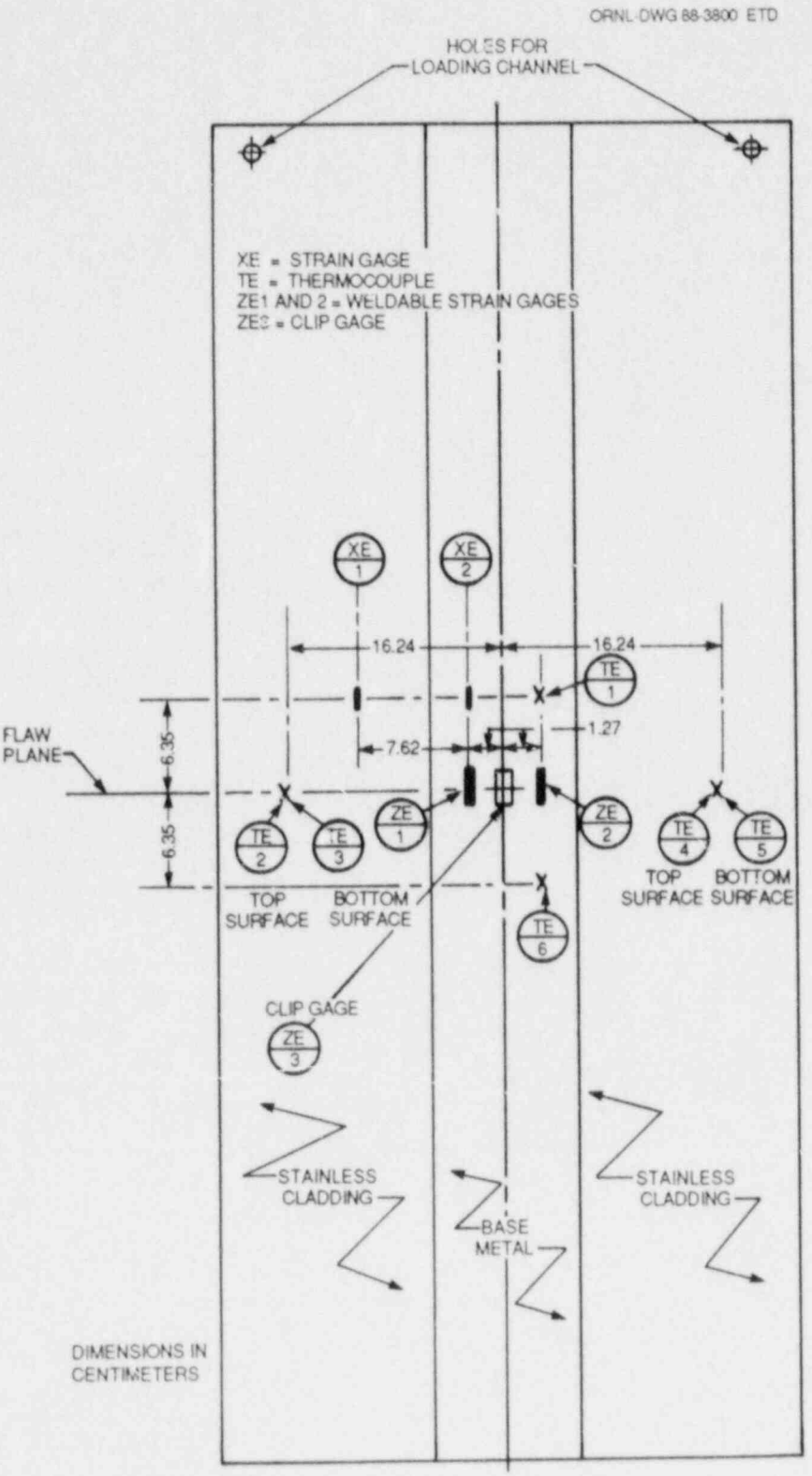

Fig. 7.2. Partially reinstrumented plate for initiation test.

Table 7.1. Target surface strains and corresponding loads for the six plates tested

Plate	Condition	Test temperature (°C)	Load (kN)		Target surface strain (%)
			Pop-in	Arrest	
CP-15	Clad	RT[a]	676	654	0.31
		−25	759	709	
		−100	600	R[b]	
CP-17	Clad	RT	890	823	0.45
	Several pop-ins occurred before rupture	−25	756/725	R	
CP-19	Clad	RT	987	689	0.65
		−50	703	R	
CP-21	Unclad	RT	676	R	0.27
CP-18	Clad	−25	823	649	0.39
		−25	698	R	
CP-20	Clad	−25	868	R	0.41

[a]RT = room temperature, ~25°C.

[b]R = plate ruptured in two pieces.

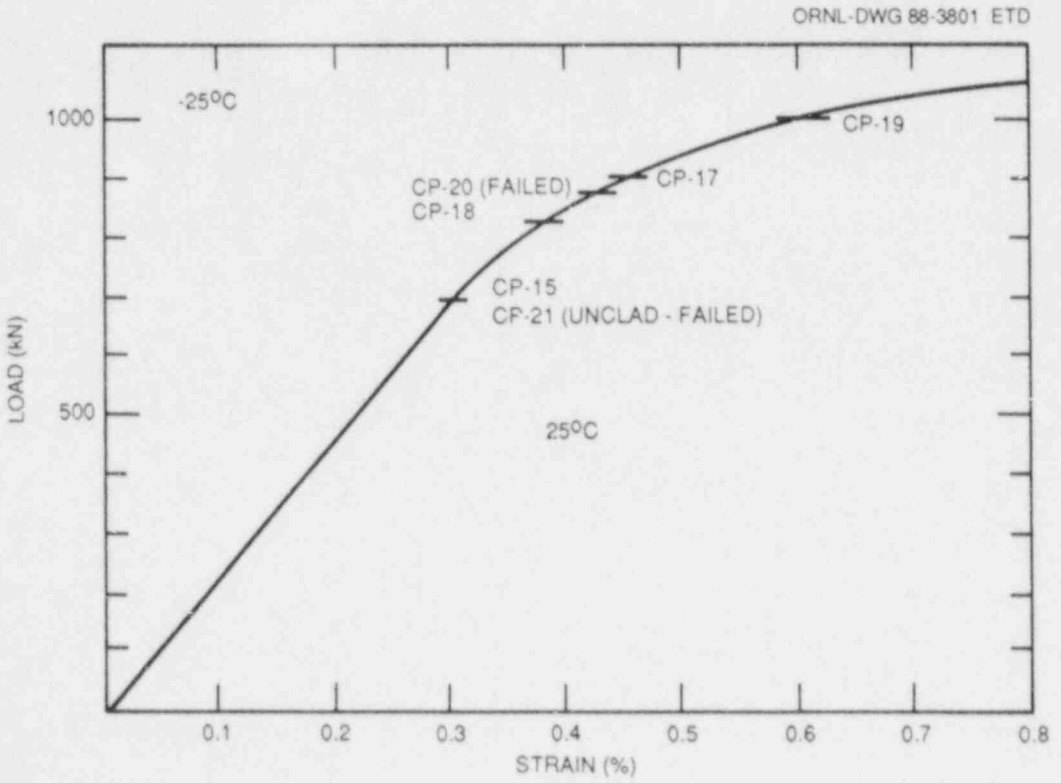

Fig. 7.3. Point on the load vs surface strain curve at which six plates have been tested.

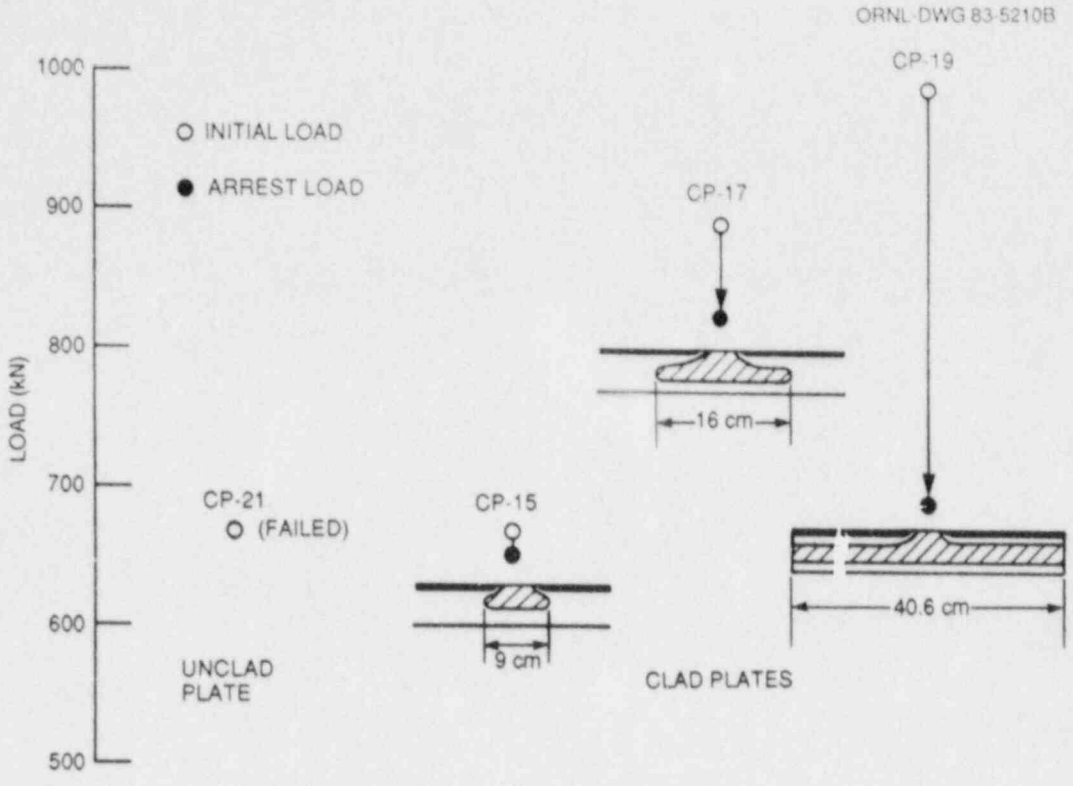

Fig. 7.4. Pop-in, arrest loads, and corresponding crack lengths for four plates tested at room temperature.

7.1.3 Testing of plate CP-15

The first three-wire clad plate was loaded at room temperature to a surface strain of ~0.31% (in the uniform moment span of the plate), corresponding to the yield stress at room temperature of the base metal of 590 MPa and requiring a load of 676 kN (152 kips). The plate was then hydrogen-charged, while the load was kept constant by using stroke control. Pop-in occurred within about 1 h. The plate was removed from the testing machine and heat-tinted at 325°C. The plate was reinstalled, cooled to −25°C, and loaded at a constant displacement rate. A second pop-in occurred at a load of 759 kN (170.6 kips). The plate was removed from the testing machine and heat-tinted at 250°C. The plate was reinstalled in the testing machine, cooled to −100°C, and the load increased at a uniform rate until the plate broke completely at 600 kN (134.8 kips). Figure 7.5 shows the two broken halves of the 150-kg test specimen with heat-tinted shapes of the first and second pop-ins. The fracture surface was examined in detail and is described in a later section.

After the first pop-in, a surface crack in the HAZ of the EB weld could be discerned, but it did not appear to have extended on the surface. Instead, a small concave dimple extended axially from the ends of the flaw, indicating that perhaps the flaw extended under the surface. The extension of the axial dimple stopped short of the cladding. The crack had actually propagated in the base metal just below the surface

M&C PHOTO YP3768

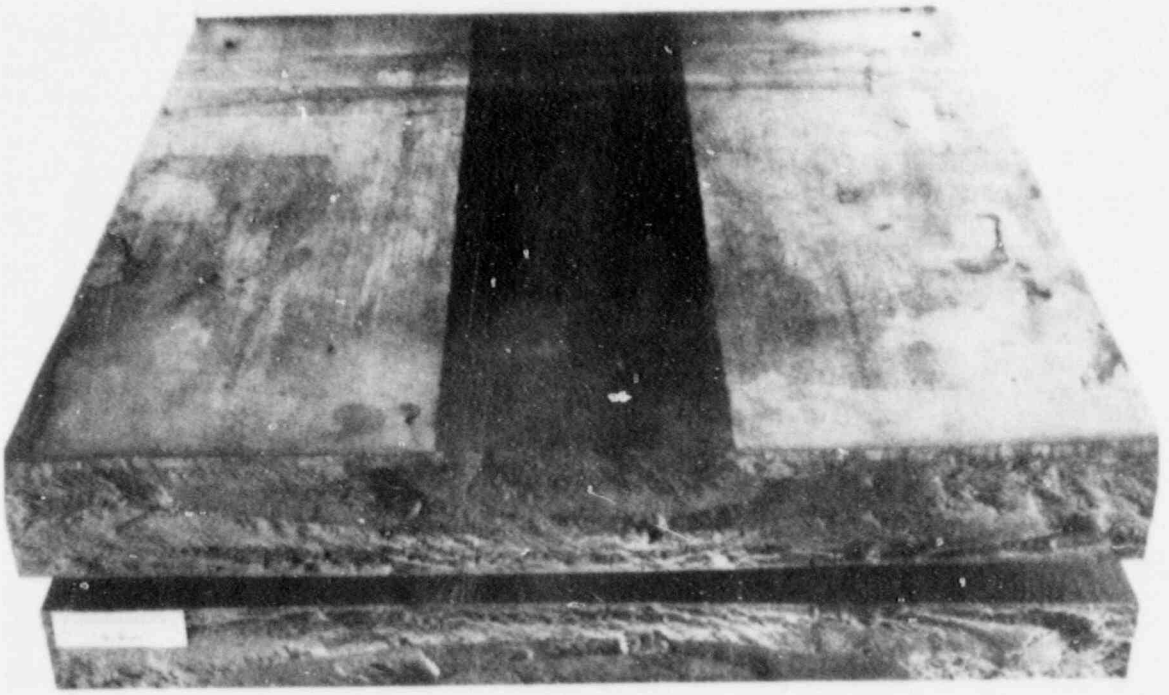

Fig. 7.5. Broken halves of the 150-kg test specimen CP-15 with heat-tinted shapes of first and second pop-ins.

until it encountered the HAZ with a very thin layer of metal covering the flaw.

During the second pop-in, the surface flaw appeared to have extended in the base metal along the previously dimpled surface to a length of about 7 cm, but still short of the 10 cm needed to reach the cladding. However, the dimple extended into the cladding ~5 to 10 mm. The surface extension of the flaw in the base metal was merely the rupturing of the thin layer mentioned previously. Figure 7.6 shows the surface crack in the HAZ of the EB weld after the second pop-in (top center), extending as dimples into the cladding on either side. The crater on the left of the crack was formed during EB welding, not during testing. Note the buckled weldable strain gages, indicating the large COD to which they had been subjected.

After the second pop-in, because of the lack of observable flaw extension along the surface, the plate was x-rayed and examined ultrasonically with dye penetrant. Both examinations indicated a subsurface flaw about 27 cm long. The dye penetrant failed to reveal any extensions of the flaw on the surface beyond those observed visually (Fig. 7.7). The thin surface layer over the portion of the flaw residing in the base metal had only partially ruptured, thus blocking the dye penetrant from indicating that portion of the flaw. The details of the dye penetrant and ultrasonic examination are given in a later section.

M&C PHOTO YP3755

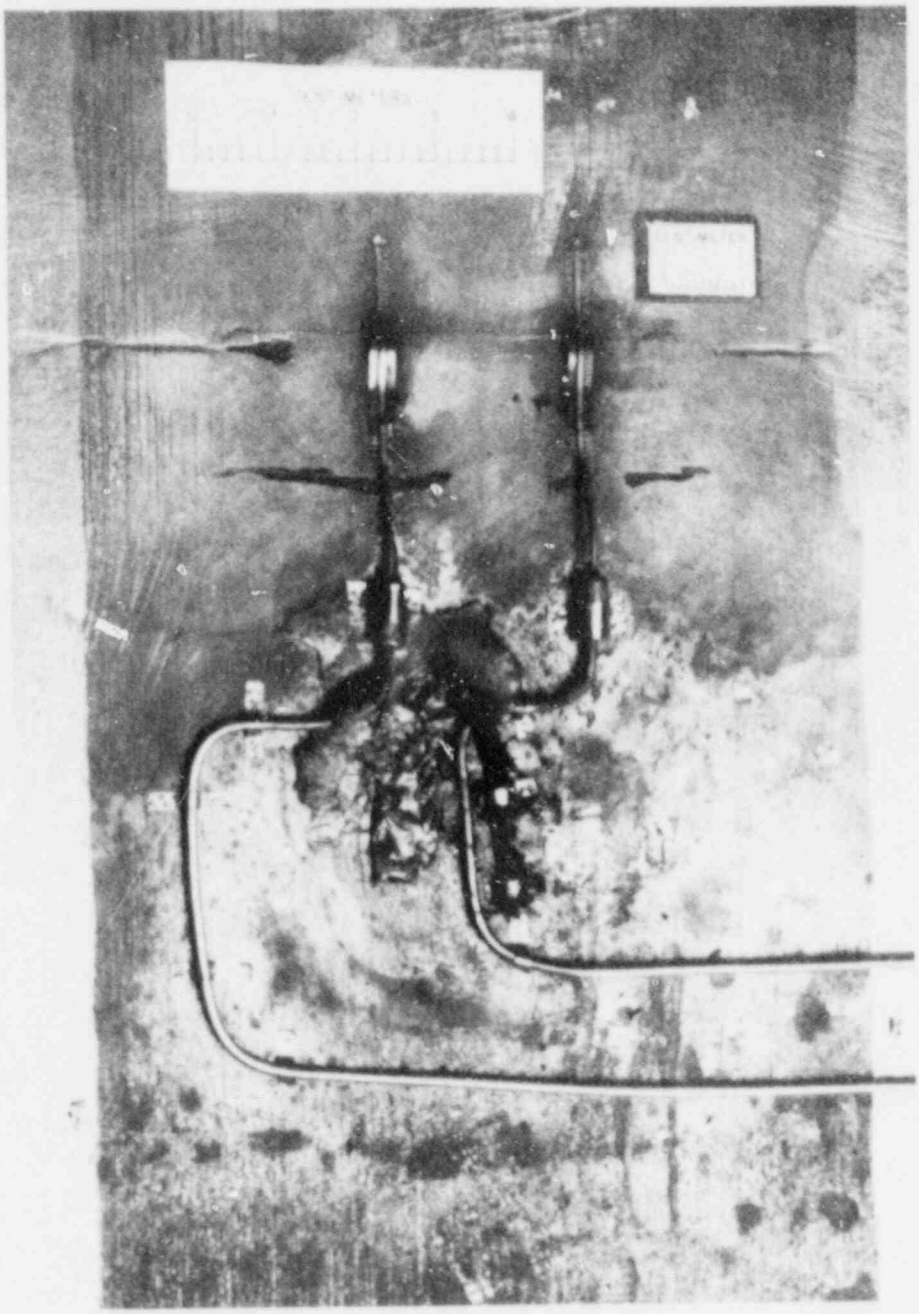

Fig. 7.6. Surface crack in HAZ of EB weld of plate CP-15 after second pop-in (top center), extending as dimples into cladding on either side. Crater on left of crack was formed during EB welding, not during testing.

M&C PHOTO YP3754

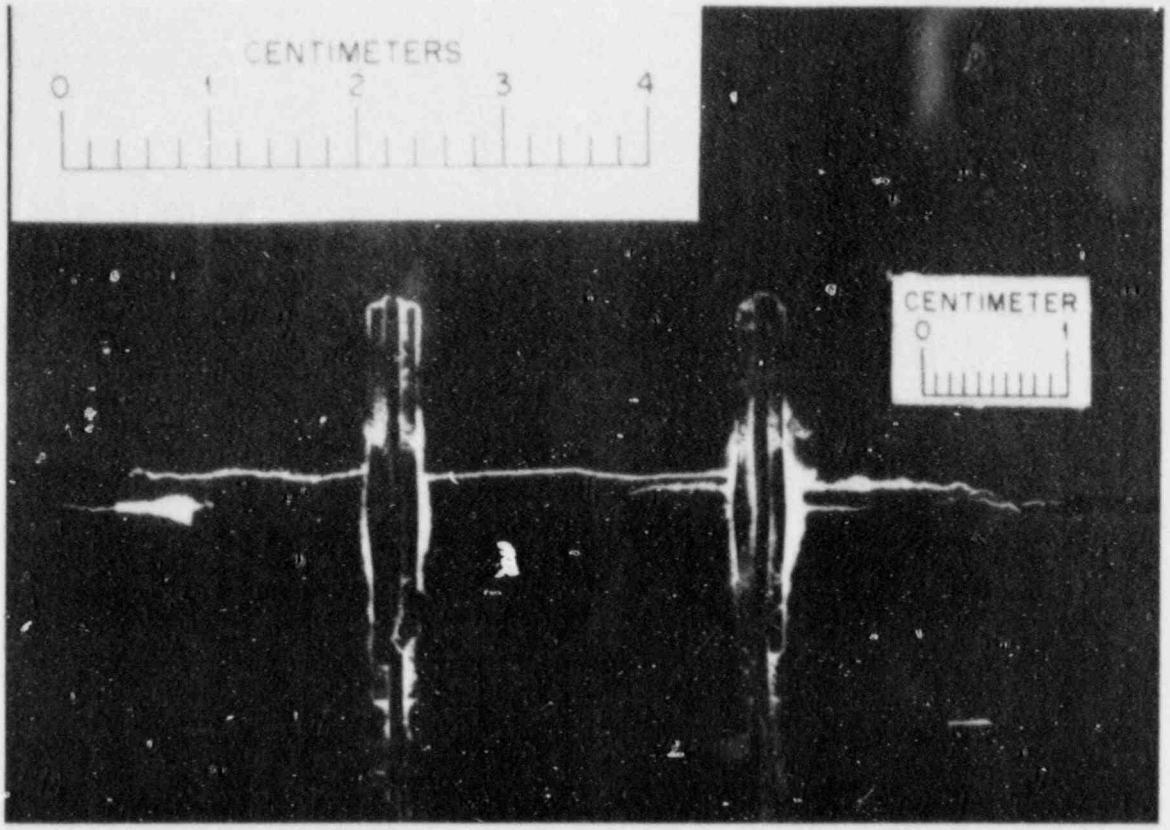

Fig. 7.7. Dye penetrant (examination of plate CP-15 after second pop-in) failed to reveal any extensions of flaw on surface beyond those observed visually.

7.1.4 Fractography of plate CP-15

The fracture surface of plate CP-15 was examined to determine the profile of the crack front at the arrest events. For this specimen, the initial fracture and arrest occurred at room temperature, the second fracture and arrest occurred at −25°C, and the final fracture of the plate was at −100°C. Heat-tinting was used to mark the crack front after the two arrest events.

Preliminary examinations were made of the fracture surface after the final fracture. Optical micrographs were also made. The fracture surfaces were then cut off of the fractured specimen halves. One of the resulting pieces was then cut into 11 sections to allow portions of the surface to be inserted into the SEM for further examination.

7.1.4.1 First fracture event. The initial event, which occurred at room temperature, initiated in the HAZ of the EB weld and propagated down into the plate as well as extending out to either side. Near the surface, the crack was arrested on either end by the HAZ associated with the cladding. The result was the bowed-out shape shown in Fig. 7.8. The

M&C PHOTO YP3763

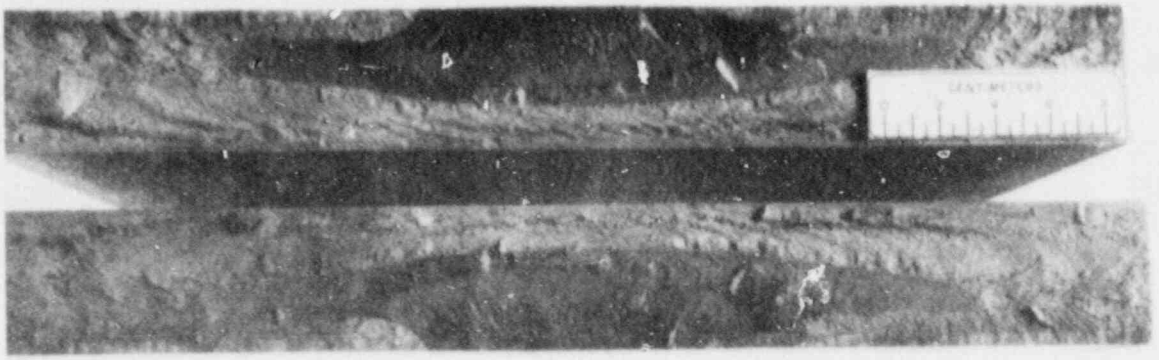

Fig. 7.8. Macrograph of fracture surface of clad plate CP-15.

fracture mode during this event was cleavage, all the way to the arrest location. No evidence of ductile fracture at the arrest point is shown in Fig. 7.9.

7.1.4.2 Second fracture event. The second fracture and arrest occurred at −25°C. The crack extended from the first arrest point into the plate, extending much further to either side and also through the thickness of the plate. SEM examination showed that the crack was again arrested by the HAZ boundary on one end of the crack, termed the "left-hand side" (LHS). Again, in this case, the fracture mode was cleavage all the way to the arrest point. In the center of the plate, the crack also extended by cleavage to its arrest location. However, at the other end of the flaw, referred to as the "right-hand side" (RHS), the flaw was able to penetrate the HAZ and did actually come into contact with the cladding. In this case, the HAZ was fractured over a distance of roughly 1 in., at which point the flaw deviated and returned to follow the HAZ boundary. The distance over which the HAZ was penetrated matched the width of the initial strip of cladding. The crack front deflection occurred at the point where the HAZ of the second strip of cladding encountered the HAZ from the first strip. The crack grew through the first strip of HAZ by a cleavage mechanism and then hit the stainless steel cladding. Near the edge of the cladding, the flaw penetrated into the cladding for as much as 0.8 mm. The amount of penetration decreased further from the edge of the cladding until the flaw followed the cladding–base metal interface. Fracture of the stainless steel cladding occurred by a ductile mechanism, because the primarily austenitic material will not cleave.

7.1.4.3 Final fracture. The final fracture at −100°C resulted in the complete fracture of the plate. Fracture occurred by cleavage through the remaining areas of base metal and HAZ. Fracture in the cladding tended to follow the ferrite phase, resulting in a relatively brittle fracture appearance. In this case, however, there was no indication that the crack had stopped at the interface between the cladding and the HAZ or at the boundary between HAZ and base metal.

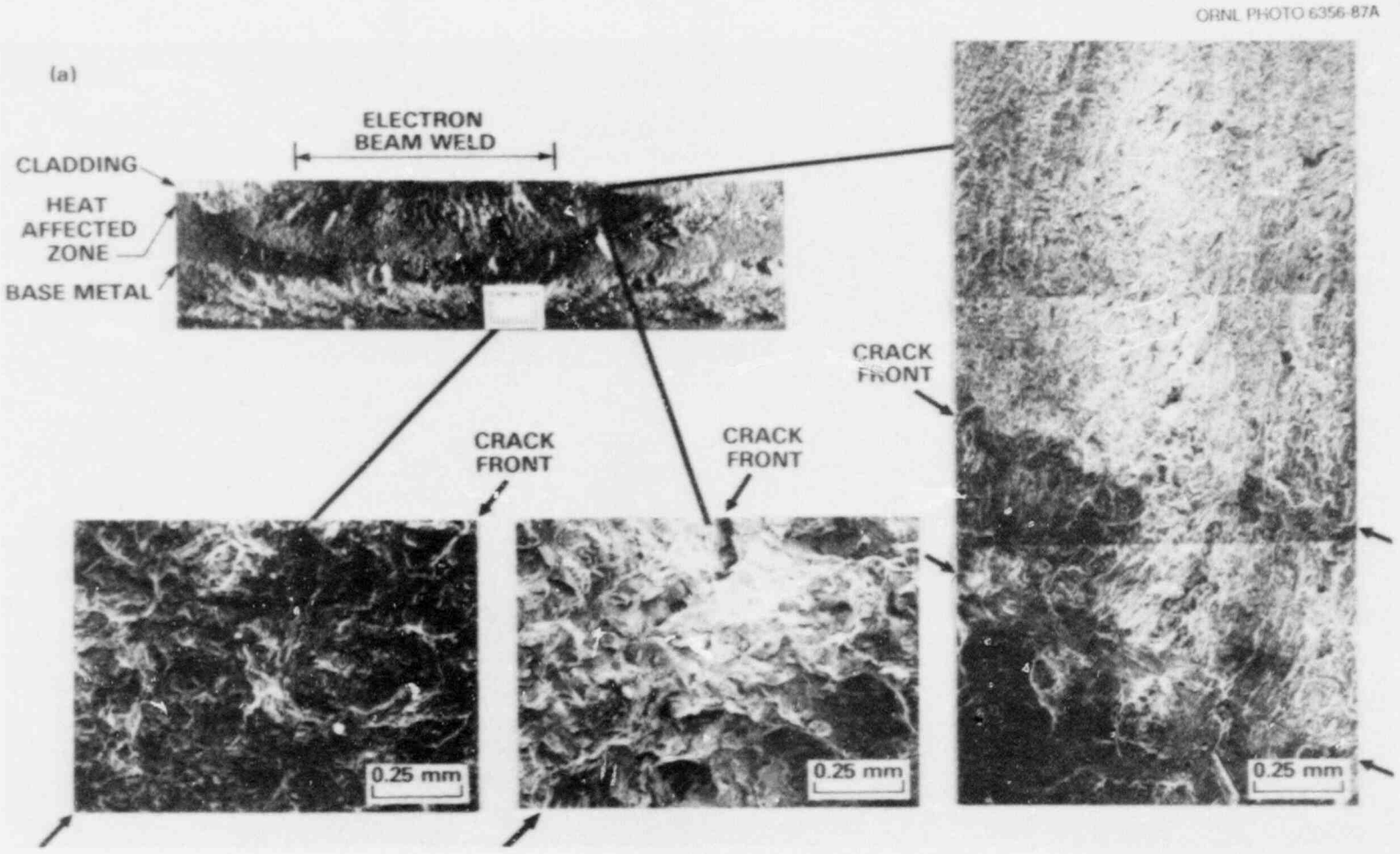

Fig. 7.9. Fractography of clad plate CP-15. There is no evidence of ductility at arrest locations. Second event resulted in crack arrest in cladding on the right-hand side of flaw.

7.1.5 Testing of plate CP-17

The test temperature of the second clad plate, CP-17, was also 25°C, and surface strains were about 0.45% during hydrogen-charging.

The loads at pop-in were 890 and 823 kN (200 and 185 kips) at pop-in and arrest, respectively. Figure 7.10 shows the crack in the HAZ of the EB weld on the surface of plate CP-17. As in plate CP-15, the crater on the right side of the crack was formed during EB welding, not during testing. Figure 7.11 shows the same area as Fig. 7.10 during dye penetrant examination.

The plate was heat-tinted then reloaded at −25°C until it ruptured. An audible pop-in occurred at 756 kN (170 kips), followed by other pop-ins before complete rupture at 725 kN (163 kips). Figure 7.12 shows the load displacement record of these events.

Figure 7.13 shows the fracture surfaces of the broken halves of plate CP-17. Figure 7.14 is a close-up of the heat-tinted, arrested flaw shape of plate CP-17 and six data points from the ultrasonic examination (see Sect. 7.1.6). The HAZ of each weld pass is clearly visible, and it appears that the HAZ of the first pass has deflected the "wing-tips" of the flaw toward the midthickness of the plate before arresting. The

M&C PHOTO YP3328

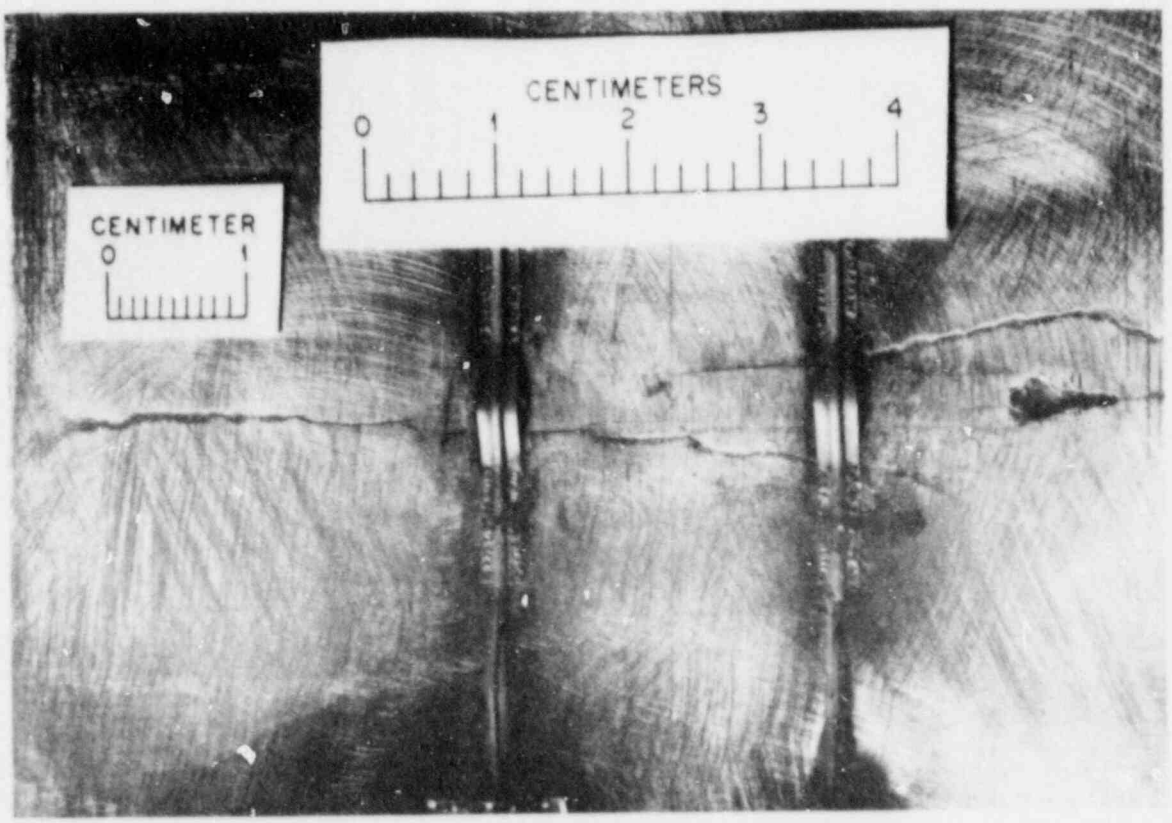

Fig. 7.10. Crack in HAZ of EB weld on surface of plate CP-17.

M&C PHOTO YP3827

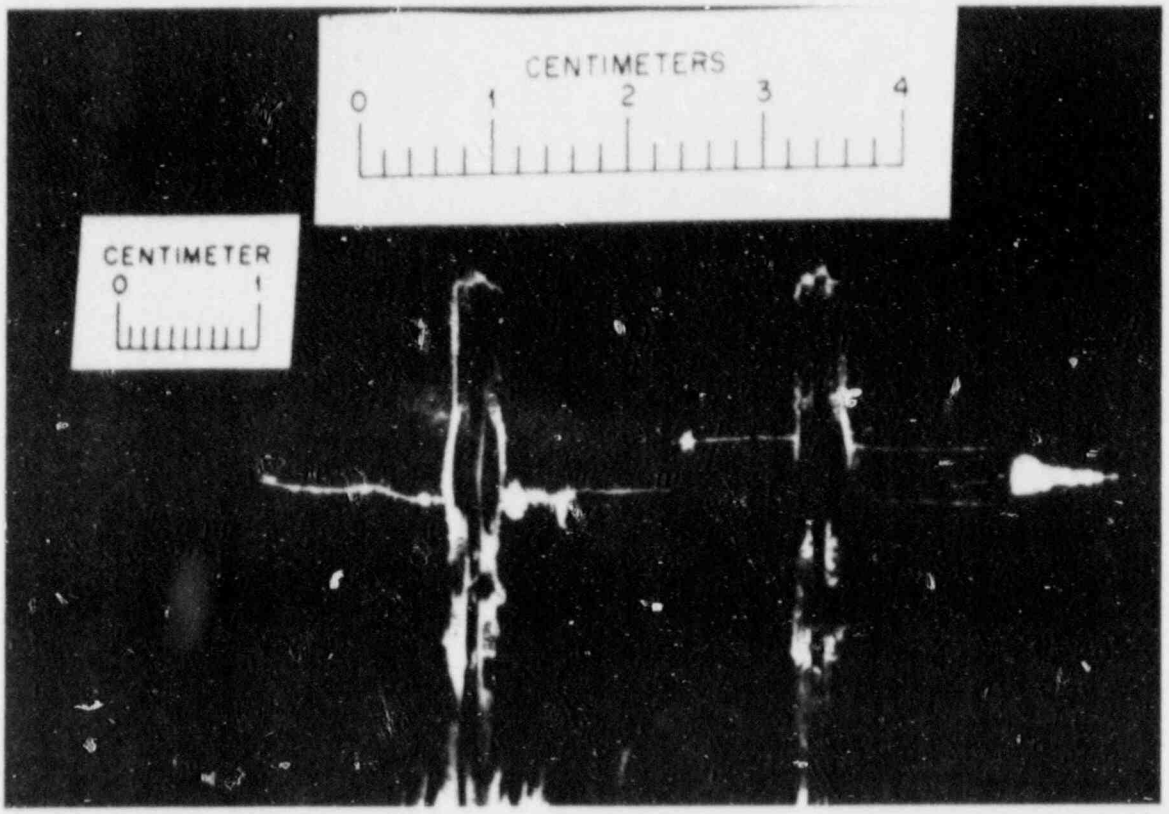

Fig. 7.11. Same area of plate CP-17 as shown in Fig. 7.10 during dye penetrant examination.

lighter colored bands are unbroken ligaments that are deeply undercut. The pop-ins observed during the final stages of loading, before rupture, may have been the breaking of these ligaments.

7.1.6 Dye penetrant and ultrasonic examination of plates CP-15 and -17

Plate CP-15 was examined after the second pop-in of the flaw, while plate CP-17 was examined after the first pop-in. Both penetrant and ultrasonic techniques were applied. The penetrant technique used a Zyglo ZL-22A material (Magnaflux product). This fluorescent dye penetrant is viewed with an ultraviolet light and is considered a high-sensitivity indicator for surface-breaking flaws. Results of the penetrant tests are documented in Figs. 7.7 and 7.11.

The ultrasonic examination was performed with a 5-MHz search unit with a contact wedge to produce a 45° shear wave in steel. The measurements depend on the detection of the tip-diffracted signals from the crack. Scanning was performed from the unclad surface in two directions (perpendicular to the crack surface) to detect the maximum through-wall crack depth as referenced to plate thickness and centerline. Initial

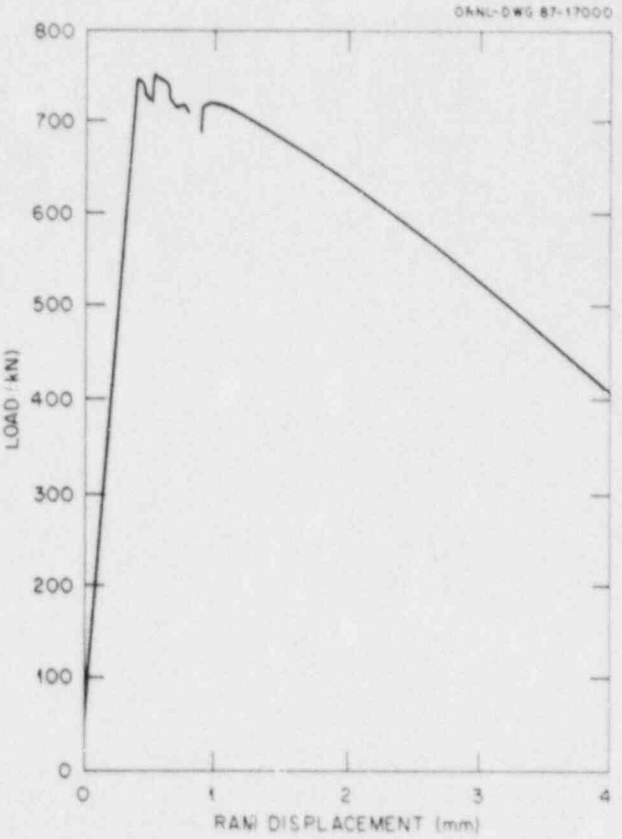

Fig. 7.12. Load-displacement record of events during rupture of plate CP-17.

M&C PHOTO YP3826

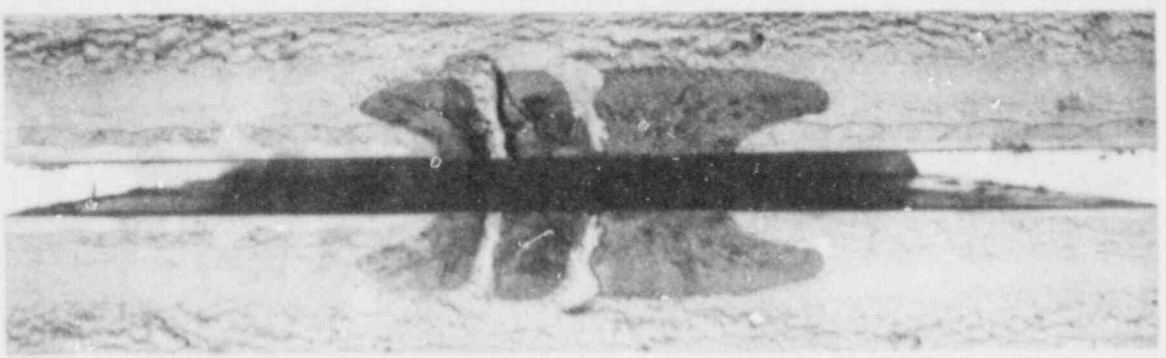

Fig. 7.13. Fracture surfaces of broken halves of plate CP-17.

M&C PHOTO YP3823A

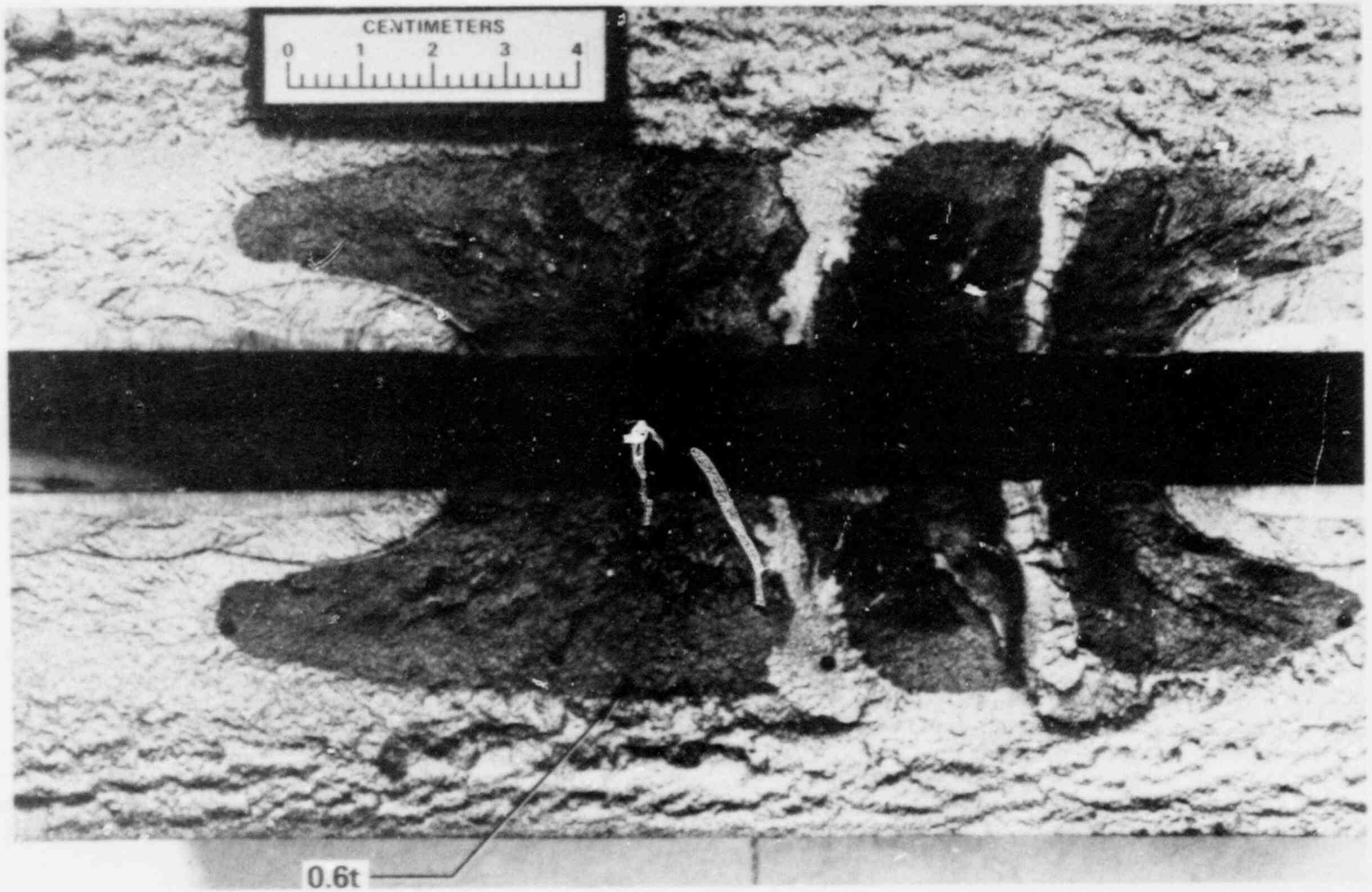

Fig. 7.14. Close-up of heat-tinted, arrested flaw shape of plate CP-17 and six data points from ultrasonic examination (see Sect. 7.1.6).

attempts on CP-15 estimated the maximum flaw depth to be about one-half the thickness (t).

Crack-tip measurements on CP-17 predicted a maximum crack depth of ~60% of the thickness [30.5 mm (1.2 in.)] at a position ~25.4 mm (1 in.) to one side of the centerline. This data point and five others have been plotted on the fracture surface and are shown in Fig. 7.14. The maximum extension under the clad was predicted to be on the same side as the 0.6t data point. The prediction of maximum flaw depth at each end was essentially the same [0.38t or 19.1 mm (0.75 in.)]. The accuracy of the tip measurements depends on the detection of the extreme crack extension and is prone to underpredict the depth if the tip is closed or highly stressed.

7.1.7 Testing of plate CP-19

This plate was loaded to a surface strain of about 0.65%, which corresponded to a load of 987 kN (222 kips). The flaw popped-in and arrested at a load of 689 kN (155 kips). Figure 7.15 shows the fairly wide but shallow crater formed on the surface of plate CP-19 as the flaw

M&C PHOTO YP3891

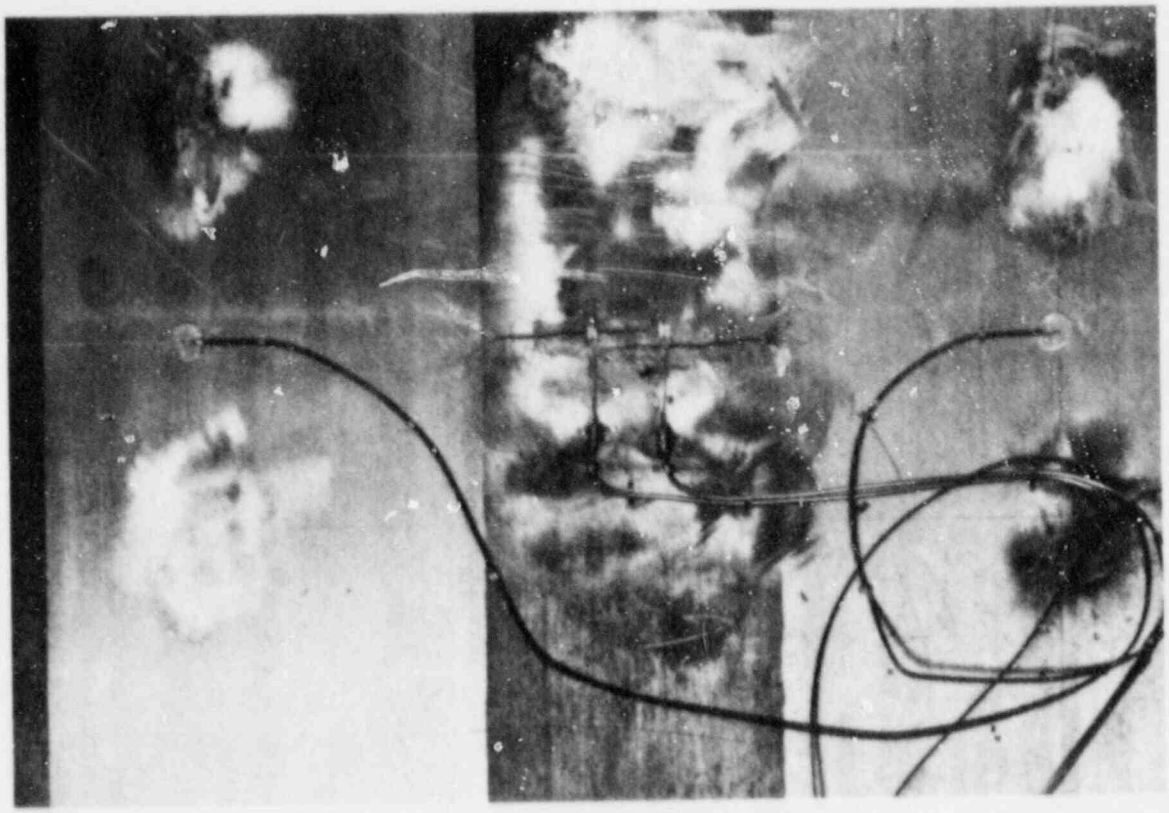

Fig. 7.15. Fairly wide but shallow crater formed on surface of plate CP-19 as flaw tunneled below.

tunneled below. The flaw ran the entire width of the plate until it penetrated the side. Figure 7.16 shows the location on the side of plate CP-19 where the propagating flaw emerged, allowing the acid used for hydrogen-charging to run out of this crevice.

Figure 7.17(*a*) shows the interesting arrested flaw shape formed in plate CP-19. The flaw ran parallel and almost symmetrically about the centerline of the plate cross section. A possible explanation of such a flaw shape is that the neutral axis of the plate during bending must have shifted to some location in the unbroken ligament on the compressive side. Figure 7.17(*b*) shows schematically the displacements (after the flaw arrested) through the plate thickness in the plane of the flaw with the neutral axis near the plate bottom (assuming plane sections remain plane). If this was the case, then the high ductility of the cladding must have sustained high strains on the tensile side as well as relieved the high strains at the tip of the flaw.

M&C PHOTO YP3893

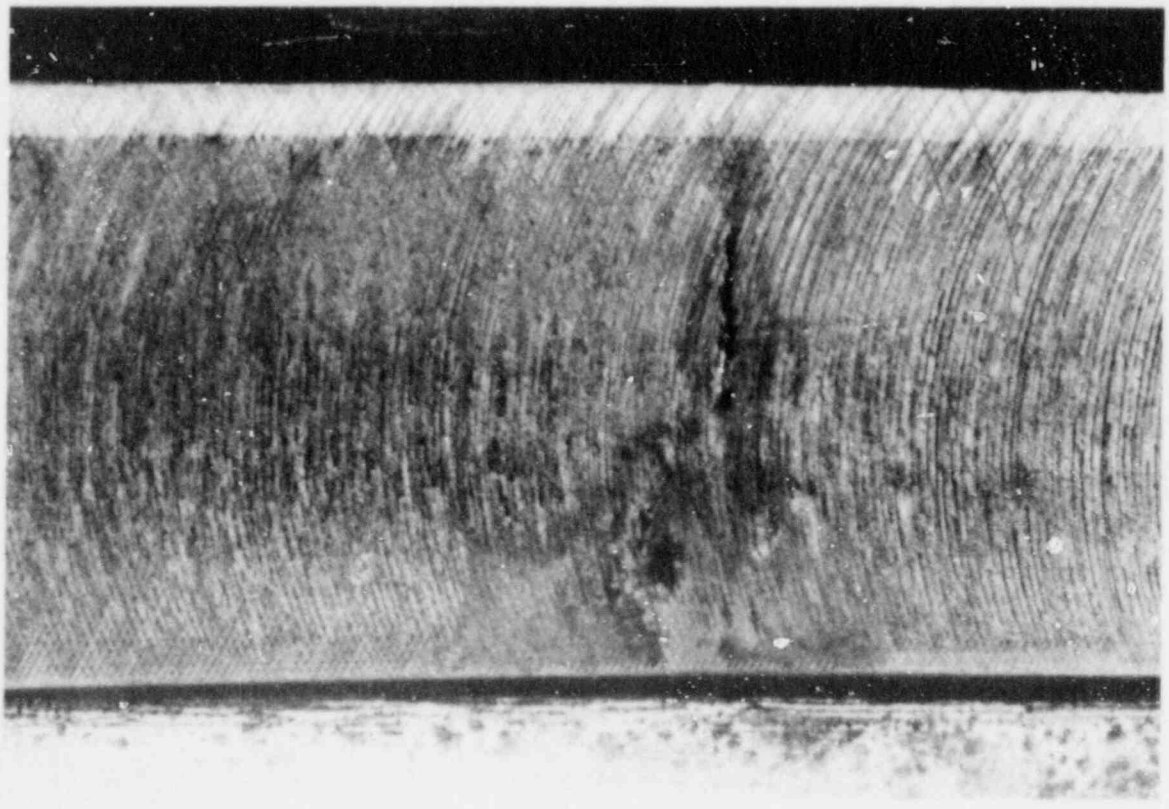

Fig. 7.16. Location on side of plate CP-19 where propagating flaw emerged, allowing acid used for hydrogen-charging to run out of this crevice.

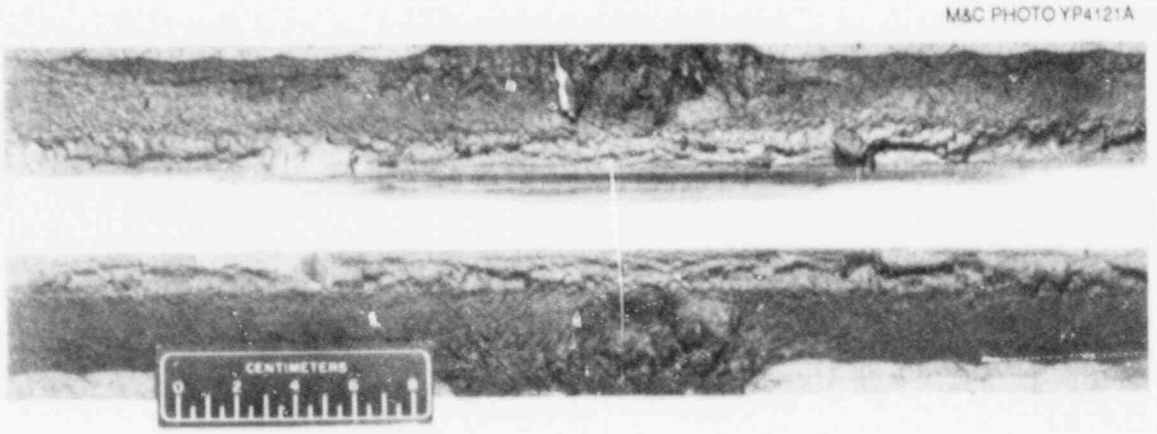

(a)

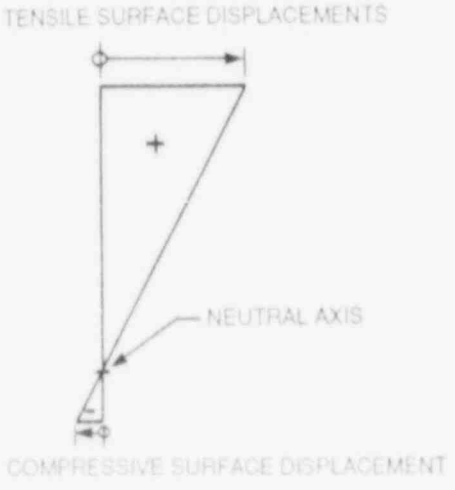

(b)

Fig. 7.17. (a) Interesting arrested flaw shape formed in plate CP-19 and (b) surface displacement after arrest of flaw.

7.1.8 Testing of plate CP-18

This plate was tested at −25°C with pop-in and arrest occurring at 823 and 649 kN (185 and 146 kips), respectively. Figure 7.18 shows the fracture surface of plate CP-18. Note the similarity to the fracture surface of plate CP-19 shown in the previous figure. The tunneling of this flaw was also accompanied by the formation on the surface of a shallow crater similar to the one in plate CP-19 (Fig. 7.15).

The sulfuric acid used during hydrogen-charging of this plate at −25°C froze, and the test had to be discontinued until a more suitable concentration was substituted. After thawing, the acid was removed, but it was the following day before the test was resumed. Just as the plate reached the target load of 823 kN, before any acid was added, and the hydrogen-charging current switched on, the flaw initiated. It is not

M&C PHOTO YP4122

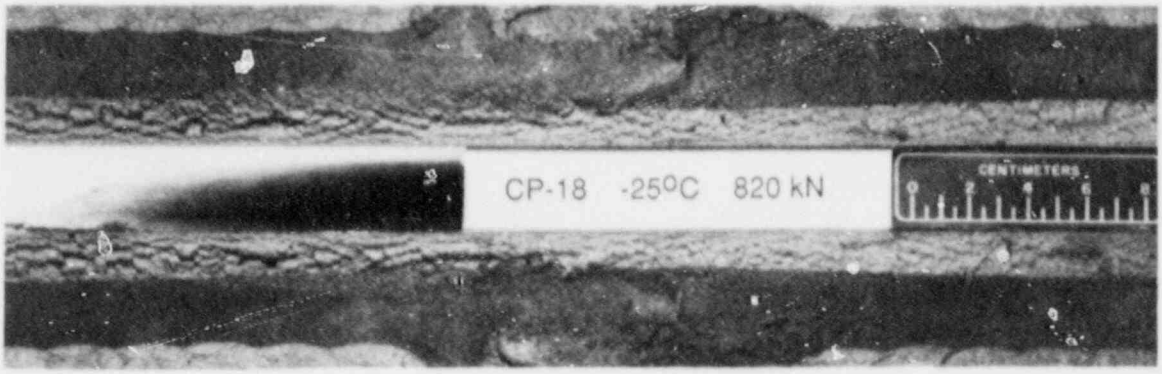

Fig. 7.18. Fracture surface of plate CP-18. Note similarity to fracture surface of plate CP-19 shown in Fig. 7.17.

clear whether a smaller flaw had already initiated in the EB weld region (triggered by the remnants of the acid in the EB weld region).

After the heat-tinting, the plate was loaded at −25°C until it ruptured at 698 kN (157 kips).

7.1.9 Testing of plate CP-21

Of the six tested, this was the only unclad plate, providing a comparison to the clad ones; it used the same load as plate CP-15, namely, the 676 kN. The test was performed at room temperature, and the plate ruptured. Figure 7.19 shows the fractured surfaces of the two broken halves of plate CP-21. The beach marks formed on the surface indicate a canoe-shaped crack front as the flaw propagated in a direction parallel

M&C PHOTO YP4123

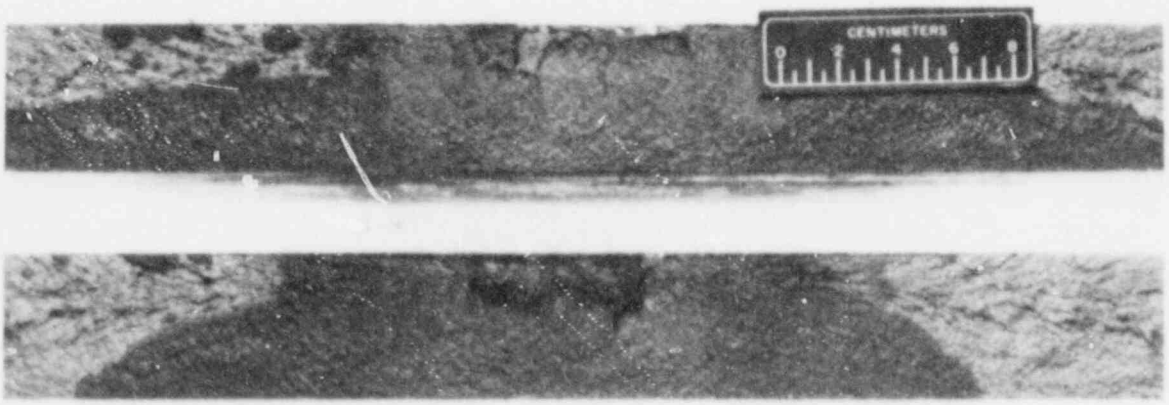

Fig. 7.19. Fracture surfaces of two broken halves of plate CP-21. Plate ruptured ~2.5 h after start of hydrogen charging.

to the top surface before the plate ruptured. The dark discoloration formed by the acid and should be disregarded.

7.1.10 Testing of plate CP-20

This was a clad plate tested at −25°C and at a target strain of 0.41% corresponding to a load of 868 kN (195 kips). The plate ruptured ~2.5 h after the start of the hydrogen-charging. The fracture surfaces of plate CP-20 are shown in Fig. 7.20.

The strain and load levels for this plate form an upper bound to the load-bearing capacity of the clad plate at −25°C. Although not easily comparable to the load (676 kN) that ruptured the unclad plate at room temperature, it does provide another indication of the enhanced crack-arrest capability of clad plates.

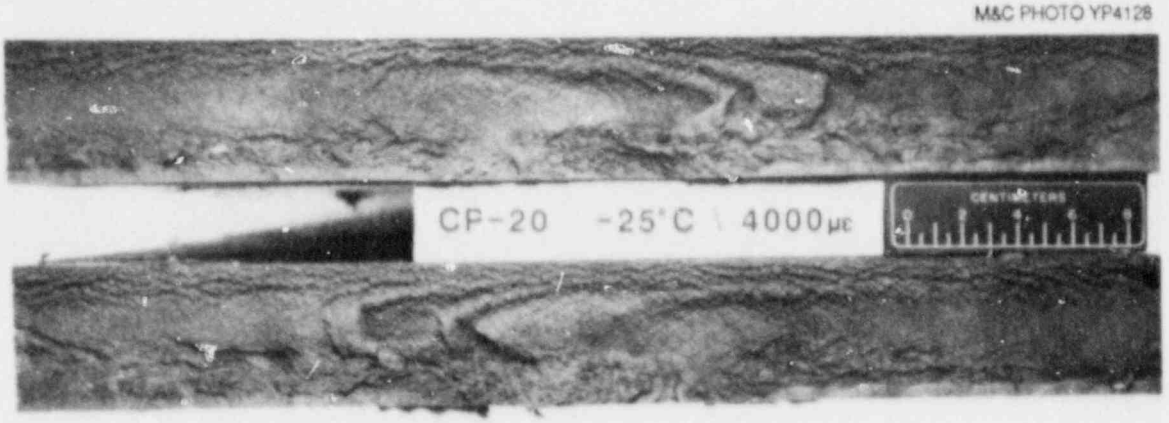

Fig. 7.20. Fracture surfaces of plate CP-20.

7.1.11 Discussion of results

The tough surface layer of cladding and HAZ seemed to have contributed significantly to the load-bearing capacity of the plates by arresting flaws at loads and temperatures that have ruptured unclad plates, as seen by comparing the results of the tests on plates CP-15 and -21. In fact, the clad plate CP-19 arrested a flaw subjected to a driving force (as measured by the target load) almost 50% higher than that which broke an unclad plate. Moreover, the residual load-bearing capacity of plates, as measured by the critical loads in initiation experiments with fairly large flaws, was generally greater than required to break the unclad plate, even though the test temperatures were lower by 50°C.

The tests indicate a propensity of propagating flaws to tunnel, even without the aid of the tough surface layer composed of cladding and HAZ; tunneling also has occurred in the base metal portion of the clad plates

and in the unclad plate. This potential for tunneling results from the location of the maximum stress-intensity factor for short flaws occurring somewhat below the surface when the flaw is in a stress gradient as in these tests.

The ductility of cladding appears to have been a necessary ingredient in increasing the load-bearing capacity of clad plates. However, it is not clear at this time whether cladding alone, without benefit of the tough HAZ that played a pronounced role in arresting propagating flaws, would have also elevated the load-bearing capacity. In case of radiation-embrittled reactor pressure vessels, the HAZ will most likely undergo toughness degradation similar to that of base metal and would therefore not play such a prominent role in arresting propagating flaws.

7.2 Flaw Characterization Studies of Clad BWR Vessel Material

K. V. Cook R. W. McClung

7.2.1 Introduction

Nondestructive examinations conducted to determine flaw density in segments of the Hope Creek Unit 2 boiling-water reactor (BWR) and Pilgrim Unit 2 pressurized-water reactor (PWR) pressure vessels were completed. A topical report, *Flaw Density Examination of a Clad Boiling Water Reactor Pressure Vessel Segment* [NUREG/CR-4860 (ORNL/TM-10364)], was published in April 1987; however, a revision to that report adds a brief comparison of the limited experimental data with the predictions from the Marshall Report and the Octavia function.[3] Results indicate that the flaw density predictions may be nonconservative for the small flaws.

An oral presentation and a paper summary, entitled "Detection and Characterization of Flaws in Segments of Light-Water Pressure Vessels," were prepared for the 15th Water Reactor Safety Information Meeting, October 27, 1987, at the National Bureau of Standards.

The experimental/prediction comparison and technical studies activities performed during this period are summarized in the following subsections of this report. Further details are available in the written material mentioned earlier.

7.2.2 Comparison of experimental and predicted results for Unit 2 Hope Creek vessel segment

A brief comparison was made between the apparent flaw density detected in this examination and the predictions made in the Marshall Report. In a 1976 version of the Marshall Report, an estimate was made of 3.6 defects (of all sizes) in a 3-m^3 volume of weld material. A table in the 1982 Marshall Report estimated that the flaw population per vessel

would be

Defects	Depth (in.)
0.92	>0.25
0.39	>0.5
0.06	>0.5
0.0076	>1.5

The 1982 Marshall Report estimates were further compared in Appendix B of a United Kingdom Atomic Energy Establishment report[4] with the Octavia function[5] and other flaw density estimates. The Octavia function was developed by the U.S. Nuclear Regulatory Commission (NRC) to calculate the probability of pressure vessel failure from operationally caused pressure transients that can occur in a PWR and determines the probability of occurrence for various size flaws. Based on "operational experience and discussions with metallurgical personnel," the Octavia function predicts fewer cracks <10 mm deep than predicted by the Marshall Report.

In the very limited examinations of the Hope Creek pressure vessel sections, the first indication of flaw density using *American Society of Mechanical Engineers (ASME) Code* procedures implied significantly more apparent flaws than would have been predicted. Clad removal demonstrated that 11 of the 12 indications were clad-associated anomalies. The one remaining indication was demonstrated by both nondestructive and destructive methods to have a through-wall dimension of about 6 mm (0.24 in.). It is recognized that examination of only 3 m (10 ft) of weldment offers very limited data when compared to the extent of welding in only a single pressure vessel. However, the detection and confirmation of the flaw in the arbitrarily selected sections demonstrate a circumstance where the Marshall Report estimates are nonconservative.

7.2.3 Nondestructive examination of sections from Pilgrim Unit 2 pressure vessel

Four sections from the as-fabricated Pilgrim vessel were purchased by the HSST Program. Three of the four sections were of adequate size for the flaw density studies; therefore, the three larger sections were screened for the expected presence of weld seams. No welds were located, so activities were restricted to a penetrant examination of the cladding and a manual ultrasonic examination of the underclad regions contained in the three larger sections. The inside clad surfaces were covered with a paintlike coating by the manufacturer to protect against erosion-corrosion effects prior to shipment to the reactor site. The coating was designed for stripping from the vessel; however, it could not be manually removed [especially in areas where the high-temperature flame-cutting (salvage) operation had melted it onto the surface]. After unsuccessful attempts to manually remove the coating, the three pieces were shipped to the K-25 Plant for acid-bath cleaning. Two cleaning operations were performed to

get the clad surface in condition for penetrant inspection. Figure 7.21 shows the three pieces of the Pilgrim vessel sitting on wooden skid pallets after acid cleaning.

7.2.3.1 Liquid penetrant inspection of three segments of Pilgrim Unit 2 vessel. After acid cleaning and an alcohol wipe of the clad surfaces, we inspected ~5 m^2 (53 ft^2) of cladding for surface-breaking flaws with a Zyglo fluorescent penetrant technique. Magnaflux ZL-22A oil-base dye-containing penetrant was applied for a minimum of 30 min. We then manually removed the penetrant with alcohol-dampened cloths. After removing the surface penetrant, we inspected for surface-breaking indications using a 100-W fluorescent light (black light) in a darkened area of Building K-1401. No significant indications were detected. A light background glow, after significant time delay, indicated surface roughness exceeding that observed on the Hope Creek pieces. We suspect that the acid cleaning performed on these sections (and not on the Hope Creek sections) provided the increased sensitivity background.

7.2.3.2 Examination for underclad cracking using manual ultrasonics. A dual-element search unit that generates nominal 70° longitudinal beams with a second angle to produce a pitch-catch maximum sensitivity to underclad cracking at a depth of about 9.5 mm (0.375 in.) was used to examine for underclad cracking. The same couplant, equipment, and technique used for the Hope Creek task was used for the Pilgrim task. The same block used to establish secondary calibration procedures for Hope Creek underclad cracking studies was used for preliminary calibration of our ultrasonic screening tests (to select one of the Pilgrim pieces for use as an underclad calibration standard). This preliminary calibration block is shown in Fig. 7.22 and was fabricated for a previous NRC activity. We arbitrarily assigned P-1, -2, and -3 identification to the three Pilgrim vessel sections (see Fig. 7.21). Section P-1 was selected for the underclad cracking calibration block. Figure 7.23 shows block P-1 with the rectangular-shaped, dual-angle, 70° search unit located on the clad surface. Note the two side-drilled hole reflectors located within the machined slot just to the lower right of the search unit and scale. Two more side-drilled holes are located in a second slot just above the metal lifting plate that has been welded to the piece (at the nearest corner of the vessel section). These four holes (reflectors) are located at two depths below the clad surface, are all the same diameter [4.76 mm (3/16 in.)], and were drilled at least 10.16 cm (4 in.) deep. The centerline depths (from the clad surface) of these reflecting surfaces are 1.42 and 3.81 cm (0.56 and 1.5 in.), respectively. The 1.42-cm reflectors provided our basic calibration. Manual scans were made both parallel and perpendicular to the ~8.9-cm-wide (3.5-in.) strip clad by 2-m-long (6.5-ft) overlay sections obvious in Fig. 7.23. The nominal practice of skewing the search unit while scanning was used. Block P-2 was the only one in which an indication of note was located. This indication's amplitude is about 5 dB less than that from the calibration reflector, and it appears to be a spotlike reflector. A stop-stare positioning of the search unit was required to obtain the maximum amplitude response. Additionally, the search unit position is difficult to relocate. This indication is physically located near a position where two of the 8.9-cm-wide strip clad sections join and at a depth of about one-half that of the calibration reflector (i.e., near the clad-to-vessel wall interface).

K/PH 87-2643

Fig. 7.21. Pilgrim Unit 2 pressure vessel pieces (arbitrarily designated as P-1, -2, and -3 with P-3 located at front of the photograph).

ORNL-DWG 81-22147A

DESCRIPTION OF FLAWS IN BLOCK 2			
		DIMENSIONS [mm (in.)]	
FLAW IDENTIFICATION	DESCRIPTION	LENGTH	DEPTH OR DIAMETER
1	MACHINED NOTCH	74.7 (2.94)	12.7 (0.5)
2	MACHINED NOTCH	69.9 (2.75)	6.4 (0.25)
3	EB WELD CRACK	76.2 (3.0)	9.5 (0.375)
5	MACHINED NOTCH	46.0 (1.9)	5.6 (0.22)
6	EB WELD CRACK	76.2 (3.0)	9.5 (0.375)
S1	MACHINED SLOT BELOW REFERENCE CLAD SURFACE	12.7 (0.5)	5.6 (0.22)
S2	MACHINED SLOT BELOW REFERENCE CLAD SURFACE	25.4 (1.0)	5.6 (0.22)
A	MACHINED HOLE	228.6 (9.0)	15.86 (5/8)
B	MACHINED HOLE	228.6 (9.0)	15.86 (5/8)
C	MACHINED HOLE	76.2 (3.0)	4.75 (3/16)
D	MACHINED HOLE	76.2 (3.0)	4.75 (3/16)
E	MACHINED HOLE	76.2 (3.0)	4.75 (3/16)
F	MACHINED HOLE	76.2 (3.0)	9.53 (3/8)
G	MACHINED HOLE	76.2 (3.0)	9.53 (3/8)
H	MACHINED HOLE	76.2 (3.0)	9.53 (3/8)

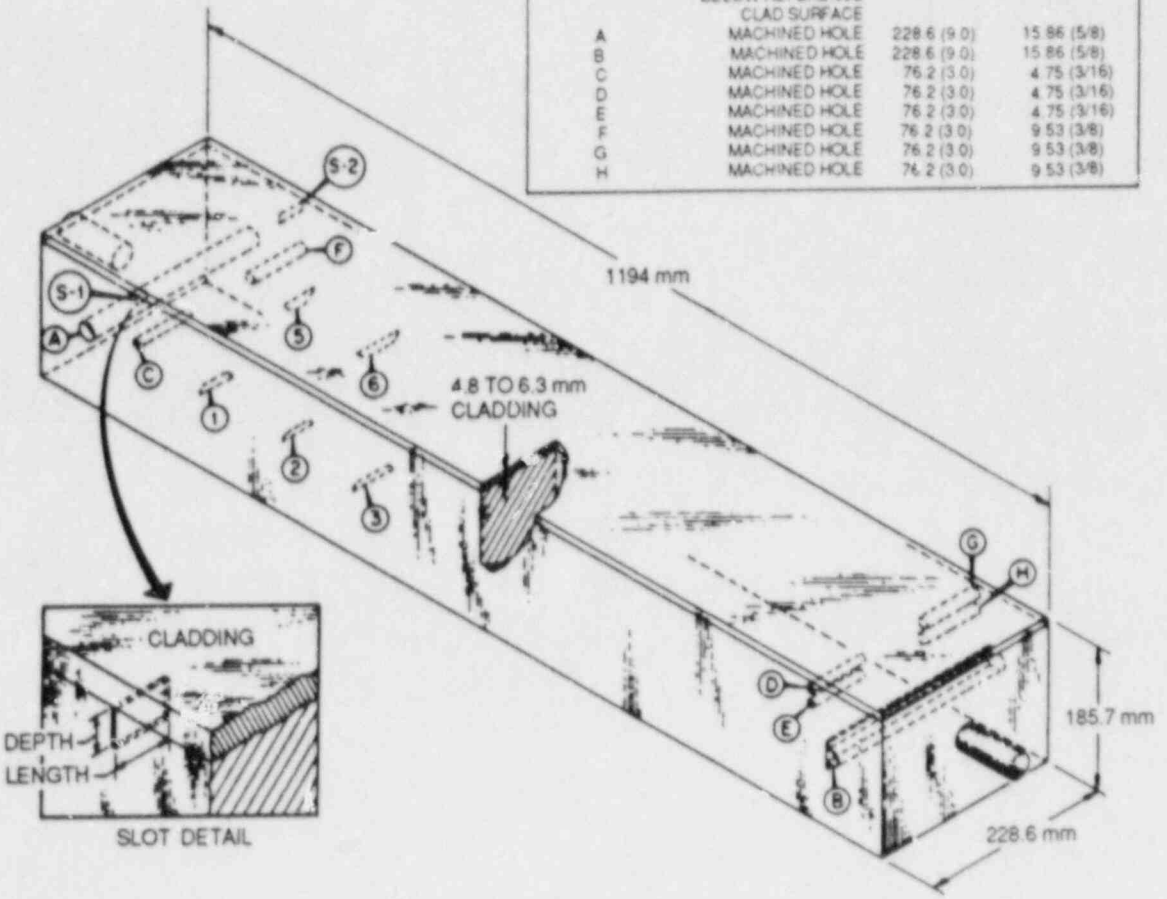

FLAWED BLOCK NUMBER 2

Fig. 7.22. Flawed block 2 used for preliminary underclad cracking calibration.

Fig. 7.23. Pilgrim Unit 2 pressure vessel piece (P-1) in which ultrasonic calibration reflectors are machined.

7.2.4 Results and conclusions

A comparison of limited experimental data taken on the Hope Creek Unit 2 segment with the predictions made by the Marshall Report and the Octavia function seem to make the predictions nonconservative for small flaws.

The nondestructive examinations completed on ~5 m^2 of clad surface contained in three pieces of the Pilgrim Unit 2 pressure vessel detected only one ultrasonic indication that compares in signal amplitude to a calibration reflector similar to that used in vessel field-type inspections. The amplitude of this indication is only about half that of the calibration reflector when maximized and appears to have very little length. Decisions have not been made on further potential exploration of this indication.

7.3 Finite-Element Analyses of Plates CP-15, -17, -18, and -19

J. S. Parrott B. A. Owens*

An elastic finite-element posttest analysis of the initial flaw of plate CP-15 was made using the ORMGEN/ORVIRT[6,7] fracture analysis system with the ADINA[8] finite-element code. The initial flaw of the CP-15 plate was located exactly in the center of the top surface. Because of the symmetry of crack location, cladding location, crack shape, loading, and support location, it was only necessary to generate a one-quarter plate model to analyze the entire plate. This model contained 3750 nodes and 733 20-noded isoparametric elements. In the model, the symmetry planes had to have certain constraints. The nodes in the X = 0 plane were constrained to have no motion in the X direction. Likewise, the nodes outside the crack front in the Z = 0 plane were constrained not to move in the Z direction. These two restrained planes are shown in Fig. 7.24.

The model was 5.08 cm thick, 20.32 cm wide, and 45.72 cm in length. A 0.508-cm layer of cladding and 0.762-cm layer of heat-affected metal were also present as portions of the top surface of the plate. The general dimensions of the model, cladding layer, and HAZ are also shown in Fig. 7.24. Material properties for the base metal (A 533 grade B chemistry steel), the cladding (three-wire, series-arc, stainless steel overlay), and the HAZ required for the analysis are tabulated in Table 7.2. These properties were Young's modulus and Poisson's ratio corresponding to a temperature of 22.2°C, which is the test plate temperature. The thermal coefficient of expansion was not needed because no thermal strain was present.

Only the first load step of a possible multistep inelastic analysis was used in this problem. This allowed the elastic first step results to be scaled to the results obtained from a fully applied elastic load. The

---

*Undergraduate student, College of Engineering, Tennessee Technological University, Cookeville, Tennessee.

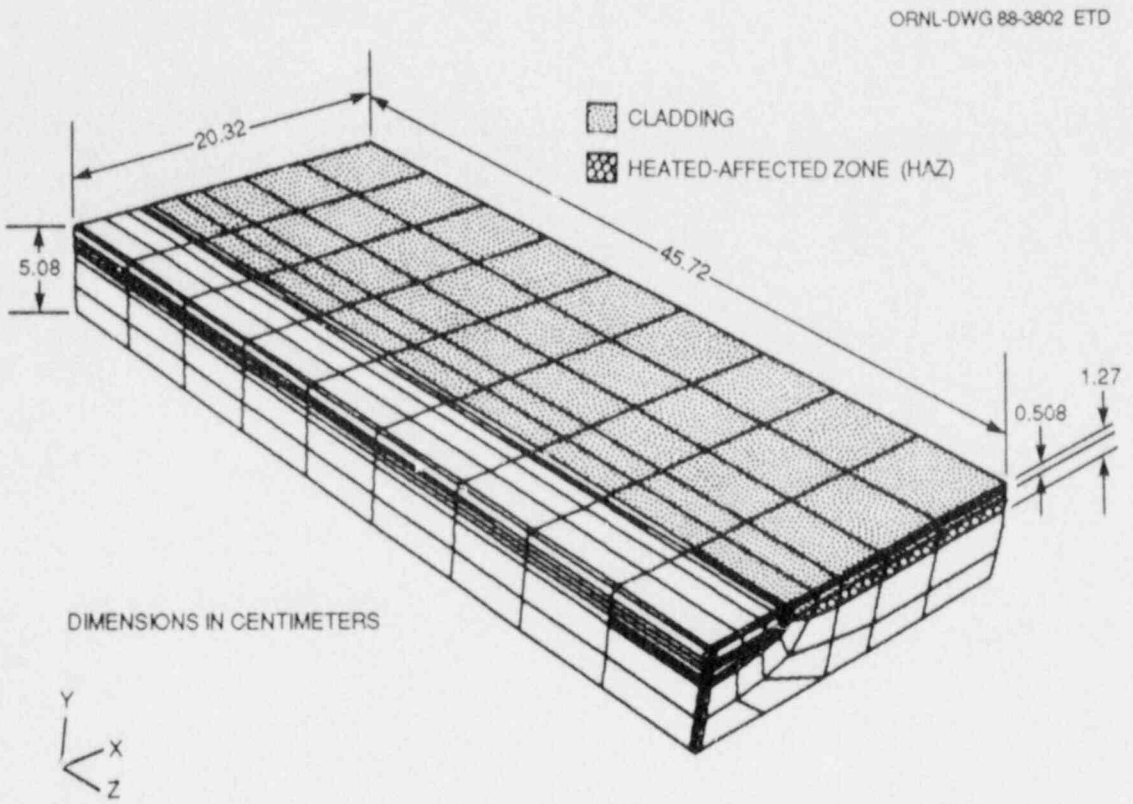

Fig. 7.24 Final element model of CP-15.

Table 7.2. Material properties

Material	Young's modulus, E [GPa (psi)]	Poisson's ratio, ν
Base metal A 533 grade B chemistry steel	206.08 (29.89 × 10^6)	0.3
Cladding 301 stainless steel	190.36 (27.61 × 10^6)	0.3
HAZ metal	198.22 (28.75 × 10^6)	0.3

total applied load of 169 kN (38 kips) (one-quarter of that applied to the entire plate), and plate supports are shown in their proper location in Fig. 7.25. Loading was applied while the plate was at a uniform temperature of 22.2°C. No thermal strain was present because of the uniform temperature and freedom of the plate to expand and contract.

The objective of the entire analysis was to determine the stress-intensity factors (K_I's) along the crack front. This was accomplished

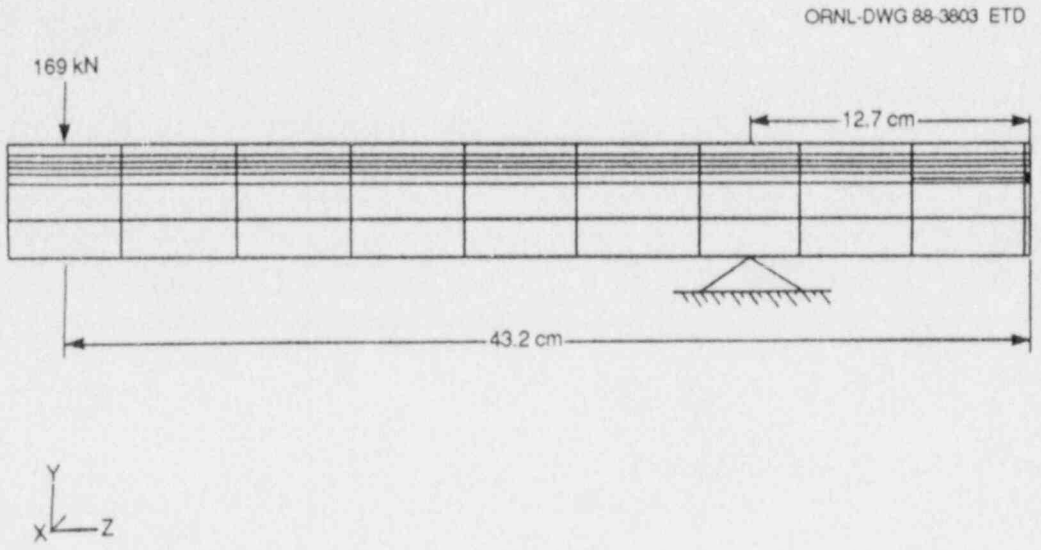

Fig. 7.25. Load and support location used on finite-element model of initial flaw of CP-15.

using ORVIRT after the mesh was generated and the plate stresses calculated. ORMGEN was used to generate the model mesh, and ADINA was employed to calculate stress throughout the model. The stress-intensity factors calculated using ORVIRT are tabulated in Table 7.3. These values are graphed vs the clockwise angle along the crack front in Fig. 7.26. The crack in the model was then closed, and ADINA was run again to find the stresses in the model. These stresses were then found to favorably compare with those obtained using simple beam theory providing confidence that the ADINA ORVIRT results with the crack open were correct.

A three-dimensional (3-D) finite-element analysis was also conducted on the intermediate flaw (right side only) of the CP-15 steel plate to determine stress-intensity factors at points along the crack surface. These analyses were performed with the ORMGEN/ORVIRT fracture-analysis system in conjunction with the ADINA-84 finite-element code. The 3-D model was comprised of a quarter segment of the original plate containing 3817 nodes with 753 20-noded isoparametric elements as shown in Fig. 7.27. The material properties for the cladding, HAZ, and the base metal used in this analysis are given in Table 7.4. In reducing the model to one-quarter the original plate, nodes were also restrained in the X = 0 and Z = 0 planes.

Only the first load step of a possible multistep inelastic analysis was used in this problem. This allowed the elastic first step results to be scaled to the results obtained from a fully applied elastic load. The total load applied to this model, 189.7 kN, which is one-quarter of the load applied to the entire plate, along with the plate supports are shown in Fig. 7.28. Because the supports are present where Y = 0 in. and Z = 12.7 cm, the nodes along this line parallel to the X axis had to be restrained in the Y direction. Due to the plate's uniform temperature of −25°C (−13°F), there is no thermal loading thereby reflecting no need for a thermal coefficient of expansion.

Table 7.3. Average stress intensity K_{AVG} along crack front

Angle[a] (deg)	K_{AVG} [MPa·$\sqrt{m}$ (ksi·$\sqrt{in.}$)]
0.00	112.2 (102.1)
2.81	78.2 (71.1)
19.69	72.2 (65.7)
36.56	77.7 (70.7)
53.44	87.2 (79.4)
70.31	89.9 (81.8)
87.19	92.2 (83.9)
90.00	92.6 (84.2)

[a]Clockwise from top surface.

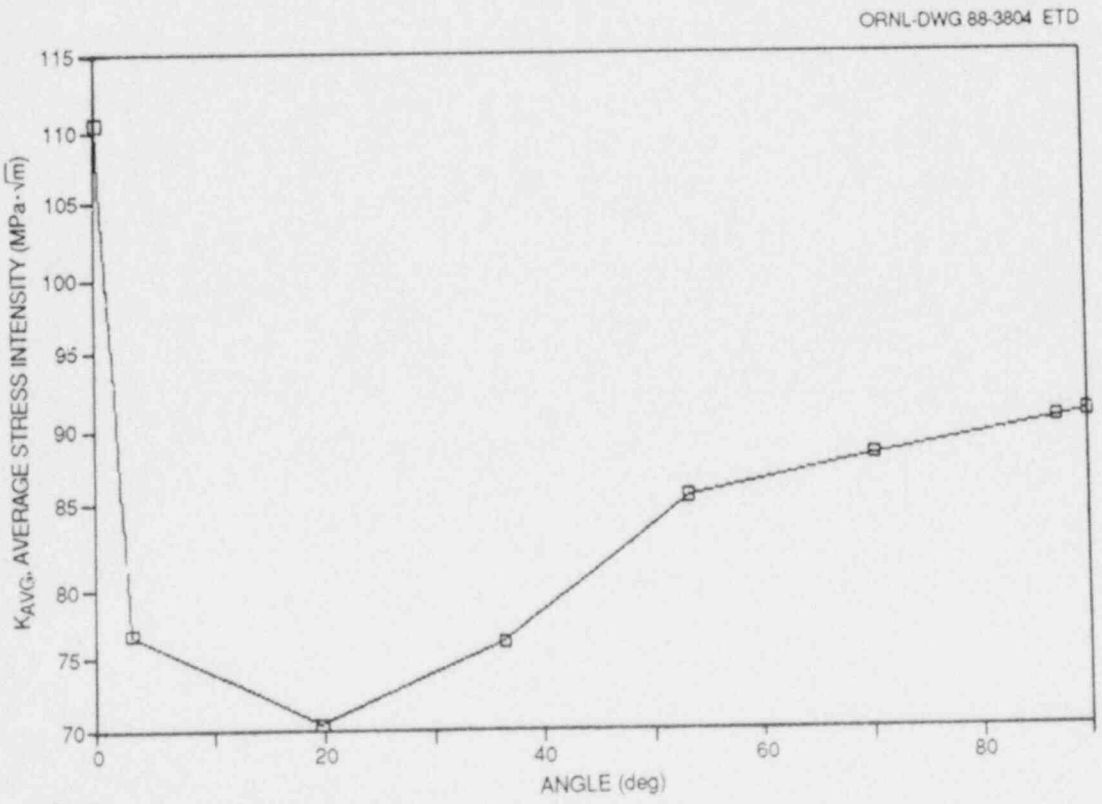

Fig. 7.26. Variation of average stress intensity as function of clockwise angle along crack front.

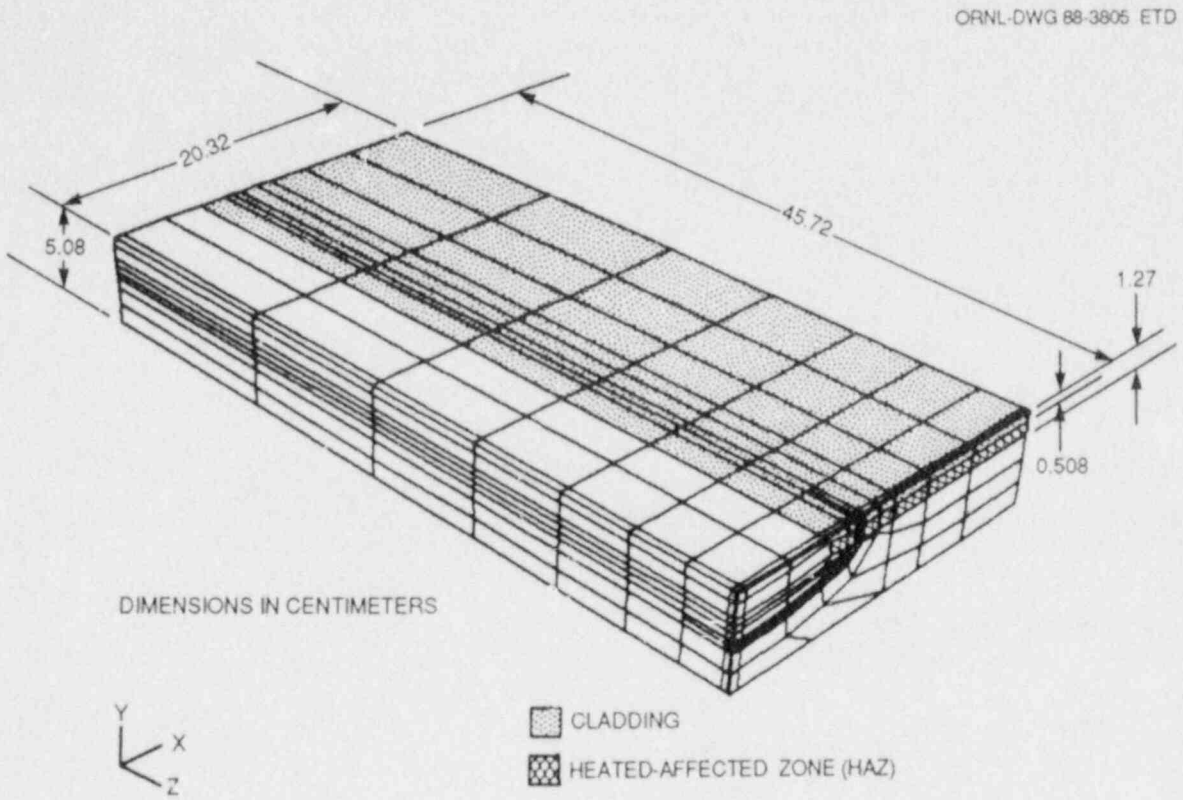

Fig. 7.27. Finite-element model of intermediate flaw of CP-15.

Table 7.4. Material properties

Material	Young's modulus, E [GPa (psi)]	Poisson's ratio, ν
Base metal A 533 grade B chemistry steel	208.63 (30.26 × 10^6)	0.3
Cladding 301 stainless steel	193.26 (28.03 × 10^6)	0.3
HAZ metal	200.91 (29.14 × 10^6)	0.3

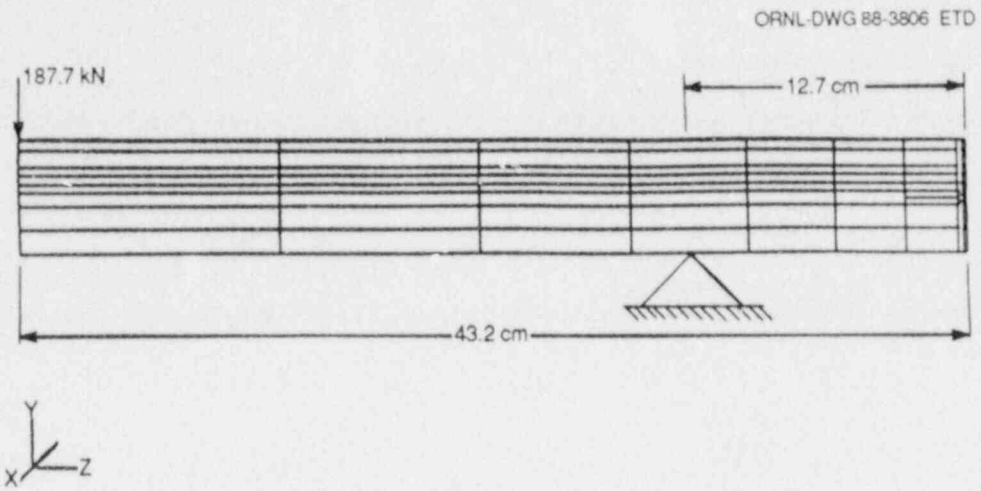

Fig. 7.28. Load and support location used on finite-element model of intermediate flaw of CP-15.

The expected stress-intensity factors (K_I's) along the crack front were determined using ORVIRT. Prior to this, however, a closed crack test was performed to ensure that ADINA was giving the same normal Z stress as was calculated using the simple beam theory.

Three situations were analyzed for the intermediate flaw. These involved having the crack (1) embedded in the cladding, (2) embedded in the HAZ, and (3) extended through the cladding to the plate surface. The analysis of situation (1) resulted in meaningless K values for the clad region nodes. Likewise, erroneous K values were produced for the nodes in the clad region and HAZ from the analysis of situation (2). These K values were therefore disregarded. All the meaningful K values are tabulated along with their corresponding clockwise angles along the crack front for each situation in Tables 7.5–7.7. These K values are graphed as a function of the clockwise angle along the crack front for each situation in Figs. 7.29–7.31.

The final pseudo flaws considered for CP-15, -17, -18, and -19 were analyzed elastically with the ORMGEN/ORVIRT and ADINA computer programs by making several simplifying assumptions:

1. Material properties were assumed to be uniform in all regions of the plate and to consist of the base material properties.
2. A semiellipse was fitted to each of the flaw profiles neglecting the actual deviation that occurs at the HAZ and at the cladding.
3. These pseudo flaws were assumed to penetrate through the HAZ and cladding to the plate surface.
4. Load at arrest was assumed to be that at initial pop-in for each plate.

Only one-quarter plate models were necessary due to symmetry of crack location, crack shape, and loading in each plate. Each model contained 2931 nodes and 589 20-noded isoparametric elements.

Table 7.5. Average stress intensity K_{AVG} of intermediate flaw of CP-15 along crack front assuming embedment of the flaw in the cladding

Angle[a] (deg)	K_{AVG} [MPa·$\sqrt{m}$ (ksi·$\sqrt{in.}$)]
3.68	44.5 (40.5)
9.13	67.4 (61.4)
10.14	49.0 (44.6)
14.45	61.6 (56.1)
22.21	76.4 (69.5)
38.45	89.6 (81.5)
79.98	94.1 (85.6)
90.00	93.2 (84.8)

[a]Clockwise from top surface.

Table 7.6. Average stress intensity K_{AVG} of intermediate flaw of CP-15 along crack front assuming embedment of the flaw in the HAZ

Angle[a] (deg)	K_{AVG} [MPa·$\sqrt{m}$ (ksi·$\sqrt{in.}$)]
9.13	8.8 (8.0)
10.14	24.0 (21.9)
14.45	33.1 (30.1)
22.21	59.1 (53.8)
38.45	84.1 (76.6)
79.98	89.5 (81.4)
90.00	88.5 (80.5)

[a]Clockwise from top surface.

Table 7.7. Average stress intensity K_{AVG} of intermediate flaw of CP-15 along crack front assuming flaw penetrates to the surface

Angle[a] (deg)	K_{AVG} [MPa•√m (ksi•√in.)]
0.00	214.5 (195.2)
3.68	155.5 (141.5)
9.13	92.8 (84.5)
10.14	78.2 (71.1)
14.45	99.1 (90.2)
22.21	107.3 (97.7)
38.45	107.1 (97.5)
79.98	108.6 (98.8)
90.00	107.8 (98.1)

[a]Clockwise from top surface.

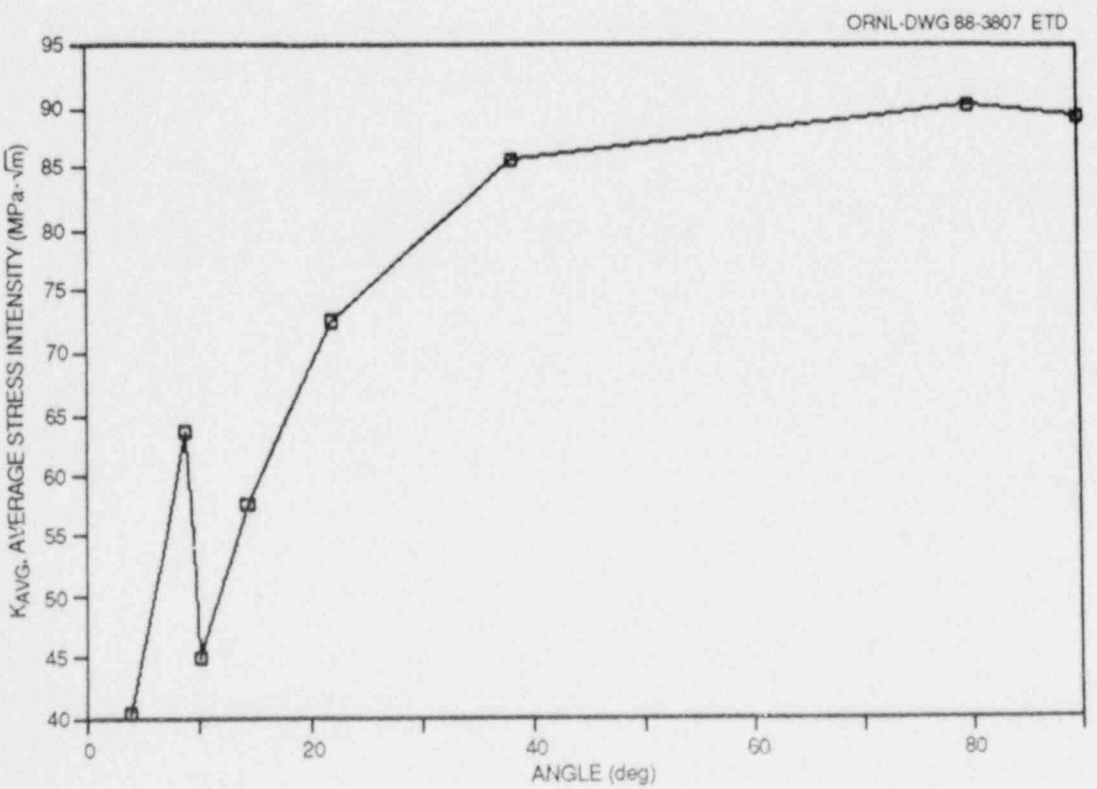

Fig. 7.29. Variation of average stress intensity of intermediate flaw of CP-15 as function of clockwise angle along crack front.

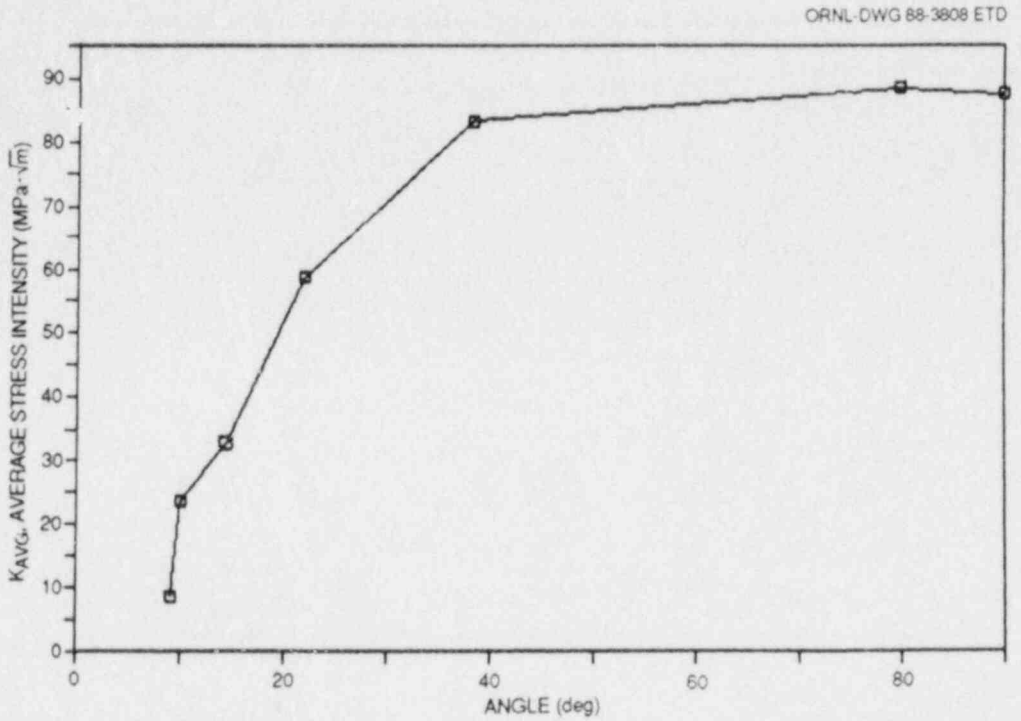

Fig. 7.30. Variation of average stress intensity of intermediate flaw of CP-15 as function of clockwise angle along crack front.

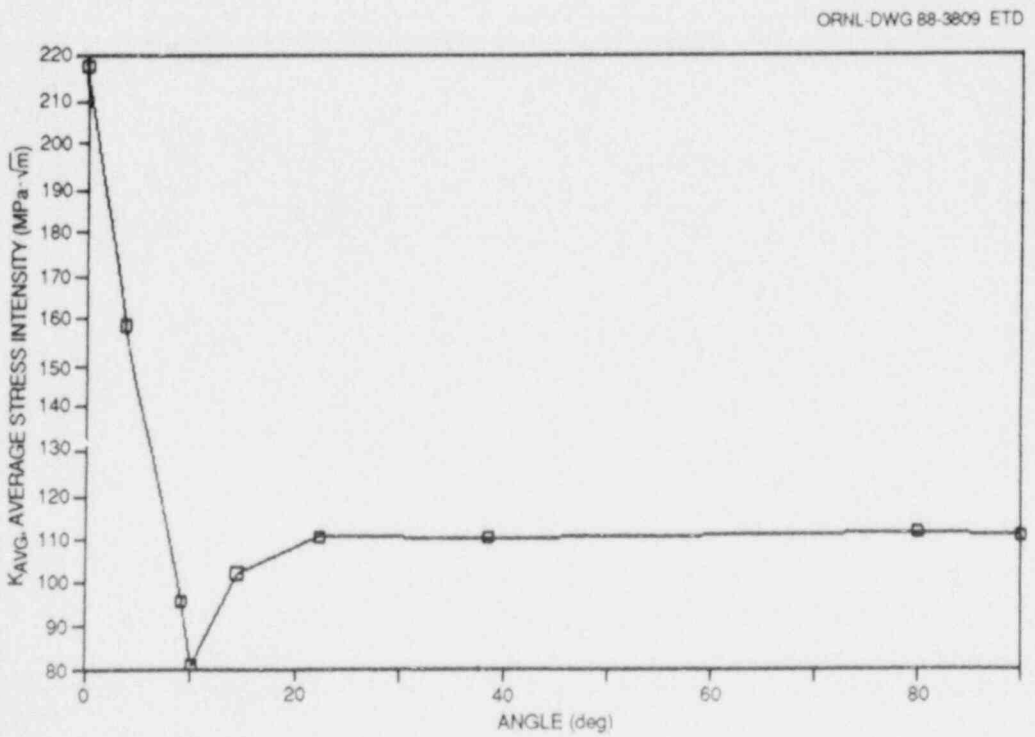

Fig. 7.31. Variation of average stress intensity of intermediate flaw of CP-15 as function of clockwise angle along crack front (flaw assumed to penetrate to surface).

For CP-15, a crack depth corresponding to the known crack width at the cladding interface could be chosen. Surface roughness changes in a crack plane photograph made this possible. There were no physical means of approximating the crack depths of CP-17, -18, and -19. Therefore, the same crack depth-to-width ratio was used for the last three plates as had been used in CP-15. The crack widths and depths as well as the load and temperature of the tests of each plate are given in Table 7.8. A typical crack plane mesh generated by ORMGEN is given by Fig. 7.32.

The average stress intensities calculated as a function of the clockwise angle along the crack front for the final pseudo flaws of CP-15, -17, -18, and -19 (based on the previous assumptions) are tabulated respectively in Tables 7.9–7.12 and plotted respectively in Figs. 7.33–7.36.

Table 7.8. Analyses parameters

Plate	Crack width (in.)	Crack depth (in.)	Load total plate (kN)	Temperature (°C)
CP-15	1.8970	0.6640	676	20
CP-17	1.9110	0.6689	890	20
CP-18	2.090	0.7316	823	−25
CP-19	1.930	0.6756	988	20

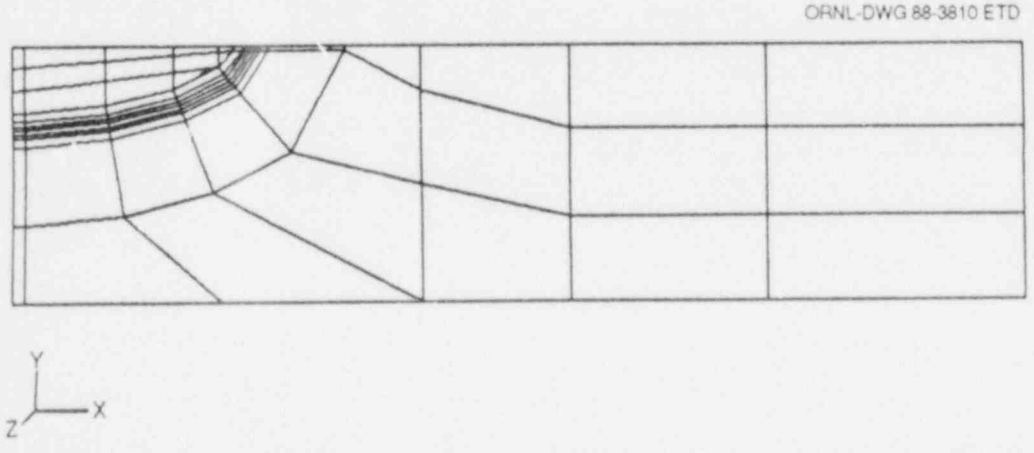

Fig. 7.32. Typical crack plane mesh for final flaws of CP-15, -17, -18, and -19.

Table 7.9. Average stress intensity K_{AVG} along crack front of final flaw of CP-15

Clockwise angle (deg)	K_{AVG} [MPa$\cdot\sqrt{m}$ (ksi$\cdot\sqrt{in.}$)]
0.00	86.5 (78.7)
3.46	84.0 (76.5)
24.23	83.6 (76.1)
45.00	87.4 (79.5)
65.77	86.9 (79.1)
86.54	87.2 (79.4)
90.00	86.4 (78.7)

Table 7.10. Average stress intensity K_{AVG} along crack of final flaw of CP-17

Clockwise angle (deg)	K_{AVG} [MPa$\cdot\sqrt{m}$ (ksi$\cdot\sqrt{in.}$)]
0.00	114.6 (104.3)
3.46	110.9 (100.9)
24.23	110.5 (100.5)
45.00	115.4 (105.0)
65.77	114.5 (104.2)
86.54	114.9 (104.6)
90.00	113.9 (103.6)

Table 7.11. Average stress intensity K_{AVG} along crack front of final flaw of CP-18

Clockwise angle (deg)	K_{AVG} [MPa·$\sqrt{m}$ (ksi·$\sqrt{in.}$)]
0.00	112.3 (102.2)
3.46	108.9 (99.1)
24.23	106.9 (97.3)
45.00	109.8 (100.0)
65.77	107.5 (97.8)
86.54	107.2 (97.5)
90.00	106.0 (96.5)

Table 7.12. Average stress intensity K_{AVG} along crack front of final flaw of CP-19

Clockwise angle (deg)	K_{AVG} [MPa·$\sqrt{m}$ (ksi·$\sqrt{in.}$)]
0.00	127.9 (116.4)
3.46	123.9 (112.8)
24.23	123.2 (112.2)
45.00	128.4 (116.9)
65.77	127.2 (115.8)
86.54	127.6 (116.1)
90.00	126.5 (115.1)

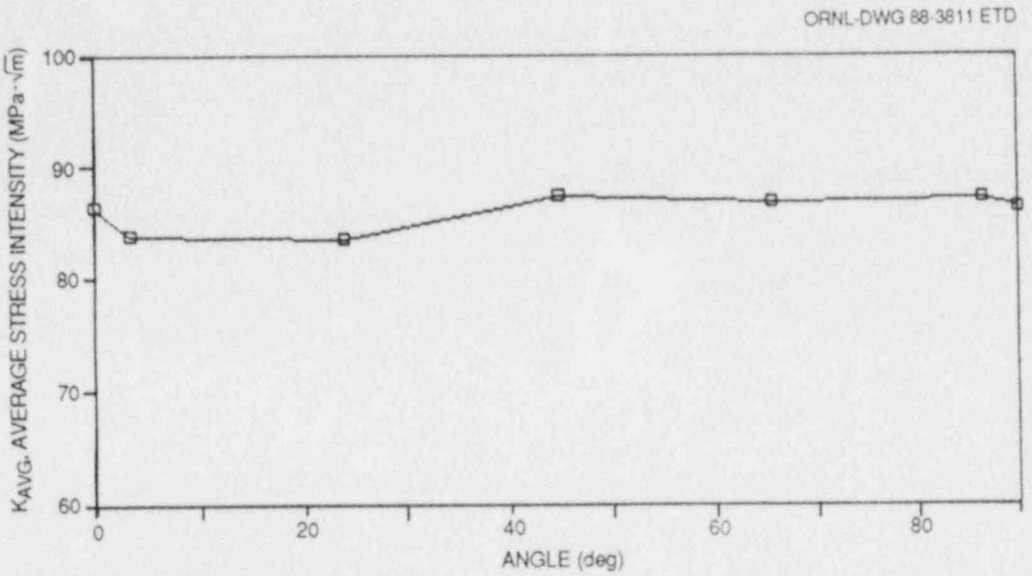

Fig. 7.33. Variation of average stress intensity of final flaw of CP-15 as function of clockwise angle along crack front.

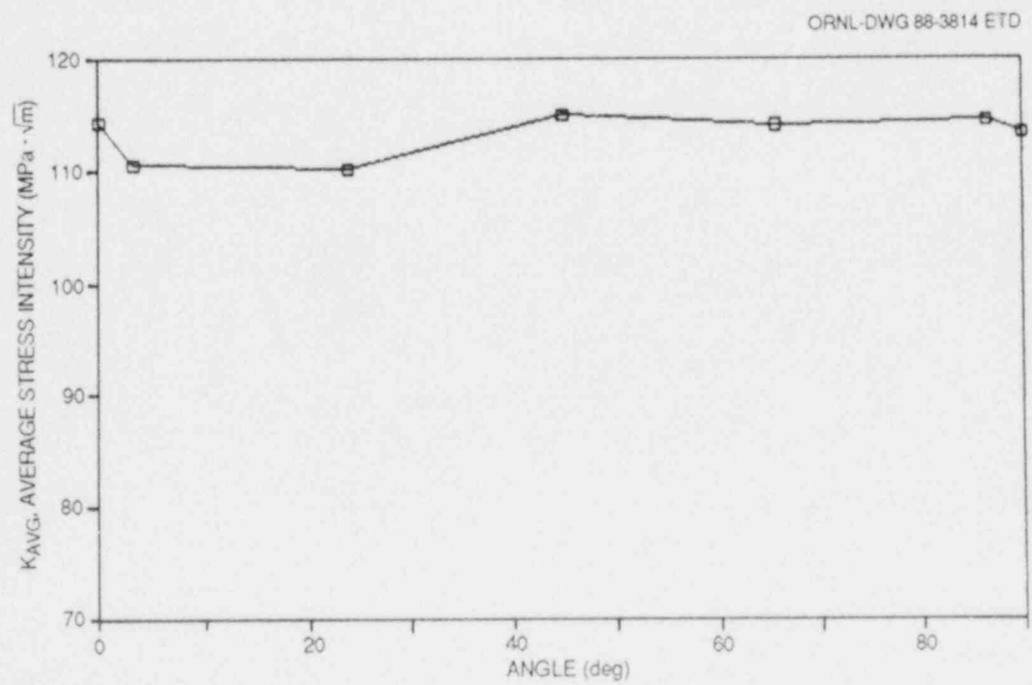

Fig. 7.34. Variation of average stress intensity of final flaw of CP-17 as function of clockwise angle along crack front.

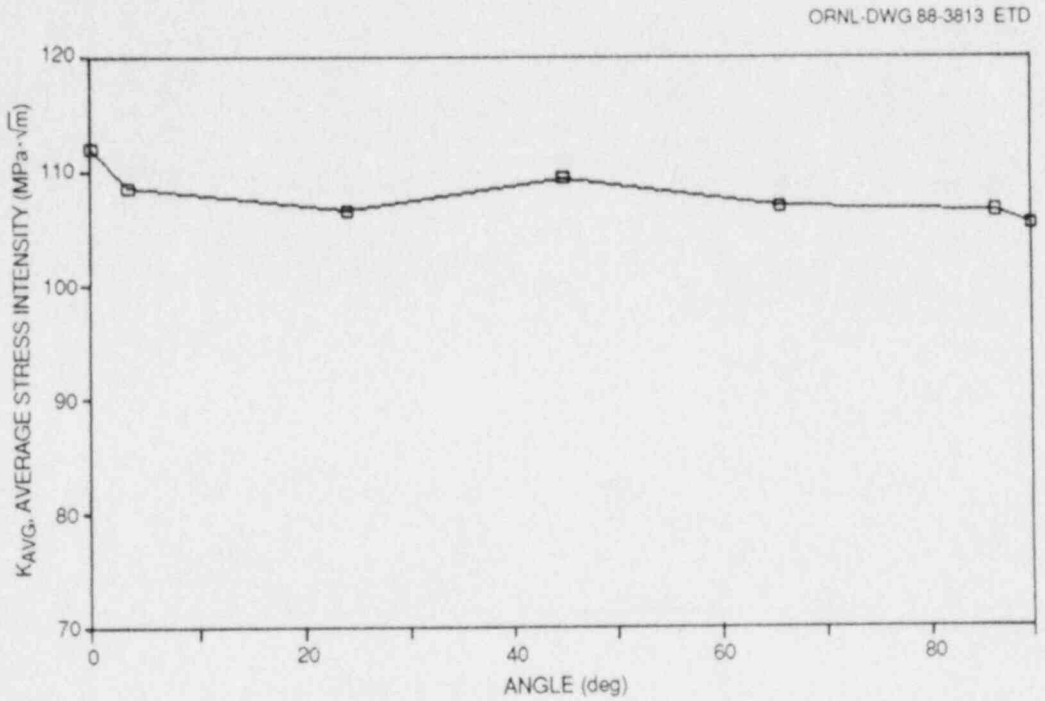

Fig. 7.35. Variation of average stress intensity of final flaw of CP-18 as function of clockwise angle along crack front.

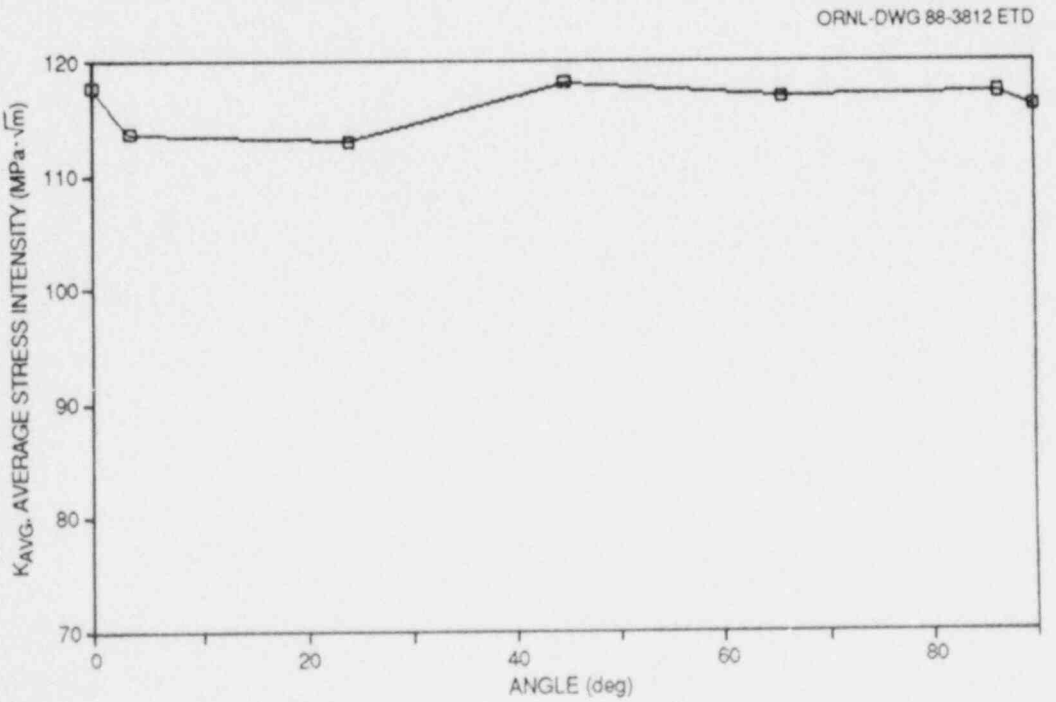

Fig. 7.36. Variation of average stress intensity of final flaw of CP-19 as function of clockwise angle along crack front.

References

1. S. K. Iskander et al., "Crack Arrest Behavior in Clad Plates," pp. 169–87 in *Heavy-Section Steel Technology Program Semiann. Prog. Rep. October 1986–March 1987*, NUREG/CR-4219, Vol. 4, No. 1 (ORNL/TM-9593/V4&N1), Martin Marietta Energy Systems, Inc., Oak Ridge Natl. Lab.

2. W. R. Corwin, "Seventh HSST Irradiation Series: Stainless Steel Cladding," pp. 70–87 in *Heavy-Section Steel Technology Program Semiann. Prog. Rep. October 1985–March 1986*, NUREG/CR-4219, Vol. 3, No. 1 (ORNL/TM-9593/V3&N1), Martin Marietta Energy Systems, Inc., Oak Ridge Natl. Lab.

3. United Kingdom Atomic Energy Authority, *An Assessment of the Integrity of PWR Pressure Vessels*, Second report of a study group chaired by Dr. W. Marshall, CBE, FRS, CEGB/S/64 (1982).

4. Private communication, J. Darlaston, Central Electricity Generating Board, United Kingdom, March 1987.

5. W. E. Vesely, E. K. Lynn, and F. F. Goldberg, *The Octavia Computer Code: PWR Reactor Pressure Vessel Failure Probabilities Due to Operationally Caused Pressure Transients*, NUREG-0258, March 1978.

6. B. R. Bass and J. W. Bryson, *Applications of Energy Release Rate Techniques to Part-Through Cracks in Plates and Cylinders, Volume 1. ORMGEN-3D: A Finite Element Mesh Generator for 3-Dimensional Crack Geometries*, NUREG/CR-2997/V1 (ORNL/TM-8527), Union Carbide Corp. Nuclear Div., Oak Ridge Natl. Lab., December 1982.

7. B. R. Bass and J. W. Bryson, *ORVIRT: A Finite Element Program for Energy Release Rate Calculations for 2-Dimensional and 3-Dimensional Crack Models*, NUREG/CR-2997, Vol. 2 (ORNL/TM-8527/V2), Union Carbide Corp. Nuclear Div., Oak Ridge Natl. Lab., February 1983.

8. K. J. Bathe, *ADINA — A Finite Element Program for Automatic Dynamic Incremental Nonlinear Analysis*, Report 82448-1, Massachusetts Institute of Technology, Cambridge, Mass., September 1975 (revised December 1978).

8. INTERMEDIATE VESSEL TESTS AND ANALYSIS

R. H. Bryan

During the previous report period, a topical report on the last intermediate vessel test V-8A was published.[1]

Intermediate test V-8A was the twelfth fracture test of a 150-mm-thick steel vessel in the Heavy-Section Steel Technology Program. This test series is a set of experiments on a scale large enough to simulate realistically important aspects of fracture behavior of reactor pressure vessels. Such experiments are the means by which theoretical models of fracture behavior can be evaluated for possible application to fracture analysis of vessels in nuclear plants.

The V-8A test was concerned with the fracture behavior of the pressure vessel steels that are particularly susceptible to irradiation damage. Several reactor pressure vessels in service contain welds that, because of high copper content, may have their Charpy upper-shelf impact-energy values reduced to relatively low levels by neutron irradiation. Such low-upper-shelf steels are known to exhibit low resistance to a ductile tearing mode of crack propagation in small (25-mm) laboratory specimens. The results of the V-8A test are intended to provide an experimental basis for judging the accuracy of analytical procedures used to evaluate the safety of reactor pressure vessels under conditions of low-upper-shelf toughness.

The test plan was formulated to (1) demonstrate on a large scale the tearing behavior of a low-upper-shelf steel and (2) facilitate the comparisons, based on elastic-plastic fracture mechanics, with experimental results of predictions of stable and unstable tearing. The test required placing a special low-upper-shelf weld seam in a test vessel and generating a large flaw in this seam.

The test vessel was a typical HSST intermediate test vessel with an outside diameter of 990 mm and a thickness of 152 mm. The vessel used for the V-8A test had been tested previously at Oak Ridge National Laboratory and repaired by the Babcock & Wilcox Company by depositing a submerged-arc seam weld especially designed to have the desired properties for the V-8A test. A 280-mm-long by 88-mm-deep fatigue-sharpened flaw was implanted in the seam. The vessel was extensively instrumented with crack-mouth-opening displacement (CMOD) gages, strain gages, and ultrasonic transducers for detecting the flaw depth throughout the test.

The vessel was heated to an isothermal condition at ~150°C and then pressurized slowly in several stages until unstable tearing was observed. Pauses in pressurization at several pressure levels allowed time for observing stable crack depths. A tearing instability was first observed while the pressure was between 138 and 140.5 MPa. Tearing was interrupted by a slight depressurization, and a second tearing instability was induced by further pressurization, which reached 143 MPa. The crack grew in depth ~6 mm before the first instability. At the end of the test, the flaw was 453 mm long and 101.4 mm deep.

Extensive elastic-plastic finite-element analyses were performed before and after the test. Before the test, estimates of instability pressure were made on the basis of these analyses and measurements of the

ductile tearing resistance of four characterization welds. The estimated instability pressures depended on the various measured resistances and fell in the range of 133 to 145 MPa. The estimated instability pressure based on tearing resistance of the vessel test weld itself measured after the test was 134.5 MPa, which is 4% lower than the actual instability pressure.

The objectives of the test were attained in spite of difficulties with high-pressure, high-temperature seals. The Charpy-impact and tearing-resistance properties of the special seam weld were as desired: impact energy was ~60 J. Ultrasonic transducers and CMOD gages performed satisfactorily. Instabilities were arrested, preserving the final crack geometry. Pretest predictions of the instability pressure made by several investigators worldwide were all within −14 to +10% of the observed instability pressure.

This experimental study demonstrated that the V-8A vessel, when pressurized in a ductile state with a large flaw in a region of low tearing resistance, is capable of withstanding a pressure twice the nominal *ASME (American Society of Mechanical Engineers) Code* design pressure. The study also indicated that accurate prediction of instability pressures of a ductile vessel requires (1) methods of analysis that account for plasticity and (2) good representations of the properties of the material with respect to tearing resistance (with proper consideration to scatter) and stress-strain behavior.

Reference

1. R. H. Bryan et al., *Test of 6-in.-Thick Pressure Vessels. Series 3: Intermediate Test Vessel V-8A — Tearing Behavior of Low Upper-Shelf Material*, NUREG/CR-4760 (ORNL-6187), Martin Marietta Energy Systems, Inc., Oak Ridge Natl. Lab., May 1987.

9. THERMAL-SHOCK TECHNOLOGY

No activity in the thermal-shock technology task during this period.

10. PRESSURIZED-THERMAL-SHOCK TECHNOLOGY

R. H. Bryan

During this reporting period, the results of the second pressurized-thermal-shock experiment, PTSE-2, were evaluated, posttest properties of the vessel insert containing the flaw were determined, and a topical report on the experiment was written.[1]

10.1 Background and Conclusions

The PTSE-2 experiment was concerned, primarily, with the behavior of a crack in material with low tearing resistance and, secondarily, with warm prestressing. Preparations for, and performance of, the experiment are reported in Ref. 1. The PTSE-1 experiment had explored, with high-toughness material, warm prestressing and the nature of crack propagation and arrest as the crack approached the ductile zone within the wall of the test vessel. The PTSE-2 experiment employed a steel that had low toughness in the ductile fracture regime so that fracture behavior representative of irradiated low-upper-shelf steel could be observed under transient conditions relevant to a flawed nuclear reactor pressure vessel.

The vessel used for PTSE-1 and two earlier fracture tests was repaired for the PTSE-2 experiment. A 1-m-long sharp flaw was implanted in a welded-in insert of low-upper-shelf material in the 148-mm-thick test vessel. The vessel was instrumented to give measurements of crack-mouth-opening displacement (CMOD), temperature profiles through the vessel wall, and internal pressure during the experiment. With this instrumentation scheme, posttest fracture analyses could be conducted on the basis of actual loads experienced during the pressurized-thermal-shock transients. This facilitated the interpretation of the fracture phenomena that transpired by eliminating, in the final analyses, the considerable uncertainties of heat transfer calculations.

Extensive experimental and analytical studies preceded the transient experiment.[2] Material properties of the special material in which the flaw resided were determined by extensive characterization tests. Numerous prospective transients were analyzed to define experimental procedures with good expectations for success in spite of uncertainties. Two transients were defined and conducted. The first transient generated the conditions necessary for the warm-prestressing investigation. In this transient, the temperature dropped from ~300°C throughout the vessel to ~8°C on the outside surface. The transient included a warm-prestressing phase in which the pressure was reduced from ~63 to 10 MPa, followed by repressurization until the flaw propagated in a brittle mode of fracture (at ~46 MPa). In the course of this transient, stable ductile tearing occurred before and after the brittle fracture. The second transient generated the conditions for a deep brittle propagation terminated by an arrest or conversion of the brittle fracture to ductile tearing under conditions conducive to a tearing instability. The initial temperature

was ~275°C, and the outside surface cooled to ~4°C while the pressure increased monotonically from 3 to 67.3 MPa. The desired conditions were attained in both transients. In the final transient the test vessel ruptured, as had been expected but not especially desired, but without damage to the test facility or loss of experimental information.

This experiment produced, for the first time with stress and toughness states representative of reactor pressure vessels, (1) the arrest of a brittle fracture with an immediate tearing instability and (2) brittle fracture following warm prestressing. Principal conclusions are that

1. low-upper-shelf material can exhibit very high arrest toughness,
2. ductile tearing promotes more-severe fractures in low-upper-shelf material,
3. warm prestressing inhibits brittle fracture to some degree even when crack driving forces are increasing with time,
4. benefits of warm prestressing are diminished by ductile tearing,
5. a simple theoretical analysis of warm prestressing represented fracture conditions reasonably well, and
6. calculations of ductile tearing based on resistance curve test data did not consistently predict the observed tearing.

10.2 Fracture Mechanics Interpretations of PTSE-2

10.2.1 Material characterization

The insert of material containing the flaw in the vessel was characterized before the PTSE-2 experiment by testing specimens cut from a piece of the plate from which the insert was made.[3] The characterization piece (PTC1) and the insert had been heat treated as nearly as practicable in an identical manner. Both were cut from the normalized but untempered plate of 2 1/4 Cr-1 Mo steel, and both were exposed simultaneously to the postweld heat treatment of the PTSE-2 vessel. Nevertheless, hardness testing of the vessel insert and PTC1 before the experiment implied that the tensile strength of the insert was significantly higher than that of PTC1. Consequently, after the experiment, material from the insert was tested to evaluate its tensile and toughness properties, as reported in Chap. 3.

For purposes of fracture analysis, the tensile properties were of greatest importance. Calculations of J_I and K_I depended upon elastic-plastic finite-element analysis for which a reasonable representation of the stress-strain behavior of the material around the flaw was necessary. The representations shown in Fig. 10.1 were used in the posttest analysis of the fracture events in PTSE-2. The geometry of the two-dimensional finite-element model used in this analysis of the test vessel is shown in Fig. 10.2 in which the vessel insert is labeled material A.

The posttest material characterization investigations could not conclusively confirm whether the PTC1 tensile properties were representative of the pretest properties of the insert because the experiment itself subjected the insert to high plastic strains, thus affecting the tensile test results. However, the posttest tensile tests demonstrated that the

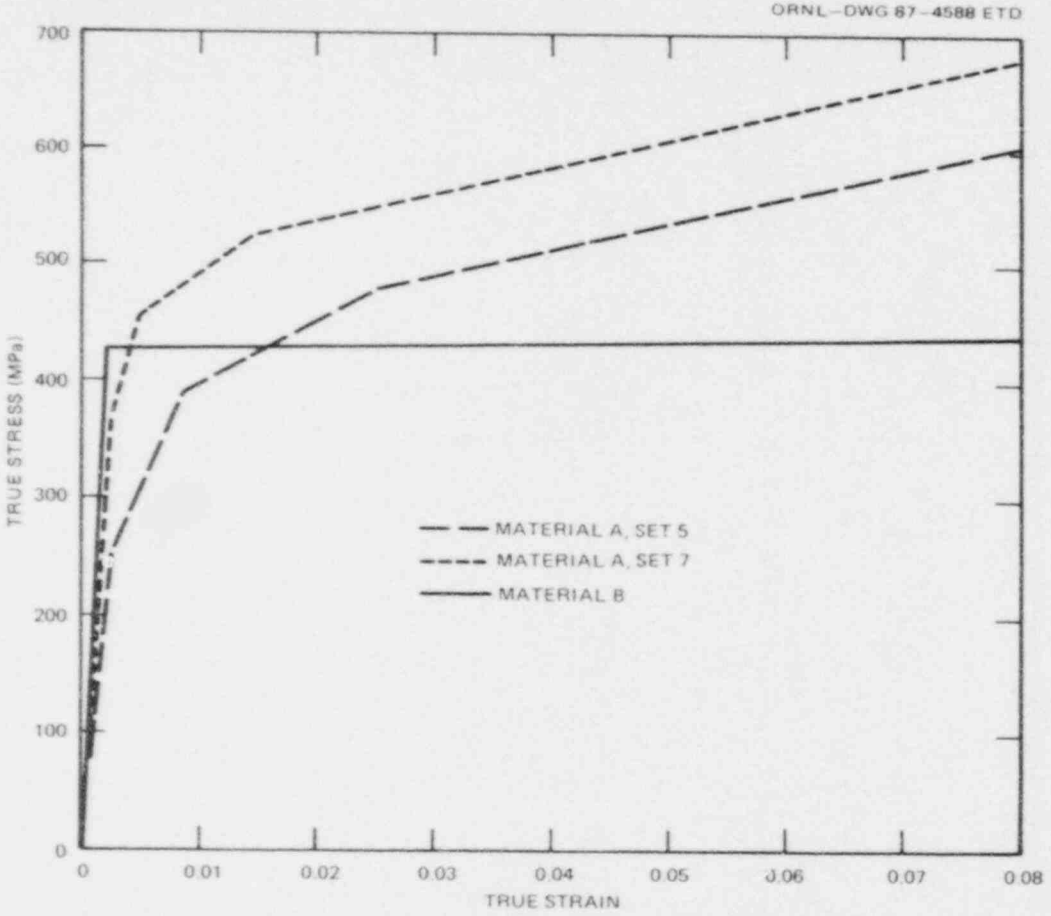

Fig. 10.1. Piecewise linear representations of the stress-strain characteristics of the low-upper-shelf insert (material A) and the base metal (material B). Property set 5 is based on PTC1 data and property set 7 on vessel insert data.

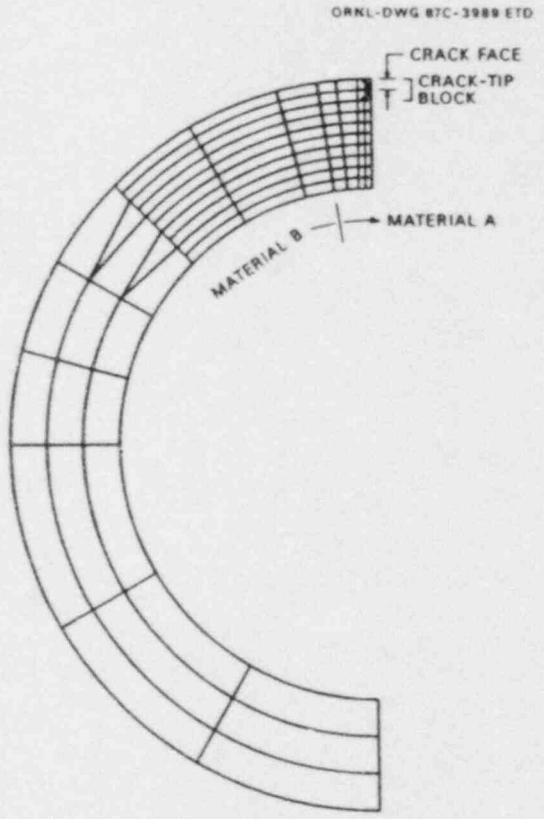

Fig. 10.2. Two-dimensional finite-element mesh for the PTSE-2 cylinder with a crack with depth-to-thickness ratio a/w = 0.1.

differences in the stress-strain behavior (Fig. 10.1) could be largely a result of strain hardening during the PTSE-2 experiment. Consequently, values of K_I and J_I reported for events in the PTSE-2A and -2B transients were based on different characterization tensile tests, namely PTC1 and the PTSE-2 insert, respectively.

10.2.2 Fracture mechanics calculations

The final calculations of K_I and J_I for the PTSE-2 experiment were made with two-dimensional elastic-plastic finite-element analysis using the ADINA/ORVIRT computer programs.[4-6] The calculations for the PTSE-2A transient were based on the same material property tensile data as reported previously,[2] but additional calculations were made to determine the K_I states relevant to all the events of that transient. The events of the second transient (PTSE-2B) were interpreted by similar analyses based on the tensile properties of the vessel insert.[1]

The fracture events are identified in Table 10.1, which presents times, crack depths, crack-tip temperatures, and K_I values for the events. The crack behavior in the PTSE-2A transient is presented in Figs. 10.3 and 10.4 in terms of CMOD and K_I, respectively. It is evident from analysis of the CMOD shown in Fig. 10.3 that the observed ductile tearing occurred in the intervals A-B, C-D, and E-F. The depth of the torn crack at points from B to C was deduced by finite-element analysis from the experimental CMOD values. The depths at the other labeled points were measured directly on the fracture surface after the experiment, as previously reported.[1]

A reconstruction of the K_I and K_{Ic} variation with time in PTSE-2A is shown in Fig. 10.4. The same transient is characterized in Fig. 10.5 in terms of K_I and K_{Ic} vs crack-tip temperature. Because the crack was warm prestressed before the cleavage propagation in PTSE-2A, at the time of cleavage initiation (point D), K_I was not equal to K_{Ic}.

In the PTSE-2B transient, K_I increased monotonically with time until the crack propagated in cleavage. Stable tearing that preceded the cleavage advanced the crack from a depth of 42.4 to 46.1 mm, as indicated in Table 10.1. The fracture behavior is described in Fig. 10.6 in terms of K_I, K_{Ic}, and K_{Ia} vs crack-tip temperature.

10.2.3 K_{Ic} determination from PTSE-2 data

Pretest measurements of K_{Ic} were made only at low temperature. At temperatures relevant to the PTSE-2 experiment, estimates of K_{Ic} based on K_{Jc} data were uncertain.[1] K_{Ic} was assumed to have a temperature dependence represented by the expression

$$K_{Ic} \text{ or } K_{Ia} = a + b \exp\left[c\,(T - T_o)\right] , \qquad (1)$$

where a, b, c, and T_o are material property parameters and T is temperature. The parameter values shown in Table 10.2 were used in pretest

Table 10.1. Events and conditions during the PTSE-2 transients

	Event[a]	Time (s)	Crack depth, a (mm)	Crack-tip temperature (°C)	K_I[b] (MPa·√m)
	PTSE-2A				
A.	Initiation of thermal shock	~112	14.5	302.8	
B.	First maximum K_I	184.6	19.6	128.0	195.7
C.	Minimum K_I	341.8	19.6	77.0	171.0
	Onset of secondary pre-cleavage tearing	341.8	19.6	77.0	171.0
D.	Initiation of cleavage	361.4	22.5	80.7	198.9
E.	Cleavage arrest	361.4	39.3	130.6	261.4
F.	Termination of tearing (by unloading)	365.6	42.4	138.0	278.7
	PTSE-2B				
A.	Initiation of thermal shock	~155	42.4	274.9	
	Onset of precleavage tearing	<575.8	42.4	[c]	[c,d]
B.	Initiation of cleavage	575.82	46.1	102.4	248.1[d]
C.	Interruption of cleavage by ductile tearing and reinitiation		69.2	146.8	361.6[d]
D.	Final cleavage arrest	575.82	78.8	162.9	419.3[d]
	Onset of ductile tearing	576.2	78.8	162.9	406.5
	Vessel rupture (and complete unloading)	576.7	147.6	216.4	

[a]The letters A–F correspond to labeled points shown in Figs. 10.3 and 10.4.

[b]K_I values were calculated from the experimentally observed pressures and temperatures by two-dimensional elastic-plastic finite-element analysis. The stress-strain parameters for material A were set 5 for PTSE-2A and set 7 for PTSE-2B (see Fig. 10.1).

[c]At t = 575.82 s, T = 94.8°C and K_I = 233.8 MPa·√m at this depth.

[d]K_I values listed for t = 575.82 s were calculated for the loading condition at 575.7 s.

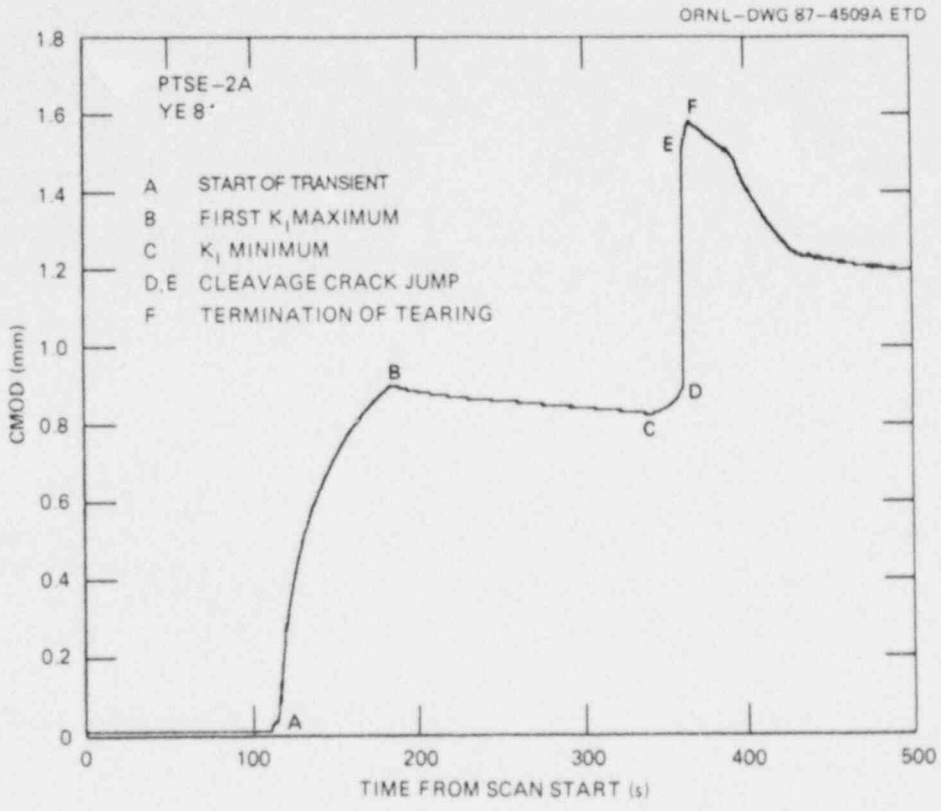

Fig. 10.3. CMOD vs time for the PTSE-2A transient.

Table 10.2. Fracture toughness

Property[a]	Parameter value[b]			
	a	b[c]	c	T_o[c]
		K_{Ic}		
Upper	39	19.666	0.02878	0
Lower	39	19.666	0.02878	30
PTSE-2B	39	19.666	0.02878	20.26
		K_{Ia}		
Upper	34	11.143	0.02413	0
Lower	34	7.96	0.02133	0

[a]Upper and lower toughnesses represented the bounds explicitly evaluated in pretest analyses. The PTSE-2B set of K_{Ic} parameter values agrees with the cleavage initiation observed in that transient.

[b]K_{Ic} or $K_{Ia} = a + b \exp [c(T - T_o)]$, where K_I is in megapascals times square root meters and T is in degrees Celsius.

[c]The parameters b and T_o are interdependent for a given value of c.

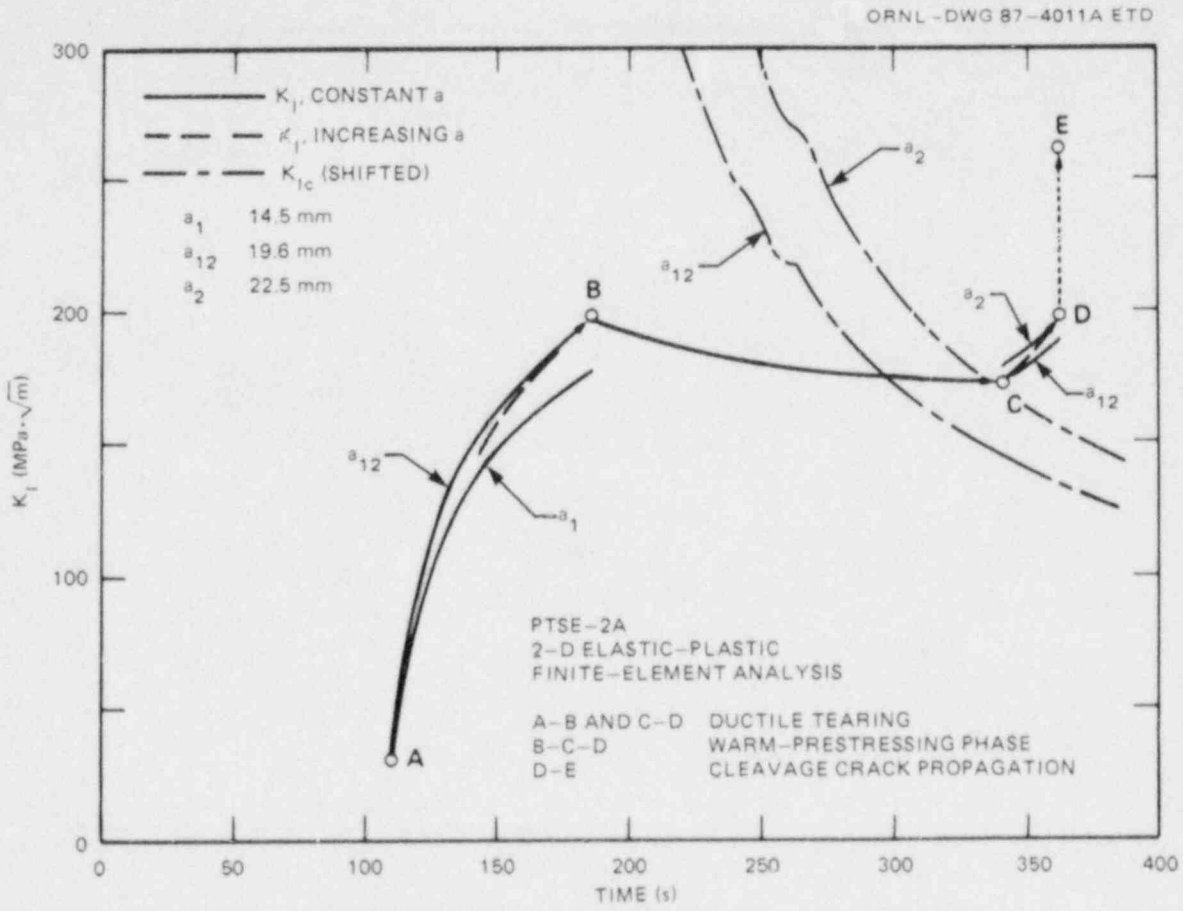

Fig. 10.4. K_I and K_{Ic} vs time from posttest elastic-plastic finite-element analyses based on actual pressure and temperatures measured in PTSE-2A for precleavage crack depths.

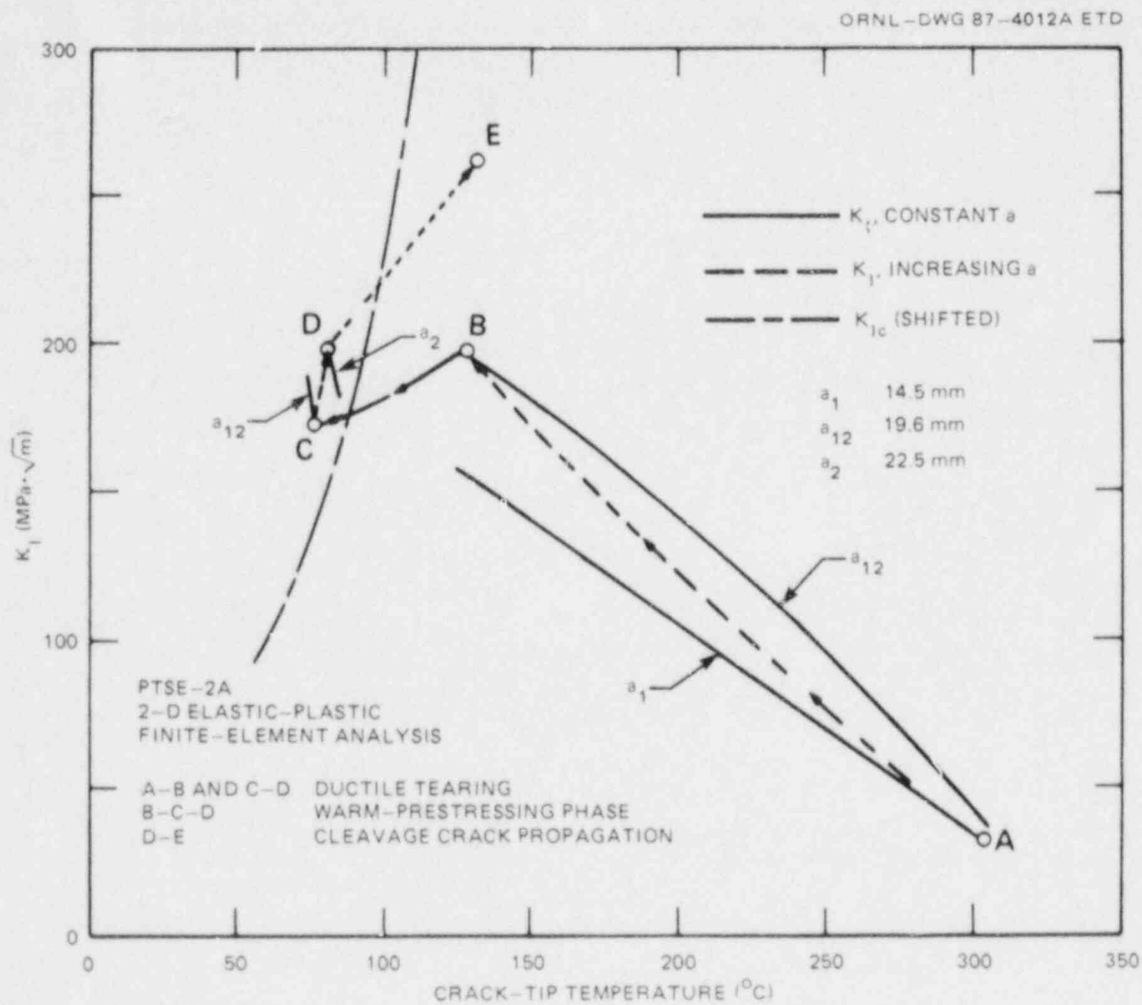

Fig. 10.5. Crack-tip conditions for precleavage crack depths from posttest elastic-plastic finite-element analysis using experimental pressure and temperature data from transient PTSE-2A: K_I and K_{Ic} vs crack-tip temperature.

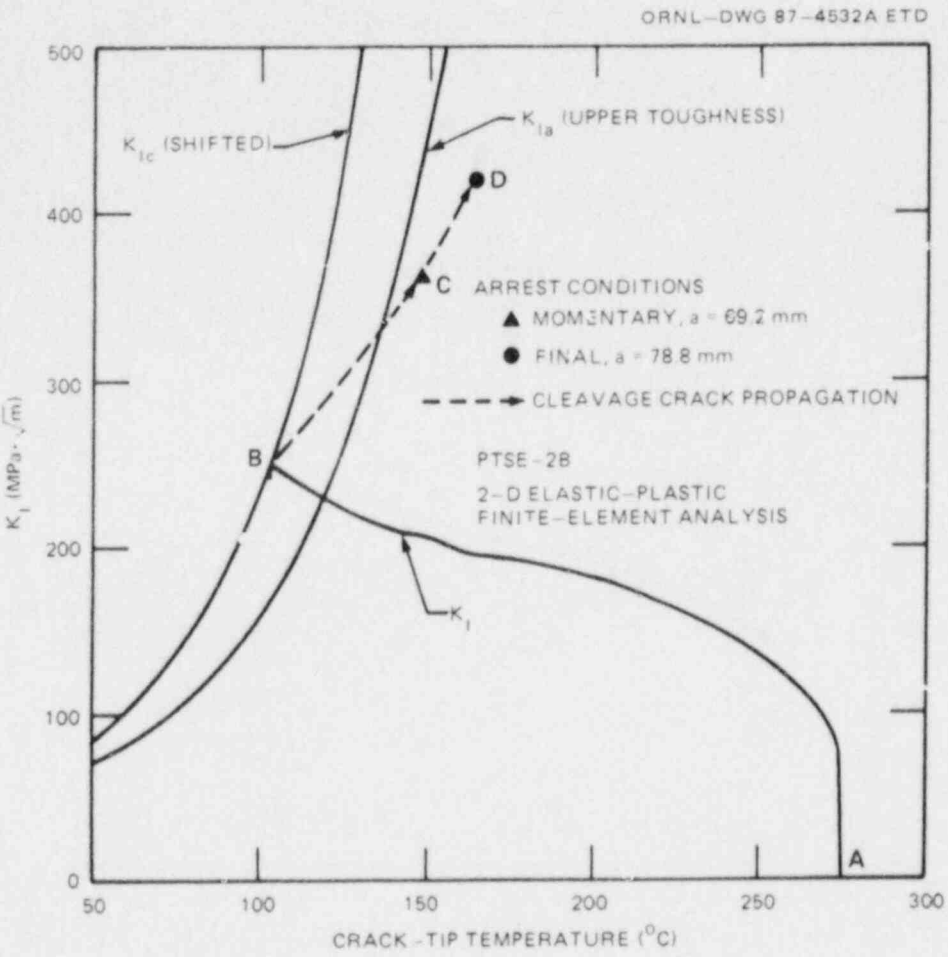

Fig. 10.6. Crack-tip conditions for the precleavage crack depth from posttest elastic-plastic finite-element analysis using experimental pressure and temperature data from transient PTSE-2B: K_I, K_{Ic}, and K_{Ia} vs crack-tip temperature.

analyses. The upper K_{Ic} case in Table 10.2 represented a particular fit to pretest K_{Ic} and K_{Jc} characterization data that was consistent with pretest K_{Ia} data, which were considered a more reliable indication of toughness at high transitional temperature than the K_{Ic} and K_{Jc} data.

An important element of the PTSE-2 experiment was to determine K_{Ic} with greater certainty. The cleavage crack initiation in the PTSE-2B transient was expected to occur when $K_I = K_{Ic}(T_{CT})$, where T_{CT} is the crack-tip temperature (see PTSE-2B event B, Table 10.1). With the values of a, b, and c unchanged, this event was presumed to define the value of the parameter T_o that best represented the intrinsic $K_{Ic}(T)$ of the material around the crack. Thus, T_o = 20.26 K fit the PTSE-2B crack initiation. This is the basis for the K_{Ic} curves (labeled "shifted") in Figs. 10.4 and 10.5 for PTSE-2A and in Fig. 10.6 for PTSE-2B.

The cleavage initiation and arrest values from the PTSE-2 experiment (given in Table 10.1) are shown in Fig. 10.7 with the upper-toughness K_{Ia} curve used in the final pretest analyses and the shifted (upward in temperature by 20.16 K) upper K_{Ic} curve. All of the PTSE-2 points fall within the uncertainty ranges evaluated in pretest analyses. The small-specimen data were adequate to permit the definition of experimental conditions that led to successful results in both transients.

10.2.4 Ductile tearing

Contrary to the behavior of PTSE-1, which had high tearing resistance,[7] the PTSE-2 experiment demonstrated that low tearing resistance promoted ductile tearing before cleavage in both transients. Furthermore, the cleavage propagation in the PTSE-2B transient was interrupted by a small band (~1 mm) of ductile tearing ~10 mm from the final cleavage arrest, and the final arrest was followed immediately by ductile tearing that proceeded until the crack penetrated the entire wall of the vessel.

The ductile tearing in the PTSE-2A transient occurred while the material at, and immediately ahead of, the crack tip was at temperatures well below the onset of the Charpy upper shelf (150°C). The final unstable ductile tearing (in the PTSE-2B transient) started in material at ~160°C.

The final tearing started with $J_I \approx 0.8$ MJ/m^2. This is much higher than J_{Ic} for normal reactor pressure vessel steels and is high enough to cause a tearing instability in the PTSE-2 transient, irrespective of any other type of instability. If the arrested crack (with a = 78.8 mm) were not deep enough to cause a tensile instability, the J_R-controlled tear would have promoted enough growth to cause a tensile instability.

The applied J_I attained at the end of each phase of tearing was used in calculating the extent of stable tearing that would occur if tearing were controlled by the condition $J_I = J_R$ for a tearing resistance curve

$$J_R = c(\Delta a)^n \quad , \tag{2}$$

in which J_R is the tearing resistance, Δa is the increment of crack depth, and c and n are parameters determined by a least-squares fitting of specimen test data to the function in this equation. The highest and lowest tearing resistances (Table 10.3) from the set of six 25-mm-thick compact specimens of the characterization material PTC1 were used in the calculations to determine the range of uncertainty of Δa estimates. The numerical results are summarized in Table 10.4. The specimen data were interpreted in two ways: in terms of (1) J based on deformation theory, as prescribed in the testing standard of Ref. 8, and (2) the J modified by Ernst.[9]

Neither the deformation theory J_R nor the modified Ernst J_R gives a consistent estimate of tearing. The lowest-resistance deformation J_R data imply tearing in the first two phases of PTSE-2A that is reasonably consistent with the actual tearing. In all other phases, this J_R implies tearing that greatly exceeds the actual tearing. The highest resistance

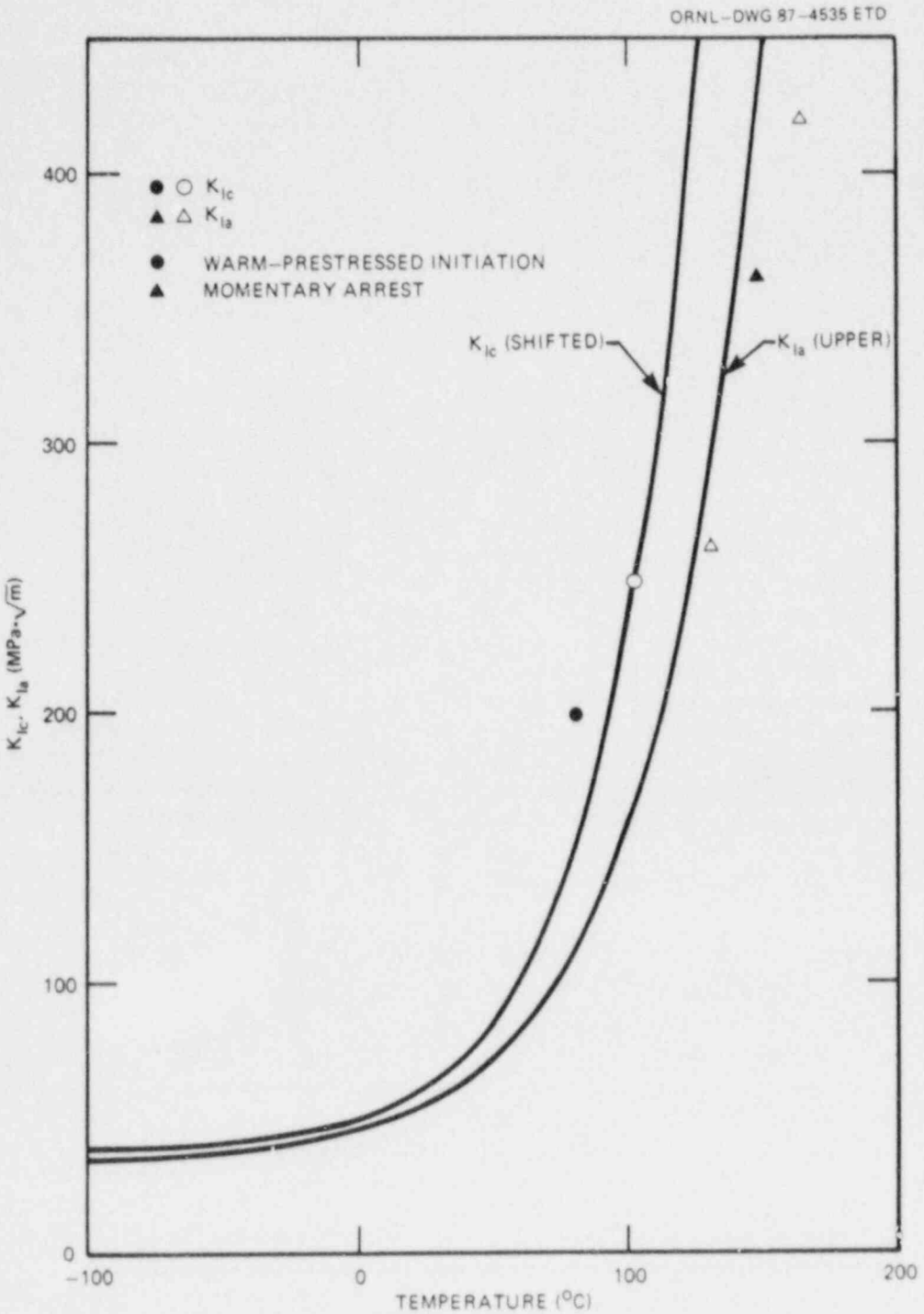

Fig. 10.7. Crack initiation K_{Ic} and arrest K_{Ia} toughness values observed in PTSE-2 compared with the shifted pretest K_{Ic} curve and the upper-toughness K_{Ia} curve.

Table 10.3. Tearing resistances for PTC1 characterization material specimens exhibiting the highest and lowest resistances[a]

Parameters	Lowest resistance[b]		Highest resistance[c]	
	Deformation theory	Modified Ernst	Deformation theory	Modified Ernst
c	0.09327	0.09592	0.1178	0.1229
n	0.2722	0.3701	0.4341	0.5372

[a] $J_R = c(\Delta a)^n$, where J_R is in megajoules per square meter and Δa is in millimeters.

[b] Specimen PI235.

[c] Specimen PI230.

specimen with the modified Ernst interpretation of J_R implies tearing in phases 3 and 4 (Table 10.4) that agrees well with actual tearing, but these J_R data are inconsistent with the actual tearing in all other phases. Furthermore, unlike the other three cases, this J_R case implies strong tearing stability in phase five during the time that the final tearing instability occurred.

10.2.5 Warm-prestressing effects

Analysis of warm prestressing in PTSE-2 was based on a theoretical procedure developed by Chell.[10-12] Chell's procedure is derived from the strip-yield model of a crack with the premise that, after warm prestressing, failure occurs when the J-integral reaches a critical value

$$J_{CRIT} = \frac{(1 - \nu^2)}{E} K_{Ic}^2 , \qquad (3)$$

where K_{Ic} is the fracture toughness of pristine material. The J-integral used in Chell's theory is defined on the basis of elastic strains only, even in regions of plasticity.[12]

In the PTSE-2 experiment, warm prestressing occurred only in transient PTSE-2A. The analysis of PTSE-2A involves the determination of K_I at the times of the first maximum and minimum in $K_I(t)$. These values, together with the flow stresses σ_{flow} at those times, define the plastic zone sizes for the first two states (i.e., the first maximum K_I and the minimum K_I) involved in Chell's theory. The third state, the loading at the time of failure, is defined by the criterion of Eq. (3).

Table 10.4. Tearing calculations based on two-dimensional elastic-plastic finite-element calculations and tearing resistance J_R-Δa data for characterization piece PTC1[a]

Tearing phase	Time (s)	Initial crack depth, a (mm)	Final J_I (MJ/m^2)	Measured Δa (mm)	Calculated Δa (mm)[b]			
					Lowest resistance		Highest resistance	
					Deformation theory	Modified Ernst	Deformation theory	Modified Ernst
			PTSE-2A					
1. Before maximum K_I	112–184.6	14.5	0.165	5.1	8.1	4.3	2.3	1.7
2. Secondary precleavage	341.8–361.4	19.6	0.171	2.9	9.2	4.7	2.3	1.9
3. Postcleavage	361.4–365.6	39.3	0.335	3.1	109	29	11	6.5
			PTSE-2B					
4. Precleavage	155–575.82	42.4	0.283	3.7	59	19	7.5	4.7
5. Postcleavage	576.2–576.7	78.8	0.759	Unstable	Unstable	Unstable	Unstable	30

[a]The initial crack depth is the depth at the beginning of the specified phase. The J_I value is for the initial depth plus the measured Δa. J_I values were calculated by the two-dimensional elastic-plastic finite-element method.

[b]Δa is calculated from $J_I = c(\Delta a)^n$, where c and n are the power-law parameters determined by least-squares fitting the test specimen data. The lowest-resistance columns are based on specimen PI235; the highest-resistance columns are based on specimen PI230. See Table 10.3.

Chell's theory was modified to take account of tearing before cleavage during the loading step that leads from state 2 (minimum K_I) to state 3 (final K_I). For this modification, it was assumed that this tearing occurred with the material at the state 3 temperature. The modification takes account of the actual change in position of the crack tip relative to the residual plastic zones generated in the states 1 and 2 loadings. It also introduces virtual crack-face tractions over the incremental surface of the crack. The virtual tractions are equal and opposite in direction to the stresses in the residual plastic zones of states 1 and 2. The modified theory is similar to a modification for subcritical crack growth that Chell described in Ref. 13, which did not come to the attention of the author of the present report until this work was completed.

Several PTSE-2 warm-prestressing sequences were analyzed to illustrate the effects of various factors. Cases for fracture without the intervention of tearing and for a variety of assumptions regarding flow stress were investigated. In all cases, K_I values for the applied loads were selected from the posttest values given in Table 10.1, and the temperature of the crack tip at the time each loading state was attained was attributed to the entire plastic zone. That is, for the purpose of determining their attributes, plastic zones were assumed to be isothermal during the respective loading steps. The temperature of the structure in state 3 was, in each case, the experimental temperature of the actual PTSE-2A crack tip at the instant cleavage propagation commenced.

In the PTSE-2A transient the initial crack (a = 14.5 mm) tore ductilely to a depth of 19.6 mm before the onset of warm prestressing (state 1). After the minimum in K_I (state 2), K_I increased, and for a short time before cleavage occurred, the crack tore ductilely to a depth of 22.5 mm. The loading conditions deduced from the PTSE-2A transient for two of the sequences analyzed are described in Table 10.5. The sequence for a fixed crack depth is important because it represents the course of events that would be predicted if there were no expectation of ductile tearing. The sequence for a variable crack depth represents the actual course as reconstructed from experimental evidence.

The results of the fixed-crack and tearing-crack sequences are shown in Figs. 10.8(*a*) and (*b*), respectively. Figure 10.8 shows the K_I at fracture calculated by the warm-prestressing theory as a function of the K_{Ic} of the material. The experimental points are the actual fracture conditions obtained from the PTSE-2 experimental data. The K_{Ic} values used for plotting the experimental points were derived from the K_{Ic} expression based on PTSE-2B.

If the crack, which was 19.6 mm deep, had not torn in the final loading step, the theory predicted that the cleavage initiation would have occurred, as shown in Fig. 10.8(*a*), at K_I ~12 MPa$\cdot\sqrt{m}$ higher than the experimental K_I for a crack of this depth. The experimental point in Fig. 10.8(*a*) would be the perceived initiation condition if one did not know that the crack tore. The calculations for the tearing crack predicted that fracture would have occurred at a K_I ~7 MPa$\cdot\sqrt{m}$ lower than the experimental point, as shown in Fig. 10.8(*b*). The important implications of the experimental and analytical results are that (1) warm prestressing, combined with the complications of precleavage tearing, elevated the fracture point (K_I = 198.9 MPa$\cdot\sqrt{m}$) significantly above the level of the

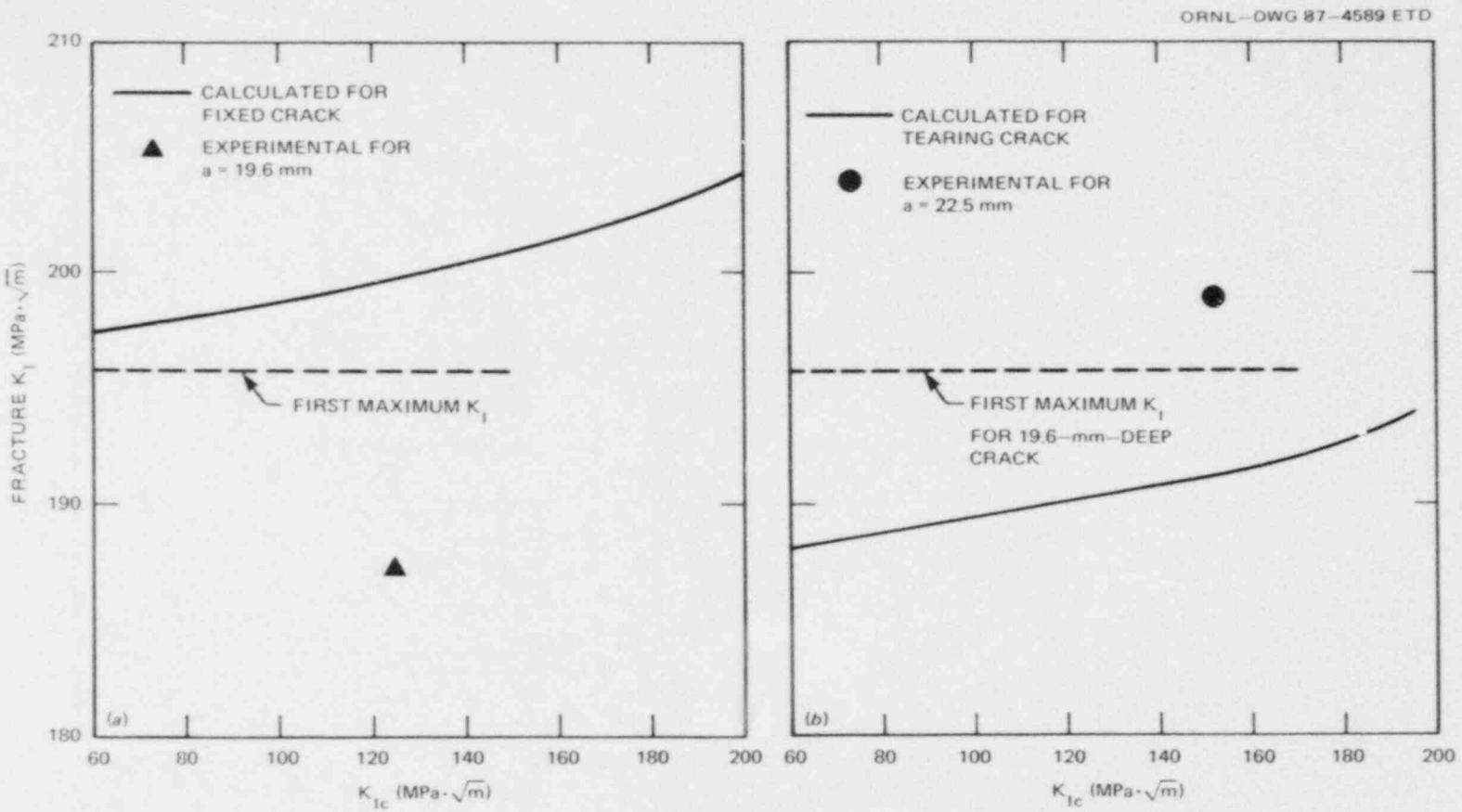

Fig. 10.8. Theoretical prediction of post-warm-prestressing fracture conditions K_I vs K_{Ic} for the PTSE-2A transient compared with actual fracture. Predictions are based on K_I values from posttest elastic-plastic finite-element analysis using measured pressure and temperatures. Plastic zones in the warm-prestressing analysis are based on measured flow stresses for characterization material PTC1. (*a*) Crack without tearing, (*b*) tearing crack.

Table 10.5. Parameters for warm-prestressing analysis of the PTSE-2A transient

Loading state	Time (s)	Crack depth (mm)	Crack-tip temperature (°C)	Flow stress[a] (MPa)	K_I[b] (MPa·$\sqrt{m}$)	K_{Ic}[c] (MPa·$\sqrt{m}$)
Fixed crack depth (19.6 mm)						
1	185	19.6	125.0	392.2	195.7	439.7
2	340	19.6	75.1	409.2	171.0	134.3
3	361.4	19.6	71.4	410.8	187.3	124.7
Variable crack depth (Δa = 2.9 mm)						
1	185	19.6	125.0	392.2	195.7	439.7
2	340	19.6	75.1	409.2	171.0	134.3
3	361.4	22.5	80.9	406.8	198.9	151.6

[a]Flow stresses as a function of temperature were obtained from a polynomial least-squares fit to tensile data for characterization material PTC1. All transversely oriented instrumented specimens were included.

[b]Values interpolated from set of 2-D elastic-plastic finite-element calculations based on PTSE-2A experimental pressure and temperatures.

[c]Values based on the pretest K_{Ic} curve shifted to agree with the PTSE-2B experiment, Eq. (1), at the crack-tip temperature.

pristine K_{Ic} (151.6 MPa·$\sqrt{m}$) and (2) the modified warm-prestressing theory predicted an elevation of the fracture point ~15% less than the observed elevation.

According to theory, the consequences of warm prestressing are very sensitive to the extent of precleavage tearing and the tensile strength of the material. The sensitivity to strength is principally a result of the contributions of virtual crack-face loading, which may in different circumstances increase or decrease the effective stress-intensity factor of the final crack.

10.3 Conclusions

Principal conclusions from the PTSE-2 experiment are that

1. low-upper-shelf material can exhibit very high arrest toughness,
2. ductile tearing promotes more-severe fractures in low-upper-shelf material,

3. warm prestressing inhibits brittle fracture even when crack-driving forces are increasing with time,
4. benefits of warm prestressing are diminished by ductile tearing,
5. a simple theoretical analysis of warm prestressing represented fracture conditions reasonably well, and
6. calculations of ductile tearing based on resistance curve test data did not consistently predict the observed tearing.

References

1. R. H. Bryan et al., *Pressurized-Thermal Shock Test of 6-in.-Thick Pressure Vessels. PTSE-2: Investigations of Low Tearing Resistance and Warm Prestressing*, NUREG/CR-4888 (ORNL-6377), Martin Marietta Energy Systems, Inc., Oak Ridge Natl. Lab., December 1987.

2. R. H. Bryan, "Pressurized-Thermal-Shock Technology," pp. 181–230 in *Heavy-Section Steel Technology Program Semiann. Prog. Rep. October 1986–March 1987*, NUREG/CR-4219, Vol. 4, No. 1 (ORNL/TM-9593/V4&N1), Martin Marietta Energy Systems, Inc., Oak Ridge Natl. Lab.

3. R. K. Nanstad et al., "Pressurized-Thermal-Shock and Wide-Plate Crack-Arrest Characterization," pp. 55–77 in *Heavy-Section Steel Technology Program Semiann. Prog. Rep. April–September 1986*, NUREG/CR-4219, Vol. 3, No. 2 (ORNL/TM-9593/V3&N2), Martin Marietta Energy Systems, Inc., Oak Ridge Natl. Lab.

4. K. J. Bathe, *ADINA — A Finite Element Program for Automatic Dynamic Incremental Nonlinear Analysis*, Report 82448-1, Massachusetts Institute of Technology, Cambridge, September 1975 (revised December 1978).

5. J. W. Bryson and B. R. Bass, *ORMGEN.PC: A Microcomputer Program for Automatic Mesh Generation of 2-D Crack Geometries*, NUREG/CR-4475 (ORNL-6250), Martin Marietta Energy Systems, Inc., Oak Ridge Natl. Lab., March 1986.

6. B. R. Bass and J. W. Bryson, *Applications of Energy Release Rate Techniques to Part-Through Cracks in Plates and Cylinders, Volume 2. ORVIRT: A Finite Element Program for Energy Release Rate Calculations for 2-D and 3-D Crack Models*, NUREG/CR-2997, Vol. 2 (ORNL/TM-8527/V2), Union Carbide Corp. Nuclear Div., Oak Ridge Natl. Lab., February 1983.

7. R. H. Bryan et al., *Pressurized-Thermal-Shock Test of 6-in.-Thick Pressure Vessels. PTSE-1: Investigation of Warm Prestressing and Upper-Shelf Arrest*, NUREG/CR-4106 (ORNL-6135), Martin Marietta Energy Systems, Inc., Oak Ridge Natl. Lab., April 1985.

8. ASTM Standard E813-81, "Standard Test Method for J_{Ic}, A Measure of Fracture Toughness," pp. 762–80 in *1983 Annual Book of ASTM Standards*, American Society for Testing and Materials, Philadelphia, 1983.

9. H. A. Ernst, "Material Resistance and Instability Beyond J-Controlled Crack Growth," pp. 191–213 in *Elastic-Plastic Fracture: Second Symposium*, ASTM STP 803, Vol. I, American Society for Testing and Materials, Philadelphia, 1983.

10. G. G. Chell, J. R. Haigh, and V. Vitek, *A Theory of Warm Prestressing: Experimental Validation and the Implications for Elastic-Plastic Failure Criteria*, RD/L/N63/79, Central Electricity Research Laboratories, Leatherhead, Surrey, England, August 1979.

11. G. G. Chell, *A Theory for Predicting the Failure Loads of Cracked Structures Subjected to Warm Prestressing. 1: Load Changes at Constant Temperature*, RD/L/N78/79, Central Electricity Research Laboratories, Leatherhead, Surrey, England, September 1979.

12. G. G. Chell, "Some Fracture Mechanics Applications of Warm Prestressing to Pressure Vessels," pp. 117–24 in *Proc. 4th Int. Conf. on Pressure Vessel Technology*, Paper C22/80, The Institution of Mechanical Engineers, London, 1980.

13. G. G. Chell, "The Effects of Sub-Critical Crack Growth on the Fracture Behavior of Cracked Ferritic Steels after Warm Prestressing," *Fatigue Fract. Engng. Mater. Struct.* 9(4), 259–74 (1986).

11. PRESSURE-VESSEL-RESEARCH USERS' FACILITY

C. E. Pugh G. C. Robinson

11.1 Procurement Activities

As previously reported[1] acquisition of a pressurized-water reactor (PWR) vessel from Combustion Engineering Company (CE) required the letting of a complementary third-party subcontract that would include the following activities:

1. barging of vessel and appurtenances from the CE Chattanooga plant site to the Oak Ridge K-25 Plant K-700 area site;
2. construction of a barge slip on the Clinch River at mile 13.2 at the K-700 area site boundary;
3. construction of a short unpaved roadway from the barge slip to a paved area immediately adjacent to the K-701, K-702, and K-703 building complex; and
4. transportation of the vessel from the barge slip and unloading at a designated temporary storage location on the paved area adjacent to the K-701, K-702, and K-703 building complex.

Implementation of these activities requires the use of equipment specifically designed to handle and transport very large equipment similar to PWR vessels. Concern that the normal bid process would not ensure that bid responses would be technically qualified for these activities interrupted advertisement of the job and led to a reformulation of the procurement package to permit bid evaluation on technical merit issues in addition to cost. In the second round of bidding, the apparent low bidder failed to provide a qualified bid bond after a prolonged period of negotiation. Implementing these procurement actions resulted in a significant slippage in schedule.

Consequences of the schedule slippage were (1) the necessity of slip construction at high-water conditions resulting in a cost increase in the bid responses and (2) the refiling of slip construction permits with the Corps of Engineers and the Tennessee Valley Authority (TVA) that resulted in the required use of silt screens during high-water slip construction and further cost increases in the bid responses.

Under normal circumstances, losses due to "acts of God" in government-funded programs must be covered by normal funding sources and not by insurance policies. However, the transportation of the PWR vessel from CE's Chattanooga site to Oak Ridge involved an unusual risk with a potential salvage cost of ~$750,000 if the worst-case hypothetical accident should occur. Contingency funds were not available to cover such a cost, and the normal policy of self-insurance was waived to permit the requirement that all-risk insurance be a part of the procurement packages. The attendant cost increases exceeded the approved funding for the project and required a revised submission and approval of the OR0638 budget approval form.

At this point delays due to the foregoing actions had become critical because of the limited construction time available before the dropping of the water level at the barge slip site. Figure 11.1 provides a schematic of TVA's operation of the Watts Bar Reservoir that controls the pool level on the Clinch River downstream from the Melton Hill Dam. As noted from Fig. 11.1, the pool level at the K-25 barge slip site normally falls on October 1.

The procurement package was, therefore, premised on a delivery of the PWR vessel and unloading prior to October 1 because the slip can only be used under full pool conditions. Figure 11.2 shows a plan view and cross section of the slip in a conceptual configuration. (Final design was a responsibility of the subcontractor.)

In spite of the constraints previously discussed, the second-low bidder, a consortia of companies headed by CMC Construction Company, affirmed that the project was feasible and was awarded the subcontract. CMC Construction Company mobilized their forces and began construction within a week of bid award.

Construction proceeded rapidly. Figure 11.3 is a view of the barge slip site showing the silt screen as installed and dredging in progress. Figure 11.4 is another view of the barge slip site showing the placement of sheet piling by a high-frequency hydraulically powered vibration unit. Typically, <2 min were required to drive each sheet pile 30 ft into the

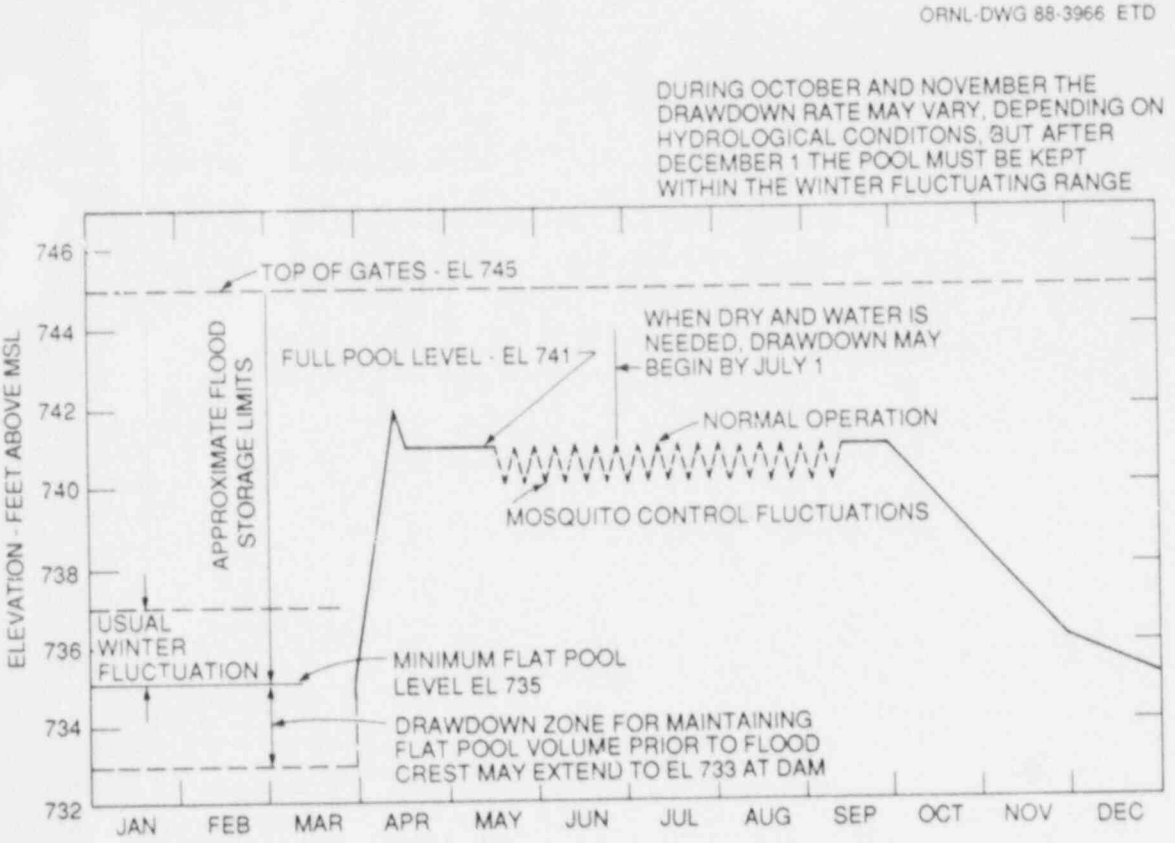

Fig. 11.1. TVA control schematic of Watts Bar Reservoir.

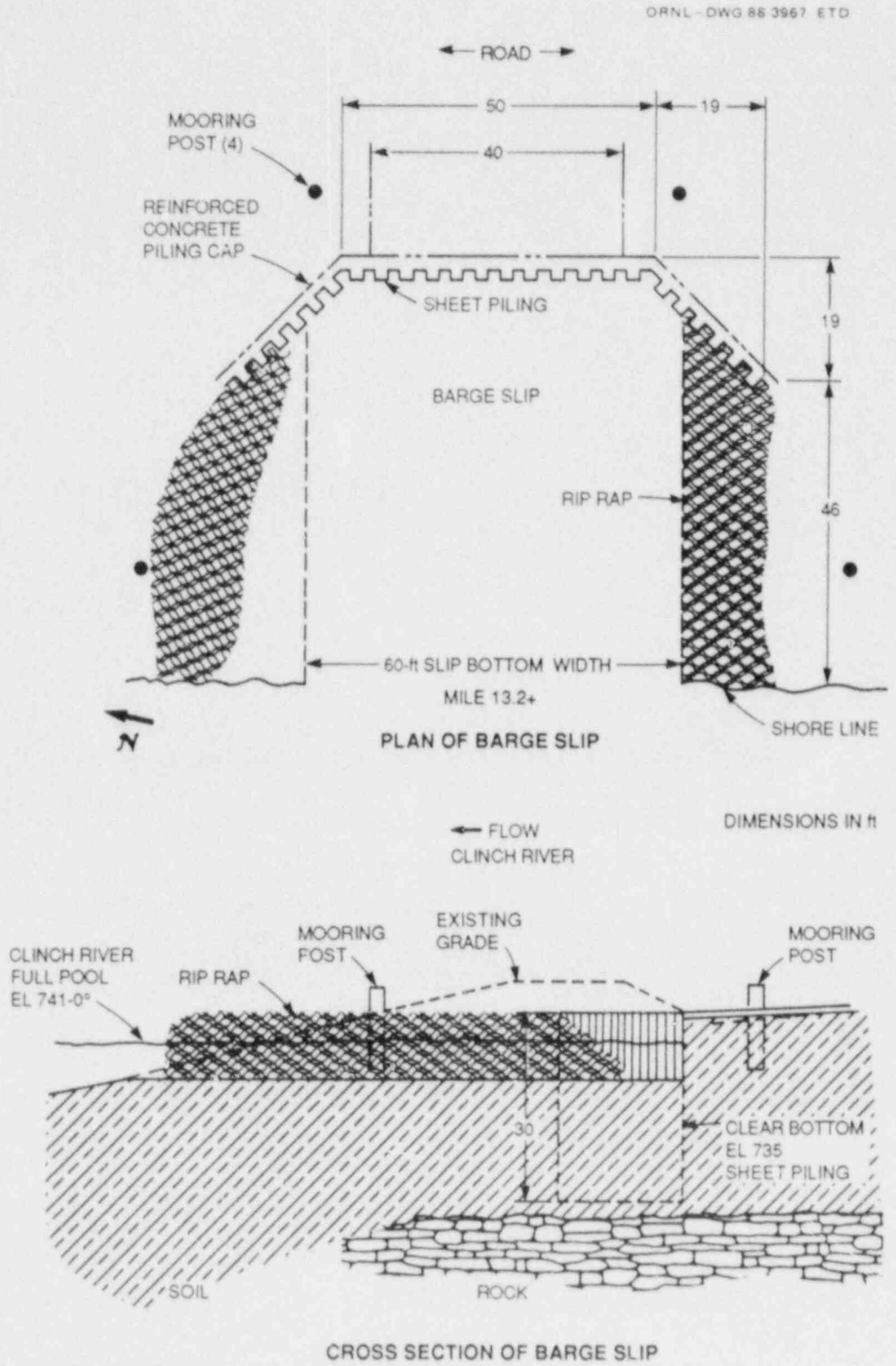

Fig. 11.2. Conceptual requirements of barge slip shown in plan and cross-section views.

PHOTO K/PH 87-3013

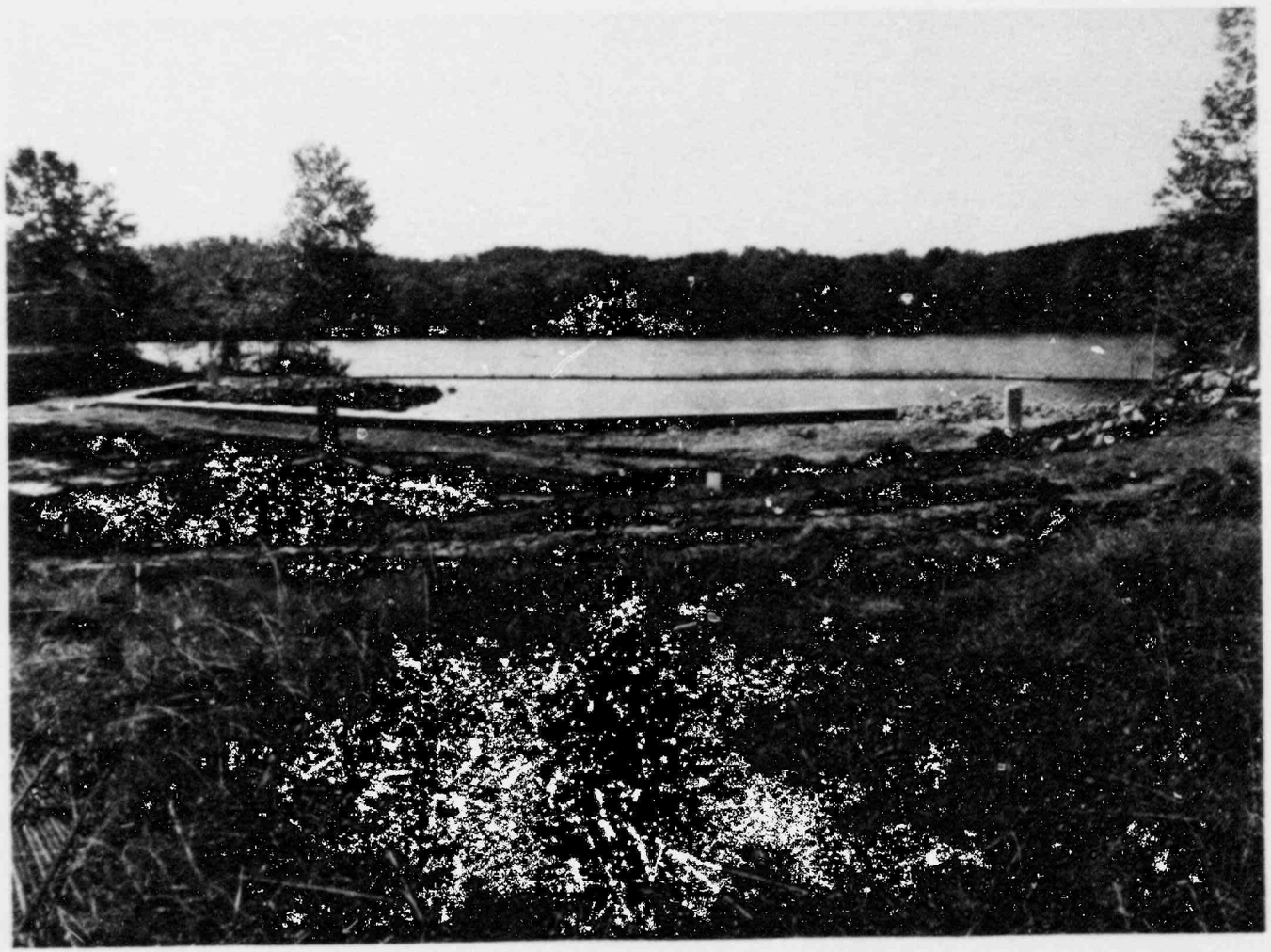

Fig. 11.3. View of barge slip site showing installed silt screen and retaining wall.

Fig. 11.4. View of barge slip site showing the driving of sheet piling for head wall.

soil. A crane supporting the vibration unit and hydraulic power supply are in the foreground. Figure 11.5 is a view of the completed barge slip. Prominent in this view are the sheet piling, mooring posts, riprap at the slip and shore line, and compacted road bed. Figure 11.6 is a view at arrival (September 26) of the tug-pushed barge (53.3 m long × 13.7 m wide × 3.3 m deep) with the PWR vessel and appurtenances mounted on the deck. Figure 11.7 is a view of the rigging for off-loading the PWR vessel head. In addition to the PWR vessel head, equipment prominently displayed in the view include the hydraulic jacks, the lifting fixture, and the 1.8-MN capacity transporter and tractor. Figure 11.8 is a view of the rigging for off-loading the PWR vessel on September 30. In addition to the PWR vessel, equipment prominently displayed in this view include the hydraulic jacks, the lifting fixture, the J-skid vessel support, and the two 1.8-MN capacity transporters and tractors. Figure 11.9 is a view of the PWR vessel loaded on the two transporters parked at the unloading site near the K-750 building complex. Figure 11.10 is a view of the PWR vessel at its unloading site.

11.2 Planning Activities

Funds for further implementation of the Pressure-Vessel-Research Users' Facility complex have not yet been allocated. Currently, an investigation is being initiated to determine the activities required to conduct a detailed NDE inspection of the PWR vessel, while it is situated horizontally on the temporary supports. The primary difficulties associated with in-place inspection are the subjection of equipment and personnel to outside temperature conditions and the virtual limitation of zones inspected to those accessible from a "down-hand" position.

Efforts leading up to the procurement of this PWR vessel included the conduct of a limited survey of potential uses of the vessel. An expansion of this effort will be initiated in FY 1988 to detail the equipment, operating personnel, utilities, and supporting maintenance craft required to support these activities and to define facility needs.

Reference

1. C. E. Pugh and G. C. Robinson, "Pressure-Vessel Research Users' Facility," pp. 231–33 in *Heavy-Section Steel Technology Program Semiann. Prog. Rep. October 1986–March 1987*, NUREG/CR-4219, Vol. 4, No. 1 (ORNL/TM-9593/V4&N1), Martin Marietta Energy Systems, Inc., Oak Ridge Natl. Lab.

PHOTO K/PH 87-3079

Fig. 11.5. View of barge slip.

PHOTO K/PH 87-3257

Fig. 11.6. View of PWR vessel and appurtenances loaded on barge at arrival at the K-25 barge slip.

PHOTO K/PH 87-3196

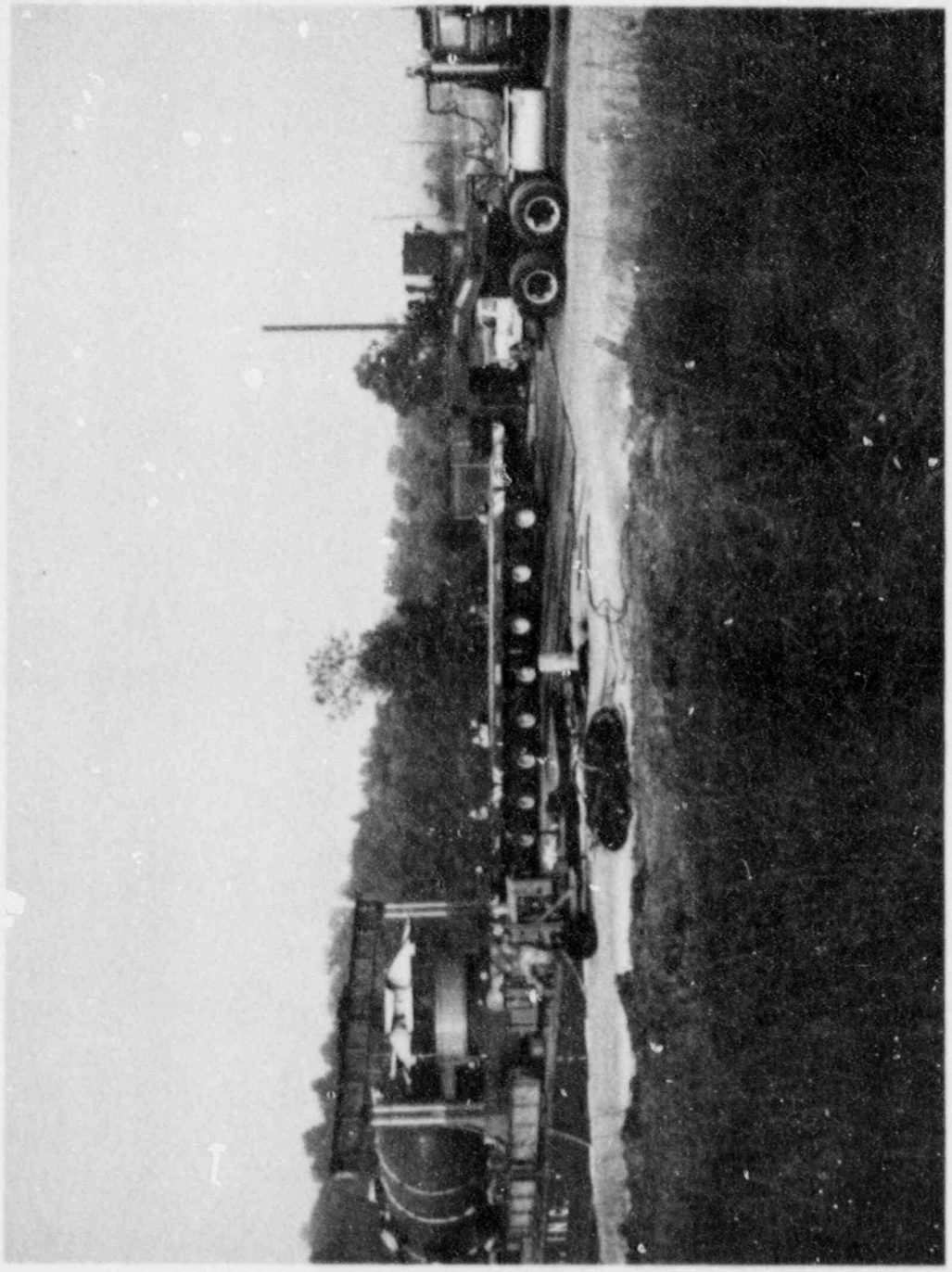

Fig. 11.7. View of rigging for off-loading of PWR vessel head.

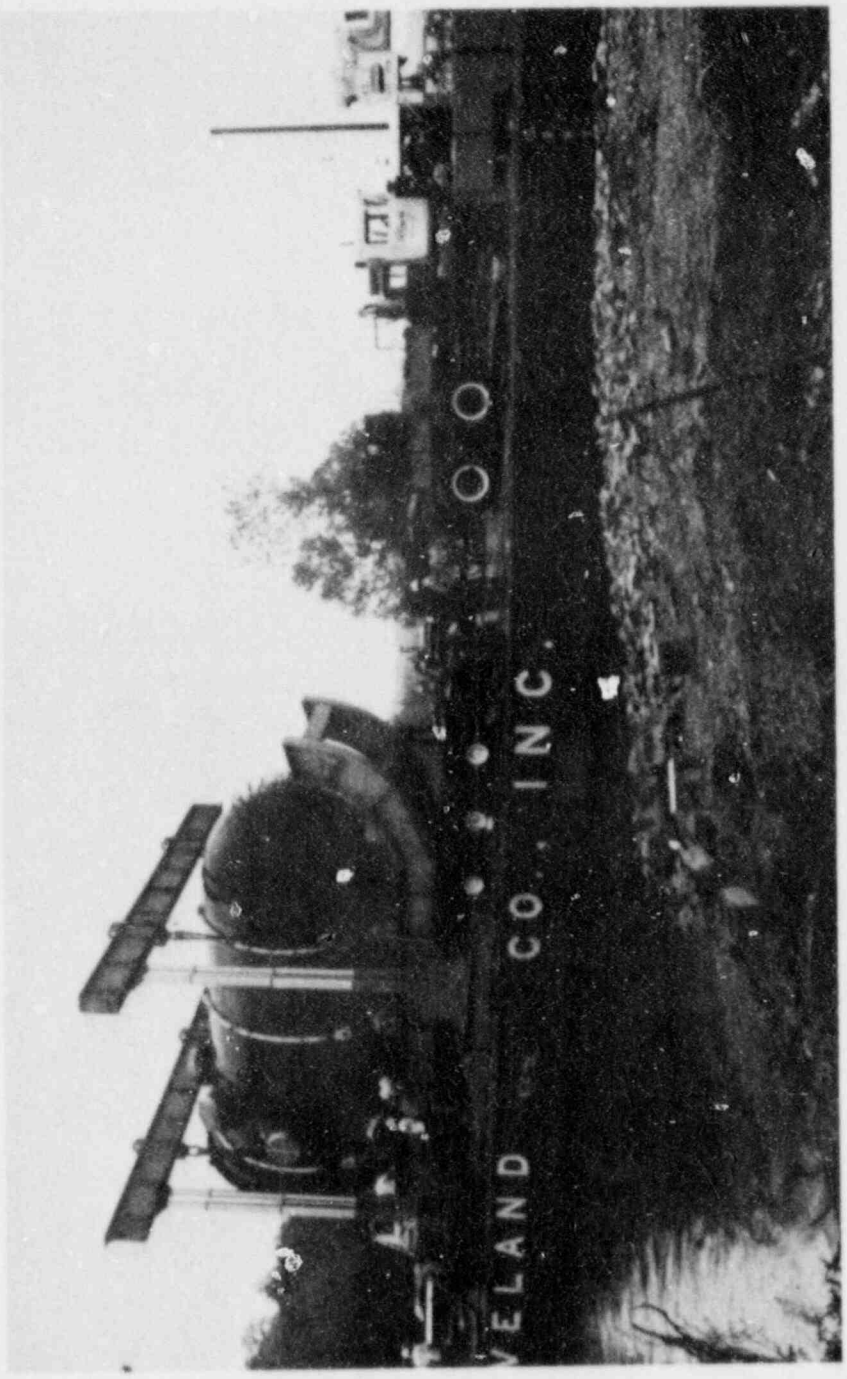

Fig. 11.8. View of rigging for off-loading of PWR vessel.

PHOTO K/PH 87-3165

Fig. 11.9. View of PWR vessel on transporters at K-700 unloading site.

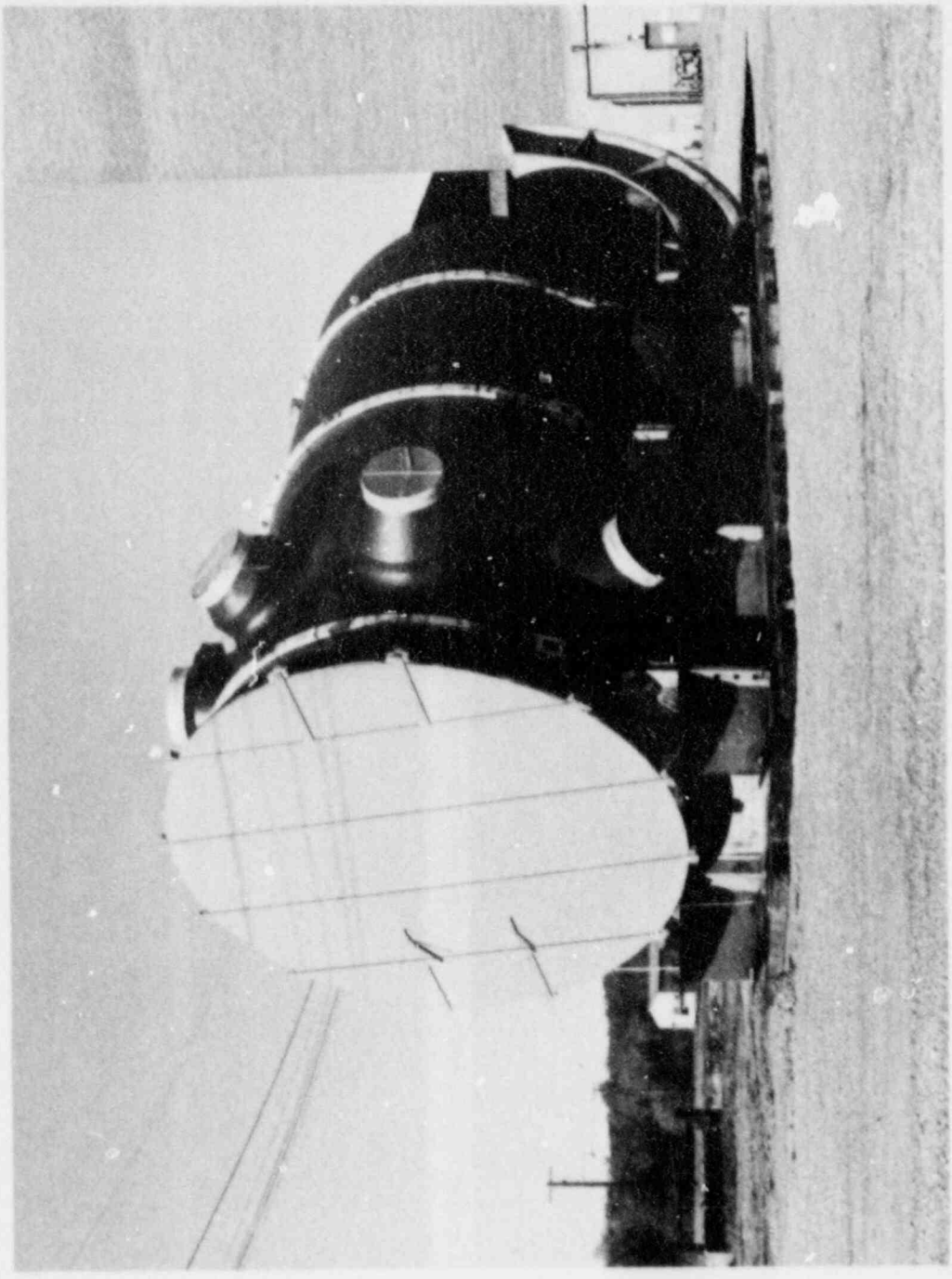

PHOTO K/PH 87-3497

Fig. 11.10. View of PWR vessel at unloading site.

12. SHIPPING CASK MATERIAL EVALUATIONS

J. G. Merkle R. K. Nanstad

12.1 Introduction*

In FY 1987, the U.S. Nuclear Regulatory Commission (NRC) added a task to the Heavy-Section Steel Technology (HSST) Program, the primary objective being to evaluate the suitability of candidate materials for use as primary structural materials in nuclear spent-fuel shipping casks. Further, a near-term objective is to concentrate evaluation on the use of nodular cast iron (NCI) for such an application. General background on the regulatory and research aspects of cask structural materials, especially NCI, were given in a previous progress report.[1] In the same report,[1] the general plan for work to be performed by Oak Ridge National Laboratory (ORNL) was discussed. In particular, a fact-finding trip to the Federal Republic of Germany (FRG) and the convening of a panel of experts on the subject of cask structural materials were described as initial tasks. The results of these initial efforts, as well as some additional background, will be discussed below.

12.2 Background

Although the problem of qualifying the primary structural materials for spent-fuel shipping casks is sometimes viewed as a "materials" problem, the truth is that it cannot be labeled that simply. The reason is that the low-probability accidental loadings that a spent-fuel shipping cask must be able to withstand without loss of safety function are highly random in nature, in the same sense as earthquakes, windstorms, fires, and floods. Consequently, although specified simplified test conditions are currently used to represent severe service loading conditions, the frequency with which the conditions of actual accidents exceed the test conditions has not been well established. In particular, the realism of the test conditions with regard to such things as sequential impacts, the reliability of impact limiters, and the durations of fires is not well known for all cask designs. A detailed study of accident modes, event sequences, and damage frequencies has only been performed for one type of cask design. This study was performed recently for the NRC by Lawrence Livermore National Laboratory (LLNL), using a conventional stainless steel shell, lead-shielded, cask design.[2] The LLNL study found that in about one rail or truck accident in every 40 million shipment miles (or once every 13 years, assuming 3 million shipment miles per year) minor functional cask damage would be expected. In about one accident every 80 million shipment miles (or once every 27 years) cask damage would be significant enough to cause a radiological hazard that could equal or slightly exceed existing compliance values (i.e., cask damage would

---

*Because of common usage and pertinent regulatory guides, metric units will not be used in this chapter.

exceed that caused by the specified simplified test conditions).[3] These findings pertain only to lead-stainless steel casks and, therefore, do not consider the effect on radiological hazards of a cask being subject to the risk of brittle fracture. This additional effect must be determined for NCI and forged steel casks.

Examples of rail accidents involving conditions some, but not all of which, exceed those used for regulatory drop and fire tests have occurred recently. In July 1986, 16 cars of a train loaded with hazardous chemicals were blown off a railroad bridge by extremely high winds and fell 108 ft into the Des Moines River near Boone, Iowa. Figure 12.1 shows the results. More than 200 teenagers were evacuated from a summer camp because of the chemicals spilled into the river.[4] The regulatory drop test for a cask is a 30-ft drop onto a "flat, horizontal, unyielding surface."[3] The bottom of the Des Moines River is probably not as hard as the regulatory drop base, but the fall distance far exceeded 30 ft. Less than 6 months later, in December 1986, a nearly empty Japanese excursion train was blown off a 135-ft-high bridge by high winds, 300 miles west of Tokyo. The train fell onto a crabmeat processing factory below, killing six people and injuring six more.[5] Evidently falls from heights exceeding 30 ft cannot be classified as extremely rare events. Consequently, the mass and hardness of targets beneath high bridges must be estimated carefully because these statistical estimates could strongly influence the outcome of hazard studies. Especially important is the hardness of shallow river bottoms, considering the fact that, geologically, rivers tend to erode down to highly resistant base levels and that the associated formations also provide good foundations for bridge abutments.

The regulatory fire test, which follows the impact tests, requires a 30-min total flame engulfment at a temperature of 1475°F (Ref. 3). Once again, the specified fire duration is by no means an upper limit. In July 1987, at least 25 train cars, including three tankers carrying methyl alcohol, derailed in Erwin, Tennessee, 75 miles east of Knoxville near the North Carolina border. Figure 12.2 shows the results.[6] One of the tankers caught fire and burned for 4 1/2 h; flame temperatures were not reported. The possible proximity of casks to other vehicles carrying flammable chemicals is an important consideration in cask safety analysis.

12.3 BAM Workshop and Seminar and Related Visits in the FRG

In June 1987, a fact-finding team composed of J. G. Merkle of ORNL, H. J. Cialone of Battelle Columbus Division (BCD), and C. Z. Serpan of the NRC traveled to the FRG to gather information needed for assessing the safety of NCI spent-fuel shipping casks. The itinerary was planned around a workshop and seminar organized by and held at the Bundesanstalt für Materialprufung (BAM) in Berlin, FRG, on June 9–10, 1987. Participation of HSST Program personnel in this activity was specifically requested by the NRC. Subsequent site visits were made to the offices and shops of the primary vendor (GNS), a casting foundry (Siempelkamp), and a machine shop (KWU) involved in the design, fabrication, and marketing of NCI casks. Visits were also made to two laboratories in the FRG (MPA, Stuttgart and IWM, Freiburg) whose work is germane to the HSST Program.

ORNL PHOTO 0057-88

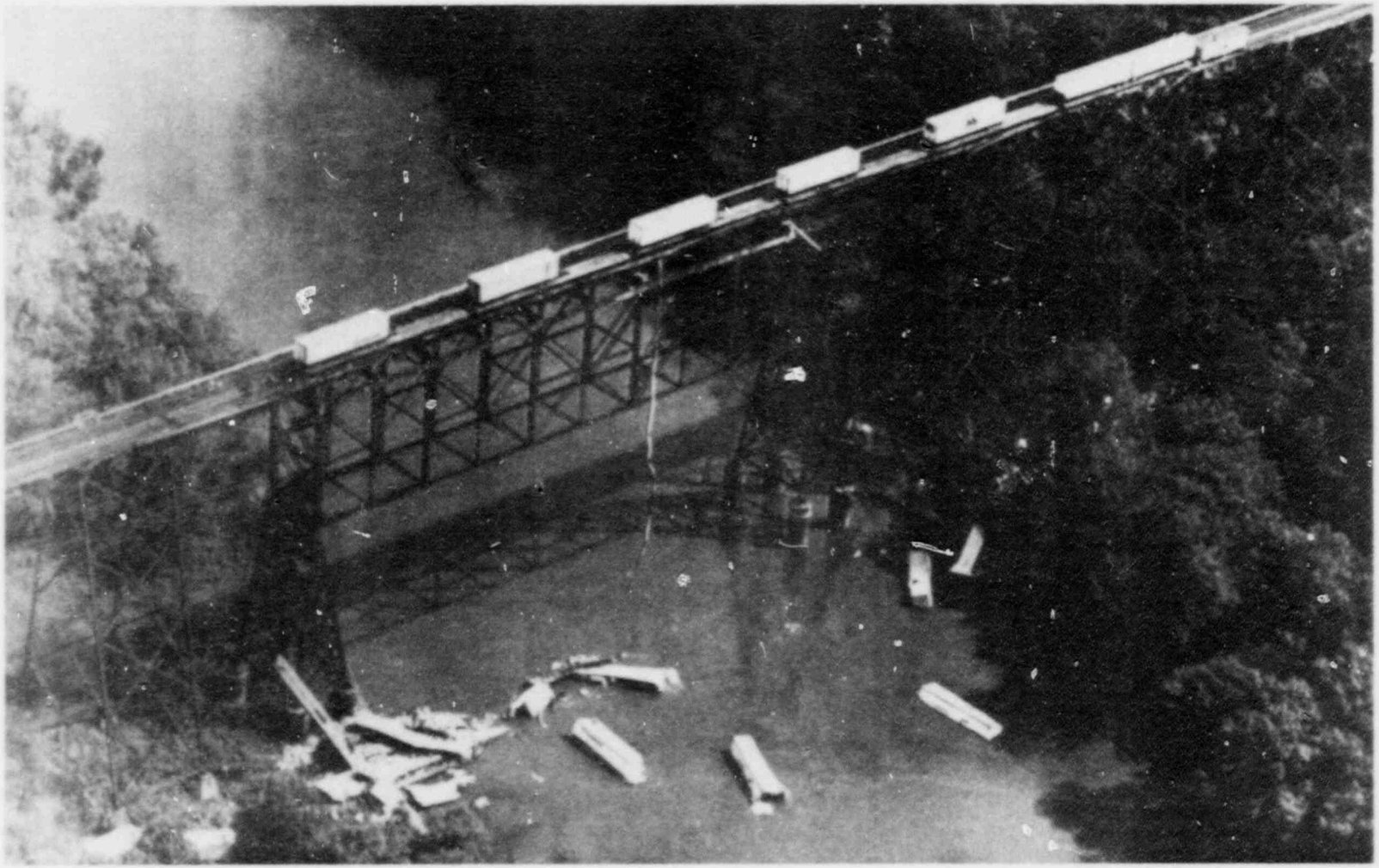

Fig. 12.1. Railcars loaded with hazardous chemicals blown by high winds off a 108-ft-high bridge into the Des Moines River near Boone, Iowa. *Source*: Associated Press photo by C. Neibergall, from the Knoxville News Sentinel, July 30, 1986.

ORNL PHOTO 0058-88

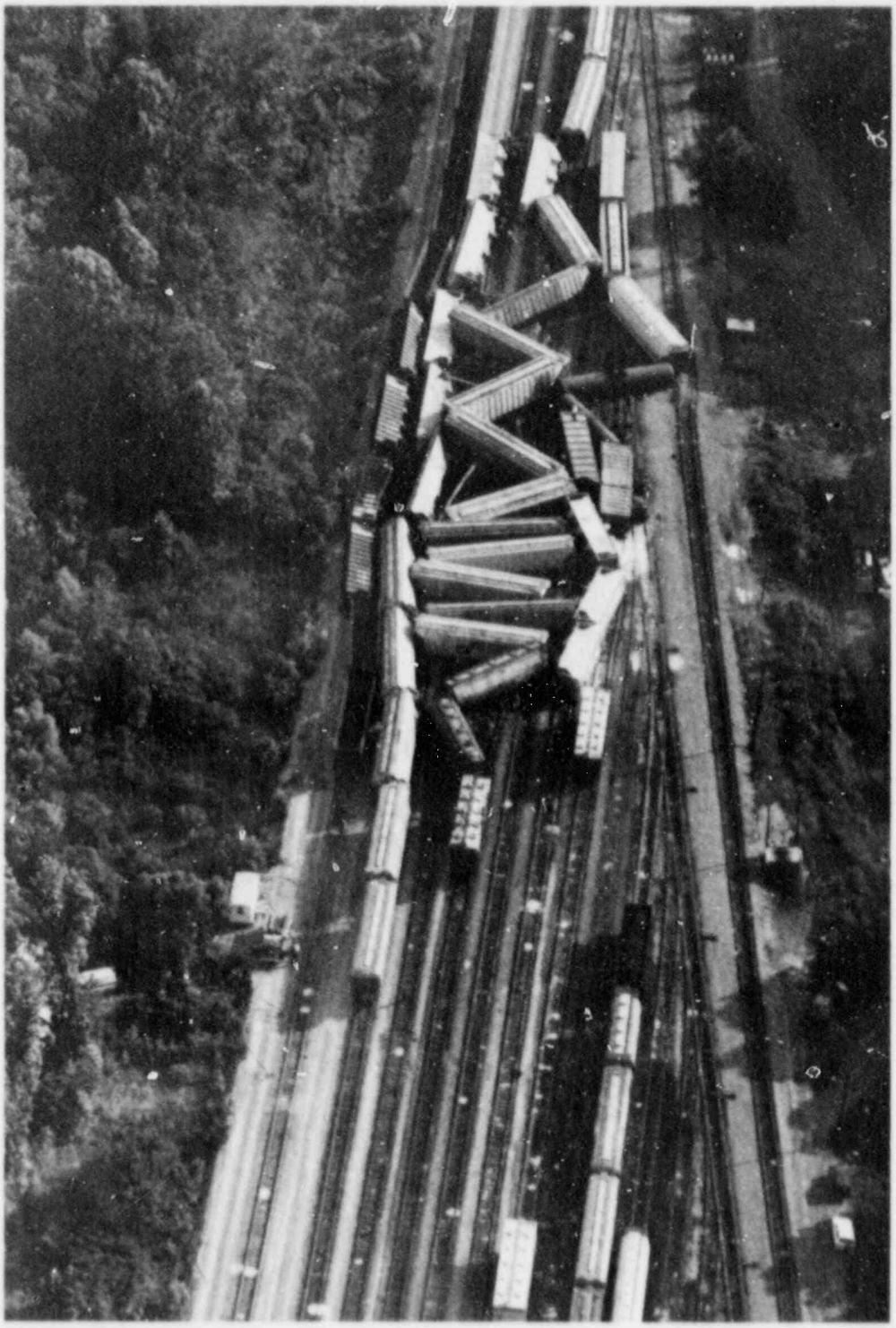

Fig. 12.2. Railcars after a derailment and fire near Erwin, Tennessee, on July 17, 1987. *Source*: Knoxville News Sentinel staff photograph by J. Miles Cary.

The primary observations of the team were as follows:

1. A great deal of progress appears to have been made during the past 5 years in developing improved nodular iron by control of chemical composition and solidification cooling rate from casting. However, while the resistance to crack initiation has been improved significantly, ductile iron still appears to have low resistance to crack propagation.
2. Many drop tests with casks have been performed under a wide range of conditions. In addition, extensive mechanical property testing has been conducted.
3. Despite the material-property improvements and extensive testing, there is still a lack of basic metallurgical and stress analysis information to explain how this material performs. Many of the tests that have been conducted were direct demonstrations of strength, but their results cannot necessarily be used to quantitatively determine safety margins with respect to flaw size, temperature, strain level, or fracture toughness.
4. The people at BAM and PTB believe in adhering closely to the prescribed rules for material testing. The problem in the present situation is that the current rules for cask validation and for material toughness testing are based largely on experience with wrought ferritic or stainless steels. For ductile iron the rules must be critically evaluated and may require modification.
5. A willingness to modify validation-test procedures by mutual agreement was expressed, both by BAM and GNS.

Both BAM and GNS have exerted a great deal of effort in improving the quality of the GNS shipping casks and in demonstrating their strength. Our overall impression of the week's tour is that NCI is probably a more ductile material than has been previously believed. Such a conclusion is clearly tentative, but also indicates the impression that we gained from a wide spectrum of sources: government research institutions (BAM and PTB), quasi-government research establishments (MPA-Stuttgart), private companies (KWU-Mulheim), plus the company GNS itself and Siempelkamp, its contractor foundry. A key feature is that cast iron simply does not behave exactly the same as steel, nor does cast iron completely fit the trends or follow the test methods developed for steel. Prima facie evidence of the apparent ductility and integrity of the NCI used for the proposed casks is the survival of casks in multiple drop tests under severe conditions.

A detailed foreign trip report has been issued.[7]

12.4 Crack-Arrest Toughness Data for NCI

A. R. Rosenfield

A preliminary experimental examination of the crack-arrest toughness of NCI was performed this reporting period at BCL. Within experimental uncertainty it appeared that the crack-arrest toughness of NCI was comparable to that of reactor pressure vessel steels over the limited range

of temperature examined (relative to the iron's transition temperature). See Sect. 5.6.1 for details.

12.5 Results of HSST Expert Panel Meeting

The first meeting of the HSST Expert Panel on Shipping Casks was held at ORNL on September 24–25, 1987. The purpose of the meeting was to consider the proposed use of NCI as a primary structural material for nuclear spent-fuel shipping casks. In preparation for the meeting, ORNL furnished the panel members with advance copies of a bibliography and a two-volume package of literature and documents concerning NCI and spent-fuel shipping casks.

The sensitivity of the mechanical properties of NCI to chemistry and microstructure was noted, and newly obtained crack-arrest toughness data for NCI, measured with duplex specimens by BCD, were studied with interest. On the basis of the information available, it was determined that NCI is qualified to be considered as a candidate primary structural material for spent-fuel shipping casks. However, the variability of properties that can occur within specified ranges of chemistry and processing conditions is substantial and must be more fully investigated. To make sound regulatory decisions, more information will be required concerning (1) the effects of strain rate and temperature on the cleavage fracture toughness; (2) the reliability of nondestructive testing; (3) chemistry and microstructural effects on toughness (especially the percentage of pearlite and graphite nodularity); (4) the random variability of flaw sizes, toughness, and accidental loads; (5) the calculated safety margins with and without impact limiters; and (6) the relative severity of presently specified full-scale test conditions.

The amount and type of material needed for the required experimental work was discussed. A large piece, ~90° × t × 4t (t = cask thickness) from a well-documented, typical cask is needed, as well as several full length by about 1-in.-diam neutron absorber hole cores. It will be important to have access to the large existing German data bank on materials properties of NCI to assess where our material resides within the entire population of castings used for shipping casks. Other axial and radial cores, plus samples from earlier casks, would be useful. Recommended testing includes Charpy V-notch, tensile, drop-weight (requires crack-starter development), static, dynamic, and crack-arrest fracture toughness, chemistry, microstructure, and nondestructive examination for flaw characterization and property estimation. Existing toughness data and the data to be obtained need to be examined to determine the presence or absence of specimen-size effects on the cleavage fracture toughness. An expanded analysis similar to the existing modal study (NUREG/CR-4829) will be conducted for an NCI cask design to determine the influence of brittle fracture variables on cask safety margins for NCI.

The panel believes that the work described above will provide a sound basis for regulatory decisions concerning the use of NCI for spent-fuel shipping casks. Written comments have been requested from the panel members to ensure that their advice is fully understood and utilized.

References

1. R. K. Nanstad and J. G. Merkle, "Shipping Cask Material Evaluations," pp. 234–38 in *Heavy-Section Steel Technology Program Semiann. Prog. Rep. October 1986–March 1987*, ORNL/TM-9593/V4&N1, August 1987.

2. L. E. Fischer et al., *Shipping Container Response to Severe Highway and Railway Accident Conditions*, NUREG/CR-4829, Vols. 1&2, Lawrence Livermore Natl. Lab., February 1987.

3. W. R. Lahs, *Transporting Spent Fuel; Protection Provided Against Severe Highway and Railroad Accidents*, NUREG/BR-011, U.S. Nuclear Regulatory Commission, March 1987.

4. "Derailed Train," *The Knoxville News Sentinel*, Knoxville, Tennessee, July 30, 1986.

5. "Wind Hits Train, Causes Fall from Bridge; 6 Killed," API Tokyo, printed in *The Knoxville News Sentinel*, Knoxville, Tennessee, December 29, 1986.

6. "Derailment Sparks Fire in Erwin," *The Knoxville News Sentinel*, Knoxville, Tennessee, July 18, 1987.

7. J. G. Merkle, H. J. Cialone, and C. Z. Serpan, Jr., *Report of Foreign Travel of J. G. Merkle, HSST Task Leader, Engineering Technology Division; H. J. Cialone (Battelle Columbus Division); and C. Z. Serpan, Jr. (U.S. Nuclear Regulatory Commission)*, ORNL/FTR-2568, Oak Ridge Natl. Lab., Martin Marietta Energy Systems, Inc., July 13, 1987.

CONVERSION FACTORS[a]

SI unit	English unit	Factor
mm	in.	0.0393701
cm	in.	0.393701
m	ft	3.28084
m/s	ft/s	3.28084
kN	lb_f	224.809
kPa	psi	0.145038
MPa	ksi	0.145038
$MPa\cdot\sqrt{m}$	$ksi\cdot\sqrt{in.}$	0.910048
J	ft·lb	0.737562
K	°F or °R	1.8
kJ/m^2	$in.\text{-}lb/in.^2$	5.71015
$W\cdot m^{-2}\cdot K^{-1}$	$Btu/h\cdot ft^2\cdot °F$	0.176110
kg	lb	2.20462
kg/m^3	$lb/in.^3$	3.61273×10^{-5}
mm/N	$in./lb_f$	0.175127
$T(°F) = 1.8\ T(°C) + 32$		

[a]Multiply SI quantity by given factor to obtain English quantity.

NUREG/CR-4219
Vol. 4, No. 2
ORNL/TM-9593/V4&N2
Dist. Category RF

Internal Distribution

1. D. J. Alexander
2. B. R. Bass
3. S. E. Bolt
4. R. H. Bryan
5. J. W. Bryson
6. R. D. Cheverton
7. J. M. Corum
8-9. W. R. Corwin
10. J. A. Getsi
11. R. C. Gwaltney
12. F. M. Haggag
13. S. K. Iskander
14. A. P. Malinauskas
15. J. G. Merkle
16-17. R. K. Nanstad
18. D. J. Naus
19. J. S. Parrott
20. N. Perrone
21-25. C. E. Pugh
26. G. C. Robinson
27. G. M. Slaughter
28. J. E. Smith
29. R. W. Swindeman
30. K. R. Thoms
31. H. E. Trammell
32. J. K. Walker
33. C. D. West
34. ORNL Patent Office
35. Central Research Library
36. Document Reference Section
37-38. Laboratory Records Department
39. Laboratory Records (RC)

External Distribution

40. C. Z. Serpan, Division of Engineering, Nuclear Regulatory Commission, Washington, DC 20555
41. M. Vagins, Division of Engineering, Nuclear Regulatory Commission, Washington, DC 20555
42. Michael F. Mayfield, Division of Engineering, Nuclear Regulatory Commission, Washington, DC 20555
43. J. R. Strosnider, Region I, Nuclear Regulatory Commission, 631 Park Avenue, King of Prussia, PA 19406
44. W. H. Bamford, Plant Engineering Division, Westinghouse Electric Corporation, Pittsburgh, PA 15230
45. R. A. Fields, Fracture and Deformation Division, National Bureau of Standards, Gaithersburg, MD 20899
46. W. L. Fourney, Department of Mechanical Engineering, University of Maryland, College Park, MD 20742
47. M. F. Kanninen, Engineering and Material Science Division, Southwest Research Institute, San Antonio, TX 78284
48. J. W. Hutchinson, Division of Applied Science, Pierce Hall, Harvard University, Cambridge, MA 02138
49. E. T. Wessel, P.O. Box 0788, Andover, OH 44003-0788
50. Office of Assistant Manager for Energy Research and Development, DOE, ORO, Oak Ridge, TN 37831
51-52. Office of Scientific and Technical Information, P.O. Box 62, Oak Ridge, TN 37831
53-302. Given distribution as shown in category RF (NTIS — 10)

NRC FORM 335 (2-84) NRCM 1102, 3201, 3202

U.S. NUCLEAR REGULATORY COMMISSION

BIBLIOGRAPHIC DATA SHEET

SEE INSTRUCTIONS ON THE REVERSE

1. REPORT NUMBER (Assigned by TIDC, add Vol No., if any)
NUREG/CR-4219, Vol. 4, No. 2
ORNL/TM-9593/V4&N2

2. TITLE AND SUBTITLE
Heavy-Section Steel Technology Program Semiannual Progress Report for April 1987 - September 1987

3. LEAVE BLANK

4. DATE REPORT COMPLETED
MONTH: March YEAR: 1988

5. AUTHOR(S)
W. R. Corwin

6. DATE REPORT ISSUED
MONTH: April YEAR: 1988

7. PERFORMING ORGANIZATION NAME AND MAILING ADDRESS (Include Zip Code)
Oak Ridge National Laboratory
P. O. Box X
Oak Ridge, TN 37831

8. PROJECT/TASK/WORK UNIT NUMBER

9. FIN OR GRANT NUMBER
B0119

10. SPONSORING ORGANIZATION NAME AND MAILING ADDRESS (Include Zip Code)
Division of Engineering
Office of Nuclear Regulatory Research
U. S. Nuclear Regulatory Commission
Washington, DC 20555

11a. TYPE OF REPORT
Semiannual

b. PERIOD COVERED (Inclusive dates)
April 1987 - September 1987

12. SUPPLEMENTARY NOTES

13. ABSTRACT (200 words or less)

The Heavy-Section Steel Technology (HSST) Program is an engineering research activity conducted by the Oak Ridge National Laboratory for the Nuclear Regulatory Commission. The Program comprises studies related to all areas of the technology of materials fabricated into thick-section primary-coolant containment systems of light-water-cooled nuclear power reactors. The investigation focuses on the behavior and structural integrity of steel pressure vessels continuing cracklike flaws. Current work is organized into twelve tasks: (1) program management, (2) fracture-methodology and analysis, (3) material characterization and properties, (4) environmentally assisted crack-growth studies, (5) crack-arrest technology, (6) irradiation effects studies, (7) cladding evaluations, (8) intermediate vessel tests and analysis, (9) thermal-shock technology, (10) pressurized thermal-shock technology, (11) Pressure Vessel Research Users' Facility, and (12) shipping-cask material evaluations.

14. DOCUMENT ANALYSIS - a. KEYWORDS/DESCRIPTORS

Pressure vessels
Ferritic steels
Weldments
Irradiation
Cladding
Flaws
Thermal shock
Fracture mechanics
Crack arrest
Crack growth

b. IDENTIFIERS/OPEN ENDED TERMS

15. AVAILABILITY STATEMENT
Unlimited

16. SECURITY CLASSIFICATION
(This page) Unclassified
(This report) Unclassified

17. NUMBER OF PAGES

18. PRICE

☆U.S. GOVERNMENT PRINTING OFFICE 1988—548-118/80005